

**Tribochemical investigation of micropitting in
rolling-element bearing applications: the influence of
lubricant additives and water contamination**

Siavash Soltanahmadi

Submitted in accordance with the requirements for the degree of

Doctor of philosophy

The University of Leeds

School of Mechanical Engineering

Leeds, UK

October 2017

II

The candidate confirms that the work submitted is his own, except where work which has formed part of jointly-authored publications has been included. The contribution of the candidate and the other authors to this work has been explicitly indicated below. The candidate confirms that appropriate credit has been given within the thesis where reference has been made to the work of others.

With regard to the papers contributing to this thesis, the candidate, first author, performed all the experiments and analyses of the data and prepared all the manuscripts. All other authors contributed to the discussion part of the manuscripts by providing insights and to the whole manuscripts by proof reading. The focused ion beam milling, transmission electron microscopy and EDX spectra collection in transmission electron microscopy were undertaken by Dr Michael Ward.

This copy has been supplied on the understanding that it is copyright material and that no quotation from the thesis may be published without proper acknowledgement.

© 2017 The University of Leeds and Siavash Soltanahmadi

Papers contributing to this thesis

1. Soltanahmadi S, Morina A, van Eijk MC, Nedelcu I, Neville A. Investigation of the effect of a diamine-based friction modifier on micropitting and the properties of tribofilms in rolling-sliding contacts. *Journal of Physics D: Applied Physics*. 2016;49(50):505302.
2. Soltanahmadi S, Morina A, van Eijk MCP, Nedelcu I, Neville A. Tribochemical study of micropitting in tribocorrosive lubricated contacts: The influence of water and relative humidity. *Tribol Int*. 2017 2017/03/01/;107:184-98.
3. Soltanahmadi S, Morina A, van Eijk MCP, Nedelcu I, Neville A. Experimental observation of zinc dialkyl dithiophosphate (ZDDP)-induced iron sulphide formation. *Applied Surface Science*. 2017 2017/08/31/;414:41-51.

Acknowledgments

I would like to express my deepest gratitude towards my primary academic supervisor, Professor Anne Neville, for her persistent support, technical advice, endless encouragement, calmness and especially for her continued positive attitude throughout the project. Also, I would like to thank her for providing me with the splendid opportunity to do this project. It has been a great pleasure meeting her and working in her group. I thank Professor Ardian Morina, my secondary supervisor, for his meticulous reviews of the manuscripts, presentations and thesis and for his guidance from start to finish.

I am grateful to Dr Ileana Nedelcu, my industrial supervisor, for all her valuable technical support and advice within the secondments in this project. Her prompt and diligent reviews of the manuscripts and presentations are greatly appreciated. I thank Dr Marcel van Eijk my meticulous industrial supervisor for his technical support who has contributed to this project through his probing and detailed questions.

Special thanks to Dr Victor Brizmer, Dr Guillermo Morales-Espejel, Dr Christine Matta, Dr Pascal Ehret, Mr Ralph Meeuwenoord, Mr Berry Peek and Mr. Elio Piras for being a wonderful host. They made the secondments in SKF truly joyful and fruitful. I am very grateful to Dr Michael Ward, Mr Adrian Eagles and Mr Stuart Micklethwaite for their extensive help. Dr Joke Speelman from AkzoNobel is gratefully acknowledged for providing this project with the amine-based additives. Many thanks to Fiona and Carol for their time and administrative support. I would also like to thank my friends, office mates and iFS members Uriel, Maksims, John, Vishal, Joe, Erfan, Ali G, Ali Alazmani, Mohammad, Frederick, Thibaut, Michael, Kim, Tayo, Kevin, Ogbemi, Bello, Mohsen, MacDonald, Farnaz, Siamak, Doris, Shahriar, Zahra, Mick, Andrew, Paul and Jordan.

The greatest gratitude to whom I have received the greatest love, motivation and support from my mother, Farideh Khoshtinat, my father, Ali Soltanahmadi, a lovely person with the most beautiful heart who is my beloved wife, Yasaman Maghzi, my sister, Solmaz, my brothers, Babak and Saman and finally my parents-in-law, Shirin Fallahzadeh and Hasan Maghzi. Maman, Yasaman, baba and Babak I would like to dedicate this work to you. Without you and your love, the completion of this thesis would not have been possible, boundless thanks for always being there for me.

Abstract

Bearings as a machine element are designed to facilitate relative motion. The expected life span for bearings in each application, depending on operation conditions, is different. Whilst numerous efforts have been focused on increasing the bearing life-time, over the last few decades, premature failures have been reported especially in automotive and wind turbine gearbox bearings e.g. hydrogen embrittlement and micropitting surface fatigue. Furthermore, Zinc Dialkyl Dithio-Phosphate (ZDDP) as an anti-wear additive, which is crucial to suppress destructive wear, accelerates micropitting. Moreover, water contamination is common in wind turbine gearboxes especially in off- and near-shore turbines which can further promote micropitting occurrence. Therefore, it is significantly important to understand the influence of ZDDP and water on micropitting and investigate the effect of low Sulphated Ash, Phosphorus and Sulphur (SAPS) additives capable of suppressing the micropitting-enhancing behaviour of ZDDP.

In this study a modified PCS instrument MicroPitting Rig (MPR) is utilised to perform micropitting experiments. The influence of ZDDP on micropitting is investigated over a range of different contact cycles and the tribochemical phenomena involved in the micropitting is addressed using X-ray Photoelectron Spectroscopy (XPS) and Energy-Dispersive X-ray (EDX) in a Transmission Electron Microscope (TEM). Employing white light interferometry a promising procedure for micropitting mapping is implemented in order to achieve a micropitting surface area in the wear scar. Experiments are undertaken in order to understand the impact of water as a contaminant on micropitting where ZDDP was used in the lubricant formulation. The influence of free and dissolved water on tribocorrosive micropitting is differentiated and clarified. A mechanistic understanding of effect of water and relative-humidity on micropitting is elucidated using XPS.

A range of organic Nitrogen-Containing-Additives (NCA) with a friction reduction capability is proposed to diminish the micropitting-enhancing behaviour of ZDDP and evaluated using MPR. The affinity of the functional group of NCAs, N, to ZDDP which brings about a delay in the tribofilm formation, their friction modification properties, changes in the tribofilm composition and being an additive with no SAPS content were the rationale behind employing NCAs in combination with ZDDP. The

tribofilm formation and frictional properties of the different lubricant formulations are examined using a mini traction machine (MTM-SLIM). To gain a full understanding of NCAs behaviours in combination with ZDDP, tribofilms are studied using XPS and EDX-TEM and atomic force microscopy.

The results in this study showed that interaction of ZDDP with the steel surface under severe rolling-sliding contacts is a profound factor to induce micropitting. While dissolved water increases micropitting nucleation and expands the nucleation across the wear scar, in free water condition micropitting appearance is suppressed due to a dominant action of mild wear. The chemical structure of NCAs significantly influences the tribological results. A careful selection of NCAs with a tailored concentration successfully reduces micropitting and protects the surface from wear simultaneously and thus NCAs are desirable additives in rolling-element bearing applications under certain conditions.

Table of Contents

Chapter 1 Introduction	- 1 -
1.2 Statement of motivation for research	- 1 -
1.3 Literature gaps, aims and objectives	- 3 -
1.4 Structure of thesis at a glance	- 4 -
Chapter 2 Background and relevant theory.....	- 6 -
2.1 Introduction to tribology	- 6 -
2.2 Friction	- 6 -
2.3 Wear	- 7 -
2.3.1 Fatigue wear	- 8 -
2.3.2 Corrosion assisted wear.....	- 9 -
2.3.3 Adhesive wear	- 9 -
2.3.4 Abrasive wear.....	- 10 -
2.3.5 Erosive wear.....	- 11 -
2.4 Lubrication	- 12 -
2.4.1 Hydrodynamic Lubrication (HL) regime	- 12 -
2.4.2 Elasto-Hydrodynamic Lubrication (EHL) regime	- 12 -
2.4.3 Boundary lubrication regime.....	- 13 -
2.4.4 Mixed lubrication regime	- 14 -
2.5 Lubricants and additives.....	- 16 -
2.5.1 Lubricants.....	- 16 -
2.5.2 Base oil.....	- 16 -
2.5.3 Synthetic base oil	- 17 -
2.5.4 Additives	- 18 -
2.6 Bearings.....	- 20 -
2.6.1 Bearing types.....	- 20 -
2.6.2 Bearing materials	- 24 -
2.6.3 Cage materials	- 27 -

2.7	Summary	- 27 -
Chapter 3 Literature review		- 29 -
3.1	Introduction	- 29 -
3.2	Rolling contact fatigue	- 29 -
3.2.1	Hydrogen embrittlement and white structure flaking	- 34 -
3.2.2	Hydrogen embrittlement mechanisms in bearing steels.....	- 35 -
3.3	Tribochemical influence of lubricant additives on fatigue and pitting life of the bearings	- 39 -
3.4	Micropitting.....	- 46 -
3.4.1	Micropitting mechanism from a metallurgical standpoint	- 48 -
3.4.2	Micropitting test rigs	- 51 -
3.5	Parameters influencing micropitting	- 53 -
3.5.1	Tribological, mechanical and physical parameters	- 53 -
3.5.2	Tribochemical parameters: the influence of lubricant additives	- 61 -
3.5.3	Interaction of ZDDP with the steel surface.....	- 72 -
3.5.4	The role of sulphur in the ZDDP interaction with the steel surfaces-	74
	-	
3.5.5	Influence of water and relative humidity as lubricant contamination....-	81 -
3.5.6	The influence of water contamination on the lubricant	- 84 -
3.5.7	The influence of water contamination on RCF and wear	- 86 -
3.5.8	Tribo-chemical influence of water in lubricant.....	- 89 -
3.5.9	The effect of water on micropitting	- 93 -
3.5.10	Micropitting and Friction Modifiers (FM).....	- 96 -
3.6	Summary	- 99 -
Chapter 4 Materials and methods.....		- 100 -
4.1	Experimental Methodology	- 100 -
4.1.1	Micropitting tests	- 100 -

4.1.2	MTM and friction tests.....	- 103 -
4.1.3	Lubricants.....	- 106 -
4.2	Surface Analysis.....	- 111 -
4.2.1	Wear scar observation.....	- 111 -
4.2.2	Scanning electron microscopy	- 112 -
4.2.3	Optical microscopy	- 112 -
4.2.4	X-ray photoelectron spectroscopy analysis.....	- 112 -
4.2.5	Transmission electron microscopy and energy-dispersive X-ray	- 113 -
4.2.6	Topographical/roughness analysis of the tribofilm.....	- 114 -
Chapter 5 Investigation of the ZDDP effect on the micropitting surface fatigue-		116 -
5.1	Introduction	- 116 -
5.2	Results	- 116 -
5.2.1	Friction and wear results of the surfaces lubricated with BO and BO + ZDDP	- 116 -
5.2.2	The effect of ZDDP on micropitting wear	- 121 -
5.2.3	The tribochemical investigation of the ZDDP tribofilms generated on the wear scars in micro-scale	- 128 -
5.2.4	Cross-sectional study of the micropitted roller	- 134 -
5.3	Summary	- 143 -
Chapter 6 The effect of water and humidity on micropitting wear.....		- 146 -
6.1	Introduction	- 146 -
6.2	Results	- 146 -
6.2.1	The effect of dissolved water on base oil performance.....	- 146 -
6.2.2	Micropitting results	- 148 -
6.2.3	Total wear volume results	- 159 -
6.2.4	Friction results.....	- 161 -
6.2.5	Tribochemistry in the presence of water in oil and humidity	- 162 -
6.3	Summary	- 168 -

Chapter 7 Nitrogen-containing additive as a friction modifier: effect of NCAs on the friction, rolling wear and tribofilm composition.....	- 170 -
7.1 Introduction	- 170 -
7.2 Results	- 170 -
7.2.1 Tribofilm thickness in SS configuration	- 171 -
7.2.2 Surface observation of disc specimens using SEM.....	- 173 -
7.2.3 Friction results in SS configuration.....	- 174 -
7.2.4 Tribofilm thickness in SR configuration.....	- 179 -
7.2.5 Friction results in SR configuration	- 182 -
7.2.6 Surface topography and wear in SR configuration	- 183 -
7.2.7 Tribochemistry of the tribofilm formation.....	- 185 -
7.3 Summary	- 190 -
Chapter 8 Nitrogen-containing-additive as a friction modifier: the effect of NCAs on micropitting	- 192 -
8.1 Introduction	- 192 -
8.2 Results	- 192 -
8.2.1 Friction results.....	- 192 -
8.2.2 Micropitting and wear results.....	- 193 -
8.2.3 Understanding the mechanism by which NCAs influence micropitting-	198 -
8.3 Summary	- 219 -
Chapter 9 Discussion	- 221 -
9.1 Overview of discussion	- 221 -
9.2 Understanding the micropitting evolution in severe rolling-sliding contacts lubricated with a ZDDP-containing oil from initiation to propagation.....	- 221 -
9.2.1 Micropitting and wear over contact cycles in the modified-MPR and the relevant tribochemical investigation	- 222 -
9.2.2 Iron sulphide formation on interface.....	- 224 -
9.2.3 Effect of the lubricant additive on surface cracks.....	- 227 -

9.2.4	Proposed mechanism for ZDDP-induced micropitting.....	- 230 -
9.3	Understanding the tribological and tribochemical influence of water as a lubricant contaminant on micropitting surface fatigue	- 233 -
9.3.1	The effect of dissolved water	- 233 -
9.3.2	The effect of free water	- 240 -
9.3.3	The micropitting mechanism in tribocorrosive environments	- 241 -
9.4	Mitigation of micropitting-enhancing behaviour of ZDDP by utilising NCAs	- 242 -
9.4.1	The influence of NCAs on the steel surface.....	- 242 -
9.4.2	The influence of NCAs in combination with ZDDP.....	- 246 -
9.4.3	The interactions between NCAs and ZDDP	- 247 -
9.4.4	NCAs and their delaying impact on ZDDP-tribofilm formation .	- 249 -
9.4.5	Interaction of NCAs with the (poly)phosphates in ZDDP-tribofilm	- 250 -
9.4.6	The impact of test parameters	- 251 -
9.4.7	The efficiency of NCAs in mitigating ZDDP-enhanced micropitting ...	- 253 -
Chapter 10	Conclusions and future work.....	- 257 -
10.1	Overarching conclusions.....	- 257 -
10.2	Future work.....	- 259 -
10.2.1	Identification of the chemical nature of the compounds inside the crack	- 259 -
10.2.2	Investigation of the mechanical properties and stability of the tribofilms	- 259 -
10.2.3	Understanding of localised reactions using advanced microscopy (TEM)	- 260 -
10.2.4	Assessing the influence of other NCAs on micropitting.....	- 260 -
10.2.5	Further elucidation of additive impact though quantifying the micropit depth	- 261 -

List of Figures

Figure 1-1. A generalized illustration of a typical wind turbine gearbox exhibiting the locations of the bearings suffer micropitting presented by a) S. Butterfield (3) and b) M. N. Kotzalas (3).....	- 2 -
Figure 2-1. Micropitting surface fatigue a) optical (18) b) electron microscopic micrographs (19).....	- 8 -
Figure 2-2. Schematic image of stress distribution in a point contact bearing assembly (22).....	- 9 -
Figure 2-3. Adhesive wear occurred on the inner ring of a bearing (24).....	- 10 -
Figure 2-4. Illustration of different types of two-body abrasion (12).....	- 11 -
Figure 2-5. a) Steady-state wear volume as a function of time or sliding distance b) transient rise in wear volume beyond a critical load or speed (28).....	- 12 -
Figure 2-6. Schematic illustrations of a) hydrodynamic lubrication and b) elastohydrodynamic lubrication (14).....	- 13 -
Figure 2-7. Schematic illustration of a) boundary and b) mixed lubrication regimes (14).....	- 15 -
Figure 2-8. Illustration of the modified Stribeck diagram (31).....	- 15 -
Figure 2-9. Illustrations of a) deep-grooved and b) double row self-aligning ball bearings (17).....	- 21 -
Figure 2-10. Schematic illustrations of a) angular contact single row b) double-row angular contact c) four-point ball bearings (17).....	- 22 -
Figure 2-11. Images of typical roller bearings a) single-row cylindrical, b) adjusted configuration of tapered, c) spherical and d) CARB (17).....	- 23 -
Figure 2-12. Comparison of a) heat generation and b) torque as a function of angular velocity of the inner ring in bearings having steel and silicon nitride balls (40) .	- 26 -
Figure 3-1. Scanning Electron Microscopy (SEM) image of a stinger of inclusions (43).....	- 30 -
Figure 3-2. Schematic illustration of surface crack initiation and propagation (46) ...	- 31 -

Figure 3-3. Stress history trend of a point below the surface in a Hertzian line contact (20).....	- 32 -
Figure 3-4. a) Formation of WEA induced by a microstructure change of that area b) crack initiation in WEA c) propagation of WEC and its progress to WSF (21)..	- 33 -
Figure 3-5. WEC induced by electric current (50).....	- 34 -
Figure 3-6. High voltage TEM cross-section images of fatigue crack tip. Left and right images show crack in helium and hydrogen environments respectively (57)	- 35 -
Figure 3-7. Optical micrograph of the crack tip of a strained sample at different hydrogen pressures (10 Pa, 0.7 Pa, vacuum) (60).....	- 36 -
Figure 3-8. a) Optical and b) SEM images of a butterfly and WEA originated from a void (62).....	- 37 -
Figure 3-9. SIM images of the a) circumferential and b) cross-section of hydrogen-charged 52100 steel on which cyclic torsion and static compressive loads are applied (59).....	- 37 -
Figure 3-10. Micrographs of WEC propagation pattern in a) martensitic b) bainitic c) case carburised steels (21).....	- 38 -
Figure 3-11. Schematic of WEA formation (21, 64-65). H and DER stands for atomic hydrogen and dark etching region respectively	- 39 -
Figure 3-12. Investigation of AW and EP influence on the fatigue life of gears using FZG gear tester at 100°C. Load stages 9 and 11 resemble Hertzian contact pressures of 1.52 and 1.86 GPa respectively (67).....	- 40 -
Figure 3-13. The influence of AW and EP additives and their concentrations on a) L_{10} fatigue life b) the depth of fatigue pits. The results are attained using a four ball tester and B1 is a mineral base oil (70).....	- 41 -
Figure 3-14. a) The influence of TCP AW additive on the fatigue lives of different bearing steels. SEM images of fatigue spalls on the surfaces of CSS steel lubricated b) without and c) with TCP in the lubricant formulation. Dioctyl-diphenyl amine and phenyl- α -naphthyl amine are antioxidants blended to a synthetic polyol ester at 1% concentration each for all the tests (72)	- 42 -
Figure 3-15. The influence of a commercial S-P EP additive at concentration of 5 wt% on fatigue life. The EP additive a) reduced L_{10} life by a factor of three in the Weibull	

statistical plots and b) enhanced the formation of multiple spalls and c) cracks accompanied with micropitting (19).....	- 43 -
Figure 3-16. Evaluation of EP influence on the bearing fatigue life. a) Weibull statistical plots for fatigue life and b) surface deterioration in the immersion test (73).....	- 44 -
Figure 3-17. Evaluation of Weibull statistical fatigue life of DPP additive (74).	- 45 -
Figure 3-18. Evaluation of the influence of different lubricant additives on the bearing fatigue lives in spherical roller bearing fatigue tests. a) the lubricant formulations used in the tests and b) Weibull statistical fatigue lives for the different lubricant formulations (76).....	- 46 -
Figure 3-19. Damage features in the roller element bearing components a) micropitting (24) b) micropitting and macropitting (81) c) spalling (24).....	- 47 -
Figure 3-20. Micropitting in gear teeth and corresponding SEM image (81).....	- 48 -
Figure 3-21. Crack initiation and growth along a) slip bands b) grain boundaries and c) interface of inclusion (80).....	- 48 -
Figure 3-22. Schematic illustration of the mechanism of micropitting incident in martensitic steels and hardness values associated with the different microstructures which occur with micropitting. a) Micropitting initiation and b) micropitting propagation (79).....	- 49 -
Figure 3-23. DER evolution over contact cycles (84).....	- 50 -
Figure 3-24. Hardness variation over depth after $\sim 165 \times 10^3$ revolutions and cross-sectional micrograph after 150×10^3 revolutions (85).....	- 50 -
Figure 3-25. Influence of lubricant entrapment inside the crack on crack and micropit propagation (44).....	- 51 -
Figure 3-26. Schematic illustration of wind turbine gearbox indicating bearing positions (2).....	- 52 -
Figure 3-27. a) PCS Instrument MPR (8), b) WAM micropitting test machine (91) and c) FZG gear test rig (7).....	- 52 -
Figure 3-28. Traction forces in the rolling-sliding contacts (12).....	- 54 -

- Figure 3-29. Traction curve measurement over different SRR under test conditions indicated inside the graph (82)..... - 55 -
- Figure 3-30. The effect of sliding distance on micropitting of rollers lubricated with PAO + ZDDP lubricant. a) Experiment under SRR of 0.5% after 7.2×10^6 contact cycles and b) experiment under SRR of 5% after 0.72×10^6 contact cycles (102). The optical images obtained from the work by Cen (102) do not have a scale bar. However, all images were taken using the same objective and magnification for a true comparison between the different test parameters - 56 -
- Figure 3-31. Micropitting performance of PAO + ZDDP lubricated surfaces of 52100 bearing-steel rollers after 72×10^4 contact cycles under different SRRs of a) 0.005, b) 0.02, c) 0.05 and d) 0.5 (102)..... - 57 -
- Figure 3-32. Micropitting performance of surfaces of 52100 bearing-steel rollers after 72×10^4 contact cycles lubricated with a commercial fully-formulated lubricant under different SRRs of a) 0.005, b) 0.02 and c) 0.05 (102)..... - 57 -
- Figure 3-33. Model prediction of the effect of SRR on micropitting area ratio A_p [%] (47)..... - 58 -
- Figure 3-34. The effect of surface finish and lubricant formulation on micropitting (8) (Where λ' is the ratio of the central film thickness to the centre-line average roughness of the ring)..... - 59 -
- Figure 3-35. The effect of surface roughness value on micropitting of surfaces having transverse surface finish and lubricated with PAO + ZDDP (1.3 wt%) (8) (Where λ' is the ratio of the central film thickness to the centre-line average roughness of the ring)..... - 60 -
- Figure 3-36. The effect of surface roughness treatment (superfinishing) on micropitting examined using a FZG gear tester based on test procedure described in "Test Procedure for the Investigation of Micropitting Capacity of Gear Lubricants," FVA Information Sheet 54/I-IV. a) Shows the micropitted area as a function of load stage and b and c) present the images from the baseline and superfinished gear teeth respectively (104)..... - 61 -
- Figure 3-37. SEM images taken from surfaces lubricated with different base oils after micropitting tests using a twin disc tester. a) Lubricant: mineral oil and material: 20MnCr5 carburised steel, b) lubricant: synthetic ester and material: 20MnCr5

- carburised steel, c) lubricant: synthetic ester and material: micro-alloyed Nb-added 20MnCr5 steel and d) lubricant: tall-oil based ester and material: micro-alloyed Nb-added 20MnCr5 steel (89)..... - 62 -
- Figure 3-38. Roller surfaces lubricated with lubricants containing 2% of ZDDP formulated using different base oils of a) PAO and b) ester under 2% of SRR and 20% of relative humidity after 72×10^4 contact cycles (102)..... - 63 -
- Figure 3-39. Bearing protection test using INA slow speed axial bearing tester using different lubricants with a mineral base-oil (5)..... - 63 -
- Figure 3-40. SEM images from gear surfaces lubricated with a) oil A5 and b) oil A3 which are specified in Table 3-2 (7) - 65 -
- Figure 3-41. The investigation of the effect of ZDDP on micropitting and the correlation between counterbody roughness variation and micropitting. The changes in a) wear depth and b) counterbody roughness with respect to the number of contact cycles (6)..... - 66 -
- Figure 3-42. The influence of ZDDP concentration on micropitting and sliding wear. a) Micropitting results from MPR at test temperature of 70°C and contact pressure of 1.71 GPa, counterbodies had longitudinal roughness with values of 0.5-0.52 and the base oil used was a mineral oil and b) pure sliding wear results obtained at 80°C (8)- 68 -
- Figure 3-43. The influence of MoDTC friction modifier on the micropitting-enhancing behaviour of ZDDP. The influence of MoDTC on a) micropitting b) counterbody roughness. Tests are carried out at temperature of 70°C and contact pressure of 1.71 GPa under SRR of 5.2%, counterbodies had longitudinal roughness with values of 0.53 ± 0.2 and the base oil used was a mineral oil base oil (92).. - 69 -
- Figure 3-44. Micropitting performance of PAO-based lubricants containing a) ZDDP at concentration of 2 wt% and b) molyvan at concentration of 5 wt% under 2% of SRR and 20% of relative humidity after 72×10^4 contact cycles (102)..... - 70 -
- Figure 3-45. Investigation of the lubricant additives impacts on fatigue life of 52100 steel under contact pressure of 3.2 GPa at 80°C and lambda ratio of 2.2 under a) pure rolling condition and b) SRR of 6.7%. c) SEM-EDX analyses of a FIB section prepared to investigate a crack on the dented disc. H B resembles the mineral base oil,

Htot is the mineral base oil + five additive and Hdet is the mineral base oil + anti-foam + detergent (106).....	- 71 -
Figure 3-46. Investigation of a) AW and b) EP activity of different metal (4-methylpentyl-2) dithiophosphates at concentration of 4 millatoms of P per 100 grams of oil for each additive using a four ball tester (123).....	- 73 -
Figure 3-47. EELS maps of a) Fe and b) S and c) EDS concentration of elements as a function of contact pressure collected from wear particles extracted from ZDDP-lubricated tribotests (118)	- 76 -
Figure 3-48. <i>In-situ</i> investigation of interaction of the ZDDP tribofilm with a and b) iron oxide and c and d) Fe surfaces in UHV conditions. a and c) tests were conducted under mild contact conditions and b and d) tests are conducted under severe contact conditions (107)	- 77 -
Figure 3-49. Schematic illustrations of ZDDP tribofilm structure suggested by a) Bell <i>et al.</i> (136) b) Smith and Bell (137), c) Martin, Grossiord and Le Mogne (127), d) Martin (122), e) Spikes (105) and f) Kim, Mourhatch and Aswath (121) (WC ball on steel cylinder under EP contact).....	- 79 -
Figure 3-50. SIMS depth profiling of ZDDP films a) outside (thermal film) and b) inside (tribofilm) of the wear track representing the ion intensities with white corresponding to high and black corresponding to low intensities (140)	- 80 -
Figure 3-51. The forms of water in oil (152)	- 82 -
Figure 3-52. Water saturation of oil as a function of temperature (153)	- 83 -
Figure 3-53. The correlation between water uptake by three different commercial gear oils and relative humidity at 38°C (155). The graphs are plotted using three-point data obtained at relative humidities of 20, 60 and 100 %	- 84 -
Figure 3-54. Bearing fatigue life in wind turbine gearbox as a function of water content in oil (23).....	- 85 -
Figure 3-55. Influence of water on oil oxidation (23).....	- 86 -
Figure 3-56. Influence of water on wear and wear track profile of ball surfaces tested using four ball machine (159)	- 87 -
Figure 3-57. The impact of water and relative humidity on sliding wear coefficient (148).....	- 88 -

Figure 3-58. Investigation of the influence of water which is added to the lubricant at different concentrations of a) 0 wt%, b) 0.5 wt%, c) 1 wt% and d) 2 wt% on RCF testes using four ball machine (151)	- 89 -
Figure 3-59. Investigation of impact of water on decomposition of ZDDP and surface film composition at 177°C (163)	- 90 -
Figure 3-60. ZDDP-tribofilm evolution over time from PAO + ZDDP and PAO + ZDDP + 2wt% water lubricants. a) Presents the tribofilm thickness obtained from XPS etching and b) exhibits the corresponding phosphate peak (P 2p _{3/2} peaks in the XPS spectra) binding energy (151)	- 92 -
Figure 3-61. a) Investigation of water effect on micropitting under different SRRs of 0.5, 2, 5 and 50% and b) SEM image from surface under SRR of 50% and RH of 20% (102)	- 94 -
Figure 3-62. Optical micrographs taken from roller surfaces after tests with PAO + OFM, PAO + EP, and PAO + AW. The larger images represent the surface against the rougher disc (0.4 μm) and the miniature images correspond to the roller against the smoother disc (0.1 μm) (9)	- 97 -
Figure 4-1. Schematic illustration of the MPR rig with the humidifier assemblies.....	101 -
Figure 4-2. Schematic illustration of PCS Instruments MTM-SLIM	- 104 -
Figure 4-3. Illustration of micropitted surface-area measurement using multiple region analysis	- 111 -
Figure 4-4. Bruker's (Dimension Icon) AFM in tapping mode (190)	- 115 -
Figure 5-1. a) Wear and friction results and b) optical micrographs of the wear scars lubricated with BO and BO + ZDDP	- 117 -
Figure 5-2. The WLI images of the wear scars and corresponding depth profiles on the roller surfaces lubricated with a) BO and b) BO + ZDDP. R and M are the profile cursors which are placed at the wear track edges	- 118 -
Figure 5-3. Friction coefficient in the contacts lubricated with BO and BO + ZDDP	119 -

Figure 5-4. SEM images of BO + ZDDP lubricated wear scars undergone 10^6 contact cycles a) before and b) after tribofilm removal. *Red arrows on the images show the rolling-sliding direction.....	- 120 -
Figure 5-5. Optical microscopy images from roller surfaces after a) 62.5K, b) 250K, c) 500K and d) 1M contact cycles.....	- 122 -
Figure 5-6. WLI 3D profile and roller image of the MPR rollers following complete removal of the tribofilm over different contact cycles of a) 62.5K, b) 250K, c) 500K and d) 1M.....	- 123 -
Figure 5-7. a) WLI wear scar profiles, b) representative surface line-profiles of the shown WLI images, c) roughness (R_q) and skewness (R_{sk}) values for the line profiles of the MPR rollers undergone 62.5 K, 250 K, 500 K and 1 M contact cycles, respectively	- 125 -
Figure 5-8. Micropitting maps and surface areas in the wear scars shown in Figure 5-7 generated using MR analysis after contact cycles of a) 62.5K, b) 250K, c) 500K and d) 1M.....	- 126 -
Figure 5-9. Total wear volume and micropitted surface area over different contact cycles.....	- 127 -
Figure 5-10. XPS detailed spectra of the ZDDP-tribofilm elements in the wear scar after 250K contact cycles showing a) O 1s, b) P 2p and Zn 3s, c) Fe 2p and d) S 2p signals.....	- 129 -
Figure 5-11. EDX spectra from ZDDP-tribofilm in different areas of the wear scar having different characteristics	- 133 -
Figure 5-12. Micrographs of wear track cross-section which is prepared transverse to the rolling-sliding direction.....	- 135 -
Figure 5-13. a-d) SEM images of the roller cross-section undergone 10^6 contact cycles lubricated with BO + ZDDP and e) corresponding EDX spectra of the inclusions.....	- 136 -
Figure 5-14. EDX elemental mapping of the tribofilm from FIB sample showing K edge maps of a) merged Fe and S, b) Zn , c) Fe , d) S , e) P and f) O	- 138 -
Figure 5-15. EDX spectra and atomic concentration ratio of the tribofilm elements at a) top layer and b) middle layer	- 139 -

- Figure 5-16. EDX elemental mapping of the tribofilm from FIB sample in the cracked zone showing K edge maps of a) merged Fe and S, b) Fe , c) S , d) P , e) Zn, f) merged Fe and P, g) merged Fe and Zn, h) O and i) merged Fe and O - 142 -
- Figure 6-1. The effect of relative-humidities on the PAO-base oil performance. a) wear results, b) friction results and c) wear profile of a surface under 90% humidity - 147 -
- Figure 6-2. Wear scar and MR profile, corresponding wear scar depth profiles and average micropitted surface area of the roller surfaces lubricated with a, c, e) BO + ZDDP and b, d, f) BO + ZDDP + 1% Water at 90°C. Abrasive marks.. - 149 -
- Figure 6-3. Wear scar and MR profile, corresponding wear scar depth profiles and average micropitted surface area of the roller surfaces lubricated with a, c, e) BO + ZDDP and b, d, f) BO + ZDDP + 1% Water at 75°C. Abrasive marks.... - 150 -
- Figure 6-4. SEM images of the roller surfaces lubricated with a) BO + ZDDP and b) BO + ZDDP + 1% Water at 75°C - 151 -
- Figure 6-5. Optical images of the wear scars lubricated with a) BO + ZDDP and b) BO + ZDDP (RH 90%) - 152 -
- Figure 6-6. Wear scar and MR profile, corresponding wear scar depth profiles and average micropitted surface area of the roller surfaces lubricated with a, c, e) BO + ZDDP (RH 60%) and b, d ,f) BO + ZDDP (RH 90%) at 75°C. Abrasive marks - 153 -
- Figure 6-7. SEM images of the roller wear scars lubricated with a) BO + ZDDP and b) BO + ZDDP (RH 60%) at 75°C - 154 -
- Figure 6-8. a) Water saturation level measured by Hydac contamination sensor and b) water concentration of the oils after the tests measured by Karl Fischer..... - 155 -
- Figure 6-9. SEM images of the micropits appear on the wear scars lubricated with a) BO + ZDDP (RH 60%) and b) BO + ZDDP + 1% Water - 156 -
- Figure 6-10. Optical images of the wear scars on the rollers after a) 62.5×10^3 and b) 1×10^6 contact cycles. Abrasive marks - 157 -
- Figure 6-11. a) Wear scar profile, b) MR profile, c) corresponding wear scar depth profiles and d) average micropitted surface area of the roller surfaces lubricated with BO + ZDDP +3% Water at 75°C. Abrasive marks..... - 158 -

Figure 6-12. Average micropitted surface area and water saturation level in oil at the end of the test in different test conditions	- 159 -
Figure 6-13. Total wear volume (material loss) in the wear scars in different test conditions and lubricants (at 75°C).....	- 160 -
Figure 6-14. Friction coefficient in the contacts lubricated in different test conditions	- 161 -
Figure 6-15. XPS detailed spectra of the ZDDP-tribofilm elements in the wear scar of the roller lubricated with BO + ZDDP (RH 60%) showing a) C 1s, b) O 1s, c) P2p and Zn 3s, d) Fe 2p, e) S 2p and f) Zn L ₃ M _{4,5} M _{4,5}	- 162 -
Figure 6-16. Sputter depth profile of the tribofilms in the wear scars lubricated with a) BO + ZDDP in laboratory conditions, b) BO + ZDDP (RH 60%), c) BO + ZDDP + 1% water in laboratory conditions and d) BO + ZDDP (RH 90%) lubricants at 75°C -	168 -
Figure 7-1. Images of oil solutions of ETDP in a) PAO, b) a fully-formulated and c) a synthetic ester	- 171 -
Figure 7-2. Tribofilm evolution over rubbing-time in the three lubricant formulations. Experiments are conducted in conditions associated with SS configuration. The circular contact zones in the interference images are 280 μm in diameter as represented in the first image of BO + ZDDP + TDP (1%) lubricated ball surface	- 171 -
Figure 7-3. Tribofilm thickness of different lubricant formulation over rubbing intervals *Error bars in the plot represent the minimum and maximum tribofilm thickness detected on the MTM balls.	- 172 -
Figure 7-4. SEM and EDX analysis on the wear scar of the disc specimen lubricated with BO + ZDDP in SS configuration	- 173 -
Figure 7-5. SEM and EDX analysis on the wear scar of the disc specimen lubricated with BO + ZDDP + TDP (0.5%) in SS configuration	- 174 -
Figure 7-6. Friction coefficient of different lubricant formulations over rubbing steps	- 175 -

Figure 7-7. Stribeck diagrams measured after certain rubbing intervals for a) BO, b) BO + ZDDP, c) BO + ZDDP + TDP (0.5%), d) BO + ZDDP + TDP (1%), e) BO + ZDDP + TA (1%) and f) BO + ZDDP + ETA (1%) lubricant formulations - 177 -

Figure 7-8. Tribofilm thickness from different lubricant formulations over rubbing intervals *Error bars in the plot represent the minimum and maximum tribofilm thickness detected on the MTM balls - 180 -

Figure 7-9. Tribofilm evolution in different lubricant formulations over 4-hours of rubbing. Experiments are conducted in conditions associated with SR configuration. The circular contact zones in the interference images are 280 μm in diameter as represented in the first image of BO + ZDDP + ETA (0.5%) lubricated ball surface. - 181 -

Figure 7-10. Friction coefficient in different lubricant formulations over 4 hours of rubbing - 182 -

Figure 7-11. Stribeck diagrams measured at the start of the tests and after 4 hours of rubbing for a) BO + ZDDP, b) BO + ZDDP + TDP (0.5%), c) BO + ZDDP + TA (0.5%) and d) BO + ZDDP + ETA (0.5%) lubricant formulations..... - 183 -

Figure 7-12. WLI-profiles taken from a) outside and b) inside the wear-scar collected from the disc lubricated with BO + ZDDP + ETA (0.5%) - 184 -

Figure 7-13. The ball-surface images after tests lubricated with a) BO + ZDDP and b,c) BO + ZDDP + ETA - 185 -

Figure 7-14. Detailed XPS spectra showing a) C 1s, b) three minor contributions to the C signal c) O 1s, d) P 2p and Zn 3s, e) S 2p, f) Zn $L_{3M_{4,5}M_{4,5}}$ and g) N 1s signals. The spectra collected from MTM balls in SR configuration lubricated with BO + ZDDP (top-plotted in red) and BO + ZDDP + TDP (0.5%) (bottom-plotted in green) lubricant formulations. N 1s signal appeared in the spectrum from BO + ZDDP + TDP (0.5%)..... - 186 -

Figure 8-1. Friction coefficient results for different lubricant formulations presented a) over the test duration and b) as average friction values within the last 30 minutes of the tests - 193 -

Figure 8-2. WLI and optical microscope images of the roller surfaces lubricated with a) BO + ZDDP, b) BO + ZDDP + TDP (0.5%) and c) BO + ZDDP + TDP (1%) lubricant formulations - 194 -

Figure 8-3. WLI and optical microscopic images of the roller surfaces lubricated with a) BO + ZDDP + TA (1%) and b) BO + ZDDP + ETA (1%) lubricant formulations. - 195 -

Figure 8-4. WLI images, micropitting surface area and wear scar cross-sectional depth profile of the wear scars on the roller surfaces lubricated with a) BO + ZDDP, b) BO + ZDDP + TDP (0.5%) and c) BO + ZDDP + TDP (1%) lubricant formulations- 196 -

Figure 8-5. WLI images, micropitting surface area and wear scar cross-sectional depth profile of the wear scars on the roller surfaces lubricated with a) BO + ZDDP + TA (1%) and b) BO + ZDDP + ETA (1%) lubricant formulations..... - 197 -

Figure 8-6. Total wear-volume on the roller surfaces lubricated with different lubricant formulations - 198 -

Figure 8-7. Wear scar WLI profiles of the rollers lubricated with a) BO + TDP (0.5%) and b) BO + TDP (1%) - 199 -

Figure 8-8. Optical microscopic images of the wear scar lubricated with BO + TDP (1%) * Arrows show the rolling-sliding direction on the surface..... - 200 -

Figure 8-9. Friction coefficient results for BO + TDP lubricant formulation.... - 201 -

Figure 8-10. AFM images and height profiles of the tribofilms induced after 15 minutes of rubbing in a &c) BO +ZDDP + TDP (0.5%) and b &d) BO + ZDDP lubricants. The height profiles obtained across the centre of the AFM images provided in (a) and (b)..... - 202 -

Figure 8-11. AFM images and height profiles of the tribofilms induced after 2 hours of rubbing in a &c) BO +ZDDP + TDP(0.5%) and b &d) BO + ZDDP lubricants. The height profiles obtained across the centre of the AFM images provided in (a) and (b) - 203 -

Figure 8-12. AFM images of the tribofilm induced after 2 hours of rubbing in a) BO +ZDDP + TDP(0.5%) and b) BO + ZDDP lubricants - 203 -

Figure 8-13. a) SLIM images showing the influence of TDP on the ZDDP tribofilm and b) the change in tribofilm thickness and friction over the test time - 205 -

Figure 8-14. TEM images and EDX mapping of the tribofilm showing K edge maps of a) merged Fe and O, b) merged Fe, O and Cr, c) Fe , d) O , e) Cr, f) Zn, g) P and h)

S from the tribofilm generated in the wear scar of MPR-roller lubricated with BO + ZDDP + TDP (1%).....	- 207 -
Figure 8-15. TEM images and EDX mapping of the tribofilm showing K edge maps of a) merged Fe and O, b) Fe, c) O, d) Al, e) Cr, f) P, g) S and h) Zn from the tribofilm generated in the wear scar of a roller lubricated with BO + ZDDP + TDP (1%) in the cracked-zone and i) L edge map of the protective Pt layer.....	- 209 -
Figure 8-16. SEM images of the tribofilm on the surface of rollers lubricated with a) BO + ZDDP and b) BO + ZDDP + TDP (1%)	- 210 -
Figure 8-17. SEM images of the tribofilm on the surface of a roller lubricated with BO + ZDDP + TDP (1%) obtained following tribofilm removal	- 211 -
Figure 8-18. Detailed XPS spectra showing a) O 1s, b) S 2p, c) N 1s and d) Fe 2p signals. The spectra collected from MPR rollers lubricated with BO + ZDDP (top-plotted in green) and BO + ZDDP + TDP (0.5%) (bottom-plotted in red) lubricant formulations. N 1s and Fe 2p signals appeared in the spectrum from BO + ZDDP + TDP (0.5%).....	- 212 -
Figure 8-19. Detailed XPS spectra showing a) Fe 2p, b) O 1s, c) P 2p and Zn 3s and d) C 1s signals. The spectra collected from MPR roller lubricated with BO + ZDDP + ETA (1%).....	- 214 -
Figure 8-20. Sputter depth profiles of the reaction layers on the surface of rollers lubricated with a) BO + ZDDP and b) BO + ZDDP + TDP (0.5%)	- 218 -
Figure 9-1. Micropitting evolution over contact cycles in the modified-MPR and the relevant tribochemical parameters	- 223 -
Figure 9-2. The influence of S and P concentrations in the reaction layers on the bearing fatigue lives (76). *Oil E is a lubricant formulated using a mineral oil base stock and consists of complex S-P additives. X_{cg} is the effective thickness of the reaction layer and C_s is the concentration of the corresponding element at the top surface	- 225 -
Figure 9-3. Enriched S concentration around the pitted area (114). a) SEM image of a worn surface under pure sliding b) S $K\alpha$ EDX map of the SEM image, c and d) Auger spectra collected from the pit (region a) and upper layer (region b) respectively after 90 min of argon ion sputtering	- 226 -

- Figure 9-4. A TEM image presenting the postulated behaviour of ZDDP-tribofilm in reducing the crack propagation by acting as a sticking plaster (106) - 229 -
- Figure 9-5. Schematic illustration of ZDDP-induced micropitting. a) illustration of features in schematics and corresponding compounds b) a ZDDP-tribofilm before crack initiation, c) a severe asperity-asperity contact and crack initiation, d) tribochemical change to the ZDDP-tribofilm and micropitting propagation..... - 232 -
- Figure 9-6. The effect of water on micropitting and relevant tribochemistry at 90°C - 234 -
- Figure 9-7. The effect of water and humid environments on micropitting and relevant tribochemistry at 75°C - 236 -
- Figure 9-8. Hydrolysis investigation of a) normal and b) basic forms of zinc di-isopropyl dithiophosphates using nuclear magnetic resonance spectroscopy in 1,2-dimethoxyethane solvent at 85°C in the presence of 6 vol% water (254) - 238 -
- Figure 9-9. The influence of boundary lubrication friction and wear on micropitting after 720K contact cycles. The model is run for contact pressure of 1.5 GPa, $\lambda = 0.15$, lubricant temperature of 75°C and the counterbody roughness of $R_q = 500$ nm. The solid lines and the dots represent the results of the model and the experiments, respectively. μ_{bl} stands for boundary friction and the model yielded a fraction of boundary-lubricated area of 0.14 for the given λ .(18) - 240 -
- Figure 9-10. Immediate elimination of the initiated micropits by mild-wear in free water conditions - 241 -
- Figure 9-11. Schematic illustration of OFM interactions with metal surfaces. a) Multilayer (260) b) suggested bonds in OFM adsorption process (261) - 243 -
- Figure 9-12. Schematic illustrations of proposed adsorption patterns of hexadecylamine on iron oxide surface a) (231) b) (264) - 244 -
- Figure 9-13. Illustration of cis and trans isomers of fatty acids with the same chemical formula. a) structure of oleic acid and the kink induced by cis bonding and b) the trans isomer of oleic acid (elaidic acid) (269) - 245 -
- Figure 9-14. Stribeck curves in base oil + OFMs and MoDTC measured a) at the start of the test and b) after two hours of rubbing under a contact pressure of 0.95 GPa, SRR of 50% and an entrainment speed of 100 mm/s at 100°C (171)..... - 246 -

- Figure 9-15. Stribeck curves measured a) at the start of the test and b) after two hours of rubbing in oil blends of OFMs and MoDTC friction modifiers blended to a ZDDP containing base oil. The tests were carried out under a contact pressure of 0.95 GPa, SRR of 50% and an entrainment speed of 100 mm/s at 100°C (171)..... - 247 -
- Figure 9-16. Illustration of the chemical states of N atoms in a) TA and b) TDP (274) - 247 -
- Figure 9-17. Metal complex formation in a and b) ZDDP + diamine solutions and c and d) ZDDP + amine/diamine solutions. Illustrations of a) chelate MC, b) bridge-type MC, c) 1:1 MC and d) 2:1 MC formation through interactions between amine/diamine and ZDDP (175) - 248 -
- Figure 9-18. The influence of sliding speed on frictional properties of a) linear amines blended to a base oil at concentration of 1wt% under mean contact pressure of approximately 3 MPa at 100°C (289) and b) 0.01 M stearylamine (saturated amine) and oleyl amine (unsaturated amine) in hexadecane under mean Hertzian contact pressure of 0.69 GPa (270)..... - 253 -
- Figure 9-19. Schematic illustrations of the tribofilms formed on the surfaces of the MPR rollers lubricated with a) PAO + ZDDP b) BO + ZDDP + TDP/TA - 254 -

List of Tables

Table 2-1. Mechanical properties of some PVD coatings (25).....	- 10 -
Table 2-2. Molecular structure of different types of mineral oils (28, 30, 33)	- 16 -
Table 2-3. Mechanical and thermal properties of silicon nitride with respect to M-50 bearing steel (40).....	- 27 -
Table 3-1. Chemical composition of additives used in the report by O'Connor (7)-	64
-	
Table 3-2. Wear and micropitting performance of different lubricants formulated with additives indicated in Table 3-1 (7)	- 64 -
Table 3-3. Wind turbine gearbox failures induced by water contamination (23) -	85 -
Table 4-1. MPR test materials and parameters	- 102 -
Table 4-2. Experimental set up of MTM (smooth ball - smooth disc) tests	- 105 -
Table 4-3. Experimental set up of MTM (smooth ball – rough disc) tests	- 106 -
Table 4-4. Molecular structure of the investigated NCAs	- 108 -
Table 4-5. Chain length distribution and degree of unsaturation of tallow (185)-	109
-	
Table 4-6. Lubricant formulation table	- 110 -
Table 4-7. Lubricant formulation matrix	- 110 -
Table 4-8. Experimental setup for topographical AFM analysis	- 115 -
Table 5-1. Binding energy values of the elements/compounds in the tribofilm and atomic concentration of the Zn, S and O normalised to P after different amounts of contact cycles	- 131 -
Table 5-2. Elemental composition of inclusions highlighted in Figure 5-13.....	- 137 -
Table 5-3. Atomic concentration ratio of the ZDDP elements at the a) crack mouth, b) middle of the crack and c) crack tip.....	- 143 -
Table 6-1. Binding energy values of the elements/compounds of the tribofilm and atomic concentration of the Zn, S and O normalised to P	- 163 -

Table 6-2. Binding energy values of the elements/compounds of the tribofilm and atomic concentration of the Zn, S and O normalised to P	- 165 -
Table 7-1. Binding energy values of the elements/compounds of the tribofilm.* The values indicated in the parentheses present the contribution of the corresponding compounds to the tribofilms in atomic percentage	- 188 -
Table 7-2. Parameters in the tribofilms and atomic concentration of the Zn, S, O, and N normalised to P	- 189 -
Table 8-1. Experimental parameters for understanding the TDP effect on the ZDDP-tribofilm	- 204 -
Table 8-2. Binding energy values of the elements/compounds in the tribofilms-	215 -
Table 8-3. Parameters and atomic concentration of the compounds/elements in the tribofilms	- 217 -
Table 9-1. The micropitting mechanisms proposed in the literature	- 230 -

Abbreviations

AES	Auger Electron Spectroscopy
-----	-----------------------------

AFM	Atomic Force Microscope
-----	-------------------------

AP	Amine Phosphate
----	-----------------

AW	Anti-Wear
----	-----------

BE	Binding Energy
----	----------------

BO	Base Oil
----	----------

BO	Bridging Oxygen
----	-----------------

DER	Dark Etching Region
-----	---------------------

DPP	Di-Phenyl Phosphonate
-----	-----------------------

EDX	Energy Dispersive X-ray analysis
-----	----------------------------------

EHL	Elasto-Hydrodynamic Lubrication
-----	---------------------------------

EP	Extreme Pressure
----	------------------

ETA	Ethoxylated (2) Tallowalkyl-Amine
-----	-----------------------------------

ETDP	Ethoxylated (3) N-Tallow-1,3-DiaminoPropane
------	---

FF	Fully Formulated
----	------------------

HE	Hydrogen Embrittlement
----	------------------------

HL	Hydrodynamic Lubrication
----	--------------------------

HSAB	Hard and Soft Acids and Bases
------	-------------------------------

MC	Metal Complex
----	---------------

MoDTC	Molybdenum Di-Thio-Carbamate
-------	------------------------------

MPR	MicroPitting Rig
-----	------------------

MR	Multiple Region analysis
----	--------------------------

MTM	Mini Traction Machine
-----	-----------------------

NCA	Nitrogen-Containing Additive
-----	------------------------------

OFM	Organic Friction Modifier
PAO	Poly Alpha Olefin
PDR	Plastically Deformed Region
RCF	Rolling Contact Fatigue
RH	Relative Humidity
SAPS	Sulphated Ash, Phosphorus and Sulphur
SCC	Stress Corrosion Cracking
SEM	Scanning Electron Microscopy
SIMS	Secondary Ion Mass Spectroscopy
SLIM	Spacer Layer Image Mapping
S-P	Sulphur-Phosphorus compounds/additives
SR	Smooth ball-Rough disc
SRR	Slide-to-Roll Ratio
SS	Smooth ball-Smooth disc
TA	Tallowalkyl-Amine
TAN	Total Acid Number
TCP	Tri-Cresyl Phosphate
TDP	N-Tallow-1,3-DiaminoPropane
TEM	Transmission Electron Microscopy
TOF-SIMS	Time-of-Flight-Secondary Ion Mass Spectroscopy
UHV	Ultra High Vacuum
VM	Viscosity Modifier
WEA	White Etching Area
WEC	White Etching Crack
WLI	White Light Interferometry
WSF	White Structure Flaking

XANES X-ray Absorption Near Edge Spectroscopy

XPS X-ray Photoelectron Spectroscopy

ZDDP Zinc Dialkyl Dithio-Phosphate

Symbols glossary

μ	Friction coefficient
μ_b	Dipole moment
Al	Aluminium
C	Carbon
Cr	Chromium
E'	Effective modulus of elasticity
Fe	Iron
H	Hydrogen
h_{\min}	Minimum lubricant film thickness
Hv	Vickers Hardness
N	Nitrogen
O	Oxygen
P	Phosphorus
P_{\max}	Maximum Hertzian Contact Pressure
R_x	Radius of curvature of specimen
S	Sulphur
U_e	Lubricant entrainment speed
Zn	Zinc
δ	Partial charge
η_0	Lubricant dynamic viscosity
λ	Lambda ratio
σ	Normal force
τ	Shear stress

Chapter 1

Introduction

1.2 Statement of motivation for research

Bearings as a machine element are designed to facilitate relative motion. The expected life span for bearings, depending on their operation conditions varies for each application. Whilst numerous efforts have been focused on increasing the bearing life-time over the last few decades considering the major growth on renewable energy, premature failures have been reported especially in automotive and wind turbine gearbox bearings e.g. white structure brittle flaking, micropitting surface fatigue and smearing. As a result of these unforeseen failure mechanisms, wind turbine gearboxes have yet to accomplish their design life expectancy of twenty years. These failure mechanism are not considered in the bearing life calculations since the mechanisms are not induced by point surface origin or inclusion associated fatigue (1). As stated by Musial, Butterfield and McNiff (2), the majority of wind turbine gearbox premature failures appear to initiate in the bearings, although most of the gearboxes are designed and developed considering the best bearing-design criteria (2). Micropitting profoundly deteriorates wind turbine reliability (3) especially affecting the planet and shaft bearings which are shown in Figure 1-1 (a). Micropitting of other bearings in wind turbines including main shaft bearing (4) and high speed intermediate shaft bearing, shown in Figure 1-1 (b), (2) also induce undesirable downtime.

Micropitting incidents, in general, involve microcrack initiation at the surface or at the area close to the surface where the lubricant film is not sufficiently thick to separate the asperities of the surfaces in contact. It is believed that widely varying loads, rapid accelerations and high vibration levels together with relatively small lubricant entrainment speeds promote micropitting (3). In these conditions, where solid-solid contacts prevalently occur, the surface reactive additives in the lubricant play a crucial role through forming interfacial films on the surfaces. Moreover, water contamination, which is common in wind turbine gearboxes especially in off- and near-shore turbines, is postulated to be a contributing factor (3). Therefore, investigation of the effects of lubricant additives and water contamination on

micropitting in order to achieve a comprehensive understanding with regard to additive action is essential. The influence of the oil additive package on micropitting has been discussed in several studies mostly addressing the tribological performance (5-8).

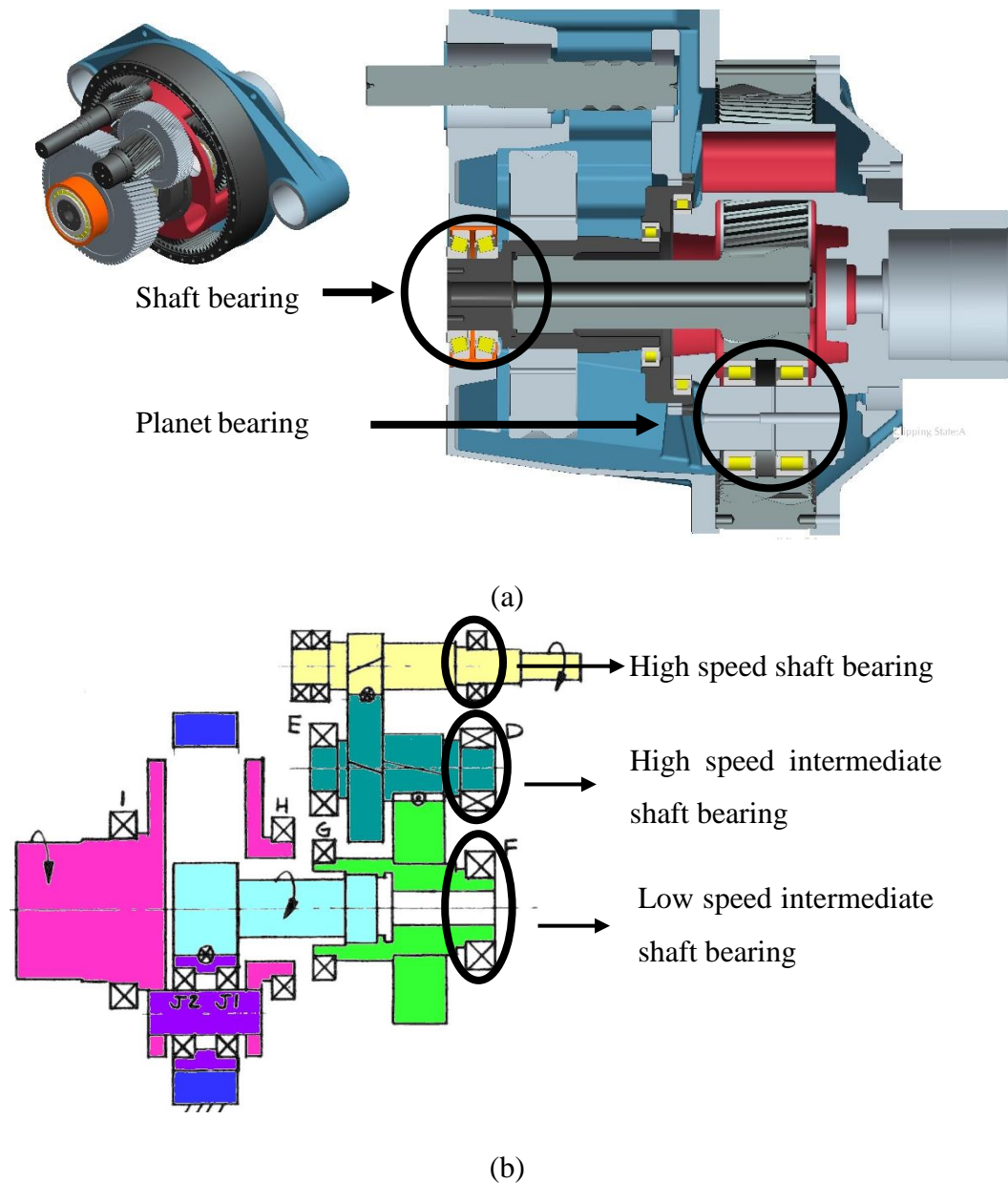


Figure 1-1. A generalized illustration of a typical wind turbine gearbox exhibiting the locations of the bearings suffer micropitting presented by a) S. Butterfield (3) and b) M. N. Kotzalas (3)

However, the literature shows that the mechanistic understanding with regard to tribochemical phenomena involved in micropitting is still lacking which makes it challenging to develop desirable additive packages to tackle micropitting. Therefore, further diligent and in detail studies are required to gain an exemplary and mechanistic

understanding of tribochemical phenomena involved in micropitting and to complement the tribological observations with tribochemical justifications.

1.3 Literature gaps, aims and objectives

At early stages of research, micropitting was investigated taking the mechanical and tribological factors into account. However, Brechot, Cardis and Murphy (5) were among the first researchers who observed and disclosed the tendency of Anti-Wear (AW) additives to accelerate micropitting revealing the important influence of tribochemistry. The micropitting-enhancing properties of Zinc Dialkyl Dithio-Phosphate (ZDDP) as an AW additive, which is crucial to mitigate the destructive wear, is experimentally verified by Benyajati and Olver (6). Following that Laine, Olver and Beveridge (8) examined the influence of varied experimental parameters on ZDDP-induced micropitting and attributed the ZDDP behaviour to its preventive effect on proper running-in wear of the rough counterbody. However, the running-in effect cannot justify firstly the enormous difference in micropitting wear of base oil and ZDDP-containing base oil and secondly, and more importantly, the influences of different additive packages and lubricant formulations observed by other researchers (7, 9). This specifies the impact of additive chemistry and indicates that different micropitting performances of different additives stem from tribochemistry involved in the contact. Therefore, the overall aim of this project is to comprehend the role of tribochemistry in ZDDP-induced micropitting. Accordingly, the goal of this work is to achieve a better understanding of tribochemical phenomena involved in micropitting at conditions relevant to the roller element bearings. In order to gain insights into the influences of water contamination and additive interactions on micropitting, it is important to attain a consensus that can clarify the mechanism of ZDDP-induced micropitting. The key objectives of the project are as follows:

- To identify the mechanism by which incipient micropitting initiates and propagates in tribological contacts lubricated with a ZDDP-containing oil employing surface analytical techniques
- To explore the chemical composition and elemental distribution of ZDDP tribofilm on top surface and throughout its depth and compare the findings with the available data in the literature
- To mechanistically understand the impact of water contamination on micropitting generated in a ZDDP-containing lubricated contacts. The influence of

Relative Humidity (RH) and dispersed water in lubricants at different concentrations will be discerned

- To examine the influence of four different types of Nitrogen-Containing-Additives (NCAs) based on an amine structure as Organic Friction Modifiers (OFMs) in combination with ZDDP on friction and wear performances in rolling-sliding contacts. The change in tribofilm thickness and composition induced by NCAs will be inspected using surface analytical techniques
- To evaluate the efficacy of NCAs in alleviating micropitting-enhancing properties of ZDDP and to comprehend the influence of NCAs on tribofilm formation and composition in order to correlate the tribological performance to tribochemical reactions. The results gained from friction tests in rolling-sliding contacts will be compared in relation to micropitting performance results in order to better understand the behaviour of amine-based OFM where it is blended into the lubricant in combination with ZDDP.

1.4 **Structure of thesis at a glance**

In Chapter 2 an introduction to the fundamentals of tribology, lubrication and wear mechanisms with respect to bearings is presented. Also, a section is dedicated to illustrate different types of roller element bearings used in industry and the materials utilised in the different segments of bearings. Chapter 3 provides a comprehensive review of literature on the roller bearing failure mechanisms with a focus on the impact of lubricant chemistry including base stock, additives and contamination (water). The substantial impact of tribochemistry on micropitting surface fatigue is elucidated in Chapter 3.

Chapter 4, clarifies the experimental set-up, sample preparation procedures and materials used throughout the project. The detailed specifications of the materials and specimens, lubricant and additives, tribological rigs and test procedures employed in the project are presented and justified in this chapter. Chapter 4 also delineates the post-experimental surface analysis techniques used to investigate the experimental parameters and specimens.

The first results chapter of the project is Chapter 5, in which the effect of ZDDP as an AW additive has been investigated on the micropitting wear. As there is a gap in the

literature on the tribochemical studies of the ZDDP effect on the micropitting, Chapter 5 examines the micropitting enhancing behaviour of ZDDP from initiation to propagation in relation to the tribofilm formation through conducting tests in four varied loading cycles.

After achieving an initial understanding of the tribochemical influence of ZDDP on micropitting, Chapter 6 explores the effect of water as a contamination on the micropitting wear. Numerous experiments are conducted in order to inspect the effects of two relative humidities and two varied concentrations of the distilled water on the tribological performance of the lubricant in terms of wear, friction and micropitting surface density. The changes in the tribofilm chemical composition and thickness have been delicately investigated in detail employing X-ray Photoelectron- Spectroscopy (XPS) surface analytical technique.

In order to tackle the micropitting-enhancing behaviour of the ZDDP a NCA capable of reducing micropitting and friction while protecting the surface from wear is introduced to the lubricant formulation. In Chapter 7 the tribological and tribochemical influences of NCA incorporation to the lubricant formulation have been evaluated using a Mini Traction Machine (MTM) and XPS. A topographical comparison of the tribofilms has been conducted employing Atomic Force Microscopy (AFM).

Chapter 8 details the beneficial effect of NCAs on micropitting reduction encountered on the rollers tested using a MicroPitting Rig (MPR) and lubricated with the different lubricant formulations obtained through blending different NCAs. The performances of the NCAs have been explored both in the presence and absence of ZDDP in order to elucidate the mechanism of action of NCAs. The wear volume and micropitting surface density measurements were performed using NPFLEX™ equipment. Comparisons of the tribofilm composition both on the very top layer and throughout its depth and the tribofilm thickness were made utilising Transmission Electron-Microscopy (TEM), Energy Dispersive X-ray (EDX) and XPS techniques.

Chapter 9 represents the overall discussion of the attained results in the project in order to reach all-embracing conclusions and advance the knowledge of tribochemical phenomena involved in micropitting. Tying together all the project findings, Chapter 10 lists the conclusions derived from this project. Also, some recommendations for future work are outlined in the final chapter.

Chapter 2

Background and relevant theory

2.1 Introduction to tribology

Amongst the developments in engineering, science and technology there is an extreme tendency to reach higher efficiency and lesser energy loss. As a result of this, a new multidisciplinary science was introduced in the late 1960s termed “Tribology”. Although the principles of tribology date back to 4000 BC the word is new. Tribology word is derived from Greek word *tribos* which means ‘rubbing’(10). As a technical field, tribology is a comprehensive scope which involves materials, mechanics, and chemical sciences. Tribology is well-defined as the science of interacting surfaces in relative motion of two components and related subjects (11). Three cornerstones of tribology are friction, wear and lubrication.

2.2 Friction

Friction is the resistance to motion encountered when one body moves tangentially over another (12). Although lubricated and smoother surfaces have less friction and traction forces, friction exists in any lubricated or dry, smooth or rough surfaces that are moving over each other. Apart from detrimental effects of friction in many applications such as engine and bearings, friction force is utilised desirably in specific applications such as brakes and clutches. Furthermore, it should be noted that very low friction in particular applications is not pleasant, for instance, if the friction coefficient is very low in large bearings, applying rapid acceleration during running-in results in high amounts of slip leading to the skid damage or surface distress damage on the surface of the bearing (13).

The simplest theory for friction coefficient is Amontons’ law (1699) which is based on the projected area (14). Based on the Amontons’ law, the friction force is proportional to the normal load between the contacting bodies. The coefficient of friction is defined by $\mu = \frac{F}{W}$ in which F is friction force and W is the applied normal load. The Amontons’ theory is established based on three laws (14):

- The tangential friction force is directly proportional to the normal load applied in sliding
- The friction force is independent of the projected contact area
- The friction force is independent of the sliding velocity

A more realistic theory called adhesion theory was announced by Bowden and Tabor in 1954, which is based on the idea of real contact pattern of two surfaces (14). They developed the theory based on the concept that contact is made up of lots of small asperities that generate atom to atom contact. According to adhesion theory: $\mu = \frac{S_0}{P_0}$ where S_0 is the shear stress and P_0 is material yield pressure. In ploughing theory $\mu = \frac{2 \tan \theta}{\pi}$ where θ is average asperity slope. Combining the adhesion and ploughing theories generates the composite theory for conical asperities (14): $\mu = \frac{S_0}{P_0} + \frac{2 \tan \theta}{\pi}$.

2.3 Wear

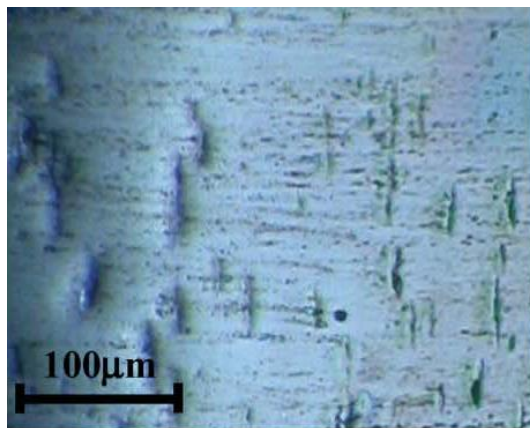
Wear is progressive damage in which material loss is involved and occurs on the surface of a body as a result of its motion over another (12). Hundreds of equations have been developed specifying certain materials and conditions; however the most well-known one is the Archard's equation (1953) which defines dimensionless wear coefficient (10) as $k = \frac{VH}{Wd}$ Where V is the wear volume (m^3), H is hardness of the material (Nm^{-2}), W is normal load (N), and d is the sliding distance (m).

In tribology, wear can be categorised into five main mechanisms (14), which are indicated below in order of importance for bearing applications from top to bottom:

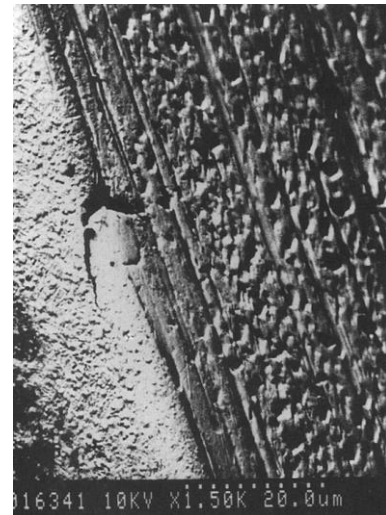
- Fatigue wear
- Corrosion-assisted wear
- Adhesive wear
- Abrasive wear
- Erosive wear

A prevalent wear mechanism and appearance happening in bearings and gears is called micropitting or surface distress (3) which is shown in Figure 2-1. Micropitting should not be confused with corrosion pitting. Micropitting is a surface fatigue mechanism happening on components lubricated under EHL or mixed/boundary regimes when the minimum lubricant film thickness (h_{min}) becomes thin leading to

solid-solid contacts of asperities (3). Asperity contacts under load impose localised elastic and plastic deformation of the surface which brings about surface fatigue (15). Due to the higher viscosity index of synthetic oils they provide better protection against micropitting compared to mineral oils having identical additive package and viscosity grade (16). Utilising oils having higher viscosity or grease alleviates micropitting to some extent (3). Around 80% of bearings are lubricated with grease (17). Grease on the other hand, due to the thicker film and higher operation temperature has a higher friction and higher oxidation risk. It should be noted that the wear progress is complex in machine elements and several mechanisms occur simultaneously (14).



(a)



(b)

Figure 2-1. Micropitting surface fatigue a) optical (18) b) electron microscopic micrographs (19)

2.3.1 Fatigue wear

Fatigue wear is defined as the continuous removal of the material induced by applied cyclic load over a certain period (14). The main fatigue mechanism in bearings is Rolling Contact Fatigue (RCF). In RCF the maximum shear stress happens in the subsurface region depending on the maximum contact pressure applied at the centre of contact (20) as shown in Figure 2-2. Subsurface defects including subsurface inclusions, voids and high strain areas act as crack nuclei and originate a crack which then propagates towards the surface leading to fatigue (11). Having been induced by the tribochemical effects of lubricant contaminants and additive chemical attack, the RCF can happen much earlier than its designed life span (up to 10% of its expected lifetime) which is known as premature fatigue (21).

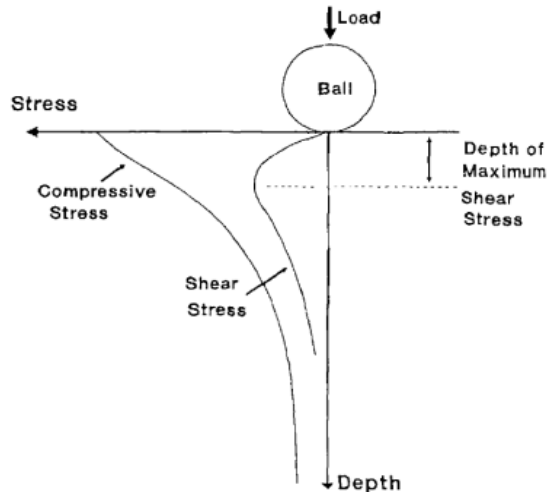


Figure 2-2. Schematic image of stress distribution in a point contact bearing assembly (22)

2.3.2 Corrosion assisted wear

The lubricant additives tend to react with the surface of the fresh metal (14). Furthermore, sliding, rubbing, and rolling increase the reaction kinetic (14). In the event of lubricant contaminant's ingress into the lubricant, especially water, the rate of chemical reactions increases high enough to induce corrosion (23). The extent of corrosive wear happening in the tribological system can be defined as the mass loss generated by the corrosion-induced wear (14). The oxidative wear, which stems from removal of the formed oxide layer on metal, is a well-known type of the corrosive wear (12).

2.3.3 Adhesive wear

Adhesive wear occurs as a result of adhesion of contact bodies. In adhesive wear material-transfer occurs from one body to the other as a result of cold welding of asperities within the contacts (12). The adhesive wear is more prevalent compared to fatigue wear and it can be prevented in bearings by preserving the lubrication regime in elastohydrodynamic within the whole operation time (12). The adhesive wear is considered as the main wear mechanism in cam and cam follower contacts (14). The AW additives such as ZDDP and ester based additives (amine neutralized phosphoric acid esters) are used in the lubricants in order to mitigate adhesive wear (14). Figure 2-3 shows the incident of adhesive wear on the inner ring of a bearing.



Figure 2-3. Adhesive wear occurred on the inner ring of a bearing (24)

The other approach to make a bearing more resistant to adhesive wear is to apply hard coatings on the surface of the bearing components. Several coatings deposited utilising Physical Vapour Deposition (PVD) are used to enhance the performance of the bearing such as: TiAlN, CrAlN, ZrN, ZrC, WC/C, W-C:H, DLC (25). Table 2-1 details mechanical properties of some PVD coatings including hardness and Young's modulus.

Table 2-1. Mechanical properties of some PVD coatings (25)

Coating	Hardness Hv	Young's modulus (GPa)	Adhesivity VDI 3198
TiAlN	25	340	5
CrAlN	19	320	2
ZrN	14	320	3
ZrC	15	200	2-3
WC/C	12	150	1
W-C:H	12	169	1

A severe adhesive wear induces high degree of tears, roughened surfaces and large plastic deformation in high temperature sliding. Severe adhesive wear is generally called galling in dry (non-lubricated) contacts and scuffing in the lubricated contacts (14).

2.3.4 Abrasive wear

Abrasive wear arises where asperities of a harder body generate grooves on the softer body within tribological contacts (14). The ploughed out material from the groove generates wear particles (14). Roller element bearings in mining, road-construction, transport, and agricultural applications suffer from abrasive wear which is prompted

by microslips between raceways and roller elements (26). The different modes of two-body abrasion are schematically shown in Figure 2-4.

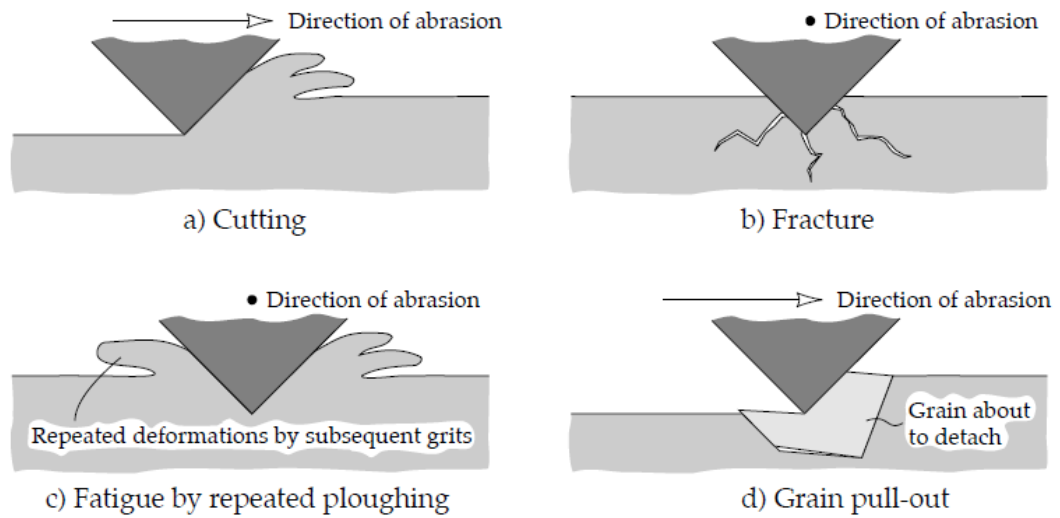


Figure 2-4. Illustration of different types of two-body abrasion (12)

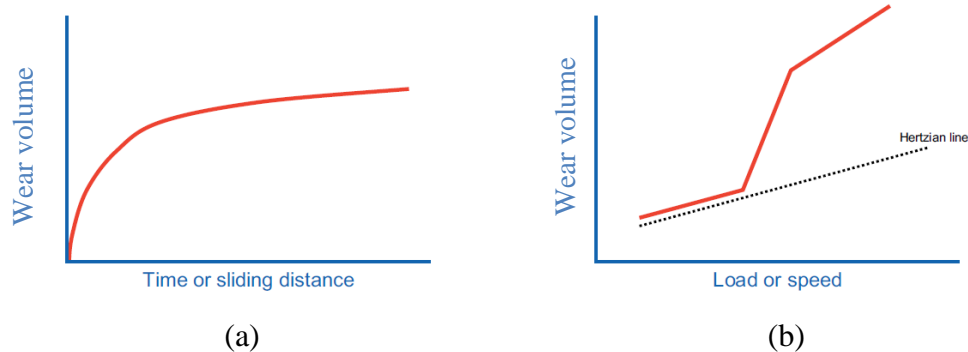
Moreover, roller element bearings operating in mineral handling applications or a desert environment undergo third-body abrasion when solid debris particles contaminate the lubricant (27). The mass loss from the roller elements associated with third-body abrasive wear is significantly higher than the mass loss from raceways (up to four times) (27). The solid abrasive particles are introduced to the lubricant as lubricant contamination e.g. sand or ploughed out particles from the surface of bearing elements.

2.3.5 Erosive wear

Erosive wear is surface damage propelled by impact forces generated through collision between hard particles carried by a fluid (flowing liquid) or by a gas on the surface (14). The wear rate depends upon the kinetic energy of the solid particles. In an event of high flow rate resulted from high pressure gradient, breakdown of gaseous bubbles near to the surface induces cavitation wear (14). Depending on the mechanical properties of the surface, ductile or brittle, repetitive impact forces leads to the fatigue wear or wear particle generation, respectively (14).

In general, the wear rate in dry contacts varies with influential factors such as material's properties and surface treatments, load and temperature (12). However, in lubricated machine elements the dominant factor controlling the wear rate is the lubricant film (14). Also, in lubricated contacts the wear volume reaches a steady state

at an established lubrication regime (28) as can be seen in Figure 2-5 (a). As shown in Figure 2-5 (b), a well-lubricated system experiences a transition stage from mild conditions to severe contacts as load or speed exceeds a certain value (29).



**Figure 2-5. a) Steady-state wear volume as a function of time or sliding distance
b) transient rise in wear volume beyond a critical load or speed (28)**

2.4 Lubrication

Lubrication is an effective interposition of a solid, liquid or gas between two bodies to reduce friction and/or wear as a body moves over the other (12). The lubrication regime in which the machine element operates depends on the following factors (12):

- Operating conditions and environmental effects: load, temperature, speed, vibration, humidity and misalignment
- Surface and material properties: metrological characteristics (e.g. roughness) and texture
- Lubricant properties: viscosity index, additive package and pour point

There are four types of lubrication regimes (14) which are briefly elucidated in the following sections.

2.4.1 Hydrodynamic Lubrication (HL) regime

In the HL regime the surfaces are utterly separated by a fluid lubricant film which is thick enough to avoid direct contacts of surfaces (14) as depicted in Figure 2-6 (a). The friction force is generated by shear forces within the lubricant (14). The lubricant film thickness is between 1-1000 μm (14).

2.4.2 Elasto-Hydrodynamic Lubrication (EHL) regime

The interfaces with low contact conformity are imposed to high loads and high contact pressures in demanding applications such as bearings and gears (14). However, the

local elastic deformations of the surface asperities and increased lubricant viscosity suppress the expected asperity-asperity contacts resulting in the EHL regime (14) as illustrated in Figure 2-6 (b). In order to achieve a favourable engineering design for roller element bearings the lubricant film between the contact surfaces have to persist and avoid solid-solid contacts (17). Therefore, EHL lubrication regime is desired throughout the entire operation time in certain applications.

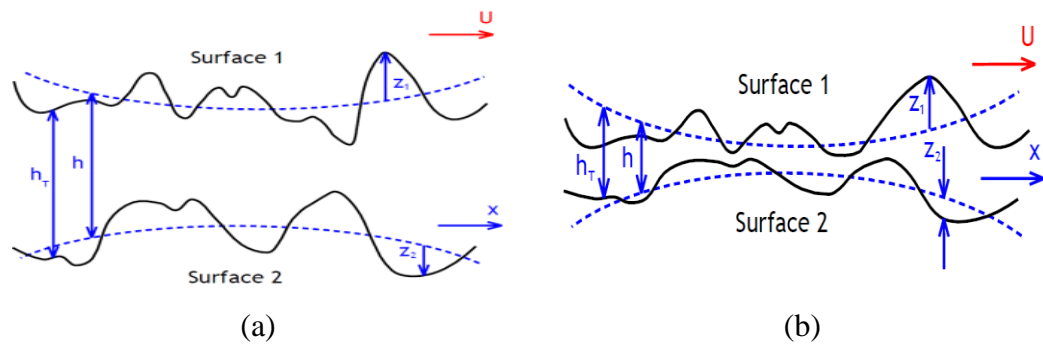


Figure 2-6. Schematic illustrations of a) hydrodynamic lubrication and b) elastohydrodynamic lubrication (14)

2.4.3 Boundary lubrication regime

In boundary lubrication the average surface roughness is greater than the average lubricant film thickness (12). As a result, the lubricant film, which is in the range of 5-100 nm in boundary conditions, cannot fully separate two contact surfaces leading to direct contacts of asperities (14). In the boundary regime, where the asperities from two bodies are in contact, the load is burdened by asperities in contact as schematically shown in Figure 2-7 (a). In this regime the dominant factors controlling the friction and wear characteristics are the surface properties of the material and additive action on the surface (14). The properties of the common thin film interposed between the contact bodies and the bulk properties of the lubricant, especially viscosity, have negligible effects on the contact (12). The friction reduction in boundary lubrication can be achieved through diminishing adhesion of the surfaces and abrasion wear and by using friction modifiers (14).

The collisions between surface asperities induce plastic deformation associated with energy dissipation and heat generation (12). A decrease in the lubricant entrainment speed, an increase in the applied load and high acceleration rate can propel the lubrication into a boundary regime which is a determining factor for the component life (30). The collisions between asperities generate a high and short-life local

temperature and nascent surface which trigger chemical interactions between surface and lubricant (21). The chemical interactions include decomposition of the base oil and additives and additive-film formation on the surface (21). Thus the chemical interactions can be sometimes beneficial in terms of reducing wear by ZDDP decomposition and tribofilm formation or detrimental in terms of increasing corrosion as a result of hydrogen release from lubricant and subsequent premature fatigue.

The boundary film, depending on its interaction with the surface, has varying film strength (12). The film strength is the resistance force by the lubricant and/or additive film to stay within the contact and suppress solid-solid contacts (14). The boundary film is formed as a result of three types of interactions between the surface and lubricant additives which are listed below in increasing order with relation to the film strength (14):

➤ Physically adsorbed layers

A one or several molecule-thick layer adsorbs to the surface by short-range between-molecular forces (Van der Waal's force).

➤ Chemically adsorbed layers

The layer formation is prompted by the molecular affinity of the additive or lubricant to the metal surface. The thickness of the layer is in the order of few nanometres. Chemical structures such as fatty acids, alkyl amines, stearic acids generate chemisorbed molecular layers.

➤ Film formed by chemical reactions

The layer is formed by the chemical reaction of the surface with the additives. In general, the reaction layers are effective in the severe operational conditions. The ZDDP molecule is the most well-known AW additive which generates a layer with a thickness of several tens of nanometre.

2.4.4 **Mixed lubrication regime**

A mixed regime corresponds to a lubrication condition in which the contact conditions can locally vary between HL and boundary lubrication (14). In other words, there are areas in the contact interface which are fully separated by lubricant film and areas in which asperity-asperity contacts take place as shown in Figure 2-7 (b). Therefore, the bulk properties of the lubricant as well as the chemical properties of the thin boundary

film have to be considered (12). The film thickness is in the range of 0.05 μm to 1 μm (14).

The lubrication regimes are well-arranged classifications which are interlinked with performance of the tribological contacts. In other words, the surfaces lubricated in the different regimes exhibit discernible wear and friction performances (14).

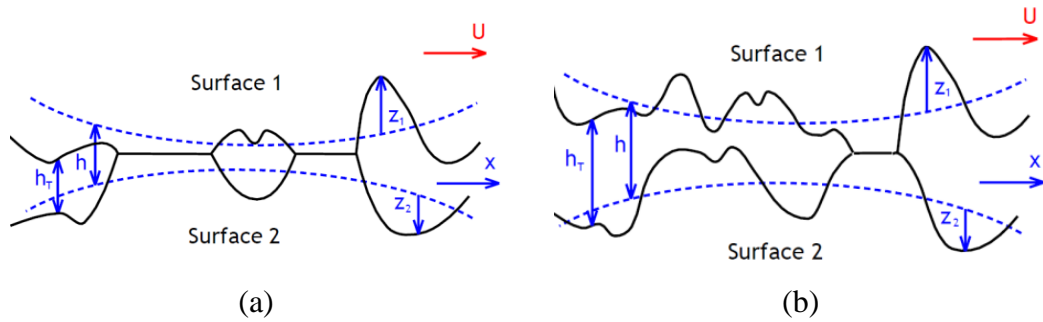


Figure 2-7. Schematic illustration of a) boundary and b) mixed lubrication regimes (14)

Shown in Figure 2-8 is a diagram developed by Richard Stribeck (1902) which clarifies the change in the friction coefficient with respect to the specific film thickness (14).

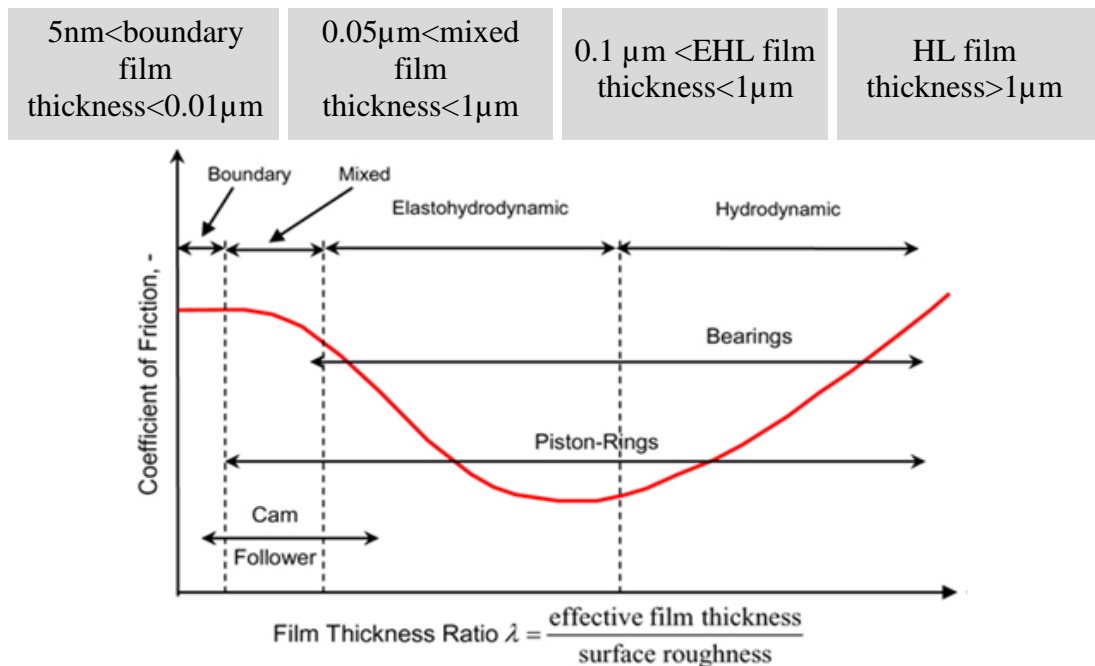


Figure 2-8. Illustration of the modified Stribeck diagram (31)

Lambda ratio (λ) is a non-dimensional parameter which specifies the lubrication regime in which the tribological system operates (14). Lambda ratio alters with a change in the lubricant properties e.g. viscosity and density, contact pressure and

geometry, lubricant entrainment speed and surface roughness of the contact bodies (32).

2.5 Lubricants and additives

2.5.1 Lubricants

A lubricant is a formulated substance composed of one or two base oils as its base stock and 1-25 wt% of additives to fulfil specific performance requirements (14). In general, the main aim to use a lubricant is to reduce friction and mitigate wear in order to have a longer and smoother operating tribological system (12).

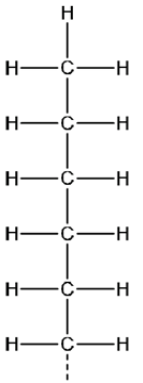
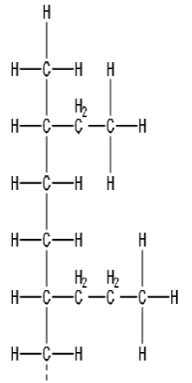
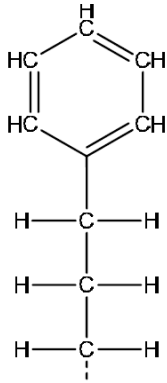
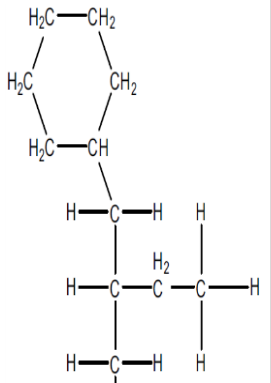
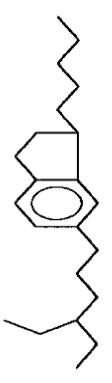
2.5.2 Base oil

As a general classification there are two types of base oils which are mineral and synthetic. The viscosity of a lubricant should be in an optimum level, since high viscosity results in high friction and heat generation due to the viscous drag and low viscosity cannot accomplish a complete separation of the two surfaces (12).

2.5.2.1 Mineral oils

The origin of mineral oils is crude petroleum oil which is composed of a blend of hydrocarbons having a chain length of 18-40 C atoms (33). There are four types of mineral oils with regard to the structure of the hydrocarbon chains in the base oil (28) which are shown in Table 2-2.

Table 2-2. Molecular structure of different types of mineral oils (28, 30, 33)

Paraffins		Aromatics	Naphthenes (cycloparaffines)	Mixed
n-paraffin	Isoparaffin			
				

The traces of S, O and N known as heteroatoms (usually less than 4 wt%) also exist in the mineral base oil (28). The typical contribution of each type of mineral oil to the chemical structure of a classically refined petroleum base stock is 5-40% (average 20%) of aromatic, 10-20% of n-paraffin and 40-85% of naphthenic compounds (33). Mineral-base lubricants commonly have 5-25 wt% of blended additives (14).

2.5.3 Synthetic base oil

The main drawback of mineral base oils is their constrained temperature range in which they are effective, hence the key aim to develop synthetic oils has been to produce oils that can operate in wide range of temperatures either very low or very high (14). The synthetic oils are derivatives of petrochemical and coal-derived feed stocks as well as animal and vegetable oils (30). There are three major types of synthetic oils (28) as follows:

- Synthetic hydrocarbons:
 - Molecules which consist of only H and C atoms: alkylated aromatics, cycloaliphatics, polybutenes, polyisobutenes, Poly Alpha-Olefins (PAO)
 - Esters: phosphate esters, dibasic acid esters, polyesters, polyol esters (neopentyl esters), aliphatic diesters, silicate esters, fatty acid esters
 - Polyether: polyglycol, polyalkyleneglycols (PAG)
- Organohalogen (halogenated hydrocarbons): perfluoropolyethers, chlorofluoroethylenes
- Silicon-containing hydrocarbons: dimethyl silicone, methylphenyl silicone, fluoromethyl silicones

2.5.3.1 Synthetic hydrocarbons

PAO: PAOs are hydrocarbons consisting of unsaturated alkenes at the chain termination (28). They exhibit good thermal and oxidation stability and excellent viscosity-temperature behaviour (viscosity index: 120-170) (28). They are used in many applications due to the similarity of their chemical composition and behaviour to the petroleum base stock. The additive dissolvability of PAOs is not much in comparison to esters (28).

2.5.3.2 Esters

They are the most common base oil employed for many applications. In general, polyesters are preferred over other types of esters due to a greater viscosity index and superior viscosity in comparison to mono-esters and diesters, respectively (28). Polyesters, polyol ester, and phosphate esters exhibit high temperature stability and excellent viscosity index (12). Also, polyesters are shown to deliver very good wear and friction performances (33).

2.5.3.3 Organohalogens

As a hydrogen atom in the hydrocarbon chain is replaced with a halogen (F, Cl, and Br), an organohalogen lubricant is derived (33). Although the hydrogen exchange leads to a less flammable substance, the chlorinated and brominated hydrocarbons exhibit severe toxicity (33). The high-cost of the perfluoropolyethers lubricant restricts its wide application in the industry (33).

2.5.3.4 Silicone analogues

The silicon polymers are one of the pioneer lubricants that have been investigated so far. However; a poor boundary lubricity and film formation capability confine its application to applications lubricated in the hydrodynamic regime (33). Also, they exhibit poor ability to dissolve additives (33).

2.5.4 Additives

Chemical substances that are blended to the lubricant to attain a certain functionality and enhance the lubricant performance are called additives (14). The desired functions are wear and friction reduction, to preserve a clean surface and lubricant and to achieve a certain viscosity index (33). Additives can be either chemically active, which includes AW and Extreme Pressure (EP) additives, organic corrosion and oxidation inhibitors and dispersants, or chemically inert such as viscosity index improvers and pour point depressants (28). The chemically active additives mostly have unsaturated chemical bonds and functional groups or molecules (from group V and VI in the periodic table: N, S, P and O). The most widely used additives (14) are as follows:

Friction modifiers are compounds that generate a film on the surface reducing the friction up to 30% (14). Friction modifiers are especially important for the contact under a boundary regime (12). Tallow and coco amines and fatty oils, fatty acid esters

and organo-metal compounds such as Molybdenum Di-Thio-Carbamate (MoDTC) are found to be effective in alleviating friction (33). There are ongoing researches on synthesis and implementation of nanoparticles of molybdenum disulphide (MoS_2) and tungsten disulphide (WS_2) (34-35) and finely dissolved graphite as potentially effective friction modifiers.

Detergents are usually metal (calcium, magnesium, barium, and zinc) based compounds that prevent insoluble oxidation and contamination-derived deposits from development on the surface (33). Detergents adsorb onto the surface as a surfactant and form microemulsion of insoluble contaminations on the surface (33). Metal sulfonates, metal phenates, metal salicylates and metal thiophosphonates are common detergents (33). In the applications where the lubricant oxidation rate is high or the operation temperature is high a certain degree of “overbasing” agents, e.g. calcium carbonate, is added to the detergent in order to neutralize acidic contaminants (14).

Dispersants are utilised to form a suspension of the insoluble oxidised products and contaminants at low temperatures (below 100°C) and usually do not have metals in their chemical structures (ashless) (33). Mannich base (amino carbonyl compounds) and Succinimide (cyclic imide) are two common types of the dispersants (33). **Pour point depressants** are paraffinic compounds that lower the pour point of the lubricant to retain the lubricant performance at lower temperatures.

Viscosity Index (VI) improvers are polymers or copolymers that have molecular weights in order of or more than 100,000 (33). Polymethacrylates, polyisobutenes, olefins and styrene-diene-copolymers are the most common VI improvers (14, 33). VI improvers are used in automatic transmission and hydraulic fluids (33). The backbone chain of the polymer should break down in high shear rates in order to fulfil shear thinning (33). Therefore, the concentration and molecular weight of the polymer should be in a certain range. Addition of 5-10% of VI improver, as an optimum concentration, leads to a considerable improvement in VI (33).

Antioxidants are additives which delay the oxidation processes in the lubricant (14). Amines such as N-phenyl α -naphthylamine, hindered phenols such as 2,6-di-tert-butyl-4-methylphenol and Sulphur-Phosphorus (S-P) compounds such as ZDDP are the most common antioxidants (33). **Anti-foam** additives are utilised to mitigate a foaming effect in the lubricant (14). Anti-foam additives are usually composed of silicon compounds (14).

Anti-wear additives are employed to suppress wear in EHL and/or mixed and boundary lubrications, particularly by forming a film on the surface (33). The most well-known AW additive is ZDDP (14). Tri-cresyl Phosphate (TCP), acid phosphates, phosphorotriesters, sulphurized terpenes, sulphurized sperm oils and metal dithiocarbamates are the other common AW additives (33). **Extreme pressure** additives are typically sulphur-based compounds that generate a film on the surface (28), particularly in boundary and severe high-load contact (14), in order to mitigate spalling on surfaces. ZDDP is the most frequently used EP additive together with dibenzylsulfide, phosphosulphurized isobutene, trichloroacetone and molybdenum disulphide which are the other EP additives (28).

Corrosion inhibitors in a lubricant are compounds that form a film on the surface either chemically or physically and reduce the cathodic or anodic (or both) chemical reactions on the surface of a metal (12). Some of the corrosion inhibitors block rust formation as rust inhibitors such as alkyl thioacetic acids, imidazolines, amine phosphates and acid phosphate esters (33). Zinc dithiophosphate, zinc dithiocarbamate, sulphurized terpenes and phosphosulphurized terpenes are the other common corrosion inhibitors (33).

2.6 Bearings

A bearing as a machine element is designed to facilitate relative motion between moving parts and to reduce friction between interfaces. The relative motion can be either linear or rotational (14).

2.6.1 Bearing types

In general, bearings can be categorised to two types which are plain and roller element bearings (17). A plain bearing does not have rolling elements and comprises a shaft and bearing surface(s). A common type of the plain bearing is the journal bearing. The second and more sophisticated type of bearing is roller element bearings (17). The roller element bearings with regard to the roller element geometry can be classified as ball bearings and barrel or cylindrical bearings (17).

2.6.1.1 Ball bearings

In ball bearings two raceways are maintained separate by ball-shaped rollers. The geometry of contact between ball and the raceway is a very small elliptical area of

contact, although it is mostly considered as Hertzian point contact (36). As a result of the small area of contact, the ball bearing applications are limited in load carrying compared to the other rolling element bearings (36). However, they provide very low friction and smooth running characteristics (36).

The simplest kind of ball bearings is deep grooved (17) which is shown in Figure 2-9 (a). The deep grooved bearing is the most popular bearing which carries axial and radial loads (36). It is a splendid bearing in light load and high-speed applications such as small electrical motors and light gearboxes (17). They commonly exhibit cool running characteristics and can be lubricated with grease allowing them to be sealed for whole life (17).



Figure 2-9. Illustrations of a) deep-grooved and b) double row self-aligning ball bearings (17)

Shown in Figure 2-9 (b) is the other type of ball bearing which is named double row self-aligning ball bearing (36). It has similar features to deep-grooved ball bearings with a second row of balls which makes it desirable to support higher levels of load and to run under dynamic miss-aligning forces (36). Therefore, it is suitable for the application such as mixing, stirring and blending machines and fans in which the shaft may deflect under the load (17).

Angular Contact Ball Bearings (ACBB), shown in Figure 2-10, are designed with a capability to carry combined radial and axial loads at a high speed with an outstanding precision (17). The contact angle is the angle between the line which connects the contact points of the ball and the raceways in the radial plane and a perpendicular line to the bearing axis (36). The axial load capacity is directly proportional to the contact angle (36). They are always assembled opposed to each other in back-to-back or face-to-face configurations. ACBB can also be double-row (having two rows of rolling elements), which is always arranged in a back-to-back configuration (17). The four-point contact bearing, shown in Figure 2-10 (c), is designed to transfer an axial

load in both directions (36). ACBB bearings are used in gearboxes, pumps and machine tools applications (17).

Another type of ball bearing designed for enhanced mounting based on the deep grooved ball bearings is the Y bearing (36). It consists of a wider inner ring, a row of balls which are embedded and secured by a cage and a spherical outer ring (17). Y bearings are lubricated with grease and sealed on both sides (17). Y bearings can also tolerate a certain degree of static miss-alignment (17). The outer ring is fitted to the housing by an intermediate matching sphere bore (36). The housing can be made of cast dye or pressed steel (17). They are used in applications with moderate speeds such as agriculture equipment, screw conveyer and fans where the load is relatively light and speed is moderate (17).

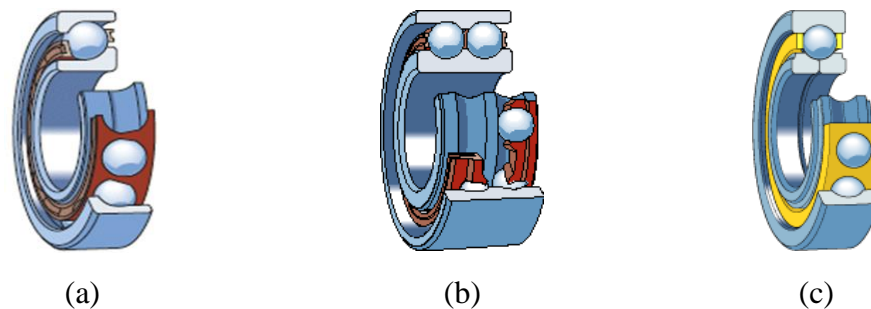


Figure 2-10. Schematic illustrations of a) angular contact single row b) double-row angular contact c) four-point ball bearings (17)

2.6.1.2 Spherical and cylindrical roller bearings

The spherical and cylindrical roller bearings are suitable for heavily loaded applications and where shock loads are encountered (36). The cylindrical roller bearing, shown in Figure 2-11 (a), is capable of accommodating high radial loads at high speeds (17). It has many types most of which are designed to facilitate relative motion under an axial load. They are usually accompanied with an axially located bearing to enhance the support to the shaft (17). Cylindrical roller bearings are employed in electrical motors, gearboxes and heavy machines e.g. rolling mills for aluminium foiling (17).

Shown in Figure 2-11 (b) is a tapered roller bearing that consists of a tapered inner ring with a set of tapered rollers secured by a steel cage called a core assembly and an outer ring called a cup (17). The cup and core are mounted separately, the core on the shaft and the cup in the housing (17). The tapered rollers are designed to carry combined and simultaneous axial and radial loads (36). Similar to angular contact bearings as

the angle increases, the axial load carrying capacity is enhanced (36). A single row tapered bearing can carry loads in one direction; thus they must be used in pairs and be adjusted opposed to each other in a back-to-back or a face-to-face configuration and be secured by a locknut (17). The tapered roller bearing can be either single row or double row (36). An adaptor or a sleeve is usually necessary for mounting the tapered bearings (36). Tapered roller bearings are utilised in applications such as truck wheels, industrial gearboxes and high-way equipment (17).

As shown in Figure 2-11 (c), spherical roller bearings are similar to the tapered cylindrical roller bearings; however they are equipped with a guide ring located between two separate cages for each roller-row (17). This design enables the bearing to render very high radial and axial-load bearing capacities in either direction with the potential to tolerate both dynamic and static miss-alignments and shock-load (17). It is appropriate for highly-loaded applications, including cranes, bridges and conveyor and heavy-duty gearboxes (17).

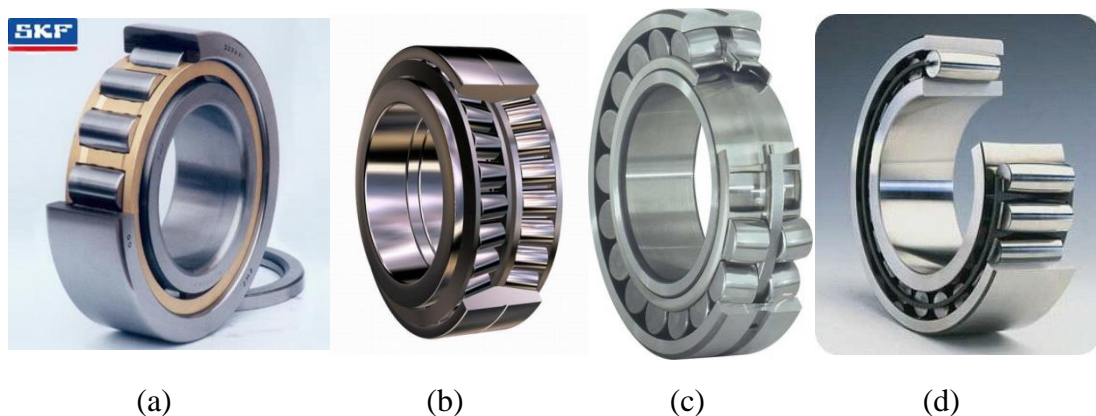


Figure 2-11. Images of typical roller bearings a) single-row cylindrical, b) adjusted configuration of tapered, c) spherical and d) CARB (17)

CARB® bearing, shown in Figure 2-11 (d), is designed to offer a self-aligning capability alongside with the axial displacement in a compact cross section (36). Although it does not carry axial loads, it provides a great freedom of axial displacement (36). It is a unique design to SKF that can carry high loads (17). The outer ring is designed to provide a torus-shaped raceway (17). It is desirable for applications in which the shaft experiences large linear expansions due to the exposed high temperatures. It is suitable for applications such as a drying cylinder in paper machines and support bearing in continuous casting machines (17).

It is essential to provide a degree of radial clearance within the bearing to avoid damages induced within pre-load conditions (17). An extravagant and out of range

clearance brings about excessive shaft movements, hence undesirably influences the bearing's performance.

An appropriate lubrication of bearings has a substantial importance in order to secure the expected life span. There are some parameters that must be considered to attain an adequate oil film thickness within the contact. These are as follows (36):

- The oil viscosity which influences oil film thickness. This is particularly important where the bearing operates at slow speeds and under high-load conditions in order to maintain oil film within the contact.
- The additive package has significant impact, especially in severe conditions, to retain the separation between the contact surfaces.
- The temperature encountered within the bearing must be considered, since the oil viscosity decreases with an increase in temperature leading to a reduction in the oil film thickness. The oils with high viscosity index constrain the influence of temperature change on the film thickness.

Grease is mostly used to lubricate bearings. Grease consists of an oil (~85%) and thickener agents (~15%) (17). The grease is a semi-solid dispersion of a thickening agent in the lubricant (14). The thickener agents are usually metal soaps (lithium, calcium and sodium) or polymers. Greases are non-Newtonian fluids and are effective in temperatures ranging from -70 to 350°C (14). The oil lubrication system is an effective way to lubricate bearings and sealing the lubricant for its life-time is a common bearing lubrication system (17). However, in certain applications the sealed for life lubrication is not effective. For example, in applications where the bearing operates in high temperatures or in harsh environments (high risk of contamination), re-greasing the bearing might be essential (17). There are other lubrication systems including the static oil bath, which is the most common type, splash and circulating lubrication (17). In most gearbox applications the bearings are lubricated by oil splash. In some applications the bearing is lubricated by a continuous lubrication system in which the lubricant is circulated in a circuit and supplied by an oil reservoir (17).

2.6.2 **Bearing materials**

The materials used in more than 90% of bearings to produce roller elements and raceways are steels and ceramics (36). There are five types of steels which have been used for manufacturing bearings as described in the next sections.

2.6.2.1 Through-hardened bearing steels

The microstructure of the whole material including bulk and surface in the bearing steel is converted to the martensite or bainite by heat treatments reaching a hardness range of 58-65 HRC (17). The steels utilised for through hardening contain approximately 1% C and 1.5% Cr (36). The cleanliness of steels is of a significant importance to industry (37). The most well-known through hardened bearing steel is 100Cr6 and its tribological behaviour has been widely investigated in the literature (37). (For the detailed information on through-hardened bearing steels and their composition and properties see Appendix 1)

2.6.2.2 Induction-hardened bearing steel

In some applications, such as flanged wheel hub bearings, the steel's surfaces with a medium C-content are hardened by the induction hardening (36). As a result, the ductile and tough nature of the bulk is maintained while a harder surface is attained at the same time (37). (For the detailed information on induction-hardened bearing steels and their composition and properties see Appendix 1)

2.6.2.3 Case-hardened bearing steels

Low C (approximately 0.15%) alloyed steels containing manganese-chromium or chromium-nickel alloying elements are utilised for case-hardening (36). In case-hardening the surface is hardened and the bulk has high toughness characteristics. They are used for applications in which the bearing is exposed to high tensile and impact loads (17). (For the detailed information on case-hardened bearing steels and their composition and properties see Appendix 1)

2.6.2.4 Stainless steels

In demanding applications, in which the bearing operates in harsh and corrosive environments, stainless steels are employed (17). Chromium and nickel as alloying elements are used at certain concentrations in stainless steels (36). The X65Cr14 and X105CrMo17 are two most common stainless steels used for bearings operating in arduous conditions (36). (For the detailed information on bearing stainless steels and their composition and properties see Appendix 1)

2.6.2.5 High-temperature resistant bearing steels

The normal case-hardened or stabilised through-hardened steels cannot resist temperatures higher than 250°C (17). Therefore, highly alloyed steels with tungsten

and vanadium are used for high temperature applications (up to 500°C) (17). (For the detailed information on high-temperature resistant bearing steels and their composition and properties see Appendix 1)

2.6.2.6 Ceramics

Ceramics are employed to produce the rolling elements for hybrid bearings. Zirconia (ZrO_2), alumina (Al_2O_3), silicon carbide (SiC), and the most common one, silicon nitride ($\beta-Si_3N_4$) (38) have been used in hybrid bearings. The density of silicon nitride is less than half of steel's density, hence ceramic balls experience significantly smaller gyroscopic moments and centrifugal forces in comparison to steel balls (39). As shown in Figure 2-12, the smaller centrifugal forces bring about 30-50% less friction force (39) leading to a considerably lower operation temperature. The lower density of silicon nitrides and its heat-resistant properties, make silicon nitride a desirable material for high speed and high temperature applications (39). Moreover, the lower density of silicon nitride diminishes the risk of false brinelling and subsequent premature failures.

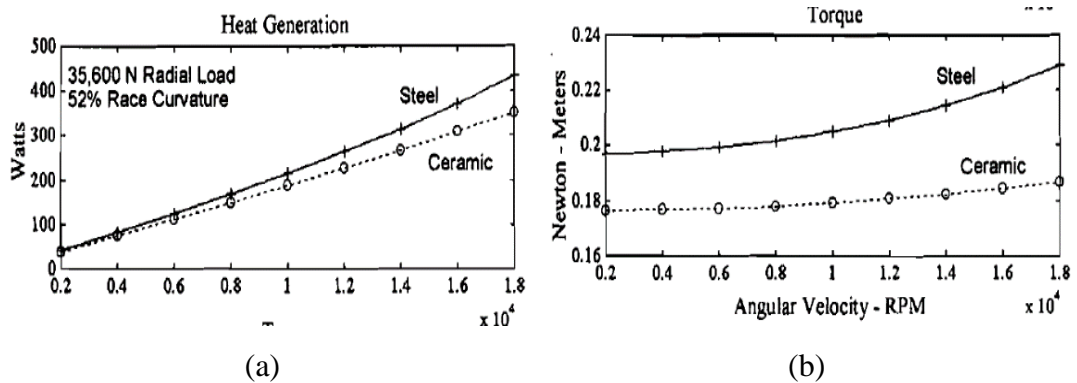


Figure 2-12. Comparison of a) heat generation and b) torque as a function of angular velocity of the inner ring in bearings having steel and silicon nitride balls (40)

The lower operation temperature alleviates the aging rate of the grease and thus a longer re-lubrication interval can be achieved (17). The silicon nitride (1600 HV10) is significantly harder than steel (700 HV10). Therefore, it is less susceptible to dent formation and micropitting surface fatigue and generates fewer wear particles in comparison to steel roller elements leading to smoother operation, less noise and less wear (17). The mechanical and thermal properties of silicon-nitride are presented in Table 2-3.

Table 2-3. Mechanical and thermal properties of silicon nitride with respect to M-50 bearing steel (40)

Material property	M-50 steel	MgO-Si ₃ N ₄
Density (g/cc)	7.8	3.16
Poisson's ratio	0.3	0.26
Elastic modulus (GPa)	207	320
Vickers hardness (GPa)	8-10	16.6
Coeff. of Therm. Expan. ($\times 10^{-6}/^{\circ}\text{K}$)	12	2.9
Specific heat (J/(Kg·K))	450	800
Thermal conductivity (W/(m·K))	30	29.3
High temperature use (K)	600	1300
Fracture toughness (MPa·m ^{1/2})	16	4.1

2.6.3 Cage materials

Metals (steel and brass) and polymers are used to produce cages (36). The materials and their compositions are briefly listed (17): (For the detailed information on the cage materials, their composition and properties see Appendix 2)

Metals:

- Steels: hot rolled low carbon steel (DD11-DD14), pressed stainless steel (X5CrNi18-10), machined steels (S355, S355GT)
- Brass: machined CuZn39Pb2

Polymers:

- Polyamides (PA66, PA46)
- Polyetheretherketone (PEEK)

2.7 Summary

In the current chapter the fundamentals of tribology as a multidisciplinary science are explained. The different and main wear mechanisms in tribological contacts, especially with respect to surface damages in bearings, are presented. Also, the most

commonly employed base oils and additives and their functionalities are elucidated. The last section is dedicated to describe different types of roller element bearings in industry and the materials utilised in bearings. In the next chapter of this thesis a comprehensive literature review regarding RCF, surface fatigue and tribochemistry involved in the surface fatigue will be presented.

Chapter 3

Literature review

3.1 Introduction

In the current chapter, the fundamentals of RCF and parameters affecting RCF, especially the influence of tribochemical parameters, are introduced at first. Following an introduction to RCF, an extensive literature review is presented with regard to surface fatigue, specifically micropitting. A comprehensive review of micropitting and the influential determinants, including tribological and tribochemical parameters, is carried out and discussed. More focus will be on the impact of ZDDP AW additive on micropitting of bearing steel surfaces and influence of water as a destructive lubricant contamination on micropitting.

3.2 Rolling contact fatigue

If a rolling bearing's components are properly manufactured with the lowest amount of S, Al (which is believed to be responsible for the majority of failures) (37), MnS, and MnS-Al₂O₃ (41) inclusions, properly loaded and well-lubricated in which lubrication remained in the EHL regime and remained free of any lubricant contamination, the bearing fails after accomplishing its expected life span (3). This affirms that the main reason of the failure would be material fatigue which depends on the mechanical properties of the material, especially fatigue life. However, in real conditions the environmental effects such as spalls, White Etching Cracks (WECs) and standstill corrosion (which is induced by moisture) and severe operation conditions leading to insufficient lubrication bring about unforeseen failures which are called premature RCF (21). RCF has been observed mostly in gears and bearings (1). In bearings the main loading is rolling but during contact, especially in running-in, sliding occurs. However, a little amount of sliding is believed to be the main factor responsible for the surface fatigue (1).

Crack initiation induced by inclusions is believed to stem from the differences in mechanical properties between the inclusion and the base metal (42). The inclusions usually prompt diagonal cracks (43). Also, as demonstrated in Figure 3-1, inclusions can be coupled together in an array to form stringers which are generally more

dangerous than a single inclusion (43). The growth of cracks then develops spalls on the surface. The spall orientation and volume depends on the extent of inclusions, crystalline orientation of the material, temperature, load and the number of the contact cycles (43).

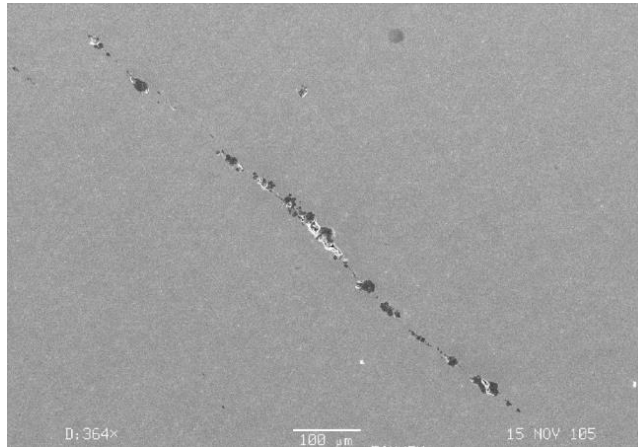


Figure 3-1. Scanning Electron Microscopy (SEM) image of a stinger of inclusions (43)

Historically, it has been believed that the microcracks responsible for RCF initiate from inclusions and in the subsurface areas of accumulated residual stresses and dislocations. The microcrack initiation is triggered by the high local contact stresses (21). However, it is currently revealed that cyclic loading induces surface-originated (surface originated micropitting) and subsurface-originated crack (subsurface originated spalling) initiation and propagation which eventually lead to failure of the bearing (21).

RCF with a subsurface origin arises when cracks initiate in the subsurface defects, mainly inclusions, and propagate toward the surface to generate a spall (20). The subsurface crack initiation usually happens in the region of maximum shear stresses (12). In conditions where the bearing components have superbly smooth surfaces, lubricated in EHL regime, and are in contacts under low surface shear stresses, the subsurface spalling fatigue is promoted resulting in a dominant subsurface RCF failure (20). The generated cracks then after propagate at a shallow angle (between 15-30 degrees) relative to surface (44).

Lai, Lund and Rydén (45) showed that under vacuum conditions the propagation of subsurface cracks is very slow compared to atmospheric conditions and the crack propagation is mostly observed in the subsurface area induced by high fatigue cycles. In other words, the vacuum crack propagation in subsurface area leads to a pure

mechanical fatigue and not a premature fatigue. This observation postulates that in premature failures the subsurface initiated crack should approach to the surface and connect to the lubricant to allow H, O and lubricant entry to the steel (45).

In contrast to subsurface originated spalling, micropitting originates from surface irregularities such as dents and scratches formed by adhesive wear or abrasive wear and surface asperities (3, 21). The surface originated crack initiation and propagation steps are schematically illustrated in Figure 3-2.

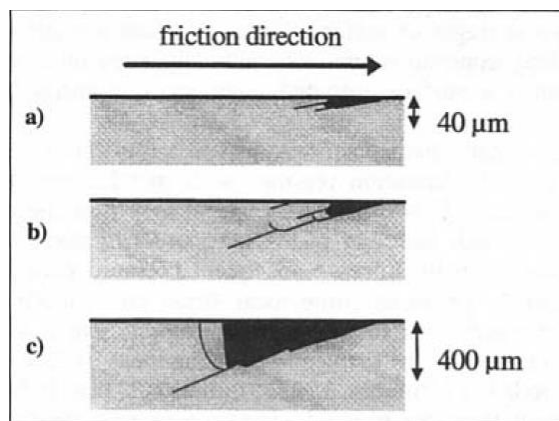


Figure 3-2. Schematic illustration of surface crack initiation and propagation (46)

Insufficient lubrication usually causes surface and near-surface crack initiation as the lubricant film fails to separate two contact bodies from solid-solid contacts (47). The bearings experiencing low load conditions at high rotational speeds and rapid accelerations are more at the risk of smearing, while bearings operating for extended periods of time under high loads, slower speeds, and in the boundary layer lubrication are more at risk of micropitting (3). It has been shown that cylindrical roller bearings undergone excessive roller-raceway slip in the area of unloaded zone leading to smearing wear (48).

Another important factor influencing the RCF life of bearing steels is the elastic response of the material in cyclic loads after shakedown (20). Plastic deformation which is prompted during running-in brings about strain-induced microstructural changes of the surface leading to a deteriorated elastic response of the material in cyclic loads (20). The decline in elastic response generates localised damage and crack initiation (20). The strain level generated by rolling contacts declines with the distance below the surface (49). The degree to which the elastic response is maintained depends on physical factors such as the applied operating temperature, magnitude of

applied stresses, extent of load cycles, and material factors such as the steel type and alloying elements, heat treatment, and extent of residual stresses (20).

Classical fatigue results cannot be directly adapted for RCF life-calculation which makes RCF challenging to predict. This results from significant differences between RCF and classical fatigue which are put forward as follows (20):

- RCF generates and occurs under multiaxial and complex stress conditions governed by Hertzian contact theory
- The hydrostatic pressure of lubricated nonconformal contact significantly contributes to the stress profile. This is in contrast to classical fatigue as it lacks the component of hydrostatic pressure
- Within a stress cycle the directions of stress axes are constantly changing leading to a continuous change in the planes of maximum shear stress in RCF
- In RCF the contact stress zone is highly localised; e.g., in bearings the contact width, typically, is in the range of 200-1000 μm
- The loading history at a certain point below the surface is nonproportional. In other words, the normal forces σ_x and σ_z are always compressive. However, the τ_{xz} has a trend as shown in Figure 3-3. Also, the rise and fall of the normal stresses do not coincide with that of shear stress (20).

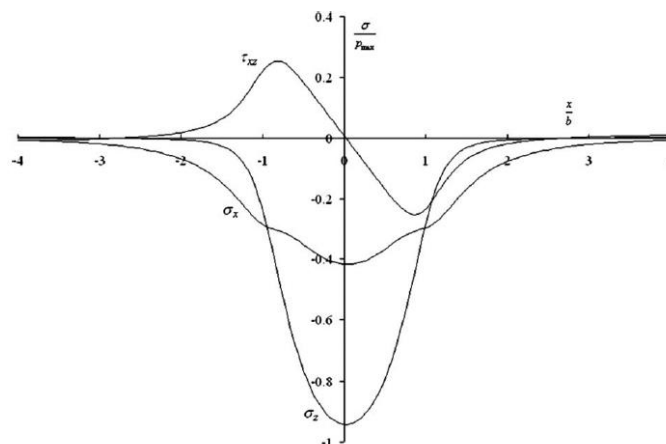


Figure 3-3. Stress history trend of a point below the surface in a Hertzian line contact (20)

A prevailing appearance in failed bearings used in wind turbine gearboxes is White Structure Flaking (WSF) (21). WSF obtained its name from the colour alteration of the cracked steel area to white, subsequent to material etching using Nital

(approximately 2% nitric acid in ethanol) (21). The formation of White Etching Areas (WEAs) and causing WSF is depicted in Figure 3-4 with a subsurface origin. At first the WEA are generated in steel at subsurface areas followed by WEC initiation and eventually WSF occurs as a result of crack propagation (21). WEA concurs with a microstructural change at the area of white appearance (21).

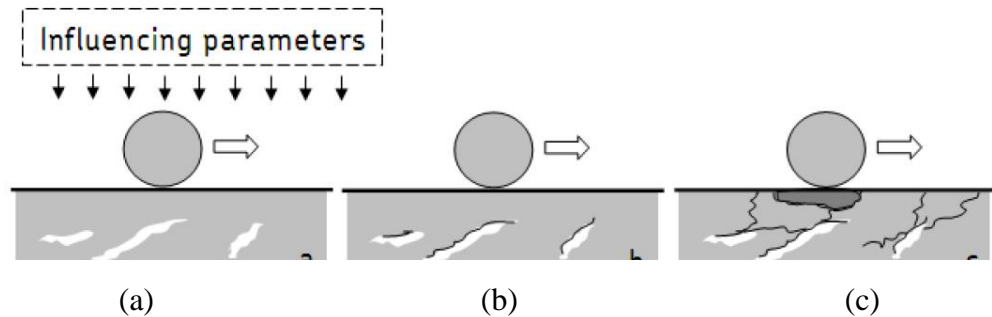


Figure 3-4. a) Formation of WEA induced by a microstructure change of that area b) crack initiation in WEA c) propagation of WEC and its progress to WSF (21)

Many factors have been reported to influence WSF (21):

1. Load and stress:

The type and extent of the load e.g. slip, vibrational stress, impact stress, stresses generated by local asperities and overload have been suggested to influence WSF.

2. Material:

The material's characteristics e.g. microstructure (martensitic, austenitic, bainite), residual compressive and tensile stresses, cleanliness (type and amount of inclusions), heat treatment and surface treatment have an important impact on WSF.

3. Lubrication and environment:

The type of lubricant and additives, operating and change of temperature, lubricant contamination (especially water introduced to the lubricant either by equipment cleaning or humidity), corrosion (standstill), hydrogen generated by lubricant decomposition and electrical current damage (shown in Figure 3-5) are postulated to be influential parameters in WSF phenomena.

4. Manufacturing and maintenance:

The quality of rolling elements in terms of the number of inclusions and surface homogeneity and smoothness, damages caused by transport, mounting of the bearing and misalignments are considered as important factors which influence WSF (21).

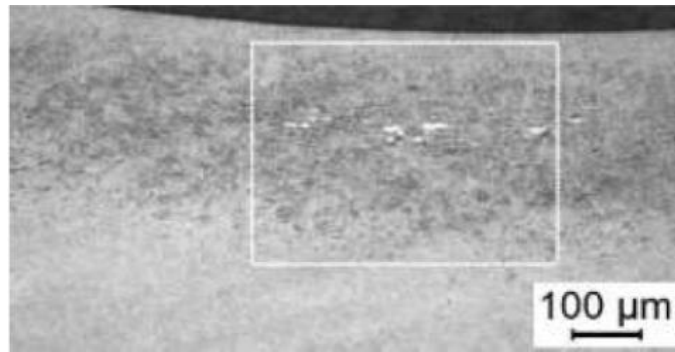


Figure 3-5. WEC induced by electric current (50)

Whether WSF originates from surface (51) or subsurface (52) initiated cracks is a subject of dispute between researchers. However, as the additive package prominently impacts the incipient WSF (53), it is conceivable to attribute the premature WSF of bearings to surface originated cracks (21). Thus, tribochemical factors to enhance WSF occurrence or retard WSF phenomena from happening should be considered for WSF investigations. Therefore, further experimental researches are required in order to clarify the influence of the additive package. WECs propagate much faster compared to classical fatigue cracks and the faster propagation is attributed to the chemical influences of lubricant contamination and additives (45). There are many reports (51-52, 54) showing that hydrogen-charged bearing steel undergoes WSF. Also, traces of hydrogen have been detected within many failed bearing crack paths (21). This postulates that diffused hydrogen into the steel causes premature failures. Therefore, it is generally believed that diffused hydrogen atoms in the steel bring about Hydrogen Embrittlement (HE) leading to the bearing's premature failure. Since hydrogen ingress into the steel takes place at the surface, surface initiated cracks (micropits and spalls) profoundly influence HE. Thus, a brief mechanistic introduction to HE is presented in this chapter.

3.2.1 **Hydrogen embrittlement and white structure flaking**

As a general term HE describes premature failure of a metal which is induced by hydrogen diffusion into the metal. The diffused hydrogen prompts a deleterious effect on metals by two general mechanisms (55):

- Hydride formation: some metals are capable of forming stable hydrides triggered by stress-induced hydride formation such as: niobium (Nb), zirconium (Zr), titanium (Ti), and vanadium (V). The formed metal hydrides are brittle leading to strain or stress-induced premature failures. At higher

hydrogen concentrations (above the solubility threshold) the hydrides precipitate on slip bands causing severe cleavage.

- Non-hydride forming metals: metals such as Fe (and steel as its alloy) and nickel (Ni) usually fracture earlier through enhancing decohesion of the grains and localised plasticity when hydrogen ingresses into the metals.

3.2.2 Hydrogen embrittlement mechanisms in bearing steels

- HE through Hydrogen-Enhanced Localised Plasticity (HELP)

Louthan, Caskey and Donovan (55) for the first time reported hydrogen interaction with dislocations. It is known that hydrogen travels to the crack tips and lattice strains since the local stress field is strengthened near to the crack tip. Due to high hydrogen concentrations around the lattice strains, the slip line becomes planar containing high shear strains around the slip plane (55). As reported by Ulmer and Altstetter (56) hydrogen induces strain localisation which is generated by slip localisation (57). Figure 3-6 shows that the rate of fatigue crack growth is greater in hydrogen environment compared to the crack propagation in helium environment. Also, a lesser number of slip planes can be observed for the sample in hydrogen environment.

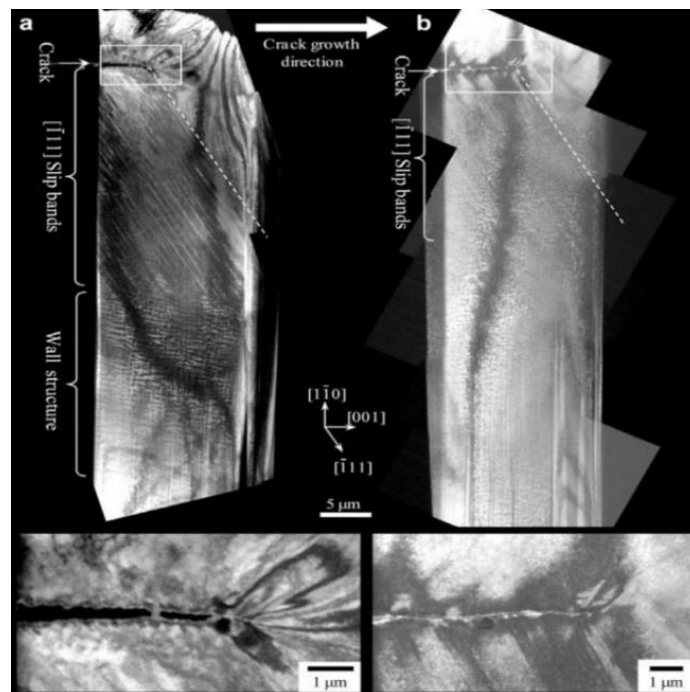


Figure 3-6. High voltage TEM cross-section images of fatigue crack tip. Left and right images show crack in helium and hydrogen environments respectively (57)

Accumulation of hydrogen atoms around the dislocations (as a high shear strain area) forms a Cottrell atmosphere around the dislocation and decreases the stacking fault energy (55). The pinned dislocation by diffused hydrogen into the dislocation gap, will migrate to the low-stress areas (55). The enhanced local-mobility of dislocation elicits local softening and plasticity leading to premature failure (58). The literature shows accelerated fatigue crack growth for hydrogen charged steel and Fe (57, 59). However, the extent of overall slip per load cycle is decreased due to the slip localisation around the crack giving rise to quasi-brittle crack growth (57).

- HE through Hydrogen-Enhanced Decohesion (HEDE)

HEDE postulates that hydrogen atoms absorb to the grain boundaries and strained regions resulting in a locally reduced atomic and lattice bonding energy (60). The declined bonding energy lowers the stress which is required to initiate a crack. It is shown that the crack tip opening angle decreases significantly (60) where higher hydrogen pressure is applied to Fe-2.6%Si alloy as a result of low energy required to initiate a crack. As a result, a cleavage fracture is encountered lacking a ductile fracture as can be seen in Figure 3-7.

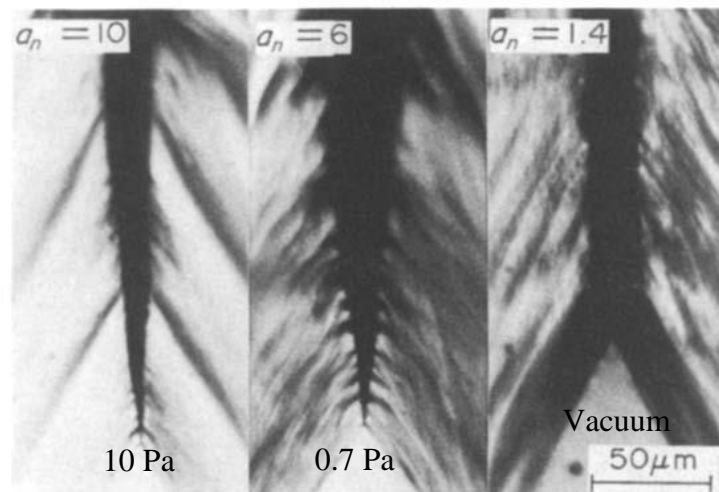


Figure 3-7. Optical micrograph of the crack tip of a strained sample at different hydrogen pressures (10 Pa, 0.7 Pa, vacuum) (60)

- HE through Hydrogen-Enhanced Strain-Induced Vacancy formation (HESIV)

HESIV postulates that hydrogen absorption promotes formation of nanovoids and vacancies under strain (61). As a result, butterflies and initiation of WECs will be enhanced. In this proposed mechanism slip localisation induces a ductile fatigue crack growth (61). Hydrogen stabilises the formed vacancies promoting crack initiation and

consequently the steel fails under ductile fracture (61). In Figure 3-8 a butterfly crack accompanied with a white structure area has been shown that is originated from a void inside the bearing steel. Premature failure is brought about by enhancement of the crack nucleation from defects (61).

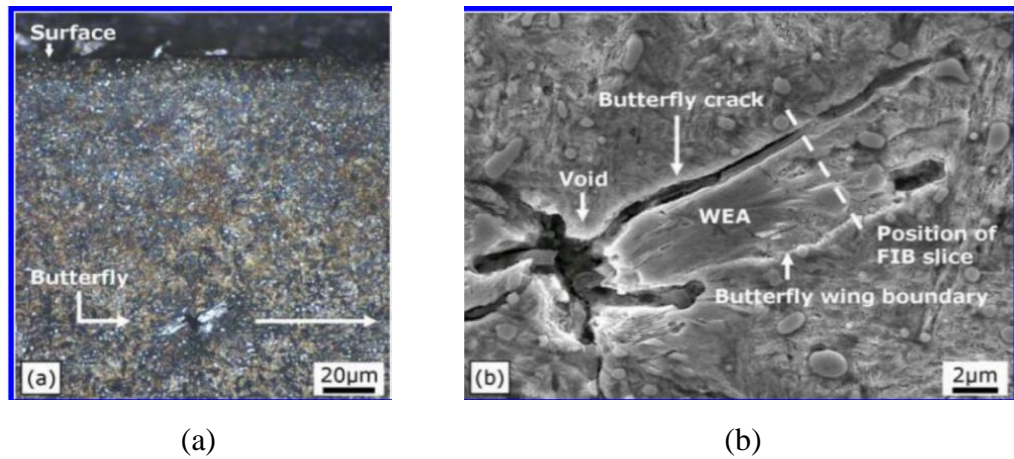


Figure 3-8. a) Optical and b) SEM images of a butterfly and WEA originated from a void (62)

- HE through Microstructural change and crack propagation

Hydrogen diffusion impels microstructural changes in the bearing steel (21). Fujita, Matsuoka and Murakami (59) employing Scanning Ion Microscopy (SIM) techniques showed that the martensitic structure of the hydrogen-charged bearing steel under cyclic torsion stresses deforms to a fibrous microstructure, as presented in Figure 3-9.

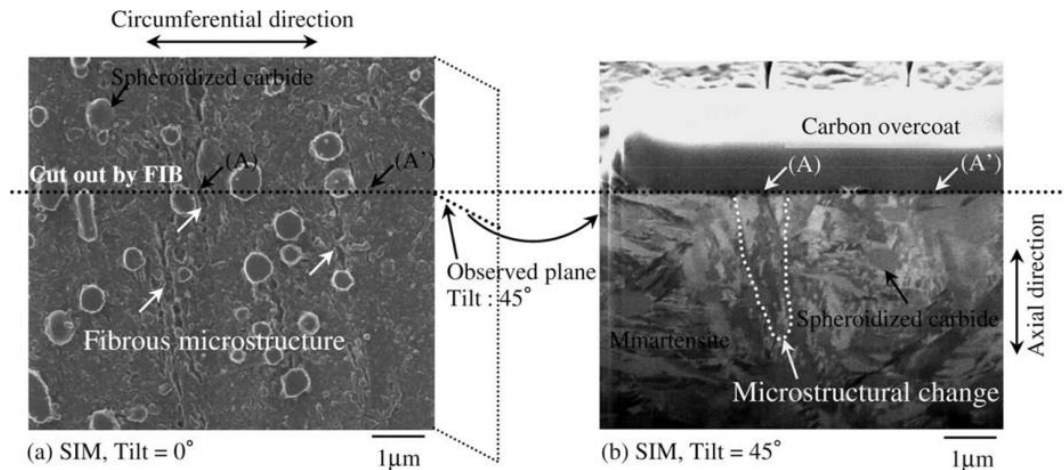


Figure 3-9. SIM images of the a) circumferential and b) cross-section of hydrogen-charged 52100 steel on which cyclic torsion and static compressive loads are applied (59)

The tribochemical impact of additives and/or lubricant, complexity of operation conditions (slip, idling, running-in and sliding) and microstructural complexity of

steel make it difficult to attribute a particular mechanism as the root cause of HE. WSF can occur within 5%-10% of the calculated life span indicating its complexity (21). Characteristics of WEC depend on the heat treatment of the material although WEC appears to happen in steels used in bearings regardless of the applied heat treatment (21).

As shown in Figure 3-10, the WEC is likely to grow axially in a martensitic structure, while in bainitic and carburised case-hardened, WEC propagates circumferentially (21). Also, the WSF occurs almost in all types of bearing configurations such as tapered, spherical, and cylindrical bearings (21). Moreover, there is a correlation between size of the bearing ring and premature failure. Slip and sliding between cage and roller elements take place more frequently in larger bearings resulting in deeper radial cracks in larger bearings under even moderate loads (63).

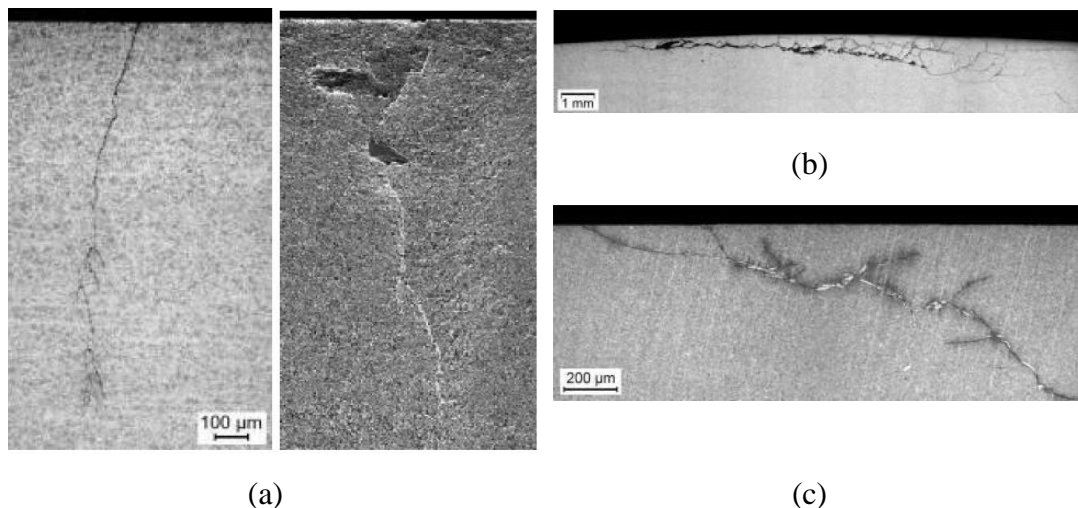


Figure 3-10. Micrographs of WEC propagation pattern in a) martensitic b) bainitic c) case carburised steels (21)

It has been postulated that WECs are generated within transient (short time) loading conditions in which high traction and contact pressures (up to 3 GPa) take place (21). In this transient period the overload and traction propel the lubrication regime to mixed lubrication regime. At the mixed regime surface cracks are initiated and lubricant and additives are forced inside the crack by capillary and hydraulic pressure effects leading to accelerated crack propagation (21). The penetrated lubricant and additives react with nascent crack surfaces and trigger corrosion fatigue crack propagation and HE by tribochemically-induced atomic hydrogen generation (21). This mechanism is schematically illustrated in Figure 3-11.

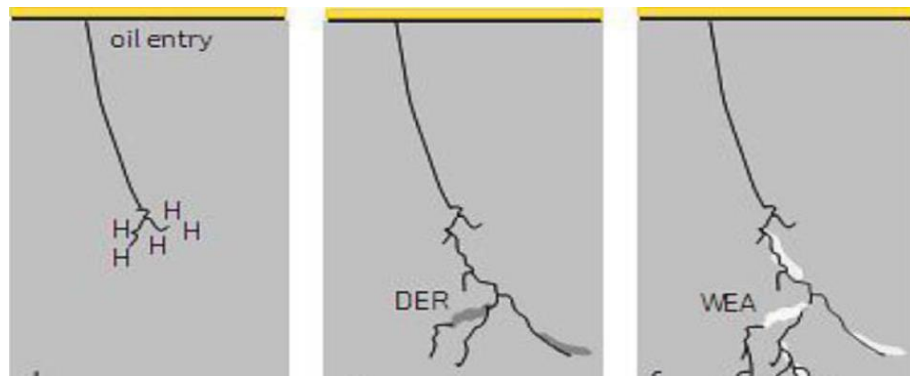


Figure 3-11. Schematic of WEA formation (21, 64-65). H and DER stands for atomic hydrogen and dark etching region respectively

3.3 Tribochemical influence of lubricant additives on fatigue and pitting life of the bearings

AW and EP (S-P compounds) additives are essential and beneficial in highly loaded gears and bearings in order to reduce scuffing and control abrasive and adhesive wear (66-68). It has been shown that AW and EP additives can improve fatigue life (67, 69-70) at low concentration (70) especially at large contact pressures (71-72). In contrast, there are reports showing S-P containing additives can be detrimental to fatigue life of bearings (19, 70, 73-76). The reduced rolling fatigue life has been suggested to be due to the chemical attack of the reactive additives which can induce crack or pit nucleation (19, 70, 73, 77).

Hong, Huston and O'Connor (67) carried out experiments using a *Forschungsstelle für Zahnrad und Getriebebau* (FZG) gear test with an initial running-in stage and investigated the effect of AW and EP additives on the gear life at two different contact pressures. The results are shown in Figure 3-12 which indicate that at a contact pressure of 1.52 GPa, elimination of the EP additive did not influence the fatigue life significantly, while fatigue life of the gear decreased dramatically by 83% by removal of the AW additive.

The influence of EP at a contact pressure of 1.86 GPa is more pronounced and removal of EP resulted in a decrease of fatigue life by 25%. Similarly, the elimination of the AW additive reduced the fatigue life by 75% when the contact pressure was 1.86 GPa. The inspection of the gear surfaces showed that in lubricants 1 and 3 where an AW additive was present the dominant fatigue mode was micropitting, while in the absence of AW additives in lubricants 2 and 4 the dominant fatigue mechanism was

spalling. The results exhibit the profound importance of AW additives in gear applications.

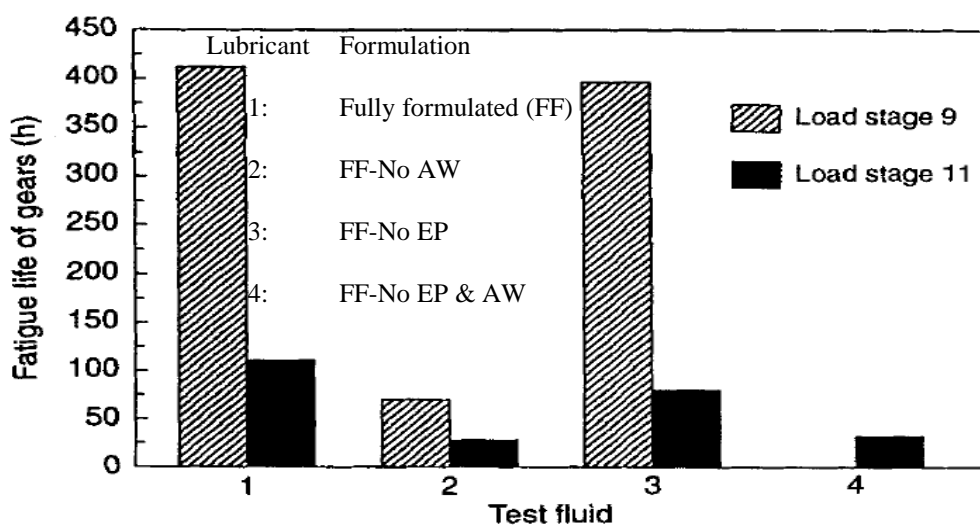
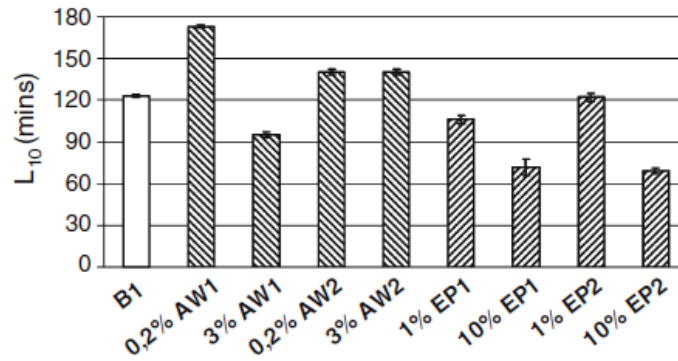


Figure 3-12. Investigation of AW and EP influence on the fatigue life of gears using FZG gear tester at 100°C. Load stages 9 and 11 resemble Hertzian contact pressures of 1.52 and 1.86 GPa respectively (67)

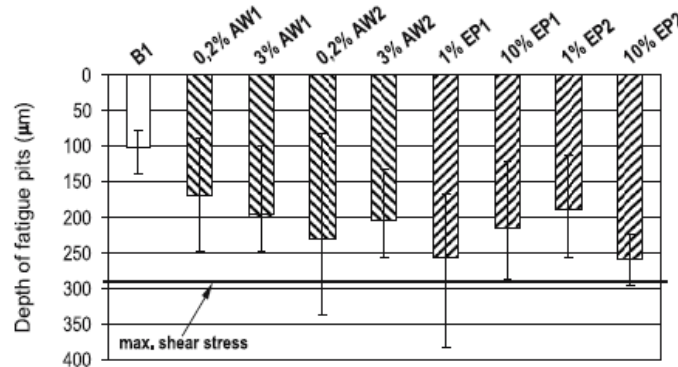
Tuszynski (70) examined the effect of two AW additives based on ZDDP and two EP additives which were organic S-P compounds at different concentrations on the fatigue life of the bearing steel using a four-ball tester. As shown in Figure 3-13, AW1 additive at a very small concentration of 0.2% improves the fatigue life, while increasing the concentration to 3% drastically deteriorates fatigue life.

EP additives at low concentration (1%) did not influence the fatigue life by high factors, while at high concentration (10%) significantly accelerated pitting occurrence. Also, the AW and EP additives tend to increase the fatigue pit depth with the highest influence observed for the EP additives. The detrimental impact of EP additives on the fatigue life was attributed to high chemical aggressiveness which leads to surface corrosion and generation of numerous depressions and micropits. Also, it is suggested that interactions of EP additives with crack faces give rise to crack propagation (70).

Trivedi, Forster and Rosado (72) investigated the effect of TCP AW additive on the fatigue life of four different bearing steel types using a ball-on-rod RCF tester in which the specimen, which is in rod configuration, is in contact against three silicon nitride balls. The tests were carried out under extremely severe contact pressure of 5.5 GPa and temperature of 177°C and the results are shown in Figure 3-14.



(a)



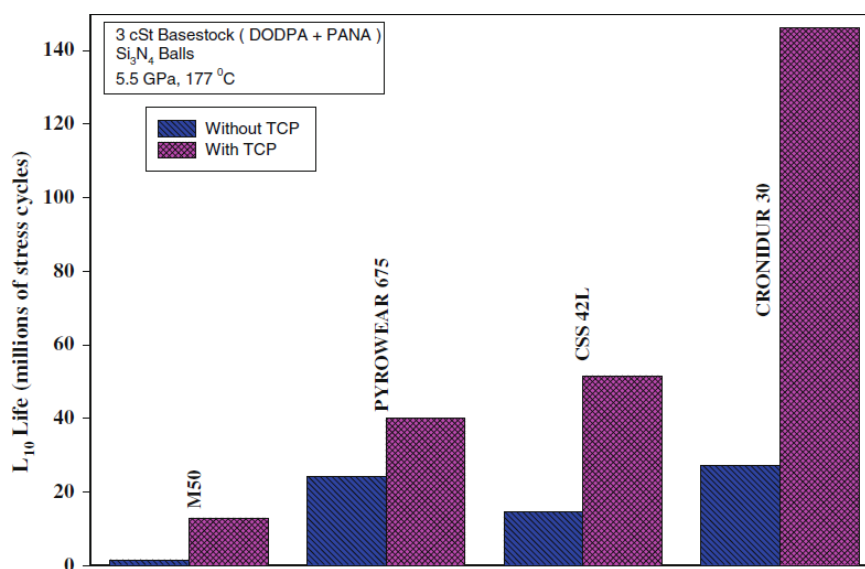
(b)

Figure 3-13. The influence of AW and EP additives and their concentrations on a) L₁₀ fatigue life b) the depth of fatigue pits. The results are attained using a four ball tester and B1 is a mineral base oil (70)

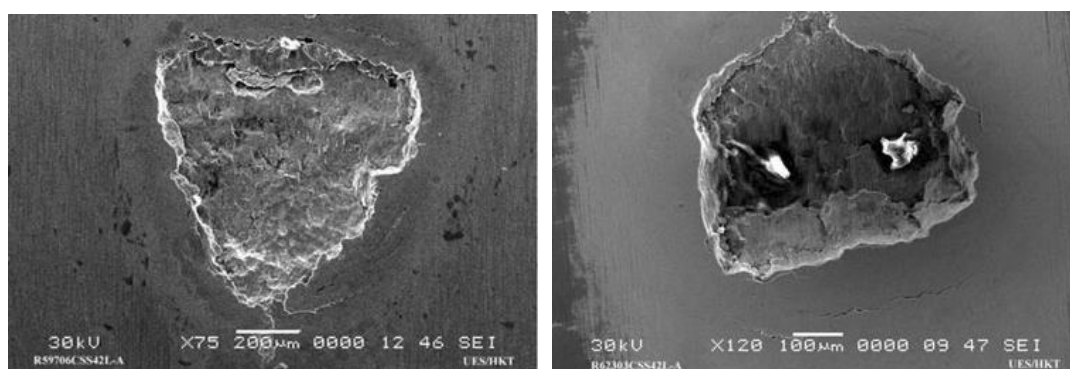
Although the appearance of the fatigue spalls is not affected by TCP, the fatigue lives of the different bearing steels, which were investigated in the report by Trivedi *et al.* (72), have been improved considerably. The most modest improvement in the fatigue life has been observed for Pyrowear 675 bearing steel. Also, it has been shown that CSS 42L and Pyrowear 675 steels having higher alloying contents (Mo, Cr and Ni) exhibit superior RCF performance over M50 steel due to the greater resistance to microstructural damage. The best RCF performance, obtained by Cronidur 30, was attributed to the reduced carbide formation in size and extent which is achieved by use of N and the modified processing.

Wang, Fernandez and Cuervo (69), using a four ball machine, showed that addition of 2% of ZDDP to a polyol ester base oil improved the fatigue life of 52100 bearing steel by a factor of two. The efficiency of ZDDP is ascribed to its action on reducing stress concentration at the asperities achieved by the reaction of ZDDP with steel surfaces. In contrast to the reports in support of the efficiency of AW and EP in improving the bearing fatigue life, Torrance, Morgan and Wan (19), Wan (74),

Nixon (78) and Pasaribu and Lugt (76) exhibited evidences that the EP and AW do not essentially enhance the fatigue life, but also can be detrimental under certain conditions.



(a)



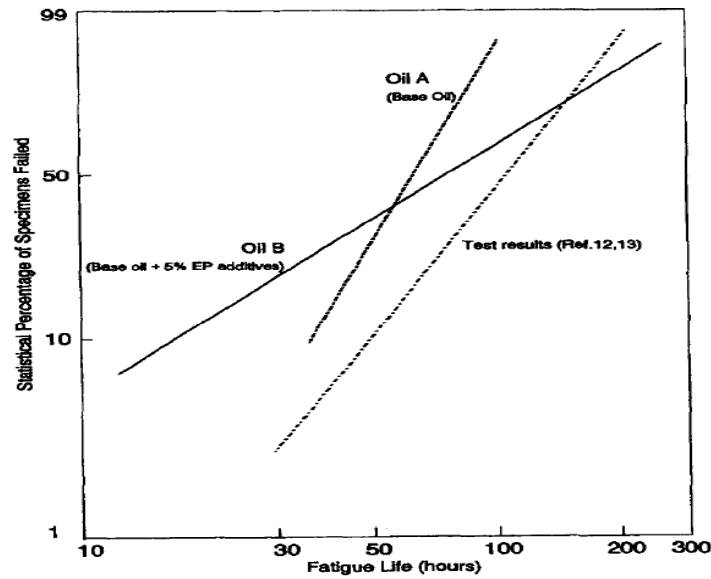
(b)

(c)

Figure 3-14. a) The influence of TCP AW additive on the fatigue lives of different bearing steels. SEM images of fatigue spalls on the surfaces of CSS steel lubricated b) without and c) with TCP in the lubricant formulation. Dioctyl-diphenyl amine and phenyl- α -naphthyl amine are antioxidants blended to a synthetic polyol ester at 1% concentration each for all the tests (72)

Torrance (19) examined the effect of a commercial S-P EP additive at a concentration of 5wt% using a RCF tester in which six balls are in contact against a rotating tubular specimen which is a ground unpolished NU 305 ring, under a contact pressure of 4.8 GPa in almost pure rolling condition. The test temperature was stabilised at 60°C. The EP additive (oil B) is shown to reduce the Weibull slope and thus the L_{10} fatigue life by almost two thirds, while providing similar L_{50} fatigue life as shown in Figure

3-15. The EP additive protected the surface against wear while induced spalls and micropitting on the surface of the raceway.



(a)



(b)

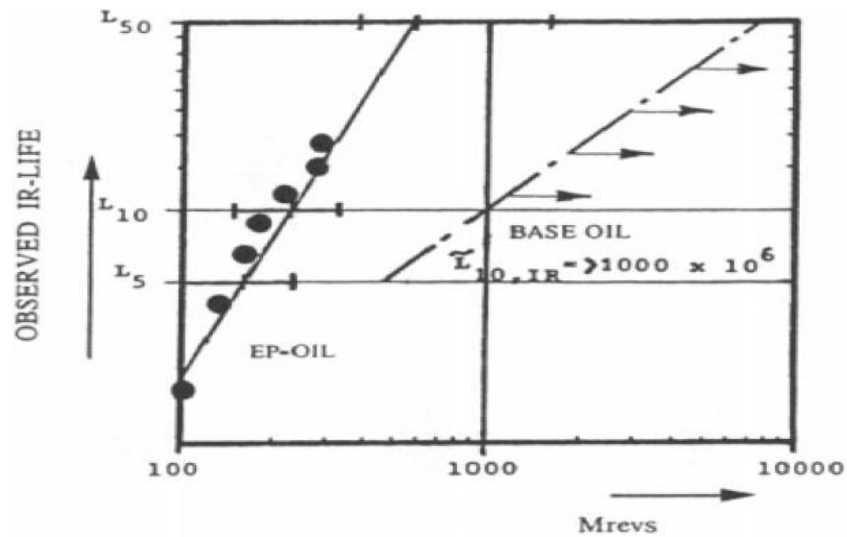


(c)

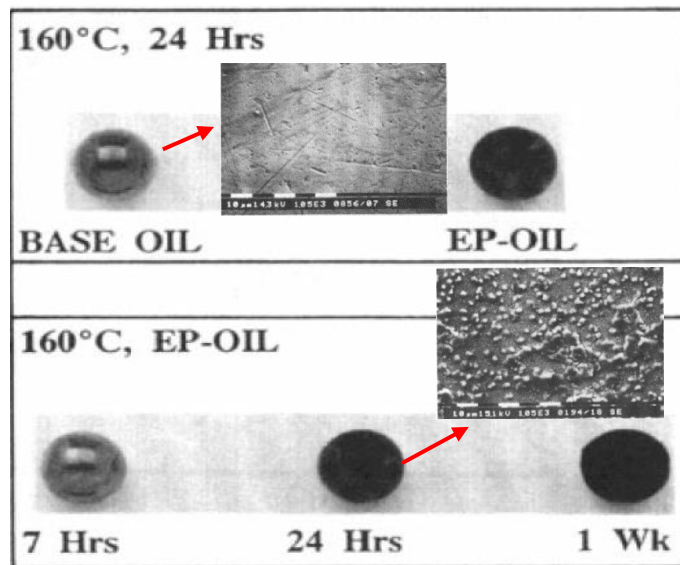
Figure 3-15. The influence of a commercial S-P EP additive at concentration of 5 wt% on fatigue life. The EP additive a) reduced L_{10} life by a factor of three in the Weibull statistical plots and b) enhanced the formation of multiple spalls and c) cracks accompanied with micropitting (19)

The detrimental influence of the EP additive is attributed to its chemical attack on surfaces generating tiny depressions on the surface. The depressions are associated with micropits which act as nuclei for pitting and a subsequent early fatigue failure known as corrosion-enhanced fatigue (19). Therefore, the reduction in mechanical distress (as a result of asperity-asperity contacts) is achieved by the compromise of a significant increase in chemical distress. Furthermore, the detrimental effect is witnessed to be more pronounced in lower contact pressures and higher temperatures (73). Wan, Amerongen and Lankamp (73) studied the effect of a S-P EP

additive at a concentration of 5% on the fatigue life of deep-grooved ball bearings under a contact pressure of 3.3 GPa on an inner ring at a lubricant temperature of 85°C and lambda ratio of 1.2 indicating a mixed lubrication regime. In this case the Weibull slope for the EP additive was more than twice the slope for base oil lubricated bearing and L_{10} fatigue life is reduced by a factor of at least 4.5 by the EP additive as shown in Figure 3-16.



(a)



(b)

Figure 3-16. Evaluation of EP influence on the bearing fatigue life. a) Weibull statistical plots for fatigue life and b) surface deterioration in the immersion test (73)

The static immersion of the 52100 steel balls at 160°C showed a discoloration of the ball surface after 24 hours in the presence of the EP additive. The SEM-EDX analyses

of the ball surfaces showed a reaction film on the surface rich in S and P. The high reactivity of the EP additive on the surface especially at the zones of high strain energy is suggested to be the reason of the EP's detrimental effect on the fatigue life. In another work, Wan (74) explored the influence of Di-Phenyl Phosphonate (DPP) additive blended to a base oil at a concentration of 0.3 vol% under 3.4 GPa of applied contact pressure producing a lambda ratio of 2.1 with an oil inlet-temperature of 60°C using a Polymet fatigue tester. The results are shown in Figure 3-17 indicating that DPP although is blended in a small concentration decreases the L₁₀ and L₅₀ fatigue lives by a factor of about five and three, respectively, in comparison to the fatigue lives with base oil. The reduced fatigue life is caused by enhanced pitting and tribochemical wear. Moreover, the Weibull slope has been reduced by almost 30% when DPP was present in the lubricant indicating a wide spread of bearing life.

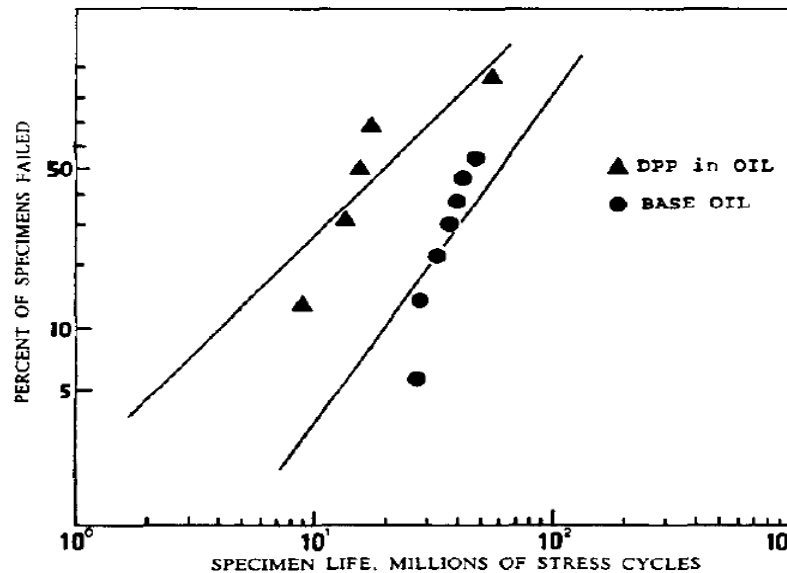


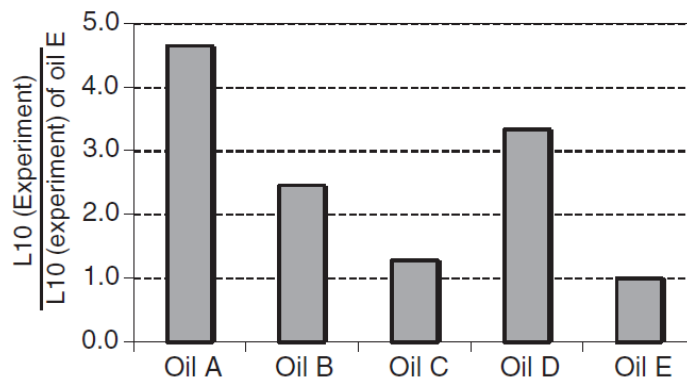
Figure 3-17. Evaluation of Weibull statistical fatigue life of DPP additive (74)

Pasaribu *et al.* (76) explored the performance of variety of commercial gear oils (indicated in Figure 3-18) having a similar viscosity under a mixed and/or boundary lubrication regime using spherical roller bearings mounted on a shaft and placed in an oil bath with an oil temperature of 90°C. At this temperature, the viscosity ratio was 0.4 to ensure the occurrence of metal-metal contacts between the rollers and raceway where use of EP additives is essential and reaction of AW and EP additives with the bearing surfaces is stimulated. The tribofilms from the different lubricant formulations on the surfaces of the inner ring of bearings were evaluated by secondary neutral mass spectrometry after 15-hour tests. The results disclosed that the best performing oil (Oil A) induced a tribofilm having an extensive concentration of O and

minor concentration of S and P. In contrast to that, the tribofilm formed from the worst performing oil (Oil E) consisted of a significant concentration of S and a low concentration of O. The enhanced performance of Oil A is attributed to high O concentration associated with a thick iron oxide layer which passivates the surface and decays the further adverse chemical attacks. Furthermore, it is suggested that S and P in the reaction layer can deteriorate the surfaces leading to a surface which is more prone to premature failures.

Lubricant	Base oil	AW-EP additive
A	PAO	Complex S-P additives
B	Polyglycol	Complex S-P additives
C	Mineral	P additives
D	PAO	ZDDP
E	Mineral	Complex S-P additives

(a)



(b)

Figure 3-18. Evaluation of the influence of different lubricant additives on the bearing fatigue lives in spherical roller bearing fatigue tests. a) the lubricant formulations used in the tests and b) Weibull statistical fatigue lives for the different lubricant formulations (76)

The results projected in the current section reveal that the additive package plays an important role in all aspects of wear performance in gears and bearings and detailed tribochemical studies of each individual additive and their interactions are required.

3.4 Micropitting

Micropitting is a prevalent Hertzian surface fatigue which is encountered locally on the surface of bearings and gears under certain conditions. Micropitting starts with a

crack initiation on the surface and is accompanied with a crack propagation into the bulk of the material (79). The propagation of cracks is shown to pursue opposite to the sliding direction into the material bulk (80) to a certain depth or length after which it can branch to the free surface that causes material removal (44). The surface initiated crack is reported to propagate at a shallow angle of 15° - 30° which is called the crack declination angle (44). Depending on the growth extent, the material removal can be categorized as micropitting, macropitting and eventually spalling in bearings or pitting in gears. A large spall or a matrix of several spalls leads to bearing failure which requires the replacement of the bearing. Micropitting adversely alters the surface geometry resulting in significant rises in the edge stresses and internal clearance which propel micropitting rapidly towards macropitting and subsequent bearing failure (3). The micropitting, macropitting and spalling features on the surface of roller element bearings are shown in Figure 3-19.

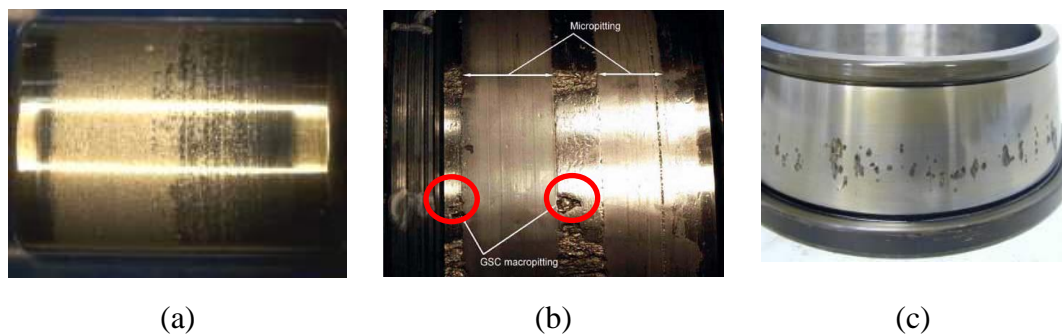


Figure 3-19. Damage features in the roller element bearing components a) micropitting (24) b) micropitting and macropitting (81) c) spalling (24)

Micropitting in gears occurs above and below the pitch lines both on the driving and driven gears. However, the extent of the micropitting differs from dedendum to addendum as the major micropitting occurrence has been observed often on the dedendum of the driving gear (82). However, in some cases micropitting has been observed only on the addendum (5).

As shown in Figure 3-20, the cracks on the driving gear (pinion) are orientated towards the pitch line, while cracks are aligned away from the pitch line on the driven gear (wheel) (81). This shows that in gears micropitting propagates opposite to the sliding direction. Micropitting in gears induces tooth profile deviation leading to an increase in noise, vibration and heat generation which requires gear replacement in some cases after as low as a million contact cycles.

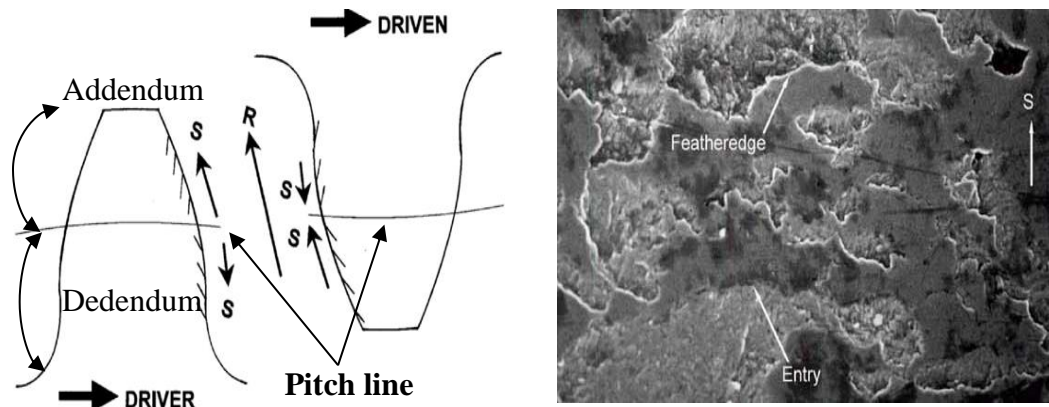


Figure 3-20. Micropitting in gear teeth and corresponding SEM image (81)

3.4.1 Micropitting mechanism from a metallurgical standpoint

From mechanical and metallurgical points of view one of the aspects that has uncertainties around it is that after a certain depth of crack propagation into the material bulk, the crack inclines back to the free surface which generates material removal. This has been ascribed to the affinity of crack propagation along the slip bands which are oriented towards the surface by dislocation's motion (80) as presented in Figure 3-21 (a). Also, cracks can grow towards the surface along the grain boundaries (Figure 3-21(b)) and on the interfaces of the non-metallic inclusions (Figure 3-21 (c)) (80), although inclusions and grain boundaries are not essentially involved in the case of surface-initiated cracks.

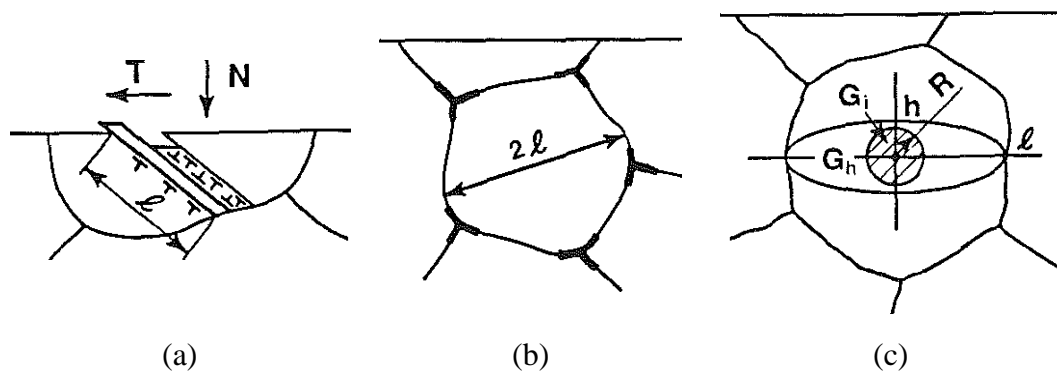
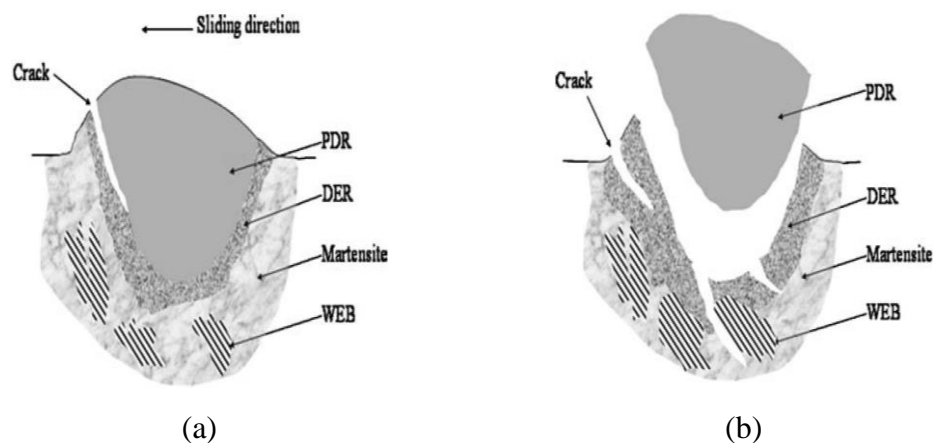


Figure 3-21. Crack initiation and growth along a) slip bands b) grain boundaries and c) interface of inclusion (80)

In through-hardened or carburised-quenched martensitic steels, micropitting is accompanied with microstructural changes in the near-surface and bulk material which are recognised to be the micropitting's main-derivative from a metallurgical point of view (79). Oila and Bull (79) showed a Plastically Deformed Region (PDR) within the area close to the surface which does not show the needle-shaped

characteristics of the martensitic phase. PDR is semi-circular in shape which is surrounded by a Dark Etching Region (DER) which is originated from prior austenite grains. PDR is induced by asperity-asperity contacts and is much harder than the martensitic matrix due to the work-hardening occurred by escalated dislocation density and temperature-induced C diffusion from carbides to the matrix. The C diffusion stimulates a re-crystallisation at the PDR boundary which generates DER with a relatively lower hardness in comparison to PDR (79). A slip band generated at this boundary favours the crack initiation and propagation along the PDR boundary. This mechanism is schematically shown in Figure 3-22 including the hardness of different microstructures after experiment. Contact cycles are essential to enhance the dislocation pile-up which results in escalated crack initiation and propagation. Since the PDR region is a semi-circular and the crack propagates along the boundary of PDR, the crack will incline back to the free surface and generate a micropit.



Microstructure	Martensite	PDR	DER	WEB
Approximate Hardness (GPa)	8	13.7	12.3	11.6

Figure 3-22. Schematic illustration of the mechanism of micropitting incident in martensitic steels and hardness values associated with the different microstructures which occur with micropitting. a) Micropitting initiation and b) micropitting propagation (79)

The DER formation and corresponding martensitic decay have been observed previously in other reports (83-84). The hardness measurements using Vickers microhardness analysis suggested an inferior hardness of DER compared to that of martensitic matrix (84). A maximum decrease of around 20% from an approximate hardness of 875 Hv to an approximate hardness of 675 Hv after 10^9 contact cycles is reported (84). Two influencing parameters in microstructural changes and

corresponding micropitting are load and extent of contact cycles. An increase in load seems to accelerate the microstructural decay (84) under certain conditions and an increase in contact cycles up to a certain extent enhances the DER formation (85) as shown in Figure 3-23.

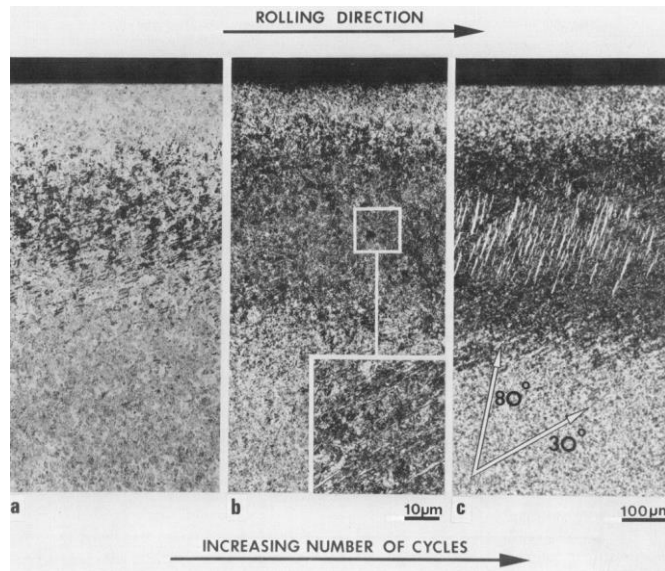


Figure 3-23. DER evolution over contact cycles (84)

Johansson, Devlin and Prakash (85) also employing Vickers microhardness reported a maximum decrease of hardness by ~40% in the DER after $\sim 165 \times 10^3$ revolutions using a four-ball tester. They observed the DER at the same depth as the depth of the maximum orthogonal shear stresses (85) having the least hardness as shown in Figure 3-24.

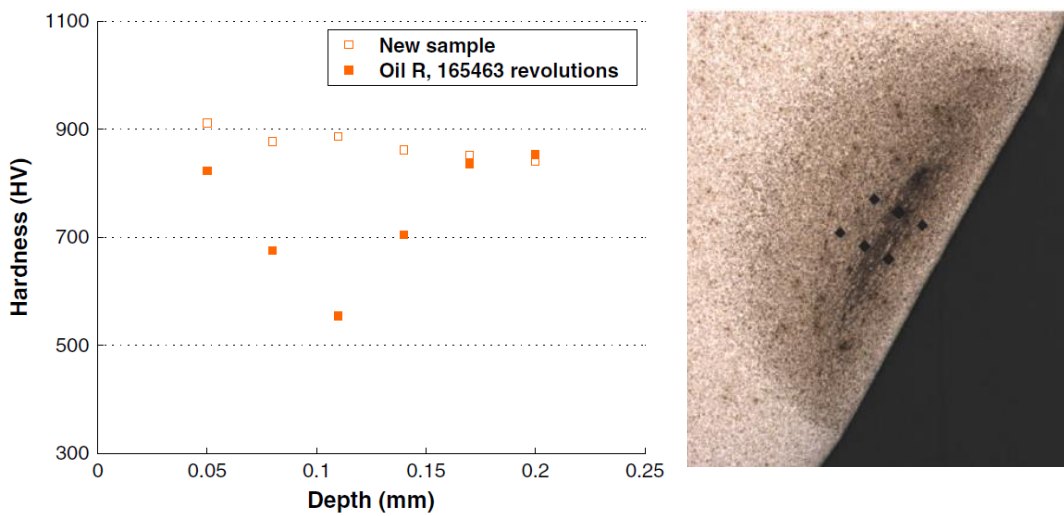


Figure 3-24. Hardness variation over depth after $\sim 165 \times 10^3$ revolutions and cross-sectional micrograph after 150×10^3 revolutions (85)

Johansson et.al observed a very rapid crack propagation, and thereby postulated that the life of the pitted ball is more controlled through crack initiation rather than crack propagation (85). These results are in contrast to the report by Oila *et al.* (79) showing greater hardness of DER with respect to martensitic matrix. They used the nanoindentation technique which is more accurate than microhardness. These controversial results suggest that the DER have grains with greater hardness which are embedded in a matrix of lower hardness.

The other proposed mechanism for micropitting propagation is the effect of hydraulic pressure of entrapped lubricant (or other fluids) inside the initiated cracks (44). This mechanism is illustrated in Figure 3-25. In this mechanism lubricant is necessary to induce the crack growth and the crack grows in the direction of loading (86). Hydraulic pressure of the trapped lubricant can cause mode I stress intensities at the crack tip (44, 87). It is also assumed that in order to induce a crack growth, the direction of the traction should be opposite to the direction of loading (88). The sliding along the rolling direction keeps the crack mouth open for the lubricant to enter (44).

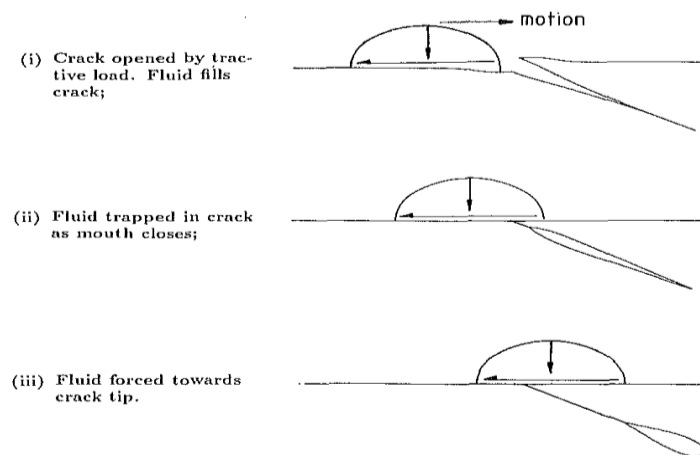


Figure 3-25. Influence of lubricant entrapment inside the crack on crack and micropit propagation (44)

3.4.2 Micropitting test rigs

Micropitting is a very complex phenomenon and is not well understood which makes it unpredictable. Moreover, micropitting happens in different applications and components (gears and bearings) which are operating in different conditions and a test rig which can emulate the different operational conditions is not available. Micropitting in wind turbine gearboxes has gained enormous attention due to its high importance (3) and a specific rig which can simulate all the rotation and sliding actions

in a wind turbine has not been yet developed. The majority of failures in wind turbine gearboxes earlier than their designed lifetime appear to originate from the bearings (2), even though the best bearing design is employed in the gearboxes. Three bearings exhibiting substantial failures in the wind turbine gearboxes are planet bearing, intermediate and high speed shaft bearings shown in Figure 3-26.

Three prevalently used rigs which have been commercially developed to evaluate micropitting include *Micropitting Rig* manufactured by PCS Instruments, *Wedeven Associates Machine* (WAM_{mp}), and FZG gear test (7) which are shown in Figure 3-27.

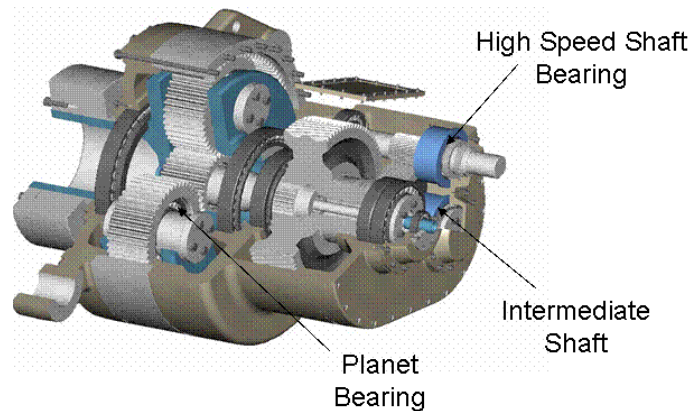


Figure 3-26. Schematic illustration of wind turbine gearbox indicating bearing positions (2)

Twin disc machines (also called two-disc or roller-disc machine) which consist of two rotating and in-contact discs have been also developed in laboratories to examine micropitting (15, 89). Furthermore, the four-ball tester (90) and the (thrust) bearing tester (38) have been employed to investigate the pitting and micropitting performances.

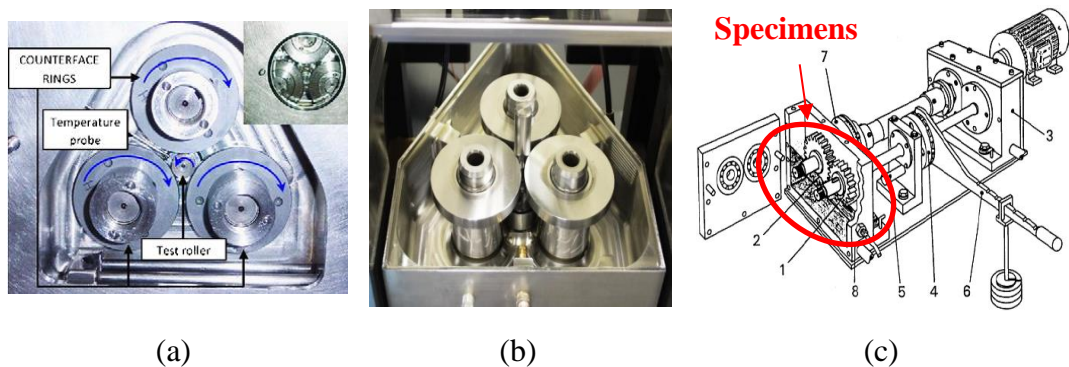


Figure 3-27. a) PCS Instrument MPR (8), b) WAM micropitting test machine (91) and c) FZG gear test rig (7)

3.5 **Parameters influencing micropitting**

The lubrication regime, type of additive package (5, 7-8, 18, 90, 92), contact pressure (93), surface roughness and topography (38, 94) and Slide-to-Roll Ratio (SRR) are among the factors which impact micropitting (15, 18).

3.5.1 **Tribological, mechanical and physical parameters**

It has been experimentally shown that as the lambda ratio drops to a certain value at which the asperities from contact bodies interact, micropitting is enhanced (8, 47). It is generally accepted that a decrease in the specific lubricant-film thickness (after a certain value) increases the probability of asperity-asperity contacts between contact bodies leading to accelerated micropitting (3, 47). This exhibits the rationale behind performing micropitting experiments in mixed and boundary conditions. However, some theoretical works (95-96) suggest that micro Elasto-Hydrodynamic Lubrication (micro-EHL) can propel the micropit initiation. Micro-EHL suggests that even in the conditions of full-fluid film lubrication, the surface roughness alters the local pressure distribution resulting in a significant rise in local pressure where the lubricant film is collapsed leading to the occurrence of surface fatigue (95).

Webster and Norbart (82) showed that at an approximately constant specific film thickness, an increase in contact pressure accelerates micropitting surface fatigue on specimens lubricated using two different lubricants containing EP and AW additives. However, they could not observe a significant improvement in micropitting associated with an enhanced λ ratio from approximately 0.9 to 2.3. The increase in lambda ratio is achieved through using a more viscous lubricant. This observation, however, is debateable due to two reasons. Firstly the increase in lambda ratio is not substantial and secondly the used lubricants contain additives which are active in both lubrication conditions to a different extent which certainly affects the results (97). An increase in contact severity through decreasing lambda ratio and consequent increase in micropitting is shown by Laine *et al.* (8).

Webster *et al.* (82) also investigated a SRR range of -20% to 20% and showed that under negative sliding micropitting was enhanced compared to positive sliding on the softer and slower contact-body, whilst the positive sliding induces minor micropitting on the harder and faster contact-body. These results suggest that micropitting is promoted on the slower contact-body, although the slower contact-body experiences

fewer stress cycles in comparison to the faster contact-body. The shorter fatigue life of the slower contact body has been shown in experimental works (82, 98). In the case of micropitting in the slower contact body, the lubricant hydraulic pressure mechanism (44, 99) supports the crack propagation opposite to the sliding direction as the tractive forces are in the favour of holding the crack mouth open as shown in Figure 3-28. However, this mechanism does not support the crack propagation opposite to the sliding direction in the faster contact-body as the crack tip confronts the compressive stresses resulted from Hertzian contact which promote crack closure and/or healing.

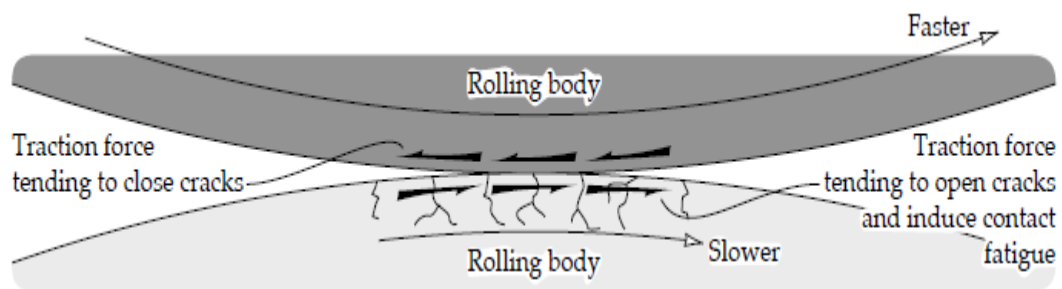


Figure 3-28. Traction forces in the rolling-sliding contacts (12)

Webster *et al.* (82) showed that at a SRR of just below -0.01 the micropitting was substantially decreased to almost no-micropitting level and wear track depth became dramatically small to an un-measurable level. This is despite the fact that the tractive force is almost the same as the tractive force in higher SRRs (shown in Figure 3-29) and surfaces undergo severe micropitting in SRRs of higher than -0.01. These observations imply that the tractive force is not the prominent parameter to influence micropitting.

However, Webster *et al.*'s observation of sharp transition from no or minor micropitting to a severe micropitting appearance just above SRR of -0.01 (82) does not comply with the recent findings by Kadiric and Rycerz (100). Kadiric *et al.* (100) showed that under controlled conditions an increase in SRR increases micropitting as a result of the increase in the number of stress cycles on a single asperity on the contact body during the contact passage. Therefore, in a condition that traction forces are within a similar range under different SRRs, a slight change in SRR from 0.0095 to 0.01 is not expected to influence micropitting to a significant extent.

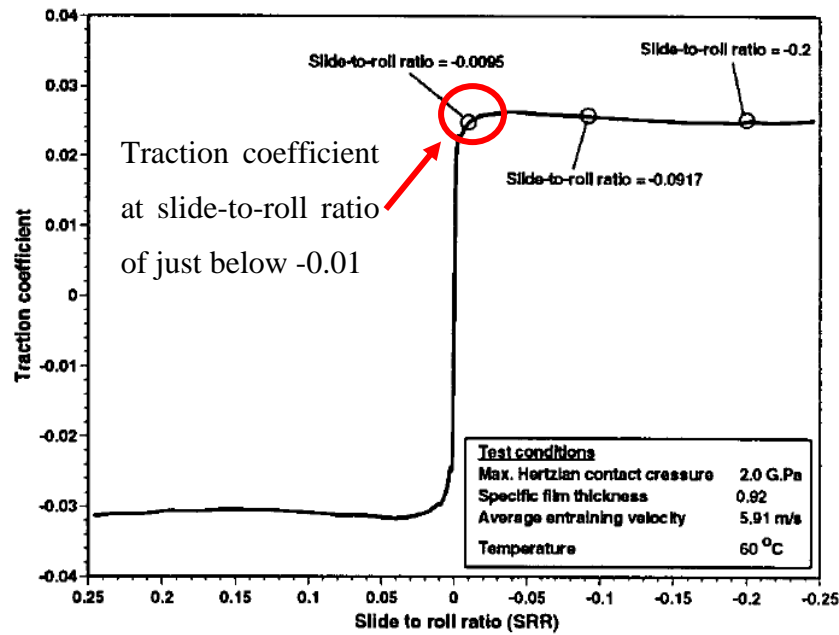


Figure 3-29. Traction curve measurement over different SRR under test conditions indicated inside the graph (82)

The effect of the material hardness is reported in a work by Olver and Spikes (101) which showed that the decrease in hardness, achieved by re-tempering the steel at higher temperature (290°C), significantly intensifies rolling contact wear. At a further step, reduction in the hardness of the counterbody (decrease in the hardness difference between contactbodies) attenuated micropitting. This phenomenon is well in agreement with the metallurgical observations suggesting that decay in the microstructure prompts micropitting. Olver and Spikes (101) showed that sliding distance does not considerably influence the wear rate (in contrast to Archard's law), when the body is slower than counterbody. This is an agreement with the observations of Cen (102), shown in Figure 3-30, where micropitting does not depend on the sliding distance. This shows that SRR and the extent of contact cycle have a pronounced influence on micropitting which are dominant over the effect of sliding distance.

The enhancing effect of SRR on micropitting, shown by Kadiric et al. (100), is applicable when the contact temperature, film thickness and other contact variables remained constant and can be controlled independently. However, in conditions where the change in SRR can alter other contact parameters such as contact temperature, the effect of SRR on micropitting is not conclusive and seems to be dependent on the other tribological factors and more importantly lubricant additives used to lubricate the contact.

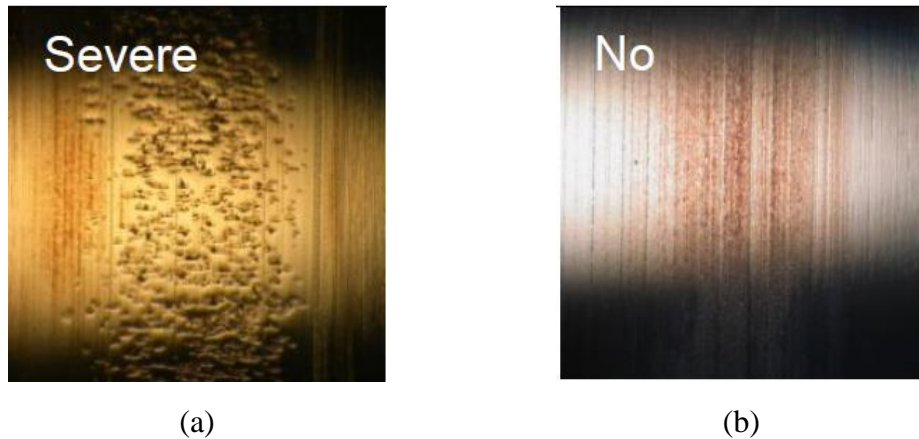


Figure 3-30. The effect of sliding distance on micropitting of rollers lubricated with PAO + ZDDP lubricant. a) Experiment under SRR of 0.5% after 7.2×10^6 contact cycles and b) experiment under SRR of 5% after 0.72×10^6 contact cycles (102). The optical images obtained from the work by Cen (102) do not have a scale bar. However, all images were taken using the same objective and magnification for a true comparison between the different test parameters

Oila *et al.* (15) assume that a higher SRR induces higher frictional forces resulting in greater heat generation and dissipation and hence accelerated martensitic decay which consequently enhances micropitting propagation. On the other hand, Morales-Espejel and Brizmer (47) experimentally and theoretically showed that an increase in SRR induces higher wear leading to removal of the fatigued layer on the surface which eventually will suppress micropitting propagation. These results are also confirmed by Cen's (102) work which is shown in Figure 3-31 for surfaces lubricated with PAO + ZDDP lubricant formulation under different SRRs.

As can be seen in Figure 3-31, while severe micropitting occurs under SRRs of 0.5% and 50%, little micropitting can be observed under a SRR of 2% and no micropitting under 5% of SRR. It should be noted that the micropit features under SRR of 50% are questionable which will be discussed more in detail in section 3.5.9.

However, as can be seen in Figure 3-32, this is not the case for all lubricants and in contrast to PAO + ZDDP lubricant, micropitting in a fully-formulated lubricant under a SRR of 2% is more severe compared to micropitting under 0.5% of SRR. The model developed by Morales-Espejel *et al.* (47), shown in Figure 3-33, predicts that the maximum micropitting surface area occurs under an approximate SRR of 1% considering the effect of wear on the removal of fatigued material on the surface.

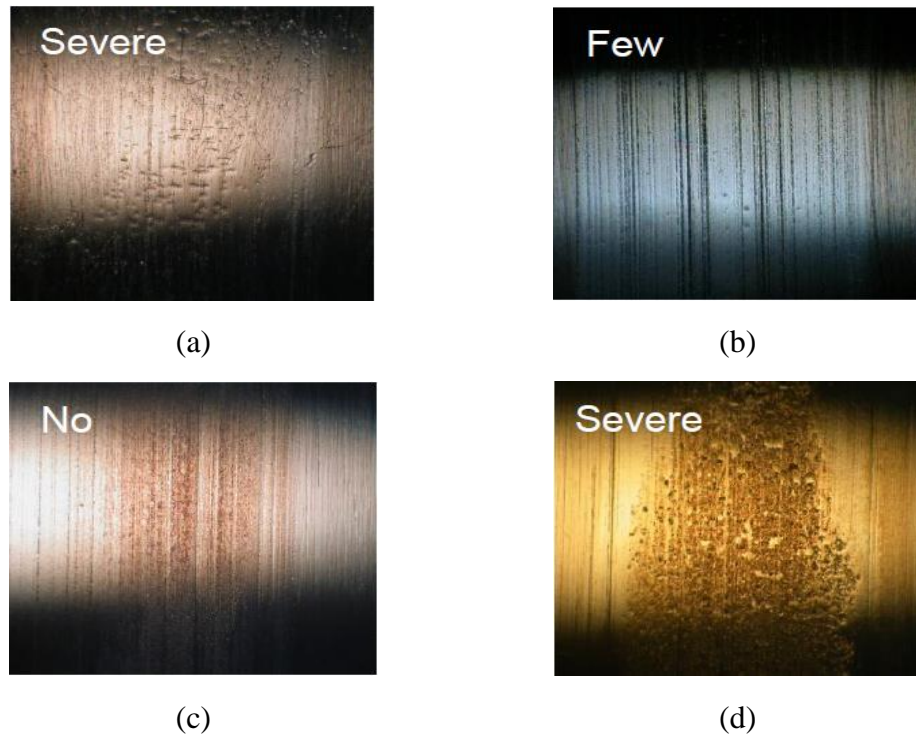


Figure 3-31. Micropitting performance of PAO + ZDDP lubricated surfaces of 52100 bearing-steel rollers after 72×10^4 contact cycles under different SRRs of a) 0.005, b) 0.02, c) 0.05 and d) 0.5 (102)

Spikes, Olver and Macpherson (101) reported that by increasing the contact pressure from 1.3 GPa to above 1.7 GPa, the wear rate significantly rises and pits appear on the surface. This may suggest that a minimum load can be considered for the onset of micropitting which is in agreement with the report by Mahmoudi, Hager and Evans (103) suggesting that micropitting occurs where the contact pressure is comparable to or greater than the material yield strength.

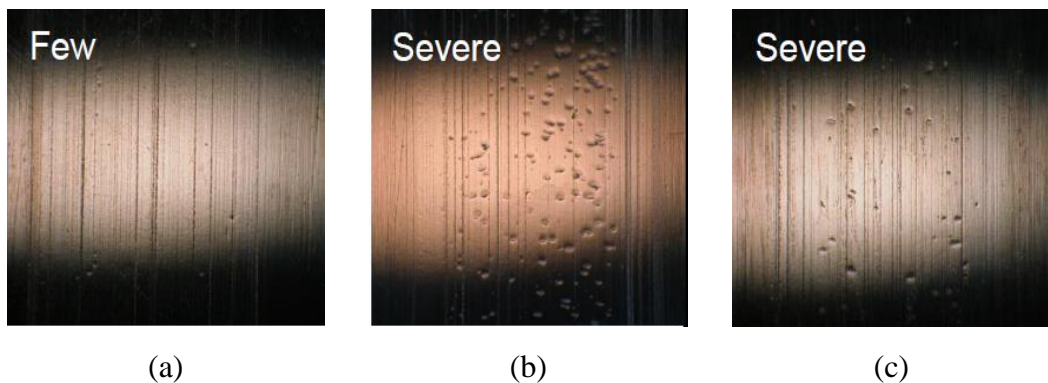


Figure 3-32. Micropitting performance of surfaces of 52100 bearing-steel rollers after 72×10^4 contact cycles lubricated with a commercial fully-formulated lubricant under different SRRs of a) 0.005, b) 0.02 and c) 0.05 (102)

Furthermore, the predominant action of contact pressure in micropitting initiation is reported by Oila *et al.* (15). They suggested that above a load threshold, mitigation of micropitting is strenuous and only improvement in the surface finish may alleviate micropitting.

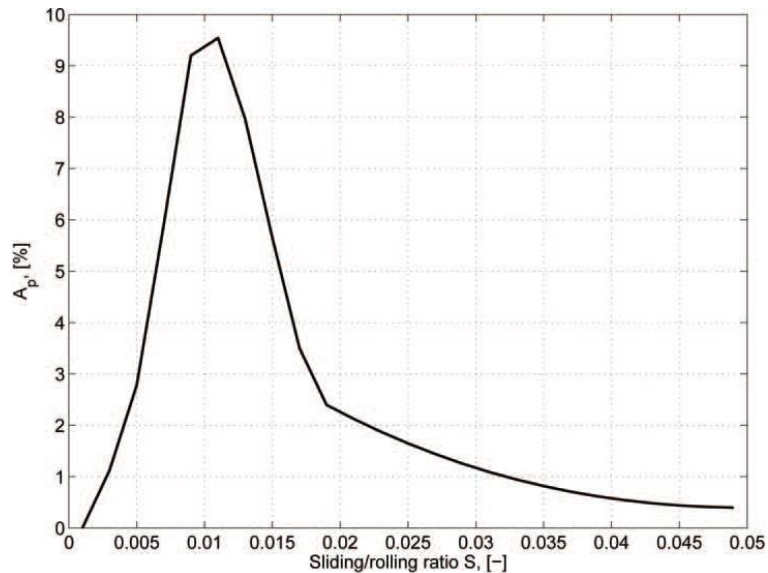
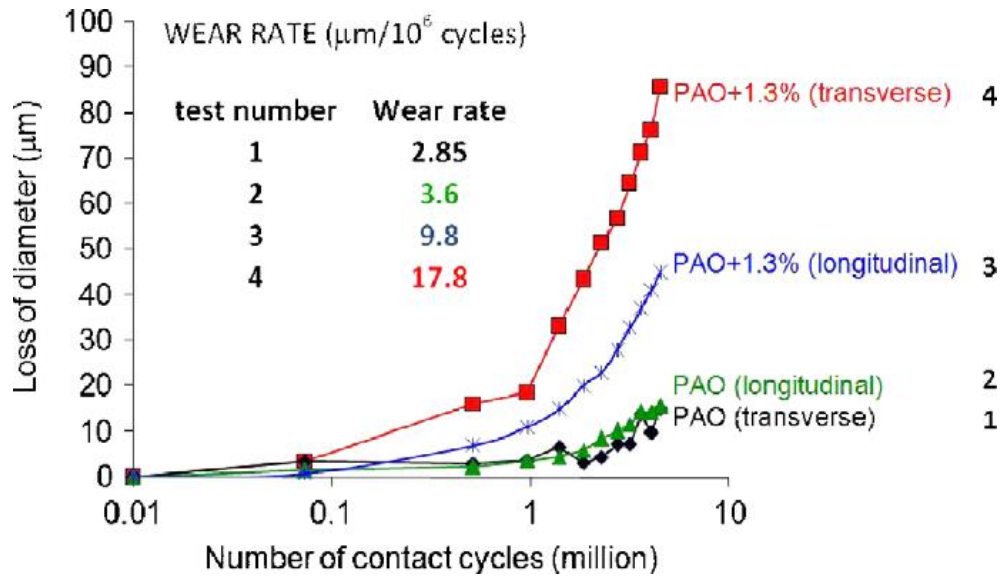


Figure 3-33. Model prediction of the effect of SRR on micropitting area ratio A_p [%] (47)

Roughness has a pronounced impact on micropitting (8). An earlier study (93) suggested that surface roughness, especially roughness characteristics after running-in, has a strong influence on the surface initiated fatigue damage to roller-element bearings. The roughness effect also is in line with the metallurgical observations, indicating microstructure decay of the micropitted area, as the greater roughness intensifies the dislocation pile-up and local plastic deformation leading to micropitting (79). However, the relative direction of rolling-sliding with respect to the direction of surface lay and roughness seems to have a more considerable impact on micropitting. Studies showed that in comparison to longitudinal or isotropic roughness of the counterbody, a transverse surface roughness enhances the micropitting incipient on the contact body in the bearings (8, 47) and gears (15). Laine *et al.* (8) investigated the effect of direction of surface finish as shown in Figure 3-34 and confirmed that with relatively constant lambda ratio and surface roughness values, a transverse roughness significantly enhances micropitting where surfaces were lubricated with PAO+ZDDP lubricant. However, as shown in Figure 3-34, the effect of surface finish on micropitting of surfaces lubricated with PAO base-oil seems to be negligible.

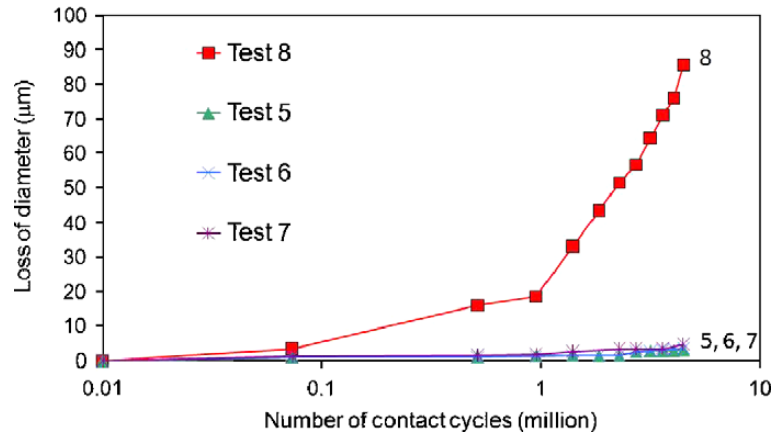


Test number	Lubricant	R _a -counterbody (µm)	λ'
1	PAO	0.50	0.14
2	PAO	0.58	0.12
3	PAO + ZDDP (1.3 wt%)	0.58	0.12
4	PAO + ZDDP (1.3 wt%)	0.55	0.13

Figure 3-34. The effect of surface finish and lubricant formulation on micropitting (8) (Where λ' is the ratio of the central film thickness to the centre-line average roughness of the ring)

In the case of transverse surface finish, the direction of lubricant entrainment is perpendicular to surface lay and thus the chance of lubricant loss within the asperity-asperity contacts is higher with respect to longitudinal surface finish (95). Therefore, transverse surface finish facilitates lubricant film thinning and collapse leading to greater micropitting.

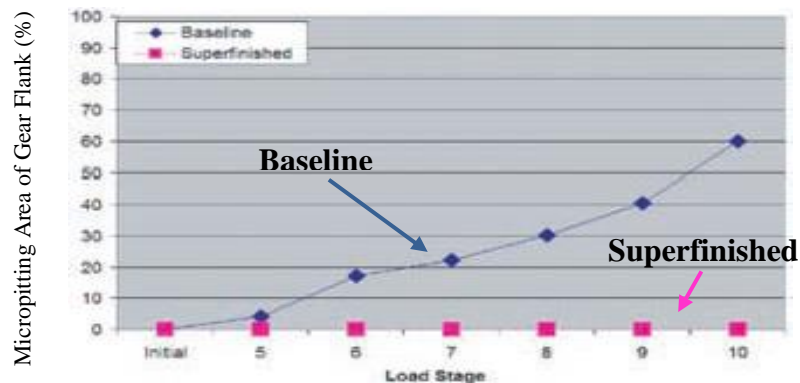
The effect of surface roughness value was also examined by Laine *et al.* (8) and shown in Figure 3-35. It has been shown that only one of the tests which was carried out using a counterbody with the highest roughness value (400-610 nm) underwent severe micropitting wear, while the roughness of 265 nm and below this value resulted in little wear. Interestingly the lambda values for roughness of 265 and 400-610 nm are almost the same which are 0.16 and 0.12, respectively. This implies that roughness predominantly influences micropitting of surfaces. Therefore, a significant reduction in surface roughness of the gear and bearing components can considerably mitigate micropitting (89, 104).



Test number	R _a -counterbody (nm)	T (°C)	λ'
5	185	76	0.4
6	195	99.7	0.22
7	265	99.7	0.16
8	400-610	76	0.12

Figure 3-35. The effect of surface roughness value on micropitting of surfaces having transverse surface finish and lubricated with PAO + ZDDP (1.3 wt%) (8) (Where λ' is the ratio of the central film thickness to the centre-line average roughness of the ring)

Winkelmann, El-Saeed and Bell (104) examined the effect of superfinishing of gear components (pinion and wheel) using a FZG gear tester and showed a dramatic reduction in micropitting. As shown in Figure 3-36 superfinishing to approximately one-fifth of the combined-baseline-roughness suppressed micropitting to almost no-micropitting level.



Baseline surface roughness (µm)	Pinion	0.52	Superfinished surface roughness (µm)	Pinion	0.13
	Wheel	0.44		Wheel	0.07

(a)



Figure 3-36. The effect of surface roughness treatment (superfinishing) on micropitting examined using a FZG gear tester based on test procedure described in "Test Procedure for the Investigation of Micropitting Capacity of Gear Lubricants," FVA Information Sheet 54/I-IV. a) Shows the micropitted area as a function of load stage and b and c) present the images from the baseline and superfinished gear teeth respectively (104)

3.5.2 Tribochemical parameters: the influence of lubricant additives

Although microstructural change of the steel under high contact pressures is accounted for micropitting in steels, the main propellant to initiate micropitting is poor lubrication which cannot suppress the interaction of the existing asperities on the surface of contact bodies (47). Therefore, an efficient lubrication and appropriate additive package are expected to effectively mitigate micropitting considering the fact that micropitting is a surface (or near surface) initiated fatigue damage. The investigation and influence of lubricant additives involve complex phenomena. Alongside the additive package, the type of base-oil used in the lubricant affects the micropitting performance (89).

Ahluos, Ronkainen and Helle (89) investigated the effect of three types of base-oils on micropitting which were a mineral oil, synthetic ester and a tall-oil-based ester. As shown in Figure 3-37, the surface lubricated with the synthetic ester showed a superior micropitting performance in comparison with the mineral oil lubricated surface. Furthermore, the tailored synthetic ester oil which was called tall-oil-based ester base oil exhibited slightly improved micropitting performance compared to the synthetic ester oil. The results suggest no clear correlation between friction coefficient and micropitting performance of the base oils used in the study (89).

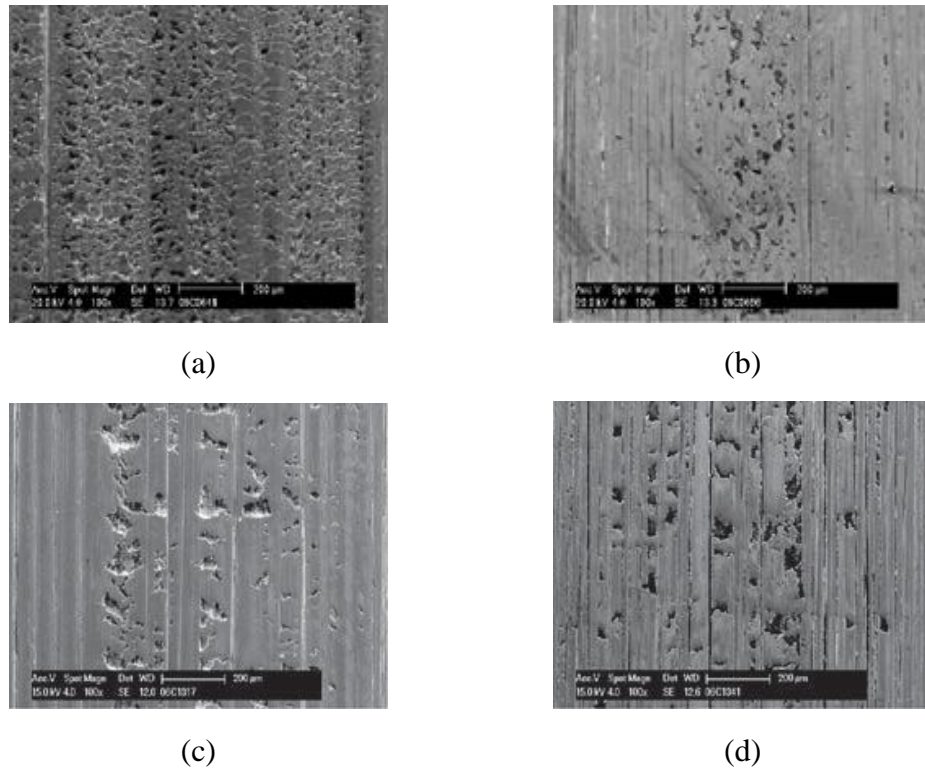


Figure 3-37. SEM images taken from surfaces lubricated with different base oils after micropitting tests using a twin disc tester. a) Lubricant: mineral oil and material: 20MnCr5 carburised steel, b) lubricant: synthetic ester and material: 20MnCr5 carburised steel, c) lubricant: synthetic ester and material: micro-alloyed Nb-added 20MnCr5 steel and d) lubricant: tall-oil based ester and material: micro-alloyed Nb-added 20MnCr5 steel (89)

Although the base oil influences the micropitting performance of the lubricant, it should be noted that the type of base oil used in a lubricant influences the reactivity of the additives in the lubricant with the steel surface (28) and thus alters the micropitting performance of the additives. Therefore, a more desirable micropitting performance of a base-oil does not essentially indicate a superior micropitting performance of a fully-formulated lubricant which uses that specific base-oil. This is manifested by the experiments carried out by Cen (102). As shown in Figure 3-38, the roller surface lubricated with PAO + ZDDP has a significantly superior micropitting performance compared to a surface lubricated with an ester + ZDDP lubricant under the same tribological test parameters. This makes the understanding of micropitting even more complex.

Although the detrimental influence of EP and AW additives on the fatigue life of bearings has been reported by several authors (19, 73, 78), Brechot *et al.* (5) were among the first researchers reporting the tendency of EP and AW additives to increase micropitting.

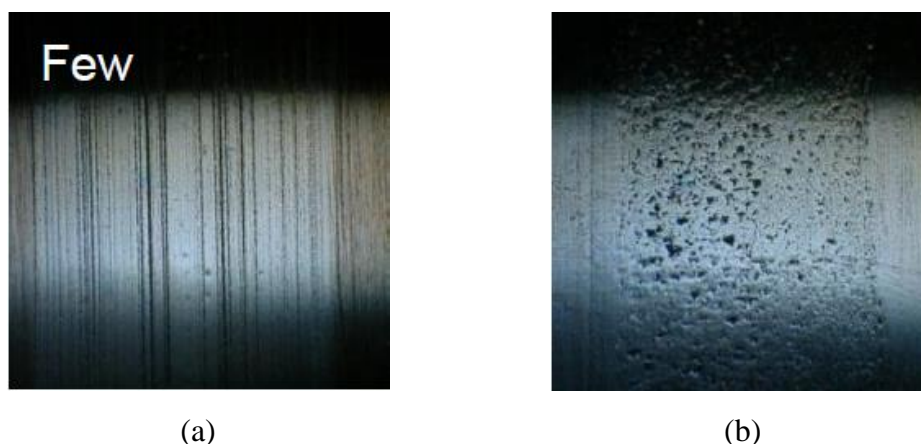


Figure 3-38. Roller surfaces lubricated with lubricants containing 2% of ZDDP formulated using different base oils of a) PAO and b) ester under 2% of SRR and 20% of relative humidity after 72×10^4 contact cycles (102)

As shown in Figure 3-39, Brechot *et al.* (5) employed two commercially sensitive and unmentioned additives to develop a “new technology” lubricant capable of reducing micropitting to a significant extent compared to two commercial gear oils (A and B) and a conventional lubricant that was not developed to tackle micropitting. As additive packages play an important role in all aspects of wear performance in gears and bearings, detailed tribochemical studies of each individual additive and their interactions are required.

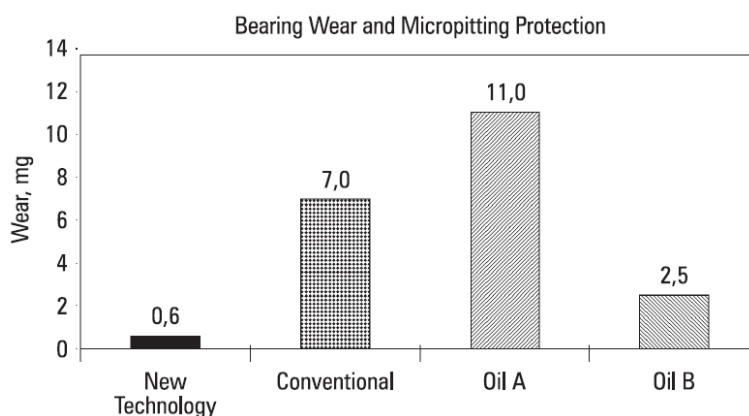


Figure 3-39. Bearing protection test using INA slow speed axial bearing tester using different lubricants with a mineral base-oil (5)

O'Connor (7) using a FZG gear tester showed that EP additives are the most effective additives to reduce micropitting. He showed that it can be misleading to assign EP or AW additives as detrimental or beneficial additive as a general statement. Thus this suggests that the action of the additives in micropitting wear depends on the

concentration, chemical structure of the additives and application. The examined AW and EP additives by O'Connor (7) are specified in Table 3-1.

Table 3-1. Chemical composition of additives used in the report by O'Connor (7)

Component	Chemical Description	Function
AW-1	Medium chain alkyl dithiophosphoric acid ester, amine salt	Antiwear (8.5% P)
AW-2	Long chain alkyl phosphoric acid ester, amine salt	Antiwear / friction modifier (5.0% P)
AW-3	Medium chain length alkyl phosphoric acid ester, amine salt	Antiwear (7.7% P)
AW-4	Long chain alkyl phosphite	Antiwear / friction modifier (5.8% P)
EP-1	Alkyl disulfide	Antiscuff (43% S)
EP-2	Alkyl polysulfide	Antiscuff (45% S)
EP-3	Alkyl polysulfide	Antiscuff / cutting agent (54% S)
EP-4	Experimental mono- and di-sulfide	Antiscuff / antioxidant (40% S)

The influence of additive chemistry and functionality on micropitting performance is detailed in Table 3-2. The micropitting investigation of the experiments when neither of EP and AW was used in the lubricant formulation was not possible since in the absence of both EP and AW additives (tests A7 and A8) enormous wear happens on the surface which indicates important functionality of these additive in protecting surfaces from wear. By comparing test A6 (EP additive only) with either A5 (EP + metal passivator additive) or A2 (EP + AW additive) it appears that the addition of the second additive to the lubricant increases micropitting which is an indication of interactions between EP and AW or a metal passivator additive.

Table 3-2. Wear and micropitting performance of different lubricants formulated with additives indicated in Table 3-1 (7)

Oil Code	A1	A2	A3	A4	A5	A6	A7	A8
Base Fluid	ISO VG 32 (100% Solvent Refined 150N)							
Additive*								
AW-1	+	+	+	+	-	-	-	-
EP-1	+	+	-	-	+	+	-	-
MP	+	-	+	-	+	-	+	-
* Balance of additive package contains appropriate levels of dispersant, demulsifier, rust inhibitor, and foam inhibitor								
**+ symbol indicates standard treat level and - symbol indicates not present								
FZG Micropit Screen Test								
Micropit area [mm ²]	17.9	23.4	24.4	24.8	18.7	9.1	NA	NA
Macropit area [mm ²]	0	0	0.2	52.4	0	8.9	NA	NA
Wt Loss [mg]	22	29	37	102	49	47	12309	4562

SEM images in Figure 3-40 compare the appearance of the micropitted areas on the surfaces lubricated without employing AW (A5) and EP (A3). As appears in Table 3-2, although the values of the micropitted areas are similar for both lubricants, the surfaces from the lubricant containing AW additive were micropitted in a substantially more severe fashion. This suggests the detrimental impact of AW additives on enhancing micropitting. It should be noted that the micropits from EP-containing lubricants are larger in size having a smooth surface around them which imply improved running-in processes.

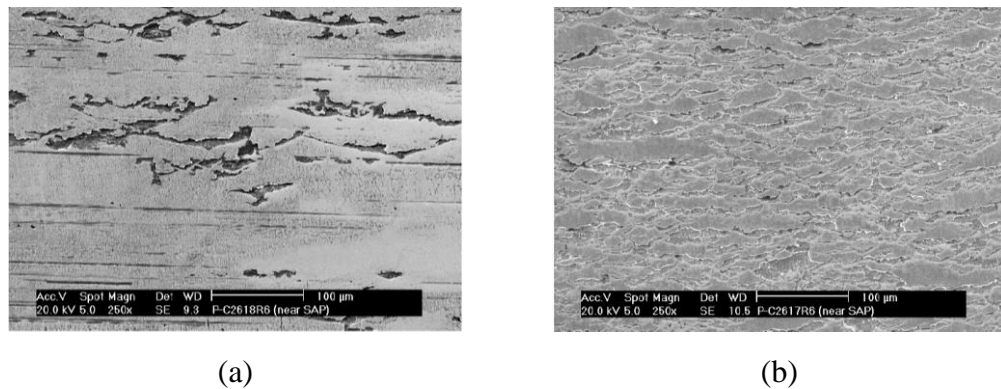


Figure 3-40. SEM images from gear surfaces lubricated with a) oil A5 and b) oil A3 which are specified in Table 3-2 (7)

In the study carried out by O'Connor (7) two approaches were considered by selecting alternative EP and AW additives to tackle micropitting. Approaches were to use AW additives having longer alkyl chains (AW-2 and AW-4) in order to reduce the asperity friction and to use more active EP additives (EP-2 and EP-3) having more functional element (S) in their chemical formula in order to increase wear and reduce micropitting subsequently. It is shown that only AW-4 resulted in a micropitting reduction while it increased macropitting. Also, both more active EP additives enhanced micropitting. The results show that friction reduction and increase in wear does not necessarily reduce micropitting. However, a change in the additive chemistry substantially influences micropitting.

ZDDP is the most well-known AW additive which enhances the performance of the lubricant beyond its wear-protection action, through its anti-oxidant and EP functionality (12). ZDDP is considered as an essential component of a lubricant formulation in most tribological applications. Some AW additives have been shown to strongly increase the incidences of micropitting (5, 8, 18, 47), whilst the enhancing effect of ZDDP on micropitting has been experimentally confirmed (6, 8, 18).

The rough nature of the ZDDP tribofilm and, more importantly, its tendency to enhance localised plastic deformation (6, 105) are attributed to be the reasons behind micropitting-enhancing properties of ZDDP. The delaying effect of ZDDP on proper running-in gives rise to asperity-asperity contacts leading to localised plastic deformation. Benyajati *et al.* (6) employing a MPR rig investigated the effect of ZDDP on micropitting of 16MnCr5 steel surface using a harder counterbody with a transverse surface finish. Experiments were carried out under a SRR of 5.2% and the results are summarised in Figure 3-41.

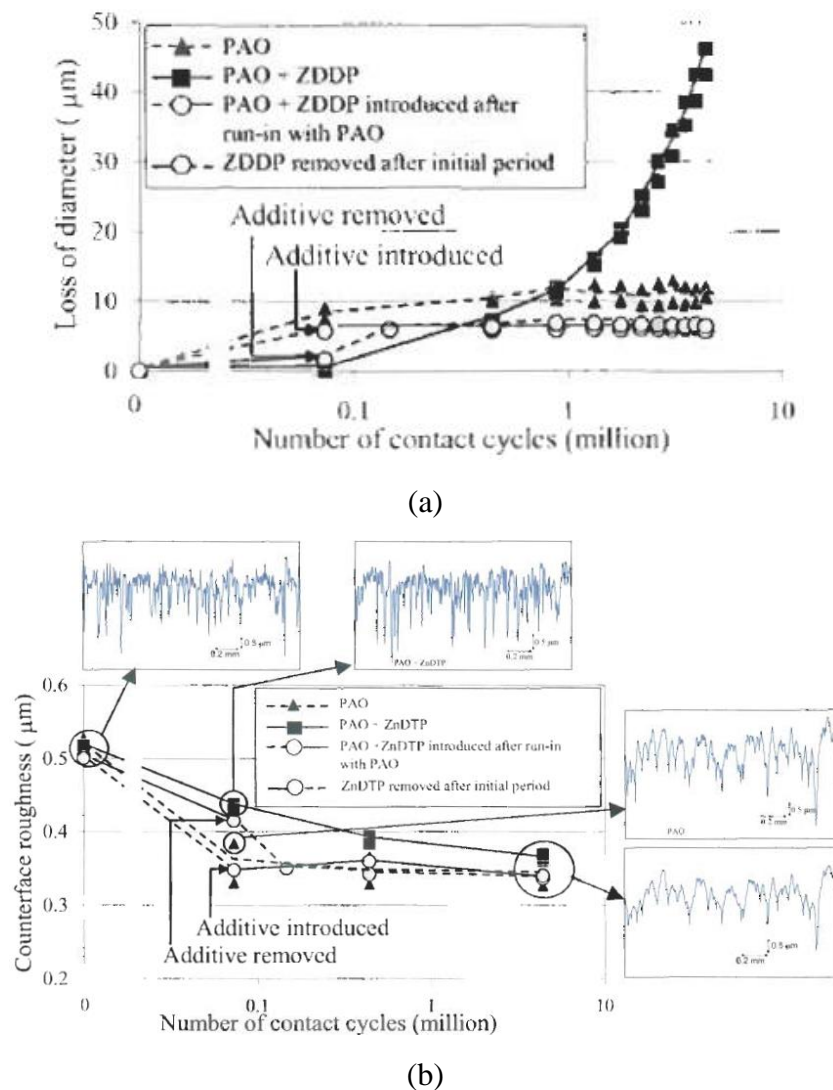


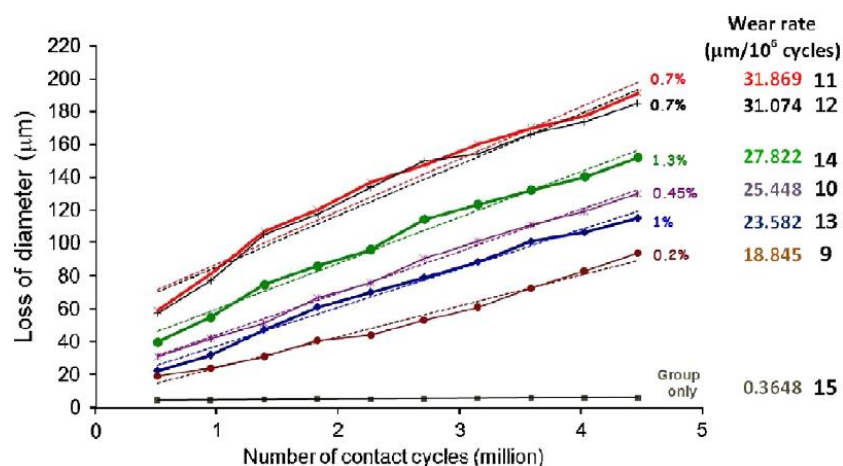
Figure 3-41. The investigation of the effect of ZDDP on micropitting and the correlation between counterbody roughness variation and micropitting. The changes in a) wear depth and b) counterbody roughness with respect to the number of contact cycles (6)

As shown in Figure 3-41, the PAO base oil lubricated specimen encountered wear at the early stage of the experiment followed by almost no wear throughout the rest of the experiment. The surface of the specimen was smooth having a dark colour and

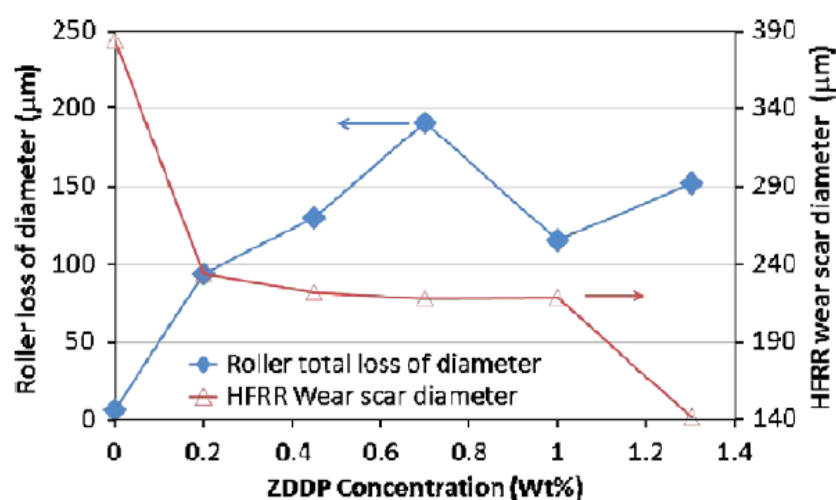
few micropits at the end of the test. The test carried out with 1.3% of ZDDP resulted in extensive micropitting on the surface with a steady wear rate. They measured the roughness of the counterbody over the same range of contact cycles in which wear depths were measured. A substantial drop in the roughness of the PAO lubricated counterbody at the early stage followed by a minor decline throughout the rest of the test was observed. In contrast to that, the roughness declines slowly during the experiment in the lubricant containing ZDDP. Thereby they proposed that ZDDP mitigates the decline in the roughness of the counterbody resulting in delayed running-in processes which lead to intensified micropitting.

Benyajati *et al.* (6) performed a test lubricated with PAO base oil for 73×10^3 contact cycles followed by a change of the lubricant to a ZDDP-containing lubricant for the rest of the test in order to determine the effect of ZDDP on running-in. As can be seen in Figure 3-41, the specimen experienced a little wear at the early stage of the test, where the lubricant was PAO base oil, and then wear was stopped as soon as ZDDP was introduced to the lubricant resulting in no micropitting on the surface of the specimen. The next experiment was performed in the reverse fashion in which first 73×10^3 contact cycles were lubricated with PAO + ZDDP and the lubricant was changed to PAO base oil for the rest of the contact cycles. In this case, as shown in Figure 3-41, little wear happens after first 73×10^3 contact cycles with a surface indicating the onset of micropitting. After removing the ZDDP from the lubricant a further small wear happened before its progression stops. Following ZDDP removal, micropitting is eliminated from the surface of the specimen generating a smooth surface with only a few micropits.

Laine *et al.* (8) carried out experiments using lubricants having different concentrations of ZDDP from 0.2% to 1.3% under a SRR of 5.2%. They did not observe a correlation between the concentration of ZDDP and the severity of micropitting, as shown in Figure 3-42, which indicates the maximum micropitting at the ZDDP concentration of 0.7%. Laine *et al.* (8) compared the wear results from the same lubricants in pure sliding conditions using a high frequency reciprocating rig with the micropitting results collected from MPR. Although there is no definitive correlation between an increase in micropitting and a decrease in wear, Laine *et al.* (8) attributed the highest micropitting at the concentration of 0.7% to the greatest rate of secondary-ZDDP tribofilm formation at the intermediate concentration of 0.7% which provides the surface with the highest protection against sliding wear.



(a)

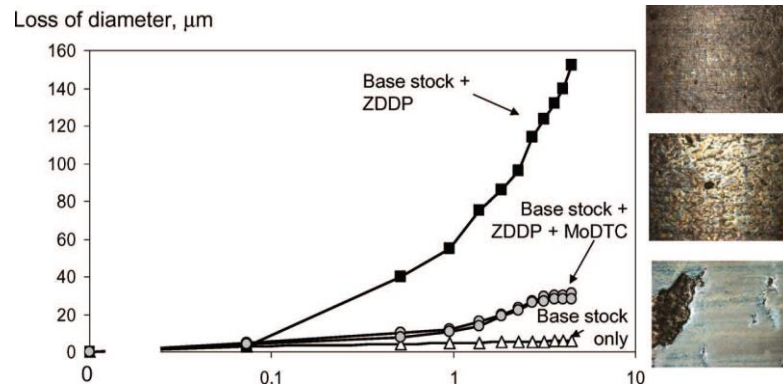


(b)

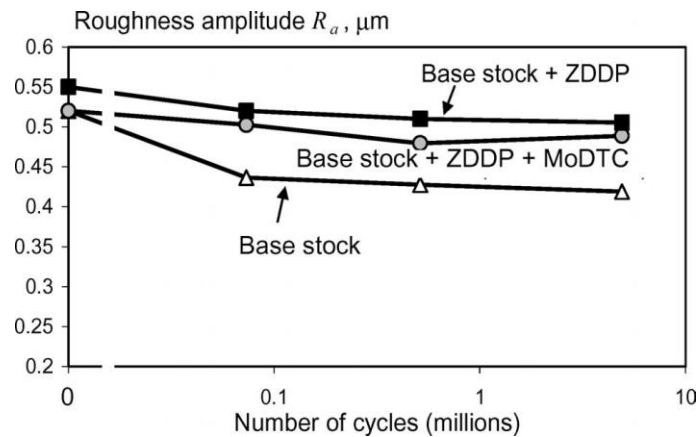
Figure 3-42. The influence of ZDDP concentration on micropitting and sliding wear. a) Micropitting results from MPR at test temperature of 70°C and contact pressure of 1.71 GPa, counterbodies had longitudinal roughness with values of 0.5-0.52 and the base oil used was a mineral oil and b) pure sliding wear results obtained at 80°C (8)

In another work by Laine, Olver AV and Lekstrom (92), the effect of a well-known friction modifier, MoDTC, used in the engine applications on ZDDP-induced micropitting was examined. They used MoDTC at the concentration of 0.35% and ZDDP at the concentration of 1.3% which were blended with a mineral oil. The relative direction of the roughness on the counterbody to the direction of rolling-sliding is not mentioned. However, it seems to be longitudinal considering the results presented in their previous report (8). The results by Laine *et al.* (92) are reflected in Figure 3-43 indicating the efficiency of MoDTC in reducing ZDDP-induced micropitting. The lubricant containing only ZDDP led to severe micropitting

wear, while the addition of MoDTC to the lubricant resulted in an initial high wear rate, which declined to nearly zero after around 10^6 contact cycles.



(a)



(b)

Figure 3-43. The influence of MoDTC friction modifier on the micropitting-enhancing behaviour of ZDDP. The influence of MoDTC on a) micropitting b) counterbody roughness. Tests are carried out at temperature of 70°C and contact pressure of 1.71 GPa under SRR of 5.2%, counterbodies had longitudinal roughness with values of 0.53 ± 0.2 and the base oil used was a mineral oil base oil (92)

The roughness on the counterbodies for two additive-containing lubricants declined very slowly, while it declined sharply for the surface lubricated with base oil. The competence of MoDTC to significantly reduce the ZDDP-induced micropitting is attributed to MoS₂ formation on the contact surfaces leading to promising boundary friction reduction (92). In contrast to the report by Laine *et al.* (92), Cen (102) examined a molyvan friction modifier, which is a organomolybdenum complex, blended to a PAO base oil and showed that molyvan lubricant generates more micropitting in comparison to the ZDDP lubricant as shown in Figure 3-44. These contradictory results can result from different additive chemistry of the molybdenum-based friction modifiers or different experimental parameters and test geometry. Also,

it is shown that MoDTC has a synergetic effect on the ZDDP functionality (105) and thus combination of ZDDP and MoDTC can be effective, while Cen (102) used molyvan friction modifier solely blended to the base oil.

Increasing oil viscosity produces thicker lubricant films in the contact and hence reduces asperity-asperity contacts which is a solution in order to mitigate micropitting. However, additives have more pronounced effects over the higher viscosity oil which can disregard the benefit of using a more viscous oil (7). In addition to that, a viscous oil can increase the churning losses and reduce the energy efficiency influencing the economics of wind turbines (7). In this regard, one of the additives that can potentially alter the micropitting performance of a lubricant significantly is a viscosity index improver which is not investigated systematically in the literature. However, the favourable influence of Viscosity Modifiers (VM) on the pitting life of the steel is addressed by Johansson *et al.* (90). Although the additive package and VMs were not clarified in the article, they suggested that VM enhances the pitting lives of the mineral oils through reducing the contact temperature and thin-film friction.

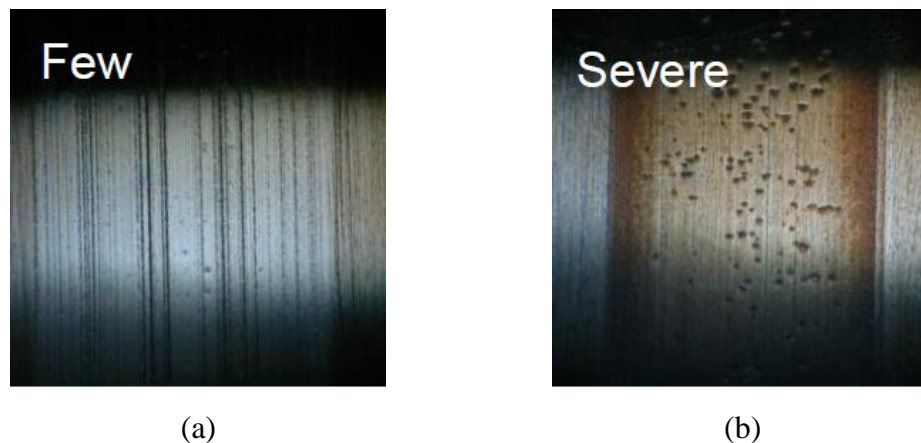


Figure 3-44. Micropitting performance of PAO-based lubricants containing a) ZDDP at concentration of 2 wt% and b) molyvan at concentration of 5 wt% under 2% of SRR and 20% of relative humidity after 72×10^4 contact cycles (102)

Meheux *et al.* (106) investigated RCF performance of three lubricant formulations under pure rolling conditions and a SRR of 6.7% using a twin-disc fatigue tester. Artificial dents were induced on the faster surface using a Rockwell penetrator in order to accelerate fatigue. The results are shown in Figure 3-45 indicating deteriorated fatigue performances of the lubricants containing additives in both SRRs. A Focused Ion Beam (FIB) milling is performed on a cracked region of the specimen which experienced 6.7% SRR and lubricated with the fully-formulated lubricant. The

EDX results showed traces of AW, EP and detergent additives inside the crack (106). The P and calcium concentration varied in a similar trend across the crack depth, while S concentration is increased towards the crack tip. They postulated that the presence of an additive-derived tribofilm on the surface can act as a sticking plaster which mitigates crack propagation (106-107). Also, they suggested that upon crack initiation and opening S firstly reacts with the nascent surface and promotes crack propagation rate (106).

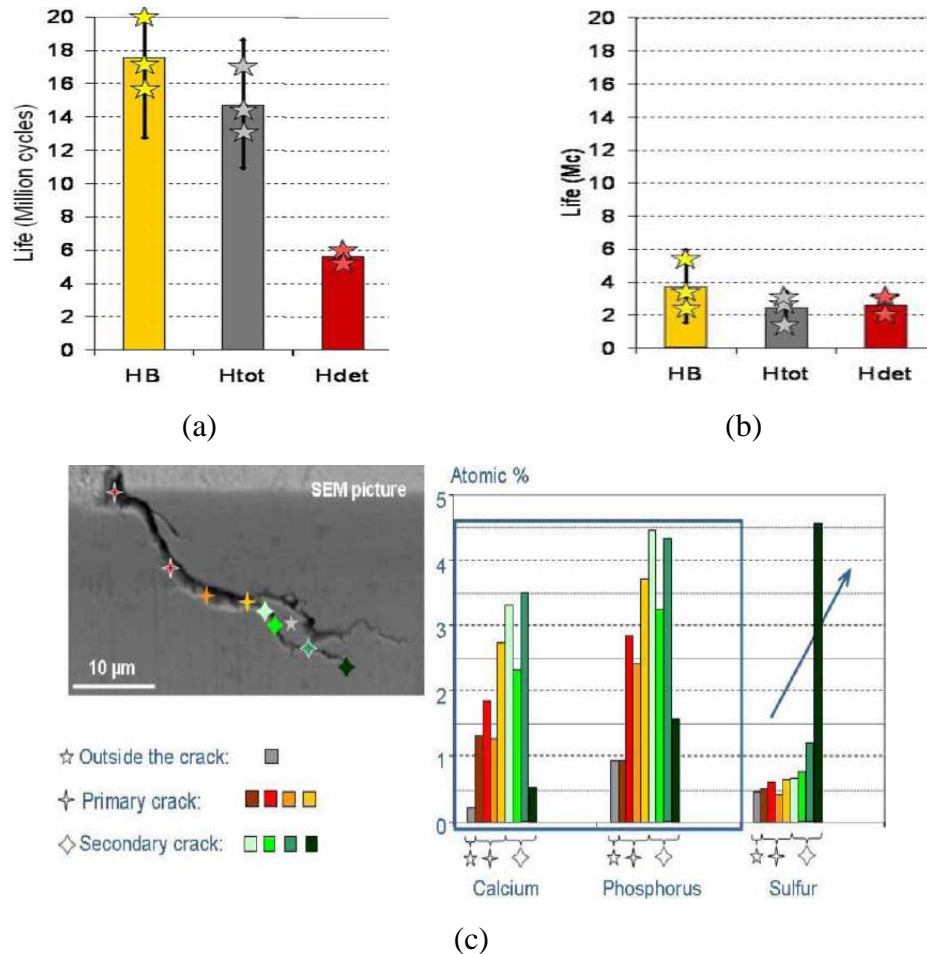


Figure 3-45. Investigation of the lubricant additives impacts on fatigue life of 52100 steel under contact pressure of 3.2 GPa at 80°C and lambda ratio of 2.2 under a) pure rolling condition and b) SRR of 6.7%. c) SEM-EDX analyses of a FIB section prepared to investigate a crack on the dented disc. H B resembles the mineral base oil, Htot is the mineral base oil + five additive and Hdet is the mineral base oil + anti-foam + detergent (106)

The enhancing effect of ZDDP on micropitting was investigated mainly taking the mechanical and tribological aspects of micropitting into account (15, 84, 101) and the tribochemical effect of ZDDP in severe micropitting wear has not been completely elucidated in rolling conditions. The current work addresses the tribochemical

phenomena involved in the micropitting enhancing behaviour of ZDDP and hence a literature review concerning the ZDDP tribofilm formation is essential. Therefore, the next section covers a brief and concise literature review regarding ZDDP-tribofilm composition and mechanisms of formation.

3.5.3 **Interaction of ZDDP with the steel surface**

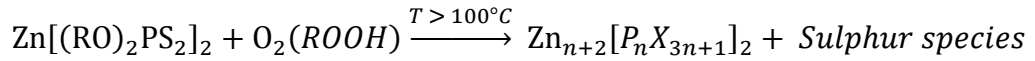
ZDDP was originally employed as an antioxidant additive in the lubricant. Its AW functionality was discovered soon after overriding its antioxidant action. Currently ZDDP is acknowledged as one of the most efficient AW additives in engine oil. However, the new environmental regulations restrict its application. Therefore, a detailed and mechanistic understanding of the ZDDP AW action is essential and has attracted enormous researches in this area in order to develop effective alternatives for ZDDP.

ZDDP as an AW additive is generally believed to protect the surface from wear through forming an adherent (poly) phosphate layer on the steel substrate (105), even though recently it has been suggested that transient tribo-products which are formed through mechanochemical reactions may protect the surface from wear and the adherent film is not necessary (108).

ZDDP also can act as an EP additive. EP activity of an additive is reflected through its load-carrying capacity. Organic sulphides are widely used EP additives which are believed to protect surfaces through surface passivation (109) e.g. forming iron-sulphur compound (12, 110-112) at high temperatures induced by high local pressure (shear and stress). A greater concentration of the sulphides was observed in the boundary film (113-117) and tribofilm on the wear particle (118) with an increase in contact load which confirms the role of sulphides in EP contacts. Using X-ray Absorption Near Edge Spectroscopy (XANES), iron sulphide formation also was confirmed in the tribofilms from ashless thiophosphates (119-121) where Zn is absent in the molecular structures of the AW additives.

Thermal degradation of ZDDP can convert most of the S in ZDDP to organic sulphides and disulphides which are oil-soluble and can act as EP additives (105). Thermo-oxidative decomposition of ZDDP in the bulk lubricant is suggested to be the main mechanism for ZDDP film formation in the absence of friction and shear forces (122). The dissolved molecular O in oil and peroxide radicals as active species

at temperatures of above 100°C react with ZDDP leading to its decomposition (122) which is represented in a simplified reaction path:



Where X denotes O atoms generating polyphosphate anions as $\text{O}(\text{PO}_3)_n^{-(n+2)}$ and S atoms which are substituted for O in the chain. Thereby, a solid film of poly(thio)phosphates deposits on the surface and sulphur species remain soluble in the oil resulting in a S-depleted solid film.

Therefore, ZDDP and other metal dialkyl dithiophosphates, as a result of decomposition to oil-soluble sulphur compounds can act as a mild EP additive (123). ZDDP shows best AW properties compared to the other metals (Bi, Ag, Pb, Sb, Sn, Cd, Fe, Ni), whilst exhibits least EP activity (123) as shown in Figure 3-46.

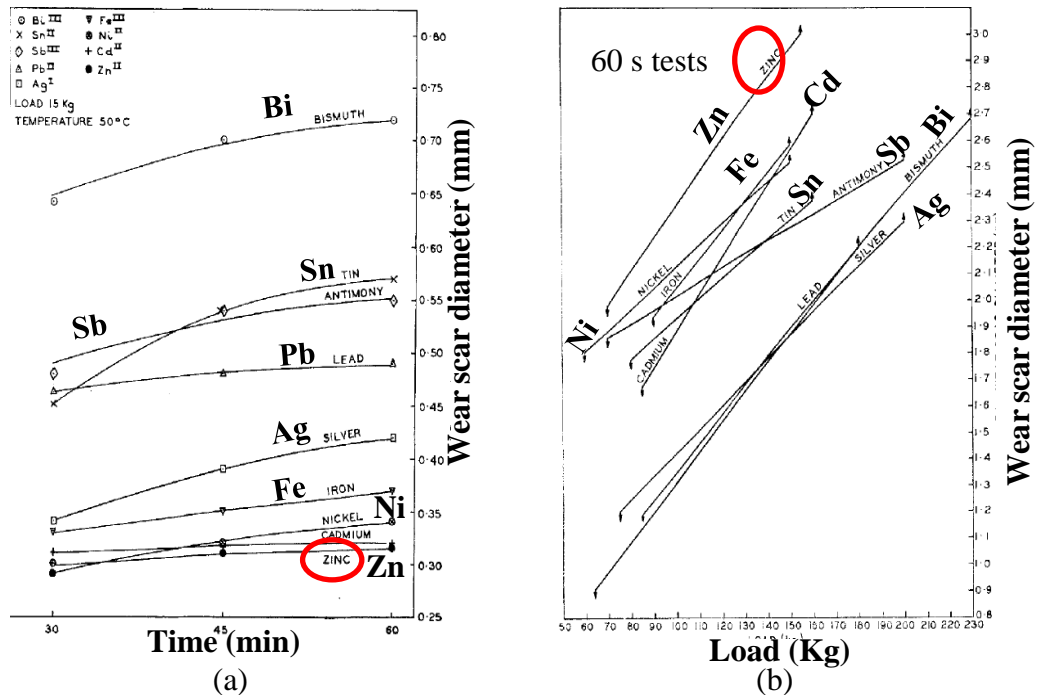
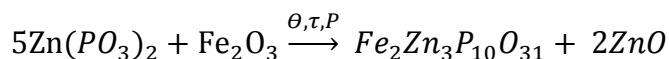


Figure 3-46. Investigation of a) AW and b) EP activity of different metal (4-methylpentyl-2) dithiophosphates at concentration of 4 millatoms of P per 100 grams of oil for each additive using a four ball tester (123)

Followed by the solid poly(thio)phosphate film formation on the surface, under external shear forces, the film reacts with the iron-oxide on surface of the iron-based substrate. The reaction is a chemical acid-base interaction which stems from Hard and Soft Acids and Bases (HSAB) principle. Phosphates and Fe^{3+} are hard Lewis bases and a hard acid, respectively. Therefore, polyphosphates react with iron-

oxide leading to elimination of iron-oxide and formation of zinc-oxide through cation exchange (122). The chemical route is as follows:

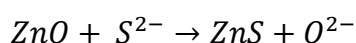


Since a unit of cation exchange (Zn^{2+} with Fe^{3+}) requires more negative charge to compensate the charge and balance the stoichiometry, this reaction leads to a decrease in polyphosphate chain length. In the wear process the distribution of the tribofilm in an uneven manner results in a continuous formation of fresh iron-oxide layer due to the reaction of atmospheric or lubricant-dissolved O with the nascent surface. The chemical reaction of freshly formed iron oxide layer with (poly)phosphates is believed to induce an intergrown layer of phosphates and interfacial iron oxide which is suggested to enhance the adhesion of the tribofilm to the surface leading to a more stable tribofilm (124). In addition, wear incidents generate iron-oxide wear particles in the lubricant which are accepted as a major source to cause severe abrasive wear on the surface (12, 122). The chemical reaction between iron oxide particles in lubricant and (poly)phosphate film eliminates abrasive wear. Both reactions result in shortening of the (poly)phosphate chain length and formation of short-chain mixed zinc and iron (poly)phosphates.

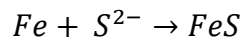
3.5.4 **The role of sulphur in the ZDDP interaction with the steel surfaces**

In spite of over thirty years of research attempting to reveal the mechanism of action of ZDDP, there are still some uncertainties around it. This is especially the case with the role of the sulphide layer formed in the tribofilm. Although iron sulphide on the substrate is hypothesised in the literature to form as a separate layer, there has been no conclusive experimental observation on the distribution of the iron sulphide as a dispersed precipitate, distinct layer at the steel substrate or both and whether the iron sulphide layer homogeneously covers the surface or locally forms at the surface.

The sulphide contribution to the bulk of the ZDDP tribofilm is expected to be mainly zinc sulphide (122, 125). Zinc oxide, produced through the reaction of zinc (poly)phosphates with iron oxide, can react with the organic sulphur species according to the following reaction path:



This reaction is thermodynamically favourable as it is exothermic ($\Delta H_{ZnO}^0=174$ Kcal/mol and $\Delta H_{ZnS}^0 = 147$ Kcal/mol) and also in accordance to HSAB principle (122). Sulphides having lower cohesive energy and being mechanically softer in comparison to the oxides having same cations, have been suggested to alleviate oxide-derived abrasive wear (122). However, the main role of sulphur species derived from EP and AW additives, including ZDDP, in tribochemical contacts is suggested to be passivation of the surface through metal-sulphide formation (12, 122). In the case of a Fe-based substrate the sulphur species are expected to react with the nascent Fe surface, generated in the event of severe wear and EP conditions, leading to formation of iron sulphide:



Formation of iron sulphide on the surface as an interfacial layer mitigates adhesive wear and decays scuffing (12). Cation exchange from zinc sulphide to form iron sulphide is not thermodynamically favourable (125-126) according to the following:



This indicates that formation of iron sulphide from zinc sulphide is unlikely and implies that iron sulphide formation can take place through reaction of organic sulphide species with the steel surfaces as also suggested by Martin (122, 127). The iron sulphide layer can be formed in the event of removal of (poly)phosphates followed by acid-base reactions of the sulphides (residual organic sulphides) with the nascent surface (122) (shown in Figure 3-49 (d)). The iron sulphide layer protects the surface from oxidation and adhesive wear (122, 128). Iron sulphide formation during the wear process as part of the ZDDP-tribofilm is shown under specific rubbing conditions (118, 122, 129), although combination of ZDDP with some other additives may inhibit formation of the iron sulphide layer (125).

Hallouis, Belin and Martin (118) performed wear tests in a lubricant containing 2 wt% of ZDDP and extracted the wear particles in order to inspect the wear particle using transmission electron microscopy. The wear particles are subjected to elemental mapping using Electron Energy Loss Spectroscopy (EELS). The EELS maps are shown in Figure 3-47 (a and b) for S and Fe $L_{2,3}$ edge. It is shown that S and Fe are locally present as a dispersed phase in the phosphate-based matrix in the form of nanometer-scale crystallites of iron sulphide. Furthermore, as can be seen in Figure 3-47 (c), they showed that increasing the contact pressure enhances the relative

concentration of S in the tribofilm on the wear particles which confirms the role of S in EP conditions.

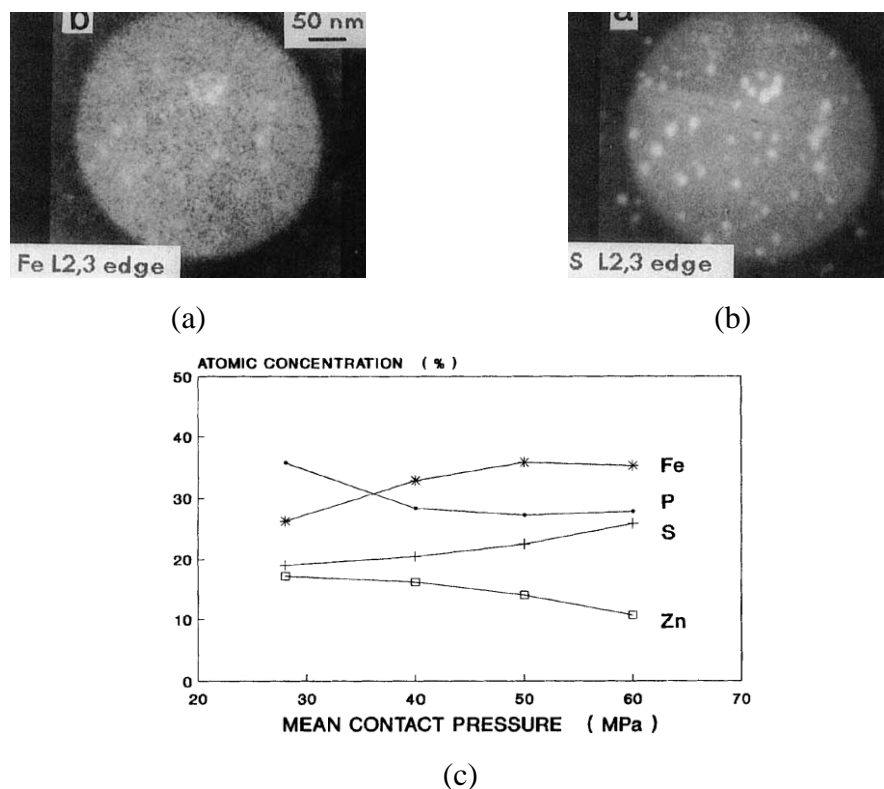


Figure 3-47. EELS maps of a) Fe and b) S and c) EDS concentration of elements as a function of contact pressure collected from wear particles extracted from ZDDP-lubricated tribotests (118)

The initial iron sulphide film can be FeS_2 and further rubbing under severe conditions can thermally decompose the FeS_2 layer to FeS (111). Also, under more severe contacts, formation of FeS may be enhanced over FeS_2 (111), which complies with the HSAB theory (122). FeS is assumed to form through reaction of nascent iron surface (Fe^0), a soft acid, with reduced sulphur (S^{-2}), a soft base, whilst FeS_2 (pyrite) formation is accounted for the reaction of Fe^{2+} (iron in FeO oxide layer), a borderline-hard acid, with S_2^{2-} anions as a borderline-hard base (111). The formed iron sulphide layer, induced by organo-sulphur additives, can protect the surface from welding under severe contacts (113, 130). The S-rich dense layer is assumed to be friable and shown distributed surrounding pits (114).

In the literature FeS (116, 122, 129), FeS_2 (122), Fe_7S_6 (131) or Fe_7S_8 (118) are suggested as the chemical nature of the ZDDP-derived iron sulphide. While FeS_2 is most probable reaction product of the iron oxide sulphidation, FeS will be formed in the sulphidation reaction of the nascent Fe surface (132). Watkins (133) hypothesised FeS formation through reaction of the alkyl sulphides with Fe_2O_3 which produces

elemental S to react with the metal surface. Iron sulphide in combination with iron oxide formation at the interface is suggested using Auger Electron Spectroscopy (AES) (128, 134) and both suggest the greater role of the sulphide layer in wear protection rather than phosphate layer. In another report, iron oxide suggested at the bottom layer rather than iron sulphide (135).

As far as ZDDP is concerned, iron sulphide formation has been observed on the wear particles as nanometre precipitates (118, 122). Hallouis *et al.*(118), using TEM diffraction pattern, suggested Fe₇S₈ as the composition of the iron sulphide nanoprecipitates. The iron sulphide precipitates could originate from iron sulphide layer on the substrate through dissolution and/or dissociation of the iron sulphide layer (125, 136). Minfray, Le Mogne and Lubrecht (107) used *in-situ* AES and rubbed a pin having iron oxide on the surface against a pre-formed ZDDP tribofilm under a severe condition in Ultra High Vacuum (UHV) ambient where lubricant was absent and observed formation of iron sulphide on the surface of the pin as shown in Figure 3-48.

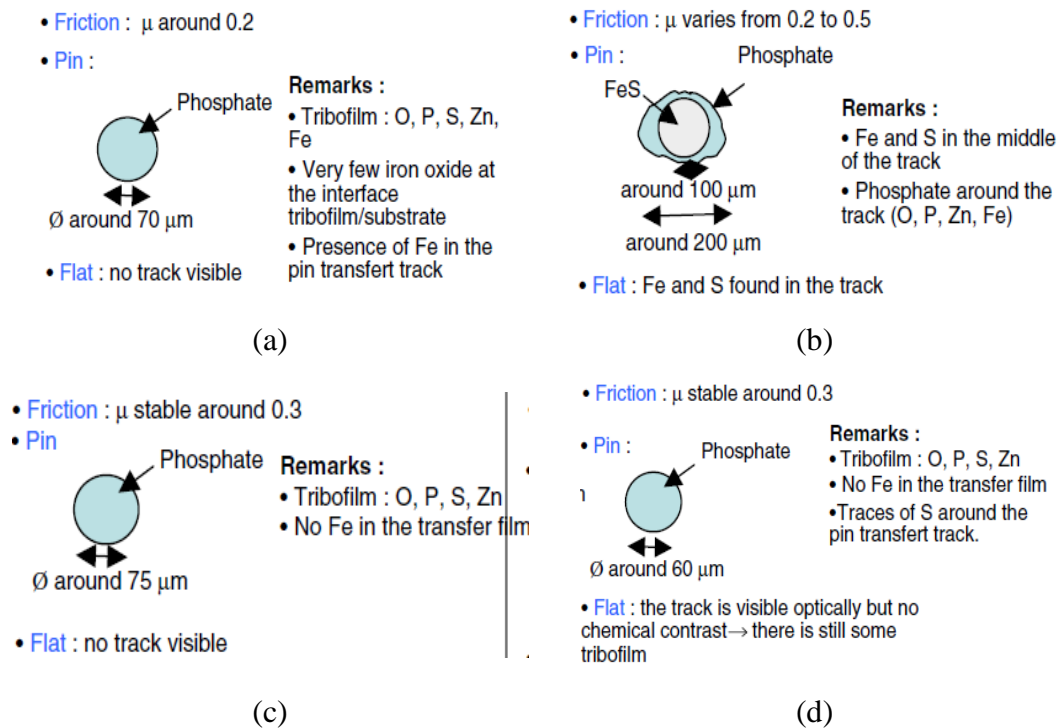


Figure 3-48. *In-situ* investigation of interaction of the ZDDP tribofilm with a and b) iron oxide and c and d) Fe surfaces in UHV conditions. a and c) tests were conducted under mild contact conditions and b and d) tests are conducted under severe contact conditions (107)

However, in mild wear conditions where iron oxide was not removed from the pin surface, the tribofilm on the pin surface consisted of mixed

zinc and iron (poly)phosphates resulting from reaction of phosphates with iron oxide surface. On the pin having the Fe surface, transfer of zinc (poly)phosphates to the pin surface is observed with no contribution of Fe under both mild and severe conditions suggesting the role of iron oxide surface in triggering the ZDDP reaction.

Bell, Delargy and Seeney (136) rubbed a pure Fe foil at 175°C in a mineral oil containing ZDTP and investigated the tribofilm by XPS, dynamic Secondary Ion Mass Spectroscopy (SIMS) and Time-of-Flight-SIMS (TOF-SIMS). The negative ion depth profile of dynamic SIMS analysis showed that S⁻ peak persists at a deeper level than PO₂⁻ and O⁻ peaks (136). They could also resolve a peak at 710.2 eV from the Fe signal and attribute the peak to the iron sulphide. They observed an increase in the intensities of the peak attributed to the iron sulphide and iron oxide peak throughout the depth (136). As a result, they suggested a representation of the tribofilm as shown in Figure 3-49 (a) having an iron sulphide and/or oxide on the substrate. Smith and bell (137) carried out SIMS and XPS depth profiling and observed patches having Zn, Fe and S in the absence of P. The XPS depth profiling showed the presence of Zn, S and O below P (137). They suggested the presence of a dense iron and/or zinc sulphide and/or oxide on the steel substrate as a distinct layer under the phosphate layer which is presented in Figure 3-49 (b). A similar structure for the ZDDP tribofilm also suggested by Tonck, Bec and Georges (138). Bec, Tonck and Georges (124), also referring to the previous results (136, 139) suggested that there is a 20 nm sulphide and/or oxide layer on the steel substrate which has a protective phosphate layer on top.

However, the three layer structure was disputed by Martin (127). Martin (127) suggested a two layer structure of ZDDP tribofilm composed of a 10nm-thin long chain poly(thio) phosphate at top and mixed zinc and iron short chain (poly)phosphates in bulk with metal sulphide precipitates embedded in its structure as can be seen in Figure 3-49 (c). Martin, Grossiord and Le Mogne (122, 127) postulated that only in very severe conditions localised iron sulphide can be formed through adhesive wear where initially formed phosphate layer and the iron oxide layer underneath the phosphate layer are disrupted from the surface providing the sulphur species with nascent Fe surface. This phenomena is schematically presented in Figure 3-49 (d).

Minfray, Martin and Esnouf (140) using AES, XPS and SIMS showed that almost no traces of iron oxide were detected near the substrate inside the wear track, while iron oxide was evident as an interfacial layer outside the wear track as can be seen in Figure 3-50. These observations imply the chemical reaction between iron oxide on the surface and ZDDP-derived (poly)phosphates in accordance to HSAB theory. Iron phosphate or/and iron sulphide were suggested to be present near the substrate in Minfray *et al.*'s study (140).

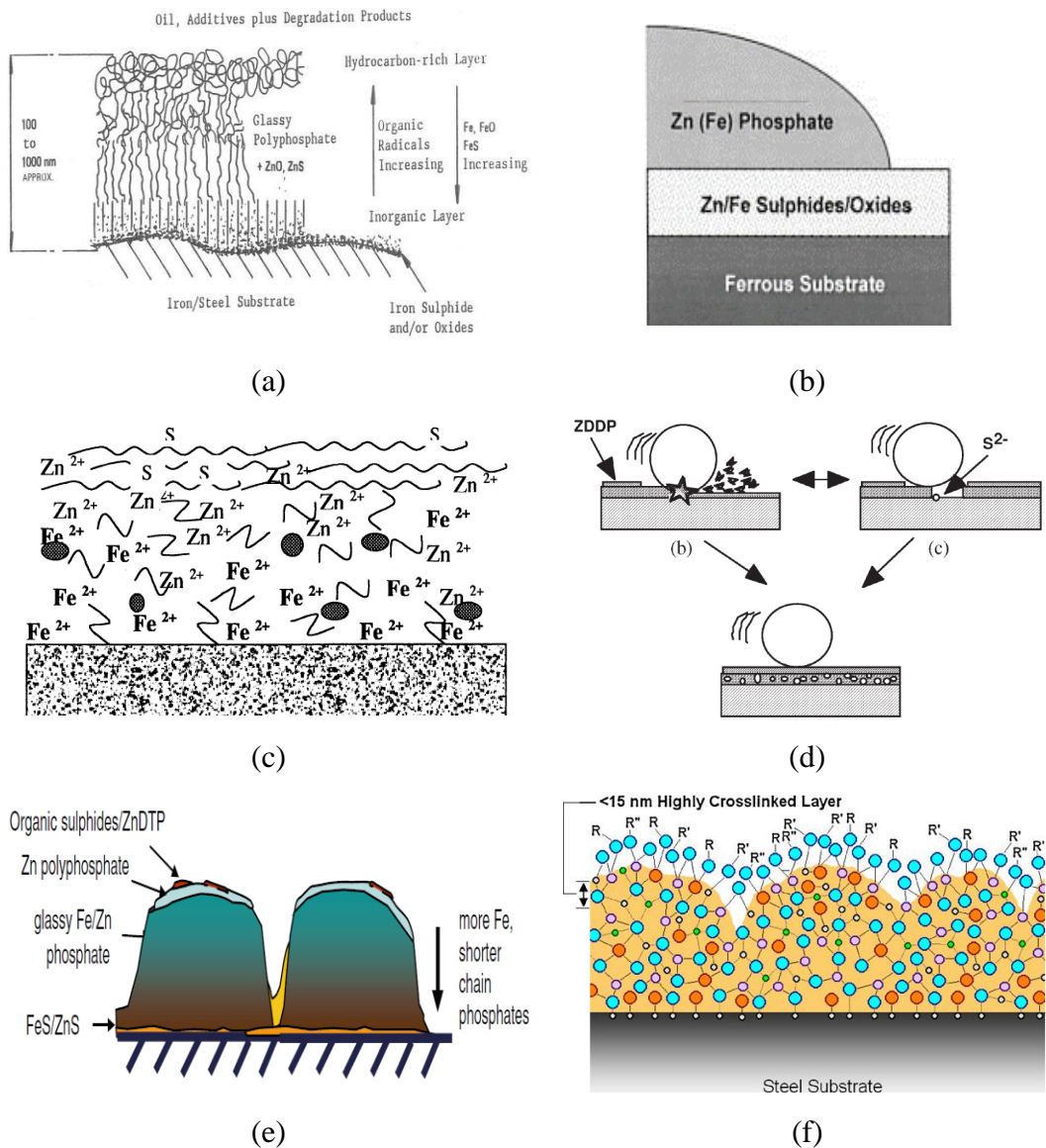


Figure 3-49. Schematic illustrations of ZDDP tribofilm structure suggested by a) Bell *et al.* (136) b) Smith and Bell (137), c) Martin, Grossiord and Le Mogne (127), d) Martin (122), e) Spikes (105) and f) Kim, Mourhatch and Aswath (121) (WC ball on steel cylinder under EP contact)

Spikes (105) in his review paper depicted the structure of the ZDDP tribofilm as shown in Figure 3-49 (e) having an iron and/or zinc sulphide at the interface of substrate and phosphate glass.

XANES reports mainly rule out the existence of iron sulphide in a fully developed ZDDP tribofilm (119-120, 129, 135, 141-142) and suggest formation of zinc sulphide. Whilst few reports, which examined the tribofilms formed under EP conditions using tungsten carbide as the counter-body, suggest contribution of the iron sulphide together with zinc sulphide and zinc and/or iron sulphate to the tribofilm throughout its depth (116, 121, 143) as shown in Figure 3-49 (f). However, excluding iron sulphide as part of the ZDDP-tribofilm (119-120, 129, 135, 141-142) in the previous XANES reports could be due to a minor contribution of dispersed iron sulphide or a very thin interfacial iron sulphide film which exists and is below the sensitivity of XANES Fluorescence Yield (FY) mode of detection on S L-edge (125, 135).

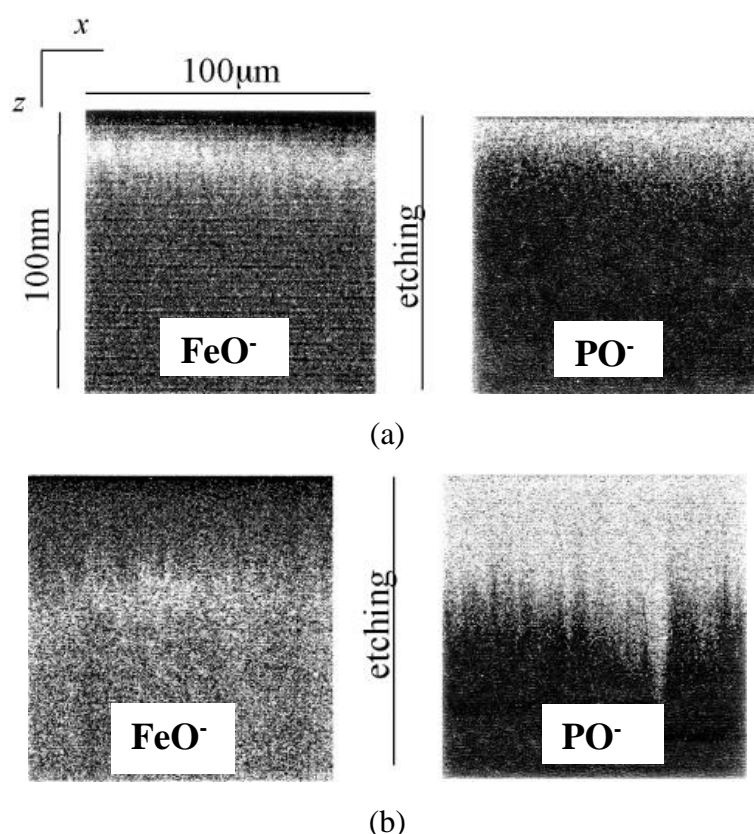


Figure 3-50. SIMS depth profiling of ZDDP films a) outside (thermal film) and b) inside (tribofilm) of the wear track representing the ion intensities with white corresponding to high and black corresponding to low intensities (140)

In addition, minor iron sulphide formation after 10 s of rubbing in Total Electron Yield (TEY) S K-edge mode was detected, although zinc sulphide was

dominant at this stage and in the further rubbing to form thick film (129). Although it cannot be concluded that the iron sulphide is present on the substrate or dispersed in the matrix of zinc sulphide and phosphates according to the results obtained by Zhang, Yamaguchi and Kasrai (129), they suggested a three layer structure of the ZDDP tribofilm having zinc sulphide and/or FeS on the substrate.

The analysis spot size in the reports by XANES is mainly varied from a few square micrometres to a few square millimetres (127, 144-145). The acquired data depths for TEY and FY are 5 and 50 nm at the S L-edges; and 50 nm and 1-3 μm at the S K-edges, respectively (116, 119). In XPS the analysed spot size is usually varied from a few tens of square micrometres to less than a square millimetre. The sampling depth of XPS for a Al K α radiation source is less than 10 nm. In both chemical analysis techniques, collected signals are consequently influenced by the averaging effect over the analysed area and sampling depth. Therefore, although XPS and XANES have produced outstanding information on the tribochemistry of lubricant additives over the years, observation of the lateral and localised chemical distribution of compounds and elements near the surface defects may not be achieved through these techniques. Furthermore, XANES possibly cannot recognise the interface layer as a separate layer on the substrate in the thick enough tribofilms.

In summary, as a result of numerous studies using a variety of analytical methods, iron sulphide formation as part of a ZDDP tribofilm has been confirmed to form under certain conditions. However, some uncertainties still remain including whether iron sulphide exists as a dispersed precipitate, as a distinct layer at the substrate or both. Also, if it presents as a layer there are still questions around the uniformity of that layer. In addition, whether the iron sulphide layer exists alone (107, 140), in combination with iron oxide (128, 136) or zinc sulphide at the substrate surface has not been confirmed. Therefore, further studies are required to understand whether iron sulphide as an interface layer entirely covers the surface or forms as a localised area.

3.5.5 Influence of water and relative humidity as lubricant contamination

Water is known as an insidious lubricant contaminant (146-147). Water is recognised as the second most destructive lubricant contaminant by Fitch and Jaggernaut (147). Water can enter into the lubricant through several sources including a humid environment (147-150) by absorption and condensation, leakage from a heat

exchanger (147), a by-product of chemical reactions (147), free water (147, 151). The water in oil can be in different configurations as shown in Figure 3-51. However, as a general definition the forms of water in oil can be classified to two categories which are “free water” and “dissolved water”. The state of water in oil as either free water or dissolved water is determined by the amount of water in oil relative to the water-saturation level of the oil. Therefore, where the amount of water in oil is in excess of the saturation level, a free water condition exists in the lubricant. Accordingly, a total water content of less than saturation level of oil indicates that water in oil is in the dissolved water state (23).

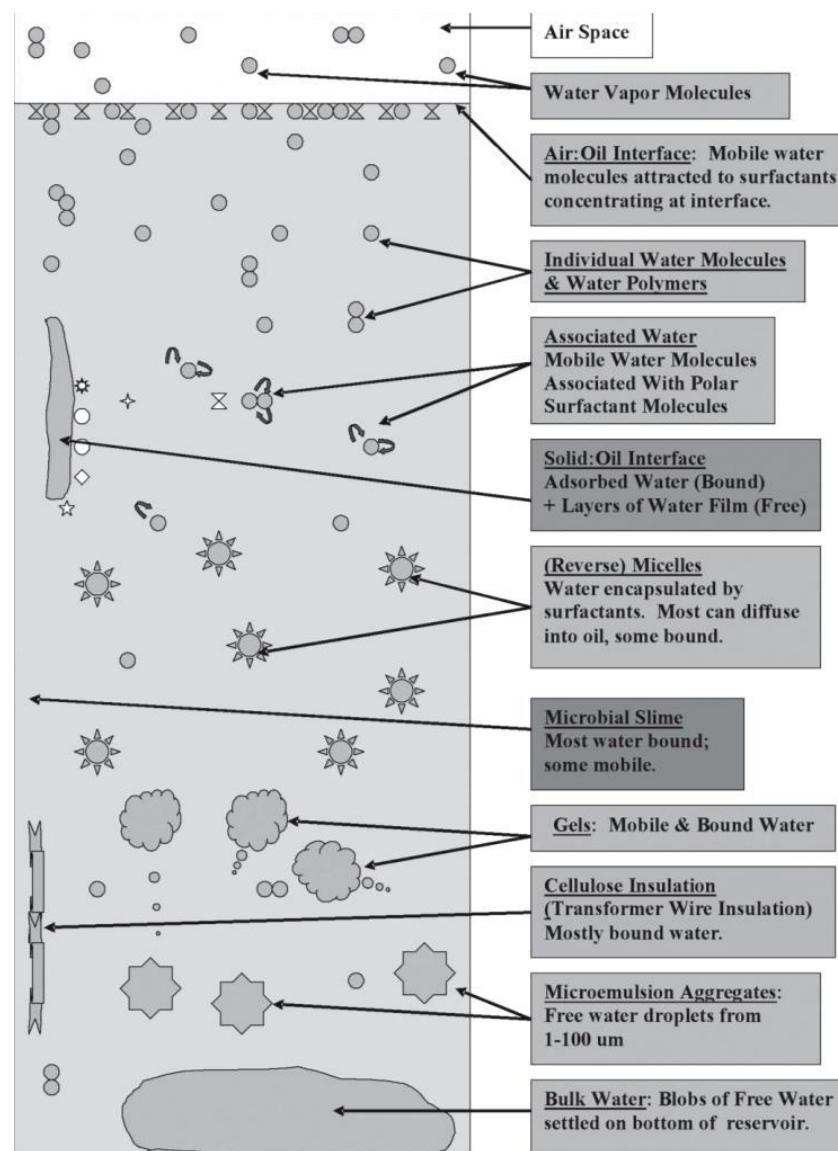


Figure 3-51. The forms of water in oil (152)

Free water in the lubricant generates water droplets in the order of 1 μm (23) and thus forms an emulsion which has an inferior load carrying capacity (12) leading to deficient lubricant performance. The cloudy appearance of oils in a certain

concentration of free water is an indication of emulsion of water in oil. Needleman (152) suggested that around 80% of water molecules in a lubricant which contains polar moieties and has a water saturation value of 500 ppm exist in reverse micelle configuration. The saturation level of a lubricant, representing its hygroscopicity, depends on the physiochemical characteristics of the base stock (viscosity and base oil polarity), additive package, environmental parameters (RH and temperature) (153) and oil condition (aged, oxidised or fresh oil) (154).

In general, the water absorption level of synthetic oils is more than mineral oils. Under 100% humidity and at 38°C some synthetic oils (diester and neopentyl polyol ester) absorb approximately 4000 ppm of water, while mineral oils absorb approximately 100 ppm of water (155). Only some synthetic oils exist that absorb low amounts of water (20-60 ppm) (155-156). Also, some additives such as those used for EP conditions (especially acid esters), have an electrostatic affinity to absorb water and can lead to the elevated amount of water in lubricant. The saturation level of an oil increases exponentially with an increase in temperature as shown in .

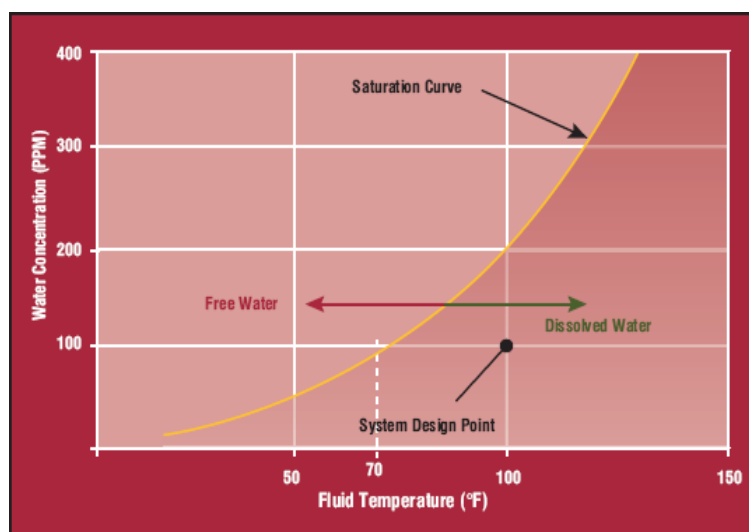


Figure 3-52. Water saturation of oil as a function of temperature (153)

The water amount in oil is proportional to the water vapour (RH) in a linear manner according to Henry's law (157). However, Henry's law is valid for an ideal-dilute solution in a static condition. This indicates that for a water-in-oil dispersion, especially in tribochemical conditions, the linear relationship between RH and water in oil is not necessarily valid. Nevertheless, an increase in RH certainly enhances the water content in lubricant (152) in tribochemical contacts. Also, it is shown the water content in oil increases linearly as a function of RH in static conditions (155).

Cantley (155) evaluated the water absorption characteristics of a range of oils including commercial, mineral and synthetic oils in a controlled condition over a week of exposure to humid environments and showed that the water content in all the oils increases with an increase in RH. The data for three commercial gear oils are shown in Figure 3-53.

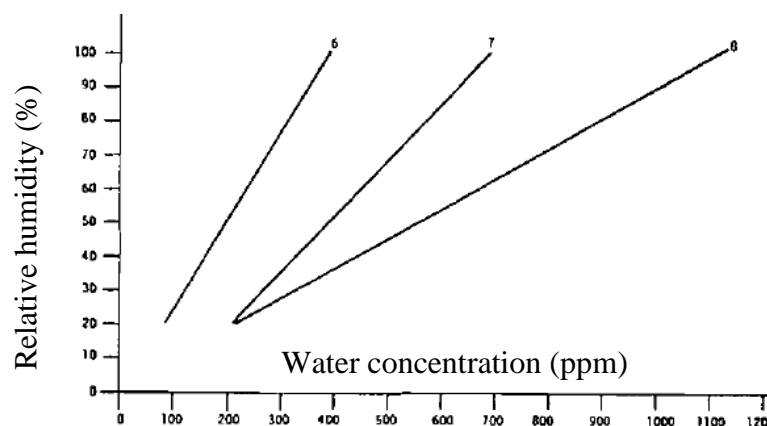


Figure 3-53. The correlation between water uptake by three different commercial gear oils and relative humidity at 38°C (155). The graphs are plotted using three-point data obtained at relative humidities of 20, 60 and 100 %

3.5.6 The influence of water contamination on the lubricant

The detrimental impact of water on bearings exceeds that of particle contamination under certain circumstances and affects a wide range of bearings from journal to rolling element bearings (3). However, this effect is highly destructive where the bearings operate under severe conditions e.g. bearings in wind turbine gearboxes especially in off- and near-shore turbines (21). An overview of the wind turbine gearbox failures resulted from water contamination is presented in Table 3-3. The water limit which is required for different applications is varied e.g. for turbine applications the limit is set to 0.2 % (2000ppm), for hydraulic system is 0.1% (1000ppm), and for dielectric system is 35 ppm (12). However, a small amount of dissolved water has a dramatic influence on bearing fatigue life. Grunberg, Jamieson and Scott (158) reported that the fatigue life of steel reduced by 52% in the presence of only 20 ppm water added to a mineral oil.

Although careful examinations and precautions are taken to control the water content of the lubricant, excessive water most of the time has been observed during operation. Furthermore, the established water threshold for turbines does not seem to be completely safe and is unlikely to prevent the damage caused by water. The water

saturation of turbine oils typically varies between 300 to 500 ppm (23). The bearing fatigue life in a wind turbine gearbox depends on the water content in the lubricant to a substantial portion. As can be seen in Figure 3-54, a decrease in water content to a target level of 75-125 ppm through improved contamination control enhances the bearing life by almost factor of three.

Table 3-3. Wind turbine gearbox failures induced by water contamination (23)

Problem	Summary
Corrosion	Due to free water, especially if acids present from oil degradation and/or microbial growth. Ion currents in aqueous solution. Leads to pitting, leakage, and breakage
Foaming	Due to free water. Leads to air blockage within the oil distribution system, and spillage
Loss of oil film	Due to free water. Water in contact zone cannot support load, allowing opposing surfaces to contact. Results in adhesive wear, high friction, and seizure
Additive drop-out	Due to free and dissolved water. Depletion of hydrophilic additives. Also breaking colloidal suspensions of additives. Leads to loss of additives and fouling of parts
Microbial growth	Due to free water. Colonization of oil by bacteria and/or fungi. Results in: acids, fouling slimes; health issues
Surface-initiated Fatigue spalling	Due to dissolved water carried by gear oil to the tips of propagating cracks. Surfaces of fresh cracks are highly reactive, dissociating water molecules into O ₂ and H ₂ . H ₂ migrates into and weakens steel by hydrogen embrittlement. Cracks spread faster, reducing life of rolling elements and resulting in fatigue spalling, pits, and craters
Accelerated oil oxidation	Due to dissolved water, especially if metal wear debris present. Increases rate of oil oxidation by up to 2 orders of magnitude. Leads to acidity, oil thickening, fouling deposits
Hydrolysis	Due to dissolved water. Decomposition of ester-based additives. Leads to loss of additives, formation of acids, and sometime fouling gels

Water can accelerate oil oxidation (23) which in turn may increase the oil Total Acid Number (TAN) resulting in standstill corrosion and corrosion-enhanced wear and fatigue (21).

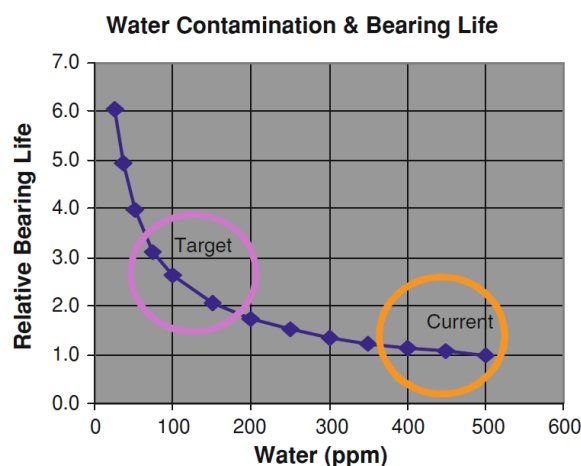
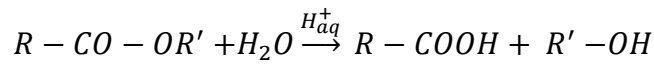


Figure 3-54. Bearing fatigue life in wind turbine gearbox as a function of water content in oil (23)

The influence of water in accelerating oil oxidation is suggested to be considerable. It has been shown that water oxidise the oil as rapidly as the presence of copper metal as an oxidation catalyst and with a faster rate compared to Fe metal (23). This is presented in Figure 3-55 also showing the extreme influence of a combination of metal (copper or iron) and water on increasing the oil acidity. Furthermore, the resultant products of an ester hydrolysis reaction are an acid and an alcohol.



Therefore, ester-based additives and base oils undergo an hydrolysis reaction as water ingresses into the lubricant and hence not only deteriorates the additive and lubricant's functionality but also the resultant acid intensifies corrosion reactions (23). Water promotes corrosion of metallic surfaces and especially standstill-corrosion encountered within the maintenance intervals in wind turbine gearboxes (24). However, contradictory results are observed by Cen (102). He performed ball-on-disc sliding experiments and showed that, after tribological tests, TAN in the PAO + ZDDP lubricant did not change with the addition of water at 1% even in combination with a high RH of 90%. However, water contamination resulted in deteriorated ZDDP AW performance.

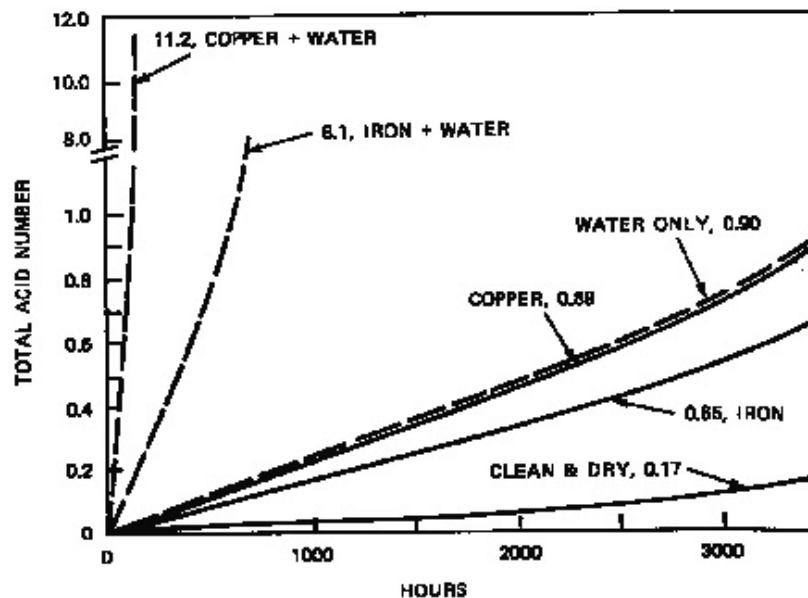


Figure 3-55. Influence of water on oil oxidation (23)

3.5.7

The influence of water contamination on RCF and wear

Schatzberg and Felsen (146) examined the influence of water in rolling contact performance of 52100 steel balls lubricated with squalene paraffinic hydrocarbon (2,

6, 10, 15, 19, 23 - hexamethyl tetracosane) using a four ball machine. A controlled water content of 100 ppm in the lubricant (65% of water saturation level) resulted in reduction of L_{10} fatigue lives by 32-48% in a range of contact pressures varying between around 6 to 9 GPa. The condensation of water inside microcracks by capillary action leading to corrosion reactions of the fresh metallic surfaces and formation of corrosion micropits, induced by dissolved water, are suggested to be the mechanism of water-accelerated fatigue (146). In another work Schatzberg (159) showed that water ingress into oil significantly promotes wear and deteriorates the wear track geometry as shown in Figure 3-56.

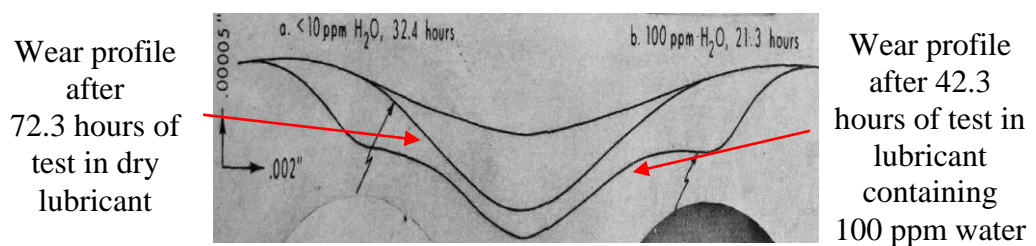


Figure 3-56. Influence of water on wear and wear track profile of ball surfaces tested using four ball machine (159)

Dissolved water can be condensed inside the microcracks through capillary effects leading to accelerated fatigue failure induced by Stress Corrosion Cracking (SCC) (146). Meanwhile, water contamination is suggested to favour hydrogen generation and permeation into the steel under tribological contacts (146, 155) which accelerate RCF, although it may not be considered as a sufficient factor to induce WEC (160). Imran, Jacobson and Shariff (161) suggested that the water dissolved in lubricant is the major source of hydrogen. Ruellan, Cavoret and Ville (160) performed fifteen tests lubricated with two water-contaminated commercial oils employing twin disc machine under different contact conditions. In contrast to Imran *et al.* (161), they observed that only one specimen underwent ramified and embrittled cracking, implying that water may not be a self-sufficient factor to induce HE.

The presence of water in the lubricant promotes wear incidents in steel-steel contacts under sliding (148) and rolling-sliding (102, 151) conditions and in metal-metal contacts under fretting (149) condition. Cen, Morina and Neville (148) examined the influence of three RH values of 20, 60 and 90% on sliding wear in lubricants containing 0 and 1wt% water and showed that increasing water content leads to an increase in wear coefficient, while the friction coefficient does not change

considerably as the result of water in oil. As can be seen in Figure 3-57, the influence of added water is more pronounced compared to tests under humid air. Cen *et al.* (148) also investigated the impact of water on ZDDP-tribofilm formation using XPS and showed that water and RH reduce ZDDP-tribofilm thickness and reduces the Zn concentration in the tribofilm.

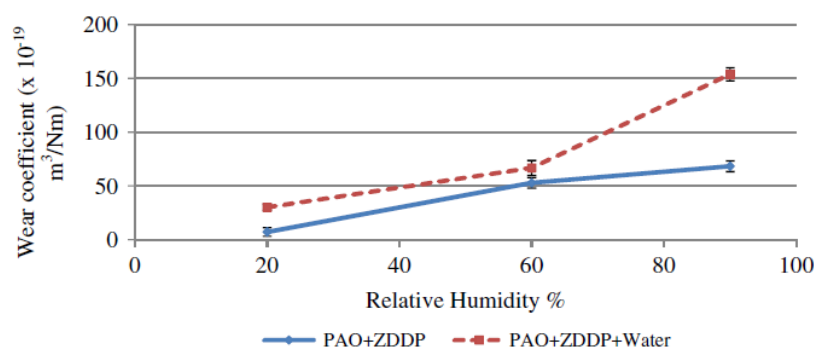


Figure 3-57. The impact of water and relative humidity on sliding wear coefficient (148)

Nedelcu, Piras and Rossi (151) examined the tribochemical influence of the addition of water into a PAO + 2 wt% ZDDP lubricant at different concentrations of 0.5 wt%, 1 wt% and 2 wt% on 52100 steel balls using a four ball machine under 3 GPa of contact pressure at 80°C. As presented in Figure 3-58, they showed an accelerated surface pitting where water was dispersed in the oil at all concentrations varying between 0.5% and 2% (151).

Magalhaes, Ventsel and MacDonald (162) immersed stainless steel balls in water-containing lubricants for eight weeks under static conditions in order to examine the effect of water at two concentrations (1% and 5%) and at two temperatures of 22 and 70°C on corrosion pitting of the balls. The elevated temperature significantly accelerated pitting corrosion. After a week of immersion, the balls kept in lubricant with salt water at 22°C were corroded, while the balls kept at 70°C were corroded both in lubricants with water and salt water. It has been found that increasing the lubricant contamination content (water and NaCl) from 1 wt% to 5 wt% would not enhance the maximum pit depth. In spite of that, the increase in the lubricant contamination content (water and NaCl) increases the extent of the localised damage on the surface. The pitting of the balls immersed in the lubricant with no added-water is attributed to the small intrinsic water in the lubricant. They also measured the hydrogen content of the balls after experiments performed at 70°C.

Results showed that water and salt, depending on the contaminant concentrations, enormously increased the hydrogen uptake by factors of around eight to ten.

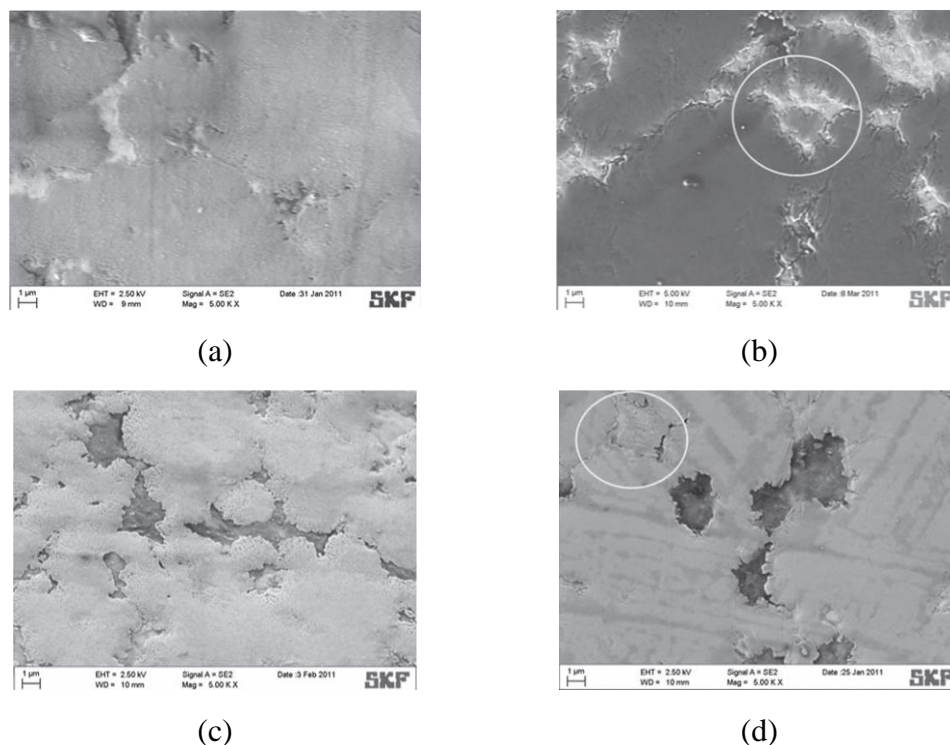


Figure 3-58. Investigation of the influence of water which is added to the lubricant at different concentrations of a) 0 wt%, b) 0.5 wt%, c) 1 wt% and d) 2 wt% on RCF testes using four ball machine (151)

3.5.8 Tribo-chemical influence of water in lubricant

Results from the work by Cen *et al.* (148) showed that water contamination does not considerably change the bulk properties of a ZDDP-containing PAO oil (viscosity and TAN), while wear performance and properties of the ZDDP-tribofilm are extensively decayed (148). This suggests that interaction of water with the lubricant additives imposes significant changes in the lubricant performance indicating the importance of tribochemical influence of water in oil.

Rounds (163) examined the influence of water at two concentrations of 0.15 and 0.5 wt% on the decomposition rate of three different types of ZDDP molecules which are blended to a mineral oil in the presence of an anti-oxidant additive using differential infrared spectrographic technique. The composition of surface precipitates generated through deposition of the ZDDP decomposition products is monitored using X-ray fluorescence. The results, illustrated in Figure 3-59, show that water diminishes induction-time for ZDDP-decomposition.

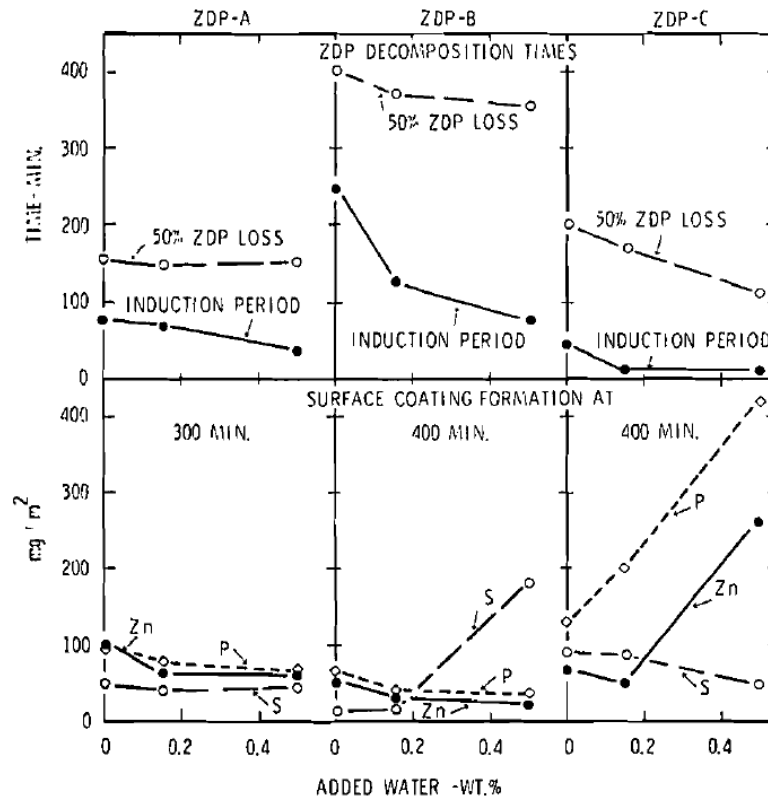


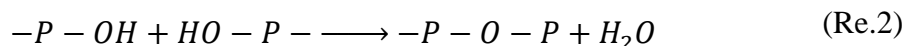
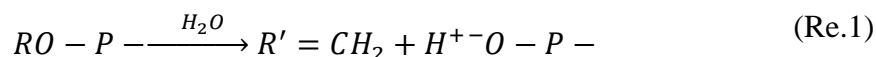
Figure 3-59. Investigation of impact of water on decomposition of ZDDP and surface film composition at 177°C (163)

Also, water decreased the half-life (time at which 50% of ZDDP molecules are decomposed) of all three different ZDDP types. This indicates that water accelerates the thermal decomposition of ZDDP which is attributed to hydrolysis activity of water on ZDDP. Moreover, the contribution of Zn and P to the surface coating is reduced by increasing the water concentration for ZDDP-A (a secondary ZDDP) and ZDDP-B (a primary ZDDP) while the opposite trend was observed for ZDDP-C (an aryl-ZDDP).

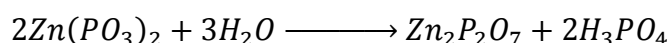
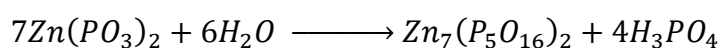
The detrimental impact of water on the AW performance of the ZDDP tribofilm has been reported in previous studies (148, 151) and hydrolysis and depolymerisation of the (poly)phosphate film formed on the surface is mainly addressed as the root cause of the deleterious influence of water (148, 151, 164-165). In addition to that, water in the lubricant (at a concentration of 2.9%) is shown to alter the tribofilm chemical composition in wet clutch contacts (166) and adversely affect the frictional properties of the ZDDP-tribofilm (167).

Spedding and Watkins (164) suggested that water plays a catalytic role in the reaction of ZDDP to form phosphoric acid (Re.1). On the other hand, water is produced in a

reaction to form polyphosphates (Re.2) and is consumed to form sulphides (Re.3) according to the following chemical paths:



Fuller (165) proposed a thermo-oxidative mechanism for the ZDDP tribofilm formation by which adsorbed ZDDP and Linkage Isomer (LI) ZDDP are decomposed to zinc polyphosphates and sulphur species. The LI-ZDDP was suggested to be a rearranged form of ZDDP molecule as a result of O substitution with sulphur, which was originally bonded to a Zn atom, leading to a bonding of sulphur to the alkyl group. As part of the mechanism, they proposed that the hydrolysis reaction is responsible for converting long polyphosphates to short (poly)phosphates:



Nedelcu *et al*, (151) examined the influence of water in oil on the ZDDP-tribofilm thickness and phosphates in the ZDDP-tribofilms. As can be seen in Figure 3-60 (a), they showed that the ZDDP-tribofilm thickness in the presence of water increased before it levels off after 3 hours of rubbing followed by a decline in thickness. However, the tribofilm thickness from the lubricant with no added-water increased constantly over contact cycles. Therefore, results suggest the hydrolysis action of water on ZDDP-derived polyphosphate films. Also, the binding energies of P 2p_{3/2} peaks in the XPS spectra collected from the tribofilms over rubbing time are in support of tribofilm thickness data. An approximately constant value of 133.3 ± 0.1 eV for the tribofilms formed in the presence of water can be observed in Figure 3-60 (b), while the binding energies of the peaks in the spectra from the lubricant with no added-water increased over time to 133.6 ± 0.1 eV. This indicates evolution of longer phosphate chains in the absence of water and hydrolysis action of water to form shorter phosphate chains. Therefore, the literature suggests that water as a ZDDP hydrolysis-catalyst (164), depolymerises long chain (poly)phosphates to shorter chain (poly)phosphates (151, 165) and reduces the tribofilm thickness (148, 151).

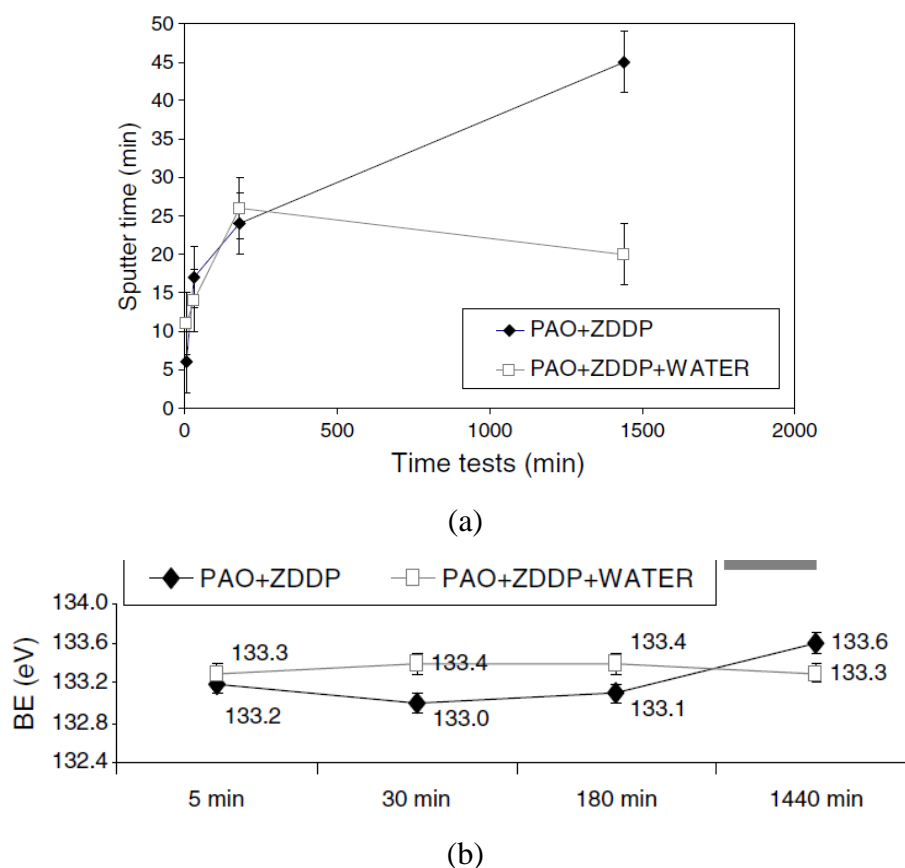


Figure 3-60. ZDDP-tribofilm evolution over time from PAO + ZDDP and PAO + ZDDP + 2wt%water lubricants. a) Presents the tribofilm thickness obtained from XPS etching and b) exhibits the corresponding phosphate peak (P 2p_{3/2} peaks in the XPS spectra) binding energy (151)

The hydrolysis effect on different types of ZDDP varies depending on their hydrolytic stability. Aryl > secondary > primary is the order of the hydrolytic stability (168). The hydrolysis of ZDDP in the presence of water is assumed to generate alkyl sulphide and zinc phosphate (164) or olefin and phosphate acid (164). In addition to hydrolysis impact of water on the ZDDP-tribofilm, water in oil is suggested to decay the stability of the ZDDP-tribofilm through impairing the tribofilm adherence to the substrate (169). Costa and Spikes (169) investigated the influence of Hydrated Ethanol (HE) and Anhydrous Ethanol (AE) fuels as lubricant contaminants on the ZDDP-tribofilm formation and stability using Mini Traction Machine-Spacer Layer Imaging Method (MTM-SLIM). AE and HE contaminants led to a delayed tribofilm formation and a significant reduction in the tribofilm thickness. However, the influence of HE which has around 6-7 wt% water was much more severe in comparison to AE. The tribofilm thickness at some points increased to a considerable value followed by a removal process suggesting that HE prevented the formation of a stable tribofilm and subsequently facilitated removal of tribofilm during rubbing.

Also, addition of HE to a fully-developed ZDDP-tribofilm resulted in a removal of the tribofilm immediately after rubbing. The more detrimental influence of HE over AE was attributed to the water which was suggested to have a localised etching properties on polyphosphates (169).

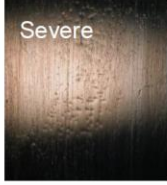
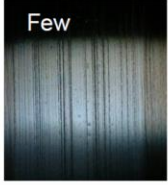

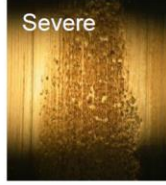
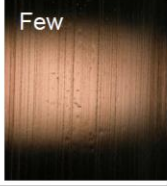


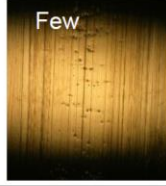

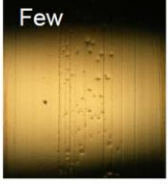


3.5.9 **The effect of water on micropitting**

As discussed in section 3.5.2, ZDDP promotes micropitting on the surface and the micropitting-enhancing properties of ZDDP is ascribed to the early and rapid ZDDP-tribofilm formation and consequent increase in local plastic deformation. Moreover, the detrimental impact of water on the fatigue life of bearings is discussed in section 3.5.7. Water contamination is also believed to enhance micropitting in rolling-sliding contacts (3, 81, 151, 170). Devlin, Ryan and Tsang (170) reported that water profoundly interferes with the functionality of additives in the wind turbine oils suppressing anti-corrosion, film formation, and friction-reducing properties of oils leading to accelerated micropitting and fatigue. Nedelcu *et al.* (151) showed that the dispersed water at different concentrations in a ZDDP-containing oil induces micropitting on the surface as presented in Figure 3-58.

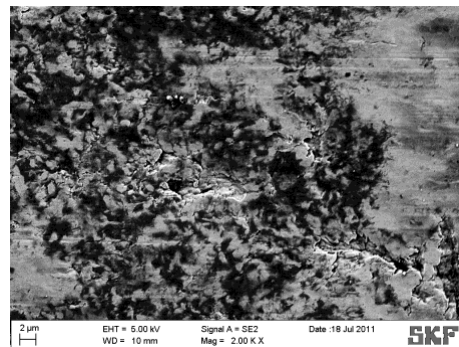
In contrast to those, Brizmer, Pasaribu and Morales-Espejel (18) reported that an increase in RH typically tends to reduce micropitting. They suggested that micropitting performance mostly depends on the boundary friction and wear and hence an increase in wear tends to decrease micropitting. Thus, as increasing RH typically leads to more intensive wear, an increase in water level is expected to decrease micropitting. The postulated inverse-correlation between mild-wear and micropitting is, however, disputed by O'Connor (7) as discussed in section 3.5.2. Furthermore, the results referred to by Brizmer *et al.* (18) are produced by Cen (102) which do not show a certain correlation between micropitting and RH.

Cen (102) qualitatively compared the influence of RH on micropitting performance of PAO + ZDDP lubricated surfaces under different SRRs of 0.5, 2, 5 and 50%. As shown in , results by Cen (102) suggest that under SRRs of 0.5, 2 and 5%, an increase in RH from 20% to 60% resulted in no considerable change (or a small decrease under SRR of 0.5%) in micropitting extent, while an increased RH value of 90% leads to a considerable increase in micropitting in comparison to both RH 20% and 60%, except under an SRR of 5% in which micropitting was not noticeably observed in all relative humidities.

PAO+ ZDDP	RH	SRR (%)			
		0.5	2	5	50
Friction	20%	0.12	0.11	0.11	0.11
	60%	0.09	0.09	0.10	0.11
	90%	0.09	0.10	0.10	0.11
Wear (10^{-10} m^3)	20%	0.27	0.40	0.44	1.20
	60%	0.35	0.42	0.51	1.21
	90%	0.38	0.49	0.57	1.26

Roller images	20%				
	60%				
	90%				

(a)



(b)

Figure 3-61. a) Investigation of water effect on micropitting under different SRRs of 0.5, 2, 5 and 50% and b) SEM image from surface under SRR of 50% and RH of 20% (102)

In the case of 50% SRR, Cen (102) reported that an increase in RH from 20% to 60% decreases micropitting, while further increase of RH to 90% enhances micropitting. However, the result for 50% SRR and RH 20% is disputable as careful inspection of the roller image may suggest that the features on the surface are not micropits and requires meticulous investigation. Furthermore, as presented in (b), the SEM image from the surface does not show any evidence of a typical micropit appearance.

Cen (102) also examined the influence of two different relative humidities of 20% and 60% over three different SRRs of 0.5, 2 and 5% for two commercial gear oils (based on PAO base stock). He observed an increase in micropitting with respect to an increase in RH over all SRRs for one of the commercial oils (Oil-A), while a completely opposite trend is observed for the other commercial oil (Oil-B) showing a substantial reduction in micropitting with increased RH. An important observation is that wear volume was increased in both oils by an increase in RH value but to significantly different extents. Higher RH resulted in increased wear by approximately 70% and 260% as an average of three different SRRs for Oil-A and Oil-B, respectively. This implies that greater RH probably intensifies micropitting unless the resultant increase in wear is substantial enough to eliminate the generated micropits.

Alongside the ZDDP effect on micropitting, water contamination is also assumed to enhance micropitting wear in the bearings and gears lubricated with fully-formulated oils (3, 81, 170), although the tribochemical changes in the reaction films were not studied in detail. The gear teeth and bearings in wind turbine gearboxes prevalently suffer from micropitting which especially affects the bearing's functionality (3). Water contamination is common in wind turbine gearboxes (3) especially in off- and near-shore turbines (21). Therefore, it is important to understand the influence of water on micropitting in bearings operating in demanding applications e.g. wind turbine gearbox.

Although, the detrimental effects of water on the RCF (146, 159, 162) and ZDDP AW performance (148, 151) have been addressed, the influence of water and ZDDP-containing oil dispersion on specifically micropitting and detailed tribochemical understanding is not universally understood. Furthermore, the literature does not differentiate the impact of free water from that of dissolved water on micropitting. In this regard, the approach taken in the current study is to assess the tribological and tribochemical phenomena involved in the micropitting performance of water-contaminated lubricants containing ZDDP as an AW additive in a specially modified tribometer (MPR) for evaluating the tribocorrosion performance of lubricants which will be presented in Chapter 6.

3.5.10 **Micropitting and Friction Modifiers (FM)**

As reported in the previous sections, most of the research in micropitting with regards to the lubricant additive effects have been carried out with a focus on EP/AW additives and fully-formulated lubricants. The efficiency of MoDTC friction modifier in micropitting reduction has been shown by Laine *et al.* (92) as presented in section 3.5.2, while this improvement was not observed in Cen (102) results where a blend of PAO + Molyvan (5 wt%) intensified micropitting.

The influence of an OFM has been studied in a work by de la Guerra Ochoa, Otero and Tanarro (9). They evaluated the influence of three different types of additives on surface fatigue life of the specimens which were in contact against rougher discs. The investigated additives were glyceride of oleic acid OFM (at 2 wt%), amine phosphates EP and ZDDP AW additives and the results are presented in . In the tests with a relatively smooth counterbody (R_a : 0.1 μm), the OFM additive was efficient in reducing friction and vibration. Also, the surface fatigue was alleviated from macropitting, observed on the base-oil lubricated surface, to micropitting. The rollers lubricated with oils containing either AW or EP additives showed increases in material loss, significant chemical etching, micropitting and increased friction and subsequently the roller lubricated with EP-containing lubricant exhibited early fatigue. A decrease in AW or EP concentration from 1 wt% to 0.3% exacerbated the fatigue performance. Therefore in low roughness the OFM reduced friction, vibration and improved surface fatigue performance, while AW and EP accelerated the fatigue process.

However, in experiments where the counterbody roughness increased to 0.4 μm a different scenario was observed. Under the contact against rougher discs, OFM was not effective and could not finish the test similar to a base oil due to flaking and pitting. On the other hand, AW and EP substantially improved the roller durability due to decayed vibration despite having pits on the surfaces. The material loss and subsequent increase in wear scar width were considerably higher for EP and AW compared to base oil and OFM which suggest that increased wear rate results in a continuous reduction in contact pressure and improved surface fatigue performance. The images of the rollers are shown in . The results are important and interesting; however performance of a blend of OFM with either AW or EP would give a more realistic insight into their efficiency in fatigue.

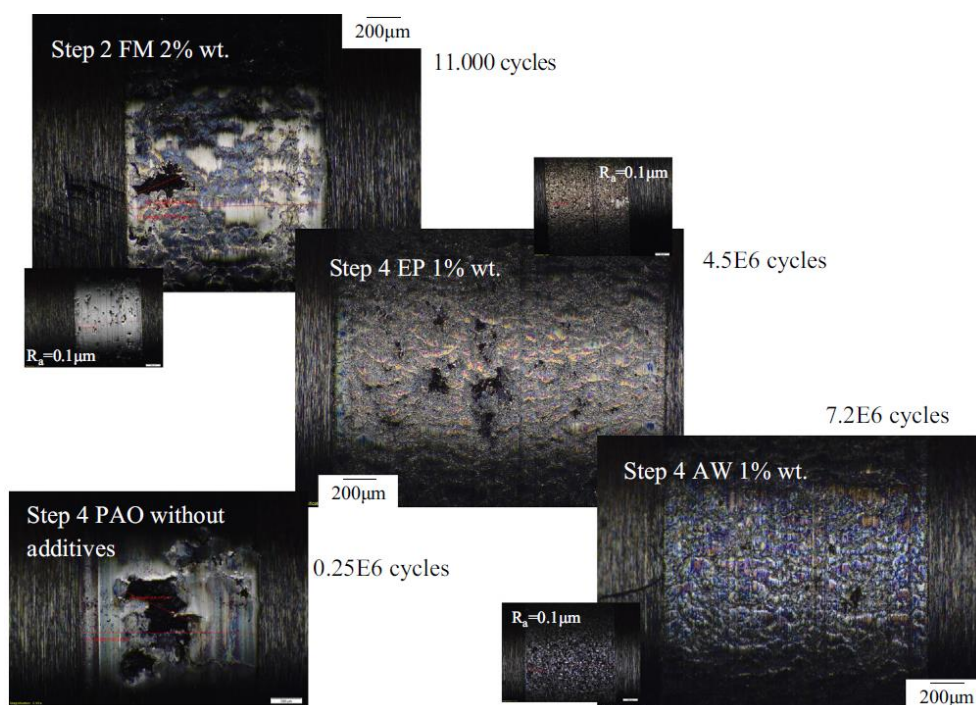


Figure 3-62. Optical micrographs taken from roller surfaces after tests with PAO + OFM, PAO + EP, and PAO + AW. The larger images represent the surface against the rougher disc (0.4 µm) and the miniature images correspond to the roller against the smoother disc (0.1 µm) (9)

As discussed, previous studies have shown that ZDDP (8, 18) and some of the other AW additives (5) can promote micropitting occurrence. However, AW additives are essential in order to suppress the wear in tribological systems and cannot be simply replaced with other types of additives. Therefore, emerging additive packages which can diminish micropitting while still offering protection of the surface from wear are of great interest to industry. Furthermore, updated fuel regulations restrict application of AW additives and other ash-containing additives like ZDDP and MoDTC. Thus, more researches are required to understand the influence and efficiency of OFMs and other more-environmentally friendly and low or no-Sulphated Ash, Phosphorus and Sulphur (SAPS) additives in tribological applications.

In this regard, OFMs should be subjected to investigations with respect to micropitting performance with the ultimate objective of developing lubricants with no or minimal environmental impact. In this work the influence of nitrogen-containing OFMs including amine, diamine and ethoxylated amine in combination with ZDDP AW additive has been studied in detail. The rationales behind employing nitrogen-containing OFMs are the efficiency of this type of OFMs in reducing friction

in combination with ZDDP (171), interactions between ZDDP and NCAs and the chemical composition of NCAs which are additive with no SAPS content.

Adsorption of ZDDP and its decomposition products on iron and/or iron-oxide surfaces has an influence on the AW performance of the ZDDP (172). It is assumed that a chemical interaction between the N in dispersants and/or amine friction modifiers and the P (173-174) and/or the Zn (175-176) in ZDDP can take place. While the interaction of the N in amine with P in ZDDP can be expected due to the difference in the dipole moment, the interaction of N as a complex ligand (electron-donor atom) with Zn as the coordination metal can form a Metal Complex (MC) which is thermodynamically stable.

The interaction of the dispersant with ZDDP propels ZDDP decomposition in oil to take place at a lower temperature compared to ZDDP alone (177-178). On the other hand, the assumed chemical MC formation in oil may lead to a reduction in the adsorption rate of ZDDP on the surface (175). Also, this chemical interaction may delay the chemisorption of ZDDP on the substrate (175, 179). As a result, the adsorption competition between free-amine and free-ZDDP and steric hindrance resulting from amine-ZDDP complex formation alter the ZDDP's AW properties (176, 179), while the enhanced thermo-oxidative decomposition of ZDDP can accelerate thermal film formation.

The change in the AW performance of ZDDP in amine-ZDDP combination depends on the chemical structure of the nitrogen-containing molecule and its concentration in oil (175-176). While Yamaguchi, Zhang and Kasrai (178) did not observe an alteration in the ZDDP AW performance as a consequence of dispersant (as a nitrogen-containing additive) addition, Zhang, Yamaguchi and Spikes (180) reported an increase in the wear rate when a dispersant is introduced to the ZDDP-containing lubricant in a prolonged rubbing test.

Knowing that the nitrogen-containing additives (organic friction-modifiers and dispersants) can alter the ZDDP tribofilm properties implies that they can alter the ZDDP tribofilm that is known to induce micropitting (8, 18). Therefore, friction modification and the affinity of the functional group of NCAs to ZDDP, which brings about a delay in the ZDDP tribofilm formation and a change in the tribofilm composition (175, 179, 181), may alleviate the micropitting-enhancing behaviour of ZDDP in NCAs + ZDDP lubricant formulation. There is no systematic understanding

of the resultant tribofilm derived from combination of nitrogen-containing OFMs and ZDDP and hence the results from this study will present new insights into the understanding of OFMs functionalities when combined with ZDDP. The results will also be critically discussed considering the existing literature in Chapter 9.

3.6 **Summary**

RCF encountered in bearings fundamentally differs from classical fatigue which makes it challenging to predict. RCF encompasses several different fatigue mechanisms including surface fatigue (micropitting, pitting and spalling), subsurface and WSF. Micropitting is a localized surface fatigue which prevalently occurs in wind turbine gearboxes. Micropitting results in altered contact geometry leading to pitting and eventually bearing failure. Tribochemical interactions of the lubricant additives significantly influence the surface fatigue performance of the bearings beyond their physical properties. Moreover, water contamination, which is common in wind turbine gearboxes, is postulated to enhance micropitting.

The remarkable AW performance of ZDDP has been the rationale behind using it in the lubricant formulations for bearing and gearboxes in order to suppress excessive abrasive, adhesive and smearing wear. ZDDP also has EP properties which can be perceived from its behaviour when the tribofilm is exposed to higher loads resulting from changes to its chemical and mechanical characteristics.

As far as micropitting is concerned, ZDDP is shown to intensify micropitting. While the decay in the martensitic structure of the steel is proposed to induce micropitting, the micropitting-enhancing properties of ZDDP are assigned to its preventive effect on proper running-in wear of the rough surfaces. However, considering the additive influence on running-in as the only influential factor, cannot justify the observations which show that micropitting performance depends significantly on the chemical structure of the additives as well as their interactions on surface and in the bulk lubricant (7). Therefore, there is a significant interlink between additive package and micropitting performance which should be investigated more in detail.

Chapter 4

Materials and methods

4.1 Experimental Methodology

4.1.1 Micropitting tests

Micropitting wear was investigated using a modified PCS Instruments MPR which is schematically represented in Figure 4-1. Two servo-controlled motors are utilised to allow rings and roller to rotate separately with different speeds which provide any combination of SRR and entrainment speed. Furthermore, the machine has the capability of controlling the load and temperature. The maximum load and temperature to be set are 1250 N and 135°C respectively.

The surface of interest is the surface of a spherical roller. The roller (12 mm in diameter) is in the middle and undergoes a cyclic load applied by three larger and equal-diameter counterbodies. The counterbodies are inner rings of a cylindrical roller bearing (designation CRB NU209) with modified roughness and outside diameter of 54.15 mm after grinding. In the present configuration, the value of contact cycles experienced by the roller is thirteen and a half times greater than the value of contact cycles experienced by each of the three ring. The roller and rings can be finished ground and/or honed to any desired roughness value and topographical pattern on the surface.

In this work all the rings in all experiments are carefully ground-finished transverse to the rotation-direction with the roughness of $R_q = 500 \pm 50$ nm and all the rollers in all experiments were circumferentially polished having a roughness value of $R_q = 50 \pm 5$ nm. In comparison to longitudinal or isotropic roughness of the counterbody (rings), a transverse roughness is shown to accelerate the micropitting incipient on the contact body (roller) having a smoother surface compared to the counterbody in the bearings (8, 47) and gears (15). Also, in this work a SRR of two percent is set for all performed experiments in accordance to a report by Morales and Brizmer (47) showing that the SRR of 0.01-0.02 can prompt the maximum surface area affected by micropitting wear.

In order to study the effect of the dissolved water, the rig is coupled with a humidifier capable of applying different RH values. The humidity control system has been

described in Morales-Espejel, Brizmer, Pasaribu and Morales-Espejel, and Cen reports (18, 47, 102). Applying humid air (with RH of 60% and 90%) into the test chamber generates dissolved water conditions in the lubricants. On the other hand, addition of water to the lubricant generates free water in the lubricant during early phase of experiments. However, due to water evaporation after the early phase of the experiment, the remaining part and most of the experiment is run in dissolved water conditions. A commercial contamination sensor, HYDAC AquaSensor AS 1000, was also employed to monitor the water saturation level in the oil. As shown in Figure 4-1, the sensor is in contact with the lubricant inside the chamber and records the saturation concentration of water relative to the oil temperature.

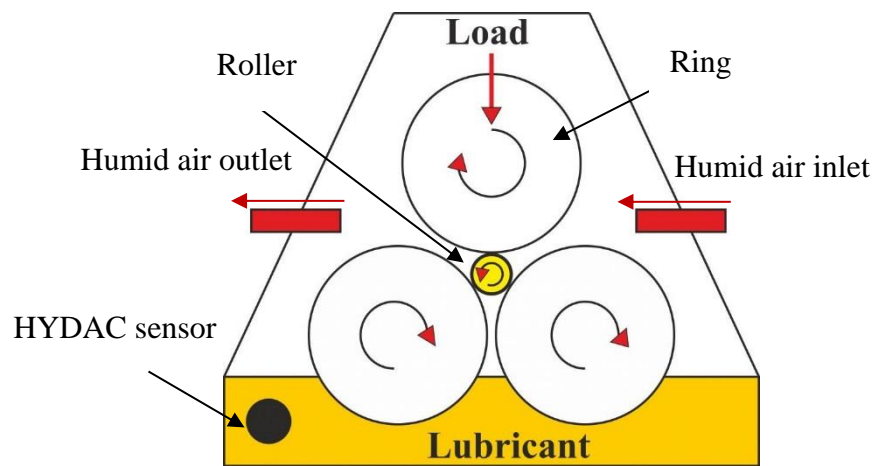


Figure 4-1. Schematic illustration of the MPR rig with the humidifier assemblies

The sensor's measurement unit which consists of a capacitive cell is inside the chamber in contact with the oil. The capacitive cell encompasses two electrodes and a dielectric polymer between the electrodes. The sensor does not measure the water content in the oil and only records the water saturation level in the oil with respect to the fully-saturated oil (100% saturation), in a percent range. 100 percent saturation corresponds to the solubility limit (saturation level) of water in the oil at the certain temperature. The state of water in oil as either *free water* or *dissolved water* is determined using the sensor. Thereby, where the sensor shows 100%, the amount of water in oil is in excess of the saturation level and thus free water conditions exist in the lubricant. Accordingly, a percentage of less than 100 indicates that water in oil is in the dissolved water state.

The micropitting test materials and parameters which are used for the current project are listed in Table 4-1. Prior to the tribological tests, rollers are thoroughly washed in acetone using ultrasound bath and rings and the MPR components and assemblies are washed using an component-cleaning equipment which uses certain solvents and hot-water. All the micropitting experiments are carried out at 90°C except those with the aim of assessing the effect of water and relative humidities which are performed at 75°C. Controlling RH at 90°C and subsequent potential condensation is arduous in the current experimental set-up which makes the results contentious. The test chamber of MPR is very large having a thick stainless-steel chamber-wall which generates temperature gradients in the test chamber especially in the high test temperatures (90°C). In this regard, the effect of dissolved water through absorption from humid air is only studied at 75°C.

Table 4-1. MPR test materials and parameters

Specimens	Roller: 52100 steel, R _q : 50 nm Hv: 785 Rings: 52100 steel, R _q : 500 nm, Hv: 745
Maximum Hertzian pressure (P _{max})	1.5 GPa
Temperature	75°C and 90°C
Entrainment speed	1 m/s
Slide-to-roll ratio	2%
Relative humidity @ 75°C	Laboratory conditions*, 60% and 90%
Contact cycles (on the roller)	62.5×10 ³ , 25×10 ⁴ , 5×10 ⁵ , 1×10 ⁶

*Laboratory conditions: T_{Environment}: 20 - 25°C and RH_{Environment}: 40 - 65%

The micropitting experiments together with the repeats for the specific conditions are performed in different seasons of the year which inevitably influences the laboratory environment conditions although the laboratory was controlled through ventilation systems. This change in the laboratory conditions is especially important for the tests investigating the influence of different RH values on micropitting. The absolute water-vapour pressure in the laboratory conditions (T_{Environment}: 20 - 25°C and RH_{Environment}: 40 - 65%) and at test temperature of 75°C are approximately 0.34 - 0.46 and 6 pounds per square inch (psia), respectively (182). Therefore, a change in the

humidity level in the laboratory conditions (25% RH) leads to a change in RH of 1.4-2% at the test conditions, which is negligible. Therefore, the influence of changes in the laboratory conditions induced by the changes in the weather conditions on the tests results is inconsiderable.

Prior and post to the actual tests there are pre-contact and post-contact (stopping) steps, respectively. The test procedure includes four pre-contact steps which are implemented in order to achieve desired speeds for rings and roller, lubricant temperature, load and SRR. The steps durations are, 30 s, 900 s, 60 s and 15 s, respectively. In order to apply desired relative humidities, the tube which is blowing humid air was connected to the chamber assembly during the last two minutes of the heating step as soon as the temperature was stabilised at the desired value. After the actual test, there is a stopping-step in which the un-loading takes place and rotation of the specimens is gradually halted. The duration of this step is approximately 1 minute and 45 seconds which is equal to approximately $6-8 \times 10^3$ cycles. These steps are essential since the tests cannot be started or stopped immediately.

4.1.2 **MTM and friction tests**

A PCS Instruments MTM-SLIM is used in this work in order to investigate the frictional behaviour and tribofilm formation properties of the additives used in the different lubricant formulations. MTM-SLIM is a ball-on-disc tribometer which is coupled with a camera capable of capturing images from the ball surface as shown in Figure 4-2. The ball which is attached to the shaft, loads against the disc. Ball and disc are driven by two independent motors to generate a mixed slide-to-roll contact. The maximum speed, temperature, and the load that can be reached by the tester are 4 m/s, 150°C, and 75 N respectively.

SLIM uses a white light source to capture the tribofilm based on the optical interferometric technique. At the end of each rubbing step, the ball was stopped and loaded in reverse against a glass window through which a static image was taken from the wear track on the ball surface using an RGB camera. The topmost surface of the glass is coated with a transparent silica space-layer, beneath which is a thin and semi-reflective chromium layer. The beams reflected from the chrome layer and the ball surface generate an interference image following recombination of the light paths. The image is frame-grabbed by the camera and analysed by the control software to

determine the film thickness. SLIM has been explained in detail by Taylor, Dratva and Spikes (183).

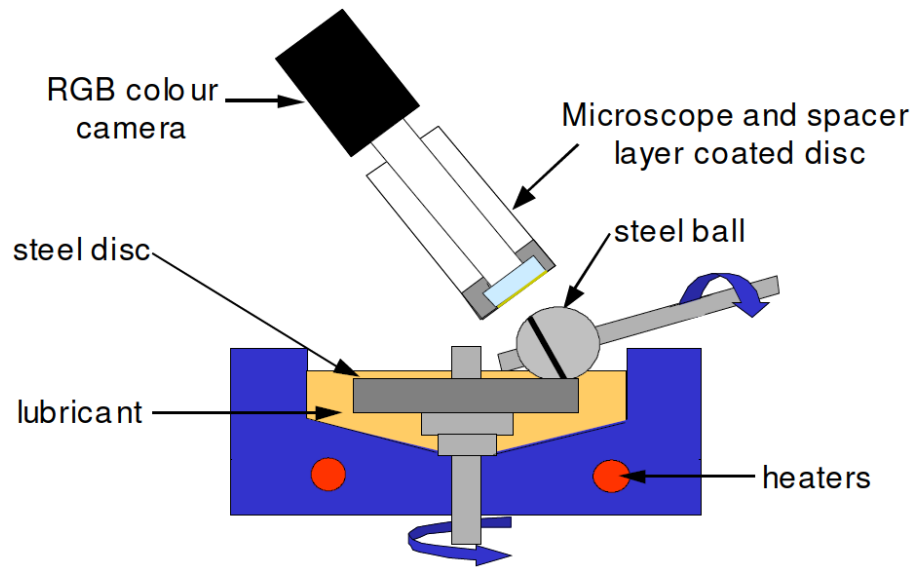


Figure 4-2. Schematic illustration of PCS Instruments MTM-SLIM

MTM tests are carried out in the standard configuration using test specimens which were a 19.05 mm (3/4") AISI 52100 steel ball with the hardness value of 800-920 Hv against a softer 46 mm diameter AISI 52100 steel disc with the hardness value of 720-780 Hv. In this work two different sets of experimental parameters are used to investigate the friction behaviour and tribofilm thickness. The temperature, SRR, entrainment speed for all rubbing steps and entrainment speed range for Stribeck curve are fixed for both sets of experiment which are 90°C, 5%, 100 mm/s and 3000-15 mm/s, respectively. The major difference between the two sets of experiments is the roughness value of the disc specimen while balls used for both sets of experiments have the same specifications including roughness and hardness values. The experimental parameters are indicated in Table 4-2 and Table 4-3.

In both configurations, applying 35 N, 1 GPa of maximum Hertzian contact pressure has been applied to the surfaces at the start of the experiments. The bulk lubricant temperature is maintained and controlled at 90°C and SRR is set to 5% during all MTM experiments. Once the oil reached a steady temperature of 90°C, the load was applied and a Stribeck curve (3000–15 mm/s) was measured which is then followed by a rubbing step at a constant entrainment speed of 100 mm/s and a SRR of 5% for a pre-defined time interval. The SLIM coupled with MTM was employed to map and

measure the thickness of the reaction film formed on the ball surface after this rubbing step.

Table 4-2. Experimental set up of MTM (smooth ball - smooth disc) tests

Specimens	Ball	Disc
Material and dimension (diameter)	AISI 52100 steel - 19.05mm	AISI 52100 steel - 46mm
Hardness (Hv)	800 - 920	720 - 780
Roughness (R_a in nm)	16	8
P_{max} (GPa)		1
Temperature ($^{\circ}C$)		90
Rubbing-step duration between Stribeck steps (in minute)	5, 10, 15, 30, 60, 60, 60	
Stribeck diagrams and mappings after total rubbing time of (min)	0 (initial), 5, 15, 30, 60, 120, 180, 240	
Slide-to-roll ratio (%) throughout the test	5	
Entrainment speed for all rubbing steps	100 mm/s	
Entrainment speed range for Stribeck curve	3000 – 15 mm/s	

In the Smooth ball - Smooth disc (SS) configuration, the three-step test procedure, based on the procedure applied by Taylor, Dratva and Spikes (183-184), was repeated several times during the experiment. Stribeck friction curves are acquired at the start of the test and then after total rubbing time of 5, 15, 30 min, 1, 2, 3 and 4 h, respectively and plotted for the different lubricants. In the Smooth ball – Rough disc (SR) configuration Stribeck friction curves are measured twice, once at the start of the test and later at the end of the test. Each test has been repeated twice and the reported results are the average of the repeated experiments.

Table 4-3. Experimental set up of MTM (smooth ball – rough disc) tests

Specimens	Ball	Disc
Material and dimension (diameter)	AISI 52100 steel - 19.05mm	AISI 52100 steel - 46mm
Roughness (R_a in nm)	16	90 - 110
P_{max} (GPa)		1
Temperature		90°C
Rubbing-step duration in order of (in minute)	5, 10, 15, 30, 60, 60, 60	
Stribeck diagrams measurement after total rubbing times of	0 (initial), 240	
Mapping after total rubbing times of	0 (initial), 5, 15, 30, 60, 120, 180, 240	
SRR% throughout the test	5%	
Entrainment speed for all rubbing steps	100 mm/s	
Entrainment speed range for Stribeck curve	3000 – 15 mm/s	

4.1.3 Lubricants

In all the experiments in this work, the base stock used is a low-viscosity PAO base oil. The kinematic viscosity of the base oil was 4.0 cSt at 100°C. The dynamic viscosity of the base stock which is used to calculate the minimum lubricant-film thickness in contact is 2.85 mPa.s at 90°C. Minimum film thickness in the contact ($h_{min} = H_{min} \times R_x$) has been calculated using the Hamrock-Dowson equation (32) indicated as Eq 1.

$$H_{min} = 3.63 \left(\frac{U_e \eta_0}{E' R_x} \right)^{0.68} (\alpha E')^{0.49} \left(\frac{W}{E' R_x^2} \right)^{-0.073} (1 - e^{-0.68k}) \quad \text{Equation 1.}$$

Where H_{min} is minimum dimensionless film thickness, $R_x \left(\left(\frac{1}{R_{x,a}} + \frac{1}{R_{x,b}} \right)^{-1} \right)$ is the effective radius of curvature in the direction of x (tangent to the path of motion), $R_{x,a}$ and $R_{x,b}$ are the radius of curvature of body a (ball or roller) and body b (disc or ring) in MTM ball-on-disc and MPR roller-rings type of contact in the direction of x, respectively, α is the viscosity-pressure coefficient ($1.1 \times 10^{-8} \text{ Pa}^{-1}$), W is the

normal load (N), U_e is the lubricant entrainment speed (m/s), η_0 is the dynamic viscosity of the lubricant (2.85×10^{-3} Pa.s at 90°C), E' is the effective modulus of elasticity, and k is the elliptical parameter which is equal to 1.03 and 4.08 in MTM ball-on-disc and MPR roller-rings type of contact respectively.

Lambda ratio (λ) is the indication of the lubrication regime in the centre of contact and is defined as the ratio of the minimum film thickness (h_{min}) to the average root mean square roughness of the two surfaces (Eq 2). Where $R_{q,a}$ and $R_{q,b}$ are the root mean square roughness of the contact body one (ball/roller) and contact body two (disc/rings) respectively.

$$\lambda = \frac{h_{min}}{\sqrt{R_{q,a}^2 + R_{q,b}^2}} \quad \text{Equation 2.}$$

The Lambda ratios in SS and SR configurations used in MTM tests are $\lambda = 0.17$ and $\lambda = 0.035$, respectively. Therefore, in SR configuration the severity of the contact is propelled to the boundary lubrication regime, while in SS configuration, surfaces experience a mixed/boundary lubrication regime. In MPR experiments the initial lambda ratio at the start of contact is $\lambda = 0.04$ and $\lambda = 0.05$ at 90°C and 75°C ($\eta_0 = 3.8 \times 10^{-3}$ Pa.s at 75°C), respectively, which is an indication of the boundary lubricated contact.

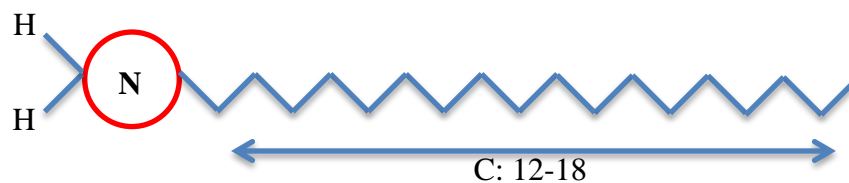
4.1.3.1 Lubricant additives

In the current work four different types of NCAs have been used which are illustrated in Table 4-4. All the NCAs are provided by AkzoNobel and are commercial products used in different industry sectors. The commercial product names are included in Table 4-4. The NCAs are amphiphilic molecules. The alkyl chain of the NCAs is their non-polar moiety and is hydrophobic. The hydrophobic part is not a chemically-functional group and influences physical parameters such as steric hindrance, solubility and Critical Micelle Concentration (CMC). Although the hydrophobic part is responsible for the friction reduction capability of the additives, the efficiency of the friction reduction is significantly influenced by the polar moiety. This results from the affinity of the hydrophilic parts to the surfaces and their interactions with the other lubricant additives. The alkyl chain of the NCA molecules is determined to be the same, tallow alkyl group, in order to eliminate the influence of hydrophobic part and investigate the effect of the functional group.

Table 4-4. Molecular structure of the investigated NCAs

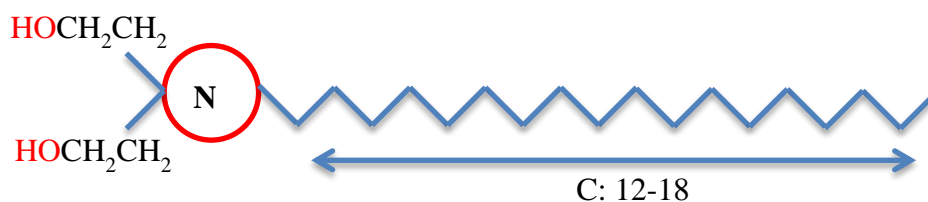
Primary Amine: Tallowalkyl-Amine (TA)

Product commercial name: Armeen TD



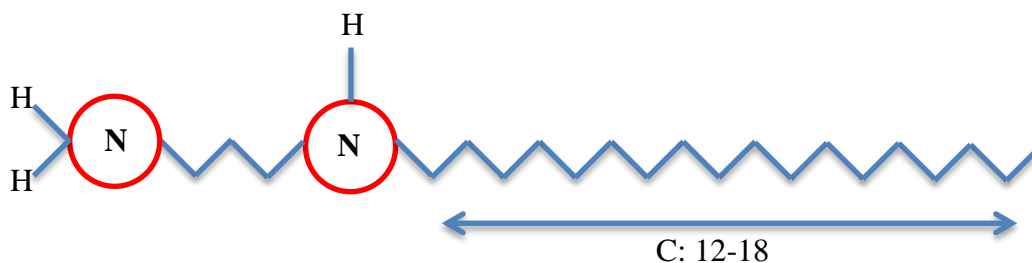
Ethoxylated Amine: Ethoxylated (2) Tallowalkyl-Amine (ETA)

Product commercial name: Ethomeen T/12



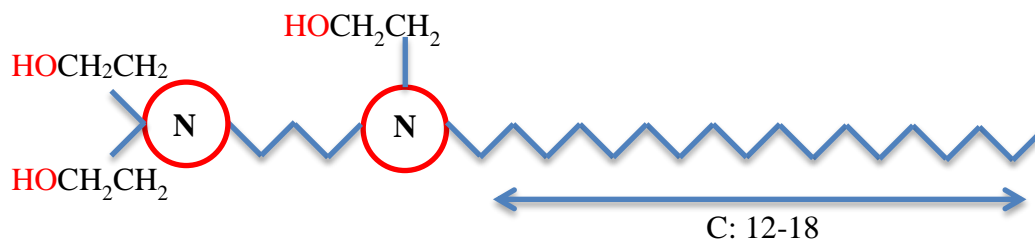
Diamine: N-Tallow-1,3-DiaminoPropane (TDP)

Product commercial name: Duomeen T



Ethoxylated Diamine: Ethoxylated (3) N-Tallow-1,3-DiaminoPropane (ETDP)

Product commercial name: Ethoduomeen T/13



The alkyl chain of the NCAs is a tallow hydrocarbon and the exact composition of the chain is not indicated in the additive MSDSs. However, a typical chain length distribution and degree of unsaturation in tallow is shown in Table 4-5.

Table 4-5. Chain length distribution and degree of unsaturation of tallow (185)

Chain length	Degree of unsaturation	Composition
C 14	None	0 – 6 %
C 16	None	20 – 37 %
C 18	None	14 – 21 %
C 16	1	3 – 9 %
C 18	1	35 – 46 %
C 18	2	4 – 10 %
C 18	3	0 – 3%

4.1.3.2 Lubricant formulations with water content

The water-lubricant dispersions are prepared by adding the required amount of deionised water to the lubricant and mechanical shaking followed by an ultrasonic mixing. The ultrasonication is carried on until water is fully dispersed in the lubricant and no noticeable deposition can be observed in the dispersion similar to the dispersing method used in the report by Nedelcu *et al.* (151). Also, the temperature of the dispersions always was kept below 40°C during mixing to avoid considerable water evaporation. Water-containing lubricant dispersions became cloudy after mixing implying creation of an emulsion phase and existence of free water in the lubricant. The lubricants to which water is added prior to the tests are denoted as the lubricants with added-water further in the text. The effect of water on micropitting wear has been examined using four lubricants; details are given in Table 4-6.

Cen *et al.* (148) carried out experiments under controlled humid environments (RH values of 60% and 90%) and using 1% water-containing lubricant. The results showed that changes in the bulk properties of the oil (viscosity and TAN) are negligible on addition of small amounts of water to a ZDDP-containing PAO oil (148). Therefore, it has been assumed that the addition of water with the concentrations used in this work is not affecting the lubrication regime and conditions (minimum film thickness), and consequently the influence of water and humidity on micropitting wear is induced by the interaction of water with the lubricant additives rather than interaction of water with the base oil.

Table 4-6. Lubricant formulation table

Lubricant formulation	Lubricant designation
PAO base oil $\nu = 4$ cSt @100°C	BO
PAO + ZDDP (0.08 wt% phosphorus)	BO + ZDDP
PAO + ZDDP (0.08 wt% phosphorus) + (1 wt%) deionised water	BO + ZDDP + 1% water
PAO + ZDDP (0.08 wt% phosphorus) + (3 wt%) deionised water	BO + ZDDP + 3% water

4.1.3.3 Nitrogen-containing additive - containing Lubricant formulations

In order to investigate and understand the influence of NCAs on the lubricant performance, experiments have been carried out using MPR and MTM tribometers. Both MTM and MPR tribological tests have been carried out using five lubricants; details are given in Table 4-7:

Table 4-7. Lubricant formulation matrix

Lubricant formulation		Lubricant name
PAO base oil $\nu = 4$ cSt @100°C		BO
PAO + ZDDP (Phosphorous: 0.08 wt%)		BO + ZDDP
PAO + ZDDP + TA	TA (wt%)	
	0.5	BO + ZDDP + TA (0.5%)
	1	BO + ZDDP + TA (1%)
PAO + ZDDP + ETA	ETA (wt%)	
	0.5	BO + ZDDP + ETA (0.5%)
	1	BO + ZDDP + ETA (1%)
PAO + ZDDP + TDP	TDP (wt%)	
	0.5	BO + ZDDP + TDP (0.5%)
	1	BO + ZDDP + TDP (1%)

The NCAs are blended to the oils using ultrasound bath at 45-50°C whilst mixing for 30 minutes.

4.2 Surface Analysis

4.2.1 Wear scar observation

The wear scar profile has been obtained utilising Bruker's NPFLEX based on Wyko (White Light Interferometry (WLI)) technology. In order to measure the wear volume in the wear track on the MPR rollers, four profiles from four different spots of each specimen have been generated and the average value of the four spots on each specimen is considered as wear volume. Prior to the wear measurement and WLI analysis, the tribofilm and residual oil on the specimen have been removed thoroughly by wiping the specimen's surface using tissue and acetone followed by ultrasonic cleaning in acetone for thirty minutes.

In this study attempts have been made to produce a representative map from the micropitted area in the wear scar on the surface of the roller by the implementation of the Multiple Region (MR) data analysis technique which has been incorporated in the Vision64 software. The process is shown schematically in Figure 4-3.

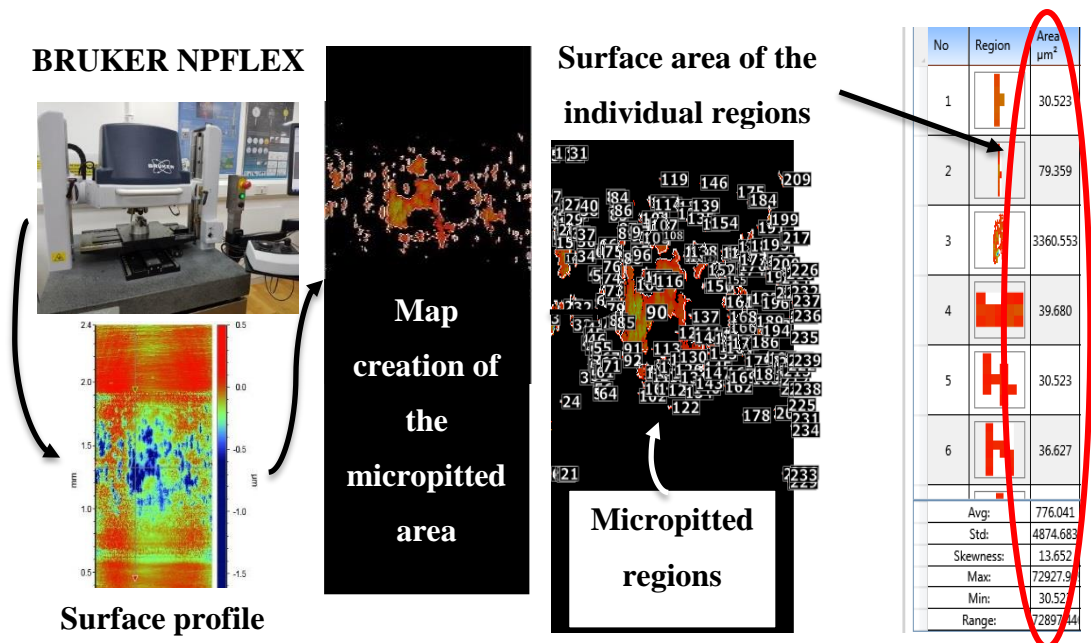


Figure 4-3. Illustration of micropitted surface-area measurement using multiple region analysis

The scanned WLI images of the wear scars are analysed using MR analysis with the minimum data pixel size set to 10. In order to screen the real data from data generated through software error, the data which are smaller than $10 \mu\text{m}^2$ in surface area were excluded from further analysis. Following careful MR analysis the total micropitted surface area on the scanned WLI images are calculated through summing up the

identified discrete micropitting regions. The average of measurements from three different specimens are reported as the average micropitted surface area.

4.2.2 **Scanning electron microscopy**

In order to inspect the wear scar and tribofilm in the wear scar and its elemental composition SEM and EDX analyses have been carried out on the specimens. Two SEM have been utilised in this study which are a Carl Zeiss Supra 55 and a Carl Zeiss EVO MA15. Supra SEM is used to capture images through secondary electron detector collecting the secondary electrons emitted from the surface of the MPR rollers. The specimen's electrons have been excited by electrons coming from the electron-gun having an acceleration voltage of 5 kV. In order to inspect the tribofilm in the wear scar, the residual lubricant on the specimen has been cleaned through flushing n-heptane followed by ultrasonic cleaning in n-heptane for three minutes prior to SEM analyses. Whilst the wear scar and micropitting features have been examined following a washing procedure of tissue wiping using acetone followed by ultrasonic cleaning in acetone for 30 minutes in order to remove residual oil and reaction film from the surfaces.

4.2.3 **Optical microscopy**

Optical images from wear scars are captured in order to inspect the wear scars of the MPR specimens lubricated over different contact cycles and with different water contents. Two optical microscopes are used in this study which are a Leica DM6000 optical microscope, appropriate for inspecting high magnification images, and a Leica Stereo Microscope M205C which is suitable for inspecting a larger overview of the wear scar. The same washing procedures as those used in WLI and SEM analyses have been employed prior to the optical microscopy.

4.2.4 **X-ray photoelectron spectroscopy analysis**

XPS surface analysis has been carried out utilising a PHI 5000 Versa Probe™ spectrometer (Ulvac-PHI Inc, Chanhassen, MN, USA) which uses a monochromatic Al K α X-ray source (1486.6 eV). Prior to the XPS analysis residual lubricant on the surface has been eliminated through flushing n-heptane followed by ultrasonic cleaning in n-heptane for three minutes. The specimen is mounted on an appropriate holder and transferred to the introduction chamber in order to achieve the desired vacuum before introducing to the main chamber. Survey spectra with an energy step

size of 1 eV were collected from different locations in order to accurately identify inside and outside of the tribological contact. Detailed High Resolution (HR) spectra have been collected from small areas inside the wear track approximately at the centre with a beam size of 100 μm and a power of 23.7 W in the fixed analysed transmission mode selecting an energy step size of 0.05 eV for the O, Fe, P, and S acquisition and 0.1 for C and Zn. The residual chamber pressure was always lower than 5×10^{-7} Pa during spectra acquisition.

The detailed XPS spectra were fitted using CASAXPS software (version 2.3.16, Casa Software Ltd, UK) with Gaussian–Lorentzian curves after subtracting a Shirley background. Aliphatic carbon Binding Energy (BE) is referred to 285.0 eV in order to correct the charging effect of the beam on specimens. In accordance with spin-orbit splitting, area-ratio-constraint of 2:1 for the two components of the signal ($p_{3/2}$ and $p_{1/2}$) has been considered to perform P (P 2p) and S (signal S 2p) signal fitting (151, 186). Also, position-difference-constrain of 0.85 eV and 1.25 eV is applied for the two components of the P and S signals, respectively (151). The detailed spectra from Zn Auger ($L_3M_{4,5}M_{4,5}$) signal were collected and fitted using two peaks in order to extract two signals (1G and 3F) (187). Modified Auger parameter (α') was calculated using Zn $2p_{3/2}$ BE and Zn $L_3M_{4,5}M_{4,5}$ 1G Kinetic Energy (KE) signals.

Following detailed analysis of the tribofilm top surface, the tribofilm is sputtered using an Ar^+ ion source (2 keV energy, $2 \times 2 \text{ mm}^2$ area and 1 μA sputter current), in order to estimate the tribofilm thickness and observe the elemental distribution of the tribofilm across its depth. The ion sputtering performed for 60 s between XPS detailed acquisitions after each sputtering. The etching rate on steel was found to be 4.5 nm per minute by Wyko (151). The sputtering time at which the concentration of O 1s signal becomes less than 5% and traces of the tribofilm elements (Zn, P, S) are not found in the detailed spectra, is considered as a measure of the reaction layer thickness (151).

4.2.5 **Transmission electron microscopy and energy-dispersive X-ray**

In order to inspect the reaction films in the wear scars, cross sections of the MPR rollers from the worn area were prepared by FIB using FEI Nova 200 NanoLab high resolution Field Emission Gun Scanning Electron Microscope (FEGSEM). FIB sectioning is collected from an area close to the edge of a micropit perpendicular to

the rolling-sliding direction. In order to protect the lamellas from the ion beam an initial layer of platinum is laid down on the surface to a thickness of 100 nm approximately. Following the initial Pt layer, a bulk platinum layer with an approximate thickness of 2 μm is deposited on the region of interest prior to etching by FIB in order to mitigate damages by ion beam (188). Subsequent to platinum deposition, the area of interest is milled by FIB from both sides to a depth of 10-15 μm to obtain a lamella. In the final step the lamella is thinned, detached from the specimen and mounted to a copper grid employing a micromanipulator.

The FIB etched lamella was examined using a transmission electron microscope. TEM images were obtained utilising a FEI Tecnai TF20 FEG-TEM/STEM. EDX analysis was employed to identify tribofilm elements within the film. An Oxford Instruments INCA 350 EDX system equipped with X-Max SDD detector and Gatan Orius SC600A CCD camera was used to produce elemental mapping. The thickness of the prepared lamella is less than 100 nm. Also the beam energy is much greater than that of SEM. As a result, the interaction volume of the electron beam with the specimen is negligible compared to EDX-SEM which brings about less beam scattering and consequently significantly higher spatial resolution compared to SEM (189).

4.2.6 **Topographical/roughness analysis of the tribofilm**

AFM analysis can provide a typical lateral resolution of less than 5 nm and vertical resolution of less than 0.1 nm. Therefore, a Bruker's (Dimension Icon) AFM, shown in Figure 4-4, was used in order to study the topographical characteristics of the tribofilms formed on the MTM disc surfaces. Separate MTM tests were carried out for AFM measurements using the BO + ZDDP and BO + ZDDP + TDP (0.5) lubricant formulations and test conditions are indicated in Table 4-8. AFM images have been taken on the tribofilm formed on the MTM discs at the approximate centre of the wear. Scans were carried out in tapping mode over areas of 20 $\mu\text{m} \times 20 \mu\text{m}$ and 5 $\mu\text{m} \times 5 \mu\text{m}$ for the tribofilm roughness and morphology study. For the AFM study, the test is halted after 15 minutes of rubbing followed by AFM analyses of the wear track on the MTM disc while the ball remained attached to the shaft. The oil was replaced with a fresh oil and a further rubbing step of 105 minutes was carried out on same specimens.

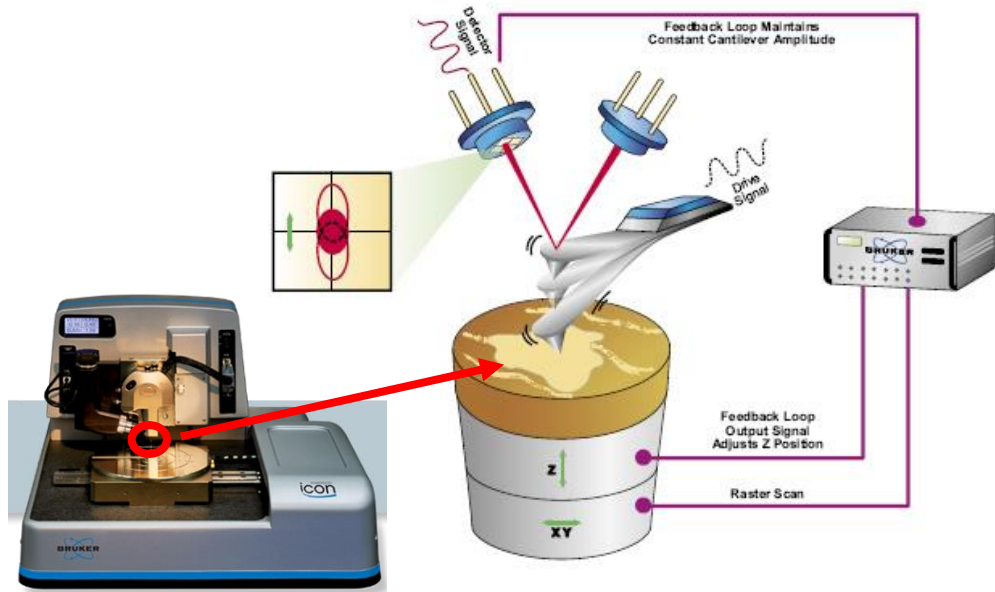


Figure 4-4. Bruker's (Dimension Icon) AFM in tapping mode (190)

The second AFM scan, performed on the disc, corresponds to the tribofilm formed after two hours of rubbing in total. The AFM scans after a rubbing duration of 15 minutes and 120 minutes were selected to represent the early and middle stage of the tribofilm formation and the established stage of the tribofilm formation (at which the friction coefficient and tribofilm-thickness will remain relatively constant), respectively.

Table 4-8. Experimental setup for topographical AFM analysis

Specimens	52100 steel R_a : ball: 16 nm, disc: 8 nm
P_{max}	1 GPa
Temperature	90°C
Slide-to-roll ratio throughout the test	5(%)
Entrainment speed	100 mm/s
Test duration	120 minutes
AFM scanning after rubbing time of	15, 120 minutes

Chapter 5

Investigation of the ZDDP effect on the micropitting surface fatigue

5.1 Introduction

The effect of ZDDP in accelerating micropitting has been shown using PCS Instrument MPR (8). However, the rig, which is used in this study, is a modified MPR in which the test specimens are a spherical roller and cylindrical rings taken from roller bearings. Therefore, understanding the micropitting evolution induced by ZDDP in the current test set-up is essential in order to carry on with the further investigations (water and potential additive effects on micropitting).

In the present chapter, firstly, the surface of rollers lubricated with BO and BO + ZDDP are inspected after 10^6 contact cycles. The wear volume on the roller surfaces and friction coefficient results in the contact are compared. The friction coefficient results are averaged and plotted over the last 30 minutes of the tests. Afterwards, the evolution of micropitting over contact cycles is inspected and addressed quantitatively and qualitatively using several surface analysis techniques including WLI, MR analysis, optical microscopy and XPS. The MR analyses are implemented in the current chapter in order to examine the change in micropitting-surface-area over contact cycles and exhibit its appropriateness in quantifying micropitting surface damage. In order to examine the ZDDP-tribofilm on nanometre scale Focused Ion Beam (FIB) sectioning is carried out in the wear scar and close to a surface micropit on the roller which has undergone 10^6 contact cycles. The FIB cross section has been investigated with TEM and EDX elemental analysis to inspect the elements throughout the tribofilm cross section.

5.2 Results

5.2.1 Friction and wear results of the surfaces lubricated with BO and BO + ZDDP

Figure 5-1 shows the total wear volume, friction coefficient and optical images of the roller surfaces lubricated with BO and BO + ZDDP after 10^6 contact cycles. The wear volume is decreased by 90% when ZDDP is present in the lubricant formulation. However, extensive surface damage can be seen in the wear scar of BO + ZDDP

(Figure 5-1 (b)), whereas BO lubricated surfaces show circumferential scratches along the rolling-sliding direction in the wear scars which suggest extensive abrasive wear on the surface. The friction coefficient during the last 30 minutes of the BO-lubricated experiment is 38% less than that of BO + ZDDP. Also, the friction coefficient of 0.054 in BO suggests a mixed/EHL lubrication regime which is propelled by high wear and the conformity of the surfaces. Therefore, the contact is not expected to be in boundary lubrication regime at the end of the experiment.

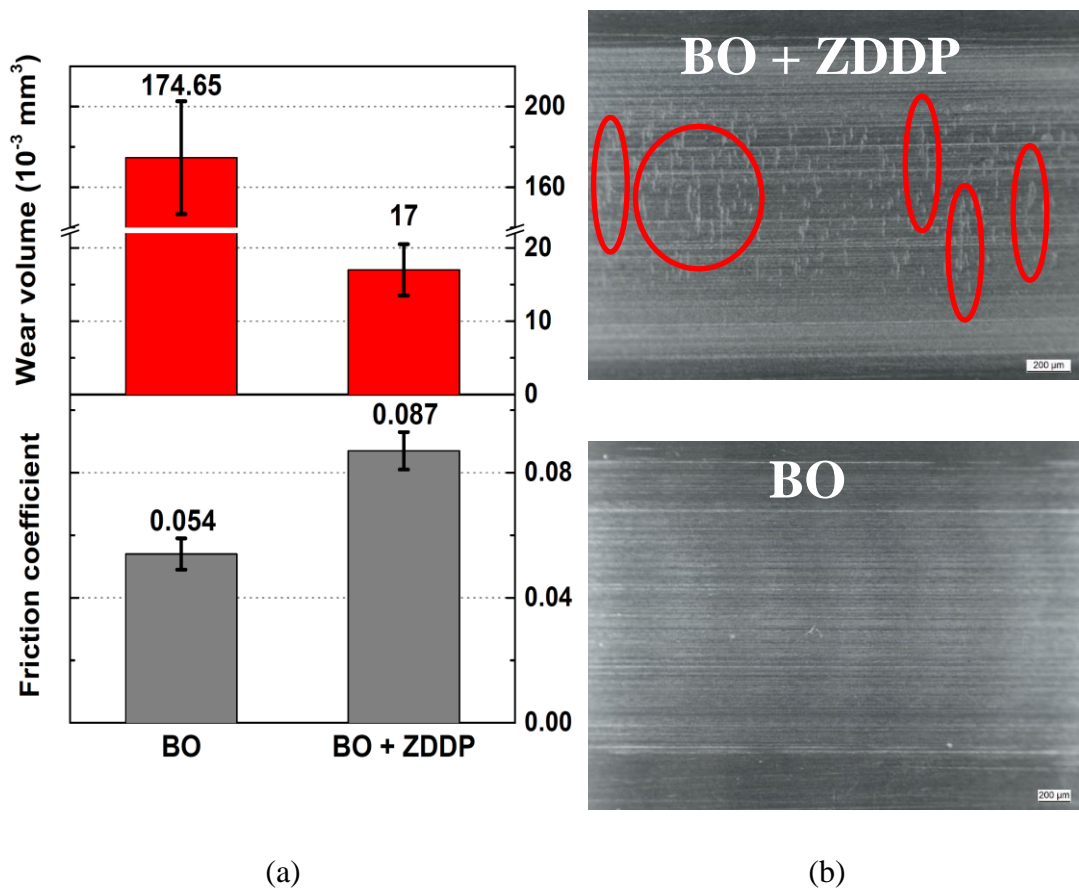
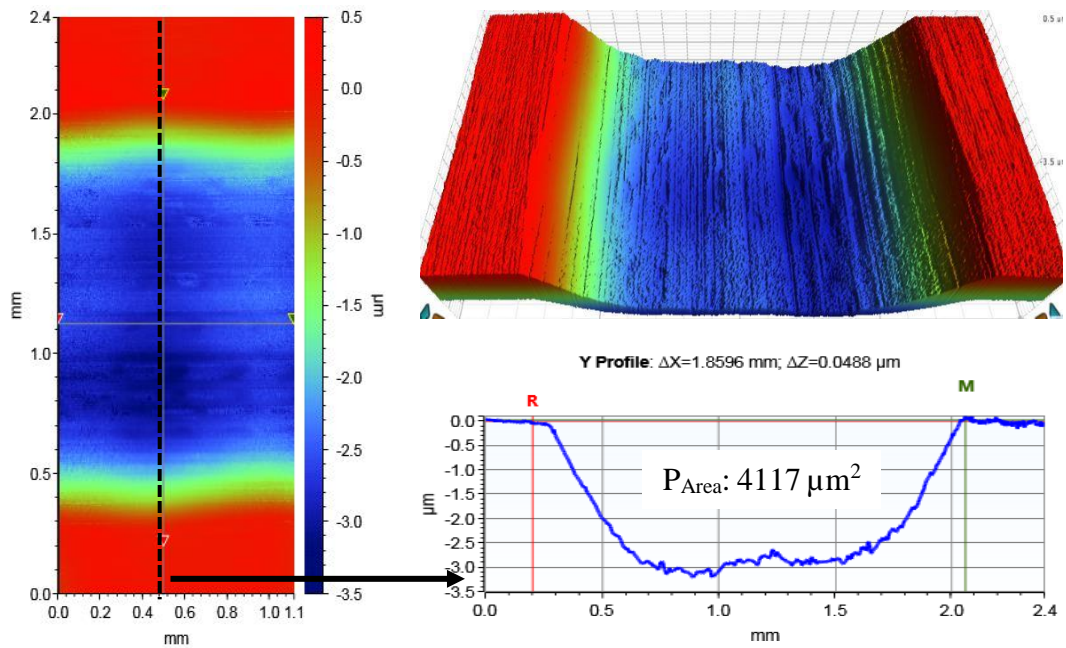


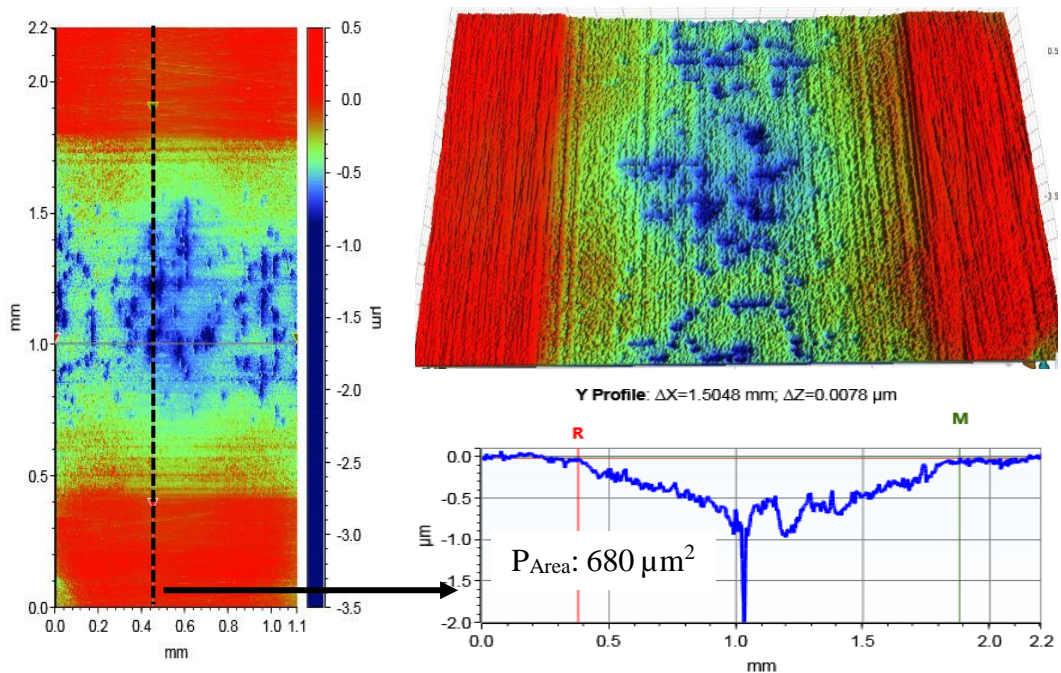
Figure 5-1. a) Wear and friction results and b) optical micrographs of the wear scars lubricated with BO and BO + ZDDP

The surface profiles of the rollers are obtained by WLI and shown in Figure 5-2 which clarify the low friction in the base-oil lubricated contacts. It is clear that 3-4 μm from the surface has been worn out in the wear scar of BO-lubricated roller. As the rollers are spherical in shape, the 3-4 μm removal of the top crest of the roller results in an increase in contact area and thus a decrease in the contact pressure. The increase in the contact area can be observed in the cross-sectional depth profiles of the wear scars shown in Figure 5-2, considering the wear width. The cross-sectional depth profile

corresponding to the black dashed line on the wear scar profile is presented on the right bottom corner of the figure.



(a)



(b)

Figure 5-2. The WLI images of the wear scars and corresponding depth profiles on the roller surfaces lubricated with a) BO and b) BO + ZDDP. R and M are the profile cursors which are placed at the wear track edges

While the wear-scar width in the BO + ZDDP lubricated rollers are approximately 1.5 mm, the wear-scar width of BO is 1.86 mm which shows an approximately 24%

increase in the wear width. Also, the significantly larger wear volume in BO wear scars relative to that of BO + ZDDP can be perceived through comparing the wear scar 3D profiles and depth profiles of rollers shown in Figure 5-2. In addition to the decrease in contact pressure, a substantial decrease in the roughness of the counter-bodies in BO-lubricated tests is the other reason behind the low friction at the end of the test. A decrease in counter-body roughness leads to an extensive increase in lubricant film thickness which avoids the further asperity-asperity contacts. In order to understand the wear process in the lubricants, the friction coefficient of BO and BO + ZDDP lubricants are plotted throughout the test duration in Figure 5-3. The friction coefficient in the BO + ZDDP-lubricated contact is around 0.1 at the start of the tests and reaches a steady state value of 0.087 ± 0.006 towards the end of the experiment. In spite of that, the BO-lubricated contact shows an entirely different trend to that of BO + ZDDP.

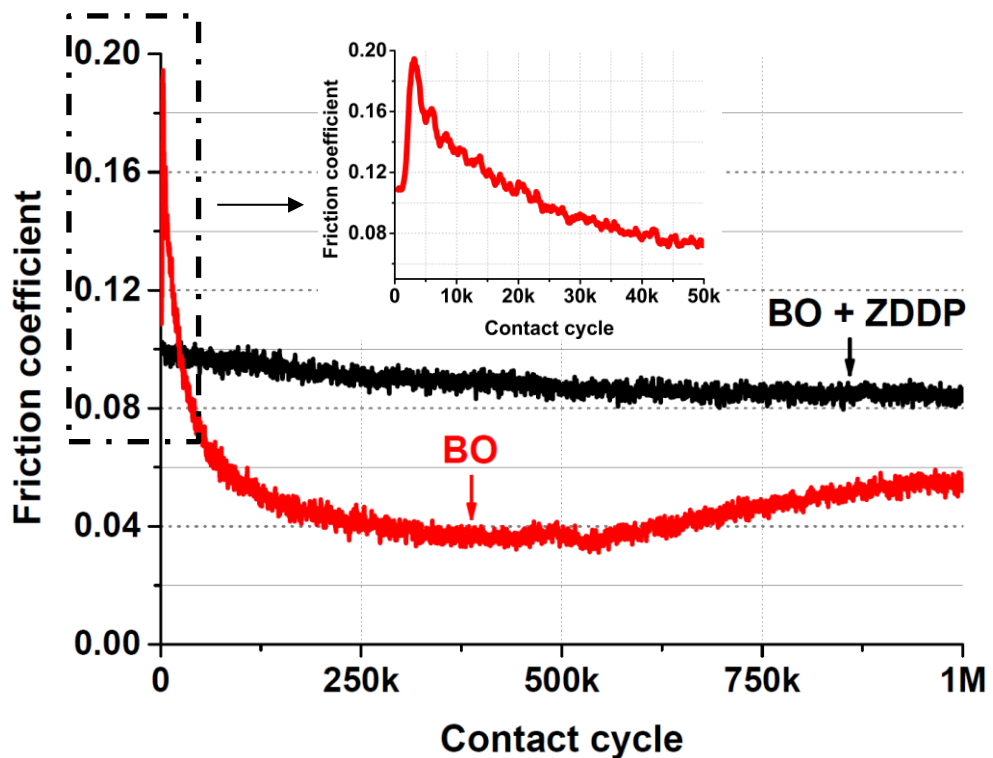


Figure 5-3. Friction coefficient in the contacts lubricated with BO and BO + ZDDP

As the shown in section 4.1.3, the λ at the start of the test is 0.04 which is an extremely severe condition. As a result of this severe tribological contact, there is a significantly sharp rise in the friction from 0.11 to almost 0.2 during first 5 K contact cycles which is close to the friction coefficient in dry contacts. Following the rise in friction there is an intense drop in friction within the next 150-200K contact cycles which results in

a friction coefficient value of 0.04. This trend suggests that in the current experimental set-up the BO-lubricated roller experiences a large material loss in the wear scar which affects the roller geometry after which the wear rate will be considerably lower. Therefore, the low friction coefficient of BO at the end of the test (Figure 5-1) results from harsh conditions in the start of the test leading to a change in the geometry of the contact.

The WLI profile of the BO + ZDDP wear scar shows that the ZDDP-tribofilm protects the surface from mild wear. However, it induces significant surface damage (micropits) on the surface, the depth of which can reach to more than 2 μm as shown in Figure 5-2 (b). SEM images of BO + ZDDP lubricated wear scars before and after tribofilm removal are shown in Figure 5-4 a and b, respectively.

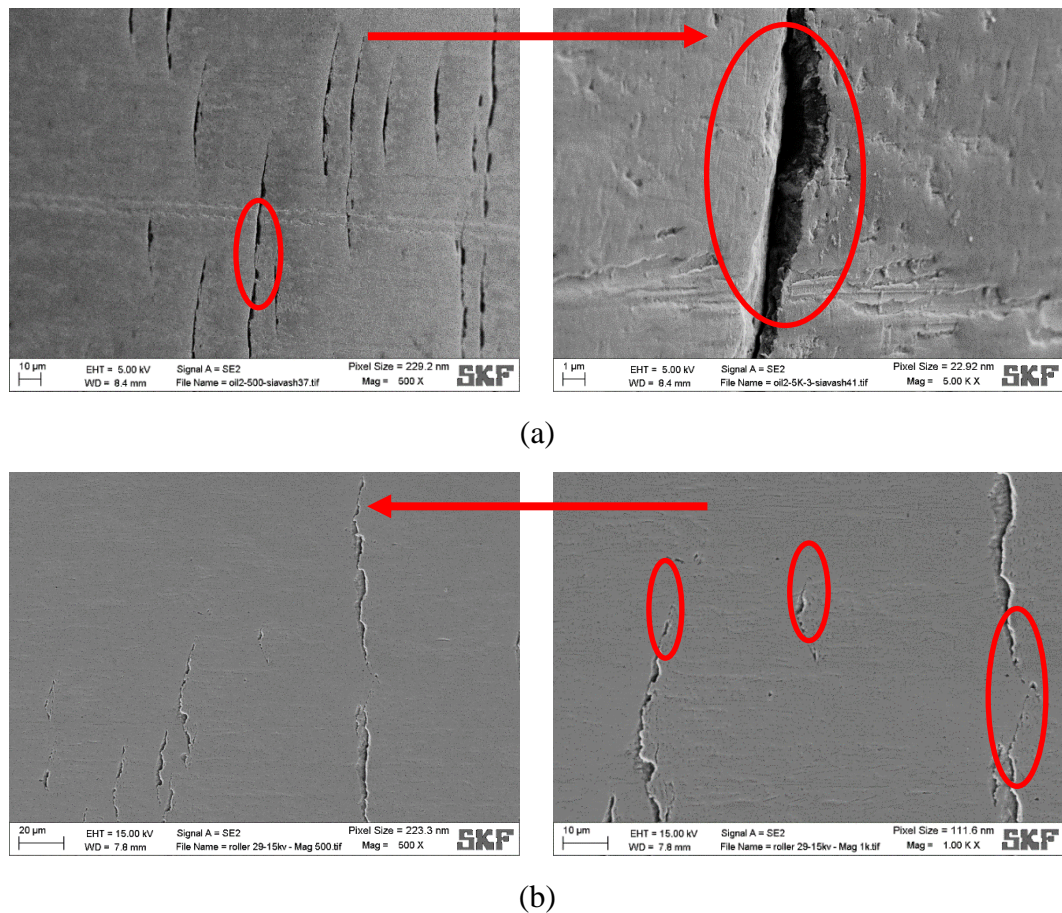


Figure 5-4. SEM images of BO + ZDDP lubricated wear scars undergone 10^6 contact cycles a) before and b) after tribofilm removal. *Red arrows on the images show the rolling-sliding direction

The SEM images show that the micropits propagate opposite to the sliding direction into the bulk of the material in agreement with Oila *et al.* (79) and also transverse to the rolling-sliding direction. Propagation opposite to the sliding direction generates

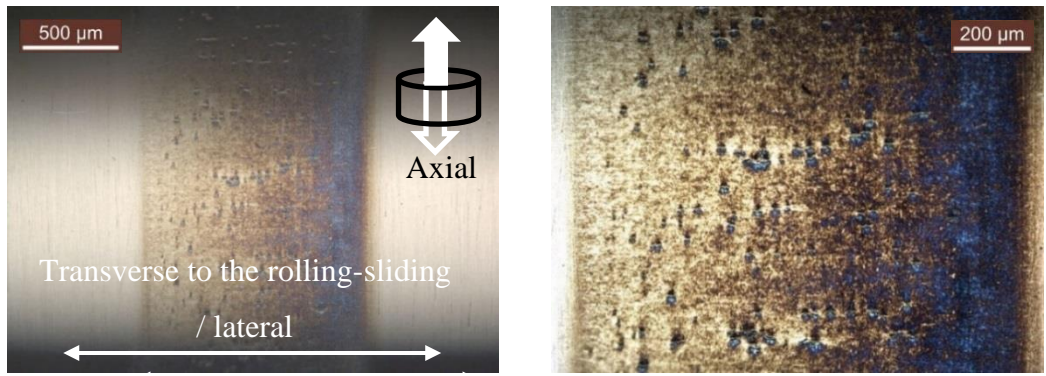
larger micropits through increasing depth of the micropit. Micropits also propagate along its length through crack opening at the edges of the micropits. The transversely propagated micropits can be coupled together to form a line of interlinked micropits. Also, as is clear in the Figure 5-1 (b) and Figure 5-2 (b), the micropits are mainly generated in the middle of the wear scar where the maximum Hertzian pressure occurs.

5.2.2 **The effect of ZDDP on micropitting wear**

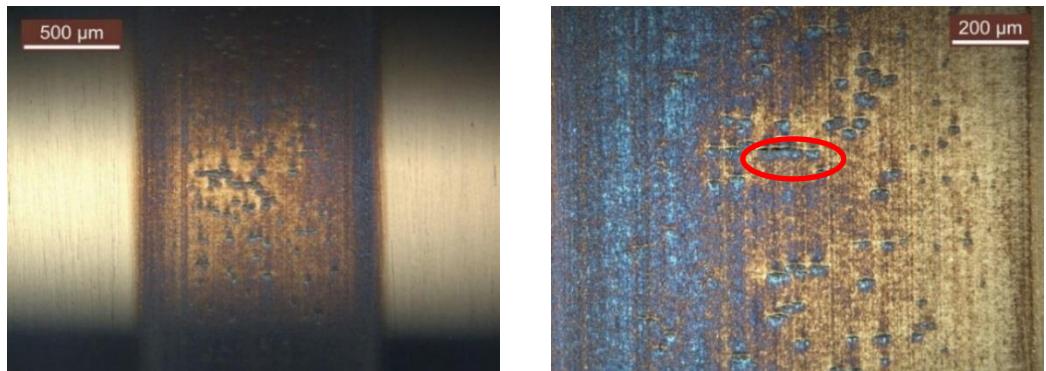
The previous section addressed the micropitting enhancing behaviour of ZDDP in the lubricant. In the current section the ZDDP effect on micropitting is evaluated from the initial stage of the experiment where micropits start to appear (micropitting nucleation) to the fully developed micropits (propagated micropits) after 10^6 contact cycles in order to observe the change in surface topography, micropitting morphology and density in the wear scars. This set of experiments helped to evaluate the capability of the modified MPR and understand the change in the micropitting extent and distribution over different contact cycles, which are required parameters to explain the effect of free and dissolved water which will be addressed in the next chapter. These stage-by-stage experiments were also designed to inspect the tribochemical change in the ZDDP-tribofilm over contact cycles which will be addressed in section 5.2.3.

The optical microscopy images of the roller surfaces are shown in Figure 5-5. As can be seen in Figure 5-5, after 62.5 K contact cycles the micropitting initiation can be observed in the wear scar. The micropitting density is small and interlinked micropits cannot be observed noticeably. With an increase in the contact cycles, micropitting surface density increases both through micropitting nucleation in the wear scar and propagation of initiated micropits to generate large micropits. The large micropits are generated through the propagation transverse to the rolling-sliding direction which are highlighted using red ovals in Figure 5-5. The roller surface after 10^6 contact cycles shows severe micropitting in the wear scar.

The micropitting propagation transverse to the rolling-sliding direction is dominant in the optical images as axial resolution in the optical images cannot be easily achieved and quantified. The axial resolution is also called depth of field or longitudinal resolution which is referred to the resolving characteristics of the lens which can be obtained parallel to the optical axis (191).



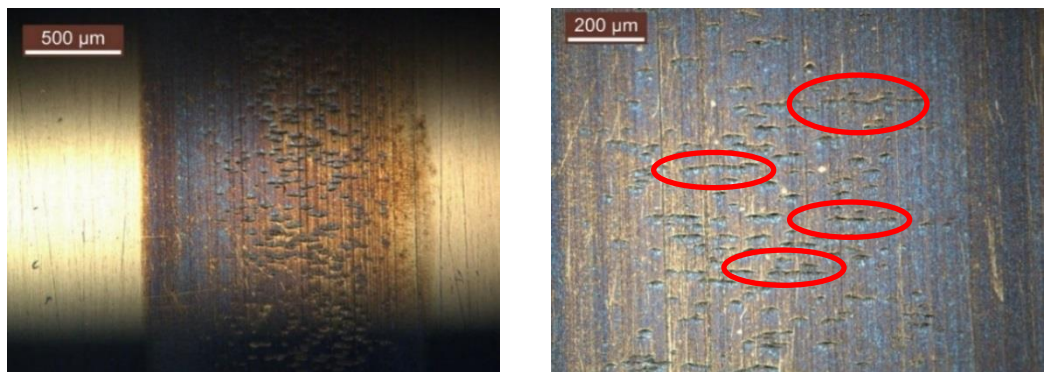
(a)



(b)



(c)



(d)

Figure 5-5. Optical microscopy images from roller surfaces after a) 62.5K, b) 250K, c) 500K and d) 1M contact cycles

In order to obtain the axial resolution to inspect the morphology and metrology, WLI images are taken and shown in Figure 5-6. Similar to Figure 5-5 the wear scar of the roller, which is undergone 62.5K cycles, shows traces of separately initiated micropits which are distributed in the wear track. Also, lateral micropitting propagation is not considerable after 62.5K cycles.

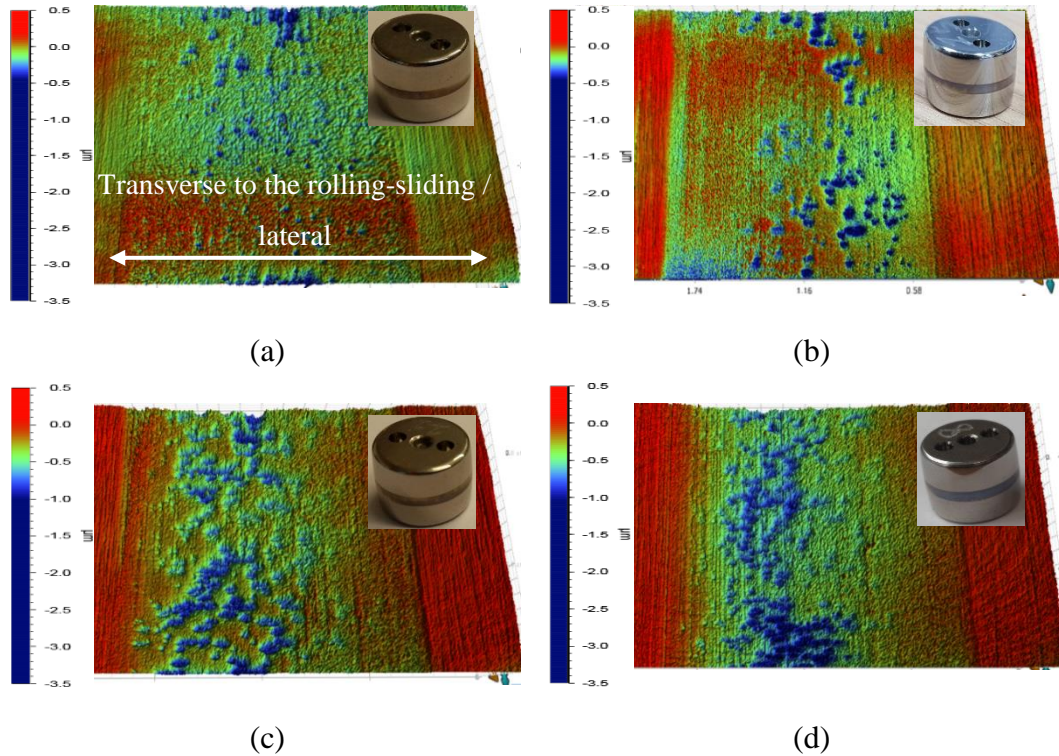


Figure 5-6. WLI 3D profile and roller image of the MPR rollers following complete removal of the tribofilm over different contact cycles of a) 62.5K, b) 250K, c) 500K and d) 1M

The WLI image does not show a considerable depression in the wear scar where there is no micropitting in the wear scar. This observation suggests that in the current experimental set-up, running-in wear is negligible and mild wear is inconsiderable in the first 62.5K contact cycles. Therefore, most of the wear volume in the first 62.5K contact cycles is originated from initiated micropits. However, mild wear can be observed in the wear scar of the roller which has undergone 250K contact cycles where a clear depression in the edge of the wear scar can be observed. Mild wear increases over contact cycles. The roller surface after 250K contact cycles shows a visible increase in micropitting initiation and minor proportion of micropits. The roller surfaces after 500K and 1M contact cycles show an increase in micropitting initiation and extensive propagation of micropits. The topographical characteristics of the wear scars are entirely different from out of the wear scar. No trace of grinding marks can

be observed in the wear scars. In order to compare the topographical characteristics of the wear scars after different numbers of contact cycles with surfaces out of the wear scars, roughness (R_q) and skewness (R_{sk}) values are measured and shown in Figure 5-7. The black dash-dotted line in Figure 5-7 (a), represents the wear scar profile, where there is no micropit on the surface, and the black solid line represents the surface profile outside the wear track. The corresponding line profile of each image is shown in Figure 5-7 (b). The roughness (R_q) and skewness (R_{sk}) values corresponding to each line profile are indicated in Figure 5-7 (c). Skewness measures the symmetry of the variation of a line or surface profile about its mean line. Surfaces with a positive skewness (>0) have relatively high spikes that protrude above the mean plane and vice versa. Thus skewness is an indication of the peak-to-valley ratio in the wear scar.

As mentioned in Chapter 3, micropitting is induced through asperity-asperity contacts and originates from a crack initiation followed by a propagation of the crack within the plastically deformed zone in the near surface zone. Therefore, positive values for skewness are expected to induce greater micropitting due to a larger proportion of the peaks above the mean plane. The impact of skewness on micropitting (38) and rolling contact life (94) has been discussed in the literature. Brizmer, Gabelli and Vieillard (38) showed that a negative value for skewness of the counter-body brings about less micropitting generation on the smoother surface compared to a positive value. As can be seen in Figure 5-7, the roughness values for the surfaces outside the wear scars are 30 - 45 nm and the skewness values are negative which exhibit a greater proportion of valleys to peaks for the initial surface after grinding. However, inside the wear scars, roughness values are 99 – 123 nm which are almost three to four times as large as that of the initial surface. Furthermore, skewness values for the inside the wear scars increased to positive values indicating a greater relative peak to valley ratio. The increase in the roughness and skewness in the wear scar significantly enhances micropitting in the wear scar as the contact continues. The rough wear scar is induced by localised plastic deformation, which is prompted by ZDDP-tribofilm, and chemical attack of ZDDP to the surface. Furthermore, the initial grinding marks cannot be observed in the wear scars. The removal of the initial grinding marks is an indication of running-in wear and/or plastic deformation of the surface due to interaction of ZDDP tribofilm with the steel surface during tribological contact.

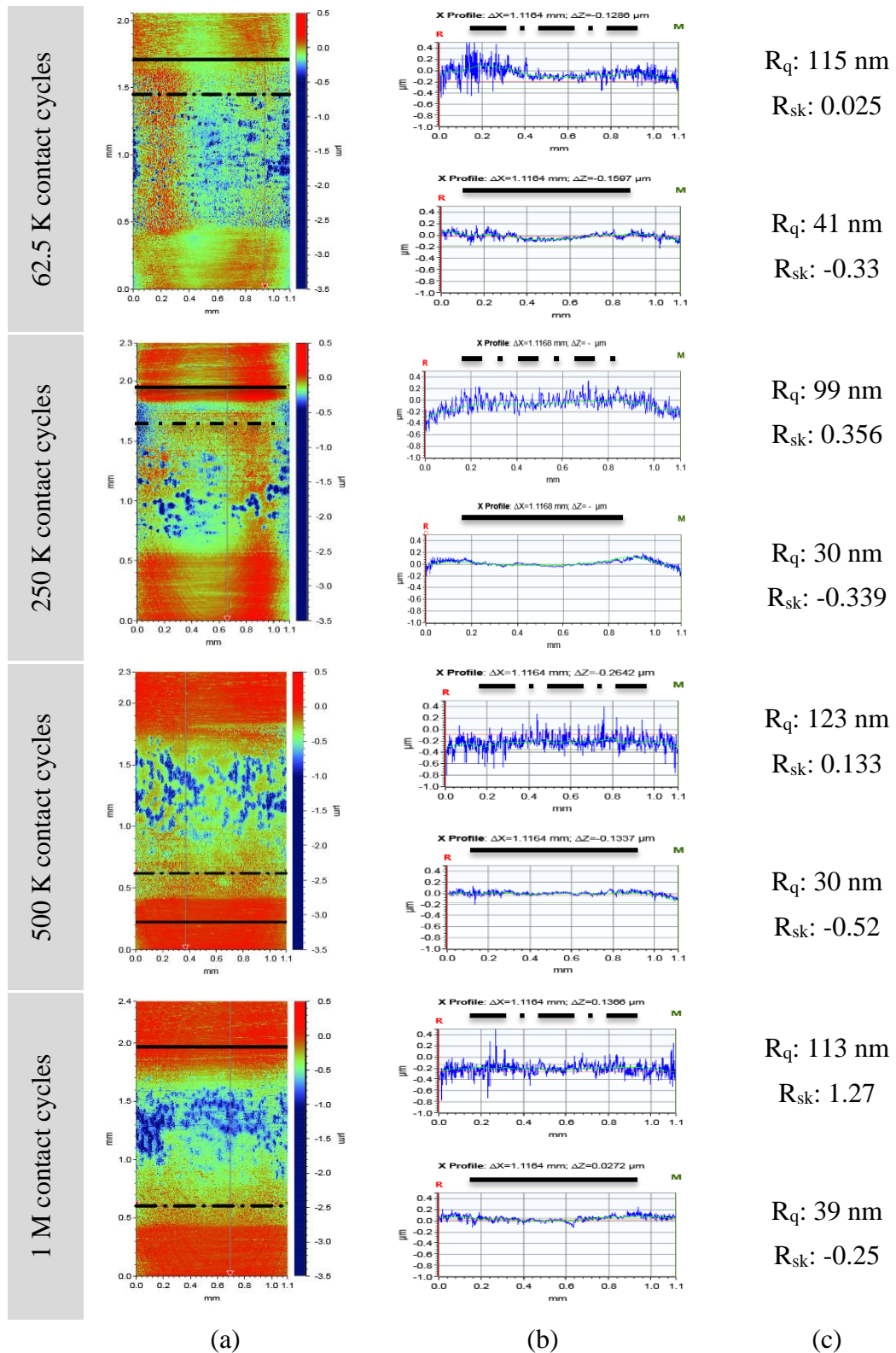


Figure 5-7. a) WLI wear scar profiles, b) representative surface line-profiles of the shown WLI images, c) roughness (R_q) and skewness (R_{sk}) values for the line profiles of the MPR rollers undergone 62.5 K, 250 K, 500 K and 1 M contact cycles, respectively

In order to quantify the micropitted surface area in the wear scars over the contact cycles, a map from micropits in the wear scar is created using MR analysis. The

generated micropitting maps of the corresponding WLI images in Figure 5-7 are shown in Figure 5-8. The MR is a strong tool to generate a well-representative micropitting map. The micropitted surface area of the generated maps is indicated on the right hand side of the map. Also, the average micropitted surface area after certain contact cycles is indicated in Figure 5-8.

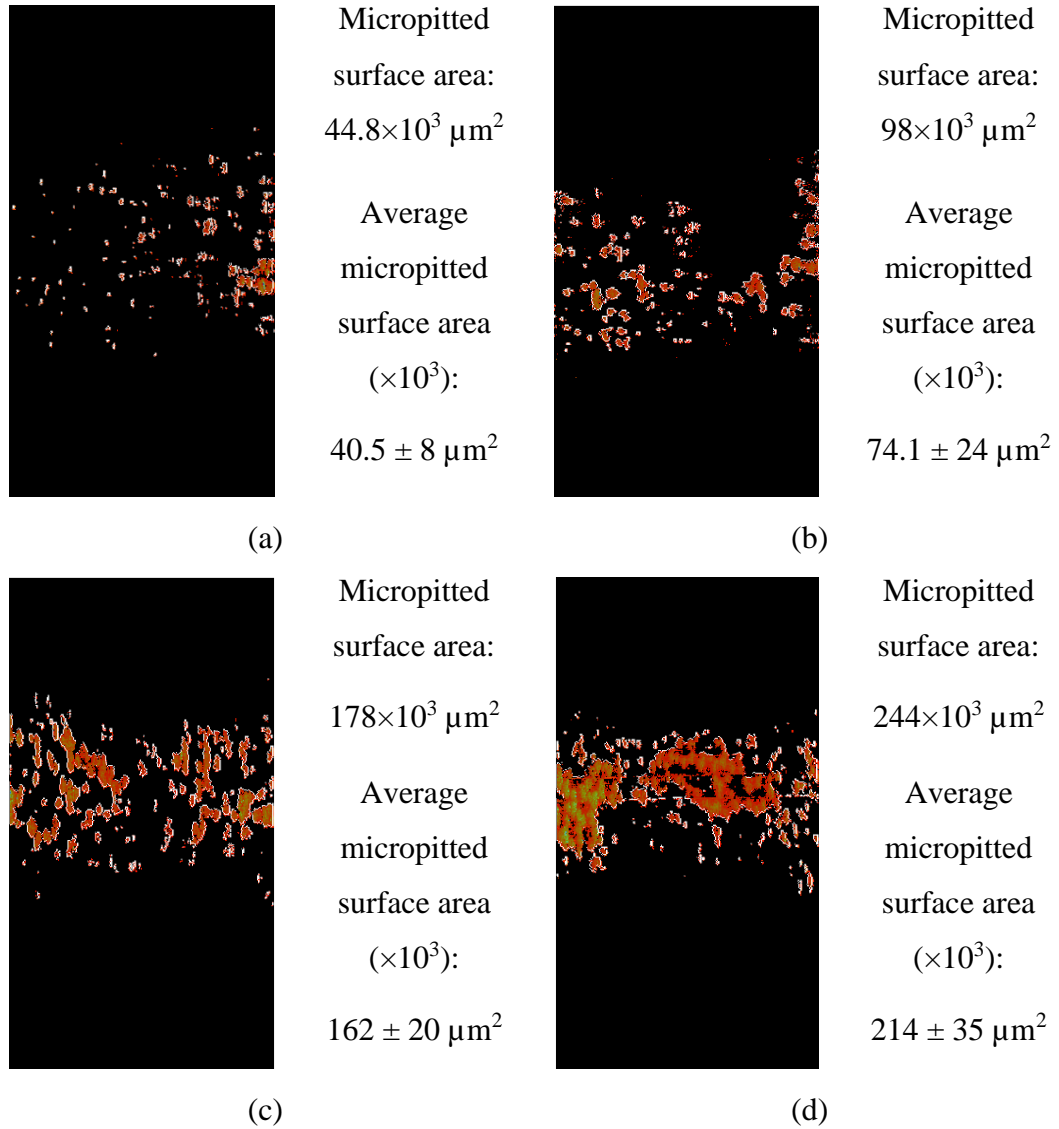


Figure 5-8. Micropitting maps and surface areas in the wear scars shown in Figure 5-7 generated using MR analysis after contact cycles of a) 62.5K, b) 250K, c) 500K and d) 1M

The total wear volume and micropitted surface area in the wear scars over different contact cycles are shown in Figure 5-9. The changes in the wear volume and micropitting surface area between each set of two consecutive amounts of contact cycles are presented below the corresponding interval in the graph.

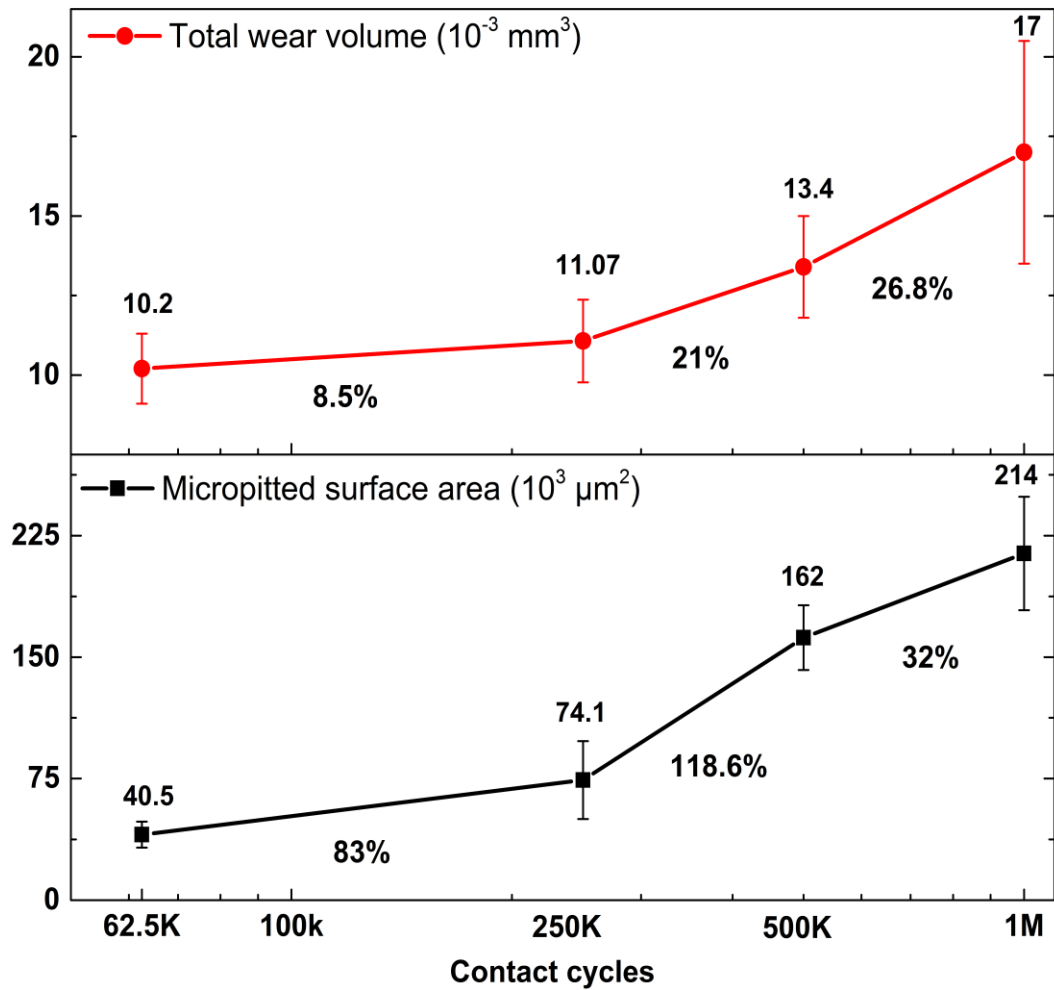


Figure 5-9. Total wear volume and micropitted surface area over different contact cycles

As can be seen in Figure 5-9, the total wear volume and micropitted surface area alter with an approximately similar trend. Interpretation of the total wear volume in the current experimental set-up is very complex and hence the correlation between micropitted surface area and total wear volume cannot conclusively suggest that the increase in wear volume is resulted from enhanced micropitting. The wear volume is a representation of the material loss induced by mild, abrasive and micropitting wear. As observed in Figure 5-7, mild wear is negligible especially in the case of the roller after 62.5K contact cycles. However, as mild wear occurs across the whole wear scar, a shallow wear scar generated by mild wear can remarkably influence the total wear volume. In addition to that, the micropits although in some cases are 2 μm in depth, locally occur in the wear scar. Thus micropitting and mild wear influence the total wear volume simultaneously.

5.2.3 The tribochemical investigation of the ZDDP tribofilms generated on the wear scars in micro-scale

In the current section the chemical nature of the ZDDP-tribofilm is investigated using XPS and EDX in order to inspect the chemical composition and elemental distribution of the ZDDP-tribofilm, respectively.

5.2.3.1 XPS chemical composition analysis

In order to compare the ZDDP tribofilm composition over different number of contact cycles, XPS survey and High Resolution (HR) spectra are collected from inside the wear scars. HR spectra are collected from ZDDP elements (P, S, Zn and O), C 1s from oil/tribofilm and Fe 2p from substrate/tribofilm. HR spectra collection were carried out on one spot on one specimen in the wear scars of all rollers that had undergone 62.5K, 250K, 500K and two specimens in the wear scar of rollers that had undergone 1 M contact cycles. The detailed XPS spectra of the O 1s, P 2p, Zn 3s, Fe 2p and S 2p signals for the roller lubricated with BO + ZDDP after 250K cycles are shown in Figure 5-10. All other spectra from other roller surfaces of different contact cycles were fitted using the same curve-fitting procedure. The detailed results from the fitted spectra are listed in Table 5-1. The decimals in Table 5-1 for 1 M contact cycles are showing the deviation from an average of the two measurements and are included in the table in order to avoid loss of detail.

The C 1s spectra collected from the wear scars of different contact cycles are resolved to four peaks. The main peak appeared at 285.0 eV assigned to aliphatic carbon (C–C and C–H) which originates from residual oil on the specimens. The three other minor contributions at 286.3 - 286.6, 287.4 – 287.6, 288.8 – 289.0 ± 0.1 eV are attributed to C–O, C–S and C=O (carbonate and/or carboxylic), respectively. The O 1s signal consists of two peaks in all wear scars. The most intense peaks at 531.4-531.6 ± 0.1 eV corresponds to Non-Bridging Oxygen (NBO), from (poly)phosphate chain (–P=O and P–O–M; where M is metal: Zn), carbonates and hydroxides (151, 192). The –P=O and P–O–M peaks cannot be resolved due to the fact that the difference in the binding energies is smaller than the energy resolution. The peak at 532.9-533.1 ± 0.1 eV corresponds to Bridging Oxygen (BO) from the phosphate chain (P–O–P). No metal oxide peak at 529-530.7 eV or Fe signal was detected in the XPS spectra collected from the top layer of the ZDDP-tribofilm (see Table 5-1 and Figure 5-10).

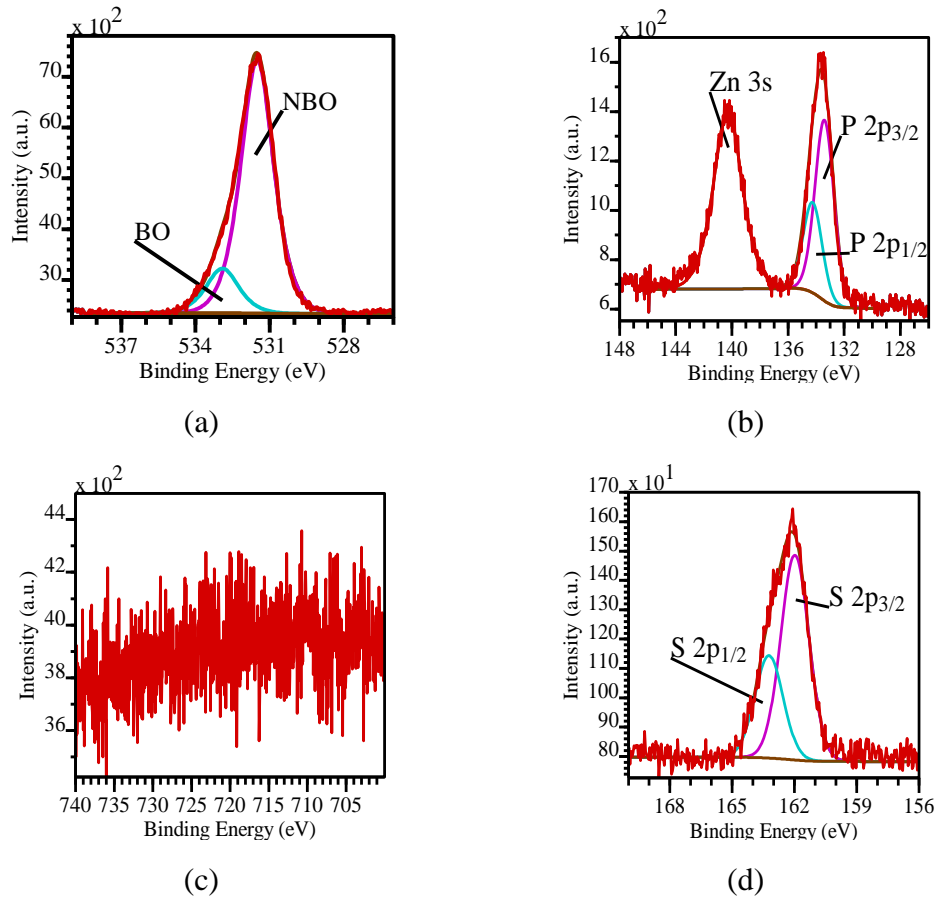


Figure 5-10. XPS detailed spectra of the ZDDP-tribofilm elements in the wear scar after 250K contact cycles showing a) O 1s, b) P 2p and Zn 3s, c) Fe 2p and d) S 2p signals

The P 2p signal originates from P in the phosphate chains of the tribofilms. The values for the P 2p_{3/2} component of the P signals from the wear scars are shown in Table 5-1, which vary between 133.3 ± 0.1 eV and 133.6 ± 0.1 eV. A peak attributed to Zn 3s is also detected next to the P 2p signal at $140.2-140.4 \pm 0.1$ eV which is considered to calculate the quantification data (elemental atomic concentration) due to the approximately same inelastic mean free path value for this peak as for P and similar to the O and S (151, 193-194).

The S 2p spectra only have a signal in the oxidation state of -2 (SII) which varies between $162.0-162.2 \pm 0.1$ eV. This signal is assigned to sulphides (195) as organic and metal sulphide (zinc sulphide here at the very top surface where Fe is not present at top) and S which is substituted for O in the phosphate chain forming (polythio)phosphate ($O-P-O \rightarrow O-P-S$) (127). The BE difference between (thio)phosphate and metal sulphide is smaller than the energy resolution and hence is not possible to decisively distinguish between these compounds using XPS. The

phosphate chain length in the ZDDP-derived tribofilm is assumed to be an important factor in determining its AW performance (105, 151) and a change in the (poly)phosphate chain length in ZDDP tribofilms during tribological contacts is reported in the literature (196).

The phosphate-chain-length estimation for ZDDP tribofilms using BO/NBO ratio is introduced by Martin et.al (122) and has been widely used to evaluate the performance of ZDDP tribofilms (122). However, the BO/NBO ratio may be affected by contaminants or overlaps with the peaks from other components. Hydroxides and C=O (carbonyl and carbonate) can contribute to NBO peak (151, 192) and P-O-C can contribute to BO peak (197). Therefore, a small change in the BO/NBO ratio is not necessarily an indication of the change in the (poly)phosphate chain length. Also, the adsorbed water at 533.3-434.3 eV can bring about errors in the BO/NBO ratio (187). Therefore, considering BO/NBO ratio for phosphate chain length estimation may bring about uncertainties and thus complementary factors are essential to conclusively confirm the change in the phosphate chain length.

An alternative parameter is the atomic-concentration-ratio of the elements (P, S, Zn, O) in the tribofilms. The higher ratio of the cations (Zn and Fe) to P (197) together with the increase in the O/P ratio in the zinc (poly)phosphate can suggest a greater metal (zinc and iron) oxide to P₂O₅ mole fraction which implies shorter (poly)phosphate chain formation (122). Also, with the more metal oxide fraction, a lower BO/NBO ratio and a shift of P 2p_{3/2} BE to lower values have been observed (187, 198-200). Also, the Zn 3s - P 2p_{3/2} BE difference ($\Delta(\text{BE})$) tends to increase with the decrease in the (poly)phosphate chain length (187, 201). The Zn 3s - P 2p_{3/2} $\Delta(\text{BE})$ is shown to have a superior potential to identify the (poly)phosphate chain length of zinc (poly)phosphate glasses compared to BO/NBO ratio (187, 199, 201). Also, if no shift in the chemical states of zinc, through interactions of zinc with other additives or lubricant contaminants, in the tribofilm is expected, consideration of Zn 3s - P 2p_{3/2} $\Delta(\text{BE})$ rather than P 2p_{3/2} BE, will eliminate the error which may arise from the calibration and sample charging. Therefore, the use of Zn 3s - P 2p_{3/2} $\Delta(\text{BE})$ in order to identify the (poly)phosphate chain length in a ZDDP-tribofilm, where no other additive or contamination (e.g. water in the case of rolling element bearings) is present in the lubricant, is favoured over using P 2p_{3/2} BE and BO/NBO ratio.

Table 5-1. Binding energy values of the elements/compounds in the tribofilm and atomic concentration of the Zn, S and O normalised to P after different amounts of contact cycles

Contact cycles		62.5 K	250 K	500 K	1 M	
Binding energy (eV)	C-C	285.0	285.0	285.0	285.0	
	C 1s	C-O	286.6	286.5	286.4	286.30 ± 0.1
		C-S	287.4	287.5	287.6	287.4 ± 0.2
		C=O	288.8	288.9	289.0	288.9 ± 0.1
		O 1s	BO	533.1	532.9	532.9
	NBO		531.6	531.5	531.4	531.55 ± 0.14
	P 2p _{3/2}	133.4	133.4	133.3	133.56 ± 0.24	
	Zn 3s	140.3	140.3	140.2	140.41 ± 0.17	
	S 2p _{3/2}	162.0	162.0	162.0	162.22 ± 0.24	
	Zn 3s - P 2p _{3/2} ΔBE	6.9	6.9	6.9	6.85 ± 0.05	
BO/NBO ratio	0.18	0.18	0.20	0.22 ± 0.02		
Atomic concentration	Zn/P	1.25	1.22	1.14	1.07 ± 0.07	
	S _(II) /P	0.62	0.73	0.62	0.71 ± 0.08	
	O _(phosphate) /P	2.4	2.2	1.85	1.75 ± 0.12	

The maximum error for the measurements of the signal binding energies was ± 0.1 eV. The decimal digits in the table indicate the maximum deviation from the mean value of two fitted spectra (average of measurements on two specimens)

As can be seen in Table 5-1, there is a small increase in the BO/NBO ratio from 0.18 to 0.22 over contact cycles and a slight decrease in Zn/P (from 1.25 to 1.07) and O/P (from 2.4 to 1.75) atomic-concentration-ratios over contact cycles which can be an indication of a minor increase in (poly)phosphate chain length. However,

Zn 3s – P 2p_{3/2} Δ (BE) in all tribofilms is approximately 6.9 which contradicts the change in other parameters (BO/NBO, Zn/P and O/P ratios). Considering P 2p_{3/2} BE values (133.3-133.6 \pm 0.1 eV), the tribofilms are not expected to consist of long (poly)phosphate chains, since P 2p_{3/2} in the pure long chain zinc polyphosphate appears at 134-135 eV (202-205). Also, with the consideration of the formula suggested by Martin (122) the phosphate contribution to the tribofilms is expected to be a mix of ortho, pyro and tripoly-phosphates for all the tribofilms generated over different contact cycles. Therefore, the change in the (poly)phosphate chain length is negligible over the contact cycles examined in this project with the current experimental set-up.

5.2.3.2 EDX elemental analysis of the ZDDP-tribofilm

XPS presents important information regarding chemical composition of the ZDDP-tribofilm. However, due to the signal collection over an area of 10⁴ μ m² in the wear scar, the generated signals present an averaged composition from inside and outside of the micropitting zone. Although EDX is an elemental analysis, it enables the user to identify the tribofilm elemental distribution in the desired areas of the surface. In this regards, EDX analysis is carried out in order to inspect the ZDDP-tribofilm in the different areas of the surface which might have different characteristics.

Figure 5-11 shows a SEM image from the roller surface after 10⁶ contact cycles in secondary electron mode and EDX spectra collected from different areas of the wear scar. Spectrum 1 is collected from an area which represents the no-micropitted area. Spectra 2 and 3 are collected in spot mode across a line which shows low contrast characteristic and from a micropit, respectively. The Zn, P and S elements originate from the tribofilm and O and Fe originate from the tribofilm and substrate. Most of the O corresponds to the ZDDP-tribofilm, since native oxide layer on the steel is believed to be removed during wear process and following ZDDP-tribofilm formation (107, 127, 206). On the other hand, most of the Fe signal is originated from the substrate electrons which emit X-rays. Therefore, the Fe atomic concentration in the EDX spectra is an indication of the tribofilm thickness.

The X-ray emissions from electrons of the substrate are collected in EDX since the signal collection depth of EDX is far larger than ZDDP-tribofilm thickness (207). The depth from which X-rays are emitted depends on the interaction volume of the

electron beam with the sample electrons. The interaction volume is a function of the electron beam characteristics (energy and angle of incident) and sample properties (e.g. atomic number, density, etc.) (207).

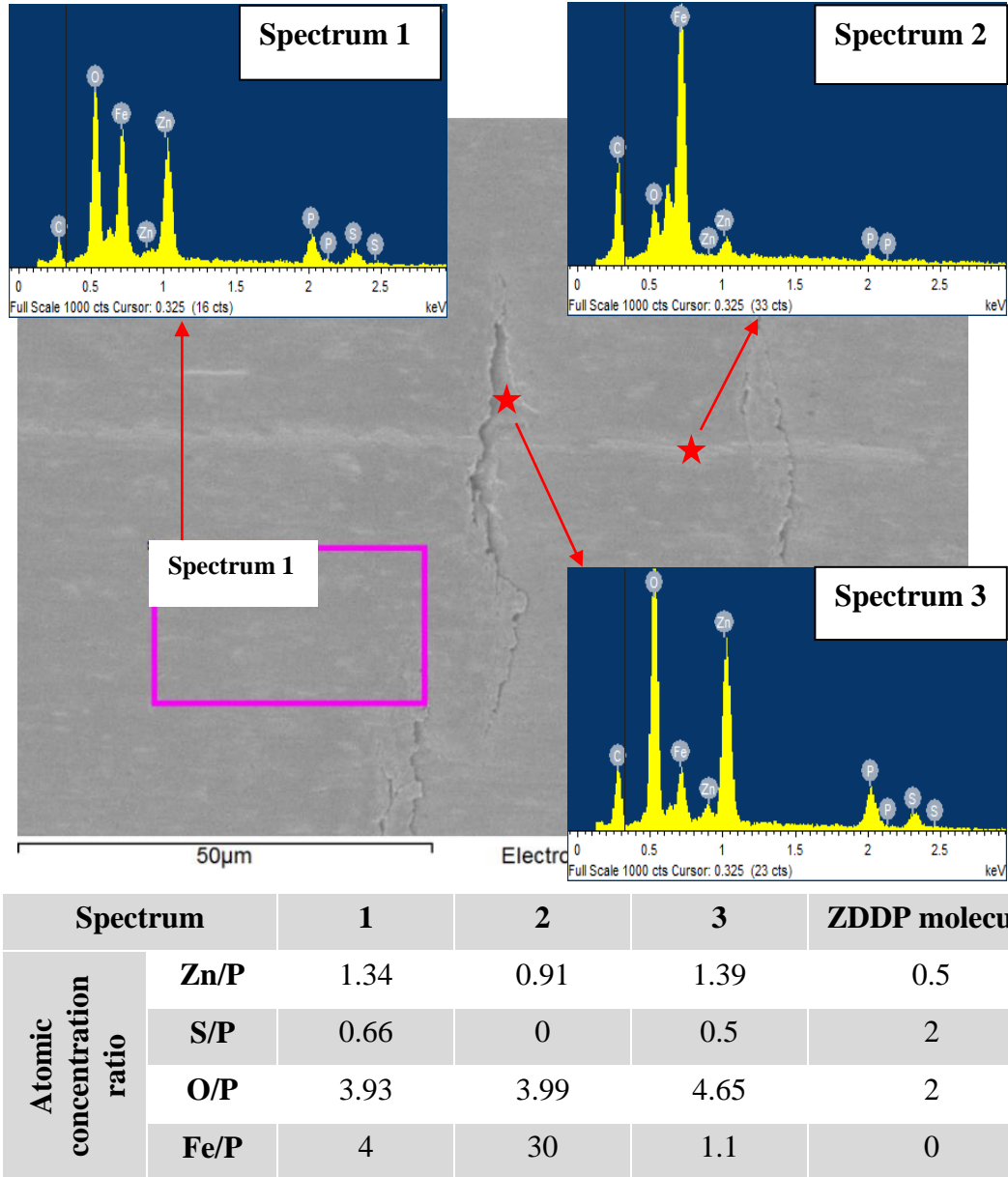


Figure 5-11. EDX spectra from ZDDP-tribofilm in different areas of the wear scar having different characteristics

As can be seen in Figure 5-11, the spectrum from no-micropitted surface has Zn/P (1.34) and S/P (0.66) ratios similar to ratios shown with XPS analysis (Table 5-1). This implies that the surface with no micropitting is covered with a ZDDP-tribofilm similar to what XPS suggests. The O/P ratio of 3.93 is much higher than what XPS shows. This is probably because of the different inelastic mean free path length of O 1s from that of S 2p and P 2p in XPS which depends on the atomic number

of the element and BE of the signal (194). Moreover, the O signal in the EDX spectra originates predominantly from O which exists throughout the entire depth of the film and partially from O in the steel, whereas O in XPS spectra stems from the top 5-10 nm of the film. Theoretically in pure zinc phosphate glasses, Zn/P ratio decreases from 1.5 (zinc orthophosphate) to 0.5 (zinc metaphosphate) with the increase in the (poly)phosphate chain length. Also, O/P ratio decreases from 4 (zinc orthophosphate) to almost 3 (zinc metaphosphate) with the increase in the phosphate chain length (122). Therefore, a ratio of 3.93 for O/P together with Zn/P ratio of 1.34 confirms the XPS data which suggests that the tribofilm consists of short chain (poly)phosphate.

Spectrum 2 in Figure 5-11 shows a strong Fe signal. Also, the Fe/P ratio (Fe/P: 30) is significantly higher than that of other spectra (which are 4 and 1.1) which shows that the tribofilm in the bright line in the SEM image is very thin compared to other spectra. This line most probably represents the tribofilm removal due to the abrasive wear which has taken place. S does not appear in spectrum 2 which also implies removal of the top layer of the ZDDP-tribofilm, as it has been shown that the S concentration is highest in the few nanometres of the top layer of the ZDDP-tribofilm and its contribution decreases towards the bulk of the ZDDP-tribofilm (105, 127, 136). The Fe/P ratio of 1.1 in spectrum 3 suggests that the micropitted area has the thickest tribofilm on the surface.

5.2.4 **Cross-sectional study of the micropitted roller**

Micropitting is a surface fatigue which commences with a surface crack initiation. The propagation of the crack into the bulk and then back to the surface creates a micropit. Therefore, subsurface inclusions (MnS, Al₂O₃, etc.) should not significantly contribute to the micropitting surface fatigue. In order to inspect this assumption a roller which had undergone 10⁶ contact cycles is cut transverse to the wear scar under metallurgical procedures.

Furthermore, the cross-sectional distribution of the ZDDP-tribofilm elements throughout its depth is important. XPS HR provides information over the top 5-10 nm layer of the tribofilm and EDX on the surface presents an elemental analysis over the whole thickness of the tribofilm. However, it has been shown that the ZDDP-tribofilm is heterogeneous over its depth (105, 127, 136, 205). In this regard, in order to observe the depth profile of the ZDDP-tribofilm a FIB sectioning is carried out in the wear

scar of a roller which had undergone 10^6 contact cycles with the ZDDP-tribofilm on the surface.

5.2.4.1 Cross-sectional observation of micropitting using optical and electron microscopy

Figure 5-12 shows micrographs of the cross-section of the wear scar transverse to the rolling-sliding direction. The specimen is etched with nital 1.5% in order to reveal the microstructural change in the steel after tribological contact (10^6 contact cycles). The PDR is shown in the micrographs below the surface and is 1-5 μm in depth. The PDR is induced during tribological contacts and also preparation procedures prior to the tests (e.g. polishing etc.).

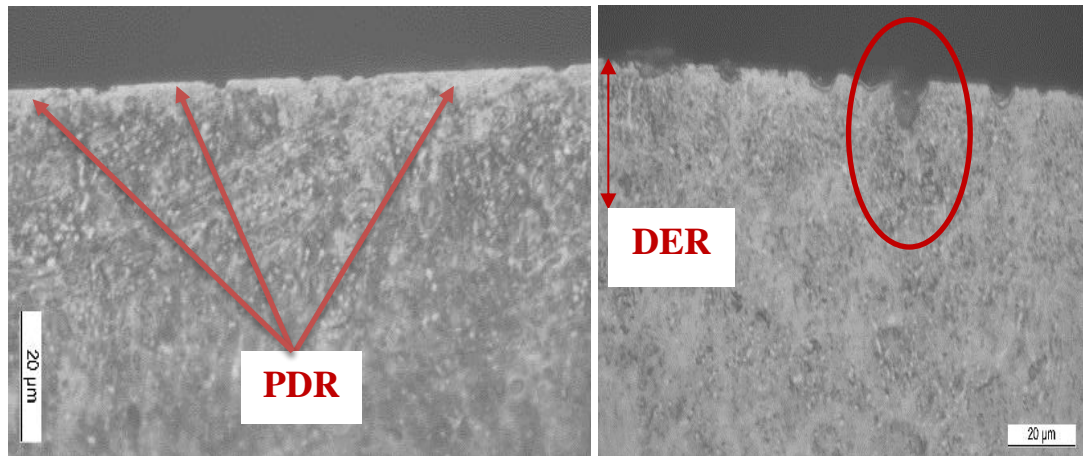


Figure 5-12. Micrographs of wear track cross-section which is prepared transverse to the rolling-sliding direction

The micropits of varied dimensions are visible on the surface. Oila, Shaw, Aylott and Bull (79, 208-209) showed that microstructural change in the martensitic steel is a factor which is involved in the micropitting initiation and propagation. The martensitic decay appears as a dark region after nital etching. DER corresponding to the structural change is clearly visible around the micropits in Figure 5-12. The DER is more visible around the bigger micropits which is highlighted in Figure 5-12. In particular, very small micropits seem to be in the PDR region. However, it should be noted that the very small defects having the shape of micropits can be also generated during sample preparation (e.g. cross-section cut) and might not be explicitly tribological-contact-generated micropits. This is probable since the resin which is used for edge retention is not 100% effective. In Figure 5-12 a large micropit with a significant surrounding-microstructural-change associated with a DER is shown using a red ellipse.

SEM image of the prepared cross-section is shown in Figure 5-13 (a). Figure 5-13 (b, c and d) show carbides embedded in the matrix of the steel located close to the surface and also in the bulk of the steel which are 1-5 μm in dimension. The inclusions are shown with pointers in the images.

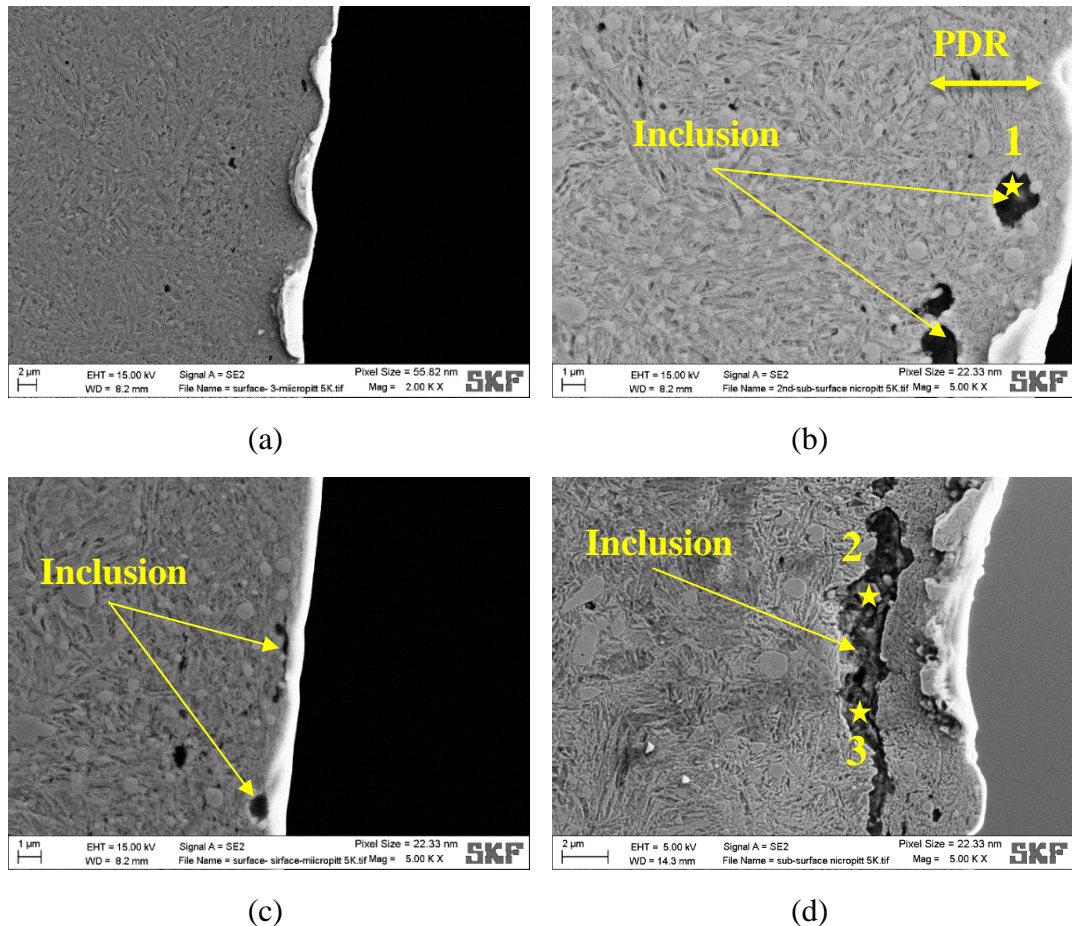


Figure 5-13. a-d) SEM images of the roller cross-section undergone 10^6 contact cycles lubricated with BO + ZDDP and e) corresponding EDX spectra of the inclusions

Data presented in Table 5-2 is obtained from EDX spectra collected from the inside of the inclusions in the areas annotated with yellow-star symbols in Figure 5-13. As expected, even a very large inclusion close to the surface and small inclusions within 1 μm of the top-surface zone, shown in Figure 5-13 d and c respectively, do not exhibit any evidence of an inclusion contribution to the micropitting surface fatigue. Therefore, the micropitting damage generated in the current experimental set-up is a surface initiated fatigue. The smaller spherical inclusions shown in Figure 5-13 (b) can be SiO_2 and Al_2O_3 . Whilst the larger inclusions shown in Figure 5-13 (d), which are irregular in shape, can be SiO_2 -Ca (O, S)- Al_2O_3 (37, 210).

Table 5-2. Elemental composition of inclusions highlighted in Figure 5-13

Element (At%)	Spectrum 1	Spectrum 2	Spectrum 3
Fe	13.3	20.3	23.8
Cr	1.6	1.45	2.7
C	75.8	30.7	59.7
O	8.85	37.7	12.8
Al	0.25	0.5	0.4
Si	0.2	5.3	0.25
Ca	-	3.75	0.15
S	-	0.3	0.2

5.2.4.2 Surface and ZDDP-tribofilm inspection at the nano-metre scale: TEM and EDX elemental analysis

In section 5.2.3 the tribochemical composition of the ZDDP-tribofilms in micropitting wear is discussed. In XPS the analysed spot size is usually varied from a few hundreds of square micrometres to less than a square millimetre. The sampling depth in XPS for Al K α radiation source is less than 10 nm. Therefore, XPS signals are consequently influenced by the averaging effect over the analysed area and sampling depth. Thus observation of the lateral and localised chemical distribution of compounds and elements near the surface defects may not be achieved through XPS, although it can produce valuable information on the tribochemistry of lubricant additives.

The ZDDP interaction with surface near and/or within the micropitted zone might not be identical to the micropit-free zone and this can influence micropitting initiation and propagation. In order to observe the local and depth profile of the ZDDP-tribofilm near the micropitted zone at nano-metre scale, a FIB milling is carried out on a roller surface after 10⁶ contact cycles. The FIB sectioning is performed close to a micropit. The FIB cross section has been investigated with TEM and EDX elemental analysis to confirm the elements throughout the tribofilm cross section. The TEM and EDX results are presented in Figure 5-14. As mentioned in section 3.5.4 there are some uncertainties around ZDDP-tribofilm especially in the case of sulphide formation in the tribofilm. It is not experimentally concluded that iron sulphide exists as a dispersed precipitate, as a distinct layer at the substrate or both. Also, if it presents as a layer there are still questions around the uniformity of that layer.

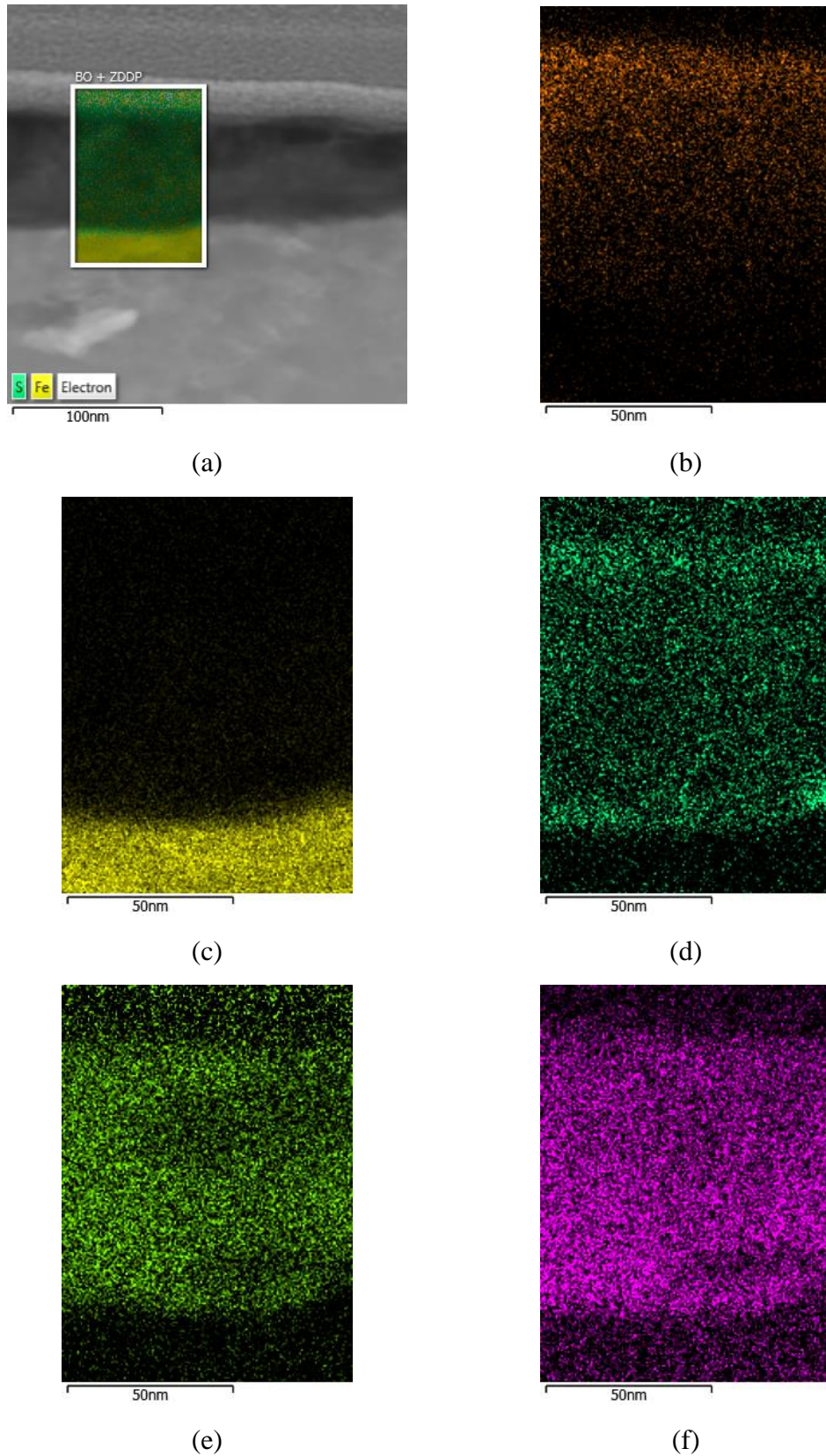


Figure 5-14. EDX elemental mapping of the tribofilm from FIB sample showing K edge maps of a) merged Fe and S, b) Zn, c) Fe, d) S, e) P and f) O

In addition, whether the iron sulphide layer exists alone (107, 140), in combination with iron oxide (128, 136) or zinc sulphide at the substrate surface has not been confirmed. In this section two sections of the FIB lamella are elementally mapped using EDX to inspect the tribofilm on the surface. Figure 5-14 shows ZDDP tribofilm formation on the steel surface with a thickness of 60-80 nm which is in agreement with the previous reports (105, 127). As shown in Figure 5-14 (Zn K-line), Zn is strongly present on the top layer while declines in concentration towards the bulk of the tribofilm. A small contribution of the Fe to the tribofilm can be detected in the bottom 30 nm of the tribofilm. Figure 5-15 (a and b) presents the composition of top and middle layer of the tribofilm, respectively.

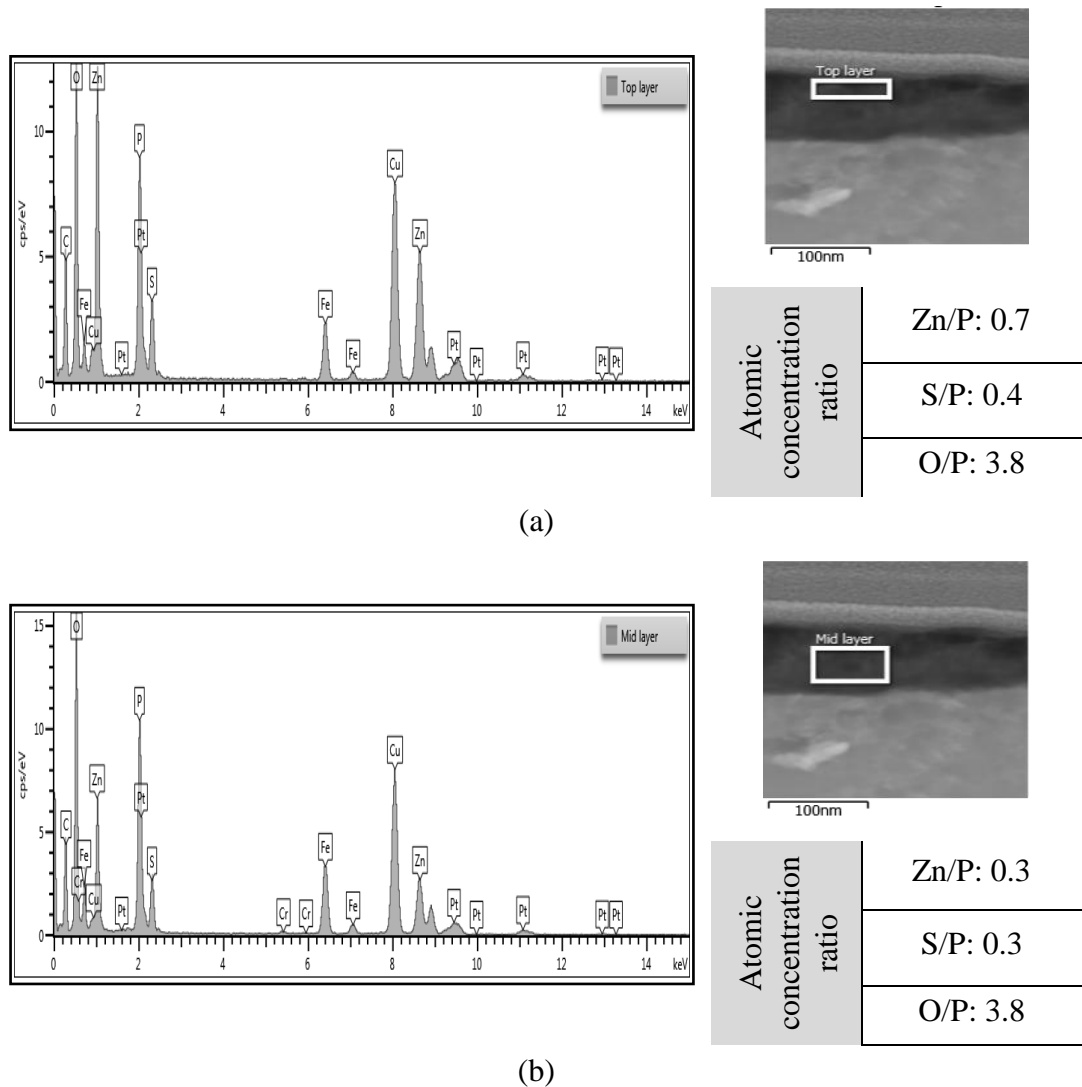
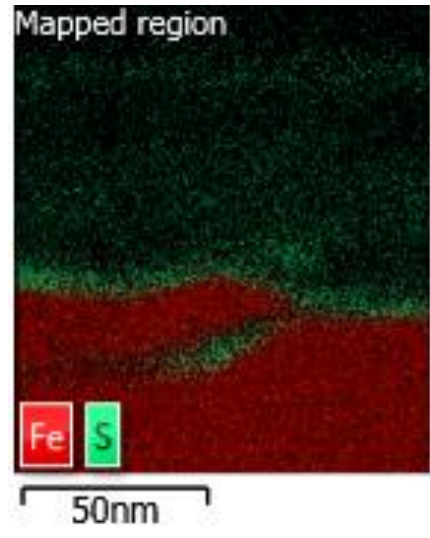
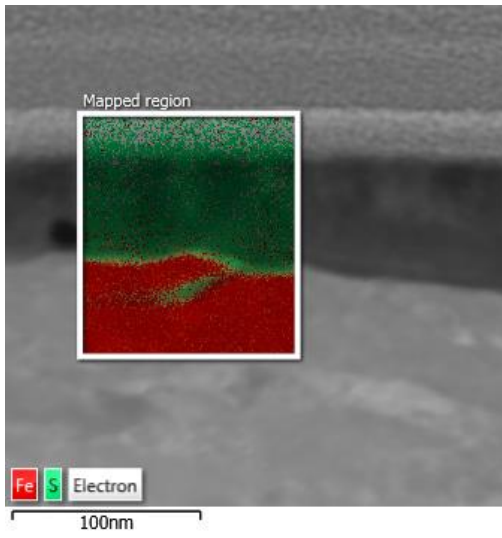


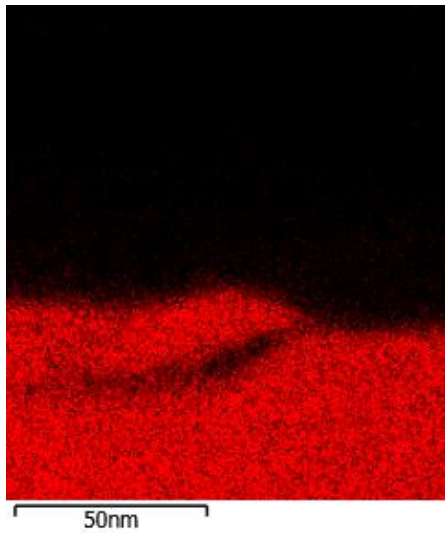
Figure 5-15. EDX spectra and atomic concentration ratio of the tribofilm elements at a) top layer and b) middle layer

Figure 5-15 shows that, while the atomic-concentration-ratio of the O to P is similar in the top-layer and mid-layer of the tribofilm, atomic-concentration-ratios of S and

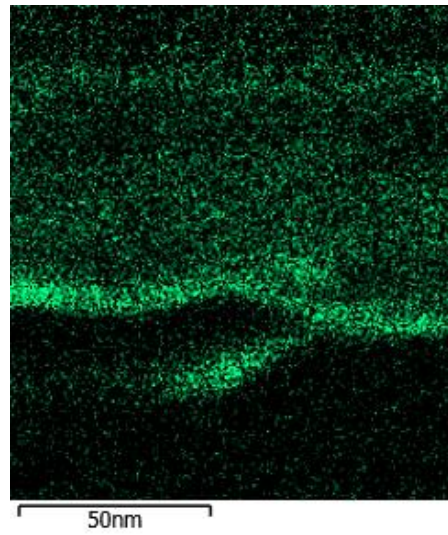
Zn to P are decreased at mid-layer compared to top-layer. This suggests a lower contribution of the sulphide to the tribofilm bulk compared to the tribofilm's very top layer. Pt and Cu signals originate from the top protective layer on the FIB lamella and the TEM grid respectively. In Figure 5-14 (S K-line) there are two distinct areas in which the presence of S is more pronounced; the very top layer and very bottom layer. Figure 5-14 (a) shows the merged mapping of the Fe and S. Since on the bottom layer of the tribofilm where S concentration is enriched, only S and Fe elements are detected and S appears as sulphide compounds, a distinct 5-10 nm iron sulphide layer formation is confirmed at the substrate of the steel. In agreement with Martin *et al.* (127) and Minfray, Martin and Esnouf (140) no iron oxide layer is observed at the interface (Figure 5-14 O and Fe K-line). The distribution of P is consistent with that of O (Figure 5-14 P and O K-line maps). P and O signals correspond to phosphates in the tribofilm. Figure 5-16 shows a TEM image from the FIB lamella where a crack is initiated on the steel surface. In agreement with Figure 5-14, in Figure 5-16 (S K-line) two distinct lines confirm the greater presence of S on the very top-layer and very bottom-layer of the tribofilm. Also, the presence of S as iron sulphide is clear at the interface in the S and Fe merged mapping (Figure 5-16 a). Interestingly the tribofilm formation in the area in which crack initiation is observed (Figure 5-16), is different from other parts of the FIB sample in which no crack was observed (Figure 5-14). In contrast to Figure 5-14, Zn greatly contributes to the bulk of the tribofilm, probably mostly as zinc (poly)phosphate together with a contribution of zinc sulphide. The concentration gradient for Zn cannot be seen in Figure 5-16. The merged mapping of O and Fe also confirms the absence of iron-oxide at the interface of tribofilm and substrate. In Figure 5-16, O and P, having similar maps, are regarded as phosphates in the tribofilm. Comparing Figure 5-14 and Figure 5-16, it is clear that the tribofilm is unevenly distributed on the surface of the roller and the thickness of the tribofilm varies from 20 nm to 100 nm. The thickness variation is probably due to the uneven wear on the surface resulting from localised surface damage. The elemental distribution of the tribofilm shown in Figure 5-14 is in agreement with the literature (105). However, Figure 5-16 shows a different elemental distribution near to the crack-initiated site at which iron sulphide formation is enhanced. This suggests that XPS data is influenced by the averaging effect over the analysed area and the distribution of the elements in the tribofilm can be different near a surface damage feature.



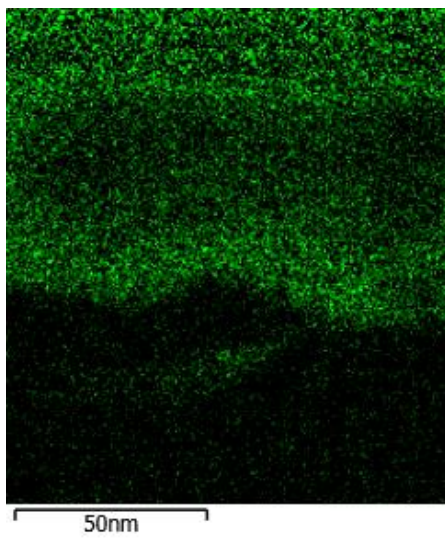
(a)



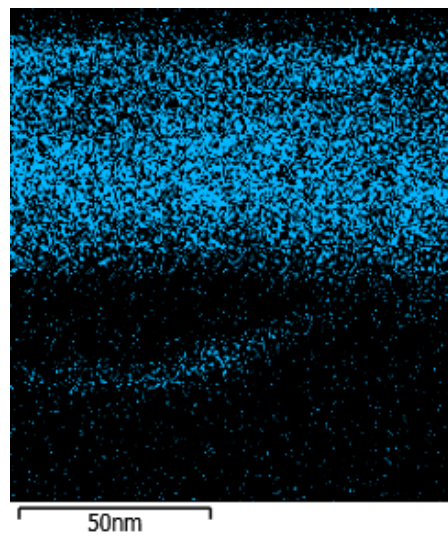
(b)



(c)



(d)



(e)

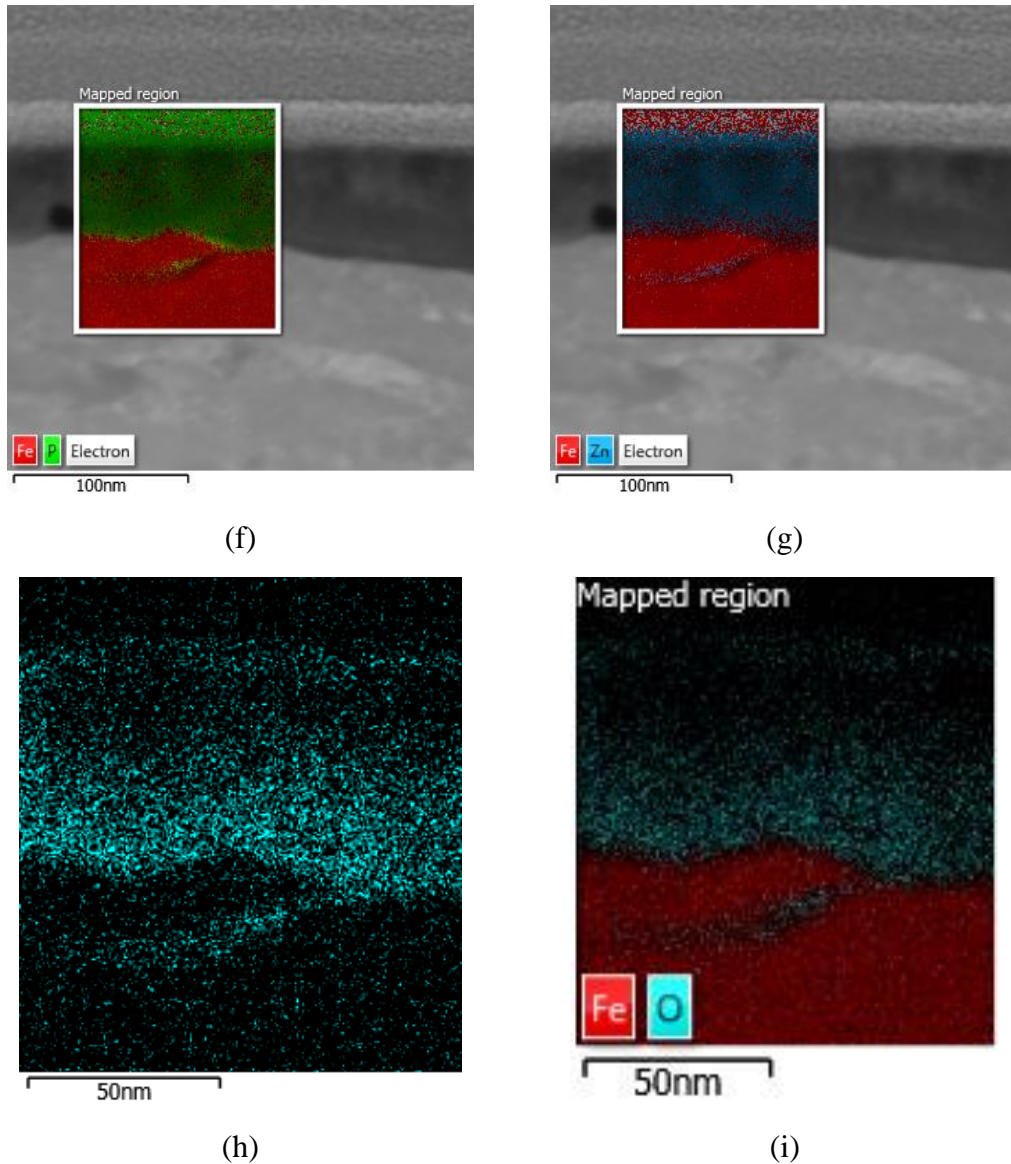


Figure 5-16. EDX elemental mapping of the tribofilm from FIB sample in the cracked zone showing K edge maps of a) merged Fe and S, b) Fe, c) S, d) P, e) Zn, f) merged Fe and P, g) merged Fe and Zn, h) O and i) merged Fe and O

In Figure 5-16 the presence of the ZDDP elements inside the crack can be clearly observed. The presence of traces of additive/tribofilm elements inside a crack which was generated prior to tribological test is reported previously in the literature (106).

Table 5-3 presents the atomic-concentration-ratios of the tribofilm elements inside the crack from the crack-mouth to the crack-tip. Comparing the atomic-concentration-ratios of the ZDDP elements from Figure 5-15 and Table 5-3, it is clear that presence of S inside the crack is enhanced compared to the bulk of the tribofilm. This observation is in agreement with the report by Meheux, Minfray and Ville (106). The S/P atomic-concentration-ratio in the top layer of the tribofilm is 0.6-0.7 as an average

(based on the XPS results presented in Table 5-1) and 0.3 in the bulk of the tribofilm. However, inside the crack the ratio is always larger than 1 and reaching 2.9 at the crack-mouth which is greater than the ratio in the ZDDP molecule ($\frac{S(at\%)}{P(at\%)} = 2$). The atomic concentration of P and Zn at the mid-crack and crack-tip remained similar while no Zn was detected at the crack-mouth. As shown in Table 5-3, in contrast to P and Zn, the S atomic concentration is higher at the crack-mouth and decreases towards the crack-tip.

Table 5-3. Atomic concentration ratio of the ZDDP elements at the a) crack mouth, b) middle of the crack and c) crack tip

Atomic concentration ratio		(a)	(b)	(c)
		Crack mouth	Mid crack	Crack tip
Zn/P		0	0.5	0.7
S/P		2.9	2.1	1.1

As shown in the current section, S from ZDDP can attack the steel surface forming iron sulphide which protects the surface from scuffing and abrasive wear. On the other hand, the presence of S inside the crack is assumed to accelerate the crack propagation (106, 211). Thus localised iron sulphide formation and interactions of the additive elements with the crack faces and tip can accelerate fatigue crack growth. The detailed discussion on the S attack to the surface and crack faces is addressed in section 9.2.

5.3 Summary

In this chapter a comparison has been made on the micropitting performance of PAO base oil and BO + ZDDP lubricant formulation followed by a detailed study of the wear scars from BO + ZDDP lubricant and ZDDP-derived tribofilm on the surfaces using optical microscopy, WLI, SEM-EDX, XPS and TEM-EDX.

In the experimental setup and conditions used in this study, the BO lubricated rollers undergo large material loss and exhibit a deep wear scar resulting in a drop in contact pressure and friction coefficient. ZDDP protects the rollers from mild wear. However the ZDDP-tribofilm induces a severe micropitting surface fatigue in the wear scars. The ZDDP-containing lubricant induces a significantly rougher interface in the wear scar compared to the initial surface together with a considerably increased skewness value. From the experiments carried out under the defined conditions following conclusions can be derived:

- The micropitting surface area and total wear volume increase over contact cycles with a similar trend.
- At 62.5×10^3 contact cycles, the micropitting is within the initiation stage and further contact cycles bring about mild wear and micropitting propagation/initiation.
- Micropits propagate opposite to the sliding direction into the material bulk and transverse to the rolling-sliding direction.
- Structural changes which surround the micropits can be observed in the cross section of the roller in the wear scar.
- A contribution of sub-surface inclusions to the micropitting initiation and/or propagation has not been observed which confirms that micropitting in the employed modified-MPR is surface initiated fatigue.
- The ZDDP-tribofilms formed in the wear scars consist of short-chain zinc phosphate and organic and zinc sulphide on the top surface and do not considerably vary in composition over contact cycles from 62.5 K to 1 M.
- The tribofilms are heterogeneous over depth and more interestingly laterally from one site to the other site. Also, the distribution of the ZDDP-elements alter in the micropits and cracks zone.
- A 5-10 nm thin iron sulphide layer is visualised on the interface as a separate layer underneath the phosphate layer with an altered distribution of tribofilm elements near the crack site. Iron sulphide reaction layer is localised on the surface of steel and enriched with higher concentration of S near the cracked site implying greater EP activity of ZDDP near the crack site.
- The ZDDP additive elements have been observed inside the crack with the enhanced contribution of the S. The ZDDP elemental distribution inside the crack is different from the crack-mouth to the crack-tip. The ZDDP traces inside the

initiated cracks, especially S, may induce stress corrosion crack propagation especially in a bearing which operates in a tribocorrosive environment where humidity and water is diffused into the lubricant. This will be discussed further in Chapter 9.

Chapter 6

The effect of water and humidity on micropitting wear

6.1 Introduction

The enhancing effect of ZDDP AW additive on micropitting is shown in the previous chapter. In this chapter modified MPR is used in order to investigate the effect of added-water and humid environments on micropitting wear. The effect of water on micropitting performance of bearings is complex and depends on different parameters including lubricant and additives, operation conditions, contaminants and component characteristics. At first the effect of two RH values of 60% and 90% is shown on the performance of the PAO base oil. Following the effect of humidity on the base oil performance, the effect of different temperatures (75 and 90°C), water concentrations (1% and 3%) and relative humidities (60% and 90% RH) has been investigated on micropitting wear under rolling/sliding contacts using a ZDDP-containing oil which is the main focus of the present chapter. In order to assess the impact of free water on micropitting, tests are carried out with 62.5×10^3 contact cycles and different added-water concentrations (1 mass% and 3 mass%). In the interpretation phase, the tribological effect of water on micropitting was addressed using WLI, SEM and optical microscopy. The tribochemical change of the reaction film is studied using XPS in the tribo-corrosion system.

6.2 Results

6.2.1 The effect of dissolved water on base oil performance

As discussed in the previous chapter micropitting features cannot be observed on the base oil lubricated surfaces due to the favoured mild-wear over micropitting wear. The results of total material loss are reported in Figure 6-1 (a). The total wear volume results, measured for the samples, show that applied humidities do not necessarily increase or decrease the wear volume and the error-bars are larger than the difference in the average wear volumes in different humidities. A wear track profile of a specimen, lubricated under 90% humidity, is shown in Figure 6-1 (c). The wear track appearance is similar to that of experiments carried out in laboratory conditions. The

friction results, presented in Figure 6-1 (b), are the average of the last 30 minutes ($\frac{3}{21} \times 10^6$ contact cycles) of the tribological tests for three measurements.

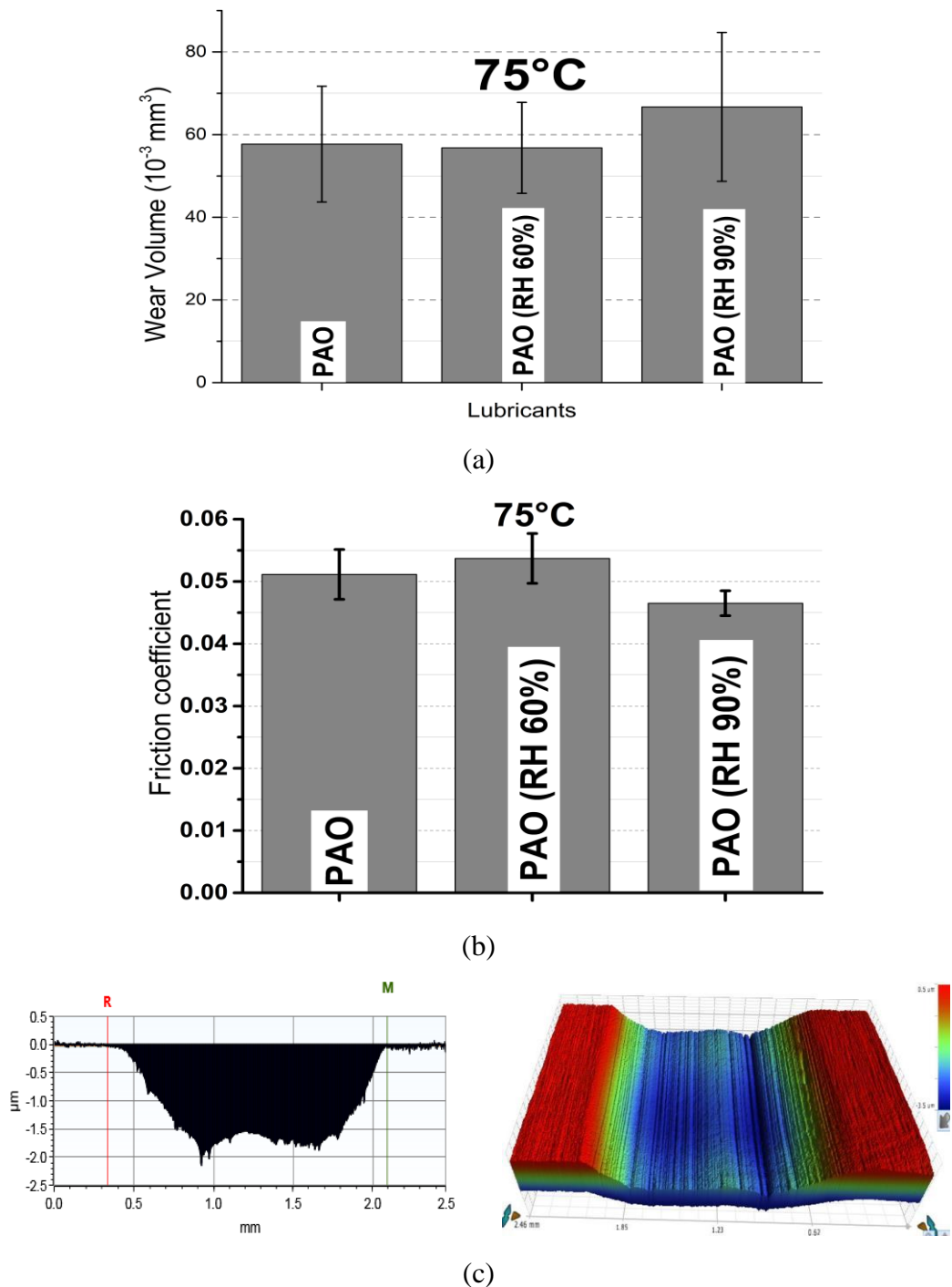


Figure 6-1. The effect of relative-humidities on the PAO-base oil performance. a) wear results, b) friction results and c) wear profile of a surface under 90% humidity

The friction graph in Figure 6-1 does not show a specific trend with respect to the dissolved water level. However, interestingly the rollers with higher wear have lower friction coefficient at the end of the test. This is expected since with increase in the

material loss, the contact pressure drops leading to a decrease in the frictional forces between the surfaces in contact. This observation suggests that the bulk properties of oil are not noticeably altered with the dissolved water in agreement with Cen *et al.* (148) and thus the performance of PAO-base oil does not significantly depend on the dissolved water level in the oil in the current experimental setup. However, the wear-performance of polar base-oils e.g. ester(s) is likely to be affected by dissolved water (102) since water interferes with the adsorption of the polar moieties of the base oil on the surface. Also, fatigue life of base-oil might be affected by dissolved water (159).

6.2.2 Micropitting results

6.2.2.1 The effect of added-water and temperature on micropitting

Following the sample washing procedure, detailed in Chapter 4, to remove the reaction layer, WLI images are scanned from the wear scar on the roller surfaces. The effect of 1 mass % added-water on micropitting at two different temperatures of 90°C and 75°C is shown in Figure 6-2 and Figure 6-3, respectively. The generated micropitting maps from the wear scars using MR analysis are shown on the right hand-side of the corresponding WLI wear scar profiles. As can be seen in Figure 6-2 and Figure 6-3, the generated micropitting maps represent the micropitted regions in the wear scars. The calculated micropitting surface areas are indicated in the lower part of the corresponding micropitting maps. The average micropitted surface area from measurements on three specimens are calculated and indicated in Figure 6-2 and Figure 6-3 (e and f). The wear scar cross-sectional depth profile, corresponding to the black dashed line on the wear scar profile of the rollers lubricated with BO + ZDDP and BO + ZDDP + 1% water, is shown below the wear scar profile in c and d, respectively. The surface areas of the wear scar cross-sectional depth profiles are indicated below the corresponding depth profiles. The wear scar cross-sectional area is representative of the extent of the material loss which is induced on the roller surfaces due to the tribological contacts. A clear increase in micropitting can be observed on the roller surfaces lubricated with added-water. 1% water increases the micropitted surface area by approximately 15% and 25% for the experiments carried out at 90°C and 75°C, respectively.

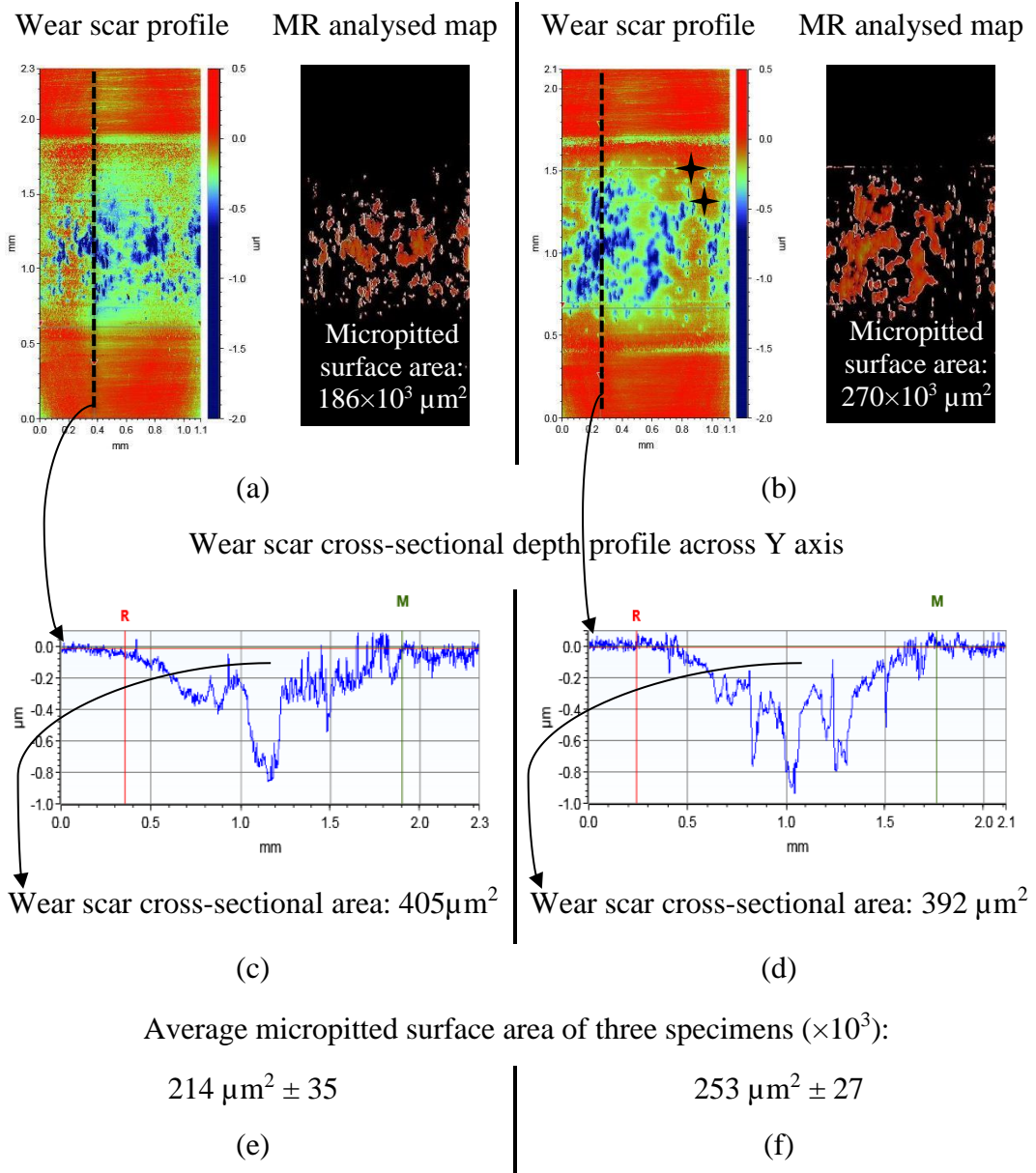


Figure 6-2. Wear scar and MR profile, corresponding wear scar depth profiles and average micropitted surface area of the roller surfaces lubricated with a, c, e) BO + ZDDP and b, d, f) BO + ZDDP + 1% Water at 90°C.

★ Abrasive marks

In BO + ZDDP lubricated contacts, there is an approximately 30% increase in micropitting when the experiments are performed at 90°C compared to the experiments performed at 75°C. A considerable rise in the wear scar cross-sectional area at 90°C compared to 75°C suggests that material loss at the higher temperature is increased. This is in agreement with the observations by Morales-Espejel *et al.* (47). They showed that an increase in the lubricant temperature from 66 to 73°C leads to a substantial increase in micropitting in full bearing tests (47). The increase in material loss and micropitting can be expected at the higher temperature (90°C) due to the increase in the severity of the contact and accelerated ZDDP-tribofilm formation (8).

Abrasive marks can be clearly observed on the wear scars of the surfaces lubricated with added-water. The abrasive marks on the wear scar profiles are designated in the images using a black-filled star symbol.

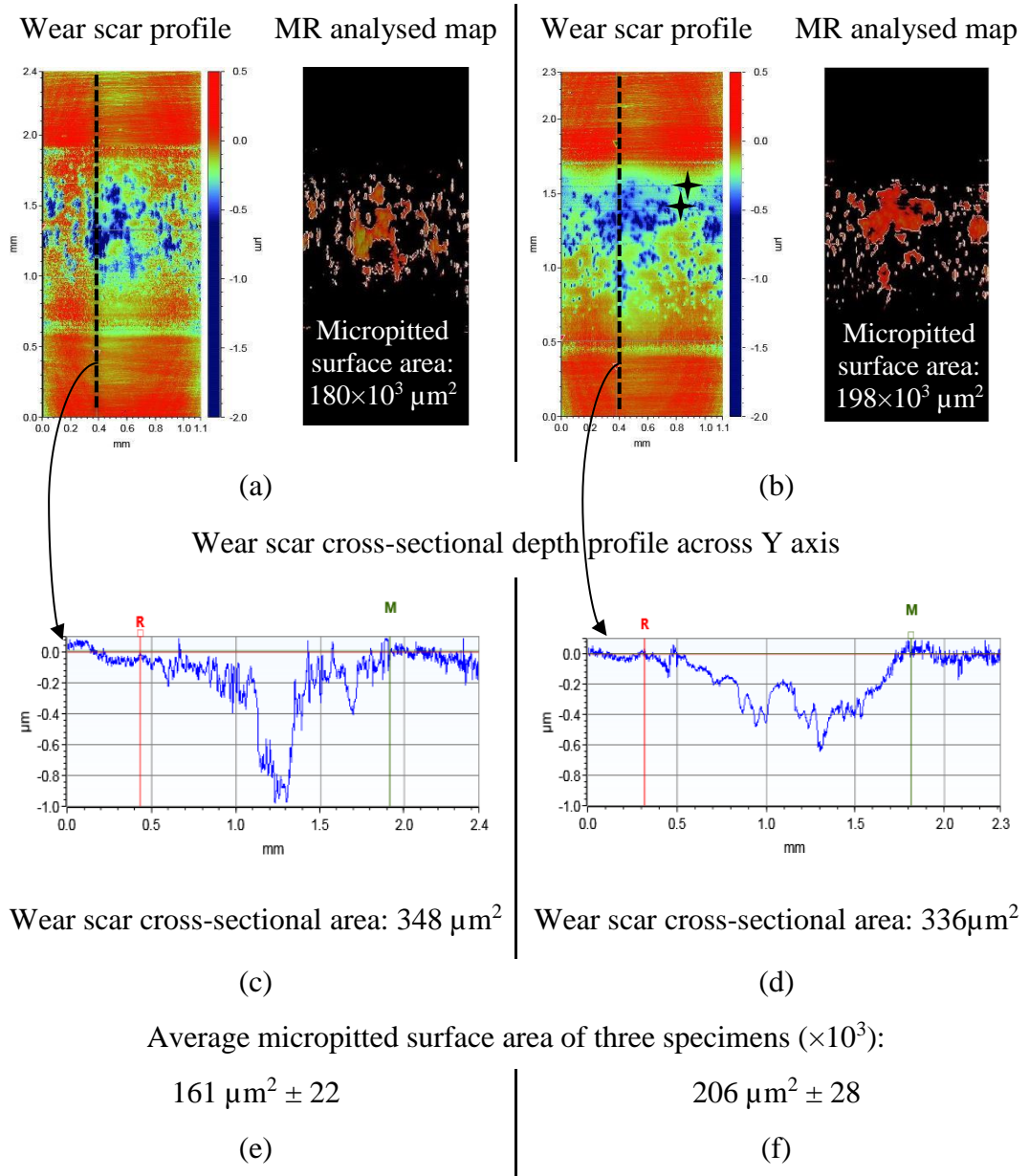


Figure 6-3. Wear scar and MR profile, corresponding wear scar depth profiles and average micropitted surface area of the roller surfaces lubricated with a, c, e) BO + ZDDP and b, d, f) BO + ZDDP + 1% Water at 75°C. ★ Abrasive marks

The wear scar cross-sectional depth profiles of the rollers lubricated with BO + ZDDP formulation, shown in Figure 6-2 (c) and Figure 6-3 (c), suggest a shallow wear track at the edge containing deep and large discrete micropits. The micropits are mainly concentrated in the middle of the wear scar which is within the zone with highest contact pressure. In contrast, the rollers lubricated with added-water, shown in Figure

6-2 (d) and Figure 6-3 (d), predominantly have a deeper wear scar depth profile at the edges suggesting mild wear on the surface. Also, surfaces lubricated with added-water exhibit more initiated micropits which are spread out across the wear scar, compared to that of BO + ZDDP. Therefore, BO + ZDDP formulation protected the surface from mild wear, while inducing large micropits and BO + ZDDP + 1% water induces larger wear and greater micropitted surface area. Figure 6-4 presents SEM images which highlight the influence of water on micropitting.

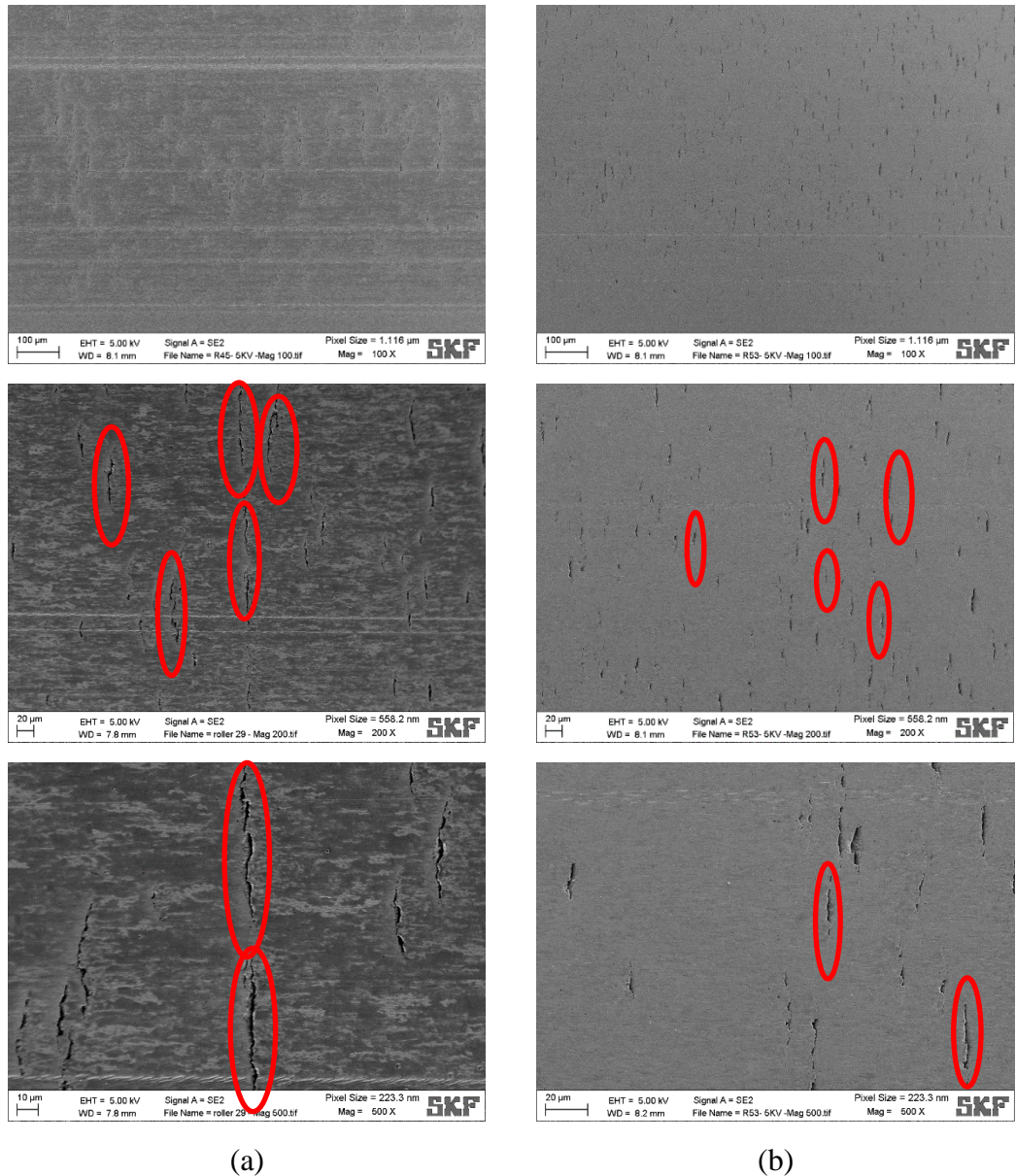


Figure 6-4. SEM images of the roller surfaces lubricated with a) BO + ZDDP and b) BO + ZDDP + 1% Water at 75°C

Furthermore, by comparing Figure 6-2 a with b, Figure 6-3 a with b and Figure 6-4 a with b, it can be observed that while the micropitting surface area is increased on the rollers lubricated with added-water, discrete micropits are smaller in size compared

to micropits in the BO + ZDDP wear scars. This suggests that the material loss, in the case of contacts lubricated with the added-water, is generated through enhanced micropitting nucleation and mild wear. However, the material loss, in the case of contacts lubricated with BO + ZDDP, is mainly induced through micropitting initiation and propagation.

6.2.2.2 The effect of relative humidity on micropitting

Figure 6-5 compares the wear scars of rollers lubricated with BO + ZDDP under laboratory conditions and 90% RH. A clear increase in micropitting damage can be observed in the 90% RH condition. The micropits are smaller in size and spread across the wear scar in RH 90%.

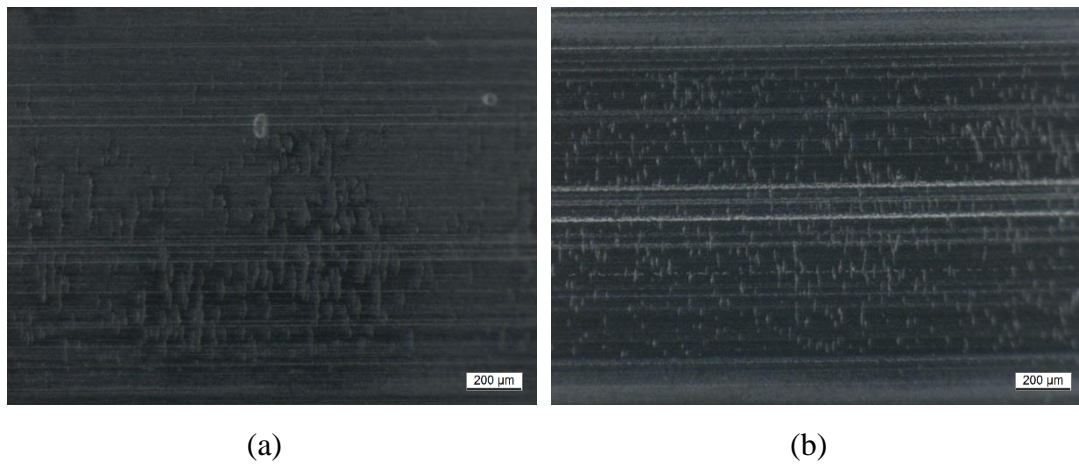


Figure 6-5. Optical images of the wear scars lubricated with a) BO + ZDDP and b) BO + ZDDP (RH 90%)

The effect of two different relative humidities (60% and 90%) on micropitting is shown in Figure 6-6 using WLI. The wear scars are extensively micropitted across the whole wear track. The micropitted surface area of the roller lubricated under 60% of RH is close to that of BO + ZDDP + 1% water lubricated surface. The micropitted surface area of the roller lubricated under 90% of RH increased by more than 60% compared to no-humidity condition. Also, abrasive marks become more intense by increasing the RH to 90%. Similar to what is observed in the case of 1% added-water, the rollers lubricated under humid environments have a deeper wear scar depth profile at the edges as shown in Figure 6-6 (c and d), showing mild wear incident on the roller surfaces. Figure 6-7 shows SEM images of the wear scars generated in the laboratory and 60% RH conditions which confirms an enhanced micropitting initiation and micropitting surface density in the case of 60% RH.

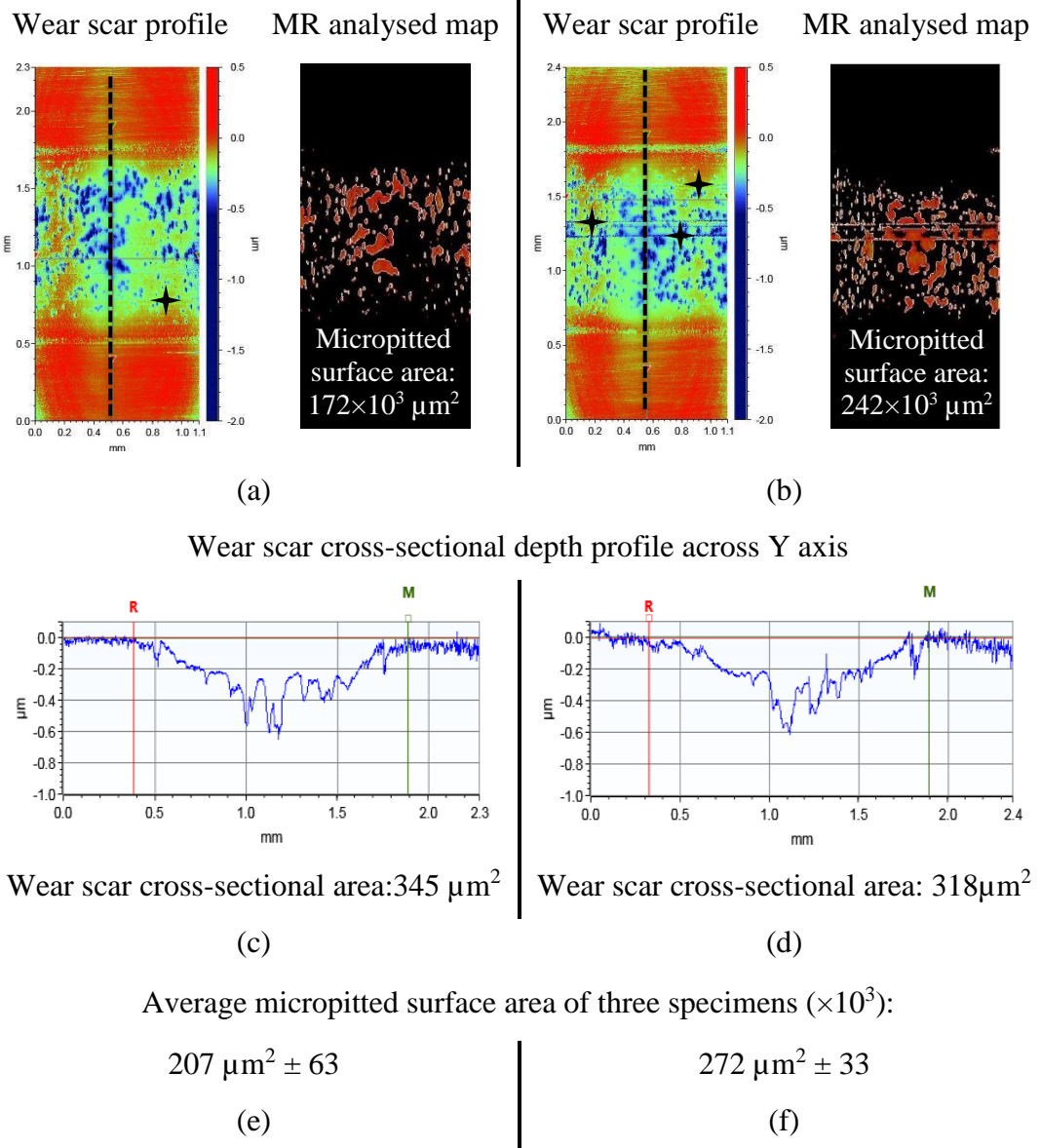


Figure 6-6. Wear scar and MR profile, corresponding wear scar depth profiles and average micropitted surface area of the roller surfaces lubricated with a, c, e) BO + ZDDP (RH 60%) and b, d, f) BO + ZDDP (RH 90%) at 75°C. ★ Abrasive marks

In Figure 6-8, the water saturation which is recorded by Hydac sensor, is shown throughout the interval of pre-contact and contact durations. Also, water concentration after each test, which is measured by Karl Fischer Titration, is indicated in the same figure. The pre-contact step which includes sub-steps of achieving the desired speed for rings and roller, lubricant temperature, load and slid-to-roll ratio, is plotted in black colour. The first 62.5×10^3 contact cycles for the lubricants with the added-water is plotted in red colour. As can be seen in Figure 6-8 (a), data acquired from water saturation sensor show that the most of the water in the lubricant with 1% of the added-water is evaporated during the pre-contact step, specifically heating sub-step,

and only approximately 7×10^3 contact cycles are carried out under the free water conditions. This indicates that most of the tribological contact is progressed under the dissolved water conditions.

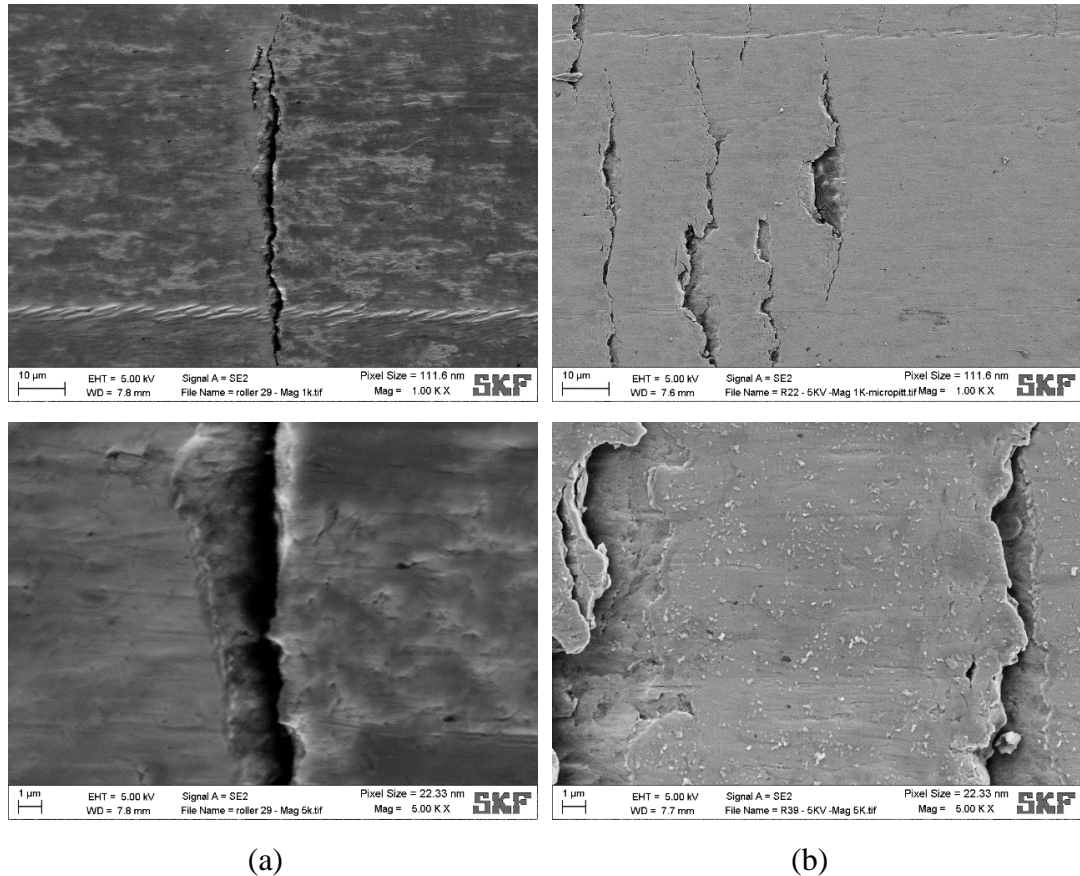
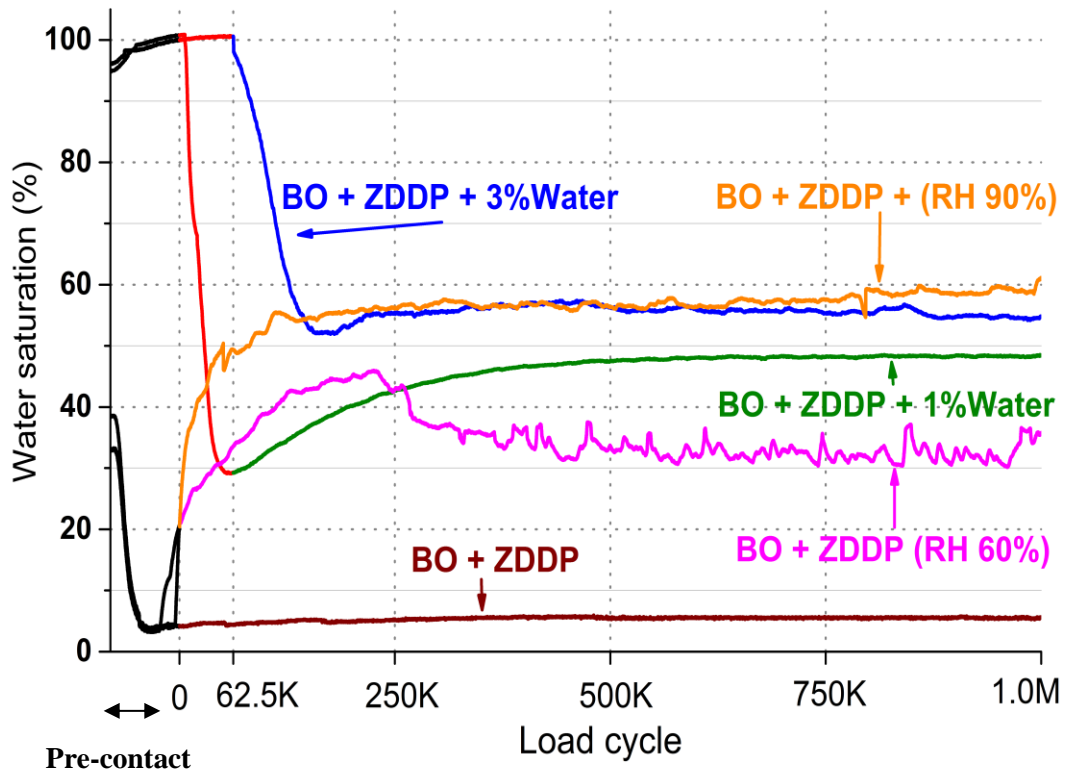


Figure 6-7. SEM images of the roller wear scars lubricated with a) BO + ZDDP and b) BO + ZDDP (RH 60%) at 75°C

The Karl Fischer measurements, which were performed after the tests, are in agreement with the sensor records. The dissolved water concentration in the lubricants reached a steady state condition after approximately 250×10^3 contact cycles. Data from the sensor and the Karl Fischer measurements show that the relative order of increasing dissolved water concentration for a series of test conditions is BO + ZDDP +3%Water & BO + ZDDP (RH 90%) > BO + ZDDP + 1%Water > BO + ZDDP (RH 60%) for the test conditions used in this study. Furthermore, the micropitted surface area and abrasive marks increase along the series of test conditions BO + ZDDP +3%Water & BO + ZDDP (RH 90%) > BO + ZDDP + 1%Water > BO + ZDDP (RH 60%). This suggests that an increase in the dissolved water concentration brings about an intensified micropitting and abrasive wear.



(a)

Water concentration after 1 million of contact cycles (mass%)

BO + ZDDP (RH 60%)	BO + ZDDP + 1% Water	BO + ZDDP + 3% Water	BO + ZDDP (RH 90%)
0.013 ± 0.001	0.017 ± 0.001	0.021 ± 0.001	0.022 ± 0.001

(b)

Figure 6-8. a) Water saturation level measured by Hydac contamination sensor and b) water concentration of the oils after the tests measured by Karl Fischer

Figure 6-9 a and b compare the micropits induced on the wear scars on the roller surfaces which were lubricated with BO + ZDDP (RH 60%) and BO + ZDDP + 1% Water, respectively. The appearance of micropits is similar and shows that the micropits propagate opposite to the sliding direction throughout the bulk of the material in agreement with Oila *et al.* (79) and also transverse to the rolling-sliding direction. Therefore, the characteristics of micropits do not appear to change by water contamination, In the Figure 6-9 (a) microcracks can be observed inside the micropits on the crack faces which can be an indication of a crack branching. The crack branching is expected for the test conditions used in this study.

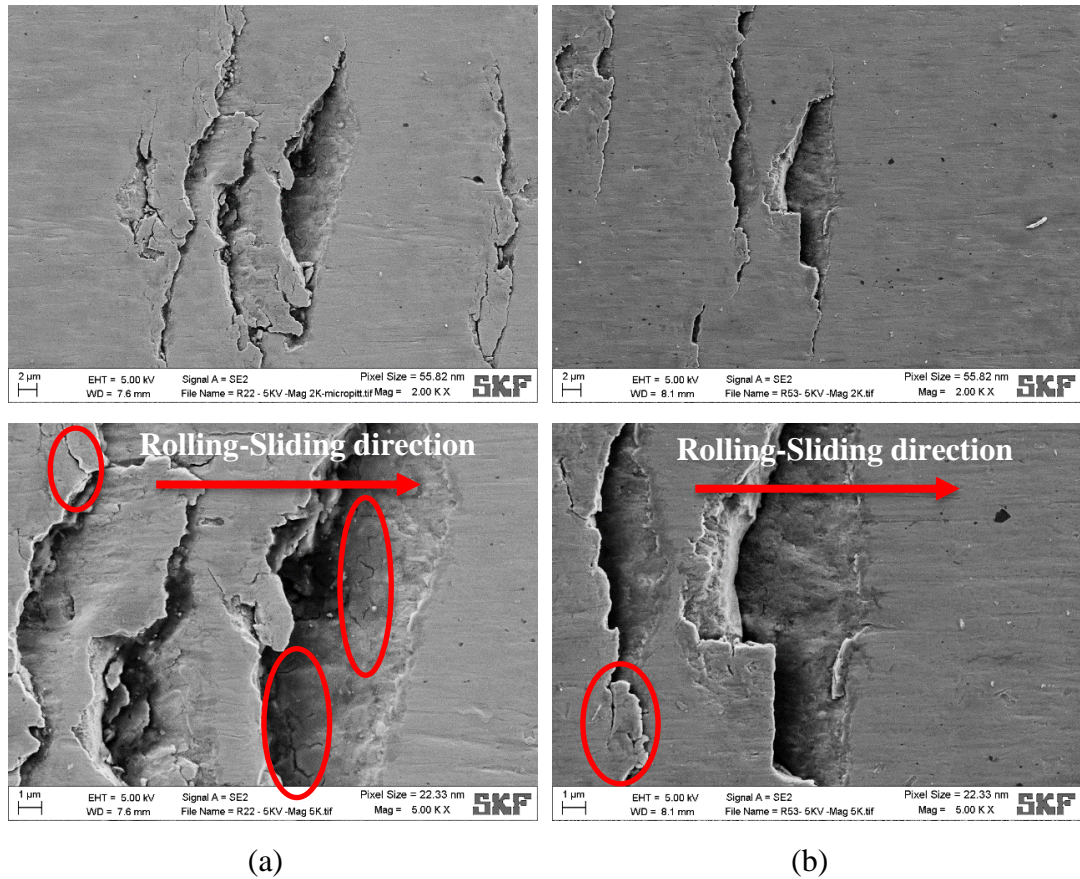


Figure 6-9. SEM images of the micropits appear on the wear scars lubricated with a) BO + ZDDP (RH 60%) and b) BO + ZDDP + 1% Water

6.2.2.3 The effect of free water on micropitting

The effect of free water on micropitting is investigated through adding 1% and 3% water and inspecting the roller surfaces after 62.5×10^3 contact cycles. The surfaces lubricated with added-water are compared with the roller surface lubricated with BO + ZDDP lubricant formulation without added-water. The change in water saturation level of the lubricant containing 3% of added-water is displayed in Figure 6-8 (a), which shows that the saturation level of the lubricant remains 100% during first 62.5×10^3 contact cycles. Therefore, the free water conditions exist throughout the tribological contacts for the roller which is lubricated with BO + ZDDP + 3% water and experienced 62.5×10^3 contact cycles. For the roller lubricated with BO + ZDDP + 1% water which experienced 62.5×10^3 contact cycles, only 11% of the test (from start of the contact) has been under tribological contacts in the free water conditions. This suggests that most of the contact cycles were performed under dissolved water for rollers lubricated with BO + ZDDP + 1% water. Optical images taken from the wear scar of the rollers lubricated with BO + ZDDP,

BO + ZDDP + 1% water and BO + ZDDP + 3% water after 62.5×10^3 and 1×10^6 contact cycles are shown in Figure 6-10 (a) and (b), respectively.

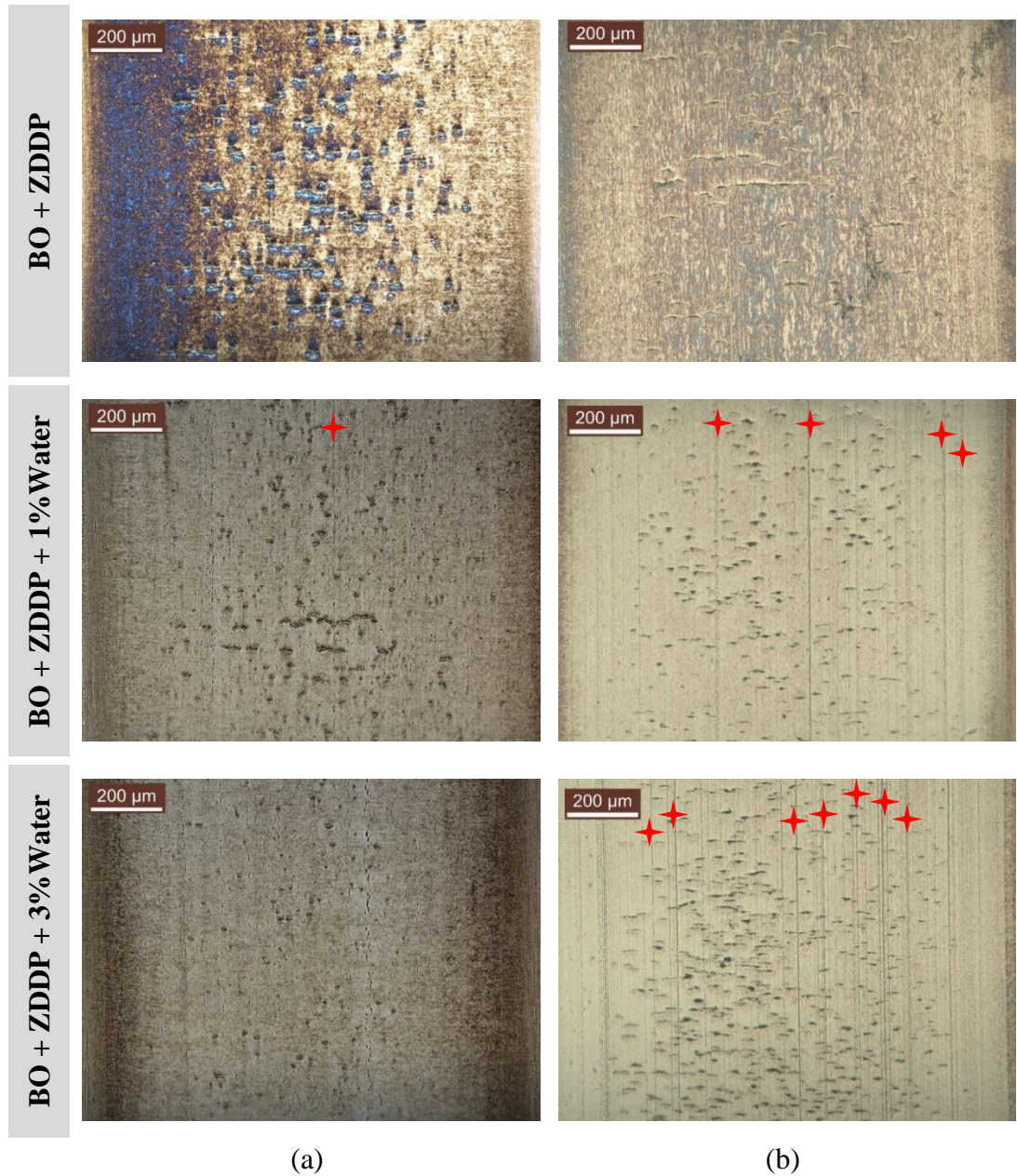


Figure 6-10. Optical images of the wear scars on the rollers after a) 62.5×10^3 and b) 1×10^6 contact cycles. ★ Abrasive marks

As can be seen in Figure 6-10 (a) the wear scar of BO + ZDDP has discrete micropits on the surface and no sign of abrasive wear can be observed. On the wear scar of the roller lubricated with BO + ZDDP + 1% water, micropits and abrasive marks are visible. The micropitting density is less compared to the BO + ZDDP lubricated roller. However, on the wear scar of BO + ZDDP + 3% water, which is lubricated in free water condition throughout the test duration (62.5 K cycles), there is almost no trace of abrasive wear and only a few and small micropits are visible. Most probably, the

negligible micropits on the surface of BO + ZDDP + 3% water lubricated roller are generated after the actual test and within the stopping-step in which the un-loading takes place and rotation of the specimens is gradually halted. The stopping-step completes approximately two minutes after the actual test which provides the lubricant with the required time to go through a transition from free water to dissolved water conditions.

In Figure 6-10 (b), which shows the wear scar of rollers after 10^6 contact cycles, micropitting and abrasive wear are enhanced in the case of lubricants with added-water. Micropitting and abrasive wear are also increased with an increase in the water concentration to 3% which is due to the increase in the dissolved water concentration as shown in Figure 6-8. This suggests that free water profoundly favours a mild wear process and subsequently micropitting is hindered. On the other hand, dissolved water facilitates mild wear and significantly enhances micropitting initiation and abrasive wear simultaneously. Figure 6-11 shows the WLI image, micropitting map and corresponding average micropitted surface area and wear scar depth profile of the roller surface lubricated with BO + ZDDP + 3% water after 10^6 contact cycles.

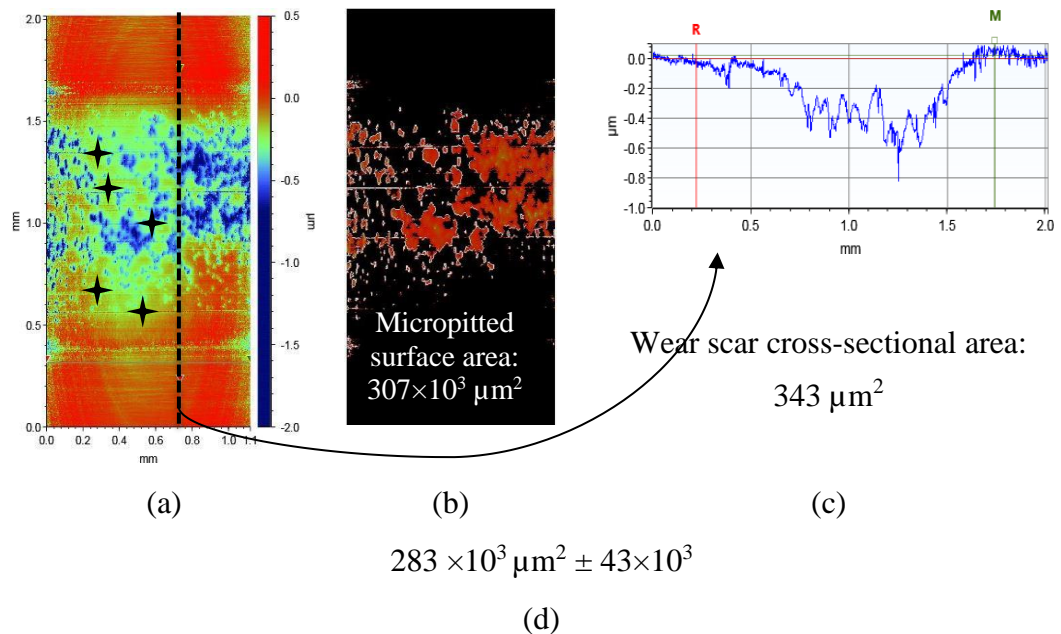


Figure 6-11. a) Wear scar profile, b) MR profile, c) corresponding wear scar depth profiles and d) average micropitted surface area of the roller surfaces lubricated with BO + ZDDP +3% Water at 75°C. ✦ Abrasive marks

Figure 6-12 compares the average micropitted surface area in the wear scars of rollers lubricated with lubricants which contain different levels of dissolved water. There is

an increase in the micropitting extent with an increase in dissolved water level. It is interesting to observe that the micropitted surface area is approximately similar in the case of BO + ZDDP (RH 60%) and lubricant with 1% added-water, although the dissolved water level of BO + ZDDP + 1%water is higher at the end of the experiment. This can be explained through a careful inspection of change in the water-saturation level of the lubricant throughout the test (Figure 6-8). The first reason is the effect of free water conditions at the start of the test ($\sim 7 \times 10^3$ contact cycles) for 1% water-containing lubricant. The free water conditions at the start of the test promote mild wear both on the roller and rough counter-parts leading to a decrease in the counter-parts roughness. The decrease in the counter-body roughness results in a consequent decrease in the micropitting extent on the roller. The second reason is that for a short period of the experiment (from 62.5 K to 250K contact cycles which almost 20% of the tests duration) the water-saturation level is higher in BO + ZDDP (RH 60%) test condition.

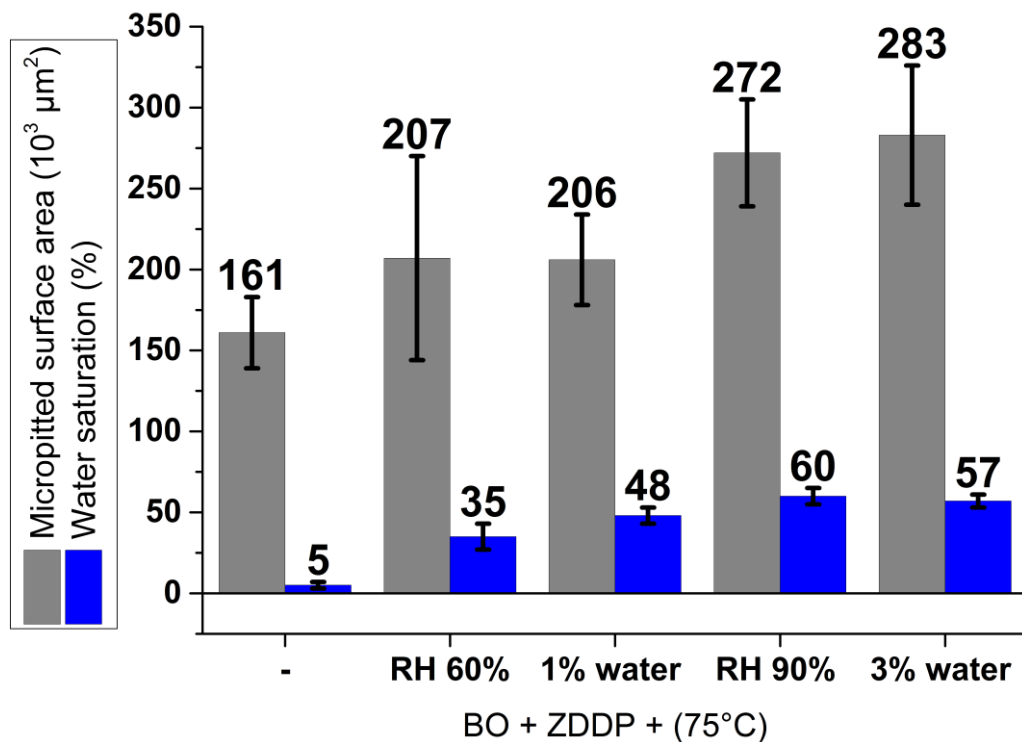


Figure 6-12. Average micropitted surface area and water saturation level in oil at the end of the test in different test conditions

6.2.3 Total wear volume results

Figure 6-13 shows the comparison of the total wear on the roller surfaces lubricated with water and humidity. The total wear volume results do not comply with the trend

which is observed for the micropitting surface area with respect to the water saturation level. Furthermore, the total wear volume on the roller surface lubricated with 1% water-containing lubricant is lower than that of BO + ZDDP. The total wear volume represents the total material loss induced by mild, abrasive, adhesive and micropitting wear. In addition, mild and micropitting wear are affected within the running-in period in which the water-saturation level in some cases (e.g. compare the water-saturation level of RH 60% with 1% Water at the beginning and end of the experiments) differs from that of the lubricants at the end of the experiment. Therefore, the total wear volume is very complex to interpret in the current experimental setup.

Alongside micropitting surface density on the surface, which increases with an increase in water saturation level in oil, micropitting depth is a strong parameter which influences the total wear volume. As shown in the previous sections (6.2.2.1 and 6.2.2.2) although mild wear and the micropitting surface area (extent of the surface damage) increases with respect to dissolved water level in the lubricant, the micropitting propagation is hindered to some extent. The decayed micropit propagation leads to a smaller and shallower micropit resulting in less material loss.

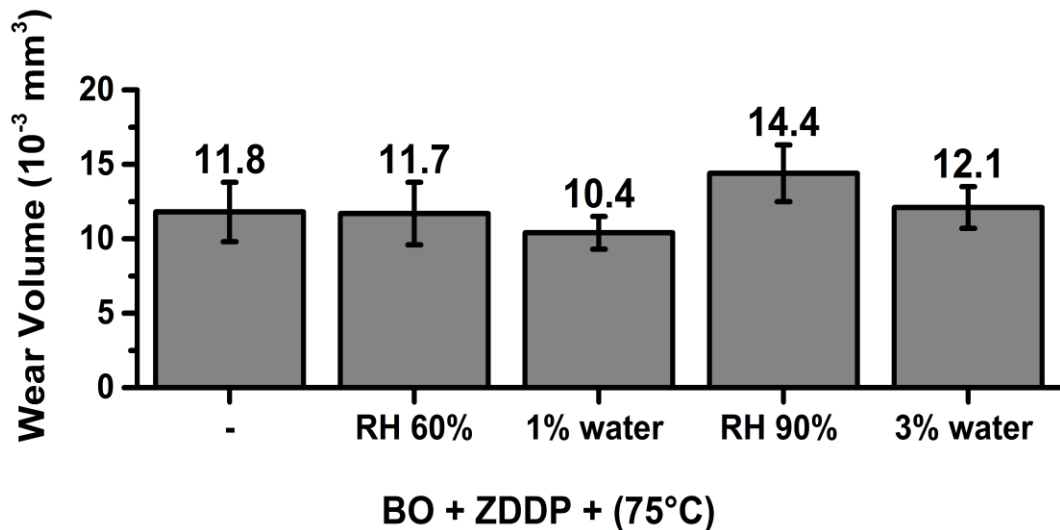


Figure 6-13. Total wear volume (material loss) in the wear scars in different test conditions and lubricants (at 75°C)

In general, the water in the lubricant induces higher mild wear. Also, high relative humidities (>RH 60%) and high concentration of added-water (>3%) bring about an increase in total wear volume in the current experimental setup.

6.2.4 Friction results

The friction results of the micropitting tests, lubricated with different lubricant formulations, are presented in Figure 6-14. The presented friction coefficient in Figure 6-14 is the average of the last 30 minutes ($\frac{3}{21} \times 10^6$ contact cycles) of the tribological tests for three measurements.

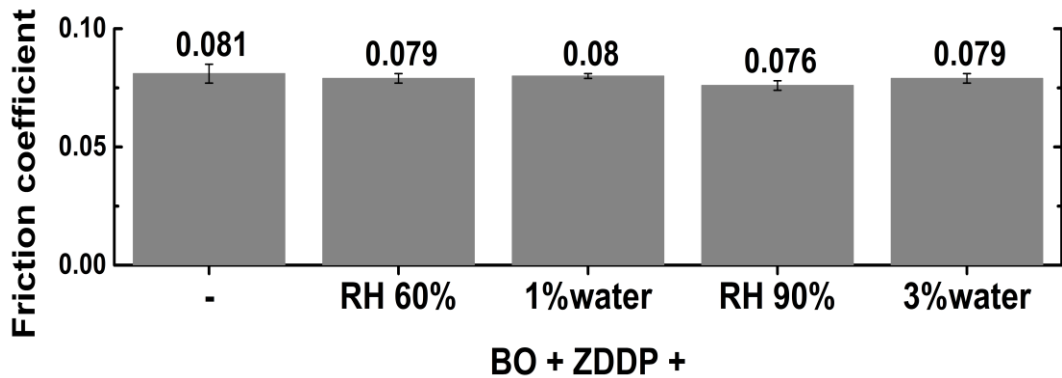


Figure 6-14. Friction coefficient in the contacts lubricated in different test conditions

As can be seen the friction coefficient results do not follow a certain trend with respect to the dissolved water level. As a general observation, it can be noted that the added-water and humidity slightly decrease the friction coefficient in the contact in the test conditions used in this project. The lowest friction coefficient can be observed in the contact which has undergone highest total wear (BO + ZDDP (RH 90%)) implying an increase in the contact area due to excessive mild-wear. The friction force, tangential to the rolling-sliding direction depends on different parameters including applied normal load, lubricant characteristics (viscosity), formed reaction layer on the surface which is induced by the interaction of lubricant additives with the surface and topography of the contact surfaces.

A severe boundary lubrication regime leads to extreme asperity-asperity contacts and consequently induces persistent changes in the surface morphology (12). As shown in the previous section (6.2.2) water and humidity alter the extent of micropitting and mild wear which profoundly influence the surface morphology. Therefore, friction coefficient, in this case, is very complex to interpret with respect to micropitting or water saturation level due to tribochemical phenomena involved in the contact and complex surface geometry which has micropits embedded in the wear scar.

6.2.5 Tribochemistry in the presence of water in oil and humidity

6.2.5.1 Chemical composition of the tribofilm top layer

In Figure 6-15 the detailed XPS spectra of the C 1s, O 1s, P 2p, Zn 3s, Fe 2p, S 2p and Zn L₃M_{4,5}M_{4,5} for the roller lubricated with BO + ZDDP (RH 60%) are shown. All other spectra from other roller surfaces were fitted using the same curve-fitting procedure. The details of the fitted spectra are listed in Table 6-1 and Table 6-2.

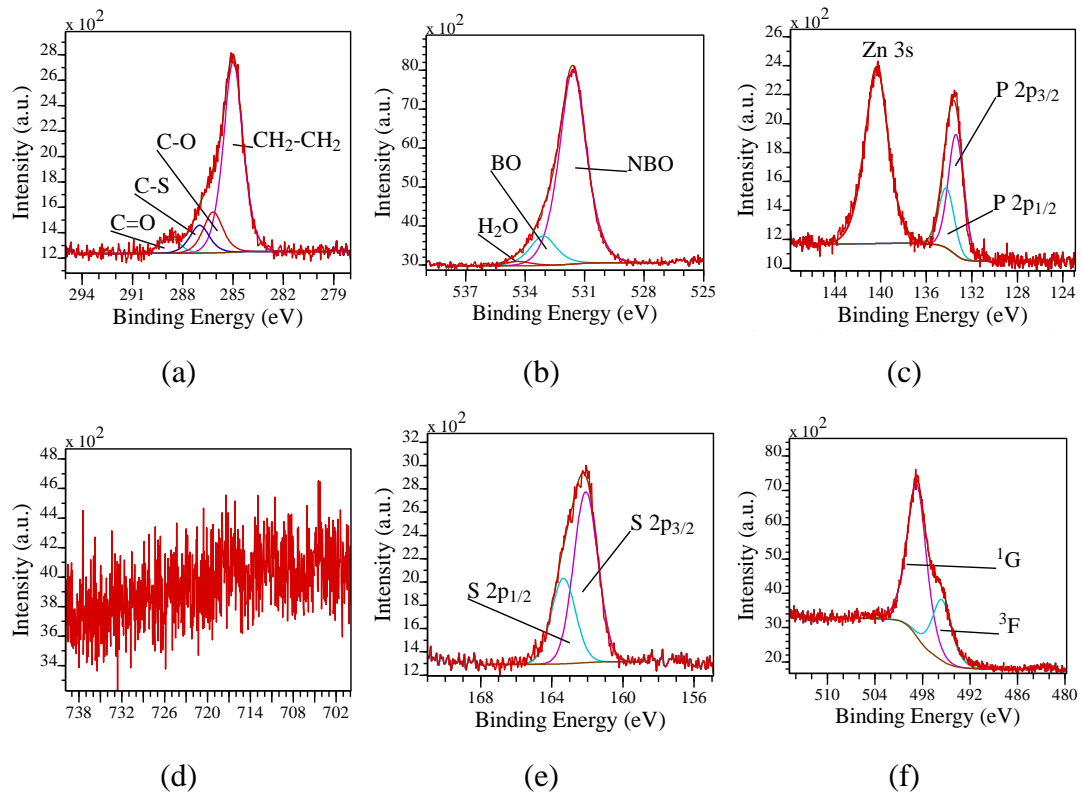


Figure 6-15. XPS detailed spectra of the ZDDP-tribofilm elements in the wear scar of the roller lubricated with BO + ZDDP (RH 60%) showing a) C 1s, b) O 1s, c) P2p and Zn 3s, d) Fe 2p, e) S 2p and f) Zn L₃M_{4,5}M_{4,5}

The C 1s spectra collected from the wear scars are resolved to four signals. The main signal appeared at 285.0 eV assigned to the aliphatic carbon (C-C and C-H). The three other minor contributions exhibited at around 286, 287, and 289 eV which are attributed to C-O, C-S and C=O (carbonate and/or carboxylic), respectively. The O 1s signal consists of two peaks in the wear scars lubricated with BO + ZDDP and three peaks in the wear scars lubricated with added-water or under humid environments. The most intense peaks at 531.5-531.7 ± 0.1 eV assigned to NBO from phosphate chain (-P=O and P-O-M; where M is a metal) and from carbonates and hydroxides (151, 192). The -P=O and P-O-M peaks cannot be resolved due to the

fact that the difference in the binding energies of them is smaller than the energy resolution.

Table 6-1. Binding energy values of the elements/compounds of the tribofilm and atomic concentration of the Zn, S and O normalised to P

	Lubricant (90°C)	BO + ZDDP	BO + ZDDP + 1% Water	
Binding energy (eV)	BO	533.07 ± 0.17	533.0 ± 0.15	
	O 1s	NBO	531.55 ± 0.14	531.5 ± 0.1
		H ₂ O/O-C	-	534.10 ± 0.1 (1.6% ± 0.2%)
	P 2p _{3/2}	133.56 ± 0.24	133.3 ± 0.08	
	Zn 3s	140.41 ± 0.17	140.3 ± 0.1	
	S 2p _{3/2}	162.22 ± 0.24	162.0 ± 0.1	
	Zn L ₃ M _{4,5} M _{4,5} ¹ G BE	499.18 ± 0.08	Not measured	
	Zn 3s - P 2p _{3/2} BE difference	6.85 ± 0.05	7.05 ± 0.02	
	Zn modified Auger parameter	2010.18 ± 0.12	Not measured	
	BO/NBO ratio	0.22 ± 0.02	0.19 ± 0.02	
Atomic concentration ratio	Zn/P	1.07 ± 0.07	1.84 ± 0.1	
	S _(II) /P	0.71 ± 0.08	1.09 ± 0.06	
	O _(phosphate) /P	1.75 ± 0.12	2.62 ± 0.2	

The maximum error for the measurements of the signal binding energies was ± 0.1 eV. The decimal digits in the table indicate the maximum deviation from the mean value (average of measurements on two specimens)

The peaks at 532.8-533.2 ± 0.1 eV correspond to BO from the phosphate chains (P-O-P). The third peaks at 534.1-534.3 ± 0.1 eV, which are observed in the wear

scars lubricated with added-water or under humid environments, can be attributed to the absorbed water (187, 192) or oxidised organic species which are adsorbed on the surface (192, 212). No metal oxide peak at 529-530.7 eV and Fe signal is detected in the XPS spectra collected from the top layer of the ZDDP-tribofilm (see Table 6-1, Table 6-2 and Figure 6-15).

The P 2p signal corresponds to P in phosphate chain and the values of the P 2p_{3/2} component of the P signals of the wear scars are shown in Table 6-2. A peak attributed to Zn 3s also is detected at 140.1-140.6 ± 0.1 eV which is considered to calculate the quantification data (elemental atomic concentrations) due to the approximately same inelastic mean free path value of this peak as P 2p and similar to the O 1s and S 2p values (151, 193-194).

The S 2p spectra have a signal in the oxidation state of -2 (SII) which is assigned to sulphides (195) as organic and metal sulphide (zinc sulphide here at the very top surface) and S which is substituted for O in the phosphate chain forming (polythio)phosphate (O-P-O → O-P-S) (127).

The modified Auger parameter ($\alpha' = \text{Zn } 2p_{3/2} \text{ (BE)} + \text{Zn } L_3M_{4,5}M_{4,5} \text{ } ^1G \text{ (KE)}$) is calculated using the zinc 2p_{3/2} signal. The zinc 2p and zinc 3s might not be a decisive and overarching signal in order to distinguish between zinc oxide and zinc sulphide. On the other hand, modified Auger parameter (α') and Wagner plot (213-214) derived from Zn 2p and Zn L₃M_{4,5}M_{4,5} are strong features in order to inspect the zinc chemical status. The α' for zinc oxide is reported to be 2009.5-2010.5 eV while to be 2010.1-2011.4 eV for zinc sulphide (215-216). The values of 2009.8-2010.2 ± 0.2 eV for α' in this study could be an indication that most of the zinc is present as zinc oxide rather than zinc sulphide in agreement with the previous reports (129, 135).

The phosphate chain length in the ZDDP-derived tribofilm is assumed to be an important factor in determining its AW performance (105, 151). The BO/NBO ratio has been widely used to evaluate the chain length of zinc phosphate glasses (122). However, the BO/NBO ratio may be affected by contaminants or overlaps with the peaks from other components. Hydroxides and C=O (carbonyl and carbonate) can contribute to NBO peak (151, 192) and P-O-C can contribute to BO peaks (197). Also, the absorbed water at 533.3-434.3 eV can bring about errors in the BO/NBO ratio.

Table 6-2. Binding energy values of the elements/compounds of the tribofilm and atomic concentration of the Zn, S and O normalised to P

Lubricant (75°C): BO + ZDDP +		-	1% Water	(RH 60%)	(RH 90%)
Binding energy (eV)	BO	533.07 ± 0.06	532.8 ± 0.15	533.06 ± 0.04	532.9 ± 0.05
	O 1s NBO	531.62 ± 0.02	531.6 ± 0.02	531.6 ± 0.02	531.5 ± 0.06
	H ₂ O/O-C	-	534.15 ± 0.15 (1.4%±0.1%)	534.3 ± 0.1 (1.6%±0.3)	534.1 ± 0.1 (1.3%±0.3)
	P 2p _{3/2}	133.52 ± 0.13	133.31 ± 0.04	133.34 ± 0.03	133.1 ± 0.07
	Zn 3s	140.4 ± 0.1	140.26 ± 0.03	140.3 ± 0.05	140.1 ± 0.05
	S 2p _{3/2}	162.15 ± 0.15	162.01 ± 0.07	162.0 ± 0.1	161.9 ± 0.1
	Zn L ₃ M _{4,5} M _{4,5} ¹ G BE	499.28 ± 0.12	498.83 ± 0.07	498.69 ± 0.08	498.70 ± 0.13
	Zn 3s - P 2p _{3/2} BE difference	6.88 ± 0.02	6.95 ± 0.02	6.97± 0.01	6.94 ± 0.03
	Zn modified Auger parameter	2009.88±0.06	2010.16±0.08	2010.19±0.07	2010.22±0.1
	BO/NBO ratio	0.18 ± 0.05	0.14 ± 0.01	0.12 ± 0.03	0.12 ± 0.02
Atomic concentration ratio	Zn/P	1.12 ± 0.15	1.73 ± 0.1	2.01 ± 0.2	2.14 ± 0.08
	S _(II) /P	0.58 ± 0.02	0.96 ± 0.13	1.32 ± 0.05	1.27± 0.09
	O _(phosphate) /P	1.96 ± 0.36	2.89 ± 0.2	2.3 ± 0.4	3.23 ± 0.33

The maximum error for the measurements of the signal binding energies was ± 0.1 eV. The decimal digits in the table indicate the maximum deviation from the mean value (average of measurements on two specimens)

Therefore, considering the BO/NBO ratio for phosphate-chain-length estimation may bring about uncertainties and thus complementary parameters are required to confirm the change in the phosphate chain length.

The higher ratio of the cations (Zn^{+2} and $Fe^{+2,+3}$) to P (197) together with the increase in the O/P ratio in the zinc (poly)phosphate can suggest a greater metal (zinc and iron) oxide to P_2O_5 mole fraction which indicates a shorter (poly)phosphate chain development (122). Also, with more metal oxide fraction a lower BO/NBO ratio and a shift of P $2p_{3/2}$ BE to lower values have been observed (187, 198-200). As far as ZDDP-tribofilms in this study are concerned, the tribofilms generated after 10^6 contact cycles are not expected to consist of long (poly)phosphate chains considering P $2p_{3/2}$ BE values ($133.1-133.6 \pm 0.1$ eV) and BO/NBO ratios of 0.12-0.23, since P $2p_{3/2}$ in the pure long chain zinc polyphosphate appears at 134-135 eV (202-205). In this study, in order to eliminate the error which may arise from the calibration and sample charging, the comparison of the (poly)phosphate chain length is also made through energy difference between Zn 3s and P $2p_{3/2}$ peaks (Zn 3s-P $2p_{3/2}$).

The Zn 3s - P $2p_{3/2}$ BE difference tends to increase with a decrease in the (poly)phosphate chain length (201). In addition, with an increase in the zinc phosphate chain length a decrease in the modified Auger parameter (α') BE has been observed (187, 193). Accordingly, to overcome the uncertainty around the BO/NBO ratio, four parameters have been used in the current study which are BO/NBO ratio, change in the ratio of Zn/P and O/P, Zn 3s - P $2p_{3/2}$ BE difference and Zn modified Auger parameter (α') to investigate the effect of water and humid environment on the (poly)phosphate chain length.

As can be seen in Table 6-1, a decrease in the BO/NBO ratio, an increase in Zn/P and $O_{(phosphate)}/P$ ratio and Zn 3s - P $2p_{3/2}$ BE difference suggest that 1% of added-water decreases the (poly)phosphate chain length in the ZDDP-derived tribofilm in agreement with a previous report (151). Also, shown in Table 6-2, a decrease in BO/NBO ratio, an increase in Zn/P and $O_{(phosphate)}/P$ ratios, Zn 3s - P $2p_{3/2}$ BE difference and the modified Auger parameter (α') can be observed in the tribofilms derived from the lubricants containing added-water or dissolved water absorbed through humid environments. This suggests that dissolved water, which is absorbed into the lubricant through added-water or humid environment, can decrease the (poly)phosphate chain length in the ZDDP-derived tribofilms.

The Zn/P, S/P and O/P ratios in the lubricants with dissolved water compared to the tests carried out in laboratory condition exhibit a significant increase. The increase in Zn/P and S/P can be an indication of enhanced formation of zinc sulphide in the tribofilms generated from lubricants with added-water and in humid environments (151).

6.2.5.2 The tribofilm thickness and elemental distribution

In order to estimate the tribofilm thickness and inspect the elemental distribution of the tribofilm in the wear scar, the tribofilms are sputtered using an Ar⁺ ion source. Although the XPS Ar⁺ ion sputtering is a valuable technique to observe the elemental distribution through the tribofilm depth, chemical substances could be altered through preferential sputtering and intermixing of compounds (217) especially in the case of transition metals. In the case of Fe, iron oxides can undergo a reduction to other oxidation states (218-220). Therefore, loss of analysis resolution is expected through depth profiling.

The sputtered profiles of the tribofilms are shown in Figure 6-16. The tribofilm thicknesses are 12, 6, 5 and 4 minutes of the etching for the surfaces lubricated with BO + ZDDP, BO + ZDDP (RH 60%), BO + ZDDP + 1%water and BO + ZDDP (RH 90%), respectively. This shows that dissolved water decreases the tribofilm thickness in agreement with the previous reports (148, 151).

As can be seen in Figure 6-16, the P concentration decreases from approximately 18% to around 10-12% as a consequence of added-water and humidity. Also, the atomic-concentration ratio of S/P is significantly increased, standing approximately ≥ 1 , throughout the tribofilm depth suggesting contribution of inferior (poly)phosphates to the bulk of the tribofilms from the lubricants with added-water and tests under humid environments.

After one step of etching the contribution of C cannot be observed for the tribofilm from BO + ZDDP lubricant until 240 s of tribofilm etching. Further contribution of C to the tribofilm bulk arises from carbides in the film. The carbide contribution originates from steel substrate and is induced through wear processes. This observation confirms the inorganic nature of the ZDDP tribofilm throughout its depth. Furthermore, in all tribofilms, the atomic concentration of Zn continuously stays above that of P and S in the tribofilm bulk which implies the contribution of Zn as zinc (poly)phosphate and zinc sulphide to the tribofilm.

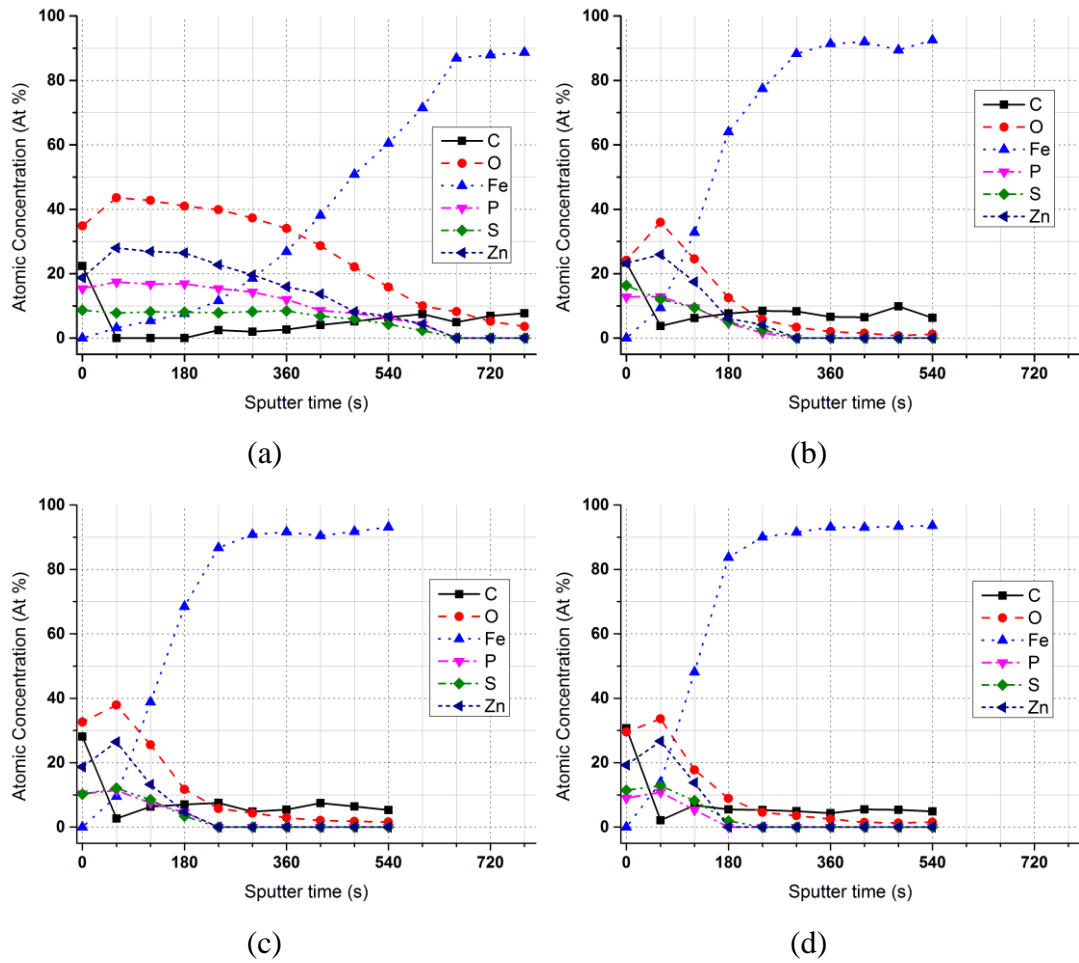


Figure 6-16. Sputter depth profile of the tribofilms in the wear scars lubricated with a) BO + ZDDP in laboratory conditions), b) BO + ZDDP (RH 60%), c) BO + ZDDP + 1%water in laboratory conditions and d) BO + ZDDP (RH 90%) lubricants at 75°C

6.3 Summary

In the current chapter the tribological and tribochemical effects of dissolved and free water on micropitting wear and friction of BO and BO + ZDDP lubricants are investigated. The PAO-base oil does not exhibit a specific trend with respect to dissolved water level in the oil in terms of friction and total wear in the test conditions applied in this study. On the other hand, the performance of BO + ZDDP lubricant significantly depends on the water content in oil. In the tests conditions defined in this study concluding remarks are as follows:

- The micropitting surface area and abrasive wear proportionally increase with an increase of dissolved water level in the lubricant absorbed through added-water or humid environments.

- In tribocorrosive environments studied in this chapter, the friction coefficient varies between 0.076 and 0.081 and the average wear volume varies between 10.4×10^{-3} and $14.4 \times 10^{-3} \text{ mm}^3$ for experiments conducted using ZDDP-containing lubricants at 75°C . Accordingly, changes in friction are negligible and changes in wear are within the standard deviations from the average in all cases. Therefore, in the conditions defined in this study, the increase in micropitting in tribocorrosive environments is influenced by tribochemical phenomena involved in the contact. This will be discussed further in the discussion chapter.
- The ZDDP-tribofilm thickness and (poly)phosphate chain length are inversely proportional to the dissolved water level in the lubricant. Also, water and humidity can alter the zinc-oxide/zinc-sulphide ratio in the ZDDP-tribofilm to a certain extent which will be discussed further in section 9.3.1.
- Water and humidity favours mild wear through interfering with ZDDP-tribofilm formation. Thinner ZDDP-tribofilm, shorter (poly)phosphate chain and less contribution of phosphate to the bulk of ZDDP-tribofilm, induced by dissolved water, are observed with an enhanced mild and abrasive wear.
- While dissolved water increases micropitting nucleation and expands the nucleation across the wear scar, in free water condition micropitting appearance is suppressed due to a dominant action of mild wear.
- Friction coefficients in the lubricants containing dissolved water are slightly lower than that of BO + ZDDP in the laboratory conditions. This could be induced through discernible changes in the ZDDP-tribofilm thickness and composition.

Chapter 7

Nitrogen-containing additive as a friction modifier: effect of NCAs on the friction, rolling wear and tribofilm composition

7.1 Introduction

The effect of ZDDP AW additive on enhancing micropitting and the influence of water contamination on the micropitting performance were shown in the previous results chapters. The efficiency of ZDDP on protecting the surfaces from wear and scuffing makes it an essential additive in the lubricant formulation. Therefore, additives that can alleviate the undesired influence of ZDDP in enhancing micropitting, while retaining the wear-protection functionality of ZDDP, are vital to the roller-element bearing and gear industries. This chapter investigates the rolling-wear and friction performances of NCAs that are ashless, with no SAPS content OFMs. The NCAs which are targeted for this project are detailed in Table 4-4. The tribochemical properties of the tribofilms derived from combination of NCAs and ZDDP are investigated employing XPS.

7.2 Results

All the additives except ETDP are soluble in the PAO + ZDDP lubricant using the mixing procedure which is indicated in section 4.1.3.3. The ETDP additive at both 0.5% and 1% was not dispersible in either PAO or PAO + ZDDP producing cloudy oils which is indicative of an emulsion formation. This results from the high polarity of the ETDP additive.

In an attempt to observe the polarity effect of ETDP on its solubility in oil, a fully-formulated oil which has 20% of ester as its base stock and a pure ester base oil are used. As can be seen in Figure 7-1, ETDP is not soluble in the fully-formulated gear-box lubricant, while it is fully-soluble in the pure ester oil. Therefore, ETDP was disregarded for the rest of the experimental plan. The first reason was that the change of base oil to an ester was not within the scope of this project. The second and more important reason for this decision was that ethoxylated amine has been found to be undesirable in the micropitting wear which will be discussed in section 8.2.2.

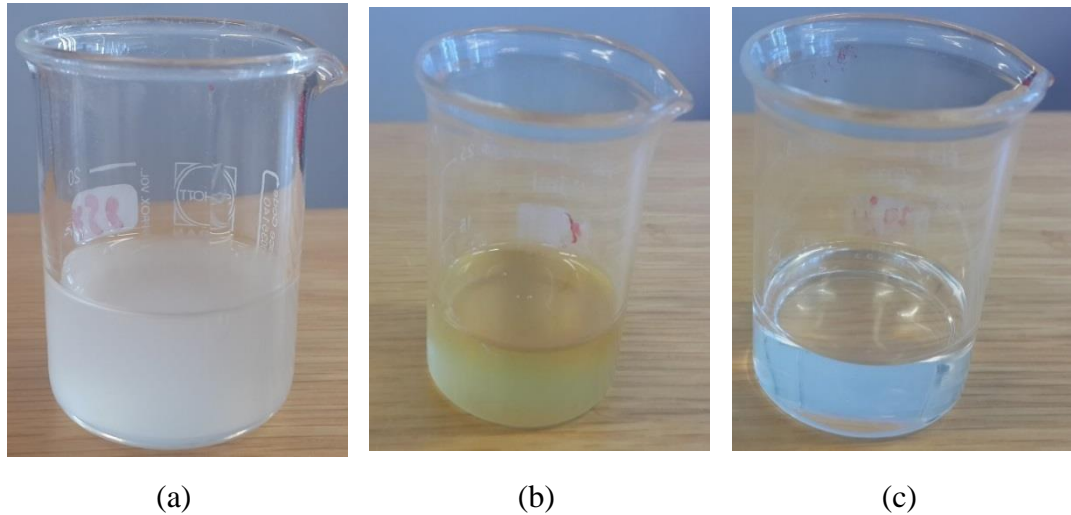


Figure 7-1. Images of oil solutions of ETDP in a) PAO, b) a fully-formulated and c) a synthetic ester

7.2.1 Tribofilm thickness in SS configuration

Figure 7-2 shows the SLIM images of tribofilm evolution over rubbing time for three lubricant formulations. The ZDDP tribofilm was seen to form on the surface after nearly five minutes of rubbing in the BO + ZDDP lubricant formulation.

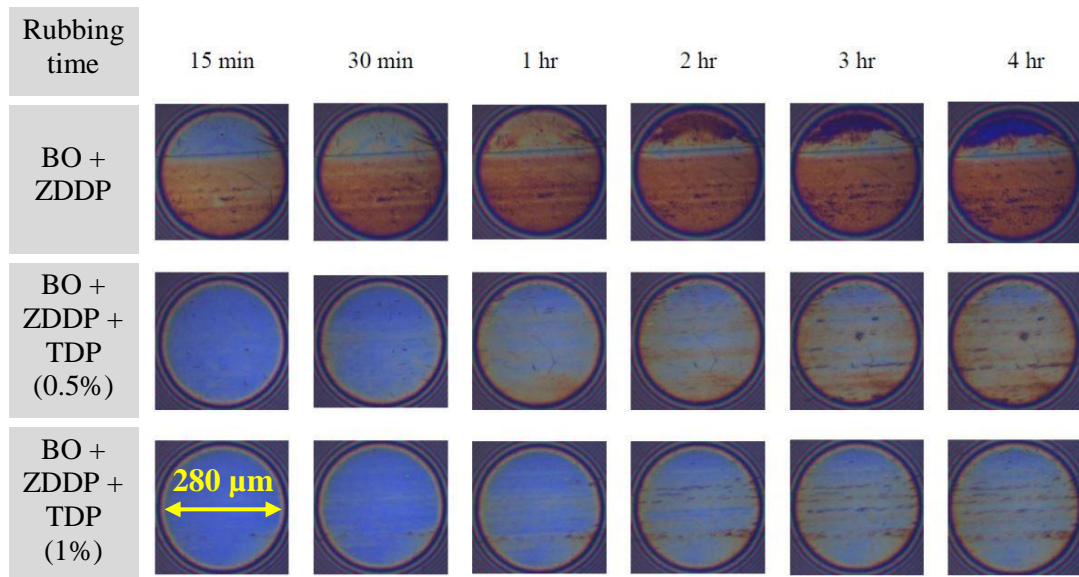


Figure 7-2. Tribofilm evolution over rubbing-time in the three lubricant formulations. Experiments are conducted in conditions associated with SS configuration. The circular contact zones in the interference images are 280 μm in diameter as represented in the first image of BO + ZDDP + TDP (1%) lubricated ball surface

For the BO + ZDDP + TDP (0.5%) and BO + ZDDP + TDP (1%) the period was delayed to thirty minutes and one hour, respectively. The delaying effect was enhanced when the concentration of TDP was doubled. Also, from images, shown in

Figure 7-2, it is clear that the tribofilms from TDP containing lubricants, at the end of the tests, are considerably thinner compared to that of BO + ZDDP.

In Figure 7-3 the tribofilm thickness is plotted for different lubricant formulations over rubbing time. It is clear that addition of NCAs delays tribofilm formation to a certain extent, depending on the concentration of the additives in the lubricant and their chemical structure. The impact of TA (1%) and ETA (1%) on delayed tribofilm formation is significantly higher in comparison to the impact of TDP.

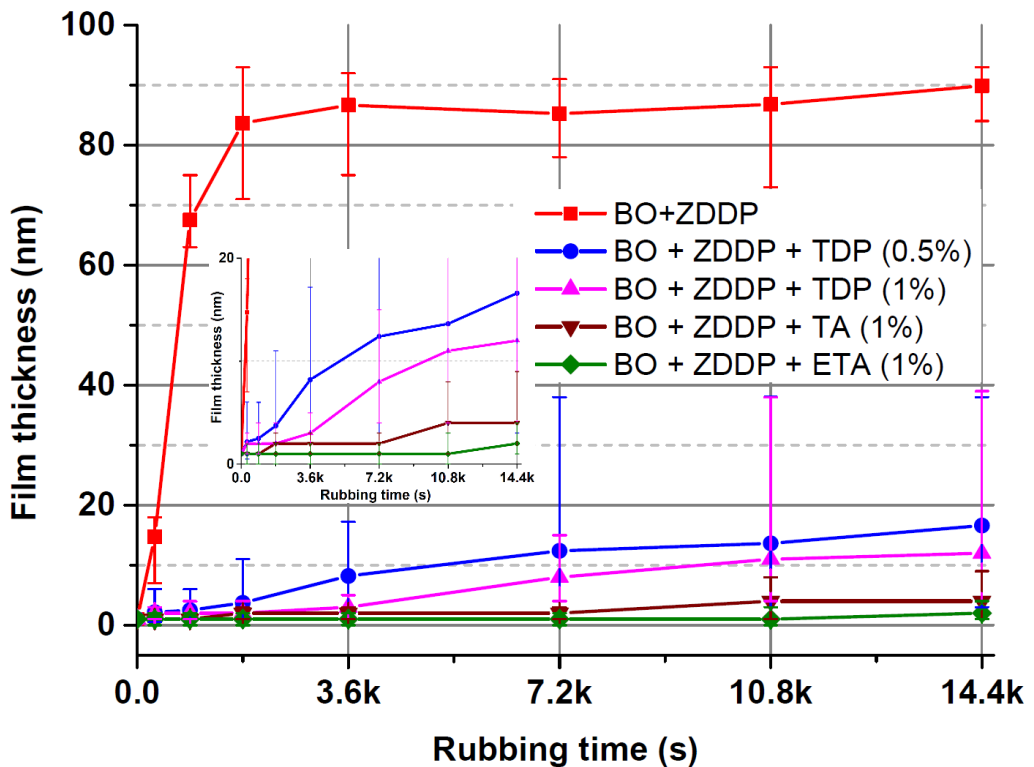


Figure 7-3. Tribofilm thickness of different lubricant formulation over rubbing intervals *Error bars in the plot represent the minimum and maximum tribofilm thickness detected on the MTM balls.

In the surface of the BO + ZDDP + TA (1%) only after 3 hours of rubbing tribofilm of few-nanometre-thick is locally formed. Almost no tribofilm is formed on the surface of BO + ZDDP + ETA (1%) until the end of the test. This shows the influence of the hydroxyl (OH) group in the ETA formulation which is chemically adsorbed on the surface, hindering ZDDP tribofilm formation. Addition of the 0.5% TDP to the lubricant, results in a 20 nm thick tribofilm, while BO + ZDDP lubricant generates a 90 nm thick tribofilm at the end of the test. Increasing the TDP concentration to 1% in the lubricant leads to a further delayed and thinner tribofilm formation.

7.2.2 Surface observation of disc specimens using SEM

The wear scars on the disc specimens, lubricated with BO + ZDDP and BO + ZDDP + TDP (0.5%), have been inspected using SEM and the images are shown in Figure 7-4 and Figure 7-5, respectively. Also, EDX analysis is carried out in order to inspect the tribofilms in the different areas of the wear scars. The areas of EDX analyses are annotated in the corresponding images and the quantitative data report the atomic concentration ratio of the elements in the corresponding annotated areas. The secondary electron mode is used to inspect the wear scars. However, high acceleration voltage (20kV) enhances the contribution of back-scattered electrons to the scan (207).

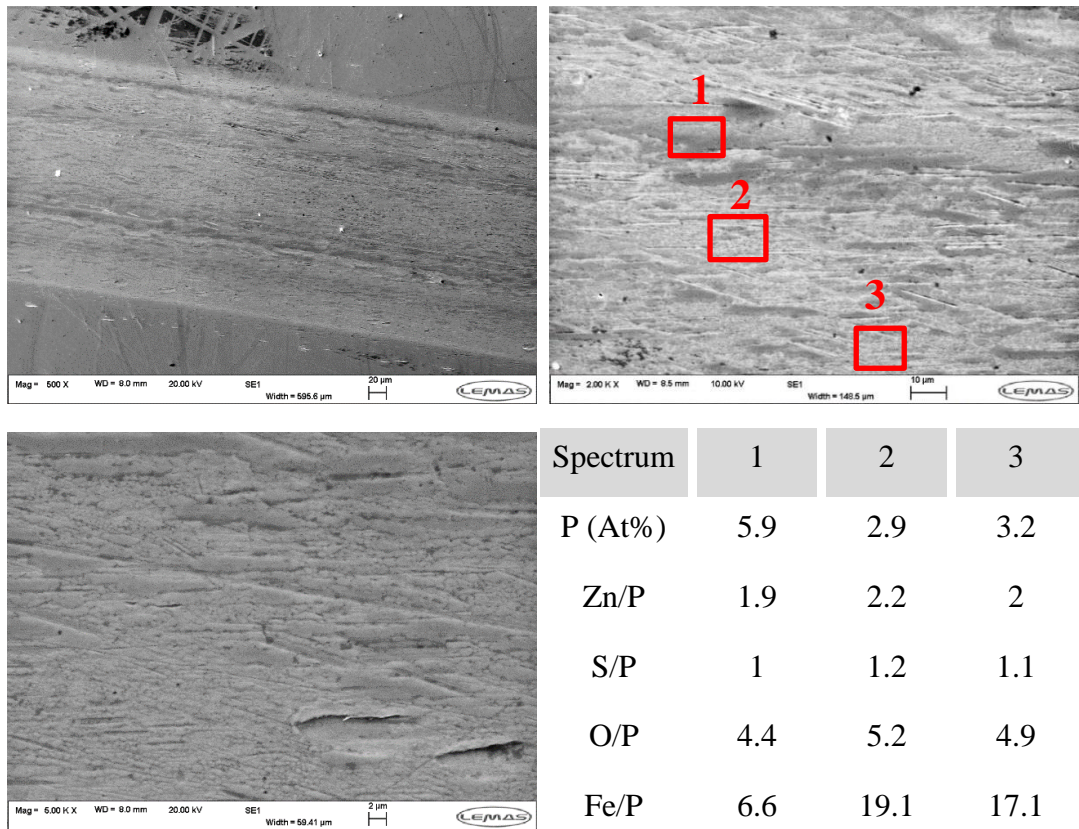


Figure 7-4. SEM and EDX analysis on the wear scar of the disc specimen lubricated with BO + ZDDP in SS configuration

The EDX analyses in Figure 7-4 show that different areas in the wear scar have a similar ZDDP elemental ratio which suggests a similar ZDDP-tribofilm composition. The Fe/P ratio in spectrum 1 is considerably lower compared to that of spectra 2 and 3 indicating thicker tribofilm in the area of spectrum 1. Therefore, in Figure 7-4 the areas of the wear scar which have a higher contrast, due to the rougher nature of the tribofilm, have a thicker tribofilm on the surface.

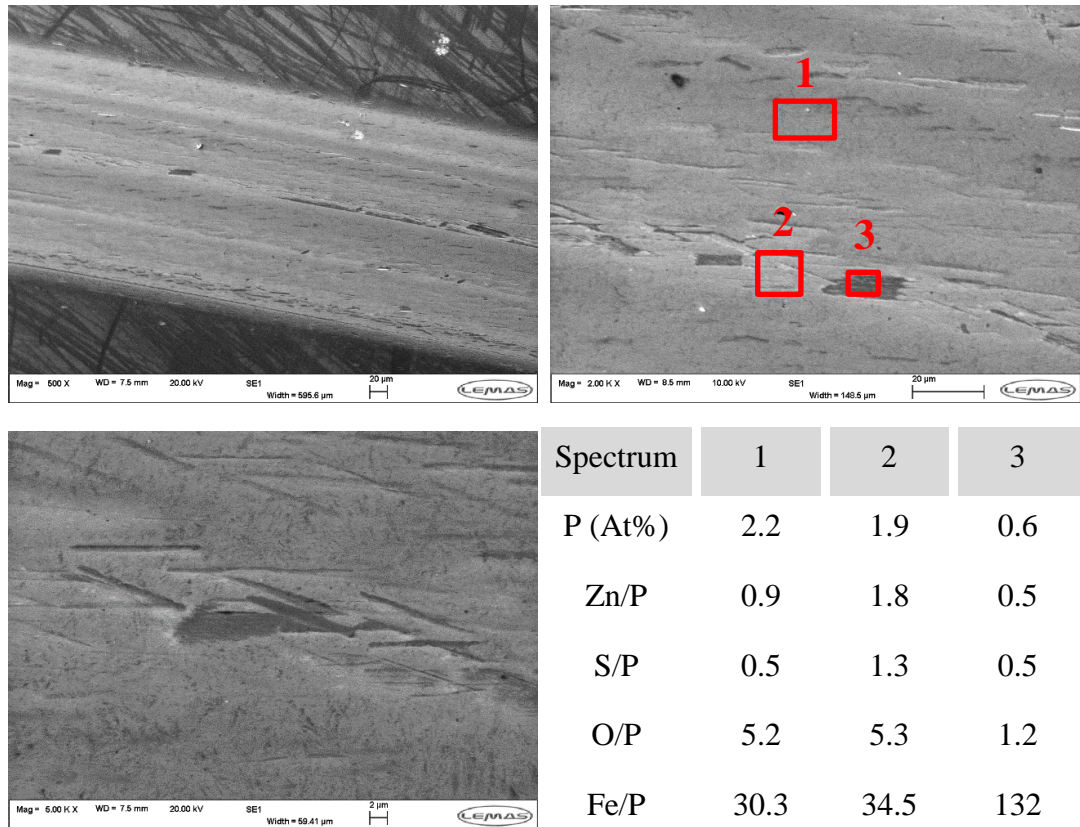


Figure 7-5. SEM and EDX analysis on the wear scar of the disc specimen lubricated with BO + ZDDP + TDP (0.5%) in SS configuration

The EDX analyses in Figure 7-5 imply that the composition of the tribofilm from BO + ZDDP + TDP is altered in different zones of contact and the tribofilm in spectrum 2 is similar to the tribofilm on the surface of BO + ZDDP. The extremely large ratio of Fe/P and a low concentration of P in spectrum 3 suggest a minor tribofilm formation in this area. Also, the high contrast suggests a worn surface having low electron escape. The higher ratio of Fe/P in tribofilm of BO + ZDDP + TDP compared to that of BO + ZDDP confirms thinner tribofilm formation in the presence of TDP (Figure 7-3). In general, the wear scar in Figure 7-5 is more uniform having less contrast compared to Figure 7-4 which points out a smoother surface and/or tribofilm from BO + ZDDP + TDP (0.5%).

7.2.3 Friction results in SS configuration

Figure 7-6 shows the friction behaviour of the different lubricant formulations over the rubbing-step. The vertical grey lines at the specific rubbing intervals show the time-periods at which SLIM mappings and Stribeck curve measurements have been carried out. A shift in friction can be observed at each Stribeck curve measurement for all the lubricants which have additives. This is due to the change in the entrainment

speed during Stribeck curve measurement. The speed goes as low as 15 mm/s leading to an enhanced tribofilm build-up and a microscopic change in the tribofilm and surface topography which results from severe contacts. Whilst in the rubbing steps with constant entrainment speed of 100 mm/s the friction remains almost unvarying.

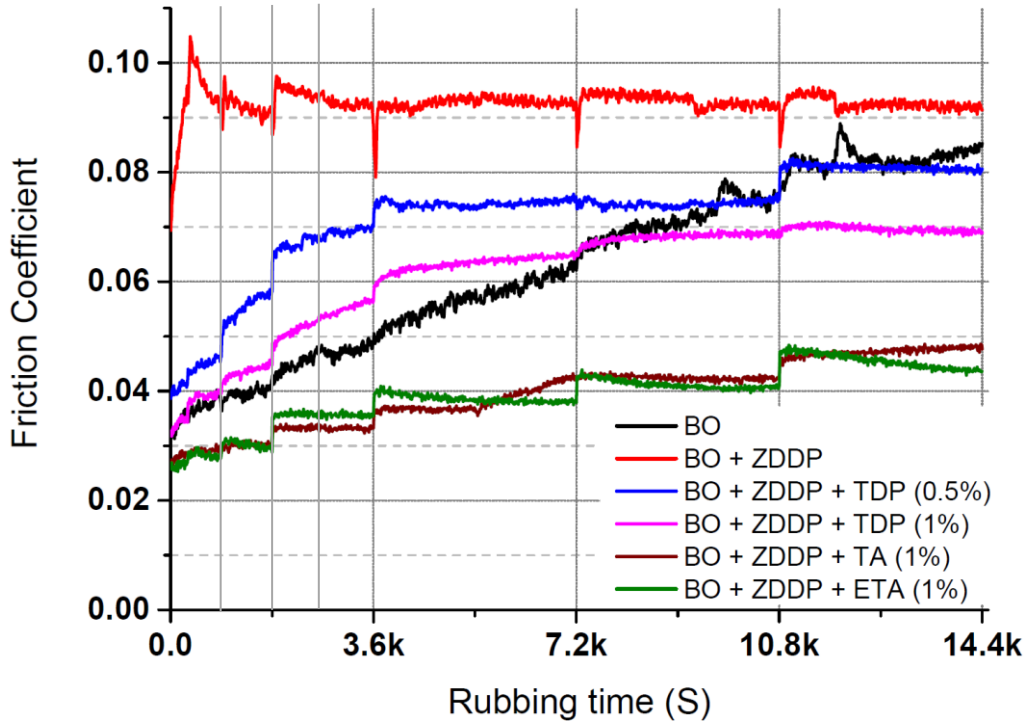


Figure 7-6. Friction coefficient of different lubricant formulations over rubbing steps

The friction coefficient of BO + ZDDP levels off at approximately 0.092 after one hour of rubbing which shows that the rate of microscopic changes in the tribofilm has reached a steady state. The friction in lubricants containing NCAs however, experiences an increase after each Stribeck curve measurement. The increase is an indication of tribofilm growth and a microscopic change in the surface topography during Stribeck curve measurements due to the more severe wear condition which is induced while the entrainment speed is decreased to 15 mm/s.

The friction coefficient in base oil has a totally different trend compared to other lubricants, reaching a friction value close to that of BO + ZDDP at the end of the test. In base oil, friction constantly increases during fixed-speed rubbing steps and Stribeck curve steps. The friction result associated with BO formulation is opposite to the trend in the micropitting test, shown in Figure 5-3, in which there was an enormous rise in friction at the very early stage of the experiment followed by a sharp drop in friction.

A different contact geometry and severity exists in the two different test set-ups which influences friction forces between two surfaces.

A similar friction coefficient is observed in TA (1%) and ETA (1%)-containing lubricants which is significantly lower than friction results for other lubricants at the end of the test. Also, friction results for TA (1%) and ETA (1%), at the start of the test are lower compared to friction in base oil. This implies that NCAs adsorb to the surface prior to the contact and diminish friction between the surfaces. The friction results for TA (1%) and ETA (1%) do not alter in accordance with friction in base oil, although tribofilm formation is inconsiderable on the surfaces in comparison to tribofilm from BO + ZDDP. This suggests that in the current lubrication conditions the NCAs can perform as an AW additive and a friction modifier simultaneously. An addition of TDP (0.5%), TDP (1%), TA (1%) and ETA (1%) leads to an approximate friction reduction of 13%, 25%, 47% and 50%, respectively compared to the friction in BO + ZDDP within the last 30 minutes of the test.

Figure 7-7 presents the Stribeck curves measured for different lubricant formulations after certain rubbing intervals. At the start of the test (at which the tribofilm has not yet formed) the initial Stribeck curve of the BO + ZDDP was similar to that of the base oil. However, the build-up of ZDDP tribofilm at the interface induces a significant increase in the Stribeck friction, especially in the intermediate speed range (200-1000 mm/s). The enhancing impact of ZDDP on the friction in the intermediate entrainment speed range has been previously reported (184). The patchy nature of the ZDDP-tribofilm on steel surfaces which inhibits the fluid-oil entrainment to the contact is postulated to be the reason behind friction-enhancing behaviour of the ZDDP tribofilm (171, 183-184).

In our experimental set-up the effect of ZDDP was observed after only five minutes of rubbing which results in the boundary/mixed condition being seen at higher intermediate speeds at which lower friction is expected. In agreement with the friction results in Figure 7-6, the Stribeck curve measured for BO + ZDDP after thirty minutes of rubbing remained similar until the end of the test implying that the tribofilm morphology, thickness and rate of microscopic-tribofilm formation and removal reached a steady state condition. The friction in the range of 15-75 mm/s after 1 hour of rubbing reached a plateau showing that the ZDDP-tribofilm effectively protects the surface in the severe boundary contacts.

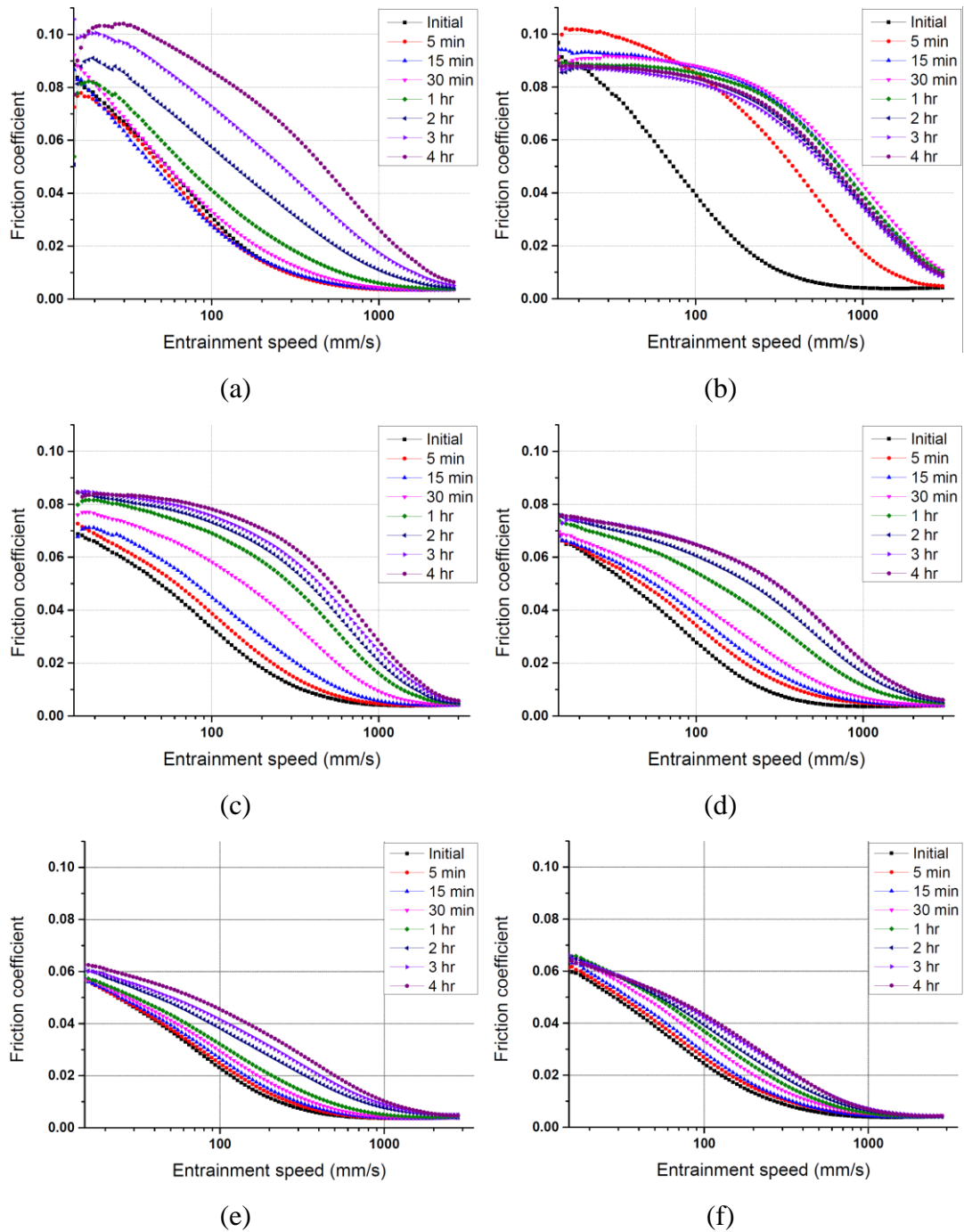


Figure 7-7. Stribeck diagrams measured after certain rubbing intervals for a) BO, b) BO + ZDDP, c) BO + ZDDP + TDP (0.5%), d) BO + ZDDP + TDP (1%), e) BO + ZDDP + TA (1%) and f) BO + ZDDP + ETA (1%) lubricant formulations

The Stribeck friction results for the BO test increase continuously after each rubbing step. The increase in friction for the BO test is induced by the wear process which influences the surface topography. Looking to the initial Stribeck curve for the BO, the friction of approximately 0.03 at 100 mm/s shows that the contact at the beginning of the test is not severe. However, during rubbing steps, asperity–asperity contacts

occur and friction increases accordingly. In fact, the gradual wear in the SS configuration increases surface roughness, leading to an increase in the probability of asperity-asperity contacts. The boundary friction (entrainment speed < 50 mm/s) shows a significant increase to above 0.1 at the end of the test which is higher than that of BO + ZDDP. In contrast to BO + ZDDP, as there is no tribofilm on the contact surfaces, the friction in the range of 15-75 mm/s increases with the decrease in the entrainment speed which results in severe asperity-asperity contacts.

As shown in Figure 7-7 (c and d), the presence of TDP in the lubricant decreases the boundary friction at the start of test compared to the BO and BO + ZDDP tests. The decrease of the boundary friction is more pronounced in the higher concentration of TDP. This can be attributed to the adsorbed film at the surface of the steel. Also, TDP reduces friction in the intermediate speed range (200-1000 mm/s) throughout the test. This indicates that TDP decays the friction-enhancing behaviour of the BO + ZDDP. A clear increase in friction occurs as soon as the tribofilm started to appear after 30 minutes and 1 hour of rubbing at TDP concentration of 0.5% and 1%, respectively. After the first hour of rubbing, the friction coefficient during each traction (fixed-speed) step remains constant followed by an increase during Stribeck friction step due to further tribofilm formation and mild wear.

As illustrated in section 2.4, in a Stribeck curve the friction coefficient is a function of Lambda ratio and hence depends on the combined roughness of surfaces which are in contact. Therefore, in the same contact conditions (e.g. load) a change in the roughness value of certain surfaces which are lubricated with a lubricant having certain characteristics, alters friction coefficient. Accordingly, the influence of additives such as ZDDP and NCAs on friction coefficient in Stribeck curves can be attributed to changes in the surface roughness resulted from surface reaction films, changes in the lubricant film thickness and accommodation of surface shear stresses by surface reaction films.

Increasing the concentration of TDP from 0.5% to 1% led to more extensive friction reduction and delay of the tribofilm formation, most probably due to a greater TDP-ZDDP interaction and less ZDDP adsorption on the surface. Although, a greater friction reduction is achieved in the higher concentration (1%) of TDP, the friction in the entrainment speed range of 15-75 mm/s has not plateaued out, in contrast to friction in TDP (0.5%) and BO + ZDDP. Attaining a plateau in the friction for

entrainment speed range of 15-75 mm/s, indicates that the film is capable of protecting the surfaces at the lower entrainment speeds. Therefore, the concentration of 0.5% for TDP has the potential to reduce the friction while protecting the surfaces at lower entrainment speeds.

The Stribeck curves of TA (1%) and ETA (1%) show a significantly lower boundary friction at the start of the test which is due to the adsorbed additives on the steel surfaces. A noticeable increase in the friction in the intermediate entrainment speed range is not observed since a tribofilm is not formed on the surfaces. The increase in friction due to the rubbing at 100 mm/s, as seen in BO, is not observed which suggests AW properties of ETA and TA in these experimental conditions. However, the boundary friction sharply increases with a decrease in the entrainment speed (<75 mm/s) implying that these additives might not protect the surface at the lower entrainment speeds (<50 mm/s) as effectively as they do at 100 mm/s.

In order to understand the performance of the additives in a more severe contact, experiments have been carried out employing a rough disc in contact against a smooth ball. The experimental parameters are presented in Table 4-3.

7.2.4 **Tribofilm thickness in SR configuration**

Figure 7-8 and Figure 7-9 show tribofilm evolution on the surface of the ball (smooth specimen) for different additive packages over 4 hours of rubbing. Two Stribeck curves have been measured at the start of the test prior to a traction step and at the end of the test after 4 hours of rubbing. It is interesting to observe that in BO + ZDDP lubricant at the initial Stribeck curve measurement, which lasts approximately 10 minutes, a 65 nanometre-thick ZDDP-tribofilm is formed on the surface. The subsequent rubbing for 5 minutes at 100 mm/s generates a further 80 nanometres of ZDDP-tribofilm which results in 145 nanometre-thick tribofilm as shown in Figure 7-9. A delay in the tribofilm formation can be observed in the presence of NCA additives. The delaying impact of NCAs on the ZDDP-tribofilm formation increases along the series of additives $ETA > TA > TDP$ in agreement with SS configuration (Figure 7-3).

The SLIM images imply that BO + ZDDP after 2 hours of rubbing reaches a steady state in terms of tribofilm thickness, whilst the tribofilm thickness in lubricants containing NCAs levels out after 3 hours of rubbing. This shows that NCAs delay both the tribofilm formation and the time required to achieve a steady-state. In

addition, ZDDP-tribofilm in BO + ZDDP lubricant reaches a plateau in tribofilm thickness after approximately 30-60 minutes of rubbing in SS configuration, while this time is delayed to approximately 60-120 minutes in the SR configuration. This suggests that in the more severe contact (with a same SRR%), the rate of the tribofilm formation, tribofilm thickness and the time required for reaching a steady-state in tribofilm thickness are increased.

Figure 7-8 shows tribofilm thickness in different lubricant formulations over rubbing time. The MTM-SLIM is able to quantify the tribofilm thickness up to the maximum value of 200 nm. After 1 hour of the rubbing, the ZDDP tribofilm thickness on the ball lubricated with BO + ZDDP reaches a value of greater than 200 nm and further mappings of the tribofilm cannot display the tribofilm thickness. The tribofilm thickness in all NCA containing lubricants levels off after 3 hours of rubbing. Among the examined NCAs, ETA induces greatest delaying effect and thinnest tribofilm (100 nm) on the surface. TA and TDP-containing lubricants generate 139 and 134 nanometre-thick tribofilms respectively. The similar thickness values can be attributed to the similar functional groups (N-H, N-CH) in TA and TDP molecular structures.

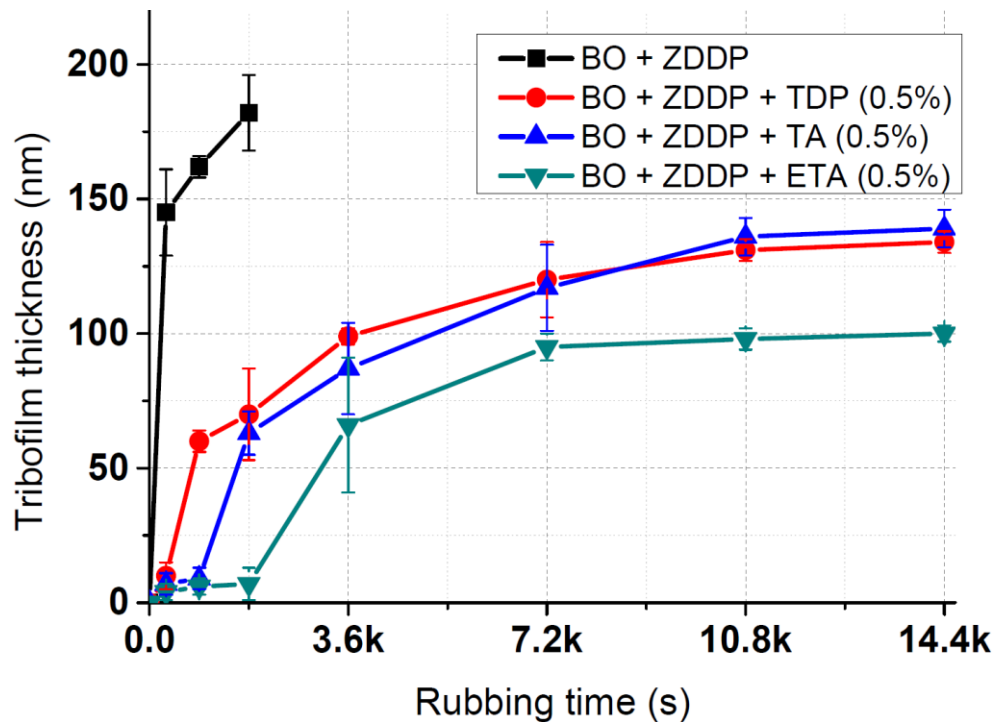


Figure 7-8. Tribofilm thickness from different lubricant formulations over rubbing intervals *Error bars in the plot represent the minimum and maximum tribofilm thickness detected on the MTM balls

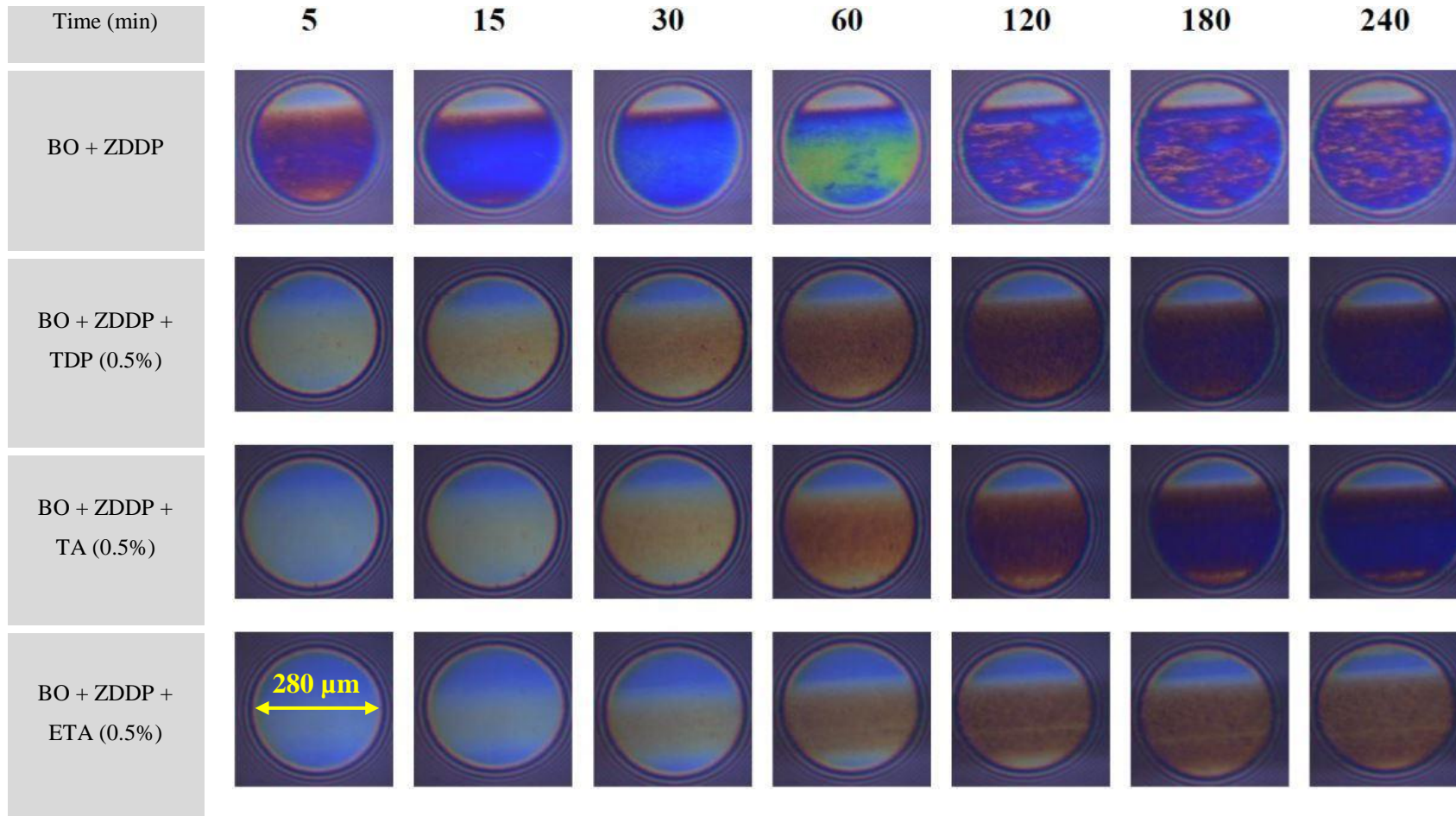


Figure 7-9. Tribofilm evolution in different lubricant formulations over 4-hours of rubbing. Experiments are conducted in conditions associated with SR configuration. The circular contact zones in the interference images are 280 μm in diameter as represented in the first image of BO + ZDDP + ETA (0.5%) lubricated ball surface

7.2.5 Friction results in SR configuration

The friction in the contact lubricated with different lubricant formulations over four-hours of rubbing at 100 mm/s entrainment speed is shown in Figure 7-10. The friction in BO + ZDDP and BO + ZDDP + TDP is stable and is 0.107 and 0.096, respectively within the last 30 minutes of the test. The average of friction within the last 30 minutes of the test is 0.088 and 0.102 in TA and ETA containing lubricants, respectively. Therefore, there is a 10%, 17% and 4% reduction in friction when TDP, TA and ETA is used in the lubricant formulation, respectively.

The friction reduction capability is significantly affected in SR configuration compared to that in SS configuration in contacts lubricated with ETA and TA. Although friction reduction capability of TA is greater than that of TDP and ETA, TDP has more stable friction in both configurations and less delaying effect on tribofilm formation.

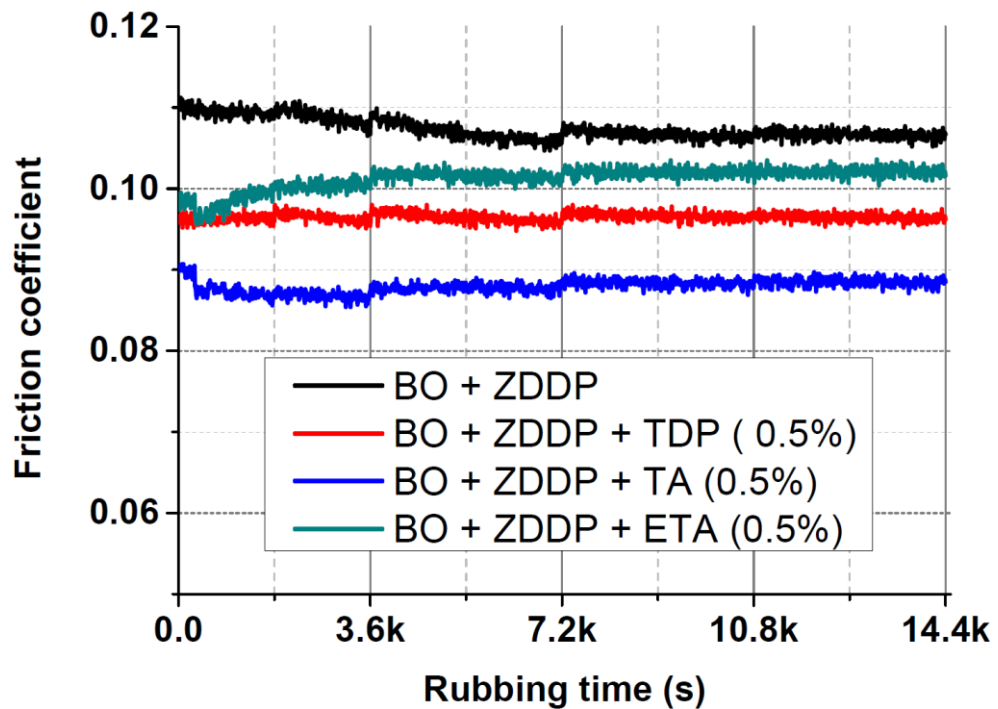


Figure 7-10. Friction coefficient in different lubricant formulations over 4 hours of rubbing

The Stribeck curves which are measured at the start and end of the tests are shown in Figure 7-11. The Stribeck friction in BO + ZDDP decreases in boundary and intermediate speed ranges (< 1 m/s) after four hours of rubbing which is opposite to SS configuration. This is due to the roughness effect. As mentioned in section 7.2.4, Stribeck measurement in SR configuration rapidly generates 65 nanometres of initial

ZDDP-tribofilm. The initial ZDDP-tribofilm is shown to be extensively patchy (105) and further rubbing can alleviate the patchiness resulting in a gentle friction reduction. Whilst in ETA an opposite trend is observed and Stribeck friction is greater after 4 hours of rubbing. The Stribeck friction in TDP and TA is stable and is not considerably affected by rubbing in the boundary and intermediate speed ranges. Also, the friction-enhancing behaviour of the ZDDP-tribofilm, which appears at speed of approximately 50 mm/s, is postponed to higher value of approximately 100 mm/s when TDP and TA are in the lubricant formulations.

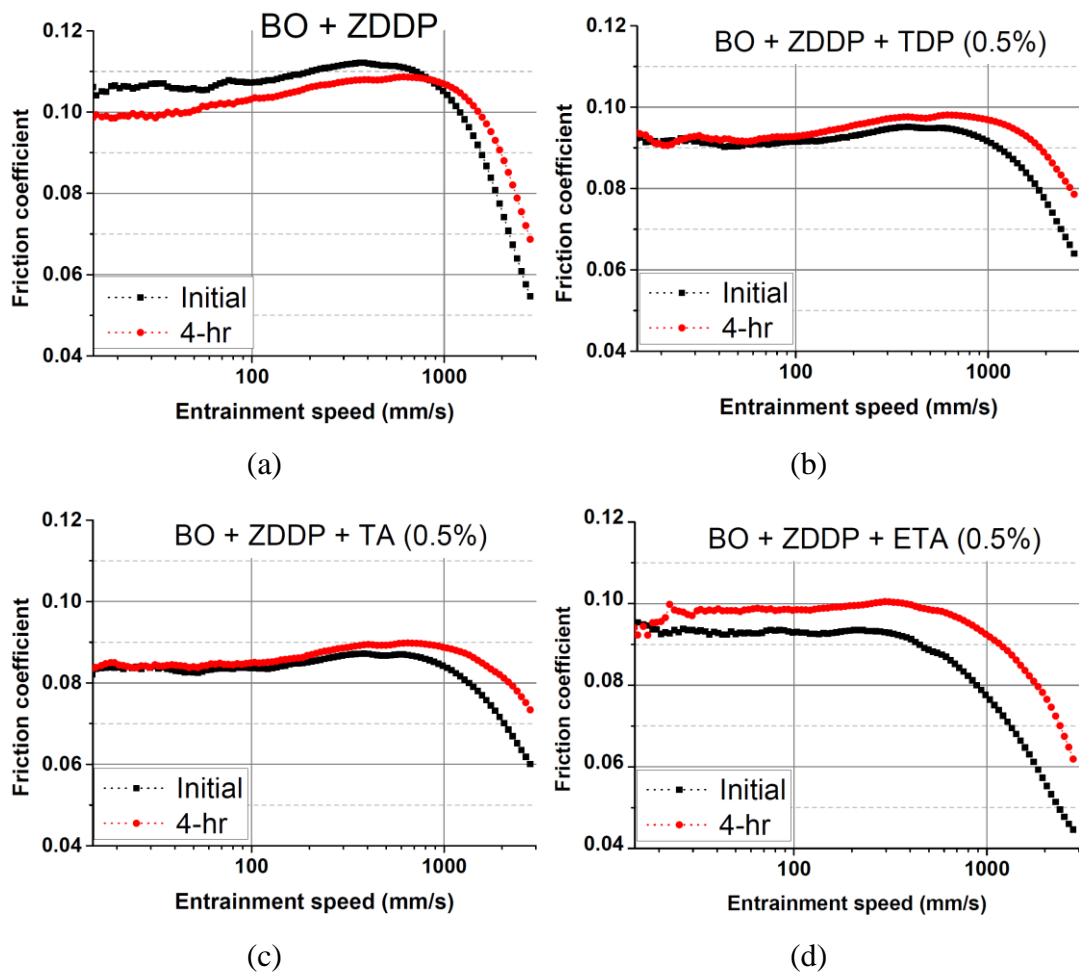


Figure 7-11. Stribeck diagrams measured at the start of the tests and after 4 hours of rubbing for a) BO + ZDDP, b) BO + ZDDP + TDP (0.5%), c) BO + ZDDP + TA (0.5%) and d) BO + ZDDP + ETA (0.5%) lubricant formulations

7.2.6 Surface topography and wear in SR configuration

Attempts have been made to measure the wear that has occurred on the contact surfaces of the discs at different magnifications using different objectives and field-of-view lenses in Vertical Scanning Interferometry (VSI) and VXI (combined VSI

and Phase Shifting Interferometry (PSI) in order to achieve higher lateral resolution) modes. However, high roughness of the discs, which was far larger than the wear depth on the discs, made the attempts unsuccessful to measure the wear. The WLI profiles are scanned from inside and outside of the wear-scar from ETA-containing lubricant which are shown in Figure 7-12. As can be seen, the profiles are almost identical and there is no discernible wear scar on the surface. The line profiles across the black-dashed line in the WLI images suggest a very gentle polishing wear on the asperities in some parts of the wear scar. Therefore, wear cannot be measured precisely on the discs and is not stated in this project to avoid reporting ambiguous results.

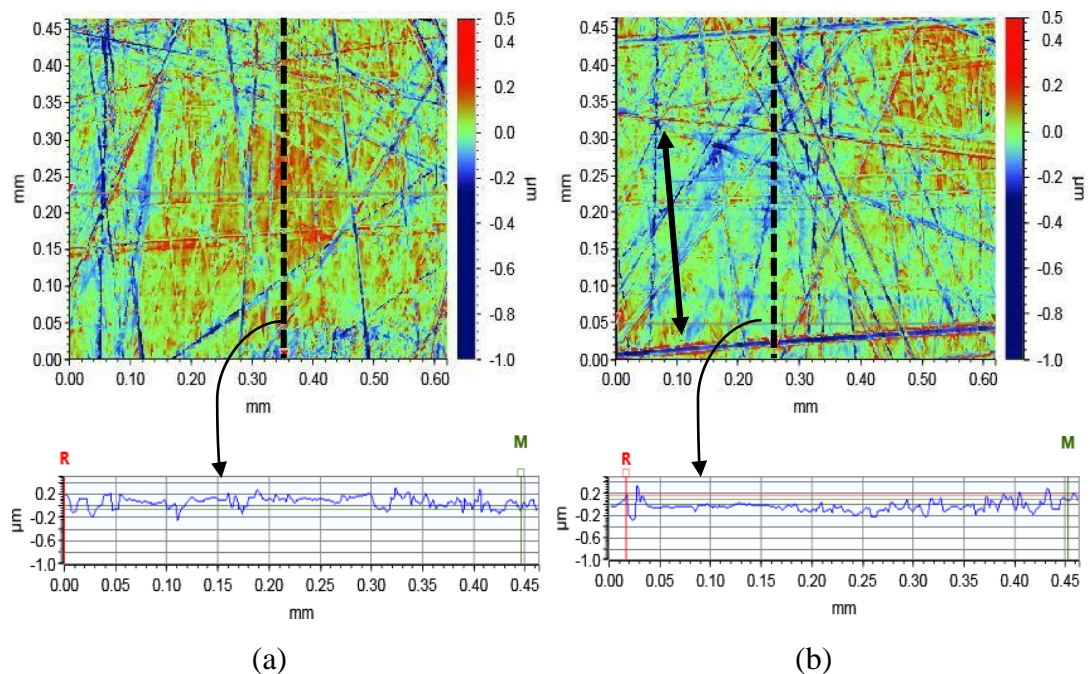


Figure 7-12. WLI-profiles taken from a) outside and b) inside the wear-scar collected from the disc lubricated with BO + ZDDP + ETA (0.5%)

Since the material loss on the disc surfaces is too small and undetectable, the balls have been considered and inspected using WLI. Ethylene-diamine-tetra-acetic acid has been used to remove the tribofilms from the wear-scars on the balls. The wear-scars on the ball surfaces of BO + ZDDP and BO + ZDDP + ETA (0.5%) are shown in Figure 7-13. Following successful removal of the tribofilms, wear-scars are not noticeable on the ball surfaces indicating negligible wear on the ball's surfaces.

Figure 7-13 (c) shows the camera image corresponding to Figure 7-13 (b) which shows that tribofilm is not utterly cleaned out of the wear scar generating dark appearance which results in spikes in WLI images. This shows that careful tribofilm

removal is essential in order to measure the wear in the super-smooth surfaces (ball) in MTM where wear is negligible. Therefore, negligible wear, which is under the measurement resolution, occurs on the MTM ball surfaces in the current experimental set-up. This is due to the thick tribofilm formation on the surfaces, low SRR and the hardness of the specimens. In MTM, ball samples are harder than discs. In general, a harder and rougher counter-body induces higher wear on the softer body. Therefore, balls with higher hardness have the potential to withstand the wear and induce wear on the discs. However, since balls are super-smooth very gentle wear happens on both contact bodies.

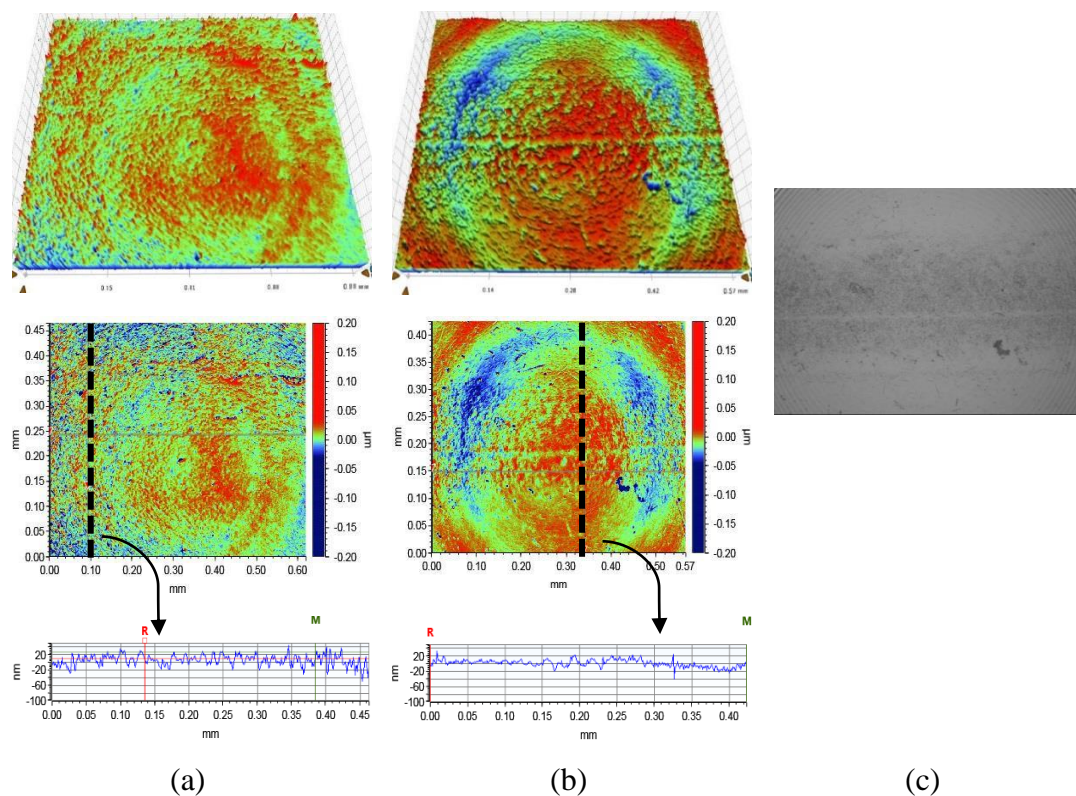


Figure 7-13. The ball-surface images after tests lubricated with a) BO + ZDDP and b,c) BO + ZDDP + ETA

7.2.7 Tribochemistry of the tribofilm formation

In this section the composition of the tribofilms generated from the lubricants containing NCAs in SR configuration is investigated using XPS. The tribofilms in SR configuration are considerably thicker compared to SS configuration and entirely cover the wear scar. Therefore, XPS analysis in SR is more suitable. The ball specimens are investigated since the high roughness of the disc specimens leads to a high scatter of the photoelectrons which results in obtaining poor signals. The HR spectra of the tribofilm elements in BO + ZDDP and BO + ZDDP + TDP (0.5%) are

compared in Figure 7-14. The detailed results from fitted spectra are listed in Table 2 and Table 3.

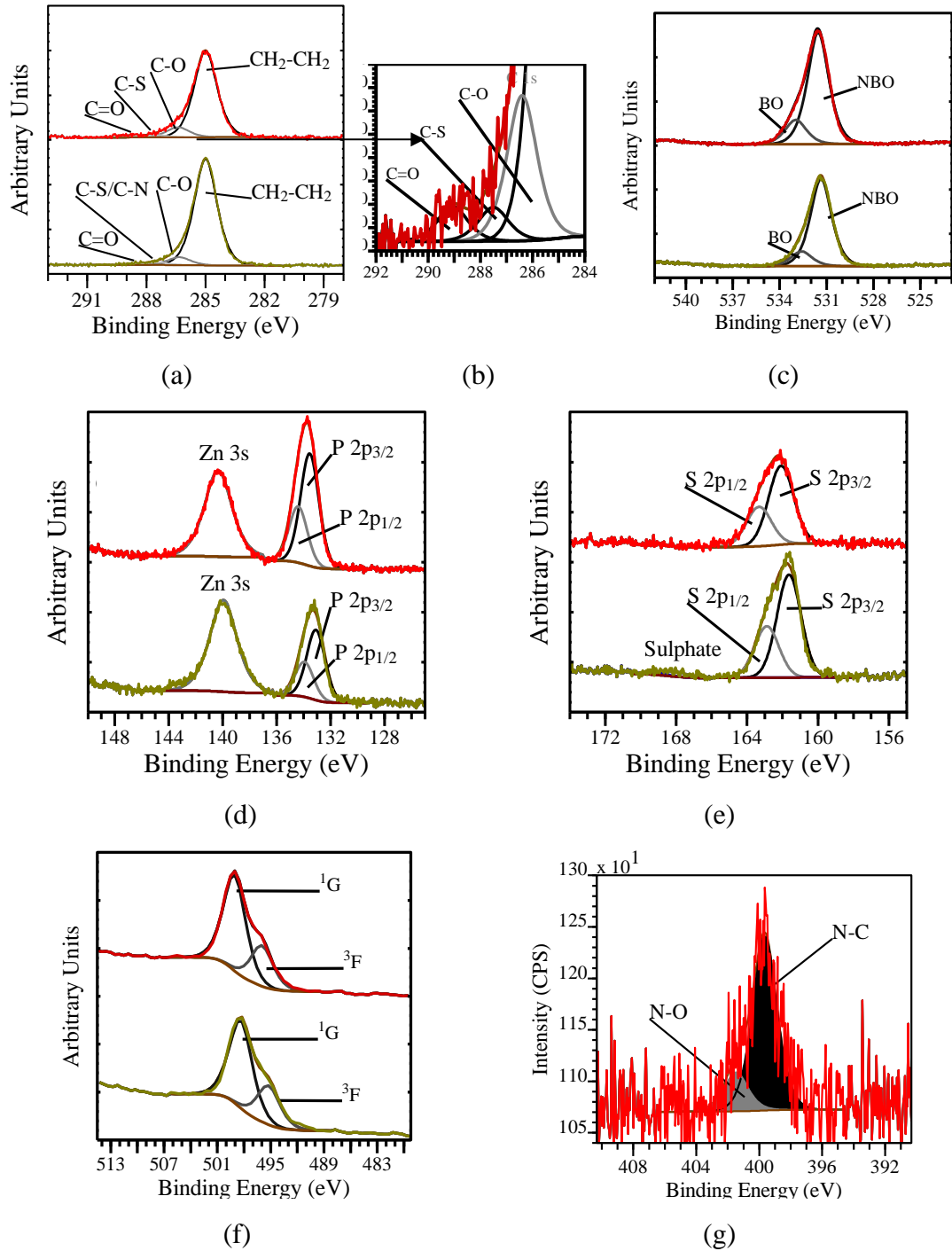


Figure 7-14. Detailed XPS spectra showing a) C 1s, b) three minor contributions to the C signal c) O 1s, d) P 2p and Zn 3s, e) S 2p, f) Zn L₃M_{4,5}M_{4,5} and g) N 1s signals. The spectra collected from MTM balls in SR configuration lubricated with BO + ZDDP (top-plotted in red) and BO + ZDDP + TDP (0.5%) (bottom-plotted in green) lubricant formulations. N 1s signal appeared in the spectrum from BO + ZDDP + TDP (0.5%)

The C 1s spectra in the MTM balls are resolved to four signals. The signals at $288.8\text{-}289.0 \pm 0.1$ eV are partly decayed in the spectra of NCAs containing-lubricants (Figure 7-14 and Table 7-1). These signals are assigned to C=O (carbonate and/or carboxylic) which can be an indication of oil oxidation. The C-O bond in the spectra of ETA is enhanced which is an indication of adsorbed ETA on the surface. However, the increase cannot be assigned explicitly to the adsorbed ETA, since it is not possible to distinguish between the C-O bond in ETA and C-O bond in base oil or phosphate chain.

The O 1s signal consists of two peaks in all tribofilms and no metal oxide peak has been found at $529\text{-}530.7$ eV. Fe also was not detected in the spectra from all tribofilms. The absence of Fe and iron oxide peaks is due to the thick tribofilms which have covered all the analysed areas. The most intense peaks at $531.4\text{-}5 \pm 0.1$ eV are assigned to NBO from phosphate chain (-P=O and P-O-Zn), carbonates and hydroxides in all tribofilms and nitrates in the tribofilms from NCAs-containing lubricants (192). This peak in the tribofilms from NCAs + ZDDP can be also attributed to ammonium phosphate (177-178) or/and Amine Phosphates (AP) (221). The peak at 533.0 ± 0.1 eV (BO + ZDDP) and $532.6 - 8 \pm 0.1$ eV (NCAs + ZDDP) corresponds to BO from phosphate chain (P-O-P).

Figure 7-14 shows the contribution of N and sulphate to the tribofilm from TDP-containing lubricant. Also, a decrease in P contribution and BO peak area is visible. Furthermore, a decrease in the P $2p_{3/2}$ BE of the tribofilms from NCAs + ZDDP can be observed in Table 7-1. A decrease in P $2p_{3/2}$ (Table 7-1) and BO/NBO ratio (Table 7-2) and an increase in modified Auger parameter, Zn/P and O/P ratios (Table 7-2) and Zn $3s\text{-P } 2p_{3/2} \Delta\text{BE}$ (Table 7-1) in the tribofilms from NCA-containing lubricants suggest a decrease in the phosphate chain length as a result of NCAs. However, the P $2p_{3/2}$ ($133.1\text{-}5 \pm 0.1$ eV) values in the lubricants indicate that the tribofilms are not expected to consist of long (poly)phosphate chains, since P $2p_{3/2}$ in the pure long chain zinc polyphosphate appears at $134\text{-}135$ eV (202-205). Considering the BO/NBO ratios (0.14 - 0.22), the phosphate contribution to the tribofilms is expected to be a mix of ortho, pyro and tripoly-phosphates for all the tribofilms (122). Also, the shift in the P $2p_{3/2}$ binding energies of tribofilms from NCAs + ZDDP are considerably higher than the increase in Zn $3s\text{-P } 2p_{3/2} \Delta\text{BE}$ of the tribofilms. Therefore, a decrease in P $2p_{3/2}$ BE of tribofilms from NCAs + ZDDP is

probably due to the (di/etho) AP formation which leads to an increase in partial positive charge on the P atoms of (di/etho) AP.

Table 7-1. Binding energy values of the elements/compounds of the tribofilm.*
The values indicated in the parentheses present the contribution of the corresponding compounds to the tribofilms in atomic percentage

BO + ZDDP +		-	TDP (0.5%)	TA (0.5%)	ETA (0.5%)
C 1s	C-C	285.0	285.0	285.0	285.0
	C-O	286.4 (10.1%)*	286.3 (6.7%)	286.5 (5%)	286.3 (12.6%)
	C-S/C-N	287.5	287.5	287.5	287.5
	C=O	289.0 (2.4%)	288.8 (1%)	289.0 (2%)	288.9 (2%)
O 1s	BO	533.0	532.6	532.6	532.8
	NBO	531.5	531.4	531.5	531.4
	P 2p _{3/2}	133.5	133.1	133.2	133.1
	Zn 3s	140.3	140.0	140.1	140.0
	Zn 2p _{3/2}	1022.4	1022.0	1022.2	1022.1
	Zn L ₃ M _{4,5} M _{4,5} ¹ G	499.1	498.4	498.6	498.2
N 1s	N-H/ N-C/ AP	-	399.7 (1.8%)	399.8 (0.8%)	399.7 (1.1%)
	N-O / (R- NH ₃ ⁺)NH ₄ ⁺	-	401.5 (0.4%)	401.6 (0.1%)	402.0 (0.2%)
S 2p _{3/2}	Sulphide	162.1	161.6	161.8	161.7
	Sulphate	-	168.0 (0.4%)	-	168.5 (0.6%)
	Zn 3s - P 2p _{3/2} ΔBE	6.8	6.9	6.9	6.9

The S 2p spectra in all tribofilms have a signal in the oxidation state of -2 (SII) assigned to sulphides (195) as organic and metal sulphides (zinc sulphide here) and S

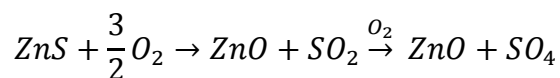
which is substituted for O in the phosphate chain forming (polythio)phosphate (O-P-O → O-P-S) (127). A contribution of sulphate generated from S in oxidation state of +6 (S_{VI}) was found in the tribofilms of TDP and ETA at 168.0 ± 1 eV and 168.5 ± 1 eV respectively (195). Sulphate is present on the top layer of the tribofilm and in the bulk of the tribofilm sulphide exists. The role of sulphate as an oxidised species is not thoroughly understood; however it is detected in thermally-decomposed ZDDP outside of the wear track and inside of the wear track of the boundary lubricated contact when water is present in the oil (148, 151). Sulphate is also identified in the wear scar of a surface lubricated with S-containing additive (222). A sulphate contribution to the ZDDP-tribofilm on the wear track has been seldom reported using XANES (143) and XPS (136).

Table 7-2. Parameters in the tribofilms and atomic concentration of the Zn, S, O, and N normalised to P

BO + ZDDP +		-	TDP (0.5%)	TA (0.5%)	ETA (0.5%)
BO/NBO		0.22	0.17	0.14	0.19
eV	α'	2009.9	2010.2	2010.1	2010.5
Atomic concentration	Zn/P	0.9	1.7	1.4	1.8
	S _(II) /P	0.5	1.0	0.75	1.25
	O/P	2.0	2.4	2.2	2.4
	N/P	-	0.24	0.07	0.13

It has been suggested that the sulphate contribution to the tribofilms originates from oxidised sulphur species while it is exposed to the air (136, 223). The S (SII) to P atomic-concentration-ratio for different lubricants is shown in Table 7-2. It is clear that the sulphide contribution is enhanced over phosphate in tribofilms formed from NCAs + ZDDP lubricants. The S_(II)/P ratio increases along the series of additives ETA (1.25) > TDP (1) > TA (0.75). Also, the extent of sulphate contribution to the tribofilms comply with the S_(II)/P trend (Table 7-1). In addition, the higher ratio of Zn/P and S/P in the tribofilms from NCA-containing lubricants implies a greater zinc

sulphide formation. Therefore, it can be suggested that the sulphate in TDP and ETA is resulted from sulphide oxidation by air exposure as a result of the enhanced sulphide contribution to the tribofilms.



Due to the lack of specific standards and low signal to noise ratio, N 1s peak is difficult to interpret. However, two peaks are extracted from N 1s signals in all spectra. A peak can be resolved at $399.7\text{-}8 \pm 0.1$ eV that can be attributed to N-C/N-H bonds in NCAs, HN-P bond (224) and AP (225). This peak can be assigned to the adsorbed NCAs to the surface or residual compound(s) of ZDDP and NCA(s) interaction(s). The second peak in the tribofilms at $401.5 - 402.0 \pm 0.1$ eV can be assigned to ammonium and/or N-O bonds in ammonium phosphate (224) and/or nitrates (192). A contribution of ammonium phosphates (177-178) or/and APs (221) to the phosphate chain in tribofilms induced by lubricants containing ZDDP and dispersants has been reported using XANES and XPS (222). The AP is formed through reaction of the pyrolytically dissociated amine group and decomposed ZDDP (221). As mentioned the shifts in P 2p_{3/2} peak in P 2p signal and also BO peak in O 1s signal are further indications of amine/ammonium phosphate formation in the tribofilms of NCAs.

The concentration of the first peak of N 1s in the TDP tribofilm is approximately twice the concentration of the first peak in the TA tribofilm which results from molecular structure of TDP. TDP has two N atoms in each molecule, while TA has one N atom per molecule. This also implies that the N-C₃H₆-N bond is not broken during contact. However, the contribution of the second peak in TDP is greater compared to that in TA which implies that TDP has more potential to prompt an ammonium phosphate formation. ETA tribofilm has a higher contribution of N compared to TA indicating its higher affinity to adsorb on the surfaces. The higher adsorption results from hydroxyl group in ETA, bringing about a greater delaying effect on the tribofilm formation.

7.3 **Summary**

In this chapter comparison has been made on the friction and wear performance of NCAs as friction modifiers and their influence on the tribofilm composition and thickness using a MTM tribometer. Tests have been carried-out using two different

discs having different roughness values in order to understand the effect of contact severity.

From the results obtained in this study with the specified test conditions it is shown that:

- NCAs compete with the ZDDP molecules in adsorption on the surface causing a delay in the tribofilm formation. The delaying influence depends on the NCAs concentration in oil and structure of the polar moiety in NCAs and is in the following increasing order: $TDP < TA < ETA$.
- The tribofilm thickness depends on the contact severity (roughness effect) in all lubricants, the NCAs concentration in the oil and the nature of the functional group and thereby increases along the series of additives $TDP \geq TA \gg ETA$.
- All NCAs have a beneficial friction-reduction influence on the friction-enhancing behaviour of ZDDP in the boundary and intermediate speed ranges which depends on the concentration of NCAs in the oil. However, the severity of contact has a significant influence on the friction-reduction potential of NCAs. The effectiveness in the friction-reduction increases in the following order: $TDP < TA \leq ETA$ in SS configuration and $ETA < TDP \leq TA$ in SR configuration.
- There is no considerable difference in the wear performance of the lubricant formulations in the experimental set-up used in this chapter.
- All tribofilms consist of short-chain phosphates and sulphides derived from ZDDP additive.
- The NCAs decrease the contribution of the phosphate to the tribofilms and enhance sulphide contribution over phosphate in the tribofilms in the tests conditions used in this chapter.
- Adsorbed NCAs are detected on the tribofilm surfaces with a concentration depending on the chemical structure of the polar moiety and is in the following increasing order $ETA \gg TDP > TA$.
- Presence of NCAs in lubricant formulations generate (di)amine/ammonium phosphates on the tribofilm surfaces. The contribution of (di)amine/ammonium phosphate to the tribofilm compositions depends on the NCA chemical structure.

Chapter 8

Nitrogen-containing-additive as a friction modifier: the effect of NCAs on micropitting

8.1 Introduction

The micropitting-enhancing impact of ZDDP AW additive and the influence of water contamination on the micropitting performance are shown in Chapter 5 and Chapter 6. The influence of NCA on friction, wear and tribofilm formation is shown in Chapter 7 employing MTM-SLIM. In the current chapter the impact of NCAs on micropitting surface fatigue where ZDDP is in the lubricant formulation is investigated using a modified-MPR. The tribochemical properties of the tribofilms derived from combination of NCAs and ZDDP are investigated employing XPS.

8.2 Results

8.2.1 Friction results

Figure 8-1 shows the friction results for the lubricants which contain NCAs in combination with ZDDP. Figure 8-1 a and b shows the friction throughout 10^6 contact cycles and the average of the last 30 minutes of the tests, respectively. As mentioned, the ETDP additive is barely soluble in PAO base-oil regardless of the presence of ZDDP and thus is not investigated in this chapter. All NCAs reduce the friction in the contact compared to BO + ZDDP formulation. The friction reduction capability of the additives, at the end of the test, increases along the series of additives $ETA (1\%) > TA (1\%)$ and $TDP (1\%) > TDP (0.5\%)$. This indicates that increasing the concentration of the TDP to 1% leads to an enhanced friction reduction which is in agreement with the MTM results presented in the previous chapter.

The friction at the start of the test is also an important parameter as seen in the Chapter 5. As can be seen in Figure 8-1 (a), the friction at the start of the test is lower for the higher concentration of TDP. While the friction results for TDP (1%) and TA (1%) are similar at the start of the tests and follow the same trend upon the end of the test, the friction in the ETA-containing lubricant is slightly higher than TDP and TA at the start of the test reaching a lower value at the end of the test. The friction within last 30 minutes of the tests (shown in Figure 8-1(b)) shows a 23%, 22% and 26% decline

in friction by adding 1% of TDP, TA and ETA additive to the BO + ZDDP lubricant, respectively. The lowest friction is observed for ETA (1%)-containing lubricant which is in agreement with MTM results in S-S configuration (Chapter 7). However, the friction results for TDP and TA appear to be approximately the same in the micropitting test set-up, while in the MTM test set-up TA exhibited a slightly lower friction compared to TDP.

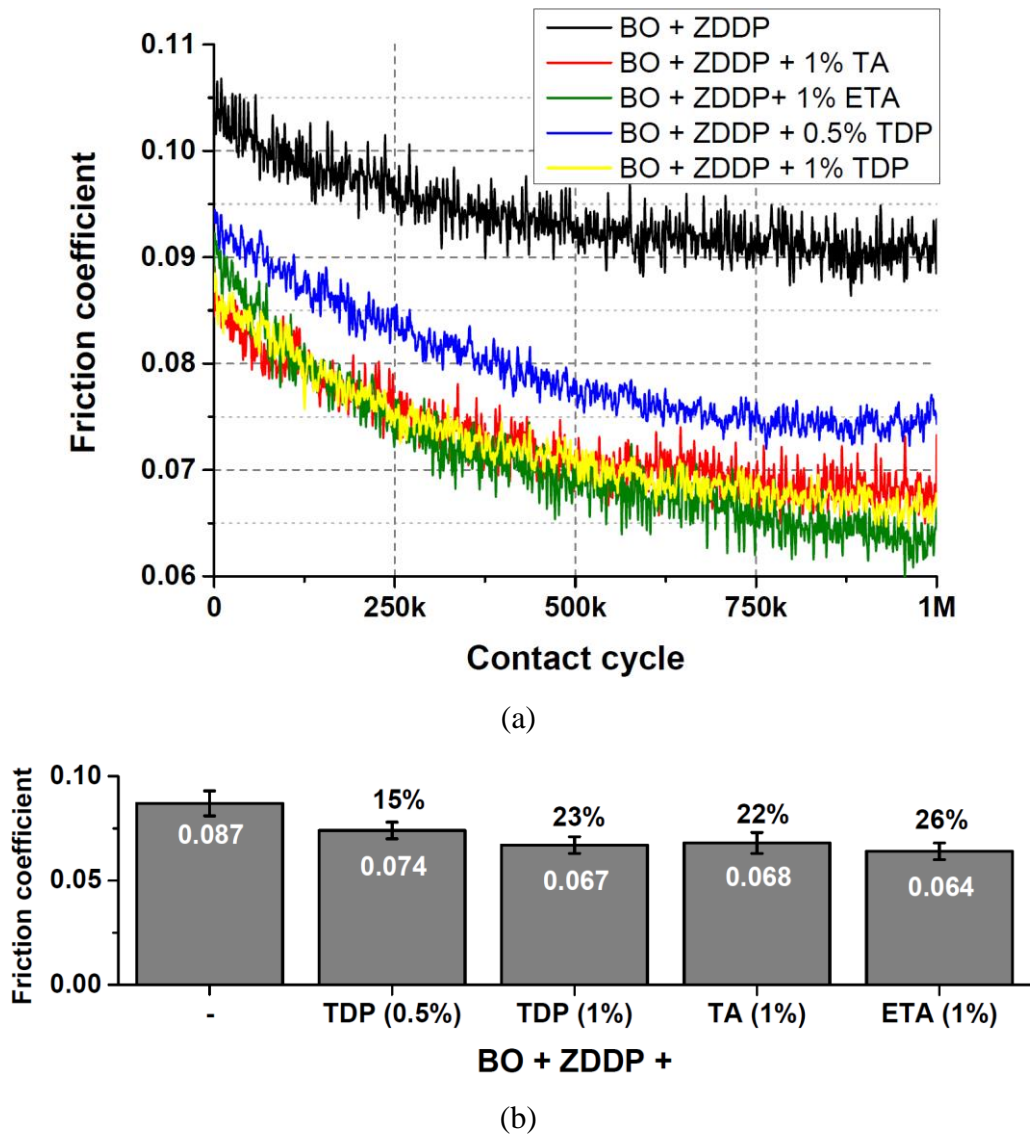


Figure 8-1. Friction coefficient results for different lubricant formulations presented a) over the test duration and b) as average friction values within the last 30 minutes of the tests

8.2.2 Micropitting and wear results

In order to inspect the wear scars corresponding to different lubricant formulations, WLI profiles and optical microscope images are obtained from roller surfaces and shown in Figure 8-2 and Figure 8-3. It can be seen that addition of NCAs mitigates

micropitting surface fatigue in the wear scars to a different extent depending on the additive used. A smaller extent of micropitting surface fatigue can be observed by increasing the TDP concentration to 1%. This indicates that increased concentration (to 1%) assists in reducing micropitting. The micropits in NCA-containing lubricants are spread separately in the wear scars and clearly show a sign of attenuated propagation.

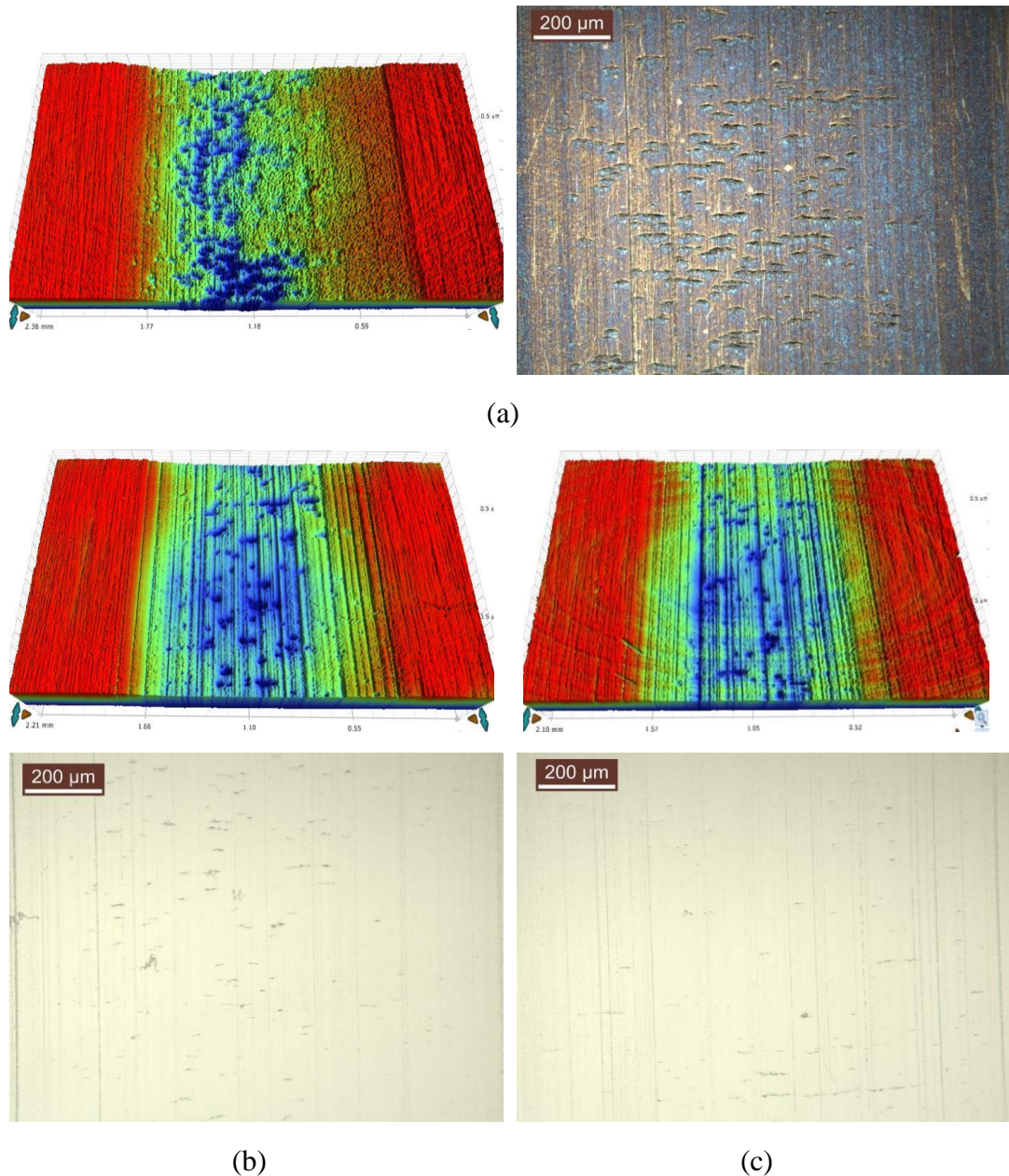


Figure 8-2. WLI and optical microscope images of the roller surfaces lubricated with a) BO + ZDDP, b) BO + ZDDP + TDP (0.5%) and c) BO + ZDDP + TDP (1%) lubricant formulations

The wear scar profiles of TDP and TA suggest shallow wear scars, while a considerable depression in the wear scar of ETA can be observed. In order to quantitatively examine the wear scars, cross-sectional depth profiles of the wear scars are shown in Figure 8-4 and Figure 8-5, across the black dashed-line in the corresponding WLI images. Also, micropitting maps from the wear scars are generated using MR analysis and presented in Figure 8-4 and Figure 8-5.

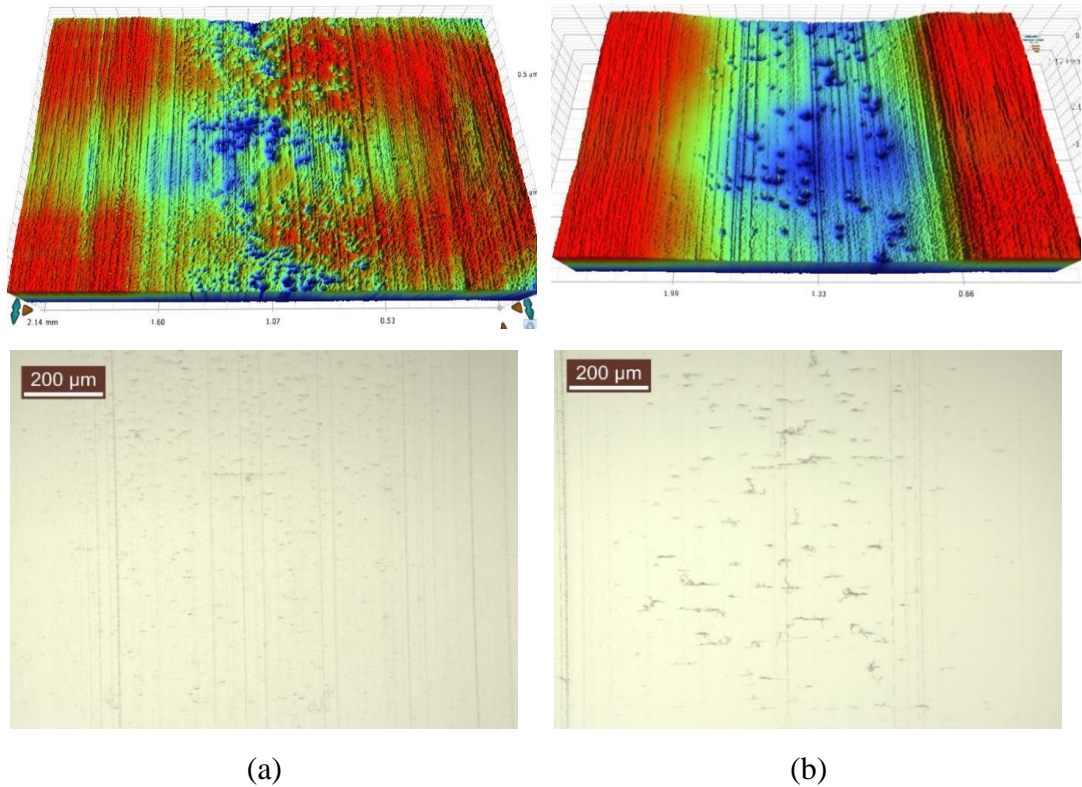


Figure 8-3. WLI and optical microscopic images of the roller surfaces lubricated with a) BO + ZDDP + TA (1%) and b) BO + ZDDP + ETA (1%) lubricant formulations

The cross-sectional area of the corresponding wear scar depth profile is presented which is an indication of the total material loss in the wear scar. As can be seen in Figure 8-4 and Figure 8-5, cross-sectional depth profiles of TDP (0.5% and 1%) and TA (1%) are considerably shallower than that of BO + ZDDP and BO + ZDDP + ETA(1%). In general, a considerable extent of the material loss in BO + ZDDP is induced by large and deeply propagated micropits on the surface, while the material loss in NCA-containing lubricants mostly produced by mild-wear and separately distributed shallow and small micropits. The wear depth-profile of ETA is a U-shaped profile similar to what is observed in BO lubricated wear scars (Figure 5-2). The wear scar is consistently deep across the wear-scar width showing a large depression together with small and shallow micropits.

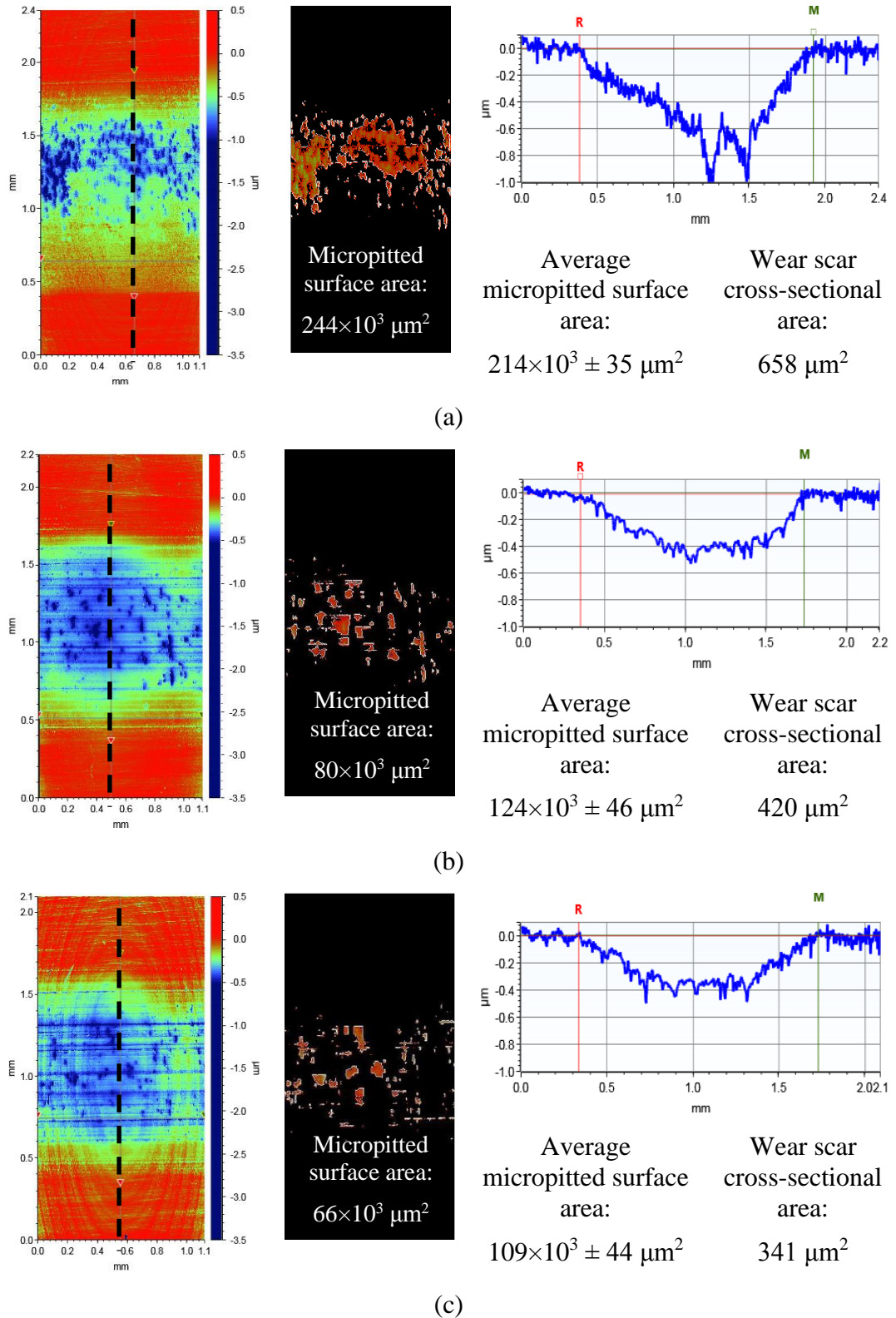


Figure 8-4. WLI images, micropitting surface area and wear scar cross-sectional depth profile of the wear scars on the roller surfaces lubricated with a) BO + ZDDP, b) BO + ZDDP + TDP (0.5%) and c) BO + ZDDP + TDP (1%) lubricant formulations

The U-shaped profile is an indication of large gradual wear on the roller surface as it is clear through comparing the cross-sectional areas of the wear scars in the different

lubricants. The micropitting surface area is decreased by approximately 50%, 40% and 34% in TDP (1%), TA (1%) and ETA (1%) containing lubricants, respectively.

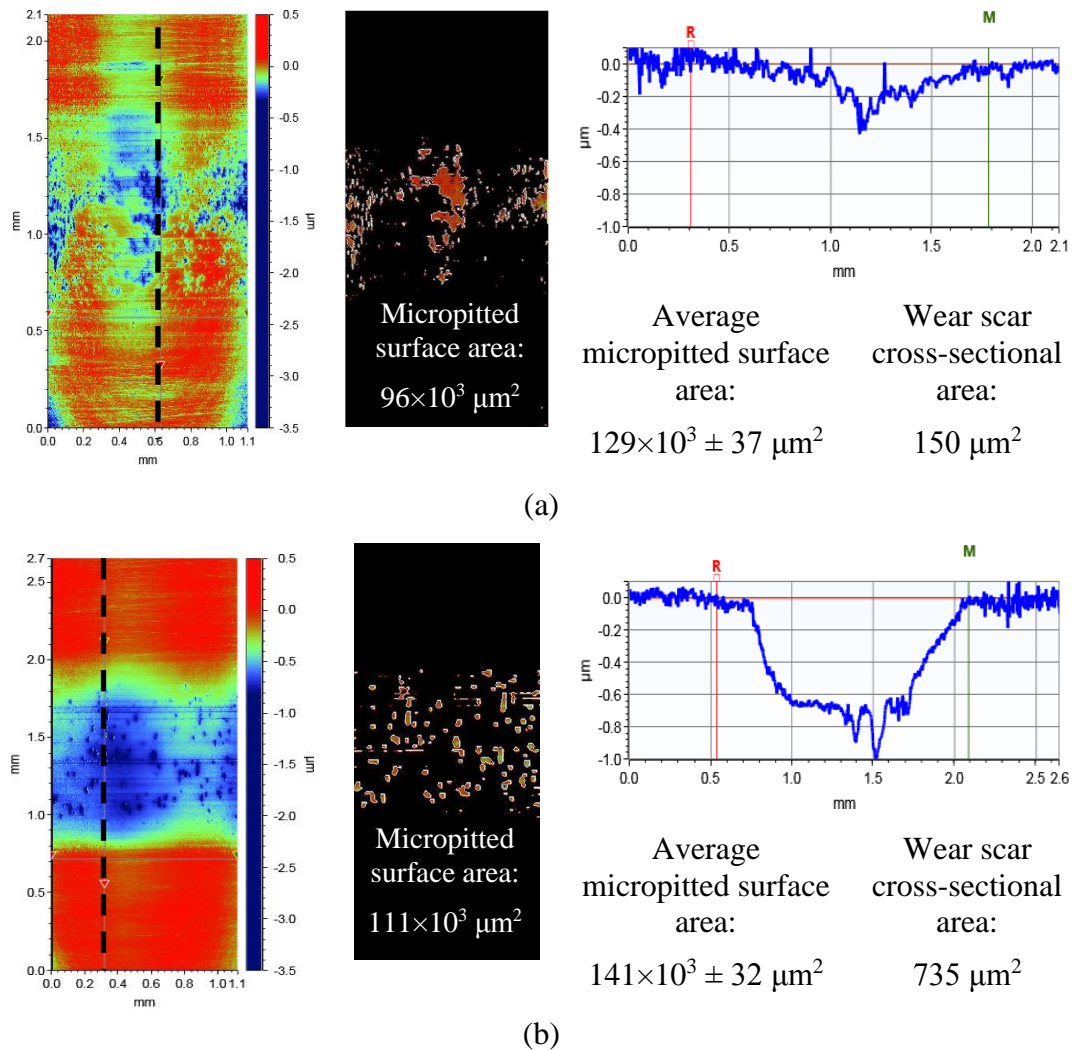


Figure 8-5. WLI images, micropitting surface area and wear scar cross-sectional depth profile of the wear scars on the roller surfaces lubricated with a) BO + ZDDP + TA (1%) and b) BO + ZDDP + ETA (1%) lubricant formulations

The wear volume on the roller surfaces is measured and presented in Figure 8-6. It is interesting to see that the addition of TA and TDP to BO + ZDDP reduces the total wear volume and alleviates the micropitting surface fatigue simultaneously, compared to BO + ZDDP. On the other hand, the addition of ETA to the BO + ZDDP increases the total wear volume by 40%, although it is effective in micropitting reduction. The wear volume of ETA is considerably less than that of BO ($\sim 175 \times 10^{-3} \text{ mm}^3$) which shows that ETA + ZDDP generates a protective reaction layer on the surface protecting the roller from wear, although its wear performance is not as effective as that of the ZDDP-tribofilm. The total wear volume is reduced approximately by 13%

and 22% by addition of TDP and TA to the BO + ZDDP lubricant, respectively. The efficiency of TDP in suppressing micropitting is slightly greater than that of TA in the experimental set-up used in this study.

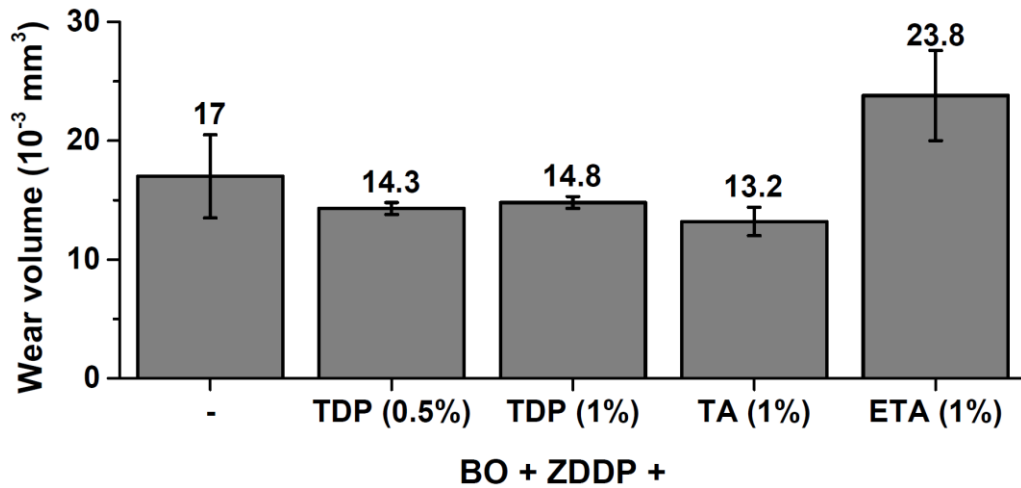


Figure 8-6. Total wear-volume on the roller surfaces lubricated with different lubricant formulations

8.2.3 Understanding the mechanism by which NCAs influence micropitting

In order to understand the mechanism by which the addition of TDP and TA to BO + ZDDP lubricant reduces the micropitting and protects the surface from wear a series of tests have been carried out using MTM and modified-MPR. Subsequently, wear scars and tribofilms are investigated using WLI, AFM, TEM-EDX, SEM and XPS. The TDP is considered as the representative additive.

8.2.3.1 Micropitting performance of BO + TDP lubricants

TDP is added to PAO base-oil where ZDDP is absent in the lubricant formulation in order to understand the behaviour of TDP as an additive when ZDDP and TDP interactions are excluded in the bulk lubricant. Therefore, the wear scars are induced through interaction of TDP with the steel surface. TDP is blended to the lubricant in two different concentrations (0.5% and 1%) and the roller surfaces are inspected after 10^6 contact cycles. The WLI images of the wear scars are shown in Figure 8-7. An interesting profile is observed for BO+TDP lubricant formulation. At the middle of the wear track (approximately a third to a half of the wear-scar width) almost no wear occurred, while two deep depressions can be observed at the edges of the wear scar. The depressions are 0.2-2 μm in depth. This wear-scar profile can be called W-shaped or double-deep wear scar geometry.

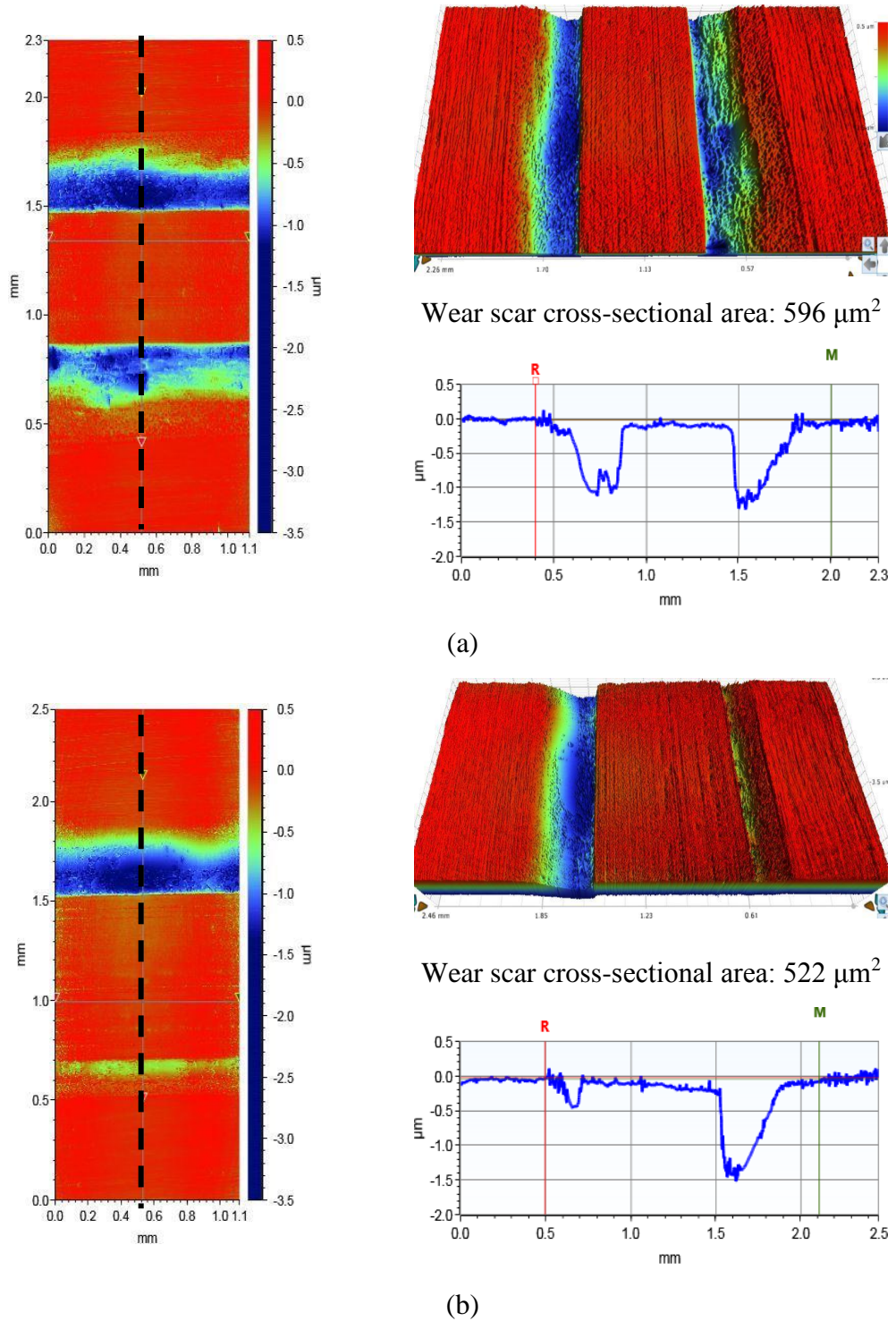


Figure 8-7. Wear scar WLI profiles of the rollers lubricated with a) BO + TDP (0.5%) and b) BO + TDP (1%)

The average wear depth at the edges and total wear volume on the rollers are decreased by increasing the TDP concentration to 1%. The total wear volume in BO + TDP wear track is substantially less than wear of BO lubricated surfaces (approximately 85-90% reduction in the total wear volume compared to BO lubricated surfaces) and is comparable to wear of BO + ZDDP lubricated surfaces. In fact the total wear volume

of BO + TDP (1%) is less than that of BO + ZDDP. This is an interesting observation and indicates that TDP performs as an AW additive in the current experimental set-up. In addition, no micropitting can be observed in the wear scars of BO + TDP and the material loss is produced by mild-wear on the wear-scar edges as can be seen in Figure 8-7 and Figure 8-8.

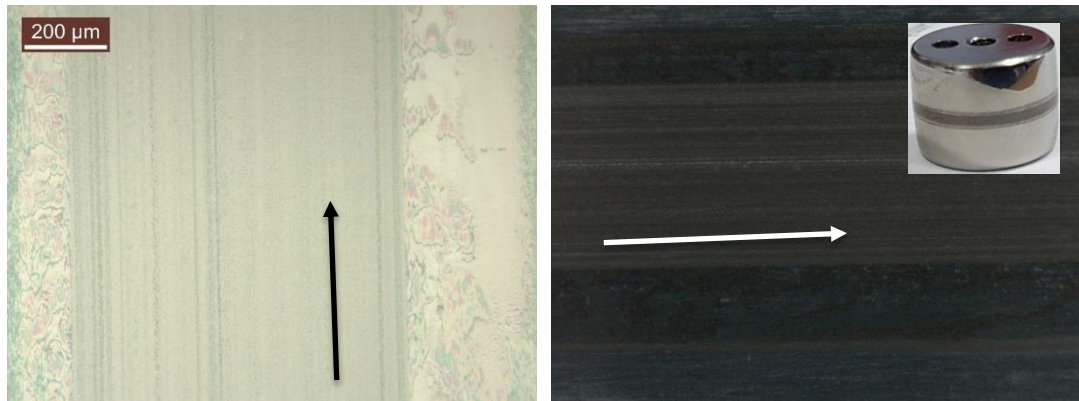


Figure 8-8. Optical microscopic images of the wear scar lubricated with BO + TDP (1%) * Arrows show the rolling-sliding direction on the surface

As shown in Figure 8-8 the middle of the wear scar, where almost no wear occurs, is turned to a brown-black appearance which is an indication of an oxidised and/or nitrated surface. The friction throughout the contact is shown in Figure 8-9. Interestingly the friction at the end of the test reaches a value similar to friction in BO-lubricated surface. There is a sharp drop in friction within the first 200K contact cycles which implies that most probably the wear on the wear-scar edges happened during early-stage of the test.

The friction reached a steady-state after 250K contact cycles. The more important phenomenon is that the intense rise in the friction from 0.11 to almost 0.2, which is observed for the BO during 5K contact cycles corresponding to large wear, disappeared in the wear scar from the TDP-containing lubricant. This indicates that TDP protects the surface at the early stage of the test and performs as an AW additive. The low friction in the contact might result from three factors. Firstly, TDP adsorbs to the surface and acts as an interfacial and low viscous layer. Secondly, the oxidised/nitrated surface of the roller enhances the wear resistance by reducing adhesive wear and finally two depressions at the wear scar edges keep the oil inside and act as a surface texturing. The depression at the wear-track-edge increases the oil

film thickness and feeds the middle of contact (non-worn area) through capillary action.

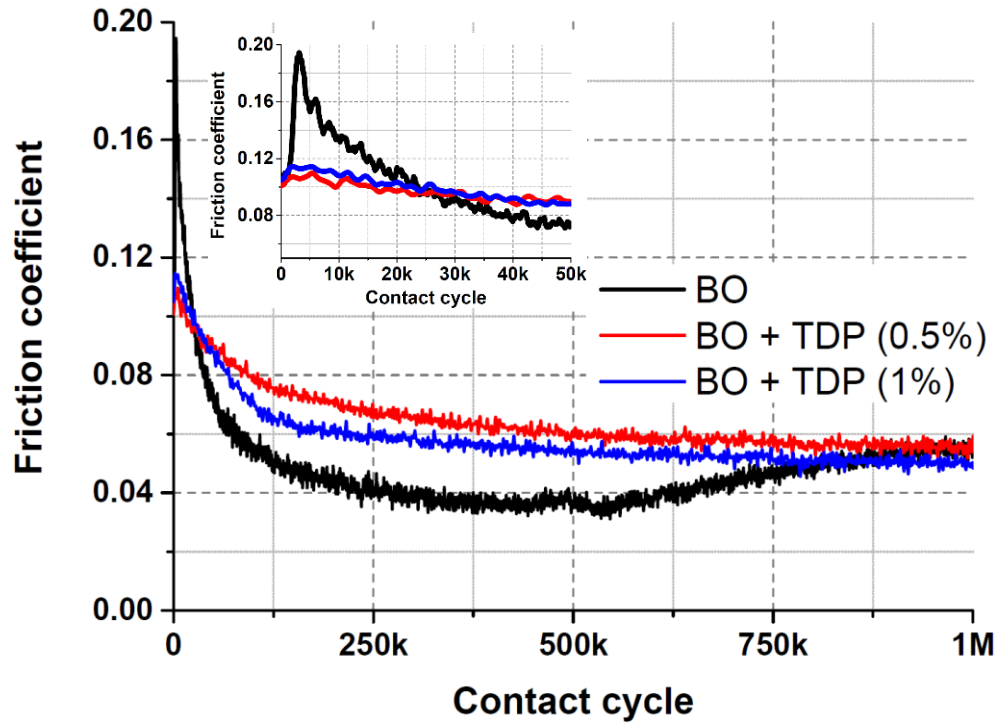


Figure 8-9. Friction coefficient results for BO + TDP lubricant formulation

Prior to this, the W-shaped wear scar is not reported in the published literature and the rationale behind it may not be conclusively evident. The most probable interpretation for W-shaped appearance in the current experimental set-up is the reactivity and interaction of the additive at high applied pressures. In other words, the TDP interaction with the steel surfaces and its subsequent AW performance depends on the applied contact pressure and is triggered under high contact pressure. Interestingly, the width of the zone in the middle of the wear track, where almost no wear occurs, is approximately 550 μm -850 μm which is close to the value of semi-major axis of the contact ellipse (550 μm). TDP molecules adsorb on to the surfaces and react with the surfaces where the maximum contact pressure exists. Therefore, the AW performance of TDP is decayed at the wear scar edges where the contact pressure is noticeably lower than that in centre due to the particular geometry of the roller.

8.2.3.2 Topographical analysis of the tribofilms

AFM was used in order to study the topographical effect of TDP on the AW tribofilm formed on the MTM disc surfaces. MTM discs are smooth and meteorologically homogenous (roughness, waviness and skewness). Also, the wear on smooth discs in the conditions used in this project is inconsiderable. On the other hand, the MPR

rollers undergo severe wear and have micropits in the wear scar which makes AFM measurements difficult. Therefore, the MTM disc is suitable to study the tribofilm morphology. Figure 8-10 and Figure 8-11 show representative AFM images of $20 \times 20 \mu\text{m}^2$ area of the tribofilm. The line profile below each image corresponds to the height profile (in Z direction) of each AFM image at the horizontal-centre of the image.

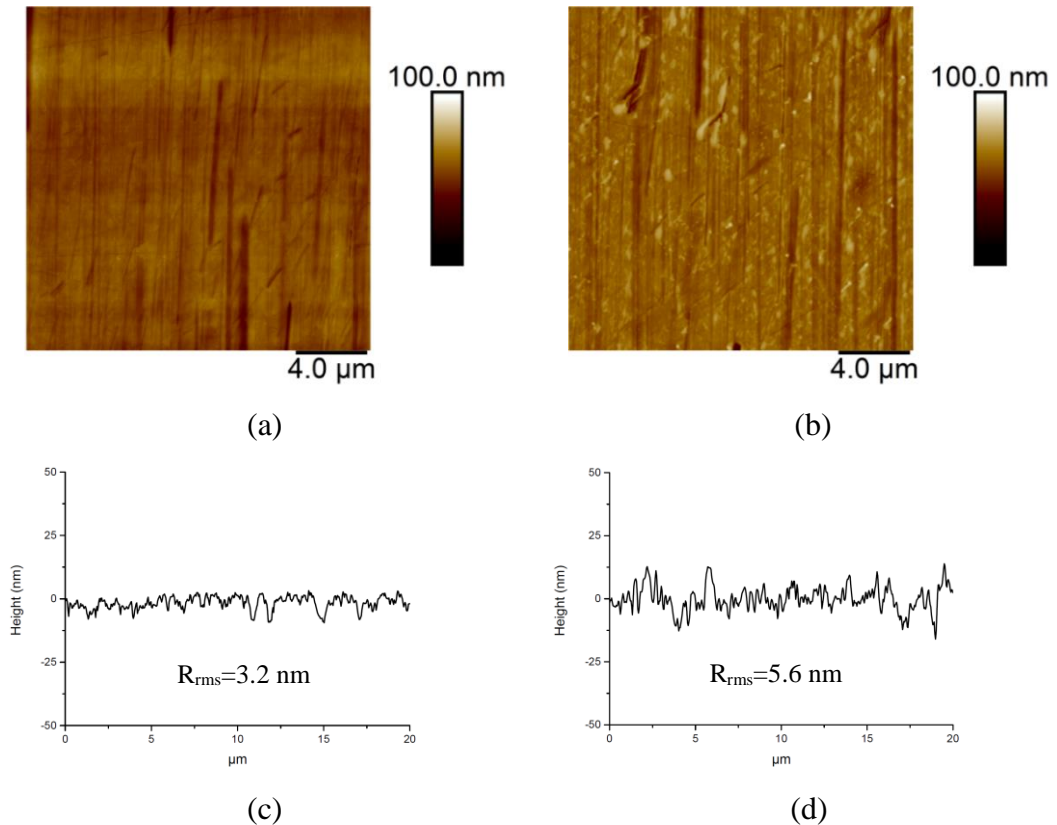


Figure 8-10. AFM images and height profiles of the tribofilms induced after 15 minutes of rubbing in a &c) BO + ZDDP + TDP (0.5%) and b &d) BO + ZDDP lubricants. The height profiles obtained across the centre of the AFM images provided in (a) and (b)

The root mean square roughness (R_{rms}) of the tribofilm across the line profile is included in the figures. The roughness value (S_q) of the tribofilm induced by BO + ZDDP is 5.1 nm and 23.3 nm after 15 minutes and 2 hours of rubbing respectively. Furthermore, the roughness value of the tribofilm induced by BO + ZDDP + TDP (0.5%) is 3.9 nm and 12.5 nm after 15 minutes and 2 hours of rubbing respectively. Accordingly, a smoother tribofilm formation can be observed when TDP is present in the lubricant formulation. Figure 8-12 presents the representative AFM images of $5 \times 5 \mu\text{m}^2$ area of the generated tribofilms after two hours of rubbing. Figure 8-12 (b) exhibits the patchy and uneven nature of the

ZDDP-derived tribofilm. A patchy structure of the ZDDP-tribofilm is well-established in the literature (105). In contrast to the tribofilm generated using BO + ZDDP, the tribofilm formed on the surface lubricated with BO + ZDDP + TDP (0.5%) appears to be smooth.

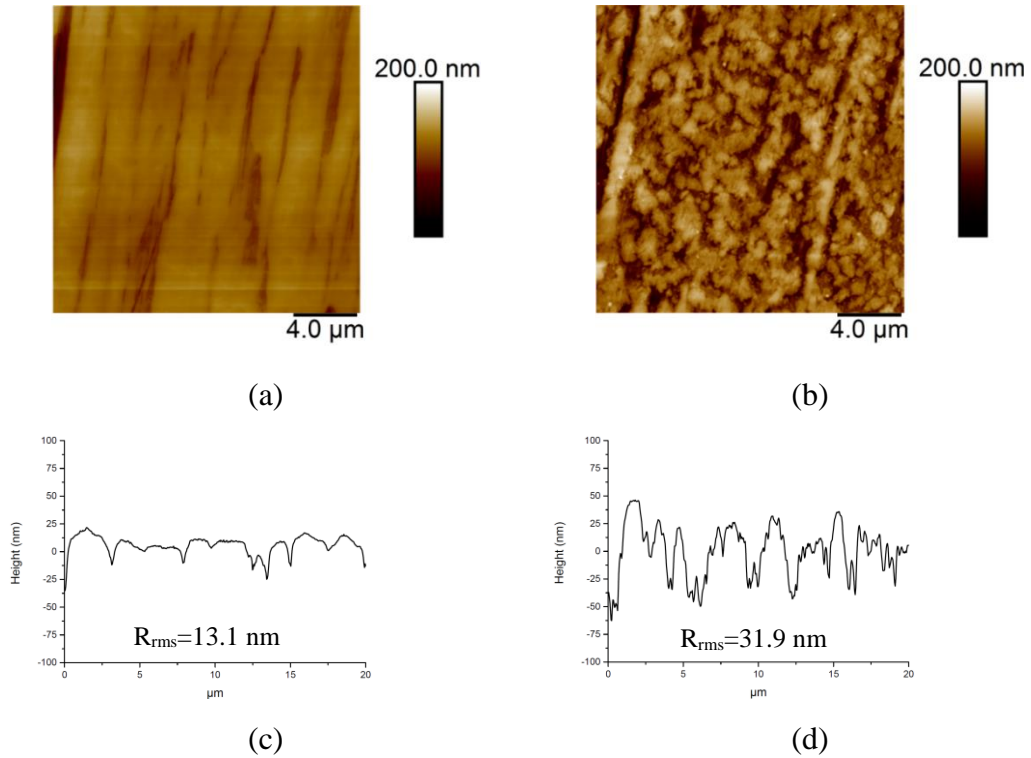


Figure 8-11. AFM images and height profiles of the tribofilms induced after 2 hours of rubbing in a &c) BO +ZDDP + TDP(0.5%) and b &d) BO + ZDDP lubricants. The height profiles obtained across the centre of the AFM images provided in (a) and (b)

Also, as shown in Figure 8-12, the tribofilm from BO + ZDDP + TDP (0.5%) seems to consist of evenly distributed pads along the sliding-rolling direction.

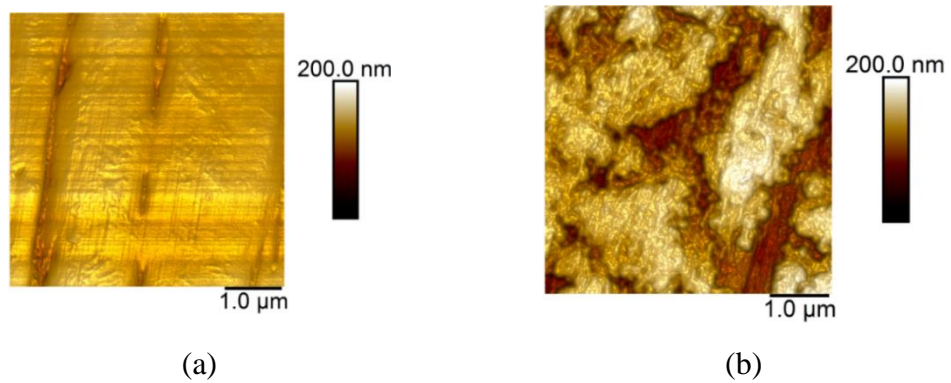


Figure 8-12. AFM images of the tribofilm induced after 2 hours of rubbing in a) BO +ZDDP + TDP(0.5%) and b) BO + ZDDP lubricants

8.2.3.3 The effect of TDP on a generated ZDDP-tribofilm: removal effect

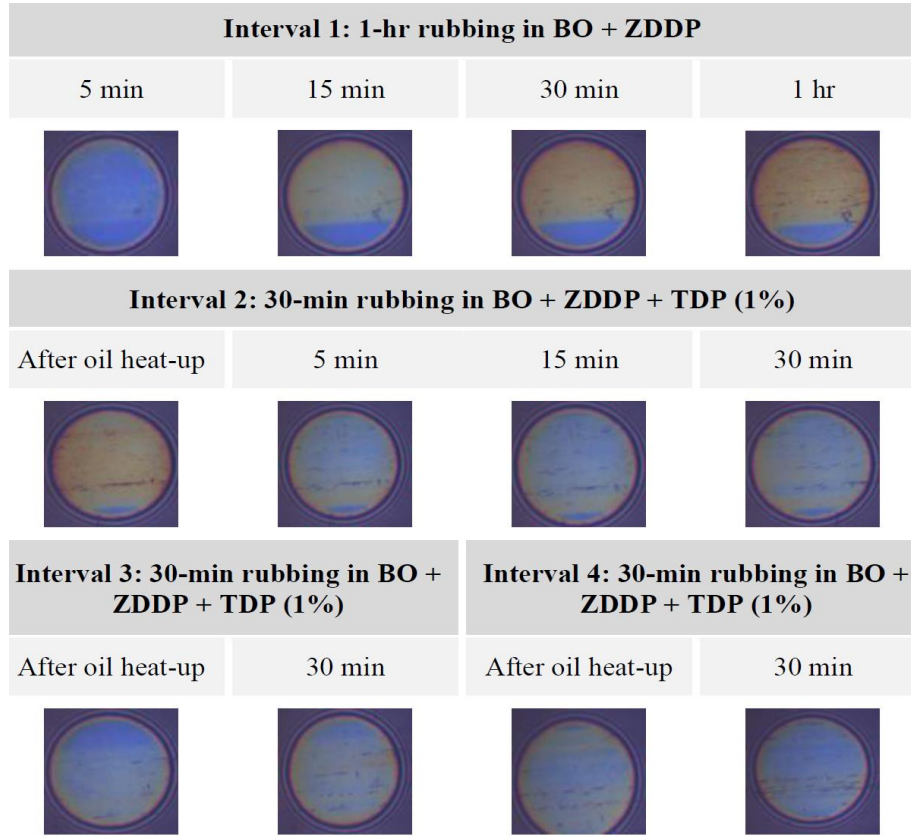
In order to inspect the effect of NCAs on an already generated ZDDP-tribofilm a test is carried out using MTM-SLIM under test conditions which are indicated in Table 8-1. The used test temperature, SRR, entrainment speed and contact pressure remained the same as that used in the previous MTM tests. A ZDDP-tribofilm is formed under tribological contacts for 1 hour and the tribofilm thickness is measured after 5, 15, 30 and 60 minutes of rubbing. At this stage the lubricant is replaced by a TDP-containing lubricant and surfaces are rubbed against each other for further 30 minutes and tribofilm thickness is measured after oil heat-up, 5, 15 and 30 minutes of the rubbing. This step is repeated three times in the current experiment. The SLIM images and corresponding tribofilm thicknesses are shown in Figure 8-13. The ZDDP-tribofilm reaches a steady state at approximately 70 nm in thickness after 30 minutes of rubbing. There is a 10-nm tribofilm loss after replacing the oil and heating the oil to 90°C. This suggests chemical interactions between TDP and the formed ZDDP-tribofilm on the surfaces.

Table 8-1. Experimental parameters for understanding the TDP effect on the ZDDP-tribofilm

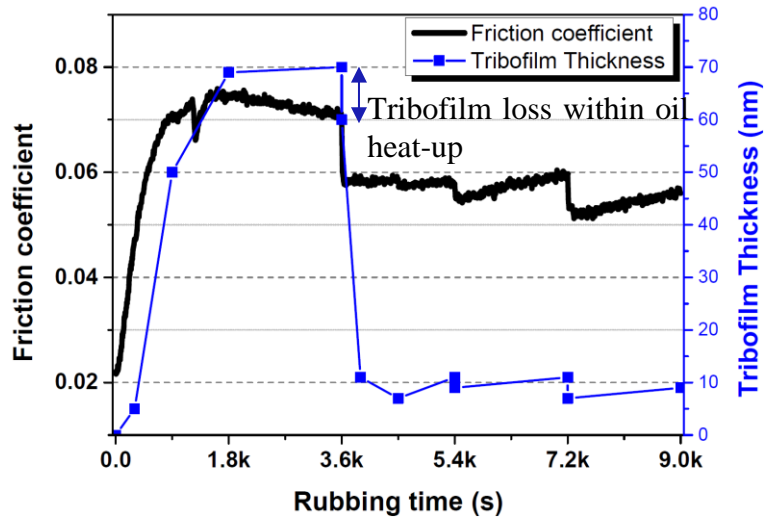
Specimens	52100 steel R _a : ball = 16 nm Disc:11 nm		
P _{max}	1 GPa	SRR	5%
Temperature	90°C	Entrainment speed	100 mm/s
Rubbing intervals	Interval 1	1-hr in BO + ZDDP	
	Interval 2	30-min in BO + ZDDP + TDP (1%)	
	Interval 3	30-min in BO + ZDDP + TDP (1%)	
	Interval 4	30-min in BO + ZDDP + TDP (1%)	

However, the interaction is significantly intensified as soon as rubbing has started. After 5 minutes of rubbing in BO + ZDDP + TDP (1%) 50 nanometres of the tribofilm is removed and the tribofilm thickness reaches a steady state at 10 nm. The enhanced interaction of TDP upon rubbing is in agreement with the observations by Campen (226). She showed that a significant friction reduction in OFMs (e.g. stearic and oleic acids) is achieved as soon as the specimen has completed one rotation

against the counterbody (226). Therefore, rubbing enhances the functionality of the NCAs.



(a)



(b)

Figure 8-13. a) SLIM images showing the influence of TDP on the ZDDP tribofilm and b) the change in tribofilm thickness and friction over the test time

Further rubbings show a minor, but persistent, tribofilm formation and removal. The tribofilm thickness varies around 6 to 12 nm. This indicates that the addition of TDP

to the lubricant formulation induces an interaction between ZDDP-tribofilm and TDP molecules generating a thinner tribofilm on the surfaces. The TDP interaction with ZDDP-tribofilm is a chemically activated reaction and the kinetics of the reaction is strongly stimulated by tribological contacts. The interaction and tribofilm removal accompanied by an approximately 20% friction reduction in average. An interesting finding is that the friction reduction is not resulted from the tribofilm removal since as soon as rubbing is started after oil change (60-nm tribofilm) friction is immediately dropped from 0.071 to 0.06. Therefore, the friction reduction is associated with the chemical interaction of the TDP with the ZDDP-tribofilm. This experiment confirms that chemical interactions occur between ZDDP-tribofilm and TDP molecules which are enhanced in tribological contacts. The chemical interaction leads to a thinner and smoother tribofilm which decays the hindering effect of ZDDP-tribofilm on oil entrainment into the contact (227) resulting in a friction reduction.

8.2.3.4 Surface and tribofilm inspection at the nano-metre scale

In order to observe the local and depth profile of the tribofilm induced by BO + ZDDP + NCAs lubricants at the nano-metre scale, a FIB milling is carried out on a roller surface having undergone 10^6 contact cycles which was lubricated with BO + ZDDP + TDP (1%). The FIB sectioning is performed close to a micropit. The FIB cross section has been investigated with TEM and EDX elemental analysis to confirm the elements throughout the tribofilm cross section. In this section two sections of the FIB lamella are elementally mapped using EDX to inspect the tribofilm on the surface and are shown in Figure 8-14 and Figure 8-15. As can be seen in Figure 8-14 the tribofilm on the surface is considerably thinner compared to the tribofilm from BO + ZDDP which is observed in section 5.2.4.2.

A part of the contact characteristics in MPR is similar to SR configuration in MTM (see Table 4-3) since a smooth roller (R_q : 50 nm) is in contact against rough rings (R_q : 500 nm). The roughness ratio of the rough specimen to the smooth specimen is approximately 10 in MPR and 6 in MTM-SR configuration respectively. Also, the λ ratio (approximately 0.04) and temperature (90°C) are also the same in MTM-SR and MPR test set-ups. In MPR experiments the contact pressure is larger compared to MTM-SR, while in MTM-SR experiments the SRR is greater compared to MPR. However, the tribofilm thicknesses are totally different. The tribofilm thickness is around 20 nm on the roller surface lubricated with BO + ZDDP + TDP (1%) (Figure 8-14).

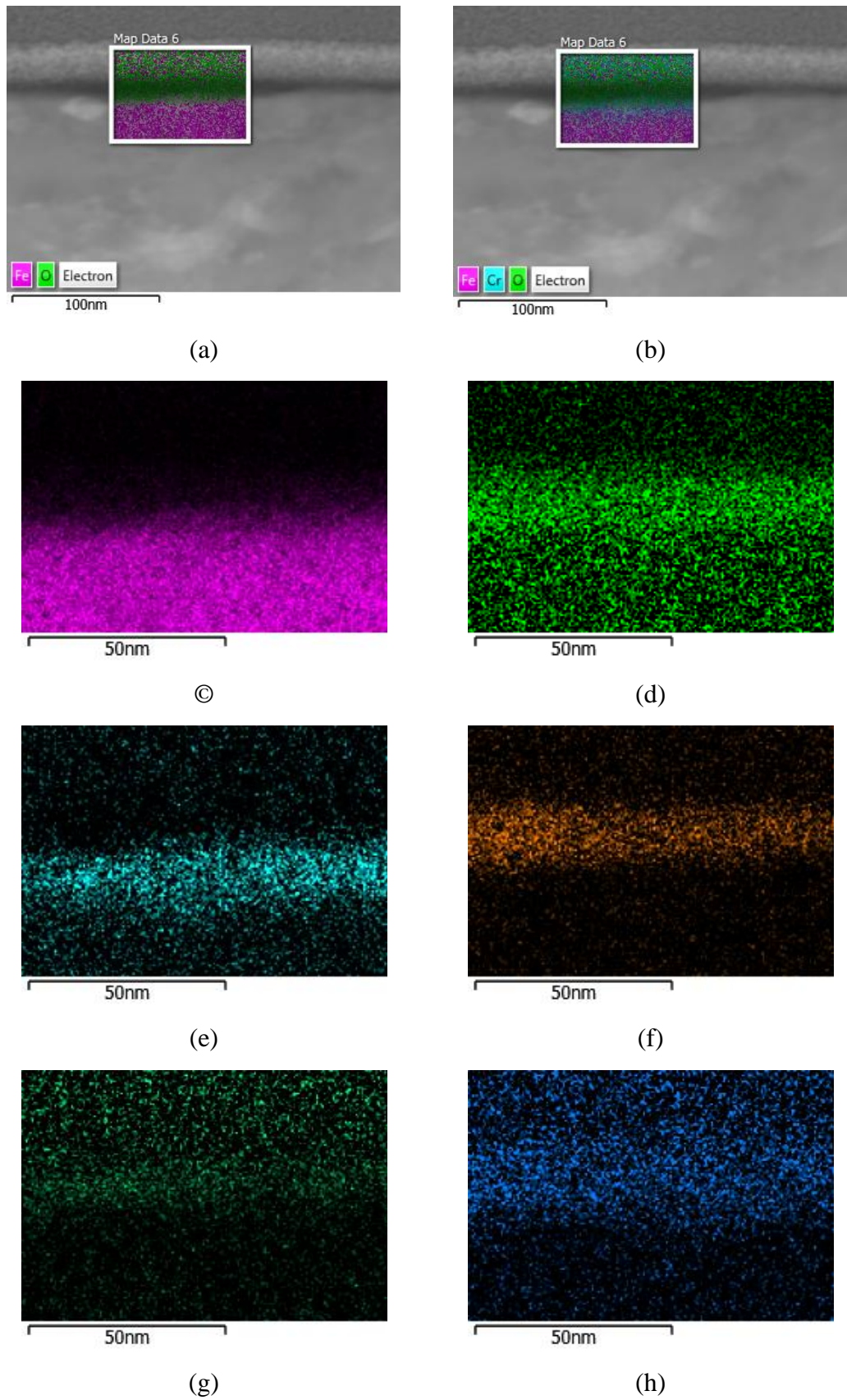
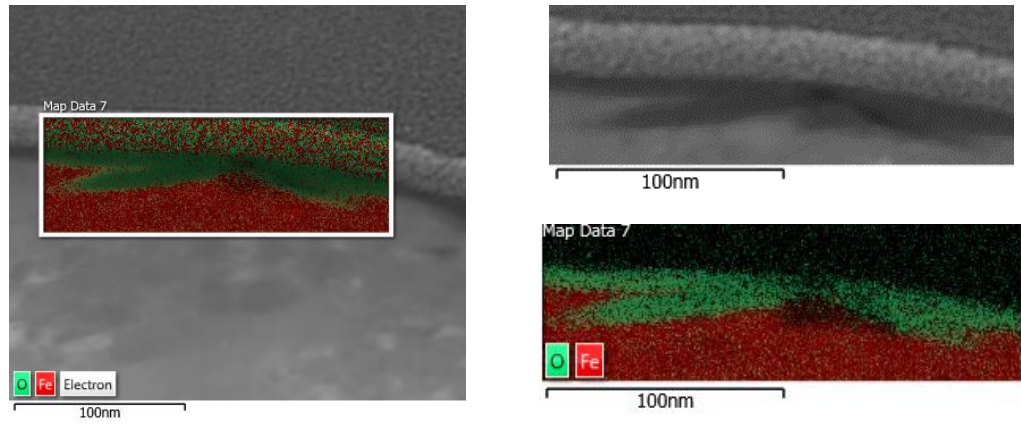


Figure 8-14. TEM images and EDX mapping of the tribofilm showing K edge maps of a) merged Fe and O, b) merged Fe, O and Cr, c) Fe, d) O, e) Cr, f) Zn, g) P and h) S from the tribofilm generated in the wear scar of MPR-roller lubricated with BO + ZDDP + TDP (1%)

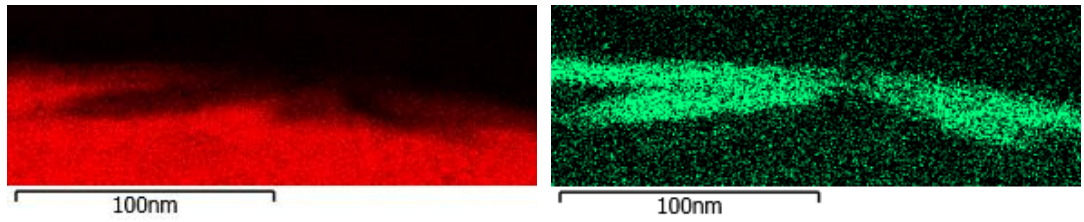
As can be observed in Figure 8-14, the phosphate contribution to the tribofilm is reduced and the presence of Zn and S is enhanced in the area where no crack was observed suggesting enhanced zinc sulphide formation. The greater zinc sulphide contribution is in agreement with XPS results reported in section 7.2.7. A greater sulphide contribution to the tribofilm bulk might be beneficial in highly loaded contacts (114-115, 117). O profoundly contributes to the tribofilm throughout its bulk implying enhanced zinc oxide formation considering the weak P signal. As showed in section 5.2.4.2, iron sulphide locally forms on the roller surfaces lubricated with BO + ZDDP, especially close to the surface crack zone. However, the interface on the roller surfaces of TDP seems to compose of iron and chromium oxide. This is an interesting and important observation. The Fe/Cr oxides are generally hard oxides that can resist crack initiation. On the other hand, the wear particles originating from interfacial Fe/Cr oxides are hard wear-particles that can promote abrasion on the contact surfaces (12, 122, 228). This is in agreement with the WLI images shown in Figure 8-2 and Figure 8-3 which show a micropitting reduction but abrasive marks in the wear scars of the lubricants containing NCAs.

A surface-initiated-crack in the wear scar is shown in Figure 8-15. The Al signal stems from the TEM grit which composed of copper and aluminium. The interface in this region is composed of iron oxide and chromium is not detected at the interface. Similar to Figure 8-14 O profoundly contributes to the tribofilm from BO + ZDDP + TDP (1%) in the cracked zone. A peak-overlapping at around 2.3-2.4 KeV occurs from the P $K\alpha$ and platinum M-line X-ray emissions which makes the P identification difficult in low concentrations and also close to the deposited protecting Pt-layer. In order to differentiate Pt from P, Pt L-line is shown in Figure 8-15 (i) in which P cannot overlap and thus a low concentration of P can be suggested to be present in the tribofilm bulk and inside the crack.

S also contributes to the tribofilm and inside the crack at low concentrations but greater than that of P. The contribution of O and Zn is significant both in the tribofilm and inside the crack implying enhanced zinc oxide formation in agreement with Figure 8-14. Also, crack faces are oxidised in this region in contrast to what is observed in Figure 5-16 for the crack in BO + ZDDP lubricated roller, in which iron sulphide formation is favoured over iron oxide.

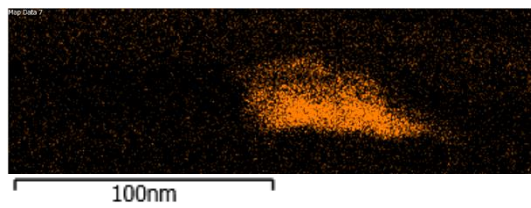


(a)

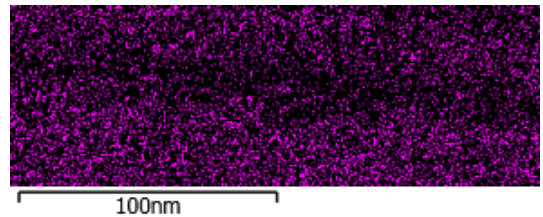


(b)

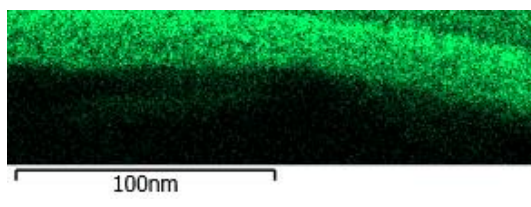
(c)



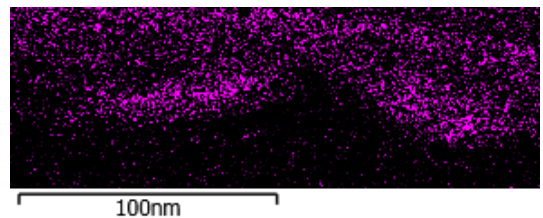
(d)



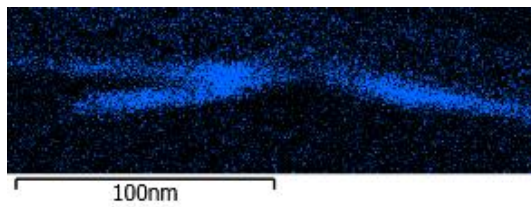
(e)



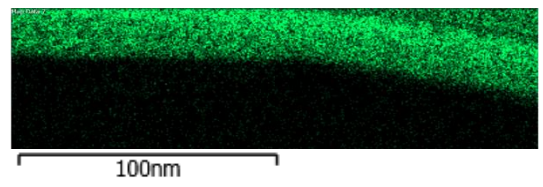
(f)



(g)



(h)



(i)

Figure 8-15. TEM images and EDX mapping of the tribofilm showing K edge maps of a) merged Fe and O, b) Fe, c) O, d) Al, e) Cr, f) P, g) S and h) Zn from the tribofilm generated in the wear scar of a roller lubricated with BO + ZDDP + TDP (1%) in the cracked-zone and i) L edge map of the protective Pt layer

8.2.3.5 An investigation on micropit morphology: SEM

In order to observe the micropit characteristics in the wear scars lubricated with BO + ZDDP + NCAs SEM images have been obtained from the roller surfaces. SEM images shown in Figure 8-16 confirm the micropitting reduction capability of the TDP additive. Also, the micropit on the surface which is lubricated with BO + ZDDP + TDP (1%) is shallower in depth. The micropits on the surface of BO + ZDDP lubricated roller are more vivid in the wear scar as can be seen in Figure 8-16.

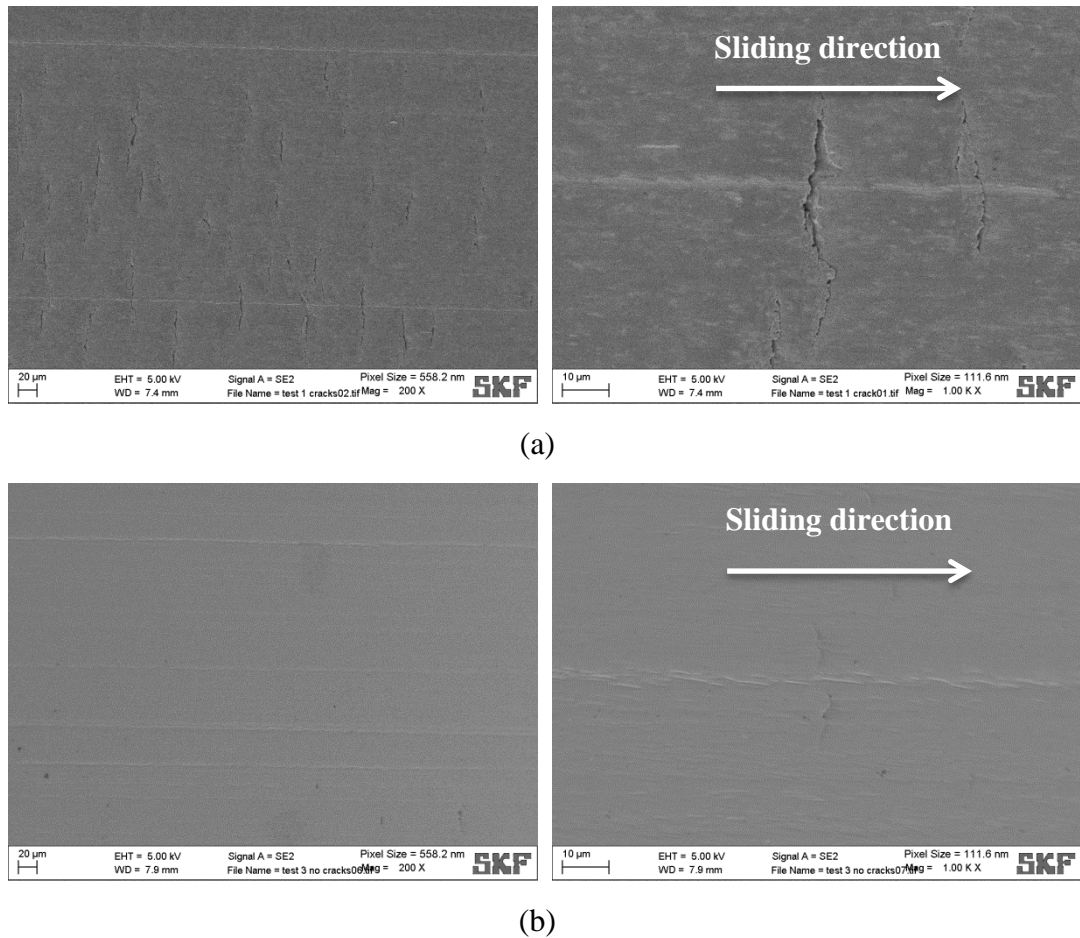


Figure 8-16. SEM images of the tribofilm on the surface of rollers lubricated with a) BO + ZDDP and b) BO + ZDDP + TDP (1%)

Micropits in the wear scar of TDP are shown in Figure 8-17 which are more visible after the washing procedure in order to remove the tribofilm. The characteristics of the micropits are similar to that observed in the case of BO + ZDDP. Micropits propagate opposite to the sliding direction into the bulk of the material and also transverse to the rolling-sliding direction. However, the micropits are smaller in size compared to the micropits in the wear scars lubricated with BO + ZDDP.

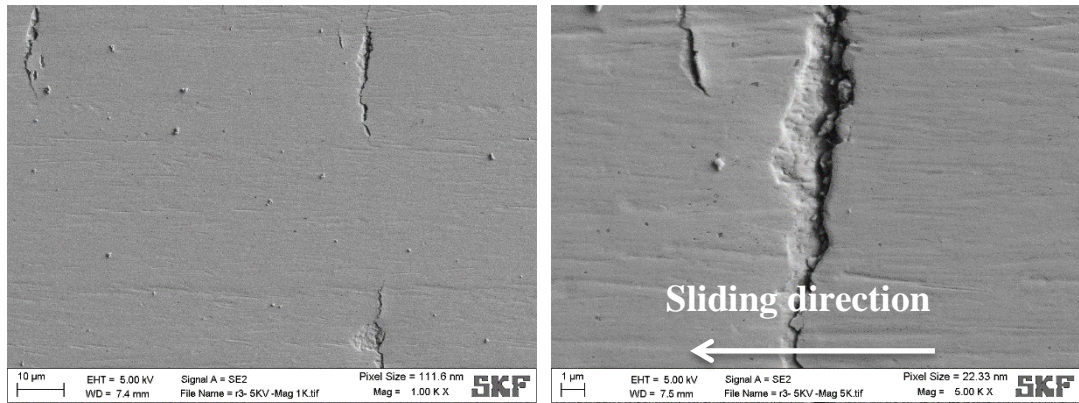


Figure 8-17. SEM images of the tribofilm on the surface of a roller lubricated with BO + ZDDP + TDP (1%) obtained following tribofilm removal

8.2.3.6 The tribochemical investigation of tribofilms generated from NCA-containing lubricants in micro-scale: XPS chemical composition analysis XPS is employed to understand how the tribochemistry can affect the changes in friction and micropitting wear seen when NCAs are used in conjunction with ZDDP. In this chapter the tribofilms in the wear scars of TDP (0.5%), TA (1%) and ETA (1%) after 10^6 contact cycles are studied. The tribofilm of TDP (0.5%) is considered in this case in order to have a similar number of N atoms in the lubricants. A TDP has two N atoms per molecule while TA and ETA have one N atom. Furthermore, the micropitting performance of TDP (0.5%) (micropitting surface area) is closer to that of TA (1%) and ETA (1%). Figure 8-18 shows a comparative fitting procedure and signal shapes in tribofilms from BO + ZDDP and BO + ZDDP + TDP (0.5%) in the wear scars of the rollers. The main differences between spectra from BO + ZDDP + TDP (0.5%) and BO + ZDDP are the appeared oxide peak in O 1s signal, sulphate in S 2p signal and iron oxide peaks in Fe 2p signal.

While a Fe signal is not detected in BO + ZDDP, Fe ($Fe\ 2p_{3/2}$) signal in BO + ZDDP + TDP (0.5%) is resolved to four peaks shown in Figure 8-18. The peak at $709.9 \pm 0.1\ eV$ and $711.1 \pm 0.1\ eV$ can be attributed to iron oxide in oxidation state of +2 and +3, respectively. The Oxide peak at $529.8 \pm 0.1\ eV$ in the O 1s signal can be attributed to the iron oxide accordingly. In addition, the peak at $712.8 \pm 0.1\ eV$ attributed to $FePO_4$, suggests the contribution of iron to the (poly)phosphate chain. As shown in Figure 8-18, the S 2p spectra from the tribofilms have a signal in the oxidation state of -2 (SII) assigned to sulphides (195) as metal sulphide (zinc sulphide) which are embedded precipitates and S which is substituted for O in the phosphate chain forming (polythio)phosphate (127). A contribution of sulphate from S (S 2p) in

oxidation state of +6 (SVI) (195) is observed for the roller lubricated with BO + ZDDP + TDP (0.5%), generating S 2p_{3/2} peak at 167.9 ± 0.1 eV. Sulphate is present on the top layer of the tribofilm and in the bulk of the tribofilm sulphide exists.

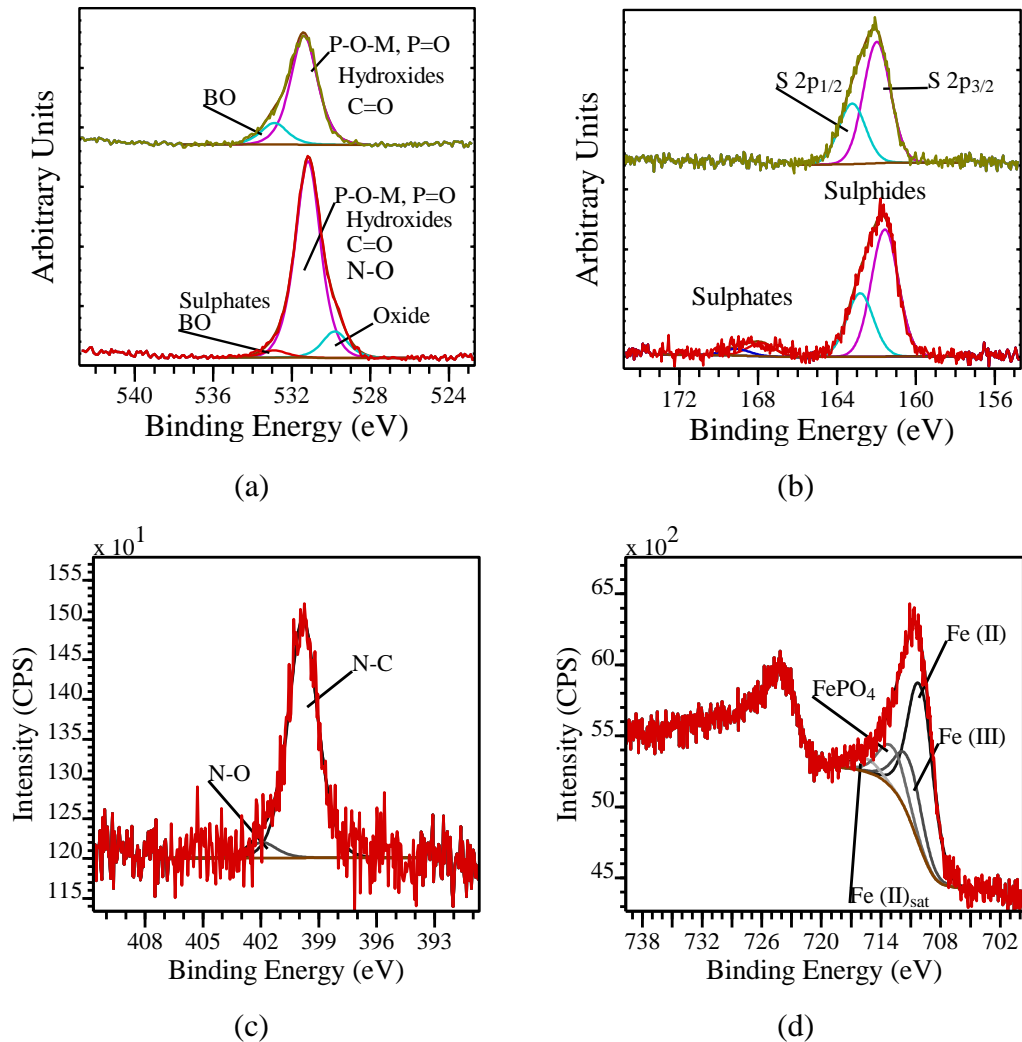


Figure 8-18. Detailed XPS spectra showing a) O 1s, b) S 2p, c) N 1s and d) Fe 2p signals. The spectra collected from MPR rollers lubricated with BO + ZDDP (top-plotted in green) and BO + ZDDP + TDP (0.5%) (bottom-plotted in red) lubricant formulations. N 1s and Fe 2p signals appeared in the spectrum from BO + ZDDP + TDP (0.5%)

The role of sulphate as an oxidised species is not thoroughly understood; however as indicated in section 7.2.7, sulphates are detected in thermal films and in the wear scar of water-contaminated contacts (148, 151). Although sulphate contribution to the ZDDP-tribofilm is shown (143), it is assumed to be a detrimental compound on the surface which can induce corrosive wear (192). The contribution of N can be observed only in the detailed spectra of the tribofilm on the roller lubricated with BO + ZDDP + TDP (0.5%) similar to what is observed in section 7.2.7. N 1s signal is difficult to interpret due to the lack of specific standards and low signal to noise ratio.

However, as shown in Figure 8-18 (c), a peak can be resolved at 399.8 ± 0.1 eV that can be attributed to N–C/N–H bonds in TDP, HN–P bond (224) and AP (225). This peak can be assigned to the adsorbed TDP on the surface or residual compound(s) of ZDDP and TDP interaction(s). The second peak in the tribofilm at 401.9 ± 0.1 eV can be assigned to ammonium, ammonium phosphate (224), N–O bonds in nitrates (192) and/or ionized organic (di)amine (225). The BE values above 400 eV is assigned to partially positive-charged and protonated N (229-230). While the N with higher electron density appears at lower binding energies in XPS (231).

The spectra in TA (1%) are similar to TDP (0.5%). However, the spectra in ETA are markedly different to other spectra. The signals and fitting procedures for ETA spectra are shown in Figure 8-19. As shown in Figure 8-19 (a), the Fe $2p_{3/2}$ signal is resolved to five peaks and the first peak at 706.8 ± 0.1 eV is attributed to the metallic Fe. No peak corresponding to metallic Fe was observed for tribofilms from TDP and TA. The contribution of the metallic Fe to the tribofilm can be an indication of high wear on the surface which is in agreement with the wear results (Figure 8-6). The O 1s signal becomes broad and a large oxide peak appears at 530.0 ± 0.1 eV. The large oxide peaks is an indication of a deficient tribofilm performance and occurrence of a considerable oxidative wear.

A carbide peak appears at 283.3 ± 0.1 eV in C 1s signal which can be attributed to chromium carbide particles (or inclusions) and/or iron carbides (cementite and etc.). The carbide contribution suggests occurrence of abrasive wear on the surface. Furthermore, the Zn contribution to the tribofilm is hindered as can be seen in Figure 8-19 (c). Also, P 2p signal is weaker compared to the spectra from other NCAs which implies the antagonistic effect of ETA on the ZDDP-tribofilm.

The BE values of the peaks and corresponding chemical compounds are summarised in Table 8-2. Also, parameters and atomic concentration of the compounds and elements in the tribofilms are indicated in Table 8-3. The C 1s spectra in all tribofilms except ETA are resolved to four peaks. The main peak at 285.0 eV is assigned to aliphatic carbon (C–C and C–H). The other three minor contributions exhibited at around 286.3-286.6, 287.4-287.7 and $288.7-289.1 \pm 0.1$ eV correspond to C–O/C–N, C–S/C–N and C=O (102, 151) (carbonate and/or carboxylic), respectively. The sixth peak appeared in C 1s signal from ETA tribofilm at 290.2 ± 0.1 eV which can be attributed to the carbonate group.

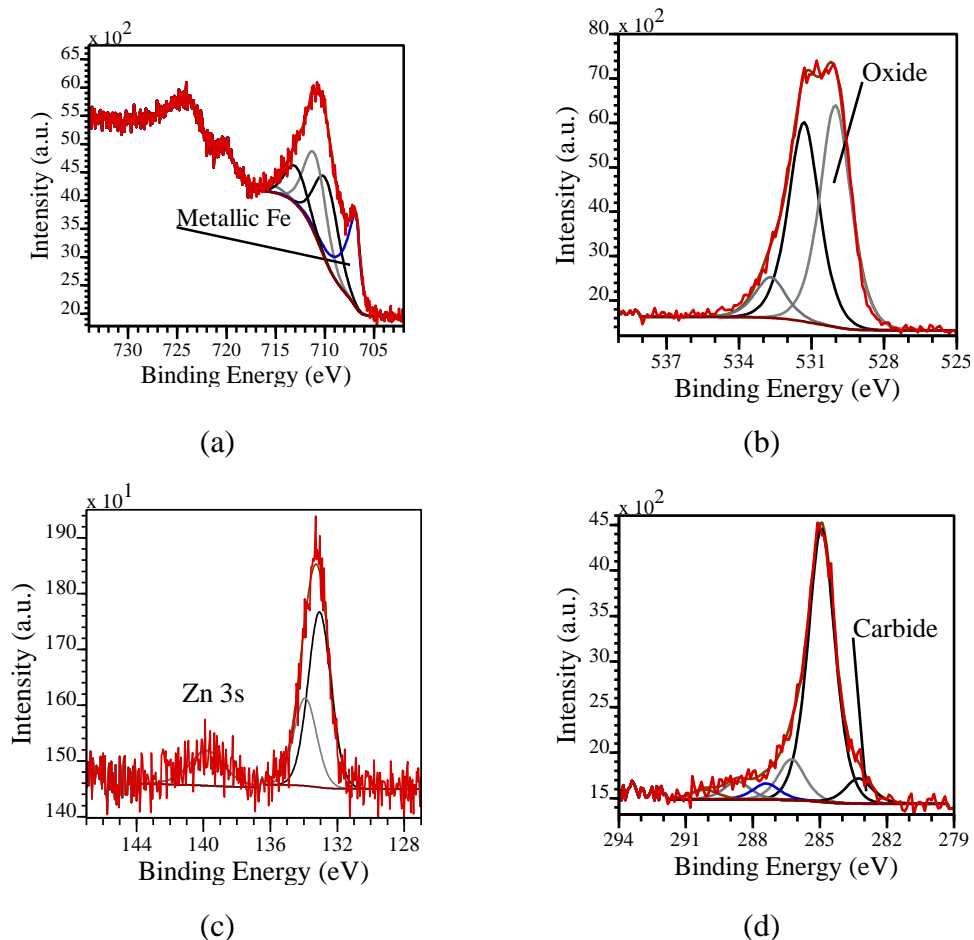


Figure 8-19. Detailed XPS spectra showing a) Fe 2p, b) O 1s, c) P 2p and Zn 3s and d) C 1s signals. The spectra collected from MPR roller lubricated with BO + ZDDP + ETA (1%)

The O 1s signal consists of two peaks in spectra from BO + ZDDP and three peaks in spectra from NCA-containing lubricants (see Figure 8-18 and Table 8-2). The peak at 529.8-530.0 eV \pm 0.1 eV in the O 1s signal of NCAs is attributed to the iron oxide (204). The peak at 531.2-531.6 \pm 0.1 eV in the tribofilms are assigned to NBO from the phosphate chain ($-\text{P}=\text{O}$ and $\text{P}-\text{O}-\text{M}$; where M is metal: Zn or Fe) (122), nitrates (192), hydroxide and carbonates. Ammonium phosphate (177-178) or AP (221) contributes to this peak. The peak at 532.-533.1 \pm 0.1 eV corresponds to BO from phosphate chain ($\text{P}-\text{O}-\text{P}$) and sulphates in NCAs tribofilms. Due to the very low P and Zn concentration and a large oxide peak in ETA tribofilm, attributing peaks to NBO and BO is controversial and thus the peak binding energies and BO/NBO ratio are not included in Table 8-2 and Table 8-3.

The P 2p_{3/2} peak at 133.0-133.6 \pm 0.1 eV is attributed to phosphate contribution to the tribofilm and neither of the tribofilms is expected to consist of long (poly)phosphate chains (202-205) in agreement with the results presented in section 5.2.3 and 7.2.7.

Similar to the procedure in previous chapters, Zn 3s is considered to calculate the quantification data (151, 194).

Table 8-2. Binding energy values of the elements/compounds in the tribofilms

BO + ZDDP +		-	TDP (0.5%)	TA (1%)	ETA (1%)
C 1s	C-C	285.0	285	285	285
	C-O/C-N	286.30 ± 0.1	286.3	286.6	286.3
	C-S/C-N	287.4 ± 0.2	287.7	287.6	287.4
	C=O	288.9 ± 0.1	288.8	289.1	288.7, 290.2
O 1s	BO	533.07 ± 0.17	532.9	532.9	-
	NBO	531.55 ± 0.14	531.2	531.4	-
	Oxide	-	529.8	530.0	530.0
P 2p _{3/2}	133.56 ± 0.24	133.0	133.2	133.1	
Zn 3s	140.41 ± 0.17	139.9	140.1	139.8	
N 1s	N-H/ N-C/ AP	-	399.8 (1.9%)	400.0 (0.6%)	399.8 (1.1%)
	N-O / (R- NH ₃ ⁺)NH ₄ ⁺	-	401.9 (0.1%)	401.6 (0.1%)	402.0 (0.2%)
S 2p _{3/2}	Sulphide	162.22 ± 0.24	161.6	161.9	161.6
	Sulphate	-	167.9	167.9	168.1
Zn 3s - P 2p _{3/2} ΔBE	6.85 ± 0.05	6.9	6.9	6.7	

The maximum error for the measurements of the signal binding energies was ± 0.1 eV. The decimal digits in the table indicate the maximum deviation from the mean value (average of measurements on two specimens)

As can be seen in Table 8-2, Zn 3s - P 2p_{3/2} ΔBE values in tribofilms from TDP and TA are similar to the ΔBE in the tribofilm from BO + ZDDP. This suggests a similar phosphate chain length for all tribofilms. However, TDP and ZDDP interactions might influence zinc states. The change in Zn states brings about a shift in Zn BE which makes the Zn 3s - P 2p_{3/2} ΔBE parameter unreliable in order to identify the

phosphate chain length (this will be discussed further in section 9.3.1). Also, the BO/NBO ratio which has been used to evaluate the chain length of zinc phosphate glasses (122) may easily be affected by contaminants or contribution of other components to BO and NBO peaks. Hydroxides and C=O (carbonyl and carbonate) can contribute to the NBO peak (151, 192). Also, sulphate and P–O–C components (197) can contribute to the BO peak. Therefore, chain length identification in the NCAs containing lubricant formulations is difficult and might be contentious. However, the increase in the cation concentration (122, 177) (Zn^{2+} , Fe^{3+} , and ionized (di)amine) together with the decrease in P 2p_{3/2} BE imply a decrease in the phosphate chain length in the tribofilms from NCAs which is not necessarily an indication of a deteriorated or improved AW performance. There are contradictory results on the performance of short and long (poly)phosphate chains in the literature (105, 201, 232).

As can be seen in Table 8-3, the sulphate contribution to the tribofilms from NCAs are similar and is not expected to induce a considerable change in the tribofilm performance. The noticeable alterations are an increase in the Fe and iron oxide concentration and a considerable decrease in the phosphate contribution to the tribofilm from ETA in comparison with the tribofilms from TA and TDP. Comparing the parameters in the tribofilm from TDP with the parameters in the TA tribofilm, it is clear that the contribution of phosphate is similar, while a slight decrease in sulphide contribution in TA tribofilm can be perceived. The presence of TDP and TDP-ZDDP compounds are greater in the TDP tribofilm. Moreover, the contribution of the first (most intense) peak in N 1s over the second peak is greater in TDP (TDP: 19, TA: 6) suggesting that TDP is less ionised on the surface and mostly presents as AP and N-C. The greater presence of TDP grants an improved micropitting-performance on the surface as shown in section 8.2.2.

In order to observe the elemental distribution of the tribofilm through its depth and obtain an estimation of the tribofilm thickness, tribofilms from BO + ZDDP and BO + ZDDP + TDP (0.5%) are sputtered with Ar⁺ ion source using XPS. The tribofilm etched profiles are shown in Figure 8-20. The sputtered profile of the tribofilm from BO + ZDDP, shown in Figure 8-20 (a), confirms a thick tribofilm formation on the surface, since after 30 minutes of etching there is a substantial proportion of the tribofilm on the surface which consists of P, S and Zn elements.

Table 8-3. Parameters and atomic concentration of the compounds/elements in the tribofilms

	BO + ZDDP +	-	TDP (0.5%)	TA (1%)	ETA (1%)
	BO/NBO	0.22 ± 0.02	0.04	0.04	-
Atomic concentration	Zn/P	1.07 ± 0.07	1.3	1.1	0.3
	S _(II) /P	0.71 ± 0.08	0.6	0.3	0.6
	O/P	1.75 ± 0.12	3.1	3.7	8.5
	N/P	0	0.2	0.06	0.3
	Fe/P	0	0.3	0.3	1.8
	P (%)	-	10.7	11.1	4.5
	Fe (%)	0	3.2	3	8.3
	N (%)	0	2	0.7	1.3
	N-C, AP / N-O, (R-NH ₃ ⁺)NH ₄ ⁺	-	19	6	5.5
	Sulphate (%)	0	0.8	0.5	0.6
	Oxide (%)	0	4.3	5.2	18.6

Fe does not appear until nine minutes of etching implying the existence of zinc (polythio)phosphates alongside sulphides (zinc sulphide and/or species in the form of (polythio)phosphate) on the upper layer of the ZDDP-tribofilm. A decrease in the Zn concentration from top layer to the bulk and an increase in the Fe concentration toward the substrate can be observed in Figure 8-20 which are in agreement with the TEM/EDX results presented in Figure 5-14. Relative S to P, O and Zn atomic ratios are larger in the very top layer compared to the bulk of the tribofilm showing a greater contribution of sulphide to the very top layer. C was not detected in the bulk of tribofilm of BO + ZDDP confirming the inorganic nature of the ZDDP tribofilm (105, 233-234).

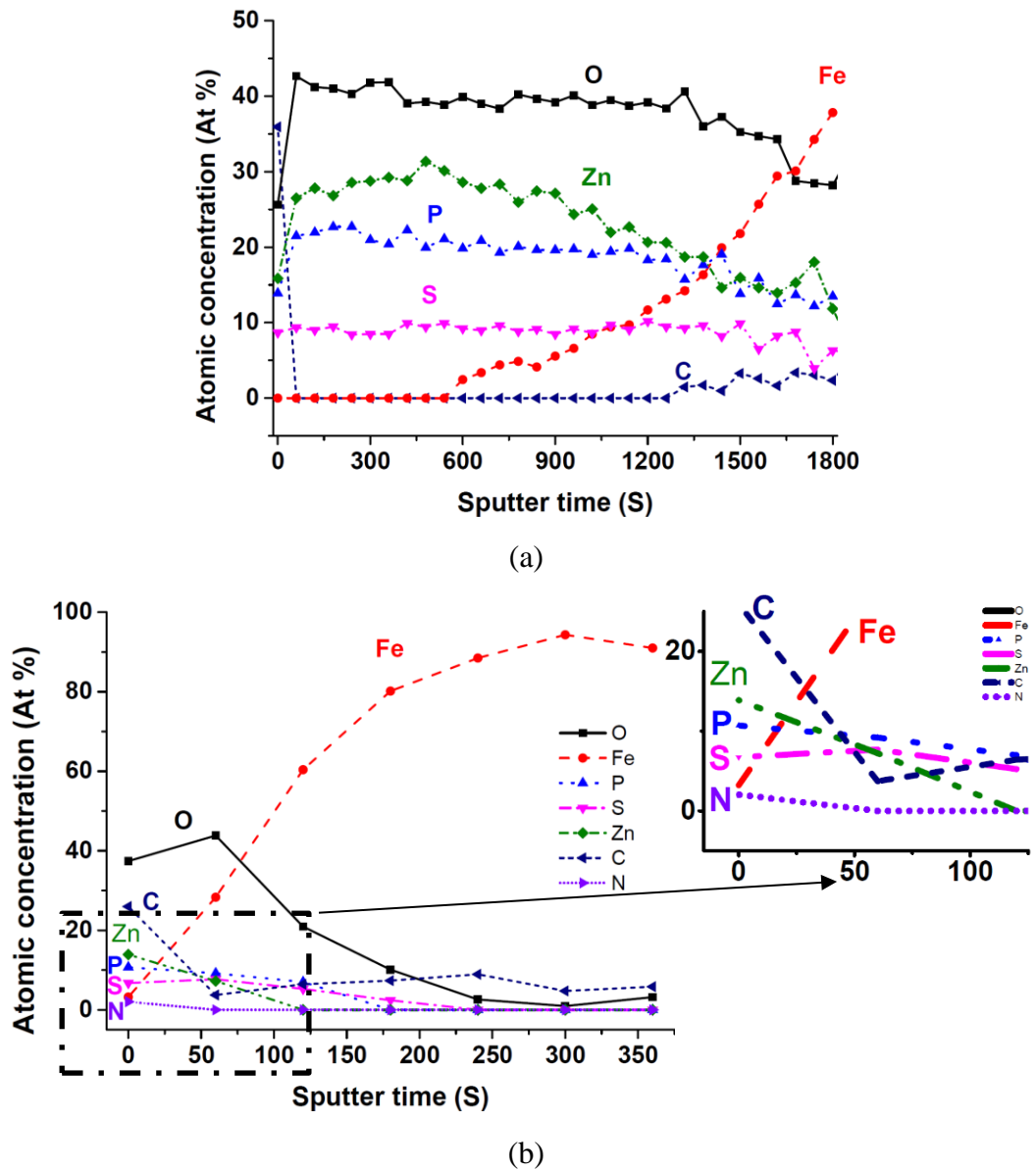


Figure 8-20. Sputter depth profiles of the reaction layers on the surface of rollers lubricated with a) BO + ZDDP and b) BO + ZDDP + TDP (0.5%)

The presence of Fe in the tribofilm spectra from ZDDP + TDP (Figure 8-18) is an indication of a thinner tribofilm formation (233). This is confirmed through etching the tribofilm, by which, after only four minutes of etching (Figure 8-20 (b)), no trace of tribofilm elements (P, Zn, and S) was observed. The thin tribofilm in the presence of TDP is also observed in Figure 8-14. A thinner tribofilm formation on the roller surface, which is driven by interactions between ZDDP and TDP, can suggest a less shear-resistant tribofilm formation in the presence of TDP. Moreover, development of a smaller extent of tribofilm-precursors (192) on the top layer to compensate the removed tribofilm in the more severe conditions (124) can also lead to a thinner tribofilm formation. However, amine-containing succinimide dispersants are shown

to enhance ZDDP decomposition (177) which rules out the lack of tribofilm-precursors.

The tribofilm from BO + ZDDP + TDP consists of short chain mixed zinc/iron (thio)phosphates with contribution of TDP residuals and (di)amine and phosphate compounds, possibly (di)-AP (222) and oxidised species (sulphates and nitrates) on the top layer. As indicated in section 7.2.7, the contribution of ammonium phosphate (177-178) or/and AP (221) to the phosphate chain in tribofilms generated from lubricants containing ZDDP and dispersants is shown in the literature (222).

Also, the relative contribution of O to P is enhanced in the tribofilm from BO + ZDDP + TDP on the top layer (O/P: 3.1) and bulk compared to the ratio in BO + ZDDP on top layer (O/P: 1.75) and bulk. This is in agreement with Pasariu *et al.* (76) results which showed a superior RCF performance of the reaction layers having a higher concentration of O rather than P. Also, no trace of N was detected after 60 s of ion sputtering the reaction layer, suggesting that TDP and its reaction products are concentrated at the surface and do not considerably contribute to the chemical composition of the tribofilm bulk.

8.3 Summary

In this chapter comparisons have been made on the micropitting performance of NCAs as friction modifiers and their influence on the tribofilm composition and thickness using a modified MPR. In general, a conclusive correlation between micropitting performance, friction coefficient and total wear volume in the wear scars was not observed in the test conditions defined in this study. The wear and micropitting performance is strongly dependent on the additive interactions in the bulk lubricant as well as with the surface in the tribofilm formation/removal procedure. A set of tests using MTM and MPR has been carried-out and tribofilm/wear scars analysed utilising AFM, WLI, SEM, TEM/EDX and XPS in order to unveil the mechanism of the action of NCAs in micropitting wear which led to interesting findings.

Experiments performed under the test conditions defined in this study showed that:

- In the modified MPR tests the friction reduction efficiency of the additives is in the following order: TDP = TA < ETA.

- All NCAs are effective in reducing micropitting at the current experimental set-up. The total wear volume is decreased with the addition of TDP and TA to the BO + ZDDP lubricant suggesting their AW action, while addition of ETA induces high wear in the wear scar which leads to greater total wear volume compared to wear volume in BO + ZDDP. Therefore, the greater wear might be partly responsible for friction reduction achieved by ETA in this case.
- TDP performs as an AW additive when it is blended to the BO in the absence of ZDDP. The AW performance of TDP depends on its adsorption on the surface and thereby is influenced by concentration, contact pressure and probably temperature.
- TDP interacts with ZDDP-tribofilm on the surface bringing about a thin and smooth tribofilm formation on the surface. A patchy ZDDP-tribofilm formation is repressed by TDP. The tribofilm from ZDDP + TDP shows a continuous tribofilm formation and removal characteristics.
- The TDP/TA and ZDDP interactions generate compounds (amine/ammonium phosphate) on the top surface of the tribofilm.
- SEM images confirmed the micropitting reduction efficiency of TDP and showed that the characteristics of the micropits do not change with the addition of TDP.
- The tribofilm composition from the TDP and TA containing-lubricants is similar with minor differences. While the tribofilm composition of ETA, which has great iron oxide and Fe contributions and low phosphate contribution, is noticeably different from that of TDP and TA.
- A slightly improved performance of TDP over TA can be attributed to the enhanced contribution of first peak in N 1s signal which is assigned to AP and N-C bonds originating from adsorbed TDP and greater contribution of sulphide to the tribofilm.

Chapter 9 Discussion

9.1 Overview of discussion

The main results obtained in this work are addressed and discussed in this chapter with regard to the available literature on micropitting and related tribochemical phenomena. Overall, results show that tribochemistry substantially influences micropitting happening in the boundary lubrication regime. The current chapter is split into three main themes that encompass the findings of this project. The three main focus areas include the following:

1. Understanding the micropitting evolution in severe rolling-sliding contacts lubricated with a ZDDP-containing oil from initiation to propagation.
2. Understanding the tribological and tribochemical influence of water as a lubricant contaminant on micropitting surface fatigue.
3. Mitigation of the micropitting-enhancing behaviour of ZDDP by utilising NCAs.

In the last section of each theme a mechanism is proposed which elucidates the observed results. The section is linked to the previous mechanism proposed for previous theme(s) leading to a comprehensive tribochemical-understanding of micropitting.

9.2 Understanding the micropitting evolution in severe rolling-sliding contacts lubricated with a ZDDP-containing oil from initiation to propagation

Micropitting occurs in bearings of wind turbines as a result of sliding between rollers and raceway at slow speeds. The excessive sliding escalates shear stresses and local temperatures in the contact zone and generates microcracks (1). Micropitting as a surface fatigue mechanism has been studied mainly taking the mechanical aspects of micropitting into account (15, 47, 80, 82, 89, 93, 209, 235-236). The influence of oil and additives has been addressed based on a comparison method (5, 18, 81, 237-239). Within the last twenty years the pronounced influence of AW additives on micropitting performance of the lubricant has been reported (7, 18, 237). It has been

confirmed that ZDDP (as the most well-known) AW additive enhances micropitting (8, 18). The detrimental effect of ZDDP on micropitting is thought to be due to its effect on promoting local plastic deformation and delaying the effective running-in. However, the tribochemical effect of ZDDP in severe micropitting wear has not been completely elucidated in rolling conditions. In this regard, the ZDDP-induced micropitting evolution over contact cycles is studied in this project in order to obtain a profound understanding of the mechanism by which ZDDP-tribofilms enhance micropitting.

9.2.1 **Micropitting and wear over contact cycles in the modified-MPR and the relevant tribochemical investigation**

In Chapter 5 results showed that ZDDP provides the surface with wear-protection while it induces micropits on the surface. The evolution of micropitting from initiation to propagation is inspected and showed that after 62.5K contact cycles the micropitting is mainly in the nucleation stage. The wear and tribochemical data obtained from the roller surfaces over contact cycles are summarised in Figure 9-1. In comparison with 10^6 contact cycles, over 50% of the total wear volume occurred in the first 62.5K cycles while the surface area affected by micropitting is around 20% of that of 10^6 cycles. Therefore, the micropitting surface area sharply increases compared to a gradual increase in total wear volume which is in agreement with experimental and numerical results by Morales-Espejel *et al.* (47). Their results showed that extensive wear can mitigate progression of micropitting and if the wear is not large enough to suppress micropitting the rate of micropitting can increase with increasing number of contact cycles. According to the micropitting results over contact cycles, the micropitting surface area in the modified-MPR used in this study is a more appropriate parameter to consider compared to total wear volume in the current set-up. However, the total wear volume provides information regarding the total material loss due to gradual wear (mild, abrasive, adhesive wear) and micropitting in the wear scar leading to an intensified complexity in interpreting the results.

The SRR of 2% typically exists in bearings (47) and the bearings in wind turbine gearboxes can experience a contact pressure of 1.5 GPa in transient conditions. Therefore, the roughness of the surfaces is the parameter which is different to the contact conditions exist in wind turbine bearings. In the laboratory experiments the

roughness of the counterbody is increased in order to accelerate the micropitting. Accordingly, micropitting initiation after 62.5K cycles and its fast progression can justify the premature failures in wind turbine bearings and hence it is essential to prevent the micropitting initiation from happening at the early stages of contacts.

Alongside micropitting surface density, the depth of the individual micropits in the wear scar is a critical parameter which influences the total wear volume and is an indication of the micropitting propagation. In addition, the micropitting depth is crucial to the rolling fatigue life of the components in roller bearings. An increase in micropitting depth enhances the chance of macropitting and spalling in the wear scar. In the wear scars of BO + ZDDP, investigated using modified-MPR, micropits vary greatly in depth which makes it impossible to generate data representing micropitting depth.

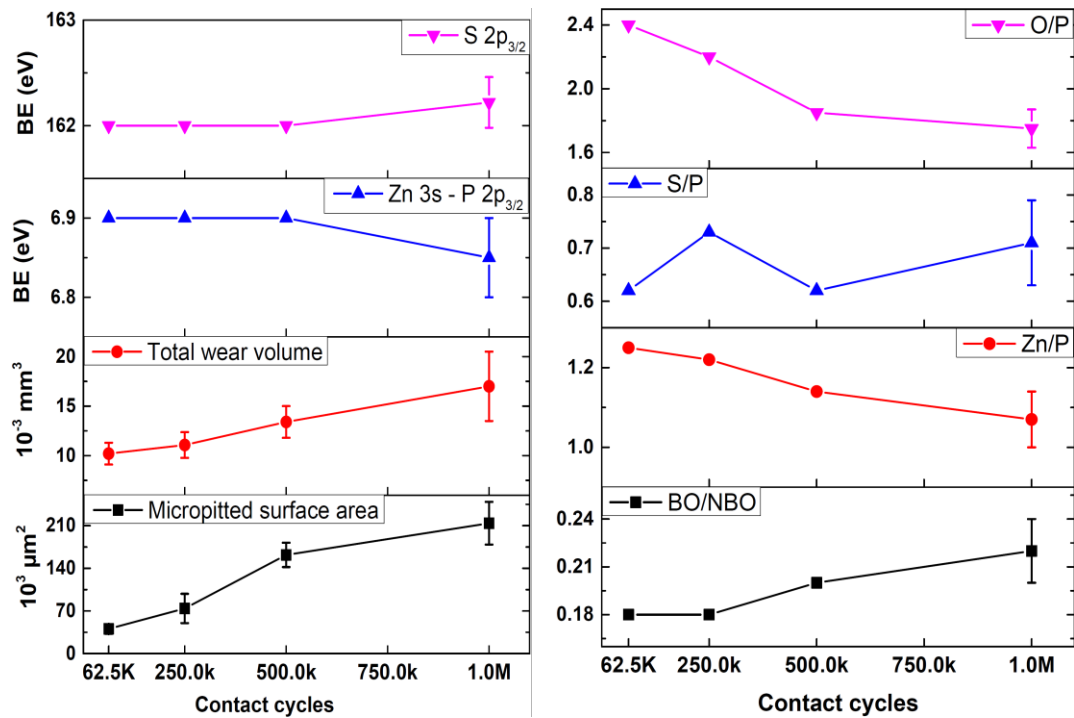


Figure 9-1. Micropitting evolution over contact cycles in the modified-MPR and the relevant tribochemical parameters

As discussed in Chapter 5, a decrease in O/P and Zn/P ratios in the ZDDP-tribofilm over contact cycles can be observed (shown in Figure 9-1). This complies with a minor increase in BO/NBO ratio suggesting a relatively slight increase in phosphate chain length over contact cycles (122, 127, 197-199, 201). However, the Zn 3s – P 2p_{3/2} ΔBE rules out the increase in phosphate chain length and indicates a similar structure over the contact cycles (187, 199, 201). In addition, an increase in

phosphate chain length over contact cycles is in contrast to the literature suggesting a decrease in the phosphate chain length of ZDDP-tribofilm over time (105, 165). Therefore, it can be assumed that phosphates in the ZDDP-tribofilms over the contact cycles exist as a mix of ortho, pyro and tripoly-phosphates. The lack of long-chain polyphosphates on top of the tribofilm which brings about viscous flows in the contact interface (105) can enhance micropitting. The viscous polyphosphate layer can accommodate the rolling/sliding shear stresses inside the tribofilm (124) and hence depolymerisation of the polyphosphates to hard and tough short-chain phosphates can provide a greater wear resistance (201), which in turn intensifies micropitting (47).

9.2.2 **Iron sulphide formation on interface**

The sputtered profile of the ZDDP-tribofilm formed in the wear scar having undergone 10^6 cycles is shown in Chapter 8. The TEM/EDX mapping of the FIB lamella in the region without crack (shown in Figure 5-14) is in agreement with the XPS sputtered profile data and previous reports (105, 127). Zn from ZDDP is strongly present on the top layer while declines in concentration towards the bulk of the tribofilm. A small contribution of the Fe to the tribofilm can be detected in the bottom 30 nm of the tribofilm. In the no-crack region, the atomic-concentration-ratio of the O to P is similar in the top-layer and mid-layer of the tribofilm while, the atomic-concentration-ratio of S and Zn to P is decreased at the mid-layer compared to the top-layer, suggesting less contribution of the sulphide to the tribofilm bulk compared to the tribofilm's very top layer (Figure 5-15) which is in agreement with the literature (105). There are two distinct areas in which presence of S is more pronounced; the very top layer and very bottom layer. The XPS sputtered profile results confirmed that S only contributes as sulphide to the tribofilm on the wear track and sulphate contribution was not observed in the bulk of tribofilms in agreement with the previous works (127, 140).

The merged mapping of the Fe and S confirmed that only S and Fe elements are present on the bottom layer of the tribofilm where S concentration is enriched. Considering that S appears as sulphide compounds throughout the tribofilm, a distinct 5-10 nm iron sulphide layer formation is confirmed at the substrate of the steel. In agreement with Martin *et al.* (127) and Minfray *et al.* (107, 140) no iron oxide layer is observed at the interface based on XPS and TEM-EDX mapping results. The native iron oxide layer on the steel surface is believed to be digested at the early stage of the

ZDDP-tribofilm formation (107, 140, 206) acting as a catalyst in the ZDDP-tribofilm formation process (172). As discussed in Chapter 3, the iron sulphide formation in the ZDDP-tribofilm has been suggested in severe wear process (127). However, Figure 5-14 and Figure 5-16 are first experimental evidences which directly show the iron sulphide on the interface of ZDDP-tribofilm and steel substrate as a separate interfacial layer. The iron sulphide formation in the area in which a crack appears on the surface is enhanced. This is an important observation since there are reports suggesting that under certain conditions, S-P containing additives can be detrimental to the fatigue life of bearings (19, 70, 73-76). Pasaribu *et al.* (76) evaluated the impact of reaction layers formed from different lubricants. According to the results presented in Figure 9-2, they showed that a high concentration of O in the reaction layer brings about a longer bearing life, while higher concentrations of P and S, derived from S-P additives, decline the Weibull slope indicating a wide spread of bearing life. The influence of additives on bearing life was discussed in Chapter 3.

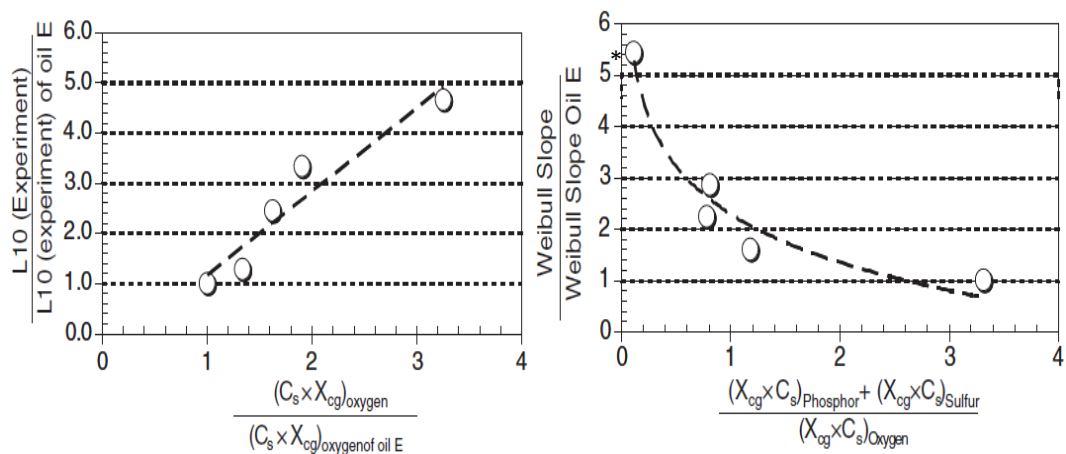


Figure 9-2. The influence of S and P concentrations in the reaction layers on the bearing fatigue lives (76). *Oil E is a lubricant formulated using a mineral oil base stock and consists of complex S-P additives. X_{cg} is the effective thickness of the reaction layer and C_s is the concentration of the corresponding element at the top surface

The reduced rolling fatigue life has been suggested to be due to the chemical attack of the reactive additives which can induce crack or pit nucleation (19, 70, 73, 77). Furthermore, in Chapter 5 the WLI images from the wear scar showed that the reaction of ZDDP with the steel surface induces greatly roughened interface in the wear scar of the roller surface with the roughness values of up to three times of the initial surface roughness. The rough interface, generated by ZDDP tribochemical attack to the steel surface, can lead to higher asperity-asperity contacts leading to an enhanced micropit

nucleation. The enhanced iron sulphide formation observed in the crack-initiated region (Figure 5-16) evidences the impact of high additive reactivity on pit nucleation. Interestingly the tribofilm formation in the area where crack initiation occurs is different from other parts of the FIB sample in which no cracks were observed. In contrast to the region without a crack, Zn greatly contributes to the bulk of the tribofilm (shown in Figure 5-16), mostly as zinc (poly) phosphate together with zinc sulphide. The different tribofilm elemental distribution near to the crack initiation site is not reported in the literature. In addition, XPS depth profiling could not detect a distinct layer on the interface implying a localised formation of the iron sulphide near the micropit. This supports previous studies (19, 114) which suggest localised enrichment of S traces around the pits. According to the results presented in Figure 9-3, Sakamoto (114) showed that the contribution of S which is derived from a S-P EP additive is enhanced in EDX and Auger spectra collected from a pit in comparison to a worn surface without pit.

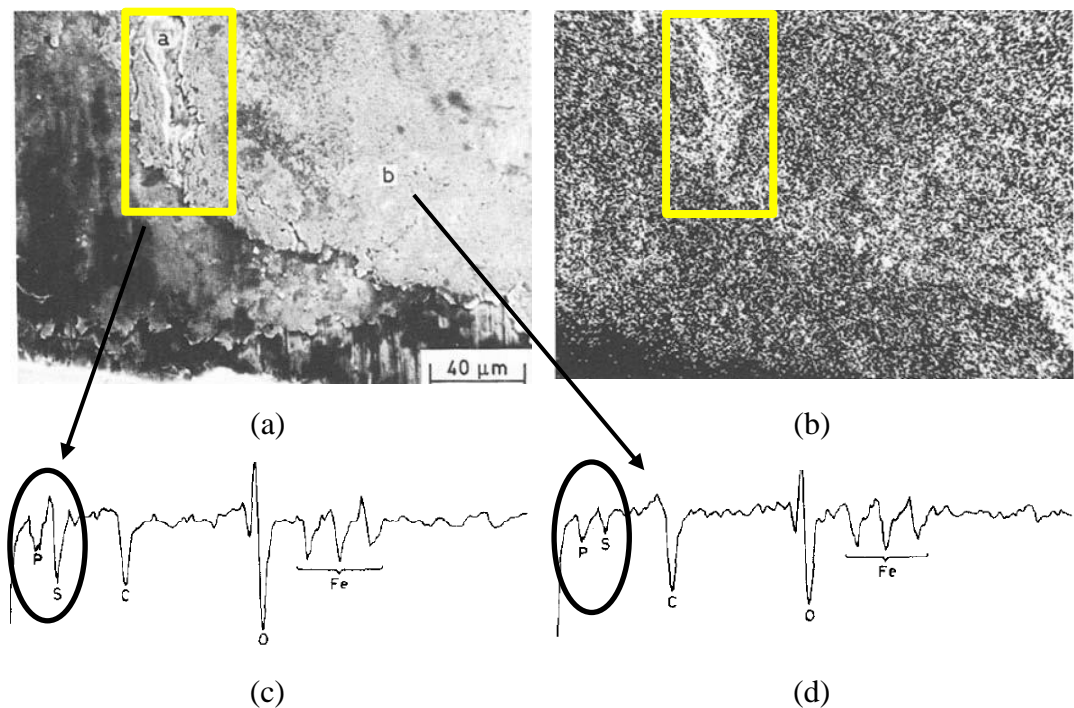


Figure 9-3. Enriched S concentration around the pitted area (114). a) SEM image of a worn surface under pure sliding b) S K α EDX map of the SEM image, c and d) Auger spectra collected from the pit (region a) and upper layer (region b) respectively after 90 min of argon ion sputtering

In agreement with the report by Sakamoto (114), the EDX-mapping results from the cracked site (Figure 5-16) show that in the tribofilm bulk, above the iron sulphide interfacial layer, S and Zn signals enhance at a same area implying an increased zinc

sulphide contribution to the tribofilm bulk associated with the cracked surface. The enhanced sulphide formation on the substrate and in the tribofilm bulk states an escalated S (re)activity in and close to the cracked site. Comparing the two mapped regions of the FIB lamella (Figure 5-14 and Figure 5-16), it is clear that the tribofilm is distributed unevenly on the surface of the roller and the thickness of the tribofilm varies from 20 nm to 100 nm. Thickness variation is probably due to the uneven wear on the surface resulting from localised surface damage. The laterally inhomogeneous nature of the ZDDP-tribofilm is also shown in Figure 5-11. The heterogeneous characteristics of the ZDDP-tribofilm throughout its depth and across wear scar is probably the reason behind the observed differences in the ZDDP-tribofilm parameters over contact cycles shown in Figure 9-1.

9.2.3 **Effect of the lubricant additive on surface cracks**

Alongside the iron sulphide formation induced by the interaction of the ZDDP elements and steel substrate, lubricant additives can also interact with surface initiated cracks (19, 106). Lubricants can enter the crack leading to an accelerated fatigue crack propagation by reducing the friction acting between the crack faces (44) or by exerting hydraulic pressure on the crack faces (44, 87). The ingress of large amounts of O and C into microcracks has been observed in a tapered roller bearing lubricated with base oil (240). Alongside base oil, additives also penetrate into the microcracks. Additive interaction with the crack faces has also been shown previously (106, 241-243). However, key understanding of this interaction with regard to reaction kinetics and chemical composition of the compounds derived from the interaction is missing. Also the effect of additive traces inside the microcracks on the crack propagation is arguable. Evans, More and Darragh (244) have not observed corrosive attack of S-P containing additives to the surface, unless the EP additive is highly active (245). On the other hand, several reports (19, 73, 75, 77-78) evidenced reduced fatigue life associated with enhanced tribochemical attack of additives.

In this work, the presence of the ZDDP elements inside the crack is clearly observed in the FIB lamella in the cracked region (Figure 5-16). Comparing the atomic-concentration-ratio of the ZDDP elements in the two mapped regions of the lamella (Figure 5-15 and Table 5-3), it is clear that the presence of S inside the crack is enhanced compared to the bulk of the tribofilm in agreement with the report by Meheux *et al.* (106) (Figure 3-45). The S to P atomic-concentration-ratio in the top

layer of the tribofilm is 0.6-0.7 as an average (according to the XPS results) and 0.3 in the bulk of the tribofilm. However inside the crack the ratio is always larger than 1 and reaching 2.9 at the crack-mouth which is greater than that of the ZDDP molecule ($\frac{S(at\%)}{P(at\%)} = 2$). The atomic concentration of the P and Zn at the mid-crack and crack-tip remained similar while no Zn was detected at the crack-mouth. In contrast to P and Zn, S atomic concentration is higher at the crack-mouth and decreases towards the crack-tip.

The affinity of the additive to interact with the crack faces and form a compound inside the crack can also be addressed through the electronic states of the molecules. At the crack tips where an increase in interatomic distance is large, due to the change in the Morse potential, activation energy of the reaction is decreased. Reduction in the required activation energy favours the reaction of the additive elements with the crack tip (109). As shown the concentration of S is high inside the crack favouring formation of iron sulphide compounds.

Iron sulphide in the presence of O can be oxidised to other types of iron sulphide (246) or magnetite iron oxide (132). While oxidation of the iron sulphide at high temperatures (around 500°C) can produce magnetite or iron oxide (which can occur in the flash temperatures happening in the asperity contacts), oxidation at the lower temperatures can lead to the conversion of iron sulphide to the other types of iron sulphides. The potentially detrimental influence of the chemical interaction of the additive with the microcracks can be considered as SCC. SCC can be induced by penetrated oil and additives (109, 211) which reduce the self-healing ability of the crack (241) and accelerate crack propagation in the presence of small amounts of water and O (211). Since iron sulphide is electro-conductive, localised formation of the iron sulphide around the pit or crack can induce localised electrolytic corrosion inside the pit (iron as an anode) in the presence of electrolyte (water) forming a local electrochemical cell (246). In other words, iron sulphide in the presence of water and O, depending on the pH of the local environment, can react to generate iron hydroxide + sulphuric acid or ferrous iron + sulphate + acidity (247). Sulphate and acidic reaction products can enhance SCC. Water ingress into the crack can be expected by considering capillary crack condensation (CCC) hypothesis (146). The CCC suggests that a small amount of dissolved water can induce a significant amount

of condensed water inside the microcracks (146). These phenomena can be addressed as stress corrosion crack propagation effects of the additive elements, especially S.

Also, the presence of additive elements inside the crack as tribofilm may reduce the friction coefficient between crack faces (248) and hence suppresses adhesion of the crack faces under rolling contacts which results in accelerated crack propagation (44). In agreement with the results in this study, the enhanced existence of the S at the crack tip was observed for the lubricant formulations with shorter fatigue lives (106, 248) which supports the SCC effect of S on the microcracks.

EP additives are also present in the lubricant formulations used to lubricate wind turbine gearboxes. As discussed in section 3.3, EP additives are S based compounds and hence the sulphur from EP additive can intensify the SCC activity of ZDDP which is observed in this study.

In contrast to the SCC negative influence, interaction of the additives with the surface and microcrack can have a beneficial impact. It is postulated that formation of the tribofilm earlier than crack initiation, as shown in Figure 9-4, can act as a sticking plaster which mitigates crack propagation (106). Furthermore, if traces of ZDDP elements inside the crack are recognised as tribofilm (248), SCC can be mitigated leading to an alleviated SCC effect.

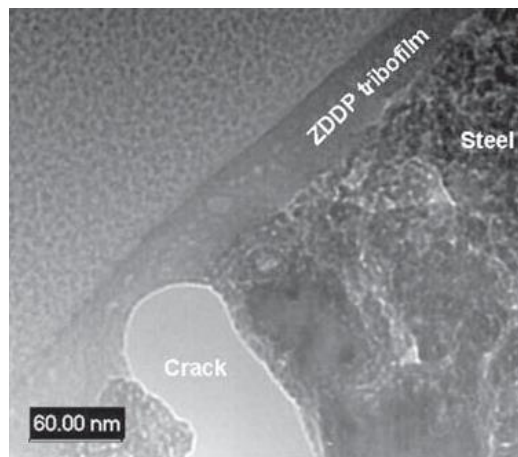


Figure 9-4. A TEM image presenting the postulated behaviour of ZDDP-tribofilm in reducing the crack propagation by acting as a sticking plaster (106)

However, the effect of water on ZDDP tribofilm removal (148, 151) and hydrolysis (133, 164-165) should also be acknowledged. In other words, if the water

in the lubricant is considerable enough to remove the tribofilm, the SCC can be intensified as a result of reactive sulphur species regardless of ascribing the additive elements inside the crack to an additive-derived film or traces of additive decomposition products.

In summary, S from ZDDP can attack the steel surface forming iron sulphide which is protecting the surface from scuffing and abrasive wear. On the other hand, localised iron sulphide formation can behave as a micropit nucleation site. Moreover, interaction of the additive elements with the crack faces and tip can induce SCC and accelerate fatigue crack growth.

9.2.4 Proposed mechanism for ZDDP-induced micropitting

The mechanisms, which are proposed to induce micropitting are detailed in Table 9-1. It is accepted that micropitting originates from surface asperities and defects. Also, it is shown that superfinishing the surfaces mitigates micropitting (104). However, superfinishing engineering-surfaces, especially bearing and gear components, is a time-consuming process and is not always economically practical. Moreover, surface defects (peaks) exist even on superfinished surfaces. Therefore, high roughness only accelerates micropitting.

Table 9-1. The micropitting mechanisms proposed in the literature

Author	Proposed mechanism
Oila <i>et al.</i> (79) and Swahn, Becker and Vingsbo (84)	Phase transformation and martensitic decay
Mahmoudi <i>et al.</i> (103) and Webster (82)	High contact pressure
Laine <i>et al.</i> (8) and Benyajati <i>et al.</i> (6)	Preventive influence of ZDDP on proper running-in wear
Laine <i>et al.</i> (8) Webster (82) Oila <i>et al.</i> (79) and Swahn <i>et al.</i> (84)	High roughness and low lubricant-film thickness
Torrance <i>et al.</i> (19), wan <i>et al.</i> (73), Pasaribu <i>et al.</i> (76), de la Guerra Ochoa <i>et al.</i> (9) and Meheux <i>et al.</i> (106)	Detrimental chemical reactivity of lubricant additives

The microstructural decay of the steels used in gearboxes and bearings is induced by high contact pressure and is inevitable within tribological contacts. The bearing steel (52100) is already a hardened steel and further hardening can result in a brittle steel which fractures due to lack of toughness. Hybrid bearings with ceramic roller

elements or raceway rule out the influence of microstructural decay and hence mitigate micropitting (38). However, reactivity of the lubricant additives with the ceramic surfaces to form an AW film is considerably lower than steel surfaces.

Therefore, optimisation of the tribochemical phenomena involved in micropitting is crucial. As far as micropitting is concerned, Laine *et al.* (92) attributed the enhancing properties of ZDDP to its preventive effect on proper running-in wear of the rough surfaces (Figure 3-43). However, considering solely the additive influence on running-in, cannot justify the O'Connor's (7) results showing that micropitting performance significantly depends on the chemical structure of the additives (Table 3-2). Furthermore, the difference between roughnesses of counterbodies in the tests with base oil and base oil + ZDDP after the tests is around 100 nm, while loss of diameter in the test with base oil was less than 10 μm and around 150 μm in base oil + ZDDP (shown in Figure 3-43). Therefore, the severe micropitting happening with ZDDP-containing lubricant cannot be justified by considering only the influence of ZDDP on running-in wear.

According to what is discussed so far a multi-parameter mechanism can be suggested for micropitting which is schematically shown in Figure 9-5. In Figure 9-5 (b) a typical ZDDP tribofilm is shown before a micropit initiates which consists of long chain zinc polyphosphates on top layer together with a thin layer of zinc/organo sulphides in agreement with the literature (127). Long chain polyphosphates accommodate shear stresses (124). As soon as a severe contact occurs between the asperities of contact-mates, a crack initiates which is associated with a phase transformation in the near-surface area (79). Simultaneously, in the cracked zone, where the phosphates tribofilm is removed, organosulphide species attack the nascent surface (122) which is exhibited in Figure 9-5 (c). Following tribochemical interaction between the sulphur species and the surface, a rough iron sulphide layer forms on the interface (Figure 5-7) which acts as a pit nuclei (19) and hence promotes micropitting initiation. As shown in Figure 5-16, in the tribofilm bulk, above the iron sulphide interfacial layer, S and Zn signals enhanced at a same area implying an increased zinc/organo sulphide contribution to the tribofilm bulk associated with the cracked surface. The enhanced sulphide formation on the substrate and in the tribofilm bulk states an escalated S (re)activity close the cracked site which resulted from severe contacts (114) and phosphate disruption. As a consequence of higher S activity,

sulphur species ingress into the crack resulting in SCC as discussed in 9.2.3. These changes to the tribofilm are demonstrated in Figure 9-5 (d).

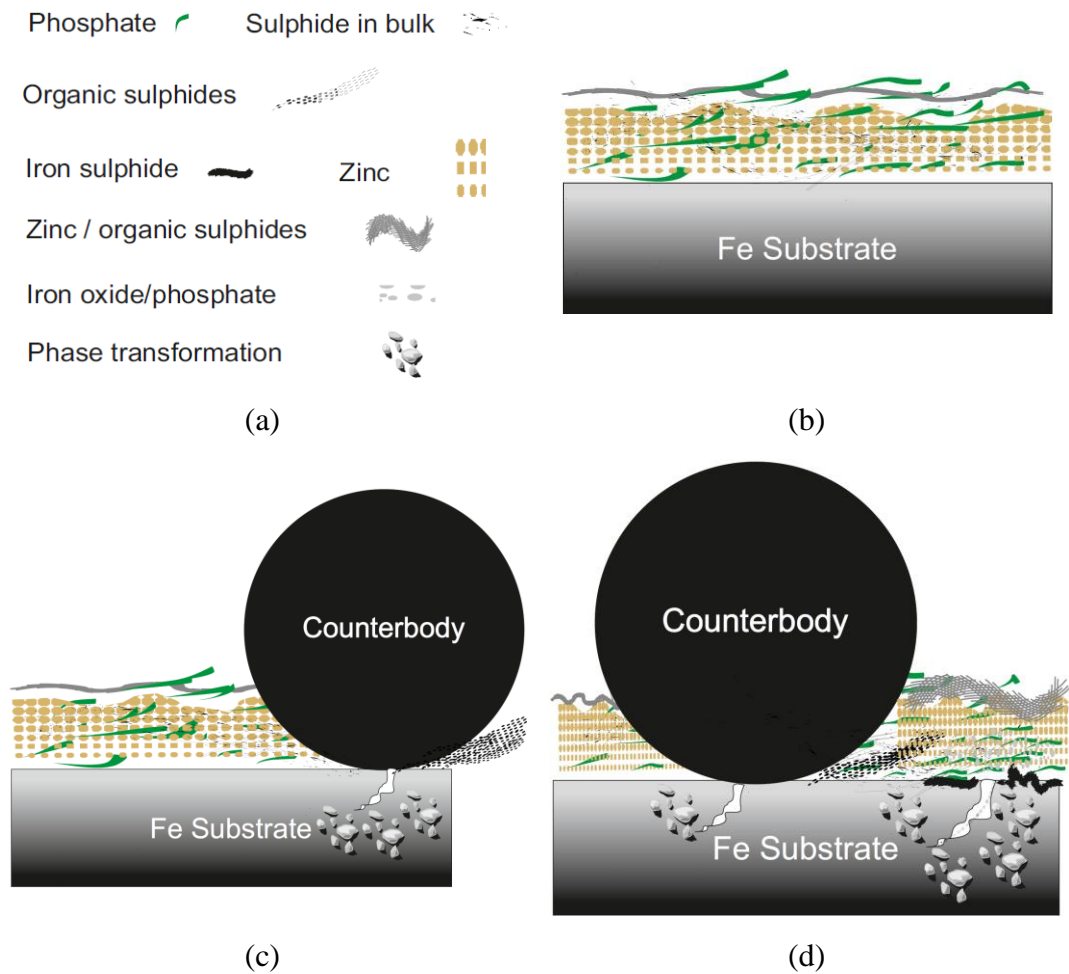


Figure 9-5. Schematic illustration of ZDDP-induced micropitting. a) illustration of features in schematics and corresponding compounds b) a ZDDP-tribofilm before crack initiation, c) a severe asperity-asperity contact and crack initiation, d) tribochemical change to the ZDDP-tribofilm and micropitting propagation

Moreover, due to the wear of the surfaces, iron oxides and/or iron phosphates are formed near the surface and polyphosphates depolymerise to shorter (zinc/iron) phosphates (127). The short chain (zinc/iron) phosphates are expected to be harder (201), probably due to the accumulation of residual compressive stresses (105), and hence are more shear-resistant. The depolymerisation of the ZDDP-tribofilm to a shear-resistant zinc (or mixed zinc and iron) short polyphosphate in the wear process is expected due to iron oxide digestion (122) or substrate iron ion diffusion to the tribofilm (105). In addition, an interfacial iron sulphide layer is postulated to make the tribofilm more durable on the surface (124). Although the durable, hard and shear-resistant tribofilm is a desirable layer for wear protection, it

induces accumulated local plastic deformation which leads to micropitting (101). Furthermore, it is shown that the ZDDP-tribofilm hinders lubricant entrainment into the contact zone (184). As presented in Figure 7-7, the deteriorated lubricant entrainment results in enhanced frictional forces in the contact interface (184). High frictional forces strongly influence micropitting propagation (92) and initiation through promoting localised plastic deformation. Therefore, S tribochemical activity accelerates micropitting initiation and propagation. Also, hard and short chain (zinc/iron) phosphates (Figure 9-1) and the tribofilm's tendency to impede lubricant entrainment (Figure 7-7) promote micropitting initiation and propagation. Severe tribological conditions such as high contact pressure and high roughness enhance the chance of asperity-asperity contacts and microstructural decay leading to accelerated micropitting.

9.3 Understanding the tribological and tribochemical influence of water as a lubricant contaminant on micropitting surface fatigue

The correlation between ZDDP and micropitting wear is discussed mechanistically in the previous section. This section discusses the mechanism by which water-contaminated lubricant intensifies the micropitting-enhancing behaviour of the ZDDP-tribofilm.

Water contamination is common in wind turbine gearboxes which shortens bearing life and can be a cause for the prevalence of micropitting in wind turbine bearings (3). Water can ingress through vents and mechanical seals and the maximum amount of the dissolved water in the wind turbine lubricants is reported to be 300-500 ppm depending on the base oil and additive package (23). The dissolved water amounts as a result of RH values examined in this study vary between 100-220 ppm which are below the reported maximum values.

9.3.1 The effect of dissolved water

The tribological and tribochemical effects of addition of 1% water to BO + ZDDP lubricant formulation at 90°C are summarised in Figure 9-6 using the information provided in Chapter 6. As can be seen, addition of water to ZDDP-containing lubricant amplifies the micropitting-enhancing properties of the ZDDP tribofilm. Addition of 1% water leads to an approximately 18% increase in the micropitting surface area.

Addition of water brings about a decrease in P 2p_{3/2} BE and BO/NBO ratio and results in an increase in O/P, Zn/P and S/P ratios and Zn 3s – P 2p_{3/2} ΔBE. The changes in all tribochemical parameters conform to each other and indicate a decrease in phosphate chain length of the tribofilm. In addition, the increase in Zn/P and S/P ratios implies enhanced zinc sulphide formation in the tribofilm.

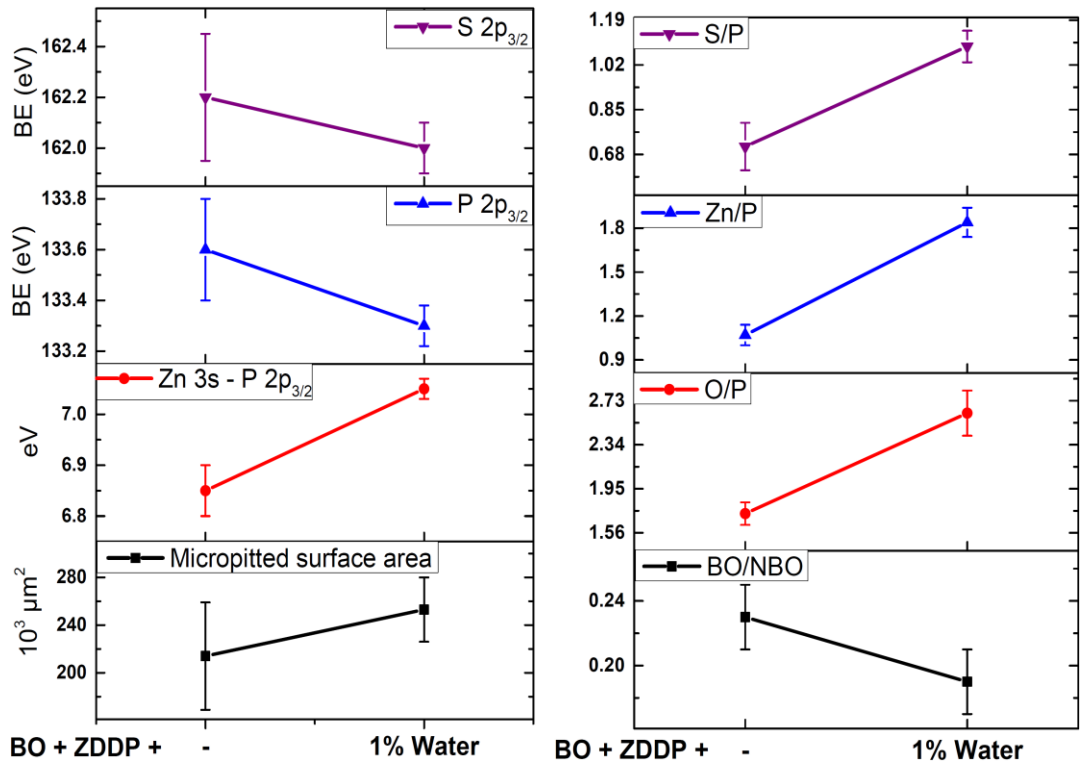


Figure 9-6. The effect of water on micropitting and relevant tribochemistry at 90°C

Figure 9-7 is plotted using the information provided in Chapter 6 and represents the tribological and tribochemical influences of water and RH on micropitting at 75°C relative to the increase in the water saturation level. Although, the detrimental effects of water on the RCF (146, 158-159, 162) and ZDDP AW performance (148, 151) have been addressed, the influence of water and ZDDP-containing oil dispersion on specifically micropitting and detailed tribochemical understanding is not universally understood. Furthermore, the literature does not differentiate the impact of free water from that of dissolved water on micropitting. Therefore, this section mechanistically discusses the effect of water on the ZDDP-enhanced micropitting.

As can be seen in Figure 9-7, the micropitted surface area proportionally increases with an increase in water saturation level. Also, an increase in water saturation level in the lubricant brings about a decrease in the ZDDP-tribofilm thickness and

P 2p_{3/2} BE. The effect of water and humid environments on decreasing the ZDDP-tribofilm thickness and phosphates BE has been reported previously (148, 151) in agreement with results in this project. Furthermore, the presence of abrasive marks in the wear scars of lubricants is enhanced in respect to an increase in dissolved water level. The decrease in P 2p_{3/2} BE can be explained considering the increase in O/P ratio in the (poly)phosphate chain which leads to an increase in partial positive charge on each P atoms (249). Therefore, a decrease in P 2p_{3/2} BE implies the presence of shorter chain (poly)phosphates in the ZDDP-tribofilms of the lubricants with dissolved water. The ZDDP-tribofilms generated under humid environments and from lubricants with added-water have an inferior BO/NBO ratio, greater ratios of Zn/P and O/P, higher Zn 3s - P 2p_{3/2} BE difference and greater α' values which confirm the effect of dissolved water on decreasing the (poly)phosphate chain length in the ZDDP-tribofilm. The tribofilm from BO + ZDDP (RH 90%) shows the least P 2p_{3/2} BE and BO/NBO ratio and a significant increase in the O/P ratio compared to tribofilms from the other lubricants. This indicates that the tribofilm from the lubricant with which has the highest level of the dissolved water, has the shortest (poly)phosphate chain length.

The enhancing impact of water and humidity on inducing mild wear at the edge of the wear scars and abrasive wear can be explained by HSAB theory which is established by Ho and Pearson (250-251) and well-implemented to ZDDP by Martin (122). Abrasive wear can be induced through hard metallic oxide (iron oxide) wear particles in the lubricant which are originated from the steel substrate. Iron oxide is a harder Lewis acid compared to zinc-oxide in zinc (poly)phosphate glass. Therefore, in compliance with HSAB the zinc (poly)phosphate glass can eliminate iron oxide wear particles through a chemical reaction to form iron phosphates and zinc oxide. In addition, a thicker tribofilm and longer-chain (poly)phosphates (hard base) in the ZDDP-tribofilm have a superior potential to digest iron oxide wear particles and avoid abrasive wear compared to a thinner and shorter-chain (poly)phosphate. Water and humidity induce thinner and shorter-chain (poly)phosphate ZDDP-tribofilm.

As far as the ZDDP molecule in the lubricant is concerned, water in the lubricant can attack the Zn atom and induce a hydrolytic reaction (164, 252-253). The rate of hydrolysis depends on the size and nature of the alkyl group (primary or secondary) (253) and the lubricant polarity which affect the availability of the Zn atom to the water attack. The final product of the hydrolytic reaction can be phosphoric

acid (252-253) which hinders polyphosphate formation. Therefore, tribofilm formation in the presence of water is mitigated through the hydrolytic effect of water leading to a thinner tribofilm formation in the presence of water.

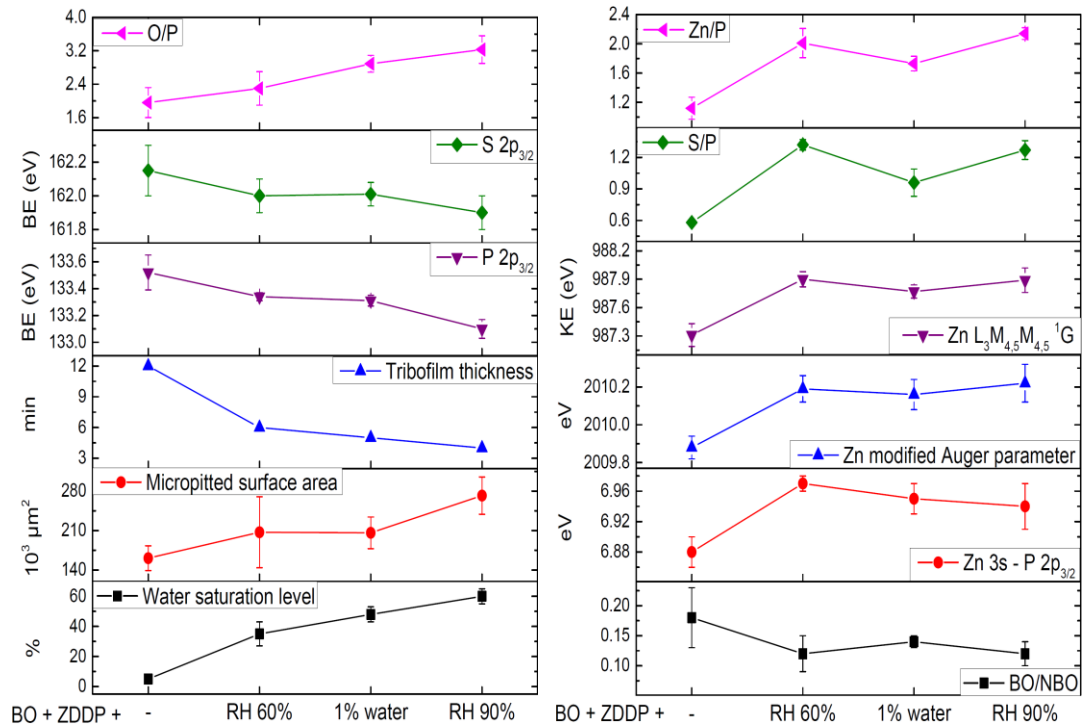


Figure 9-7. The effect of water and humid environments on micropitting and relevant tribochemistry at 75°C

Furthermore, it has been suggested that absorbed water in the lubricant depolymerises the long-chain (poly)phosphates in the thermal/tribo film to the short-chain (poly)phosphates (165). This can be the case especially in the event of high contact pressure and shear stress (199, 201). As shown in Figure 6-8, the absorbed water to some extent (approximately 5% of the lubricant-water-saturation), is present in the BO + ZDDP lubricant formulation which can have a catalytic influence on short-chain (poly)phosphate formation. Thereby, an increase in the dissolved water level accelerates water hydrolytic effect leading to a shorter-chain (poly)phosphate.

Also, as shown in Figure 6-16, the P concentration, corresponding to (poly)phosphate, is significantly decreased throughout the depth of ZDDP-tribofilms with dissolved water compared to the test in lab conditions. A thinner ZDDP-tribofilm formation having a shorter chain (poly)phosphate with less (poly)phosphate contribution to the tribofilm bulk is the reason behind the emergence of the abrasive wear and mild wear

at the edge of the wear scars lubricated with the lubricants containing added-water or under humid environments.

Higher ratios of Zn/P and S/P in the ZDDP-tribofilm induced under humid environments and lubricants with added-water can be observed in Figure 9-7 which can be an indication of an enhanced formation of zinc sulphide in the ZDDP-tribofilms of the lubricants with dissolved water (151). The Zn $L_{3}M_{4,5}M_{4,5} 1G$ in zinc sulphide appears at higher Kinetic Energies (KE) (lower binding energies) compared to zinc oxid (195, 215), thereby an increase in Zn $L_{3}M_{4,5}M_{4,5} 1G$ (KE) (Figure 9-7) might be an indication of enhanced zinc sulphide formation. Also, an increase in α' in Wagner plot also can suggest that zinc sulphide formation is partly enhanced (215). Therefore, changes in Zn/P and S/P ratios, Zn $L_{3}M_{4,5}M_{4,5} 1G$ (KE) and α' values can represent the states of Zn in the ZDDP-tribofilm. The Zn/P and S/P ratios alter with a similar trend with respect to the dissolved water level. In addition, Zn $L_{3}M_{4,5}M_{4,5} 1G$ (KE) and Zn modified Auger parameter (α') follow a similar trend to that of the Zn/P and S/P ratios (see Figure 9-7). The trend observed for Zn/P and S/P ratios, Zn $L_{3}M_{4,5}M_{4,5} 1G$ (KE) and α' shows greater zinc sulphide formation in the ZDDP-tribofilm of the lubricants with dissolved water. Also, it can be suggested that the effect of the humidity on enhancing zinc sulphide formation is more influential than that of added-water in the test conditions used in this study.

The importance of zinc oxide in the ZDDP-tribofilm and ZDDP-thermally decomposition products can be addressed due to its ability to inhibit ZDDP hydrolysis (254-255). Burn, Dewan and Gosney (254) showed that zinc oxide which is generated from breakdown of basic ZDDP to normal ZDDP inhibits the hydrolytic activity of water as shown in Figure 9-8. The normal ZDDP molecules undergo a complete hydrolytic breakdown within approximately 9 h (Figure 9-8 a). However, under the same conditions, the corresponding basic form requires 9-10 days for a complete hydrolysis (Figure 9-8 b) due to the zinc oxide product. The normal ZDDP which is generated from basic form did not undergo hydrolysis until a complete elimination of the basic form.

Although an increase in Zn 3s - P 2p_{3/2} BE difference for the lubricants with dissolved water is an indication of a shorter (poly)phosphate chain, as can be seen in Figure 9-7, the Zn 3s - P 2p_{3/2} BE difference is not following the trend of P 2p_{3/2} BE. This is arisen from the change in the Zn states which affects the Zn 3s BE. Therefore, the

Zn 3s – P 2p_{3/2} BE difference is influenced by the change in (poly)phosphate chain length and Zn states. As a result, in the lubricant formulations where a shift in the Zn states is expected, the Zn 3s - P 2p_{3/2} BE difference is not a self-sufficient parameter in order to determine the (poly)phosphate chain length.

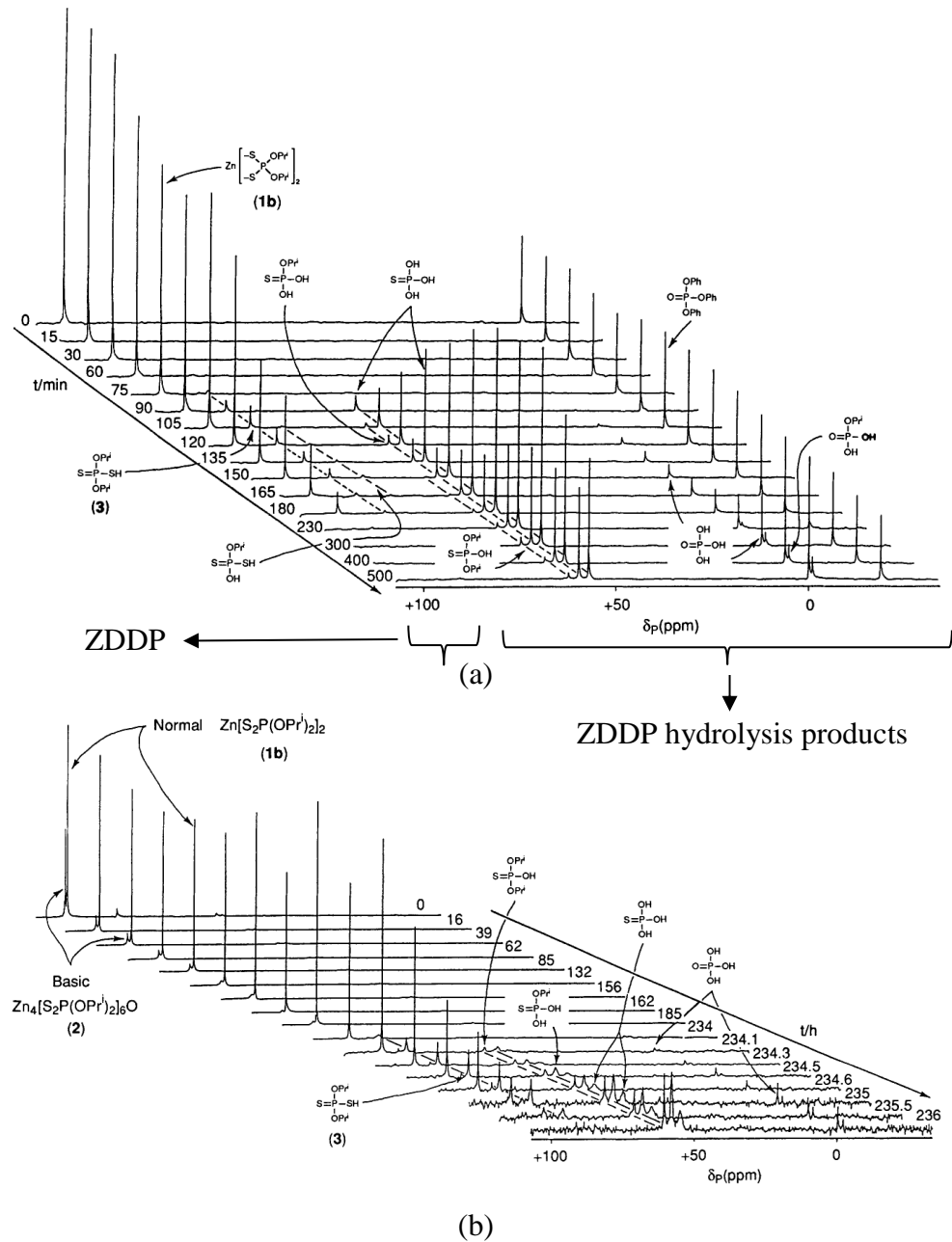


Figure 9-8. Hydrolysis investigation of a) normal and b) basic forms of zinc di-isopropyl dithiophosphates using nuclear magnetic resonance spectroscopy in 1,2-dimethoxyethane solvent at 85°C in the presence of 6 vol% water (254)

As discussed in section 3.5.9, Brizmer *et al.* (18) have observed a decrease in micropitting in tribocorrosive environments. Results presented in this study are not contradictory to those observed by Brizmer *et al.* (18). As shown in Figure 9-9,

Brizmer *et al.*'s work (18) elucidates the influence of wear coefficient and boundary friction on micropitting. In their study (18) the increase in RH from 20% to 60% enhanced wear coefficient by a factor of seven as highlighted in Figure 9-9 using black circles. In contrast to that and as shown in section 6.2.3, changes in the wear volume occur within the ranges of standard deviations from average values and the average total wear volumes changed by a maximum value of 40% for the tests at 75°C. Also as shown in section 6.2.4, changes in the friction coefficient are not considerable. Therefore, the increase in micropitting surface area by the dissolved water is not induced by changes in friction and/or wear in the test conditions used in this study. Accordingly, the addition of a tribochemical term to the Brizmer *et al.*'s model (18) can be suggested that takes tribofilm thickness and composition into account.

The cross sectional profiles presented in sections 6.2.2.1 and 6.2.2.2 suggest an approximate material removal of 200 nm in the wear scars where no micropitting is apparent. If this is considered as the central wear groove depth in Brizmer *et al.*'s model (18) and all assumptions explained in the model are relevant to the conditions defined in this study, the coefficient of fully-lubricated wear can be estimated to be 6.3×10^{-10} which is pointed by black arrows in Figure 9-9. As shown in section 6.2.2, the average micropitting surface area varies between $161 \times 10^3 \mu\text{m}^2$ and $283 \times 10^3 \mu\text{m}^2$ and the approximate wear scar width is 1.5 mm and consequently the micropitting surface fraction varies between 10% and 17%.

With the coefficient of boundary friction values close to 0.08 in this study, the model suggests a micropitting surface fraction between 15% and 25% in the wear scars after 720K contact cycles which is in a good agreement with the experimental results. The fraction of boundary-lubricated area is assumed to be 0.14 which is the value that the model predicted for $\lambda = 0.15$. In fact, the lubrication conditions in this study are more severe ($\lambda = 0.05$) which lead to lower values for coefficient of lubrication wear and hence lower micropitting surface fractions. Furthermore, the micropitting surface fraction values indicated here using Figure 9-9 are estimated for surfaces after 720K contact cycles, while the micropitting surface area in this study is evaluated for surfaces after 10^6 contact cycles. The increase in the number of contact cycles is shown to enhance the micropitting surface area (47). Therefore, the values indicated in this section are estimated values and are not produced by the actual model.

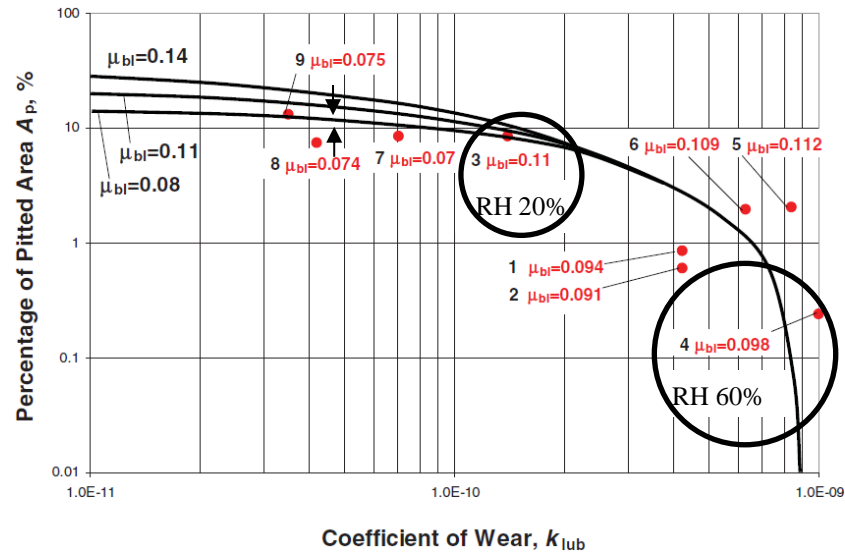


Figure 9-9. The influence of boundary lubrication friction and wear on micropitting after 720K contact cycles. The model is run for contact pressure of 1.5 GPa, $\lambda = 0.15$, lubricant temperature of 75°C and the counterbody roughness of $R_q = 500$ nm. The solid lines and the dots represent the results of the model and the experiments, respectively. μ_{bl} stands for boundary friction and the model yielded a fraction of boundary-lubricated area of 0.14 for the given λ .(18)

9.3.2 The effect of free water

In contrast to the observations when dissolved water is present, micropitting is not observed in free water conditions. As shown, dissolved water prompts thinner ZDDP-tribofilm formation and enhances mild and abrasive wear. In free water conditions ZDDP-tribofilm formation is totally hindered and mild wear exceeds micropitting wear. Therefore, micropitting propagation is suppressed and nucleated micropits will be immediately worn out by the accelerated mild wear. This mechanism of micropitting elimination by mild wear is schematically presented in Figure 9-10.

A similar competition mechanism between mild wear and micropitting is proposed by Cen (102) and Morales-Espejel *et al.* (47). Extending the tribological contact to 10^6 contact cycles, the water saturation level fell below 100% (Figure 6-8) and dissolved water condition will dominate the contact. As observed in Figure 9-7, the micropitting is enhanced under dissolved water conditions and the lubricant with a greater dissolved water shows intensified micropitting in the wear scar. The average micropitted surface area in the wear scar of the roller lubricated with 3% water-containing lubricant is $283 \times 10^3 \mu\text{m}^2$ which has the largest micropitting surface area among the all lubricants tested at 75°C showing an approximately 75% increase in micropitting compared to micropitting in BO + ZDDP.

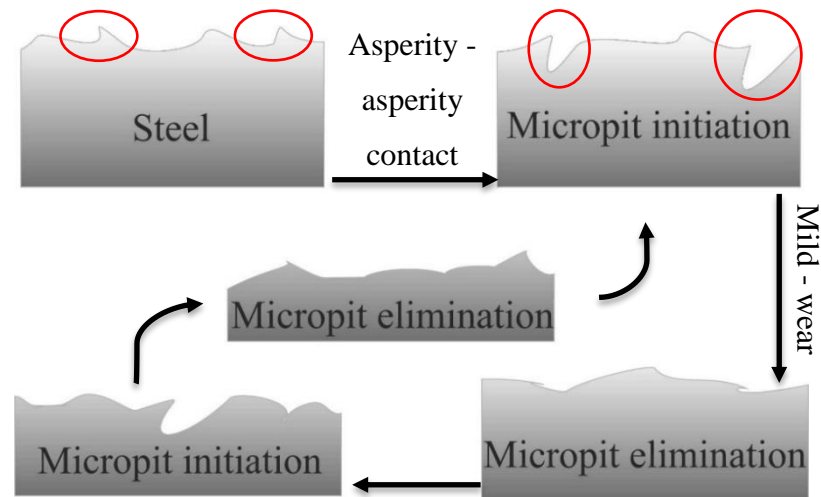


Figure 9-10. Immediate elimination of the initiated micropits by mild-wear in free water conditions

9.3.3 The micropitting mechanism in tribocorrosive environments

As shown in Chapter 6 micropitting nucleation is enhanced in the presence of water and humidity and micropits can be observed spread out across the wear scars. The dissolved water contamination is common in wind turbines operating in humid environments. Accordingly, the results in this study suggest that micropitting might be accelerated in off-shore wind turbines. As discussed in 9.3.1, dissolved water hydrolyses tribofilm to induce thinner and shorter chain phosphates. The ZDDP-tribofilm enhances micropitting incidences at the contact zone having highest contact pressure (Figure 6-2) and promotes micropitting propagation. On the other hand, the ZDDP-tribofilm is an interfacial layer which assists in maintaining the contact bodies separated and accommodating contact pressure. Therefore, the thinner ZDDP-tribofilm leads to a higher probability of asperity-asperity contacts and consequently promotes micropitting nucleation.

Also, mild wear in the wear scars of the lubricants with the dissolved water increases the contact area which leads to nucleation of micropits across the wear scar and expansion of the micropitting nucleation to the edge of wear scar (as can be seen in Figure 6-6). Therefore, in tribocorrosive conditions micropitting initiation is due to the deteriorated action of the tribofilms in preventing asperity-asperity contacts.

As shown in Chapter 6, although water enhances micropitting nucleation, the micropits are smaller in size. Also, as discussed in 9.2.4, shorter chain phosphates can promote localised plastic deformation if phosphates become stable through iron

sulphide interfacial layer. However, it has been shown that water in oil significantly decays the stability of ZDDP-tribofilm through impairing the tribofilm adherence to the substrate (169). This is due to the chemical-localised etching (169) or hydrolysis effects of water on tribofilm and also adsorption-competition between water molecules and ZDDP molecules (or decomposition products). Therefore, as tribofilm is less durable in tribocorrosive conditions, propagation of micropits is less pronounced. Furthermore, the smaller micropits can also be attributed to mild wear which is intensified in tribocorrosive conditions (section 9.3.1). As indicated in section 9.3.2 mild wear can attenuate micropitting propagation.

9.4 Mitigation of micropitting-enhancing behaviour of ZDDP by utilising NCAs

NCAs are categorised as OFMs. In the current time, the understanding on the mechanism of action of OFMs and their interaction with the ZDDP as the most well-known additive is limited. Organometallic friction modifiers such as MoDTC are widely used in lubricants especially in engine applications (12, 256). MoDTC is shown to diminish ZDDP-induced micropitting using standard PCS MPR (92). However, using modified-MPR it has been shown that MoDTC does not effectively mitigate micropitting (102). Furthermore, the downside of MoDTC is formation of MoO_x (most probably MoO_3) as a reaction product which acts as an abrasive hard metal-oxide particle (257). Moreover, MoDTC aggravates the SAPS content in the lubricant, while OFMs are additives with no SAPS content. Thereby, NCAs as effective ashless OFMs are of a great interest.

9.4.1 The influence of NCAs on the steel surface

OFMs are believed to reduce the friction on the surfaces through adsorption or chemical-reaction on the metal surfaces using their polar heads as shown in Figure 9-11. With the concentrations used in the lubricant formulations in this project, the OFMs usually form monolayers on the rubbing surfaces (258). Depending on the chemical structure of polar heads in OFMs, an increase in the concentration of the OFMs leads to generation of OFM multilayers on the rubbing surfaces as shown in Figure 9-11 (a), although multilayer formation of OFMs is not expected to take place in the case of TDP and TA (231, 258-259). Therefore, it is expected that TDP and TA

form adsorbed layers on the steel in the form of monolayers on MTM and MRR specimen surfaces.

The adsorbed layers have anti-compressive characteristics which assist in separating the rubbing surfaces (260). The anti-compressive behaviour of the film depends on the chain length of non-polar moiety and its degree of unsaturation, pack-density (surface coverage) of the OFM on the surface and number of OFM layers on the surface (259, 261). Variety of forces are playing role in the adsorption of OFMs on the iron oxide surface, some of which are demonstrated in Figure 9-11 (b).

The interaction of amines with steel surfaces is a combined physiosorption and chemisorption process (259, 262-263). The chemisorption occurs through a process in which the lone electron pair of N is donated to the Fe^{3+} ion (231) (Figure 9-12 (a)). The adsorbed molecular tilt angle is shown to be 40° - 60° from the surface (231, 264). The N coordinates to the positive sites of the iron oxide and hydrogen to the negatively charged sites (264) as shown in Figure 9-12 (b). The tilt angle can also be influenced by contact pressure. It can be assumed that under large contact pressures the tilt angle in NCAs is reduced and the tallow chain might tilt closer towards the surface (265). The smaller tilt angle of the molecule relative to the metal surface blocks more sites which are available for the adsorption of the other additives and results in load-dependent properties of NCAs.

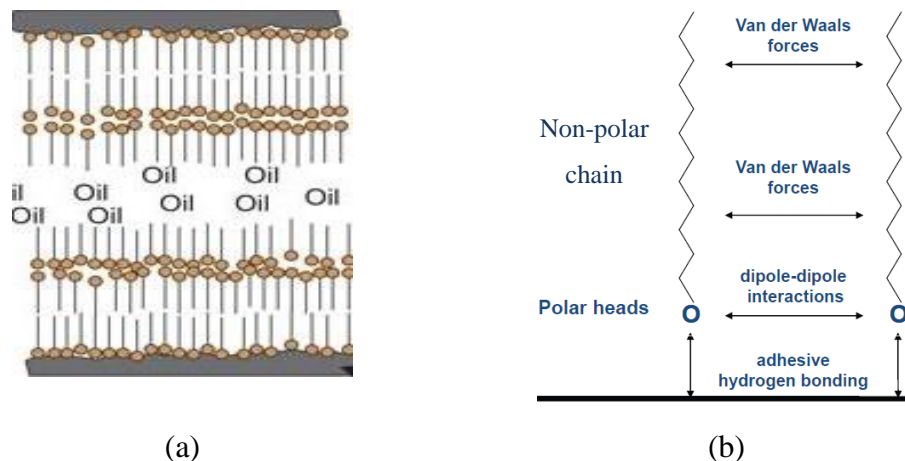


Figure 9-11. Schematic illustration of OFM interactions with metal surfaces.
a) Multilayer (260) b) suggested bonds in OFM adsorption process (261)

The packing density is strongly influenced by van der Waals interactions between the hydrocarbon chains (265) of the adsorbed NCA molecules. Thereby, the stronger and the more van der Waals forces between methylene groups of neighbouring saturated-alkyl chains lead to higher load-bearing capacities of the monolayer. This justifies the

greater friction reduction capability of the OFMs having longer chain alkyl group (266) resulted from greater van der Waals forces. Also, the greater van der Waals forces in closely-packed monolayers results in an increase in the friction with respect to the increase in load (267) which is induced due to the greater repulsive forces between the terminal methyl groups of the opposing monolayers on the surfaces which are rubbed against each other. The extent of van der Waals interactions depends on hydrocarbon chain length and its unsaturation level.

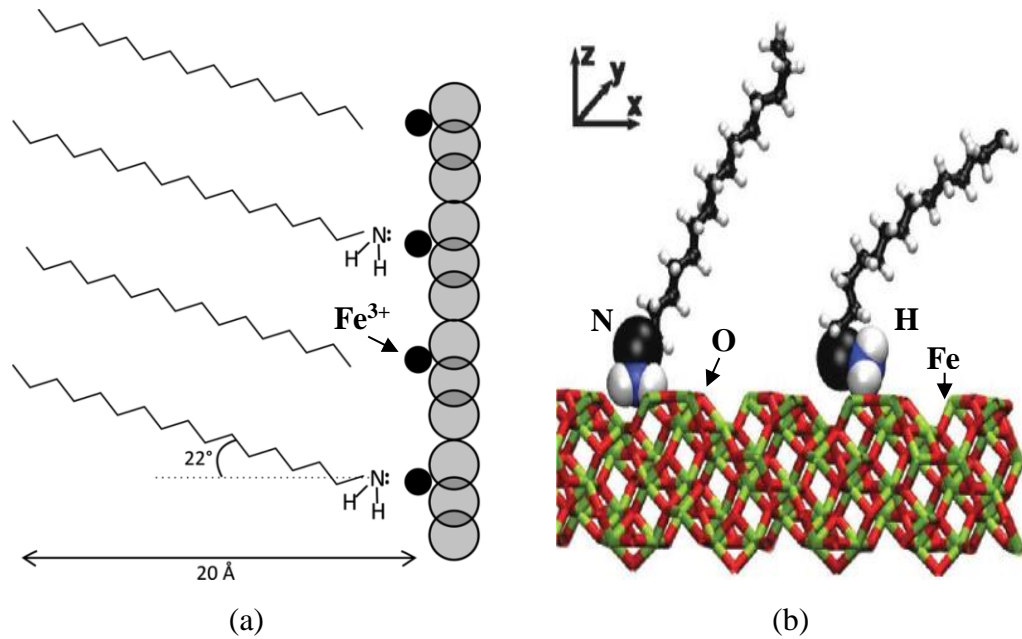


Figure 9-12. Schematic illustrations of proposed adsorption patterns of hexadecylamine on iron oxide surface a) (231) b) (264)

The tallow alkyl chain has a cis to trans ratio of 8-20 (268) which indicates the presence of several kinks in the alkyl chain group depending on the relative position of cis bonds in the alkyl chain. Figure 9-13 shows a kink induced by cis bonding for fatty acids with the same chemical formula but different molecular structures. The kinks in the alkyl chain's back bone can reduce the packing density of the adsorbed molecules on the surface (269) and affects the friction performance of OFMs (270). The kinks in the hydrocarbon chain generally reduce the interactions between hydrocarbons of different molecules in the adsorbed monolayer (271) which can reduce the load bearing capacity of the adsorbed layer. The unsaturated bonds in the tallow chain with cis configuration might induce pressure-dependent performance as they reduce the van der Waals interaction between neighbouring molecules and can consequently result in the hydrocarbon chains being tilted towards the surface blocking free surface available for the other additives. Thereby, the thinner tribofilms

formed on MPR rollers (Figure 8-14 and Figure 8-20) compared to tribofilms on MTM specimens (Figure 7-3 and Figure 7-8) might be attributed to the higher contact pressure used in MPR tests.

The presented adsorption mechanisms shown in Figure 9-12 correspond to the hexadecylamine molecule which does not have unsaturated bonds within its hydrocarbon chain. In molecular structures like TA and TDP in which unsaturated carbon bonds (C=C) exist, the adsorption mechanism most probably is the same but with an alteration in the orientation of hydrocarbon chain and a decreased monolayer packing-density. N atoms in amines are partially negatively-charged due to having higher electronegativity (~3) compared to the C atoms (~2.5). Therefore, amines can impose nucleophilic properties on the basic iron oxide surface.

The adsorption of ETA is more complex as a consequence of the OH group. In ETA, two adsorption pathways can be assumed. One results from N and iron cation interaction and the second interaction results from the hydroxyl group which can be a weak hydrogen bonding (OH in ETA with O in iron oxide) (Figure 9-11 (b)) or a strong chemical bonding of O in ETA and iron in iron oxide surface layer.

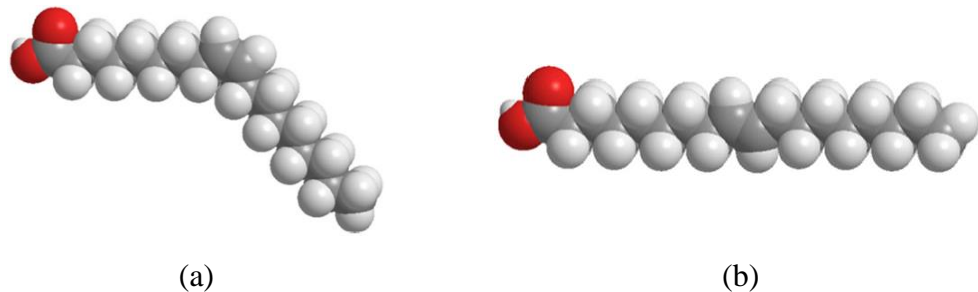


Figure 9-13. Illustration of cis and trans isomers of fatty acids with the same chemical formula. a) structure of oleic acid and the kink induced by cis bonding and b) the trans isomer of oleic acid (elaidic acid) (269)

The mentioned mechanisms elucidate the adsorption in the static conditions. It has been shown that rolling contacts can trigger thicker and more robust OFM layers on the steel and enhance the friction performance (272). This effect is attributed to stacking of the molecules from the solution (272). Thus, rubbing, especially a rolling contact, enhances the interaction of NCAs with the steel surface (259).

In a report (171) using MTM smooth specimens in the absence of ZDDP, it has been suggested that amine OFMs are not effective in friction reduction on the steel surface at the start of the test. As can be seen in Figure 9-14 all the friction modifiers to some extent reduce friction on the steel surfaces which is indicative of the OFMs adsorption

on the steel. Polycondensed Fatty Acid ester (PFA) shows greatest friction reduction which is due to highest polarity enabling PFA to strongly bond to the surface. However, most stable friction behaviour at the start of the test and after 2 hours of rubbing (comparing Figure 9-14 a and b) can be observed for amine, amide and MoDTC FMs. This suggests that amine is capable of protecting the surface as an AW additive.

The results in Chapter 8 showed that the AW behaviour of the amine is enhanced by an increase in amine concentration and stimulated by high contact pressures. It is probable that amines adsorb on the surface and tilt towards the surface to form a protective layer rather than standing up. This layer supports the oil entrainment into the contact by its orientation which is aligned with the shear stress direction. The hydrophobic alkyl chain of the amine also provides an oil-retention property for the contact.

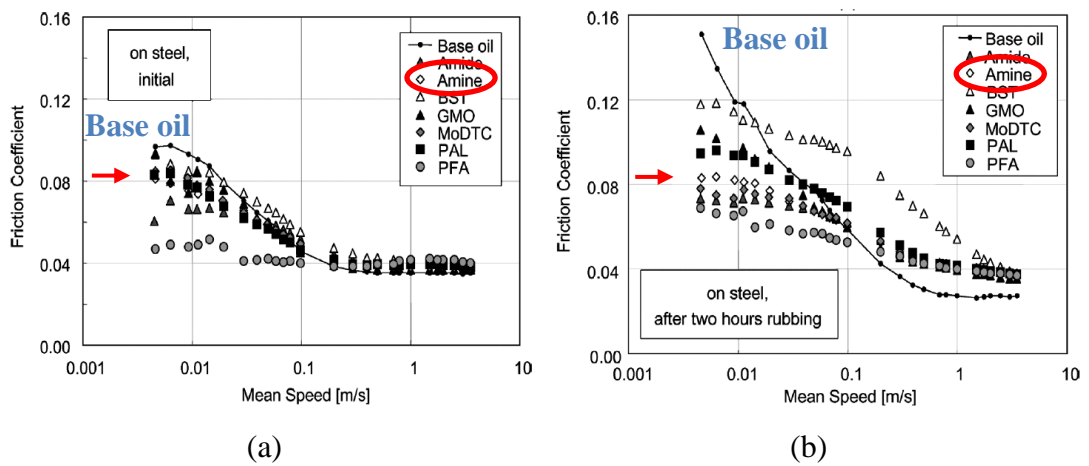


Figure 9-14. Stribeck curves in base oil + OFMs and MoDTC measured a) at the start of the test and b) after two hours of rubbing under a contact pressure of 0.95 GPa, SRR of 50% and an entrainment speed of 100 mm/s at 100°C (171)

9.4.2 The influence of NCAs in combination with ZDDP

In an application where AW additives are not present in the lubricant formulation, the friction efficiency of OFMs, to a considerable extent, depends on adsorption of OFMs on the surface. However, AW additives as an essential lubricant additive has to form a sacrificial layer on the surface and thus the OFMs are required to adsorb on the AW film to fulfil their friction reduction function. Miklozic, Forbus and Spikes (171) studied the friction performance of the same FMs shown in Figure 9-14 in combination with ZDDP which is presented in Figure 9-15.

As can be seen in Figure 9-15, PFA is no longer able to reduce the relatively high boundary friction possessed by the ZDDP-tribofilm after 2-hours of rubbing. MoDTC reduces the boundary friction at the start of the rubbing while after 2-hours of rubbing is not as effective as it was at the start of the test. The most effective OFMs are amide and amine which can mitigate friction-enhancing behaviour of the ZDDP throughout the test in agreement with the results shown in Chapter 7 and Chapter 8. It is shown that the combination of ZDDP with amine/amide lead to a considerably thin tribofilm on the surface in agreement with the results shown in Chapter 7 and Chapter 8.

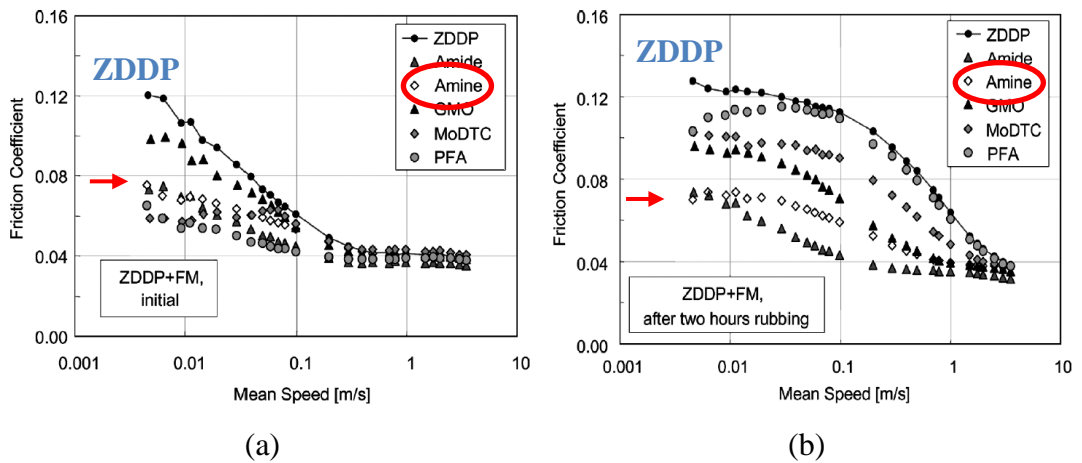


Figure 9-15. Stribeck curves measured a) at the start of the test and b) after two hours of rubbing in oil blends of OFMs and MoDTC friction modifiers blended to a ZDDP containing base oil. The tests were carried out under a contact pressure of 0.95 GPa, SRR of 50% and an entrainment speed of 100 mm/s at 100°C (171)

9.4.3 The interactions between NCAs and ZDDP

In the presence of ZDDP in the lubricant, N can act as a ligand having a lone pair of electrons in hybridized sp^3 orbital (273) as shown in Figure 9-16.

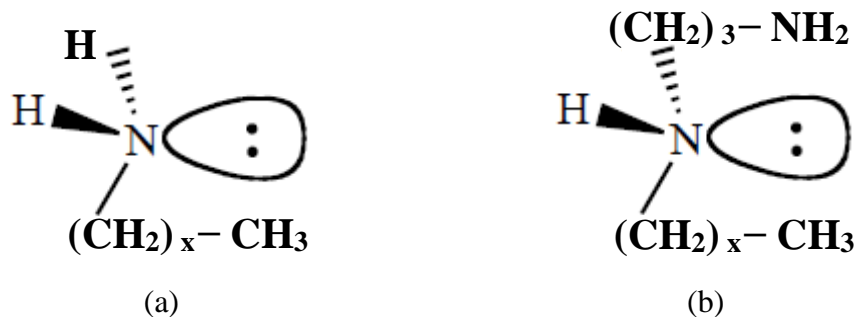


Figure 9-16. Illustration of the chemical states of N atoms in a) TA and b) TDP (274)

Amines as ligands can form MCs with the Zn atom in ZDDP (175). Therefore, in the absence of ZDDP, amines adsorb on the surface of iron oxide, while in the presence

of ZDDP in the lubricant formulation, N atom (s) in amines can induce a MC formation together with the Zn atom in the ZDDP molecule (175). The simplified illustration of the MC formation in the ZDDP + NCAs solution is shown in Figure 9-17. The chelate type of MC with a 5-membered ring is the most stable chelate compound (275) although 4, 6 or 7-membered rings can also be formed. Therefore, the 6-membered chelate in ZDDP+TDP may not be stable. Also, the steric hindrance imposed by long-tallow alkyl chain in NCAs probably favours 1:1 MC formation in NCAs used in this study.

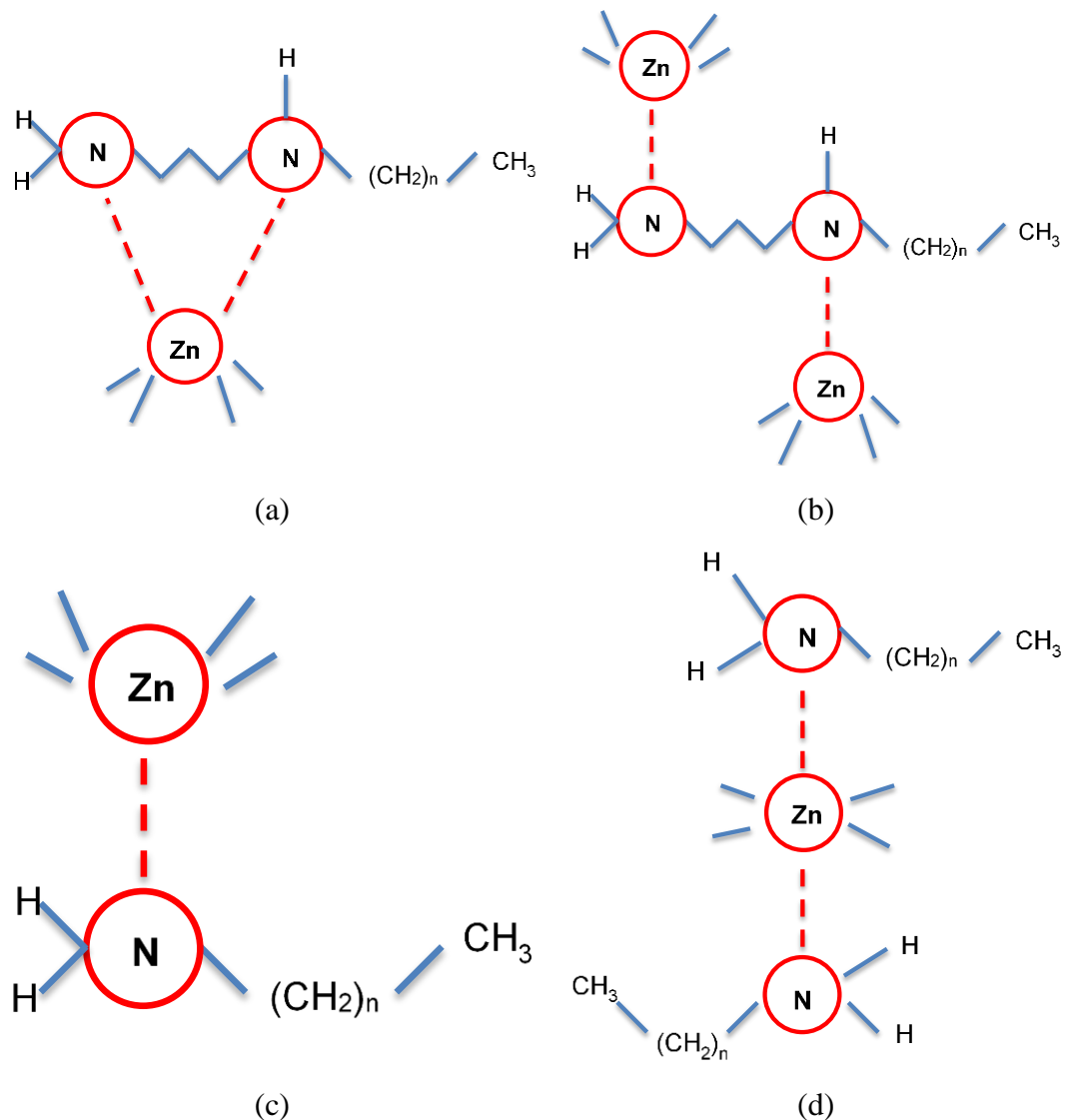


Figure 9-17. Metal complex formation in a and b) ZDDP + diamine solutions and c and d) ZDDP + amine/diamine solutions. Illustrations of a) chelate MC, b) bridge-type MC, c) 1:1 MC and d) 2:1 MC formation through interactions between amine/diamine and ZDDP (175)

The AW film formation in the ZDDP + OFMs lubricant formulation is believed to be governed by competitive adsorption of ZDDP and OFM molecules on the

surface (171, 175-176, 276). A rapid and strong adoption of OFM molecules on the surface blocks the sites on which ZDDP decomposition products can adsorb and nucleate ZDDP-tribofilms. The metal surface can be exposed to the ZDDP decomposition products through removal of OFMs from metal surface due to shear stress and wear in the tribological contact leading to ZDDP-tribofilm formation.

In the case of NCAs the interactions between ZDDP and NCAs in the bulk lubricant may induce further delay in the ZDDP-tribofilm formation. The generated MCs lead to a reduction in the concentration of free ZDDP molecules. In addition, the generated MCs are large molecules which results in larger steric hindrance and inferior adsorption on the surface.

9.4.4 NCAs and their delaying impact on ZDDP-tribofilm formation

Figure 7-3, Figure 7-8 and Figure 7-9 showed that the delaying effect of TA is stronger than that of TDP. This can be explained considering the chemical structure of the TA and TDP. TA has a smaller molecular structure indicating that TA can adsorb more easily on the metal surface due to having less steric hindrance. In addition to that, Siegel, Herrera and Cappelle (277) showed that diamine has a greater dipole moment (μ_b) compared to amine while μ_b in diamine is not twice the μ_b in amine. Dipole moment is a value, expressed in terms of Debye unit (10^{-18} statcoulomb-centimetre), which represents the polarity of a molecule (278). The polarization of a molecule results from the bonds between the atoms which have different electronegativity values and hence a more polar molecule has a larger dipole moment (278). Since μ_b in diamine is not twice the μ_b in amine and the dipole moment in diamine associates with two N atoms, the partial negative charge (δ^-) density on N atom in amine is superior to δ^- density on the terminal N atom in diamine. This suggests an enhanced adsorption of amine (TA) on the surface. As a result, the TA molecules more rapidly adsorb on the surface leading to a greater delaying effect. The ETA has hydroxyl groups which makes it both a basic and acidic substance. However, ETA donates H^+ easier than OH^- which results in being a strong nucleophile and a weak electrophile. Therefore, it preferentially adsorbs on the metallic surfaces (coordinating to the positive sites e.g. iron cations) and forms a densely packed monolayer (258). The more densely packed nature of ETA and stronger nucleophilic characteristic of ETA compared to TDP and TA are the reasons behind its enhanced

delaying effect on ZDDP tribofilm formation and also thinner tribofilms (Figure 7-3, Figure 7-8 and Figure 7-9). The interaction of ZDDP molecule with ETA in the bulk lubricant might also affect the adsorption kinetics and extent. The hydroxyethyl group ((CH₂)₂OH) in ETA exerts large steric hindrance on the N which might reduce the extent of complex formation between Zn and N resulting in more free ETA to adsorb on the surface and hence decays ZDDP-tribofilm formation. A certain degree of delay in AW film formation might be beneficial in the wind turbine bearings as it can improve the running-in through polishing wear which partly smoothens grinding marks on the bearing surfaces.

9.4.5 **Interaction of NCAs with the (poly)phosphates in ZDDP-tribofilm**

Amines are strong bases. According to Brønsted–Lowry theory (279) amines, having a lone electron pair, can bind to a proton (H⁺) to form R-NH₃⁺ (conjugate acid). The basicity of amines depends on the availability of the lone electron pair (278, 280) and thus is influenced by the R (hydrocarbon) chain type (alkyl group provide greater basicity compared to aryl groups) and length. Also, based on HSAB theory H⁺ and (di)amine are a hard acid and base, respectively. Thereby, formation of ammonium ions as a result of a chemical interaction between H⁺ and (di)amine can be expected. In Chapter 7 and Chapter 8, XPS results suggest formation of (ionised)-(di)-AP which is an indication of acid-base reaction between phosphate from ZDDP-tribofilm and (di)amine conjugate acid. Also, TDP, which provides two lone electron pairs per molecule, enhanced the formation of (ionised)-(di)-AP compared to TA (Table 7-1 and Table 8-2).

Ammonium phosphate has been used as the phosphate source in the preparation of zinc phosphate glasses (199, 281) and iron phosphate glasses (282-283). Contributions of ammonium phosphate (177-178) and AP (221) to the phosphate chain in tribofilms induced by lubricants containing ZDDP and dispersants have been reported using XANES and XPS (222). The AP is formed through reaction of the pyrolytically dissociated amine group and decomposed ZDDP (221). This confirms the contribution of the NCAs to the phosphate chain as (ionised)-(di)-AP and indicates the chemical interaction between NCAs and ZDDP-derived (poly)phosphates.

NH₄⁺ (R-NH₃⁺) is a hard Lewis acid and based on HSAB theory it can react with hard bases such as (poly)phosphates. The orthophosphates are believed to be harder bases

compared to polyphosphates (127) and hence ammonium ions are expected to have a higher affinity to the shorter (poly)phosphates. Furthermore, formation of ammonium cations enhances the cation concentration in the lubricant leading to depolymerisation of the long (poly)phosphates (122, 177) or suppressed polyphosphate formation. Therefore, it can be assumed that ionised-(di)amines depolymerise the longer (poly)phosphate chains which preferentially exist on the top-layer in ZDDP-tribofilm patches (105, 127, 145, 284-285) and subsequently react with the shorter phosphates in the bottom layers of the ZDDP-tribofilms. The mentioned reactions lead to removal of patches in the ZDDP-tribofilm resulting in a smooth and thinner tribofilm formation (Figure 8-11 and Figure 8-12).

Formation of an oxide interface on the roller surface lubricated with BO + ZDDP + TDP is confirmed employing TEM-EDX in Chapter 8 (Figure 8-14 and Figure 8-15). It has been suggested that shorter chain (poly)phosphate formation, induced by tribological contacts and native iron oxide digestion, enhances the adhesion of tribofilm to the substrate (286). It is probable that the high affinity of ammonium ion to (poly)phosphates suppresses the chemical reactions between phosphates and the native oxide (or other oxides formed under tribological contacts) which results in a less adherent tribofilm on the surface. The less adherent tribofilm shears off the surface resulting in a dynamic tribofilm removal and formation process as shown in Chapter 7 and Figure 8-13. A hard oxide interfacial layer on the steel surface and a less shear resistant and smooth tribofilm on the surface suppress the local plastic deformation properties of the ZDDP-tribofilm resulting in a reduction in micropitting.

9.4.6 **The impact of test parameters**

As observed in Chapter 7 the delaying time, tribofilm thickness and friction reduction efficiency which are prompted in NCA-containing lubricants depend not only on the additive chemistry and its concentration in the lubricant but also on the contact conditions. Increased severity of the tribological contact by employing a rougher disc specimen in the MTM set-up decreases the delaying time and increases the tribofilm thickness in all lubricants (Figure 7-3 and Figure 7-8). This indicates that intensified contact severity favours the ZDDP reactivity with contact surfaces and adsorption of the NCAs on steel-surfaces is hindered by ZDDP's dominant action on the surface. However, the degree of reactions on the interface of ZDDP-tribofilm, which leads to

ZDDP-tribofilm removal, follows the same trend as observed for SS configuration since the overall tribofilm thickness decreases in the following order: $TDP \geq TA > ETA$.

With the increased contact severity the friction reduction capability of ETA is significantly reduced while TDP/TA are not considerably affected. This indicates that ETA is effective on the steel surface, while TDP and TA perform well both on ZDDP surface as well as steel surface. The mentioned behaviour of ETA originates from the hydroxyl group in its chemical structure as discussed in 9.4.1, 9.4.3 and 9.4.5 sections.

The contact severity in MTM SR configuration ($\lambda = 0.035$) and MPR ($\lambda = 0.04$) test set-ups is similar considering the Lambda ratios in the contact. The lubricant temperature was set to 90°C and the smoother specimen (roller in MPR and ball in MTM-SR) on which the tribofilms are inspected is slower in speed compared to the counter-body in both test set-ups. The SRR is 5% and 2% in MTM-SR and MPR, respectively, which is not expected to cause a considerable difference in the tribofilm thickness and composition. Two profound dissimilarities between two test set-ups are contact pressure and entrainment speed. The contact pressure employed in MPR (1.5 GPa) is 50% larger than contact pressure in MTM (1 GPa). Therefore, it can be assumed that under the larger contact pressure (1.5 GPa) the reactivity of NCAs is escalated over ZDDP both on metal surface and on ZDDP-tribofilm. The influence of load on defect formation in monolayer films i.e. decrease in monolayer thickness and change in chain tilt is shown by Salmeron (265). Therefore, it can be assumed that a larger load applied in MPR set-up triggers the activity of the NCAs which complies with the load-dependent nature of NCAs as discussed in 9.4.1 and 9.4.2 sections and Chapter 8.

An increase in friction coefficient with the increase in the sliding speed has been often observed for OFMs (270, 272, 287-289) in which the alkyl chains are fully-saturated and linear including amine-based OFMs (289) as presented in Figure 9-18 (a). However, the unsaturated alkyl chain in the amine structure makes the OFM independent of sliding-speed to some extent, in certain sliding-speed ranges (10^{-4} to 10^{-7} ms^{-1}), which is shown in Figure 9-18 (b) (270). Therefore, tallow chain which consists of unsaturated alkyl chains is anticipated to be more responsive to the contact load rather than sliding speed.

The configurations of MPR and MTM tribometers substantially differ from each other affecting the lubricant (and additives) entrainment manner. In MPR, the lubricant is supplied into the contact by means of rotation of two lower rings. However, in MTM the contact zone is fully immersed in the lubricant. The different lubrication systems employed in the MPR and MTM might influence the tribofilm's thickness and composition. The probable impact of lubrication systems employed in MTM and MPR on tribofilm thickness and composition is not addressed in the literature and is complex to interpret, although this is a factor which should not be easily ignored and might be of an interest to future works.

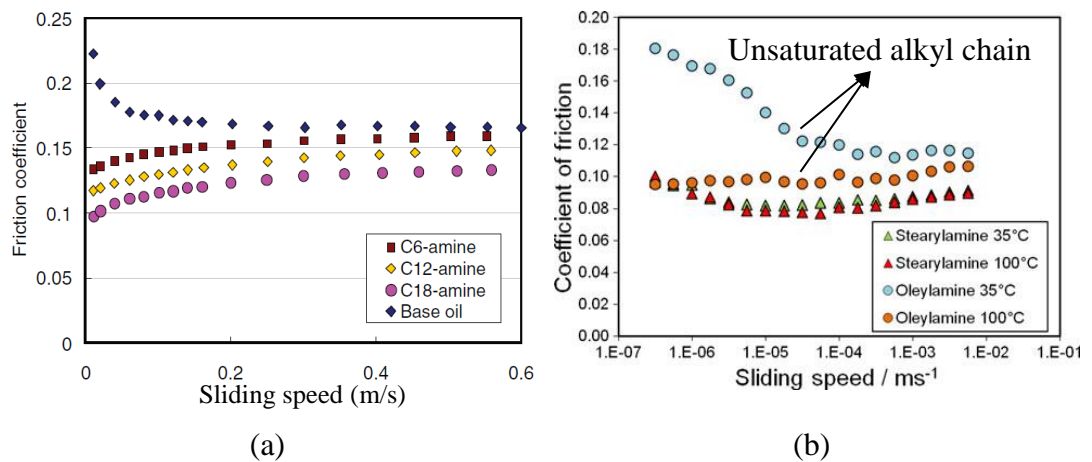


Figure 9-18. The influence of sliding speed on frictional properties of a) linear amines blended to a base oil at concentration of 1wt% under mean contact pressure of approximately 3 MPa at 100°C (289) and b) 0.01 M stearylamine (saturated amine) and oleyl amine (unsaturated amine) in hexadecane under mean Hertzian contact pressure of 0.69 GPa (270)

9.4.7 The efficiency of NCAs in mitigating ZDDP-enhanced micropitting

Considering the findings presented in the results chapters, the schematic illustration of the tribofilms formed in the wear scar of the roller surfaces lubricated with BO + ZDDP and BO + ZDDP + TDP/TA are presented in Figure 9-19. Adsorption of NCAs onto the ZDDP-tribofilm and their chemical interactions result in less frictional forces on the interface by considering three principles. Firstly, the adsorbed NCAs onto the ZDDP-tribofilm and orientation of alkyl chains in TDP/TA facilitate lubricant entrainment into the contact (this is demonstrated in Figure 7-7 and Figure 7-11). Thereby, asperity-asperity contacts are decayed through an increase in the lubricant film thickness and anti-compression and AW characteristics of TDP/TA (this is exhibited in Figure 8-7).

Secondly, the chemical interactions of TDP/TA with phosphates on the top of ZDDP-tribofilm induce a smoother tribofilm in the wear scar (shown in Figure 8-11 and Figure 8-12 and discussed in 9.4.5). The friction-enhancing impact of the ZDDP-tribofilm, having fissures between the pads, is attributed to inhibition of lubricant entrainment into the contact arising from the rough and patchy nature of the ZDDP-tribofilm (171, 184, 227). Thereby, a smoother tribofilm promotes lubricant entrainment. Enhanced lubricant entrainment into the contact and less frictional forces provided by TDP/TA mitigates local plastic deformation and thus micropitting.

The third influence can be ascribed to a less adherent and shear-resistant tribofilm in the wear scar induced by TDP/TA which is derived from the chemical interactions of TDP/TA with the phosphates in the ZDDP-tribofilm and the steel surfaces. The adsorption competition between NCAs and ZDDP and their chemical interactions hinder sulphide attack to surface (as shown in Figure 8-14 and Figure 8-15) leading to a less adherent tribofilm on the surface according to what was discussed in sections 9.2.4 and 9.4.5. The less shear-resistant tribofilm can alleviate the micropitting-enhancing behaviour of ZDDP tribofilm.

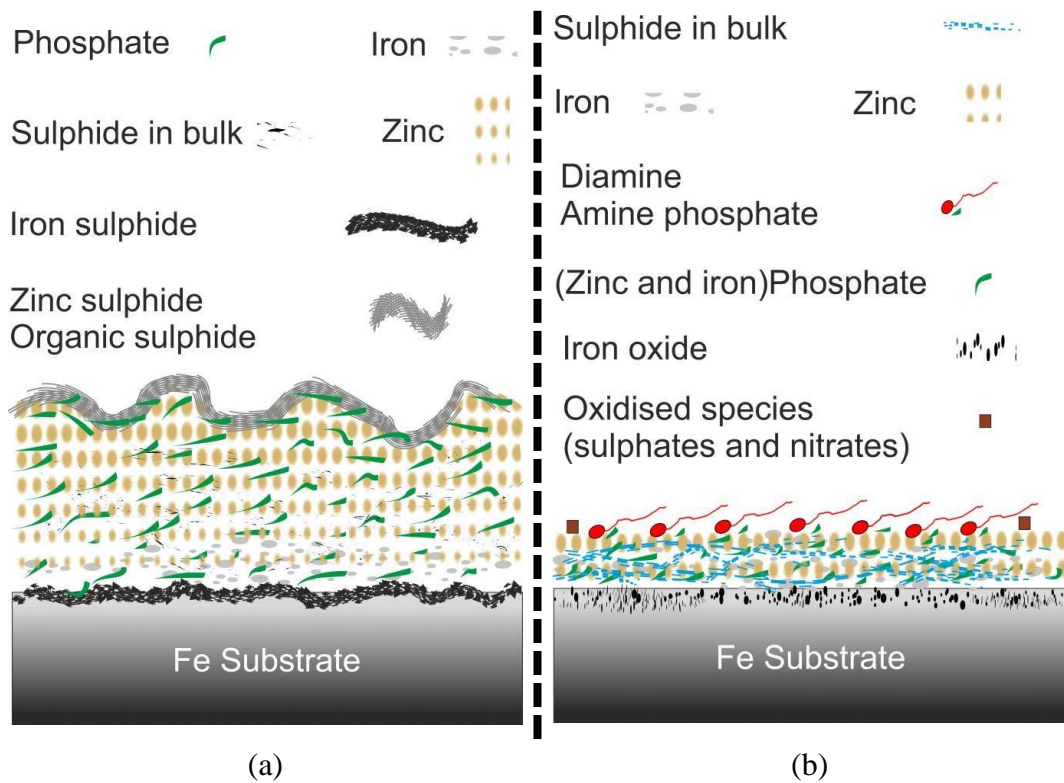


Figure 9-19. Schematic illustrations of the tribofilms formed on the surfaces of the MPR rollers lubricated with a) PAO + ZDDP b) BO + ZDDP + TDP/TA

Furthermore, the oxide formation on the interface of TDP/TA containing-lubricants (Figure 8-14) might have a beneficial impact on micropitting. An iron oxide interface is harder than iron sulphides. Therefore, iron oxide is expected to exhibit superior micropitting resistance properties. Also, as discussed in sections 9.2.3 and 9.2.4 enriched S ingress into cracks, induced by the ZDDP-tribofilm, triggers crack propagation, whereas Zn and O (probably as zinc oxide) are enriched inside the crack initiated on the surface lubricated with BO + ZDDP + TDP (shown in Figure 8-15). In addition, as shown in Table 8-3 the $S_{(II)}/P$ ratios of the tribofilms from TDP/TA containing lubricants are smaller compared to $S_{(II)}/P$ in the ZDDP-tribofilm which imply inferior S tribochemical attack to the crack surfaces.

Moreover, the relative contribution of O to P is substantially enhanced (Table 8-3) in tribofilms from TDP/TA on the top layer together with a comparatively escalated Zn/P ratio. This is in agreement with Pasaribu *et al.* (76) results showing superior RCF performance of the reaction layers having higher concentration of O rather than P. They attributed greater rolling contact performance to a passivated surface by oxide layers which can suppress further unfavourable surface reactions. The formation of an oxide interfacial layer in the tribofilm derived from TDP containing lubricant is confirmed by TEM results in Figure 8-14 and Figure 8-15.

However, it should be noted that oxide interfaces during wear incidents can introduce detrimental iron oxide wear particles to the lubricant causing abrasive wear (127). Also, as shown in Chapter 7 and Chapter 8, TDP and TA bring about inferior phosphate contributions to the top-layer and bulk of the tribofilms. As shown in Figure 8-2 and Figure 8-3, in some cases abrasive marks can be observed on the wear track of rollers lubricated with TDP/TA-containing lubricants which can be explained by HSAB theory. As elucidated in section 9.3.1, the thin tribofilms having less phosphate contribution resulted from TDP/TA which consist of short-chain (poly)phosphates cannot thoroughly digest the iron oxide wear particles. The iron oxide wear particles lead to abrasive wear which is a drawback of the TDP/TA lubricant formulations. Abrasive wear which is induced by three body particles (such as sand) or wear particles is detrimental to bearing's fatigue life in wind turbines. Therefore, use of NCAs in the wind turbine lubricants should be subjected to full-bearing tests in order to examine the extent of abrasive wear induced by the additions of NCAs.

Shorter chain phosphates from BO + ZDDP + TDP/TA lubricants can be induced within wear process (as discussed section 9.2.4) and also through TDP/TA reactions with the (poly)phosphates. Subsequent to the TDP/TA interactions with (poly)phosphates a thin and smoother tribofilm is formed. The smoother and chemically-modified tribofilm which offers less frictional forces, improved lubricant entrainment and a resistant oxide-interface layer accompanied with hindered S attack to the crack surfaces are the reasons behind micropitting reduction achieved by ZDDP + NCA formulations.

Chapter 10

Conclusions and future work

10.1 Overarching conclusions

In this thesis experiments have been carried out in order to obtain an overarching understanding of the tribochemical phenomena involved in ZDDP-induced micropitting. The micropitting surface area is quantified and tribochemical influence of water and humidity, as the most important lubricant contaminant in roller bearing applications, is examined. NCAs are employed to alleviate frictional forces and mitigate micropitting as a result of chemical interactions which occur between NCAs and ZDDP. The most prominent findings obtained from the experiments using the test conditions defined in this study are as follows:

1. Prior to this study, the early ZDDP-tribofilm formation which hinders proper running-in of the rough surfaces (8, 18, 105) and decay in the microstructure of steels are proposed to induce micropitting. The results in this study show an upsurge of S reactivity and its localised attack under severe conditions leading to an intensified iron sulphide formation and subsequent S ingress into the crack. The S to P atomic-concentration-ratio inside the crack is larger than 1 reaching 2.9 at the crack mouth which is greater than that of the ZDDP molecule ($\frac{S(at\%)}{P(at\%)} = 2$). The localised S attack acts as a pit nuclei and the interaction of the S with the crack faces and tip can induce SCC and accelerate fatigue crack growth. In addition, the lack of viscous and soft long-chain polyphosphates on the top layer of the ZDDP tribofilm as a result of its depolymerisation to shear-resistant zinc (or mixed zinc and iron) short polyphosphate enhances micropitting through accumulation of localised plastic deformations. Therefore, a substantial role of enhanced chemical attack of the additive-derived compounds especially sulphur species in micropitting-enhancing behaviour of ZDDP is put forward alongside attributing the behaviour of ZDDP to its tendency to impede lubricant entrainment.

2. The metallurgically cut specimen showed no evidence of contribution of non-metallic inclusions to the micropitting suggesting a surface initiated mechanism. This elucidates the strong influence of additives on micropitting.
3. The dissolved water in ZDDP-containing lubricant promotes micropitting nucleation through inducing a deteriorated ZDDP-tribofilm. A thinner tribofilm consisting of a lower contribution of zinc oxide and phosphates is observed in tribocorrosive conditions. The results show that the micropitting surface area and abrasive wear proportionally increase with an increase of dissolved water level in the test conditions used in this study.
4. Although dissolved water enhances micropitting nucleation and expands the nucleation across the wear scar, in free water condition micropitting feature is suppressed as a result of dominant action of mild wear.
5. Employing the NCAs, used in this study, in combination with ZDDP brings about promising tribological performances in rolling bearing applications. Results show reduction in frictional forces and micropitting.
6. All NCAs used in this study delay ZDDP tribofilm formation to a certain extent depending on its chemical structure and concentration in lubricant and induce a thinner reaction film compared to ZDDP alone lubricant.
7. All NCAs used in this study form nanometre-thick films resulted from adsorption and chemical reactions with phosphates from ZDDP leading to attenuated frictional forces and micropitting.
8. The wear and micropitting performances of NCAs strongly depend on the structure of their polar moiety. In general the more polar NCA (ETA) has a stronger influence on friction reduction (in MTM SS and MPR configuration) especially in less severe contacts (MTM SS) but is less effective in micropitting reduction. This is most probably due to the strong interaction of the more polar molecule with the steel surface which hinders available surface for ZDDP interactions. Moreover, the more polar molecule (ETA) strongly enhances wear on the surface in severe MPR tests.

9. The most promising overall performance was observed for TDP when employed at concentration of 1 wt%. TDP has shown to perform as AW additive when blended to BO, reduce friction and protect surface in the region of largest contact pressure.
10. TDP in combination with ZDDP has shown to form a smooth tribofilm capable of alleviating micropitting and friction-enhancing properties of ZDDP. TDP forms a reaction film (less than 10 nm) on top of ZDDP tribofilm leading to attenuated frictional forces on the surface.
11. The steel-tribofilm interface in the TDP-containing lubricant is an oxide layer which is postulated to be more micropitting resistant. Furthermore, the aggressive interactions of S with crack faces are restrained by the enriched presence of Zn and O compounds inside the crack.

In conclusion, a careful selection of NCAs with a tailored concentration successfully impedes micropitting while protecting the surface from wear simultaneously. Thus NCAs are favourable additives in rolling-element bearing applications when employed meticulously.

10.2 **Future work**

10.2.1 **Identification of the chemical nature of the compounds inside the crack**

EDX mappings obtained from the FIB lamellas show the elemental composition and distribution of the reaction layers. It is important to further understand the reactions happening inside the crack when elements from additives or additive's decomposition products ingress into the crack. Therefore, a TOF-SIMS chemical analysis can be performed on the FIB lamella in order to discern the chemical composition of the reactive layer inside the crack. The chemical composition of compounds inside the crack and interface layer at the crack faces will reveal the extent of chemical attack inside the crack.

10.2.2 **Investigation of the mechanical properties and stability of the tribofilms**

Although it is challenging to examine the shear flow or rheological properties of the tribofilm, the mechanical properties of the tribofilm give insight to its influence on

micropitting. Scratch test using AFM will provide useful information on the stability of the tribofilm on the surface and hence its impact on inducing local plastic deformation. Moreover, by comparing the scratch results from mild contacts (MTM tests) and severe contacts (MPR tests) in which iron sulphide layer formation is observed, the role of tribofilm formation in severe conditions on micropitting can be understood.

10.2.3 Understanding of localised reactions using advanced microscopy (TEM)

The results in this study disclose the importance of detailed study of reaction films throughout the tribofilm depth, especially in studies concerning surface fatigue. Although chemical analysis (XPS and XANES) techniques have produced outstanding information on the tribochemistry of lubricant additives over years, observation of the lateral and localised chemical distribution of compounds and elements near the surface pits/cracks may not be achieved through these techniques, since collected signals are influenced by an averaging effect over the analysed area and sampling depth. As an examples, XANES cannot recognise the interface layer as separate layer on the substrate in the thick enough tribofilms. Therefore, techniques such as TEM/EDX and TOF-SIMS on FIB lamella are essential in order to achieve a comprehensive understanding of additive influence on surface fatigue. The detailed and nano-scale local investigation of substrate-additive interactions may clarify enormous extent of disagreements around the tribochemical influence of additives on surface fatigue. In this project, TEM studies in tribocorrosive conditions (influence of water and humidity) were not conducted. Future work should locally investigate the influence of water contamination near cracks using TEM. Moreover, the additive ingress and the direction of crack propagation can be tracked inside the crack through 3D reconstruction of a micropit/crack using TEM and EDX which has not been conducted for tribochemical purposes in the literature.

10.2.4 Assessing the influence of other NCAs on micropitting

In this study the influence of some NCAs is investigated mainly focusing on the impact of the polar moiety. Further work would include another group of OFMs which is also a NCA known as amides. The properties of amides and their influence on micropitting can be explored and compared to the results obtained in this study. Moreover, as discussed in section 9.4, the structure of the alkyl chain in OFMs has a

prominent impact on its tribological properties. Accordingly, an interesting work would consider saturated alkyl chain amines/diamines for roller bearing applications. Examples of saturated amines are dodecylamine and octadecylamine which are also commercially available through AkzoNobel known by the product name “Armeen 12D” and “Armeen 18D” respectively. The alkyl chain-length (C number) in dodecylamine and octadecylamine is 12 and 18 respectively. In general OFMs with a saturated alkyl chain are more effective to reduce friction when a base oil is used to lubricate the contact. However, a comparison between saturated and unsaturated alkyl chains, when ZDDP is used in the lubricant formulation, has not been made in the literature.

10.2.5 Further elucidation of additive impact though quantifying the micropit depth

In this study a technique is implemented in order to quantify the micropitting through evaluation of the micropitted surface area which is in agreement with the quantification approaches taken in previous micropitting studies. The micropitting surface area provides information on the extent of micropitting nucleation and propagation happening transverse to the rolling/sliding direction. However, the technique used in this study cannot meticulously and quantitatively compare the micropitting propagation towards the bulk of the substrate (radial direction) induced by additives or water contamination. The radial crack/micropit propagation provides further information on the additive or contamination influence on micropit propagation. Accordingly, future work would consider a serial sectioning of the material through metallurgical cutting or ion beam milling followed by a statistical evaluation of crack depth in various experimental conditions (different additives or water contamination).

References

1. Doll GL, Kotzalas MN, Kang YS. Life-limiting wear of wind turbine gearbox bearings: Origins and solutions. Proceedings of European wind energy conference exhibition (EWEC 2010)2010. p. 2559-68.
2. Musial W, Butterfield S, McNiff B. Improving wind turbine gearbox reliability. European Wind Energy Conference, Milan, Italy2007. p. 7-10.
3. Sheng S. Wind turbine micropitting workshop: a recap. National Renewable Energy Laboratory (NREL), Golden, CO., 2010.
4. Kotzalas MN, Doll GL. Tribological advancements for reliable wind turbine performance. Philosophical Transactions of the Royal Society of London A: Mathematical, Physical and Engineering Sciences. 2010;368(1929):4829-50.
5. Brechot P, Cardis A, Murphy W, Theissen J. Micropitting resistant industrial gear oils with balanced performance. Ind Lubr Tribol. 2000;52(3):125-36.
6. Benyajati C, Olver A. The effect of a ZnDTP anti-wear additive on micropitting resistance of carburised steel rollers: AGMA; 2004.
7. O'connor B. The influence of additive chemistry on micropitting. Gear Technology. 2005;22(3):34-41.
8. Laine E, Olver A, Beveridge T. Effect of lubricants on micropitting and wear. Tribol Int. 2008;41(11):1049-55.
9. de la Guerra Ochoa E, Otero JE, Tanarro EC, Munoz-Guijosa J, del Rio Lopez B, Cordero CA. Analysis of the effect of different types of additives added to a low viscosity polyalphaolefin base on micropitting. Wear. 2015;322:238-50.
10. Khonsari MM, Booser ER. Applied tribology: bearing design and lubrication: John Wiley & Sons; 2008.
11. Hutchings IM. Tribology: friction and wear of engineering materials. 1992.
12. Stachowiak G, Batchelor AW. Engineering tribology: Butterworth-Heinemann; 2013.
13. Tassone B. Roller bearing slip and skidding damage. Journal of Aircraft. 1975;12(4):281-87.
14. Priest M. Principles of Tribology. Lecture notes, [MECH5570 Introduction to Tribology]: University of Leeds; 2013.
15. Oila A, Bull S. Assessment of the factors influencing micropitting in rolling/sliding contacts. Wear. 2005;258(10):1510-24.
16. Errichello R. Selecting and Applying Lubricants to Avoid Micropitting of Gear Teeth. Machinery Lubrication.
17. The SKF web page 2014. Available from: www.skf.com.
18. Brizmer V, Pasaribu H, Morales-Espejel GE. Micropitting performance of oil additives in lubricated rolling contacts. Tribol Trans. 2013;56(5):739-48.
19. Torrance A, Morgan J, Wan G. An additive's influence on the pitting and wear of ball bearing steel. Wear. 1996;192(1):66-73.
20. Sadeghi F, Jalalahmadi B, Slack TS, Raje N, Arakere NK. A review of rolling contact fatigue. J Tribol. 2009;131(4):041403.
21. Stadler K, Stubenrauch A. Premature bearing failures in industrial gearboxes. Antriebstechnisches Kolloquium (ATK)2013. p. 19-20.
22. Erdemir A. Rolling-contact fatigue and wear resistance of hard coatings on bearing-steel substrates. Surface and Coatings Technology. 1992;54-55, Part 2(0):482-89.
23. Terrell EJ, Needelman WM, Kyle JP. Wind turbine tribology. Green Tribology: Springer; 2012. p. 483-530.

24. Stadler K, Han B, Brizmer V, Pasaribu R. Benefits of using black oxidized bearings in wind applications. SKF Evolution. 2015.
25. Gold P, Loos J. Wear resistance of PVD-coatings in roller bearings. *Wear*. 2002;253(3):465-72.
26. Yampolski GY, Kragelskii I, Yushakov I. Abrasive wear of rolling bearings. *Tribol Int*. 1981;14(3):137-38.
27. Dwyer-Joyce R. Predicting the abrasive wear of ball bearings by lubricant debris. *Wear*. 1999;233:692-701.
28. Suarez AN. The Behaviour of Antiwear Additives in Lubricated Rolling-Sliding Contacts [Doctoral dissertation]: Luleå tekniska universitet; 2011.
29. International A. ASM handbook: Friction, lubrication, and wear technology: ASM International; 1992.
30. Hsu SM, Gates R. Boundary lubricating films: formation and lubrication mechanism. *Tribol Int*. 2005;38(3):305-12.
31. Priest M, Taylor C. Automobile engine tribology—approaching the surface. *Wear*. 2000;241(2):193-203.
32. Hamrock BJ, Dowson D. Isothermal elastohydrodynamic lubrication of point contacts: Part III—Fully flooded results. *J Tribol*. 1977;99(2):264-75.
33. Bhushan B. *Modern Tribology Handbook, Two Volume Set*: CRC Press; 2010.
34. Gullac B, Akalin O. Frictional characteristics of IF-WS2 nanoparticles in simulated engine conditions. *Tribol Trans*. 2010;53(6):939-47.
35. Lahouij I, Dassenoy F, De Knoop L, Martin J-M, Vacher B. In situ TEM observation of the behavior of an individual fullerene-like MoS₂ nanoparticle in a dynamic contact. *Tribol Lett*. 2011;42(2):133-40.
36. SKF. *Rolling bearings* In: group S, editor. 2016.
37. Bhadeshia H. Steels for bearings. *Progress in materials Science*. 2012;57(2):268-435.
38. Brizmer V, Gabelli A, Vieillard C, Morales-Espejel GE. An experimental and theoretical study of hybrid bearing micropitting performance under reduced lubrication. *Tribol Trans*. 2015;58(5):829-35.
39. Aramaki H, Shoda Y, Morishita Y, Sawamoto T. The performance of ball bearings with silicon nitride ceramic balls in high speed spindles for machine tools. *J Tribol*. 1988;110(4):693-98.
40. Cento P, Dareing DW. Ceramic materials in hybrid ball bearings. *Tribol Trans*. 1999;42(4):707-14.
41. Evans MH, Richardson AD, Wang L, Wood RJK. Effect of hydrogen on butterfly and white etching crack (WEC) formation under rolling contact fatigue (RCF). *Wear*. 2013 8/30;306(1–2):226-41.
42. Becker P. Microstructural changes around non-metallic inclusions caused by rolling-contact fatigue of ball-bearing steels. *Metals Technology*. 1981;8(1):234-43.
43. Alley ES. Influence of microstructure in rolling contact fatigue of bearing steels with inclusions [Doctor of Philosophy]: Georgia Institute of Technology; 2009.
44. Bower A. The influence of crack face friction and trapped fluid on surface initiated rolling contact fatigue cracks. *J Tribol*. 1988;110(4):704-11.
45. Lai J, Lund T, Rydén K, Gabelli A, Strandell I. The fatigue limit of bearing steels—Part I: A pragmatic approach to predict very high cycle fatigue strength. *International Journal of Fatigue*. 2012;38:155-68.
46. Nélias D, Dumont M, Champiot F, Vincent A, Girodin D, Fougères R, Flamand L. Role of inclusions, surface roughness and operating conditions on rolling contact fatigue. *J Tribol*. 1999;121(2):240-51.

47. Morales-Espejel GE, Brizmer V. Micropitting modelling in rolling–sliding contacts: Application to rolling bearings. *Tribol Trans.* 2011;54(4):625-43.
48. Kang YS, Evans RD, Doll GL. Roller-raceway slip simulations of wind turbine gearbox bearings using dynamic bearing model. *STLE/ASME 2010 International Joint Tribology Conference: American Society of Mechanical Engineers*; 2010. p. 407-09.
49. Hahn G, Bhargava V, Chen Q. The cyclic stress-strain properties, hysteresis loop shape, and kinematic hardening of two high-strength bearing steels. *Metallurgical Transactions A.* 1990;21(2):653-65.
50. Gegner J, Nierlich W. Hydrogen accelerated classical rolling contact fatigue and evaluation of the residual stress response. *Mater Sci Forum: Trans Tech Publ*; 2011. p. 249-54.
51. Ruellan A, Ville F, Kleber X, Arnaudon A, Girodin D. Understanding white etching cracks in rolling element bearings: The effect of hydrogen charging on the formation mechanisms. *Proceedings of the Institution of Mechanical Engineers, Part J: Journal of Engineering Tribology.* 2014;228(11):1252-65.
52. Evans M-H, Richardson A, Wang L, Wood R, Anderson W. Confirming subsurface initiation at non-metallic inclusions as one mechanism for white etching crack (WEC) formation. *Tribol Int.* 2014;75:87-97.
53. Ruellan A, Kleber X, Ville F, Cavoret J, Liatard B. Understanding white etching cracks in rolling element bearings: Formation mechanisms and influent tribochemical drivers. *Proceedings of the Institution of Mechanical Engineers, Part J: Journal of Engineering Tribology.* 2015;229(8):886-901.
54. Kino N, Otani K. The influence of hydrogen on rolling contact fatigue life and its improvement. *JSAE Review.* 2003;24(3):289-94.
55. Louthan Jr MR, Caskey Jr GR, Donovan JA, Rawl Jr DE. Hydrogen embrittlement of metals. *Materials Science and Engineering.* 1972;10:357-68.
56. Ulmer D, Altstetter C. Hydrogen-induced strain localization and failure of austenitic stainless steels at high hydrogen concentrations. *Acta metallurgica et materialia.* 1991;39(6):1237-48.
57. Takahashi Y, Tanaka M, Higashida K, Noguchi H. Hydrogen-induced slip localization around a quasi-brittle fatigue crack observed by high-voltage electron microscopy. *Scripta Materialia.* 2009;61(2):145-48.
58. Szost B, Rivera-Díaz-del-Castillo P. Unveiling the nature of hydrogen embrittlement in bearing steels employing a new technique. *Scripta Materialia.* 2013;68(7):467-70.
59. Fujita S, Matsuoka S, Murakami Y, Marquis G. Effect of hydrogen on mode II fatigue crack behavior of tempered bearing steel and microstructural changes. *International Journal of Fatigue.* 2010;32(6):943-51.
60. Vehoff H, Rothe W. Gaseous hydrogen embrittlement in FeSi- and Ni-single crystals. *Acta Metallurgica.* 1983;31(11):1781-93.
61. Nagumo M. Hydrogen related failure of steels—a new aspect. *Materials Science and Technology.* 2004;20(8):940-50.
62. Evans M. White structure flaking (WSF) in wind turbine gearbox bearings: effects of 'butterflies' and white etching cracks (WECs). *Materials Science and Technology.* 2012;28(1):3-22.
63. Kim T, Olver A, Pearson P. Fatigue and fracture mechanisms in large rolling element bearings. *Tribol Trans.* 2001;44(4):583-90.
64. Gegner Jr. Tribological aspects of rolling bearing failures. *Tribology–Lubricants and Lubrication: InTech*; 2011. p. 33-94.

65. Gegner J, Nierlich W. Mechanical and tribochemical mechanisms of mixed friction induced surface failures of rolling bearings and modeling of competing shear and tensile stress controlled damage initiation). *Tribologie und Schmierungstechnik*. 2011;58(1):10-21.
66. Wu X, Zhang J, Qi W, Gu X, Zhang L. The effect of SP gear oil on load capacity of carburized gears. *World congress on gearing and power transmission 16-18 March 1999; Paris, France 1999*. p. 2223-29.
67. Hong HS, Huston M, O'Connor B, Stadnyk N. Evaluation of surface fatigue performance of gear oils. *Lubr Sci*. 1998;10(4):365-80.
68. Haizuka S, Nemoto R, Naruse C. Study on Limiting Load for Scuffing and Specific Wear of Spur Gears: Effects of Lubricating Oil and Tooth Form. *JSME international journal Ser C, Dynamics, control, robotics, design and manufacturing*. 1995;38(1):149-59.
69. Wang Y, Fernandez J, Cuervo D. Rolling-contact fatigue lives of steel AISI 52100 balls with eight mineral and synthetic lubricants. *Wear*. 1996;196(1):110-19.
70. Tuszyński W. An effect of lubricating additives on tribochemical phenomena in a rolling steel four-ball contact. *Tribol Lett*. 2006;24(3):207-15.
71. Trivedi H, Forster N, Saba C. Rolling contact fatigue testing of a 3 cSt polyolester lubricant with and without TCP and DODPA/PANA at 177 C. *Tribol Lett*. 2004;16(3):231-37.
72. Trivedi HK, Forster NH, Rosado L. Rolling contact fatigue evaluation of advanced bearing steels with and without the oil anti-wear additive tricresyl phosphate. *Tribol Lett*. 2011;41(3):597-605.
73. Wan G, Amerongen E, Lankamp H. Effect of extreme-pressure additives on fatigue life of rolling bearings. *J Phys D: Appl Phys*. 1992;25(1A):147-53.
74. Wan G. The performance of one organic phosphonate additive in rolling-contact fatigue. *Wear*. 1992;155(2):381-87.
75. Nixon HP, Zantopulos H. Lubricant additives, friend or foe. What the equipment design engineer needs to know. *Lubr Eng*. 1995;51(10):815-22.
76. Pasaribu H, Lugt P. The composition of reaction layers on rolling bearings lubricated with gear oils and its correlation with rolling bearing performance. *Tribol Trans*. 2012;55(3):351-56.
77. Torrance A. Chemical and microstructural changes induced in bearing steel by rolling contact. *Wear*. 1988;122(3):363-76.
78. Nixon HP. Effects of extreme pressure additives in lubricants on bearing fatigue life. *Iron and steel engineer*. 1998;75(12):21-26.
79. Oila A, Bull S. Phase transformations associated with micropitting in rolling/sliding contacts. *Journal of materials science*. 2005;40(18):4767-74.
80. Zhou R, Cheng H, Mura T. Micropitting in rolling and sliding contact under mixed lubrication. *J Tribol*. 1989;111(4):605-13.
81. Errichello R. Morphology of Micropitting. *Gear technology*. 2012;4:74-81.
82. Webster M, Norbart C. An experimental investigation of micropitting using a roller disk machine. *Tribol Trans*. 1995;38(4):883-93.
83. Bush J, Grube W, Robinson G. Microstructural and residual stress changes in hardened steel due to rolling contact. *ASM Trans*. 1961;54:390-412.
84. Swahn H, Becker P, Vingsbo O. Martensite decay during rolling contact fatigue in ball bearings. *Metallurgical transactions A*. 1976;7(8):1099-110.
85. Johansson J, Devlin M, Prakash B. Investigations into the occurrence of pitting in lubricated rolling four-ball tests. *Lubr Sci*. 2015;27(2):103-26.

86. Fujita K, Yoshida A. The effect of changing the rolling direction on the rolling contact fatigue lives of annealed and case-hardened steel rollers. *Wear*. 1977;43(3):315-27.
87. Kaneta M, Murakami Y. Effects of oil hydraulic pressure on surface crack growth in rolling/sliding contact. *Tribol Int*. 1987;20(4):210-17.
88. Nakajima A, Ichimaru K, Hirano F, Nishimura M. Effects of combination of rolling direction and sliding direction on pitting of rollers. *Journal of Japan Society of Lubrication Engineers*. 1982;27(10):743-50.
89. Ahlroos T, Ronkainen H, Helle A, Parikka R, Virta J, Varjus S. Twin disc micropitting tests. *Tribol Int*. 2009;42(10):1460-66.
90. Johansson J, Devlin MT, Prakash B. Lubricant additives for improved pitting performance through a reduction of thin-film friction. *Tribol Int*. 2014;80:122-30.
91. Wedeven Associates - WAM micropitting tester. Available from: <http://wedeven.com/wammp.html>.
92. Lainé E, Olver AV, Lekstrom MF, Shollock BA, Beveridge TA, Hua DY. The effect of a friction modifier additive on micropitting. *Tribol Trans*. 2009;52(4):526-33.
93. Berthe D, Flamand L, Foucher D, Godet M. Micropitting in Hertzian contacts. *J Lubric Technol(Trans ASME)*. 1980;102(4):478-89.
94. Akamatsu Y, Tsushima N, Goto T, Hibi K. Influence of surface roughness skewness on rolling contact fatigue life. *Tribol Trans*. 1992;35(4):745-50.
95. Evans HP, Snidle BW. Analysis of micro-elastohydrodynamic lubrication for engineering contacts. *Tribol Int*. 1996;29(8):659-67.
96. Patching MJ, Evans HP, Snidle RW. Micro-EHL Analysis of Ground and Superfinished Steel Discs Used to Simulate Gear Tooth Contacts. *Tribol Trans*. 1996;39(3):595-602.
97. Fujita H, Spikes H. The formation of zinc dithiophosphate antiwear films. *Proceedings of the Institution of Mechanical Engineers, Part J: Journal of Engineering Tribology*. 2004;218(4):265-78.
98. Soda N, Yamamoto T. Effect of Tangential Traction and Roughness on Crack Initiation/Propagation During Rolling Contact. *A S L E Transactions*. 1982;25(2):198-206.
99. Hanson MT, Keer LM. An Analytical Life Prediction Model for the Crack Propagation Occurring in Contact Fatigue Failure. *Tribol Trans*. 1992;35(3):451-61.
100. Kadiric A, Rycerz P. Influence of Contact Conditions on the Onset of Micropitting in Rolling-Sliding Contacts Pertinent to Gear Applications. AGMA Technical Paper 16FTM21, AGMA, Virginia, USA. 2016.
101. Spikes H, Olver A, Macpherson P. Wear in rolling contacts. *Wear*. 1986;112(2):121-44.
102. Cen H. Effect of water on the performance of lubricants and related tribochemistry in boundary lubricated steel/steel contacts [Doctor of Philosophy]: University of Leeds; 2012.
103. Mahmoudi B, Doll G, Hager C, Evans R. Influence of a WC/aC: H tribological coating on micropitting wear of bearing steel. *Wear*. 2016;350:107-15.
104. Winkelmann L, El-Saeed O, Bell M. The effect of superfinishing on gear micropitting. *Gear Technol*. 2009;2:60-65.
105. Spikes H. The history and mechanisms of ZDDP. *Tribol Lett*. 2004;17(3):469-89.
106. Meheux M, Minfray C, Ville F, Mogne T, Lubrecht A, Martin J-M, Lieurade H-P, Thoquenne G. Effect of lubricant additives in rolling contact fatigue.

Proceedings of the Institution of Mechanical Engineers, Part J: Journal of Engineering Tribology. 2010;224(9):947-55.

107. Minfray C, Le Mogne T, Lubrecht A, Martin J-M. Experimental simulation of chemical reactions between ZDDP tribofilms and steel surfaces during friction processes. *Tribol Lett.* 2006;21(1):65-76.

108. Konicek AR, Jacobs PW, Webster MN, Schilowitz AM. Role of tribofilms in wear protection. *Tribol Int.* 2016;94:14-19.

109. Fischer T. Tribochemistry. *Annual Review of Materials Science.* 1988;18(1):303-23.

110. Zhang Z, Najman M, Kasrai M, Bancroft G, Yamaguchi E. Study of interaction of EP and AW additives with dispersants using XANES. *Tribol Lett.* 2005;18(1):43-51.

111. Najman M, Kasrai M, Bancroft G. X-ray absorption spectroscopy and atomic force microscopy of films generated from organosulfur extreme-pressure (EP) oil additives. *Tribol Lett.* 2003;14(4):225-35.

112. Costello MT, Kasrai M. Study of surface films of overbased sulfonates and sulfurized olefins by X-Ray Absorption Near Edge Structure (XANES) spectroscopy. *Tribol Lett.* 2006;24(2):163-69.

113. Coy R, Quinn T. The use of physical methods of analysis to identify surface layers formed by organosulfur compounds in wear tests. *ASLE Transactions.* 1975;18(3):163-74.

114. Sakamoto T, Uetz H, Föhl J, Khosrawi M. The reaction layer formed on steel by additives based on sulphur and phosphorus compounds under conditions of boundary lubrication. *Wear.* 1982;77(2):139-57.

115. Sieber I, Meyer K, Kloss H, Schöpke A. Characterization of boundary layers formed by different metal dithiophosphates in a four-ball machine. *Wear.* 1983;85(1):43-56.

116. Mourhatch R, Aswath PB. Tribological behavior and nature of tribofilms generated from fluorinated ZDDP in comparison to ZDDP under extreme pressure conditions—Part 1: Structure and chemistry of tribofilms. *Tribol Int.* 2011;44(3):187-200.

117. Nehme G, Mourhatch R, Aswath PB. Effect of contact load and lubricant volume on the properties of tribofilms formed under boundary lubrication in a fully formulated oil under extreme load conditions. *Wear.* 2010;268(9):1129-47.

118. Hallouis M, Belin M, Martin J. The role of sulphur in ZDDP-induced reaction films formed in the presence of ZDDP: Contribution of electron spectroscopic imaging technique. *Lubr Sci.* 1990;2(4):337-49.

119. Najman M, Kasrai M, Bancroft G. Chemistry of antiwear films from ashless thiophosphate oil additives. *Tribol Lett.* 2004;17(2):217-29.

120. Zhang Z, Yamaguchi E, Kasrai M, Bancroft G. Tribofilms generated from ZDDP and DDP on steel surfaces: Part 1, growth, wear and morphology. *Tribol Lett.* 2005;19(3):211-20.

121. Kim B, Mourhatch R, Aswath PB. Properties of tribofilms formed with ashless dithiophosphate and zinc dialkyl dithiophosphate under extreme pressure conditions. *Wear.* 2010;268(3):579-91.

122. Martin JM. Antiwear mechanisms of zinc dithiophosphate: a chemical hardness approach. *Tribol Lett.* 1999;6(1):1-8.

123. Allum K, Forbes E. The load-carrying properties of metal dialkyl dithiophosphates: the effect of chemical structure. *Proceedings of the Institution of Mechanical Engineers, Conference Proceedings: SAGE Publications; 1968. p. 7-14.*

124. Bec S, Tonck A, Georges J-M, Coy R, Bell J, Roper G. Relationship between mechanical properties and structures of zinc dithiophosphate anti-wear films. *Proceedings of the Royal Society of London A: Mathematical, Physical and Engineering Sciences: The Royal Society*; 1999. p. 4181-203.
125. Kasrai M, Fuller MS, Bancroft GM, Yamaguchi ES, Ryason PR. X-ray absorption study of the effect of calcium sulfonate on antiwear film formation generated from neutral and basic Zddps: Part 2—sulfur species. *Tribol Trans.* 2003;46(4):543-49.
126. Chase Jr M, Davies C, Downey Jr J, Frurip D, McDonald R, Syveraud A. JANAF thermodynamic tables. *J Phys Chem Ref Data.* 1985;14(Suppl. 1).
127. Martin JM, Grossiord C, Le Mogne T, Bec S, Tonck A. The two-layer structure of Zndtp tribofilms: Part I: AES, XPS and XANES analyses. *Tribol Int.* 2001;34(8):523-30.
128. Glaeser W, Baer D, Engelhardt M. In situ wear experiments in the scanning Auger spectrometer. *Wear.* 1993;162:132-38.
129. Zhang Z, Yamaguchi E, Kasrai M, Bancroft G, Liu X, Fleet M. Tribofilms generated from ZDDP and DDP on steel surfaces: Part 2, chemistry. *Tribol Lett.* 2005;19(3):221-29.
130. Bird R, Galvin G. The application of photoelectron spectroscopy to the study of EP films on lubricated surfaces. *Wear.* 1976;37(1):143-67.
131. De Barros M, Bouchet J, Raoult I, Le Mogne T, Martin J, Kasrai M, Yamada Y. Friction reduction by metal sulfides in boundary lubrication studied by XPS and XANES analyses. *Wear.* 2003;254(9):863-70.
132. Watanabe M, Sakuma M, Inaba T, Iguchi Y. Formation and oxidation of sulfides on pure iron and iron oxides. *Materials transactions-JIM.* 2000;41(7):865-72.
133. Watkins R. The antiwear mechanism of zddp's. Part II. *Tribol Int.* 1982;15(1):13-15.
134. Jahanmir S. Wear reduction and surface layer formation by a ZDDP additive. *J Tribol.* 1987;109(4):577-86.
135. Yin Z, Kasrai M, Fuller M, Bancroft GM, Fyfe K, Tan KH. Application of soft X-ray absorption spectroscopy in chemical characterization of antiwear films generated by ZDDP Part I: the effects of physical parameters. *Wear.* 1997;202(2):172-91.
136. Bell J, Delargy K, Seeney A. Paper IX (ii) The Removal of Substrate Material through Thick Zinc Dithiophosphate Anti-Wear Films. *Tribology series.* 1992;21:387-96.
137. Smith G, Bell J. Multi-technique surface analytical studies of automotive anti-wear films. *Applied surface science.* 1999;144:222-27.
138. Tonck A, Bec S, Georges J-M, Coy R, Bell J, Roper G. Structure and mechanical properties of ZDTP films in oil. *Tribology Series.* 1999;36:39-47.
139. Bell J, Coy R, Spikes H. Cryogenic studies of zinc dialkyl dithiophosphate anti-wear films. *Proceedings of the Japan International Tribology Conference 1990.* p. 505-10.
140. Minfray C, Martin J, Esnouf C, Le Mogne T, Kersting R, Hagenhoff B. A multi-technique approach of tribofilm characterisation. *Thin Solid Films.* 2004;447:272-77.
141. Yin Z, Kasrai M, Bancroft GM, Laycock KF, Tan KH. Chemical characterization of antiwear films generated on steel by zinc dialkyl dithiophosphate using X-ray absorption spectroscopy. *Tribol Int.* 1993;26(6):383-88.

142. Pereira G, Munoz-Paniagua D, Lachenwitzer A, Kasrai M, Norton PR, Capehart TW, Perry TA, Cheng Y-T. A variable temperature mechanical analysis of ZDDP-derived antiwear films formed on 52100 steel. *Wear*. 2007;262(3):461-70.
143. Sharma V, Erdemir A, Aswath PB. An analytical study of tribofilms generated by the interaction of ashless antiwear additives with ZDDP using XANES and nano-indentation. *Tribol Int*. 2015;82:43-57.
144. Canning G, Fuller MS, Bancroft G, Kasrai M, Cutler J, De Stasio G, Gilbert B. Spectromicroscopy of tribological films from engine oil additives. Part I. Films from ZDDP's. *Tribol Lett*. 1999;6(3-4):159-69.
145. Nicholls M, Najman M, Zhang Z, Kasrai M, Norton P, Gilbert P. The contribution of XANES spectroscopy to tribology. *Can J Chem*. 2007;85(10):816-30.
146. Schatzberg P, Felsen IM. Effects of water and oxygen during rolling contact lubrication. *Wear*. 1968;12(5):331-42.
147. Fitch J, Jaggernauth S. MOISTURE--The Second Most Destructive Lubricant Contaminate, and its Effects on Bearing Life. *P/PM Technology*. 1994;12:1-4.
148. Cen H, Morina A, Neville A, Pasaribu R, Nedelcu I. Effect of water on ZDDP anti-wear performance and related tribochemistry in lubricated steel/steel pure sliding contacts. *Tribol Int*. 2012;56:47-57.
149. Goto H, Buckley D. The influence of water vapour in air on the friction behaviour of pure metals during fretting. *Tribol Int*. 1985;18(4):237-45.
150. Lancaster J. A review of the influence of environmental humidity and water on friction, lubrication and wear. *Tribol Int*. 1990;23(6):371-89.
151. Nedelcu I, Piras E, Rossi A, Pasaribu H. XPS analysis on the influence of water on the evolution of zinc dialkyldithiophosphate-derived reaction layer in lubricated rolling contacts. *Surface and Interface Analysis*. 2012;44(8):1219-24.
152. Needelman W, LaVallee G. Forms of Water in Oil and Their Control. *Noria Lubrication Excellence Conference; Columbus Ohio2006*.
153. Bauer C, Day M. Water contamination in hydraulic and lube systems. *Practicing Oil Analysis Magazine*. 2007;9(9-10).
154. Needelman WM, Barris MA, LaVallee GL. Contamination control for wind turbine gearboxes. *Power Engineering*. 2009;113:112-20.
155. Cantley RE. The effect of water in lubricating oil on bearing fatigue life. *ASLE Transactions*. 1977;20(3):244-48.
156. Beercheck RC. How dirt and water slash bearing life. *Machine Design*. 1978;50(16):68-73.
157. Atkins P, de Paula J. *Atkins' Physical Chemistry*: OUP Oxford; 2014.
158. Grunberg L, Scott D. The acceleration of pitting failure by water in the lubricant. *J Inst Petrol*. 1958;44(419):406.
159. Schatzberg P, Felsen IM. Influence of water on fatigue-failure location and surface alteration during rolling-contact lubrication. *Journal of Lubrication Technology*. 1969;91(2):301-07.
160. Ruellan A, Cavoret J, Ville F, Kleber X, Liatard B. Understanding white etching cracks in rolling element bearings: State of art and multiple driver transposition on a twin-disc machine. *Proceedings of the Institution of Mechanical Engineers, Part J: Journal of Engineering Tribology*. 2016;231(2):203-20.
161. Imran T, Jacobson B, Shariff A. Quantifying diffused hydrogen in AISI-52100 bearing steel and in silver steel under tribo-mechanical action: Pure rotating bending, sliding-rotating bending, rolling-rotating bending and uni-axial tensile loading. *Wear*. 2006;261(1):86-95.

162. Magalhaes J, Ventsel L, MacDonald D. Environmental effects on pitting corrosion of AISI 440C ball bearing steels-experimental results. *Tribology & Lubrication Technology*. 1999;55(6):36-41.
163. Rounds FG. Some factors affecting the decomposition of three commercial zinc organodithiophosphates. *ASLE Transactions*. 1975;18(2):79-89.
164. Spedding H, Watkins R. The antiwear mechanism of zddp's. Part I. *Tribol Int*. 1982;15(1):9-12.
165. Fuller MLS, Kasrai M, Bancroft GM, Fyfe K, Tan KH. Solution decomposition of zinc dialkyl dithiophosphate and its effect on antiwear and thermal film formation studied by X-ray absorption spectroscopy. *Tribol Int*. 1998;31(10):627-44.
166. Fatima N, Minami I, Holmgren A, Marklund P, Larsson R. Surface chemistry of wet clutch influenced by water contamination in automatic transmission fluids. *Tribol Int*. 2016;96:395-401.
167. Fatima N, Minami I, Holmgren A, Marklund P, Berglund K, Larsson R. Influence of water on the tribological properties of zinc dialkyl-dithiophosphate and over-based calcium sulphonate additives in wet clutch contacts. *Tribol Int*. 2015;87:113-20.
168. McDonald RA. Zinc dithiophosphates. *Lubricant Additives: Chemistry and Applications*: CRC Press; 2003. p. 29-44.
169. Costa HL, Spikes HA. Impact of ethanol on the formation of antiwear tribofilms from engine lubricants. *Tribol Int*. 2016;93, Part A:364-76.
170. Devlin M, Ryan H, Tsang V, Corbett P, Strand L, Turner TL, Wallo C, Jao T-C. The effect of water contamination and oxidation on the fatigue life performance of wind turbine lubricants. *NLGI Annual Meeting; Hilton Head, SC: [Kansas City, Mo.] National Lubricating Grease Institute.*; 2003. p. 22-30.
171. Miklozic KT, Forbus TR, Spikes HA. Performance of friction modifiers on ZDDP-generated surfaces. *Tribol Trans*. 2007;50(3):328-35.
172. Plaza S. The adsorption of zinc dibutyldithiophosphates on iron and iron oxide powders. *ASLE transactions*. 1987;30(2):233-40.
173. Inoue K, Watanabe H. Interactions of engine oil additives. *ASLE transactions*. 1983;26(2):189-99.
174. Gallopoulos NE, Murphy CK. Interactions between a zinc dialkylphosphorodithioate and lubricating oil dispersants. *ASLE Transactions*. 1971;14(1):1-7.
175. Shiomi M, Tokashiki M, Tomizawa H, Kuribayashi T. Interaction between zinc dialkyldithiophosphate and amine. *Lubr Sci*. 1989;1(2):131-47.
176. Shiomi M, Mitsui Ji, Akiyama K, Tasaka K, Nakada M, Ohira H. *Formulation Technology for Low Phosphorus Gasoline Engine Oils*. SAE Technical Paper, 1992.
177. Zhang Z, Kasrai M, Bancroft G, Yamaguchi E. Study of the interaction of ZDDP and dispersants using X-ray absorption near edge structure spectroscopy—part 1: thermal chemical reactions. *Tribol Lett*. 2003;15(4):377-84.
178. Yamaguchi E, Zhang Z, Kasrai M, Bancroft G. Study of the interaction of ZDDP and dispersants using X-ray absorption near edge structure spectroscopy—part 2: tribochemical reactions. *Tribol Lett*. 2003;15(4):385-94.
179. Rounds FG. Additive interactions and their effect on the performance of a zinc dialkyl dithiophosphate. *Asle Transactions*. 1978;21(2):91-101.
180. Zhang J, Yamaguchi E, Spikes H. The antagonism between succinimide dispersants and a secondary zinc dialkyl dithiophosphate. *Tribol Trans*. 2014;57(1):57-65.

181. Harrison PG, Brown P, McManus J. ³¹P NMR study of the interaction of a commercial succinimide-type lubricating oil dispersant with zinc (II) bis (O, O'-diisobutyldithiophosphate). *Wear*. 1992;156(2):345-49.
182. Sonntag RE, Borgnakke C, Van Wylen GJ, Van Wyk S. *Fundamentals of thermodynamics*: Wiley New York; 1998.
183. Taylor L, Dratva A, Spikes H. Friction and wear behavior of zinc dialkyldithiophosphate additive. *Tribol Trans*. 2000;43(3):469-79.
184. Taylor L, Spikes H. Friction-enhancing properties of ZDDP antiwear additive: part I—friction and morphology of ZDDP reaction films. *Tribol Trans*. 2003;46(3):303-09.
185. Ivan J, Boyer CLB, Bart Heldreth. *Safety Assessment of PEGs Cocamine and Related Ingredients as Used in Cosmetics*. 2015.
186. Chastain J, King RC, Moulder J. *Handbook of X-ray photoelectron spectroscopy: a reference book of standard spectra for identification and interpretation of XPS data*: Physical Electronics Eden Prairie, MN; 1995.
187. Crobu M, Rossi A, Mangolini F, Spencer ND. Chain-length-identification strategy in zinc polyphosphate glasses by means of XPS and ToF-SIMS. *Analytical and bioanalytical chemistry*. 2012;403(5):1415-32.
188. Kato NI. Reducing focused ion beam damage to transmission electron microscopy samples. *J Electron Microsc*. 2004;53(5):451-58.
189. Williams DB, Carter CB. *The transmission electron microscope*: Springer; 1996.
190. Atomic Force Microscopy (AFM) - Tapping mode. Available from: <http://blog.brukerafmprobes.com/category/guide-to-spm-and-afm-modes/page/2/>.
191. Bass M, America OSo. *Devices, measurements, and properties*: McGraw-Hill; 1995.
192. Martin J, Grossiord C, Le Mogne T, Igarashi J. Role of nitrogen in tribochemical interaction between Zndtp and succinimide in boundary lubrication. *Tribol Int*. 2000;33(7):453-59.
193. Eglin M. *Development of a combinatorial approach to lubricant additive characterization [Doctor of Philosophy]*: Technische Wissenschaften ETH Zürich; 2003.
194. Seah M, Dench W. Quantitative electron spectroscopy of surfaces. *Surface and interface analysis*. 1979;1(1):2-11.
195. Brion D. Etude par spectroscopie de photoelectrons de la degradation superficielle de FeS₂, CuFeS₂, ZnS et PbS a l'air et dans l'eau. *Applications of Surface Science*. 1980;5(2):133-52.
196. Fuller MS, Fernandez LR, Massoumi G, Lennard W, Kasrai M, Bancroft G. The use of X-ray absorption spectroscopy for monitoring the thickness of antiwear films from ZDDP. *Tribol Lett*. 2000;8(4):187-92.
197. Rossi A, Piras F, Kim D, Gellman A, Spencer N. Surface reactivity of tributyl thiophosphate: effects of temperature and mechanical stress. *Tribol Lett*. 2006;23(3):197-208.
198. Liu H, Chin T, Yung S. FTIR and XPS studies of low-melting PbO-ZnO-P₂O₅ glasses. *Materials chemistry and physics*. 1997;50(1):1-10.
199. Crobu M, Rossi A, Mangolini F, Spencer ND. Tribochemistry of bulk zinc metaphosphate glasses. *Tribol Lett*. 2010;39(2):121-34.
200. Heuberger RC. *Combinatorial study of the tribochemistry of anti-wear lubricant additives [Doctor of Philosophy]*: Technische Hochschule ETH Zürich; 2007.

201. Crobu M, Rossi A, Spencer ND. Effect of chain-length and countersurface on the tribochemistry of bulk zinc polyphosphate glasses. *Tribol Lett.* 2012;48(3):393-406.
202. Onyiriuka E. Zinc phosphate glass surfaces studied by XPS. *Journal of non-crystalline solids.* 1993;163(3):268-73.
203. Brow RK, Tallant DR. Structural design of sealing glasses. *Journal of Non-Crystalline Solids.* 1997;222:396-406.
204. Eglin M, Rossi A, Spencer ND. X-ray photoelectron spectroscopy analysis of tribostressed samples in the presence of ZnDTP: a combinatorial approach. *Tribol Lett.* 2003;15(3):199-209.
205. Yin Z, Kasrai M, Bancroft G, Fyfe K, Colaianni M, Tan K. Application of soft X-ray absorption spectroscopy in chemical characterization of antiwear films generated by ZDDP Part II: the effect of detergents and dispersants. *Wear.* 1997;202(2):192-201.
206. Minfray C, Martin J-M, De Barros M, Le Mogne T, Kersting R, Hagenhoff B. Chemistry of ZDDP tribofilm by ToF-SIMS. *Tribol Lett.* 2004;17(3):351-57.
207. Hawkes PW, Reimer L. *Scanning Electron Microscopy: Physics of Image Formation and Microanalysis*: Springer Berlin Heidelberg; 2013.
208. Oila A, Shaw B, Aylott C, Bull S. Martensite decay in micropitted gears. *Proceedings of the Institution of Mechanical Engineers, Part J: Journal of Engineering Tribology.* 2005;219(2):77-83.
209. Oila A. *Micropitting and related phenomena in case carburised gears [Doctor of Philosophy]*: Newcastle University; 2003.
210. Ånmark N, Karasev A, Jönsson PG. The effect of different non-metallic inclusions on the machinability of steels. *Materials.* 2015;8(2):751-83.
211. Jahanmir S. Examination of wear mechanisms in automotive camshafts. *Wear.* 1986;108(3):235-54.
212. Mangolini F, Rossi A, Spencer ND. Tribochemistry of triphenyl phosphorothionate (TPPT) by in situ attenuated total reflection (ATR/FT-IR) tribometry. *The Journal of Physical Chemistry C.* 2012;116(9):5614-27.
213. Wagner C. Auger lines in x-ray photoelectron spectrometry. *Analytical Chemistry.* 1972;44(6):967-73.
214. Moretti G. Auger parameter and Wagner plot in the characterization of chemical states by X-ray photoelectron spectroscopy: a review. *Journal of electron spectroscopy and related phenomena.* 1998;95(2):95-144.
215. Deroubaix G, Marcus P. X-ray photoelectron spectroscopy analysis of copper and zinc oxides and sulphides. *Surface and Interface Analysis.* 1992;18(1):39-46.
216. Dake L, Baer D, Zachara J. Auger parameter measurements of zinc compounds relevant to zinc transport in the environment. *Surface and Interface Analysis.* 1989;14(1-2):71-75.
217. Wagner C, Briggs D, Seah M. *Practical surface analysis. Auger and X-ray Photoelectron Spectroscopy.* 1990;1:595.
218. Paparazzo E. XPS analysis of iron aluminum oxide systems. *Applied surface science.* 1986;25(1):1-12.
219. Lad RJ, Henrich VE. Structure of α -Fe₂O₃ single crystal surfaces following Ar⁺ ion bombardment and annealing in O₂. *Surface Science.* 1988;193(1):81-93.
220. Mills P, Sullivan J. A study of the core level electrons in iron and its three oxides by means of X-ray photoelectron spectroscopy. *Journal of Physics D: Applied Physics.* 1983;16(5):723.
221. Zhang Z, Yamaguchi E, Kasrai M, Bancroft G. Interaction of ZDDP with borated dispersant using XANES and XPS. *Tribol Trans.* 2004;47(4):527-36.

222. Komvopoulos K, Do V, Yamaguchi E, Yeh S, Ryason P. X-ray photoelectron spectroscopy analysis of antiwear tribofilms produced on boundary-lubricated steel surfaces from sulfur-and phosphorus-containing additives and metal deactivator additive. *Tribol Trans.* 2004;47(3):321-27.
223. Morina A, Zhao H, Mosselmans JFW. In-situ reflection-XANES study of ZDDP and MoDTC lubricant films formed on steel and diamond like carbon (DLC) surfaces. *Applied Surface Science.* 2014;297:167-75.
224. Hersh L, Onyiriuka E, Hertl W. Amine-reactive surface chemistry of zinc phosphate glasses. *J Mater Res.* 1995;10(08):2120-27.
225. Matsumoto K. Surface chemical and tribological investigations of phosphorus-containing lubricant additives [Doctor of Philosophy]: Technische Wissenschaften ETH Zürich; 2003.
226. Campen SM. Fundamentals of organic friction modifier behaviour. [Doctor of Philosophy]: Imperial College London 2012.
227. Taylor LJ, Spikes HA. Friction-enhancing properties of ZDDP antiwear additive: part II—influence of ZDDP reaction films on EHD lubrication. *Tribol Trans.* 2003;46(3):310-14.
228. Onodera T, Martin JM, Minfray C, Dassenoy F, Miyamoto A. Antiwear chemistry of ZDDP: coupling classical MD and tight-binding quantum chemical MD methods (TB-QCMD). *Tribol Lett.* 2013;50(1):31-39.
229. Möhrle H, Kampe C, Herbke J, Nowak H-J, Wendisch D, Storp S. Doppelsalzbildung bei Amiden und vinylogenen Amiden. *Monatshefte für Chemie/Chemical Monthly.* 1978;109(6):1295-303.
230. Greenberg A, Breneman CM, Liebman JF. *The Amide Linkage: Structural Significance in Chemistry, Biochemistry, and Materials Science*: Wiley; 2002.
231. Wood MH, Welbourn RJ, Charlton T, Zarbakhsh A, Casford M, Clarke SM. Hexadecylamine Adsorption at the Iron Oxide–Oil Interface. *Langmuir.* 2013;29(45):13735-42.
232. Yue W, Gao X, Wang C, Li X, Wang S, Liu J. Synergistic effects between plasma-nitrided AISI 52100 steel and zinc dialkyldithiophosphate additive under boundary lubrication. *Tribol Trans.* 2012;55(3):278-87.
233. Piras FM, Rossi A, Spencer ND. Combined in situ (ATR FT-IR) and ex situ (XPS) study of the ZnDTP-iron surface interaction. *Tribol Lett.* 2003;15(3):181-91.
234. Willermet P, Carter R, Boulos E. Lubricant-derived tribochemical films—an infra-red spectroscopic study. *Tribol Int.* 1992;25(6):371-80.
235. Al-Tubi IS, Long H. Prediction of wind turbine gear micropitting under variable load and speed conditions using ISO/TR 15144-1: 2010. *Proceedings of the Institution of Mechanical Engineers, Part C: Journal of Mechanical Engineering Science.* 2013;227(9):1898-914.
236. Martins R, Seabra J, Magalhaes L. Austempered ductile iron (ADI) gears: Power loss, pitting and micropitting. *Wear.* 2008;264(9):838-49.
237. Brimble K, Atkins I, Blencoe K, Aylott C, Shaw B. A comparison of micropitting performance of identical oils using standard FZG test gears and helical test gears. *British Gear Association Annual Congress*; London, UK2001. p. 44-50.
238. Martins R, Seabra J, Ruis-Moron L. Influence of oil formulation on gear micropitting and power loss performance. *Proceedings of the Institution of Mechanical Engineers, Part J: Journal of Engineering Tribology.* 2011;225(6):429-39.
239. Martins R, Seabra J. Micropitting performance of mineral and biodegradable ester gear oils. *Ind Lubr Tribol.* 2008;60(6):286-92.

240. Evans RD, More KL, Darragh CV, Nixon HP. Transmission electron microscopy of boundary-lubricated bearing surfaces. Part I: Mineral oil lubricant. *Tribol Trans.* 2004;47(3):430-39.
241. Galvin G, Naylor H. Effect of lubricants on the fatigue of steel and other metals. *Proceedings of the Institution of Mechanical Engineers.* 1964;179(1):857-75.
242. Phillips M, Dewey M, Hall D, Quinn T, Southworth H. The application of Auger electron spectroscopy to tribology. *Vacuum.* 1976;26(10):451-56.
243. Aldana PU, Dassenoy F, Vacher B, Le Mogne T, Thiebaut B, Bouffet A. Anti spalling effect of WS₂ nanoparticles on the lubrication of automotive gearboxes. *Tribol Trans.* 2016;59(1):178-88.
244. Evans RD, More KL, Darragh CV, Nixon HP. Transmission electron microscopy of boundary-lubricated bearing surfaces. Part II: mineral oil Lubricant with sulfur-and phosphorus-containing gear oil additives. *Tribol Trans.* 2005;48(3):299-307.
245. Evans RD, Nixon H, Darragh CV, Howe JY, Coffey DW. Effects of extreme pressure additive chemistry on rolling element bearing surface durability. *Tribol Int.* 2007;40(10):1649-54.
246. Pessu FO. Investigation of pitting corrosion of carbon steel in sweet and sour oilfield corrosion conditions: a parametric study: University of Leeds; 2015.
247. Sullivan PJ, Yelton JL, Reddy K. Iron sulfide oxidation and the chemistry of acid generation. *Environmental Geology and Water Sciences.* 1988;11(3):289-95.
248. Hostis BL VC, Minfray C, Frégonèse M, Jarnias F, Alder Da-Costa D'Ambros. Impact of lubricant formulation on pitting of manual transmission gears. In: 42nd Leeds-Lyon symposium on tribology, Lyon, France, 7-9 September 2015.
249. Beletskii I, Yatsimirskii K. Electronic structure of polyphosphate ions. *Theoretical and Experimental Chemistry.* 1988;23(6):621-27.
250. Ho T-L. Hard soft acids bases (HSAB) principle and organic chemistry. *Chemical Reviews.* 1975;75(1):1-20.
251. Pearson RG. *Chemical hardness: Wiley-VCH; 1997.*
252. Burn A, Dewan S, Gosney I, Tan P. ³¹P NMR Study of the Mechanism and Kinetics of the Hydrolysis of Zinc (II) O, O-Diethyl Dithiophosphate and Some Related Compounds. *ChemInform.* 1990;21(34).
253. Burn AJ, Gosney I, Warrens CP, Wastle JP. Phosphorus-31 NMR investigation of the heterogeneous hydrolytic decomposition of zinc (II) bis (O, O-dialkyl dithiophosphate) lubricant additives. *Journal of the Chemical Society, Perkin Transactions 2.* 1995 (2):265-68.
254. Burn AJ, Dewan SK, Gosney I, Tan PS. Inhibition of hydrolysis of 'normal' zinc (II) O, O'-di-isopropyl dithiophosphate by the 'basic' form. *Journal of the Chemical Society, Perkin Transactions 2.* 1990 (8):1311-16.
255. Harrison PG, Kikabhai T. Proton and phosphorus-31 nuclear magnetic resonance study of zinc (II) O, O'-dialkyl dithiophosphates in solution. *Journal of the Chemical Society, Dalton Transactions.* 1987 (4):807-14.
256. Morina A, Green J, Neville A, Priest M. Surface and tribological characteristics of tribofilms formed in the boundary lubrication regime with application to internal combustion engines. *Tribol Lett.* 2003;15(4):443-52.
257. Morina A, Neville A, Priest M, Green J. ZDDP and MoDTC interactions in boundary lubrication—the effect of temperature and ZDDP/MoDTC ratio. *Tribol Int.* 2006;39(12):1545-57.
258. Eriksson K. *Fatty Amines as Friction Modifiers in Engine Oils - Correlating Adsorbed Amount to Friction and Wear Performance [Master].* Gothenburg, Sweden: Chalmers University of Technology; 2014.

259. Spikes H. Friction modifier additives. *Tribol Lett.* 2015;60(1):1-26.
260. Green L. When and How to Use Friction Modifiers. Available from: <http://www.machinerylubrication.com/Read/30336/friction-modifiers-use>.
261. Rudnick LR. *Lubricant Additives: Chemistry and Applications*, Second Edition: CRC Press; 2009.
262. Spikes H, Cameron A. A comparison of adsorption and boundary lubricant failure. *Proceedings of the Royal Society of London A: Mathematical, Physical and Engineering Sciences: The Royal Society*; 1974. p. 407-19.
263. Block A, Simms BB. Desorption and exchange of adsorbed octadecylamine and stearic acid on steel and glass. *J Colloid Interface Sci.* 1967;25(4):514-18.
264. Doig M, Camp PJ. The structures of hexadecylamine films adsorbed on iron-oxide surfaces in dodecane and hexadecane. *PCCP.* 2015;17(7):5248-55.
265. Salmeron M. Generation of defects in model lubricant monolayers and their contribution to energy dissipation in friction. *Tribol Lett.* 2001;10(1-2):69-79.
266. Jahanmir S. Chain length effects in boundary lubrication. *Wear.* 1985;102(4):331-49.
267. Deryaguin B, Karassev V, Zakhavaeva N, Lazarev V. The mechanism of boundary lubrication and the properties of the lubricating film: short-and long-range action in the theory of boundary lubrication. *Wear.* 1958;1(4):277-90.
268. Farn RJ. *Chemistry and Technology of Surfactants*: Wiley; 2008.
269. Campen S, Green J, Lamb G, Spikes H. In situ study of model organic friction modifiers using liquid cell AFM; saturated and mono-unsaturated carboxylic acids. *Tribol Lett.* 2015;57(2):1-20.
270. Campen S, Green J, Lamb G, Atkinson D, Spikes H. On the increase in boundary friction with sliding speed. *Tribol Lett.* 2012;48(2):237-48.
271. Beltzer M, Jahanmir S. Role of dispersion interactions between hydrocarbon chains in boundary lubrication. *ASLE transactions.* 1987;30(1):47-54.
272. Nakano K, Spikes HA. Process of Boundary Film Formation from Fatty Acid Solution. *Tribology Online.* 2012;7(1):1-7.
273. Dwyer F. *Chelating Agents and Metal Chelates*: Elsevier Science; 2012.
274. Nitrogen Inversion. Available from: http://www.chem.ucla.edu/~harding/tutorials/nitrogen_inversion.pdf.
275. Madan RL. *B.SC.Chemistry - II (UGC)*: S Chand & Company Limited; 2012.
276. Ratoi M, Niste VB, Alghawel H, Suen YF, Nelson K. The impact of organic friction modifiers on engine oil tribofilms. *RSC Advances.* 2014;4(9):4278-85.
277. Siegel GG, Herrera F, Cappelle P, Huyskens PL. Dipolar study of primary aliphatic amines and diamines. *Journal of Molecular Structure.* 1987;159(3):355-63.
278. Johnson AW. *Invitation to Organic Chemistry*: Jones and Bartlett Publishers; 1999.
279. Myers R. *The Basics of Chemistry*: Greenwood Press; 2003.
280. Ramanathan E. *AIEEE Chemistry*: Sura Books.
281. Tischendorf B, Otaigbe JU, Wiench JW, Pruski M, Sales BC. A study of short and intermediate range order in zinc phosphate glasses. *Journal of Non-Crystalline Solids.* 2001;282(2-3):147-58.
282. Joseph K, Jolley K, Smith R. Iron phosphate glasses: Structure determination and displacement energy thresholds, using a fixed charge potential model. *Journal of Non-Crystalline Solids.* 2015;411:137-44.
283. Li H, Liang X, Yu H, Yang D, Yang S. Studies of structure of calcium-iron phosphate glasses by infrared, Raman and UV-Vis spectroscopies. *Indian Journal of Physics.* 2016;90(6):693-98.

284. Nicholls MA, Do T, Norton PR, Kasrai M, Bancroft GM. Review of the lubrication of metallic surfaces by zinc dialkyl-dithiophosphates. *Tribol Int.* 2005;38(1):15-39.
285. Aktary M, McDermott MT, McAlpine GA. Morphology and nanomechanical properties of ZDDP antiwear films as a function of tribological contact time. *Tribol Lett.* 2002;12(3):155-62.
286. Minfray C, Le Mogne T, Martin J-M, Onodera T, Nara S, Takahashi S, Tsuboi H, Koyama M, Endou A, Takaba H. Experimental and Molecular Dynamics Simulations of Tribochemical Reactions With ZDDP: Zinc Phosphate–Iron Oxide Reaction. *Tribol Trans.* 2008;51(5):589-601.
287. Brewer NJ, Beake BD, Leggett GJ. Friction force microscopy of self-assembled monolayers: influence of adsorbate alkyl chain length, terminal group chemistry, and scan velocity. *langmuir.* 2001;17(6):1970-74.
288. Briscoe B, Evans D. The shear properties of Langmuir-Blodgett layers. *Proceedings of the Royal Society of London A: Mathematical, Physical and Engineering Sciences: The Royal Society;* 1982. p. 389-407.
289. Ingram M, Noles J, Watts R, Harris S, Spikes H. Frictional Properties of Automatic Transmission Fluids: Part I—Measurement of Friction–Sliding Speed Behavior. *Tribol Trans.* 2010;54(1):145-53.

Appendixes

Appendix 1 The designation, composition and properties of steels used for elements and rings in roller bearings

Through-hardened bearing steel

Through-hardened bearing steel designations	
ISO(683-17, 1999,2013)	W.Nr. DIN/EN (10027-2:1992)
100Cr6 (52100)	1.3505
100CrMnSi4-4	1.3518
100CrMnSi6-4	1.3520
100CrMnSi6-6	1.3519
100CrMo7	1.3537
100CrMo7-3	1.3536
100CrMo7-4	1.3538
100CrMnMoSi8-4-6	1.3539

Through-hardened bearing steel composition												
Steel designation		Chemical composition ^a [% (m/m)]										
Name	No.	C	Si	Mn	P max.	S max.	Cr	Mo	Ni	V	W	Others
Through-hardening bearing steels												
100Cr6	B1	0,93 to 1,05 ^b	0,15 to 0,35 ^c	0,25 to 0,45	0,025	0,015 ^d	1,35 to 1,60	max. 0,10	-	-	-	
100CrMnSi4-4	B2	0,93 to 1,05 ^b	0,45 to 0,75	0,90 to 1,20	0,025	0,015 ^d	0,90 to 1,20	max. 0,10	-	-	-	Al: max. 0,050
100CrMnSi6-4	B3	0,93 to 1,05 ^b	0,45 to 0,75	1,00 to 1,20	0,025	0,015 ^d	1,40 to 1,65	max. 0,10	-	-	-	Ca: ^e
100CrMnSi6-6	B4	0,93 to 1,05 ^b	0,45 to 0,75	1,40 to 1,70	0,025	0,015 ^d	1,40 to 1,65	max. 0,10	-	-	-	Cr: max. 0,30
100CrMo7	B5	0,93 to 1,05 ^b	0,15 to 0,45	0,25 to 0,45	0,025	0,015 ^d	1,65 to 1,95	0,15 to 0,30	-	-	-	O: max. 0,0015 ^f
100CrMo7-3	B6	0,93 to 1,05 ^b	0,15 to 0,45	0,60 to 0,80	0,025	0,015 ^d	1,65 to 1,95	0,20 to 0,35	-	-	-	Tr: ^g
100CrMo7-4	B7	0,93 to 1,05 ^b	0,15 to 0,35	0,60 to 0,80	0,025	0,015 ^d	1,65 to 1,95	0,40 to 0,50	-	-	-	
100CrMnMoSi8-4-6	B8	0,93 to 1,05 ^b	0,40 to 0,60	0,80 to 1,10	0,025	0,015 ^d	1,80 to 2,05	0,50 to 0,60	-	-	-	

Through-hardened bearing steel properties					
Steel designation	As annealed Brinell Hardness (HR 30)	Application	Hardness when hardening in water		Hardness when hardening in oil
1.3505	<207	<30mm	66 HRC		65 HRC
1.3520	<217	>30mm	-		66 HRC
1.3536	<217	>50mm	-		65 HRC
Steel designation	Hot working °C	Soft annealing °C	Hardening temperature for quenching in water	Hardening temperature for quenching in oil	Tempering temperature °C
1.3505	850-1100	780-800	800-830	830-870	150-170
1.3520	850-1100	750-800	-	830-870	150-170
1.3536	850-1100	750-800	-	830-880	150-170

Case-hardened bearing steels

Case-hardened bearing steel designations	
ISO(683-17, 1999,2013)	W.Nr. DIN/EN (10027-2:1992)
20Cr3	1.3559
20Cr4	1.7027
20MnCr4-2	1.3515
17MnCr5	1.3521
19MnCr5	1.3523
15CrMo4	1.3566
20CrMo4	1.3567
20MnCrMo4-2	1.3570
20NiCrMo2	1.6522
20NiCrMo7	1.3576
18CrNiMo7-6	1.6587
18NiCrMo14-6	1.3533
16NiCrMo16-5	1.3532

Case-hardened bearing steel composition

Steel designation		Chemical composition ^a [% (m/m)]										
Name	No.	C	Si	Mn	P max.	S max.	Cr	Mo	Ni	V	W	Others
20Cr3	B20	0,17 to 0,23	max. 0,40	0,60 to 1,00	0,025	0,015 ^d	0,60 to 1,00	-	-	-	-	Al: max. 0,050 Ca: ^e Cu: max. 0,30 O: max. 0,0020 ^f Ti: ^g
20Cr4	B21	0,17 to 0,23	max. 0,40	0,60 to 0,90	0,025	0,015 ^d	0,90 to 1,20	-	-	-	-	
20MnCr4-2	B22	0,17 to 0,23	max. 0,40	0,65 to 1,10	0,025	0,015 ^d	0,40 to 0,75	-	-	-	-	
17MnCr5	B23	0,14 to 0,19	max. 0,40	1,00 to 1,30	0,025	0,015 ^d	0,80 to 1,10	-	-	-	-	
19MnCr5	B24	0,17 to 0,22	max. 0,40	1,10 to 1,40	0,025	0,015 ^d	1,00 to 1,30	-	-	-	-	
15CrMo4	B25	0,12 to 0,18	max. 0,40	0,60 to 0,90	0,025	0,015 ^d	0,90 to 1,20	0,15 to 0,25	-	-	-	
20CrMo4	B26	0,17 to 0,23	max. 0,40	0,60 to 0,90	0,025	0,015 ^d	0,90 to 1,20	0,15 to 0,25	-	-	-	
20MnCrMo4-2	B27	0,17 to 0,23	max. 0,40	0,65 to 1,10	0,025	0,015 ^d	0,40 to 0,75	0,10 to 0,20	-	-	-	
20MnNiCrMo3-2	B28	0,17 to 0,23	max. 0,40	0,60 to 0,95	0,025	0,015 ^d	0,35 to 0,70	0,15 to 0,25	0,40 to 0,70	-	-	
20NiCrMo7	B29	0,17 to 0,23	max. 0,40	0,40 to 0,70	0,025	0,015 ^d	0,35 to 0,65	0,20 to 0,30	1,60 to 2,00	-	-	
18CrNiMo7-6	B30	0,15 to 0,21	max. 0,40	0,50 to 0,90	0,025	0,015 ^d	1,50 to 1,80	0,25 to 0,35	1,40 to 1,70	-	-	
18NiCrMo14-6	B31	0,15 to 0,20	max. 0,40	0,40 to 0,70	0,025	0,015 ^d	1,30 to 1,60	0,15 to 0,25	3,25 to 3,75	-	-	
16NiCrMo16-5	B32	0,14 to 0,18	max. 0,40	0,25 to 0,55	0,025	0,015 ^d	1,00 to 1,40	0,20 to 0,30	3,80 to 4,3	-	-	

Case-hardened bearing steel properties							
Steel designation	Brinell Hardness HB 30	Yield Stress (MPa) 11 mm	Yield Stress (MPa) 30 mm	Tensile strength (MPa) 11mm	Tensile strength (MPa) 30mm	Impact value 11mm (J)	Impact value 30mm (J)
1.7027	149-197	-	-	-	-	-	-
1.6522	161-212	785	590	980-1270	780-1080	41	41
1.6587	179-229	835	785	1180-1420	1080-1320	41	41

Induction-hardened bearing steels

Induction-hardened bearing steel designations	
ISO(683-17, 1999,2013)	W.Nr. DIN/EN (10027-2:1992)
C56E2	1.1219
56Mn4	1.1233
70Mn4	1.1244
43CrMo4	1.3563

Induction-hardened bearing steel composition

Steel designation		Chemical composition ^{a, b} [% (m/m)]										
Name	No.	C	Si	Mn	P max.	S max.	Cr	Mo	Ni	V	W	Others
Induction-hardening bearing steels												
C56E2	B40	0,52 to 0,60	max. 0,40	0,60 to 0,90	0,025	0,015 ^d	-	-	-	-	-	Al: max. 0,050
56Mn4	B41	0,52 to 0,60	max. 0,40	0,90 to 1,20	0,025	0,015 ^d	-	-	-	-	-	Ca: ^e , Cu: max. 0,30
70Mn4	B42	0,65 to 0,75	max. 0,40	0,80 to 1,10	0,025	0,015 ^d	-	-	-	-	-	O: max. 0,0020 ^f
43CrMo4	B43	0,40 to 0,46	max. 0,40	0,60 to 0,90	0,025	0,015 ^d	0,90 to 1,20	0,15 to 0,30	-	-	-	Ti: 9

Induction-hardened bearing steel (1.3563 designation) properties					
Yield stress 17-40 mm (MPa)	Yield stress 41-100 mm (MPa)	Tensile strength 17-40 mm (MPa)	Tensile strength 41-100 mm (MPa)	Impact value 17-40 mm (J)	Impact value 41-100 mm (J)
760	640	980-1180	880-1080	35	35
Hot working °C	Soft annealing °C	Hardness Brinell HB 30 °C	Hardening Temperature for quenching in Water °C	Hardening temperature for quenching in oil °C	Temper °C
850-1050	680-720	<255	820-850	830-860	540-680

Stainless bearing steels

Stainless bearing steel designations	
ISO(683-17, 1999,2013)	W.Nr. DIN/EN (10027-2:1992)
X47Cr14	1.3541
X65Cr14	1.3542
X108CrMo17	1.3543
X89CrMoV18-1	1.3549

Stainless bearing steel composition

Steel designation		Chemical composition ^{a, b} [% (m/m)]										
Name	No.	C	Si	Mn	P max.	S max.	Cr	Mo	Ni	V	W	Others
X47Cr14	B50	0,43 to 0,50	max. 1,00	max. 1,00	0,040	0,015 ^d	12,5 to 14,5	-	-	-	-	-
X65Cr14	B51	0,60 to 0,70	max. 1,00	max. 1,00	0,040	0,015 ^d	12,5 to 14,5	max. 0,75	-	-	-	
X108CrMo17	B52	0,95 to 1,20	max. 1,00	max. 1,00	0,040	0,015 ^d	16,0 to 18,0	0,40 to 0,80	-	-	-	
X89CrMoV18-1	B53	0,85 to 0,95	max. 1,00	max. 1,00	0,040	0,015 ^d	17,0 to 19,0	0,90 to 1,30	-	0,07 to 0,12	-	

Stainless bearing steel properties					
Steel designation	As annealed Brinell Hardness (HB 30)	Hardness when hardening in water	Hardness when hardening in oil	Hardening temperature for quenching in water	Hardening temperature for quenching in oil
1.3543	<260	62 HRC	62 HRC	1030-1060	1030-1060
1.3549	<255	-	60 HRC	-	1040-1070
Steel designation	Hot working °C	Soft annealing °C	Tempering temperature °C		
1.3543	800-1100	800-850	100-200		
1.3549	800-1100	820-860	100-200		

SKF stainless steel (1.4125)

Density (Kg/dm ³)	E 20 (°C)	E100 (°C)	Mean coefficient of thermal expansion between 20°C and 100°C
7.7	215	212	10.4×10 ⁻⁶ k ⁻¹
Mean coefficient of thermal expansion between 20°C and 200°C	Thermal conductivity at 20°C (W/mK)	Specific thermal capacity at 20°C (J/Kg.K)	Electrical resistivity at 20°C (Ωmm ² /m)
10.8×10 ⁻⁶ K ⁻¹	15	430	0.8

High-temperature bearing steels

High-temperature bearing steel designations	
ISO(683-17, 1999,2013)	W.Nr. DIN/EN (10027-2:1992)
80MoCrV42-16 (M50)	1.3551
13MoCrNi42-16-14	1.3555
X82WMoCrV6-5-4	1.3553
X75WCrV18-4-1	1.3558

High-temperature bearing steel composition												
Steel designation		Chemical composition ^{a, b} [% (m/m)]										
Name	No.	C	Si	Mn	P max.	S max.	Cr	Mo	Ni	V	W	Others
80MoCrV42-16	B60	0,77 to 0,85	max. 0,40	0,15 to 0,35	0,025 ^b	0,015 ^b	3,9 to 4,3	4,0 to 4,5	-	0,90 to 1,10	max. 0,25	Cu: max. 0,30
13MoCrNi42-16-14	B61	0,10 to 0,15	0,10 to 0,25	0,15 to 0,35	0,015	0,010	3,9 to 4,3	4,0 to 4,5	3,20 to 3,60	1,00 to 1,30	max. 0,15	Cu: max. 0,10 ^f
X82WMoCrV6-5-4	B62	0,78 to 0,86	max. 0,40	max. 0,40	0,025	0,015	3,9 to 4,3	4,7 to 5,2	-	1,70 to 2,00	6,0 to 6,7	Cu: max. 0,30
X75WCrV18-4-1	B63	0,70 to 0,80	max. 0,40	max. 0,40	0,025	0,015	3,9 to 4,3	max. 0,60	-	1,00 to 1,25	17,5 to 19,0	Cu: max. 0,30

High-temperature bearing steel properties			
Steel designation	As annealed Brinell hardness (HB 30)	Hardness when hardening in oil	Hardening temperature for quenching in oil (°C)
1.3551	<248	64 HRC	1070-1120/500-600
1.3553	<300	66 HRC	1180-1230/500-560
Steel designation	Hot working (°C)	Soft annealing (°C)	Tempering temperature (°C)
1.3551	850-1050	800-820	530-550
1.3553	900-1100	780-820	540-560

Appendix 2 Cage materials

Hot-rolled low carbon sheet steel (EN 10111:1998)

Hot-rolled low carbon sheet steel composition and properties														
Designation in accordance with EN 10027-1 and IC 10	Designation in accordance with EN 10027-2	Method of deoxidation	Chemical composition (max) from ladle analysis ^b				Tensile properties ^c						Bend test radius ^d	Validity of mechanical properties
							R_{eL} N/mm ²		R_m max	Minimum elongation after fracture %				
			C	Mn	P	S	1,5 ≤ e < 2	2 ≤ e ≤ 8						
							N/mm ²	1,5 ≤ e < 2	2 ≤ e < 3	3 ≤ e ≤ 8				
DD 11	1.0332	At the discretion of the manufacturer	0,12	0,60	0,045	0,045	170 – 360	170 – 340	440	23	24	28	1e	1 month
DD 12	1.0398	Fully killed	0,10	0,45	0,035	0,035	170 – 340	170 – 320	420	25	26	30	0	6 months
DD 13	1.0335	Fully killed	0,08	0,40	0,030	0,030	170 – 330	170 – 310	400	28	29	33	0	6 months
DD 14	1.0389	Fully killed	0,08	0,35	0,025	0,025	170 – 310	170 – 290	380	31	32	36	0	6 months

^a The mechanical characteristics relate only to hot rolled non-descaled or chemically descaled and oiled products, skin-passed or not.
^b Unless otherwise agreed at the time of ordering, nitrogen-fixing elements such as titanium and boron may be added at the discretion of the manufacturer.
^c As long as the width of the product permits, the test pieces of the tensile tests shall be taken perpendicular to the direction of rolling.
^d See EURONORM 6 and EURONORM 12.

Pressed stainless steel X5CrNi18-10 (EN10088-1:1995) - Steel 1.4301

Steel 1.4301 properties			
Density (Kg/dm ³)	E at 20 ° C	E at 100°C	Mean coefficient of thermal expansion between 20°C and 100°C
7.9	200	194	16.0×10 ⁻⁶ k ⁻¹
Mean coefficient of thermal expansion between 20°C and 200°C	Thermal conductivity at 20°C (W/mK)	Specific thermal capacity at 20°C (J/Kg.K)	Electrical resistivity at 20°C (Ωmm ² /m)
16.5×10 ⁻⁶ K ⁻¹	15	500	0.73

Machined steel cages

Machined steel designations											
Designation		Method of deoxidation	Sub-group ⁴⁾	C in % max. for nominal product thickness in mm			Mn % max.	Si % max.	P % max.	S % max.	N ²⁻³⁾ % max.
According EN 10027-1 and ECISS IC 10	According EN 10027-2			≤16	>16 ≤40	>40 ⁵⁾					
S355JR	1.0045	FN	BS	0,27	0,27	0,27	1,70	0,60	0,055	0,055	0,011
S355J0 ⁸⁾	1.0553	FN	QS	0,23	0,23 ⁹⁾	0,24	1,70	0,60	0,050	0,050	0,011
S355J2G3 ⁸⁾	1.0570	FF	QS	0,23	0,23 ⁹⁾	0,24	1,70	0,60	0,045	0,045	-
S355J2G4 ⁸⁾	1.0577	FF	QS	0,23	0,23 ⁹⁾	0,24	1,70	0,60	0,045	0,045	-
S355K2G3 ⁸⁾	1.0595	FF	QS	0,23	0,23 ⁹⁾	0,24	1,70	0,60	0,045	0,045	-
S355K2G4 ⁸⁾	1.0596	FF	QS	0,23	0,23 ⁹⁾	0,24	1,70	0,60	0,045	0,045	-

Machined steel composition							
Grade	Chemical composition						
	C % max.	Si % max.	Mn % max.	P % max.	S % max.	Nb % max.	V % max.
S235	0.22	0.50	1.60	0.0050	0.050		
S275	0.25	0.50	1.60	0.0050	0.050		
S355	0.23	0.50	1.60	0.0050	0.050	0.003-0.10	0.003-0.10

SKF:S355GT (ST52)

Steel 1.0580 composition								
C %	Si %	Mn %	P %	S %	Cr %	Cu %	N,Pb %	Other
<0.22	<0.55	<1.60	<0.025	<0.025	-	-	-	AL,Nb ,Ti

Brass

Machined brass cage composition						
CuZn39Pb2	ISO number	Cu %	Al	Pb	C	Fe
	CW612N	59-60	0-0.05	1.6-2.5	-	0-0.3
	Ni	Sn	Zn	Others total	Density (g/cm ³)	
	0-0.3	0-0.3	remaining	0-0.2	8.4	